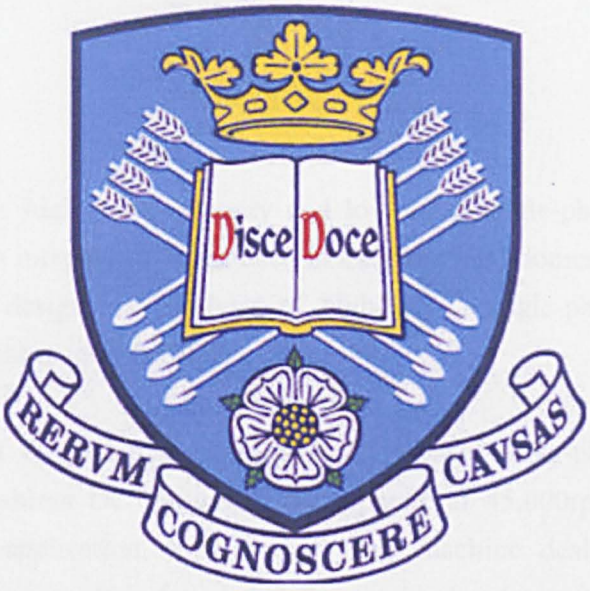

High-Speed Single-Phase Permanent Magnet Brushless DC Motor

Yu Chen

A thesis submitted for the degree of Doctor of Philosophy

Department of Electronic and Electrical Engineering

University of Sheffield

Mappin Street, Sheffield, S1 3JD

October 2009

ABSTRACT

Due to high efficiency, high power density and low cost, single-phase permanent magnet brushless DC motor has increasingly been used in industrial and domestic applications. This thesis focuses on the design and analysis of high-speed, single-phase, conventional and flux-switching permanent magnet brushless DC motors.

This thesis presents a comparative study of conventional three-phase and single-phase permanent magnet brushless DC motors, which operate at 45,000rpm with 1.1kW output power for the pump application, in terms of their machine design, drive system and electromagnetic performance. It is found that the single-phase permanent magnet brushless DC motor has a relatively lower drive system cost without significantly compromising the electromagnetic performance. Further, significant rotor eddy current loss exists in both motors. Hence, the analytical models are developed to predict the rotor eddy current loss which is resulted from the armature reaction field. By comparing with the 2D finite element method (FEM) predicted results, good agreement is obtained over the full speed range if the eddy current reaction field is taken into account. FEM is further employed to investigate open-circuit, armature and on-load rotor eddy current losses of the permanent magnet brushless DC motors. Particular emphasis is placed on the single-phase motor having an eccentric airgap with consideration for degree of airgap eccentricity, excitation current waveform, magnet segmentation, thickness and electrical conductivity of the retaining sleeve.

The single-phase flux switching permanent magnet motor, which operates at 100,000rpm with 1.2kW output power for the automotive electrical turbo-charger application, is also investigated. Its operational principle is introduced and winding topologies are investigated. In addition, the chamfered rotor pole is optimised to improve the starting capability. In order to investigate the influence of significant end leakage-flux, a 3D lumped circuit magnetic model is developed to predict the back-EMF and the inductance and validated through experiment. This model is also employed to optimise the rotor pole width for increasing the motor power density and to investigate the relationship between the magnet dimensions and the motor end effect.

Finally, the dynamic simulation models are developed to predict the dynamic electromagnetic performance and experimentally validated for a three-phase and a single-phase permanent magnet brushless DC motor, and a single-phase flux switching permanent magnet motor.

ACKNOWLEDGEMENTS

I would like to express my deepest gratitude to my supervisors Prof. Z. Q. Zhu and Prof. D. Howe for all their guidance, help and encouragement provided during my PhD study at The University of Sheffield.

I would also like to thank all the members of The Electrical Machines and Drives Group at The University of Sheffield for their invaluable support. Special thanks to Dr. Yong Pang who gave me enormous help and discussions; Dr. Yi Li who provided the drive circuit to test the prototype motors; Mr. John Wilkinson and Mr Lawrence Obodo who built up the prototype motors and test rigs.

Finally, a special thank to my parents and my wife for their continuous support and encouragement, particularly during my PhD study and research work.

TABLE OF CONTENTS

Design and Analysis of Single-Phase and Three-Phase PM Brushless DC Motors

LIST OF SYMBOLS

A	Magnetic vector potential (A/m)
$\boldsymbol{B_r}$	Magnet remanence (T)
B_r	Radial component of magnetic flux density (T)
B_α	Circumferential component of magnetic flux density (T)
B_m	Amplitude of flux density in stator iron (T)
B_g	Amplitude of flux density in airgap (T)
D_o	Stator outer diameter (m)
D_s	Stator bore diameter (m)
e_a, e_b, e_c, e_{PM}	Instantaneous phase back-EMF (V)
F	Magnetomotive force (A)
f	Frequency (Hz)
$\boldsymbol{H_c}$	Magnet coercive force (A/m)
H_r	Radial component of magnetic field (A/m)
H_α	Circumferential component of magnetic field (A/m)
I	Rated current (A)
I_{ph}	Amplitude of the sinusoidal phase current (A)
I_{rms}	Root mean square of the phase current (A)
I_u	Magnitude of u^{th} harmonic current (A)
i, i_1, i_2, i_a, i_b, i_c	Instantaneous phase current (A)
J	Rotor inertia ($Kg \cdot m^2$)
J_m	Eddy current density in permanent magnet (A/m^2)
J_{sl}	Eddy current density in sleeve (A/m^2)

J_s	The equivalent current density (A/m)
k_p	Winding packing factor
k_h	Hysteresis loss factor
k_e	Eddy current loss factor
k_{fe}	Lamination stacking factor
K_{sov}	Slot opening factor
K_{pv}	Coil-pitch factor
L	Self-inductance (H)
M	Mutual-inductance (H)
N_c	Number of turns per coil
N_{cm}	Least common multiple
N_{ph}	Number of turns of phase windings
N_s	Number of stator slots
P_c	Classical eddy current loss density (W/kG)
P_{cu}	Winding copper loss (W)
P_d	Eddy current loss density (W/kG)
P_e	Excess eddy current loss density (W/kG)
P_h	Hysteresis loss density (W/kG)
P_m	Eddy current loss in permanent magnet (W)
P_r	Rotor eddy current loss (W)
P_s	Stator iron loss (W)
P_{sl}	Eddy current loss in sleeve (W)
P_t	Stator iron loss density (W/kG)

p	Number of pole pairs
R	Phase resistance (Ω)
R_a	Radius of the middle airgap (m)
R_m	Permanent magnet outer radius (m)
R_r	Rotor outer radius (m)
R_s	Stator inner radius (m)
T	Average electromagnetic torque (Nm)
T_c	Cogging torque (Nm)
T_{em}	Electromagnetic torque (Nm)
T_f	Friction torque (Nm)
T_{load}	Load torque (Nm)
T_{iPM}	PM excitation torque (Nm)
T_r	Reluctance torque (Nm)
u	Time harmonic order
v	Space harmonic order
V	Motor volume (m^3)
v_1, v_2, v_a, v_b, v_c	Instantaneous terminal voltage (V)
v_{DC}	DC link voltage (V)
W_1, $W2$	Stored co-energy in the winding (Joules)
α	Angular position (rad)
α_h	Hysteresis loss factor
α_{cp}	Coil-pitch
α_{cu}	Temperature coefficiency of copper resistance (oC-1)
α_p	Pole-arc of per magnet segment

θ_r	Rotor position ($^{o}_{mech}$)
θ_u	Angle of u^{th} harmonic current (rad)
ρ	Mass density (kG/m^3)
ω_r	Rotation speed (rad/s)
λ	Flux linkage (Wb)
λ_{PM}	Permanent magnet flux linkage (Wb)
λ_w	Armature reaction flux linkage (Wb)
μ_0	Permeability of free space, (N·A^{-2})
μ_m	Permanent magnet relative recoil magnetic permeability
μ_{sl}	Sleeve relative recoil magnetic permeability
σ	Electrical conductivity (Ω^{-1}·m^{-1})
σ_{cu}	Copper electrical conductivity (Ω^{-1}·m^{-1})
σ_m	Permanent magnet electrical conductivity (Ω^{-1}·m^{-1})
σ_{sl}	Sleeve electrical conductivity (Ω^{-1}·m^{-1})

CHAPTER 1

Introduction

1.1 Introduction

It has become feasible to design and operate the electric motors at high-speed for a wide range of applications such as compressor, pump, vacuum cleaner and machine tools. This is due to the rapid development of the converter technology and the bearing reliability. For a given output power of an electric machine, the machine volume is inversely proportional to the machine operating speed. Hence, the main advantages of the electrical machine running in a high-speed range are either the increase of the power density or the reduction of the machine size. Further, some applications require a high-speed drive to achieve the best system efficiency. For example, traditionally a drive unit such as a gas turbine is connected to the speed-increasing gear driven by a conventional electric motor to achieve the high operating speed. However, the high-speed electric motor can directly drive the gas turbines by removing the mechanical gearbox and the coupling system. Consequently, the overall system can be more efficient and compact, and less expensive and lower maintenance [2].

There are two types of electric machines, namely, brush machines and brushless machines. In a brush machine, the brushes make mechanical contact with a set of mechanical commutators or slip rings which are affixed to the rotor and provide the connection with different armature coils at different rotor position. Due to its mature design and manufacture technology, and its simple controller, the cost of the brush machines is relatively low. However, there are a few disadvantages of mechanical commutation:

- Brushes are subjected to wear and require regular maintenance.
- Less efficiency due to the brush voltage drop and brush friction.
- Large level of electrical noise and interference due to arcing between the commutator bars and brushes.

- Limited motor operating speed due to the limitations of the mechanical commutation system.
- More acoustical noise due to brush bounce, especially at high speed.

A brushless machine, as its name suggests, is a machine without brushes, mechanical commutators or slip rings, which is replaced by an electronic controller. Therefore, compared to the brush machines, the brushless machines have a higher efficiency and reliability, reduced noise, longer lifetime (no brush erosion), elimination of ionizing sparks from the commutators, and overall reduction of electromagnetic interference. Particularly, it can run over a wider speed range by removing the mechanical limitations. Over past a few years, the cost of brushless machines has been falling over due to advances in magnet technology, improvements in motor control electronics and capital investment in the manufacture. Therefore, brushless machines have attracted more attention for high-speed applications. There are mainly three types of brushless high-speed machines on the present-day market: induction machines, reluctance machines and permanent magnet machines. They will be reviewed in the following section.

1.2 Review of high-speed machines

1.2.1 Induction machines

Induction machines are traditionally manufactured using laminations and a die-cast or soldered squirrel cage as shown in Figure 1.1. Power is supplied directly to the stator winding which induces a voltage in the rotor conductors. The torque is produced by the interaction of the rotor current with the stator flux. Induction machines are potentially the least expensive. This is due to its mature technology, manufacture line and low maintenance requirement. It also can be easily started and realize an open loop speed regulation by variable frequency inverters without a rotor position or speed sensor. Hence, it could be used for cost sensitive applications [3]. Induction machines have no permanent magnets, and therefore are suitable

for relatively harsh temperature environments [4]. However, the mechanical strength of electrical steel limits the surface speed of the laminated rotor to ~200m/s [5]. Further, the squirrel cage would probably fail to withstand the centrifugal forces and heat expansion at the high operating speed. Hence, as shown in Figure 1.2, the pure solid-rotor induction machines, with no separate rotor winding, are suitable for high-speed applications [5-7]. Inherently, solid-rotor induction machines have a high mechanical strength, high thermal durability and simple structure. However, due to absence of the well-conducting windings on the rotor, the output power and power factor are lower than squirrel-cage induction machines with a laminated rotor. Further, the rotor loss will be increased. Consequently, the rotor temperature becomes a concern and the motor efficiency will be less. So different rotor structures, such as composite solid rotor [8] and diffusion welded copper cage solid rotor [9], are employed to improve its electrical performance.

1.2.2 Reluctance machines

Reluctance machine is a single excited machine. There are no windings or permanent magnets on the rotor. The torque is produced by the tendency of its moveable part to move to a position where the inductance of the excited winding is maximized. There are a few characteristics to make the reluctance machines suitable for high-speed applications. Firstly, the rotor is free of permanent magnets and windings. Hence the rotor has a simple structure and inherently robust. It also has potential to run in very high temperature environment which is only limited by the insulation system. Secondly, the cost of reluctance machines is relatively less than permanent magnet machines, particularly at high power range. Thirdly, there is no excitation field at zero torque, thus the electromagnetic spinning loss can be eliminated. In its variants, synchronous reluctance machines and switched reluctance machines are most suitable topologies for the high-speed applications.

The stator of synchronous reluctance machines is similar to that of the induction machines as shown in Figure 1.2. Hence the use of standard components in the stator and winding

configuration means that it requires minimum re-investment in its manufacture line. There are several forms of rotor structure. The simplest one is shown in Figure 1.3 (a). Due to its simplicity of the rotor structure, it has been investigated for high-speed applications [10]. However, it suffers from low power factor, low torque capability and high volt-ampere ratings of the inverter due to its relatively small L_d / L_q ratio. Further, the salient shape leads to a significant aerodynamic loss at the high operating speed [11]. Also, if the solid rotor is used, the rotor loss will be significant at the high operating speed. In order to reduce the aerodynamic loss, the rotor can be drilled and slitted as shown in Figure 1.3 (b) and (c), which is proposed in [12]. Nevertheless the saliency ratio is still not high enough. However, the saliency ratio can be increased successfully by laminating the rotor. As shown in Figure 1.3 (d), the rotor is laminated with flux barriers punched into steel. Figure 1.3 (e) shows that the rotor is laminated in axial direction [13]. However, a laminated rotor makes it difficult to contain these laminations at the high operating speed. Hence, [14] proposed a rotor which consists of alternating layers of ferromagnetic and nonmagnetic steel as shown in Figure 1.3 (f) . It was reported in [15] that the efficiency could be 91% at a 10kW 10,000rpm operating point.

A typical switched reluctance machine is shown in Figure 1.4. It has salient poles on both the rotor and the stator. The stator consists of simple concentrated windings which can be externally wound and slipped over the salient stator poles making the stator assembly process simple and inexpensive. Since the torque is independent of the direction of the winding current, the winding current can be unidirectional which can simplify the topology of the inverter circuit. Due to these advantages, the switched reluctance machines have attracted attentions for high-speed applications. For example, in [16] it is employed for direct-drive gearless starter-generator for aircraft engines which operate at 50,000rpm with 32kW. In [17], it proposed the switched reluctance machines in the flywheel energy storage system. Although switched reluctance machines are simple, it requires a smaller airgap than induction or permanent magnet machines to achieve a good electromagnetic performance. However, due to its doubly salient structure, switched reluctance machines are inherently noisy and vibratile.

One way to reduce the acoustic noise and vibration is to increase the airgap, which will compromise the electromagnetic performance.

Due to the lack of the permanent magnets or excited windings on the rotor, the power density and power factor is generally lower than that of induction machines and permanent magnet machines. If the salient rotor is used in the reluctance machines, the aerodynamic loss will be prominent. As a consequence, the efficiency will be decreased. In addition, for acceptable performance, it may require an accurate shaft position feedback signal which could be achieved from encoder, resolver or Hall sensor or alternatively, a sophisticated sensorless control strategy.

1.2.3 Permanent magnet brushless machines

Currently, three main types of permanent magnets, viz. ferrite magnets, alnico magnets and rare earth magnets, are commercially available. Some typical properties of these different permanent magnets are listed in Table 1.1.

- Ferrite, also known as ceramic magnets, are widely available since 1950's. Beneficial characteristics of ferrite magnets include low cost, high coercive force, resistance to corrosion, and high heat tolerance. Drawbacks include their low energy product, low mechanical strength.
- Alnico magnets are made up of an alloy of aluminium (Al), nickel (Ni) and cobalt (Co) with small amounts of other elements. Alnico magnets have good temperature stability, good resistance to corrosion, high mechanical strength but low energy product, high cost and low coercive force which makes them prone to demagnetisation.
- The most common commercial available rare earth magnets are Neodymium-Iron-Boron (NdFeB) and Samarium Cobalt (SmCo). NdFeB magnets have very high-energy product, very high coercive force and moderate temperature stability, but low mechanical strength, low corrosion resistance if without properly coated or plated. SmCo magnets have high corrosion resistance, high-energy product and high temperature stability, but high cost and very low mechanical strength.

Table 1.1 Typical properties of different magnet materials.

	Ceramic 5	Cast Alnico 5	NdFeB 45M	Sm_2Co_{17}
Magnet remanence B_r (T)	0.38	1.25	1.35	1.04
Coercive force H_c (A/m)	191000	51000	970000	765000
Max Energy product (MGOe)	3.4	5.5	45	26
Temperature coefficient of B_r (%/°C)	-0.2	-0.02	-0.12	-0.035
Temperature coefficient of H_{ci} (%/°C)	0.27	0.01	-0.6	-0.2
Maximum service temperature (°C)	800	525	100	350
Density (g/cm^3)	4.9	7.3	7.4	8.3

Thanks to the recent progress of the permanent magnet material technology, high power density magnets such as neodymium-iron-boron (NdFeB) and samarium-cobalt (SmCo) can be manufactured at a reasonable cost. The permanent magnet machines (see Figure 1.5) have attracted increasing attention in a wide range of applications due to a few advantages. Firstly, due to the high energy-product permanent magnets, the high power density can be achieved. In addition, the relatively large airgap length is acceptable without significantly sacrificing the machine performance. Secondly, due to the absent of the windings on the rotor, there is no copper loss on the rotor. Further, non-overlapped windings can be employed which ease the manufacture and reduce the end winding length. In general, permanent magnet machines have a higher efficiency than induction machines and reluctance machines. Thirdly, the excitation flux is generated by the permanent magnets rather than the windings. Hence permanent magnet machines have a high power factor which can reduce the inverter volt-amperes ratings. However, if the permanent magnet machines are operated at a high speed, a number of challenges arise.

Firstly, the significant eddy current loss may be generated in the permanent magnet due to stator slot openings, time and space magnetic motive force (mmfs) harmonics. The eddy current loss can raise the temperature beyond that allowed for the permanent magnet material, which potentially leads to irreversibly partial demagnetisation of the permanent magnets. For example, NdFeB magnets may be easily demagnetise at about 120°C. Thus, the machine efficiency and power density will be reduced. In order to overcome this problem, a few

techniques have been employed.

- In [18], a super high-speed permanent magnet machine, with the ratings of 5kW at 150,000rpm, has been designed for machine tools by employing a larger airgap to reduce the flux ripple resulting from the stator slot openings and reduce the rotor eddy current loss.
- In [19-20], the author compared the performance of a slotless permanent magnet machine with that of conventional slotted permanent magnet machine with ratings of 1kW and 30,000rpm. Due to the slotless structure, the eddy current loss associated with slot openings can be eliminated. The larger effective airgap length reduces the rotor eddy current loss associated with time and space mmfs harmonics. Further, the lower flux density value leads to a lower iron loss. However, the end winding length is longer than that of slotted permanent magnet machines which yields more machine overall space and more copper loss. Also, winding manufacture becomes more complex. In [21], a slotless ring-wound permanent magnet machine with ratings of 1kW and 40,000krpm for electro-mechanical battery system has been proposed. The ring-wound stator is geometrically simple and can be easily fabricated. Compared to conventional slotted permanent magnet machine, a slotless ring-wound permanent magnet machine exhibits a higher power density and efficiency by eliminating the rotor loss and reducing the iron loss, even though the copper loss is higher due to longer end winding length. However, slotless structure has a relatively large effective airgap length which affects the machine power density.
- In order to compensate the lower open-circuit field due to the large airgap length or the slotless structure, the Halbach magnets array is an alternative topology. It can deliver a relatively strong open-circuit field. Due to its self-shielding magnetisation, rotor back-iron is not necessarily required which can reduce the rotor inertia resulting in a fast response. Further, the iron loss and idling loss are low, which make it suitable for high-speed applications such as the motor/generator in flywheel energy storage system [21-23].
- Circumferential or axial segment permanent magnet is another way to reduce the eddy current loss [24-27]. However, it may increase the construction complexity of the rotor

and the difficulty of assembly process, leading to a high manufacture cost.

- Compared to sintered magnets, bonded magnets have a higher electrical resistivity. Hence, it is a good candidate for reducing the eddy current loss in the permanent magnets [4]. In addition, bonded magnets are easily fabricated and can achieve precise dimensions without post-process which can reduce the cost. However, bonded magnets exhibits a low remanence which results in a low power density.
- Compared to NdFeB, SmCo has a higher maximum operation temperature. Hence, SmCo is generally chosen in high temperature environment, such as combined heat and power system [28], motor/generator for electrical vehicles [29]. The drawback of SmCo is that the cost is higher than NdFeB.

The second challenge is that the permanent magnet has a low bursting stress of around 80MPa [30]. It may break apart due to high centrifugal force when the machine is operated at a high speed. For the mechanical perspective, special attention needs to be paid to protect the permanent magnets. Generally, there are two different rotor constructions, that is, surface mounted magnets and interior magnets. They need different design procedures to make sure the permanent magnets can survive at the high-speed operation. For surface mounted permanent magnet machines, generally it is contained within a non-magnetic sleeve which could be made by stainless steel, carbon or glass fibre, aluminium or titanium. Consequently, the effective airgap length will be longer, thus reducing the machine power density. For interior permanent magnet machine, the magnets are buried within the rotor iron, the rotor iron itself fixes the magnets without requiring the sleeve, thus reducing the airgap length. However, the rotor structure has to be designed carefully in terms of the mechanical strength [31]. Hence, the rotor structure becomes complicated. By comparing these two configurations with the permanent magnet machines operating at 40kW and 40,000rpm, [32] shows that surface mounted magnets contained by a carbon fibre are the better choice. Considering complicated structure of interior magnets configuration, surface mounted magnets configuration is a common choice for high-speed application.

1.2.4 Alternative permanent magnet machines

For conventional permanent magnet machines, as the magnets are located in the rotor, it needs special consideration to prevent it from breaking apart due to significant centrifugal force associated with the high-speed operation. In addition, heat on the rotor is difficult to be dissipated, consequently the magnets suffers from the possibility of irreversible demagnetisation under high temperature. Hence, alternative permanent magnet machines having the permanent magnets in the stator rather than the rotor become attractive for high-speed applications. The structure of this type of permanent magnet machines is identical to that of the switched reluctance machines except the permanent magnets are inserted in the stator core. Similar to switched reluctance machines, the benefits are simplicity, mechanical integrity and robustness of the rotor. In addition, they have high power density just like conventional permanent magnet machines. Meanwhile, since the permanent magnets are located in the stator, there is no mechanical limit on the permanent magnets which is always a risk for conventional permanent magnet machines running at high speed. Further, since the stator can be easily cooled by natural or forced cooling, the risk of permanent magnets' irreversible demagnetization is reduced. For this reason, it is well suited to high-speed applications. Generally, this type of permanent magnet machines can be categorized into three different types, namely, doubly salient permanent magnets machines (DSPM), flux reversal permanent magnet machines (FRPM) and flux switching permanent magnet machines (FSPM). As shown in Figure 1.6, Figure 1.7 and Figure 1.8, these three machines have doubly salient stator and rotor structure, and permanent magnets and concentrated armature windings are located in the stator. The differences lie in the location of the permanent magnets in the stator.

In DSPM, the permanent magnets are buried in the stator back iron and concentrated windings are wound on each stator tooth. By neglecting the fringing flux, a uni-polar linear variation of open-circuit flux-linkage is generated with the rotor position, which leads to a trapezoidal back-EMF waveform. In [33], it reported that DSPM machines can deliver about 2.5 times the torque and power as that of the induction machine housed in the same frame size. Due to the

existence of permanent magnets, the reluctance path for the armature reaction flux is very high and thus the phase inductance is small, which makes it suitable for high-speed operation.

In FRPM machines, multipole permanent magnets of alternate polarity are place on each stator salient pole face embraced by concentrated windings. The permanent magnet flux linking the concentrated windings reverses polarity as the rotor rotates. Thus, an ideal bipolar triangular open-circuit flux-linkage leads to a trapezoidal generated waveform. Naturally FRPM has a low phase inductance (similar to DSPM machines). However, there is a notable flux fringing (leakage) which deteriorates the machine performance in terms of power density [34]. In [35], as shown in Figure 1.7 (c), a concave-type stator pole and a rotor with a flux barrier are used to reduce the flux leakage.

In FSPM machine, the permanent magnets are located between the stator teeth and the concentrated windings are wound around the two adjacent stator teeth and a piece of permanent magnet, as shown in Figure 1.8. FSPM machine has a sinusoidal bipolar flux-linkage waveform leading to a sinusoidal back-EMF waveform. Further, compared to DSPM and FRPM machines, FSPM machines use more permanent magnet material and utilise flux focusing to achieve a large airgap flux density. Hence, among these three types of doubly salient permanent machines, FSPM machines can deliver a highest power density with considerable cost penalty and reduced winding slot area [36-37]. In addition, the armature flux path is parallel with magnet flux path, thus FSPM machines can cope with relatively high demagnetisation current. Similar to DSPM machines, FSPM machines suffer from significant external flux leakage and end flux leakage which compromises the machine power density. In Chapter 5.5, a 3D lumped circuit model will be developed to explain its end effect in details. However, it still can have a slightly higher torque capability than interior permanent magnet machines [38]. Due to its complicated stator topology, the process cost in the production line will be relatively high.

Since above three types of permanent magnet machines are relatively new machine topologies, publications to date are generally focused on their theoretical characteristics at early machine

design stage as 'proof-of-concept' machines. High-speed applications are not covered extensively in the literatures. In [39], a single-phase FRPM machine with the ratings of 2kW, 40,000rpm has been proposed for high-speed vacuum cleaners. However, the machine performance is not presented in detail. As new machine topologies, more work needs to be done to investigate their feasibility for high-speed applications, as will be carried out in this thesis.

1.2.5 Summary of high-speed machines

A few electric machine topologies are suited to the high-speed applications. It is hard to identify which one is the best solution. It is heavily dependant on the application fields, and the designer's skill and bias as well as a thorough understanding of the system attributes. Table 1.2 summaries their advantages and disadvantages. Generally speaking, induction machines are suitable for cost sensitive application fields. Reluctance machines are suitable in the harsh environment and permanent magnet machines have the best electrical performance. Table 1.3 lists some high-speed electric machines that were selected form the results of a literature search on IEEE/IEE Electronic Library and sources from Internet. It hints that the induction machines are more likely used in moderate and large power range applications, and the permanent magnet machines are more employed in small and moderate power range applications. Table 1.3 also indicates that reluctance machines are less popular than induction machines and permanent magnet machines. Due to its prominent electromagnetic performance, this thesis will focus on the high-speed permanent magnet machines.

Table 1.2 Advantages and disadvantages of high-speed machines.

	Advantages	Disadvantages-
Induction machine	• Low cost • Open loop speed regulation without position sensor • Low windage loss • Low maintenance	• Copper loss on rotor • Laminated rotor is vulnerable to mechanical vibration • Solid rotor generates significant loss • Less efficiency than PM machines • Lower power factor than PM machines
Synchronous reluctance machine	• Simple and robust rotor • Low idle speed loss • High temperature capability • Low acoustic noise and vibration	• Low efficiency • Low power factor • High windage loss • Low power density • Less tolerant of big airgap length • Position sensor require
Switched reluctance machine	• Simple and robust rotor • Low idle speed loss • High temperature capability • Highly fault tolerant	• Acoustic noise and vibration • Low efficiency • Low power factor • High windage loss • Low power density • Less tolerant of big airgap length • Position sensor required
PM machine	• High efficiency • High power density • High power factor • Low windage loss • Quite operation	• Low rotor mechanical integrity • Low temperature capability • Needs sleeve to protect surface mounted magnets • Position sensor required
DSPM/FRPM/ FSPM	• High efficiency • High power density • High power factor • Simple and robust rotor	• Significant flux leakage • High windage loss • Complicated stator structure • Immature technology • Position sensor required

Table 1.3 Some high-speed electric machine selected from literature.

Power [kW]	Speed [rpm]	Machine type	Reference
21	47,000	Induction machine, laminated rotor	[3], centrifugal compressor
45	93,000	Induction machine	[4], turbo-charger
200	12,000	Induction machine, caged solid rotor	[7], prototype
5,220	5500	Induction machine, caged solid rotor	[40], gas compressor
6,000	10,000	Induction machine, laminated rotor	[41], gas compressor
6,300	8,600	Induction machine, solid rotor	[9], turbo compressor
10,000	12,000	Induction machine, caged solid rotor	[42], gas compressor
0.372	48,000	Synchronous reluctance machine	[10], prototype
20	20,000	Synchronous reluctance machine, solid rotor	[12, 43], prototype
60	48,000	Synchronous reluctance machine	[14], flywheel energy storage system
1.6	88,000	Switched reluctance machine	[44], hand dryer
32	26,000	Switched reluctance machine	[16], electric starter-generator
0.01	150,000	Permanent magnet machines, SmCo	[45], motorised handpiece
0.2	104,000	Permanent magnet machines	[46], vacuum cleaner
0.5	150,000	Permanent magnet machines, SmCo	[47], turbo-charger
0.7	100,000	Permanent magnet machines	[30], prototype
1	12,000	Permanent magnet machines, interior magnets	[48], prototype
1	40,000	Permanent magnet	[19], hand tool

		machines, slotless, sintered NdFeB	
1	40,000	Permanent magnet machines, slotless, Halbach array magnets	[22], flywheel for electro-mechanical battery
1.2	120,000	Permanent magnet machines	[49], prototype
2	40,000	FRPM, single-phase	[39], vacuum cleaner
2 to 5	100,000 to 140,000	Permanent magnet machines, 4-pole	[29], turbo-charger
5	150,000	Permanent magnet machines, large airgap	[18], machine tool
5	240,000	Permanent magnet machines, inconel sleeve	[50], centrifugal compressor
11	50,000	Permanent magnet machines, interior Halbach magnets	[51], machine tool
14	12,000	Permanent magnet machines	[52], air compressor
21	47,000	Permanent magnet machines, bonded NdFeB	[4], centrifugal compressor
131	70,000	Permanent magnet machines	[53], micro-turbine

1.3 Single-phase permanent magnet machines

Compared to polyphase permanent magnet machines, single-phase permanent magnet machines have a simpler construction and control circuit, and are, therefore, less expensive. For this reason, single-phase permanent magnet machines have been widely used in low-power household applications where the cost is one of most important aspects. For example, line-start single-phase permanent magnet machines can be used instead of the conventional induction machines for applications in pumps, air conditioners and fans [54-55]. As shown in Figure 1.9, the stator is the standard conventional induction motor's stator which is well suited for mass production. The rotor consists of an electrically conducting squirrel cage and pairs of permanent magnets. Due to the usage of permanent magnets, its efficiency, power factor and power density are higher than conventional induction machines. Further,

without requiring the inverter and position signal, this machine can start and operate in steady-state as a conventional synchronous machine, where the rotor speed is mainly voltage-source frequency dependant. Hence, the cost is very low. However, it is not suitable for high-speed applications due to complex rotor structure and inherent limited speed.

Another well developed single-phase permanent magnet machine is shown in Figure 1.10 and Figure 1.11, where the structure can be either with cylindrical rotor and U-shape stator, or cylindrical rotor and cylindrical stator. U-shape is easily manufactured, and thus low cost. However, it has higher stator flux leakage than cylindrical shape stator, which reduces its performance [56]. Compared to polyphase permanent magnet machines, the primary advantage is reduced inverter components and position sensors. Thus, they are superior to polyphase machines in applications where cost is of greater importance than performance such as vacuum cleaner, pumps, CD-ROM DVD and HDD drives [57-59].

A single-phase flux reversal permanent magnet motor, Figure 1.12, has been reported in [39] for high-speed vacuum cleaner application. Also, a single-phase flux switching permanent magnet motor, Figure 1.13, is presented in [60]. Both of them are well suited to high-speed applications as discussed in the previous section.

As single-phase permanent magnet machines have null-points in their torque waveforms, it may fail to start. A few technologies have been employed to overcome this problem. An additional magnet may be used to force the rotor to park at the position where starting torque can be achieved, albeit with increased cost [61]. A notch on the stator can also be employed to assist the start [62-63]. Four different types of asymmetric airgap, namely, tapered airgap, stepped airgap, asymmetric airgap and slotted teeth are compared in [64], and it was found that the tapered airgap is the most appropriate since it results in a smoother resultant torque waveform. Tappered airgap has been widely adopted to introduce the starting torque [39, 61, 64-66]. Hall sensor is usually adopted to provide the appropriate signals to the drive switches for delivering required torque. A sensorless approach is also presented in [66-67] which has a relatively complicated circuit logic and layout.

Overall, from the cost point of view, single-phase permanent magnet machines are very attractive. However, unlike three-phase permanent magnet machines, very few single-phase permanent magnet machines have been well developed and analyzed for high-speed applications.

1.4 Rotor eddy current loss of permanent magnet machines

1.4.1 Review of rotor eddy current loss calculation

In the low and moderate speed three-phase permanent magnet brushless machines, the eddy current loss in the rotor is usually neglected [68], since the rotor rotates in synchronism with the fundamental stator mmf. However, because of relatively simpler manufacture, less copper loss and potential higher efficiency, as a result of relatively shorter end winding. The concentrated and non-overlapping windings are widely employed in the new machine topologies [27, 69-70], which introduces additional space harmonics of the stator mmfs which rotate at different speeds from that of the rotor. Thus, the eddy current induced in the rotor results in a significant eddy current loss. Further, three-phase permanent magnet brushless DC machines are supplied by an alternating pulse of rectangular current of 120° electrical and with a 120° electrical shift between the three phases of the stator. Therefore, compared to brushless AC machines, brushless DC machines may have a relatively greater eddy current and associated ohmic loss, due to significant time harmonics in the winding current waveforms, with a fixed six-step commutation mode (that is by 60° electrical) [71-75]. PWM current control strategy may introduce high frequency current ripple which may cause an additional eddy current loss [76]. Therefore, the overall rotor eddy current loss associated to the space and time harmonics of the stator mmfs, which is designated as armature rotor eddy current loss, may be significant.

In addition to the space harmonics of the winding distribution and the time harmonics of the

winding current, the stator slot opening is another potential cause for the eddy current loss [77-80]. Due to the stator slot opening, there exists the airgap permeance harmonics which can cause a variation of the magnet working point when the magnet is passing under the stator slot openings. Hence the eddy current and associated ohmic loss, which is designated as open-circuit rotor eddy current loss, can be induced. However, because of the relatively small stator slot openings, the open-circuit rotor eddy current loss is generally considered to be negligible.

Unlike the rotating field of the stator mmfs in the three-phase permanent magnet brushless machines, the single-phase permanent magnet brushless machines inherently have a pulsating stator mmf. Fundamental and higher order time harmonics of the winding current results in a pulsating instantaneous airgap field distribution, which can be resolved into forward and backward components. Both forward and backward rotating harmonic mmfs, which do not rotate in synchronism with the rotor, may induce a significant armature rotor eddy current loss.

Further, in contrast to the symmetric airgap in the three-phase permanent magnet brushless machines, an eccentric airgap is usually employed to improve the starting capability and facilitate the unidirectional rotation in the single-phase permanent magnet brushless machines [64, 81-83]. This eccentric airgap will introduce more airgap permeance harmonics which result in a considerable open-circuit rotor eddy current loss.

The rotor eddy current loss may be aggravated further when the motor operates at high speed or has a high pole number. It not only reduces the overall machine efficiency, but also may cause a significant heating of the permanent magnets, due to the relatively poor heat dissipation from the rotor, and even worse if the sleeve is fitted to protect the permanent magnet against the centrifugal force [75, 78] and [20, 84-87]. It may irreversibly demagnetise the partial permanent magnet, particularly for sintered NdFeB magnets, which have relatively high temperature coefficients of remanence and coercivity and a moderately high electrical conductivity. As a result, the overall machine performance is significantly reduced.

It is essential, therefore, to predict the rotor eddy current loss as accurately as possible at the motor design stage.

1.4.2 Analytical model

The rotor eddy current loss can be predicted by either time-stepped finite element method (FEM) or analytical models. Compared to FEM, analytical models can give a deeper insight into the way of the eddy current loss facilitates optimisation of the motor design with less calculation time at motor design stage, provided it is applicable and of acceptable accuracy.

In [77], an analytical model formulated in Cartesian coordinates is presented to determine the harmonic content in the flux pattern of permanent magnet synchronous machines due to the slotting of the stator and the corresponding eddy current loss in the magnets and retaining sleeve. However, it is only valid for the diametrically magnetised magnets. In [80], an analytical model based on a 2D polar coordinate is developed for calculating the open-circuit rotor eddy current loss of the machines having diametrically magnetized magnets. However, both analytical models ignore the eddy current reaction and are inappropriate for the single-phase machines which have asymmetric airgap.

In terms of different motor topologies and operating conditions, corresponding analytical models have been developed to determine the armature rotor eddy current loss. The armature rotor eddy current loss, in the conducting retained sleeve, may be considered. If the ratio of the rotor diameter to the pole pitch is relatively high, the rectilinear coordinate is appropriate [77, 88]. Otherwise, a polar coordinate system [27, 69, 72, 76, 80] is a better option to account for curvature, particularly 2-pole motors, which are often preferred for high-speed applications. If the skin depth associated with induced field harmonics is relatively greater than the pole arc and the radial thickness of the permanent magnets, the induced eddy current loss can be assumed to be resistive limited and the influence of the eddy current reaction field

can be neglected [27, 69]. Otherwise, the effect of the eddy current reaction field should be considered [72-73, 75-77].

Up to date, existing papers have been mainly restricted to three-phase/multi-phase PM brushless machines. However, the rotor eddy current loss in the single-phase permanent magnet brushless machines, which cannot be neglected due to an eccentric airgap and pulsating stator mmf, has not been reported in literature. Hence, in this thesis, analytical models developed for calculating the armature rotor eddy current loss of the three-phase permanent magnet motors are extended to the single-phase permanent magnet brushless machines.

1.4.3 Finite element model

Due to an eccentric airgap, it is relatively difficult for analytical model to account for the open-circuit rotor eddy current loss in the single-phase permanent magnet brushless machines. Therefore, FEM is used to calculate the open-circuit rotor eddy current loss, even though FEM is time-consuming and may not provide as much insight as an analytical solution.

Though a few publications have addressed how to predict the rotor eddy current loss with FEM or analytical models, relatively little work has been presented on on-load rotor eddy current loss which denotes the total harmonic loss occurring under the load condition due to the stator slot openings, the eccentric airgap and the stator mmf, particularly in the single-phase permanent magnet machines. Particularly for PM machines where the fundamental airgap flux density is strongly affected by the load condition, superposition does not apply, which means the open-circuit rotor eddy current loss and the armature rotor eddy current loss cannot be simply added to give the on-load rotor eddy current loss. Therefore, compared to analytical model, FEM is advantageous to directly calculate the on-load rotor eddy current loss.

Further, FEM is able to analyse the influence of axial and circumferential segment of the permanent magnet on the rotor eddy current loss. Meanwhile the effect of the eddy current redistribution can be taken into account with high level of accuracy.

Basically, in FEM the study domain is represented by multiple, linked, simplified representations of discrete regions, i.e. finite elements. For electromagnetic devices, such as electrical machines, which are governed by electromagnetic fields, nonlinear partial differential equations can be derived from the Maxwell's equation. In conjunction with applicable physical model, nonlinear partial differential equations are applied to each element, and a set of simultaneous system equations is constructed. The equations can be solved to obtain the magnetic potentials and subsequently the field strength and flux density etc. While being an approximate method, the accuracy of the FEM can be improved by refining the mesh in the model using more elements and nodes.

In general, there are three phases in the procedure of the FEM analysis:

(1) Pre-processing – define the finite element model and environmental factor to be applied to it.

- Constructing the geometry of an object: For example, commercial FE package FLUX2D, which will be used to analysis the rotor eddy current loss in Chapter, has access to parameters which can help in both the construction of the geometry and in modifying the geometry. Firstly, the points are defined. Secondly, the lines are constructed by the previously defined points. The last step is to define the surface regions which can be constructed from one or several closed surfaces limited by the lines.
- Discretizing the field regions, such as stator iron, winding, airgap, sleeve, magnet, rotor iron and shaft for the PM BLDC motor, by creating the mesh which is required by the FEM to subdivide the study domain into elements. The user of FLUX2D can use the automatic mesh generator to generate triangular mesh by using the subdivisions on those lines having been used for the geometry definition. In general, the airgap and tooth tips should have a relative smaller mesh size to achieve the

accurate results. For the high-speed applications of the PM BLDC motors, the influence of the skin effect on the rotor eddy current loss can not be neglected. Therefore, the regions for the sleeve and the magnet have fine mesh elements.

- Defining the physical properties: to define the material properties such as nonlinear B/H characteristics of the steel, relative permeability and remanent flux density of the permanent magnet, electrical conductivity of the permanent magnet and sleeve, to assign materials and sources to different regions.
- Selecting the modules of application: In this thesis, magnetostatics and transient magnetics modules of the FLUX2D are used to analyze the motor performance. Magnetostatics module gives a fast computation, however, the skin effect cannot be taken into account and the eddy current loss cannot be obtained directly. The rotor position needs to be defined before starting the computation. In contrast, transient magnetics module can give the eddy current loss straightforward with consideration of the skin effect, but need relatively longer computation time. The motor speed and rotation step also needs to be defined before solving the model.

(2) Analysis solver – solve the discretized partial equations under specified boundary conditions.

(3) Post-processing – process, plot, analyze and export the results of a problem. In terms of the electromagnetic problem such as PM BLDC motors, FLUX2D can generate the flux density, flux linkage, back-EMF, inductance, torque, iron loss and eddy current loss and so on, which are dependent on the settings in the pre-processing.

1.5 Scope of research and contributions of the thesis

In this chapter, different machine topologies for high-speed applications and the associated rotor eddy current loss in permanent magnet machines have been reviewed. Conventional high-speed permanent magnet machines suffer from the rotor eddy current loss and the risk of

irreversible partial demagnetisation of permanent magnets. Therefore, accurate prediction of the rotor eddy current loss is essential at the machine design stage. Further, new topology of high-speed permanent magnet machines such as flux switching permanent magnet mahcines, is a potential solution. The outline of this thesis is described below:

Chapter 2: Three-phase and single-phase permanent magnet machines having the same power ratings are comparatively studied. Two three-phase permanent magnet machines, namely, **Design A** and **Designed B**, are analysed at the design stage, and Design A is prototyped for further analysis. Four single-phase permanent machines, namely **Design C**, **Designed D, Design E and Design F**, having different stator airgap and slot openings, are analysed at the design stage, and **Design E** is prototyped. The comparison of simulated and tested phase current is presented.

Chapter 3: Firstly, the static and improved analytical models for three-phase permanent magnet brushless machines are developed to predict the armature rotor eddy current loss in both the permanent magnet and the conducting retained sleeve (if fitted). Secondly, the above static and improved analytical models are extended to predict the armature rotor eddy current loss of the single-phase PM brushless machines which have a symmetric airgap. Thirdly, with aid of FEM to derive the boundary conditions, modified static and improved analytical models are developed to predict the armature rotor eddy current loss of the single-phase permanent magnet brushless machines having an eccentric airgap.

Chapter 4: FEM is used to predict the open-circuit, armature and on-load rotor eddy current loss of the single-phase and three-phase permanent magnet machines. Further, the influences of the current waveform and the level of airgap asymmetry, the thickness and electrical conductivity of the retaining sleeve (if employed), and the magnet segmentation on the rotor eddy current loss of the single-phase permanent magnet machines are investigated by FEM.

Chapter 5: The operation principle of the single-phase FSPM motor is introduced. Three different winding topologies, full-pitched, short-pitched and toroidal, are investigated. The

starting issue is addressed and the starting capability is improved by optimizing the chamfered rotor pole. A 3D LPMC model is developed to analyse the end effect, to optimise the rotor pole width to increase the motor torque/power density. Further, it is employed to investigate the effect of the magnet dimensions and motor axial length on the end-effect. Finally, a simulation model is developed to investigate the motor dynamic performance.

Chapter 6: General conclusions of the research and suggestions for future work.

The major contributions of the thesis include:

1. Development of analytical models to predict the rotor eddy current loss in three-phase and single-phase permanent magnet brushless DC motors with/without accounting for the eddy current reaction field.
2. Investigation of open-circuit, armature and on-load rotor eddy current losses in the permanent magnet brushless DC motors by the finite element method, with particular emphasis on the single-phase motor having an eccentric airgap with consideration for degree of airgap eccentricity, excitation current waveform, magnet segmentation, thickness and electrical conductivity of the retaining sleeve.
3. Development of 100,000rpm, 1.2kW, single-phase flux switching permanent magnet motor with an optimised chamfered rotor pole to improve the starting capability for the automotive electrical turbo-charger application.
4. Development of a 3D lumped circuit magnetic model of single-phase flux switching permanent magnet motor, with due account for significant end leakage flux, to predict the back-EMF and the inductance, to optimise the rotor pole width for increasing the motor power density, and to investigate the relationship between the magnet dimensions and the motor end effect.

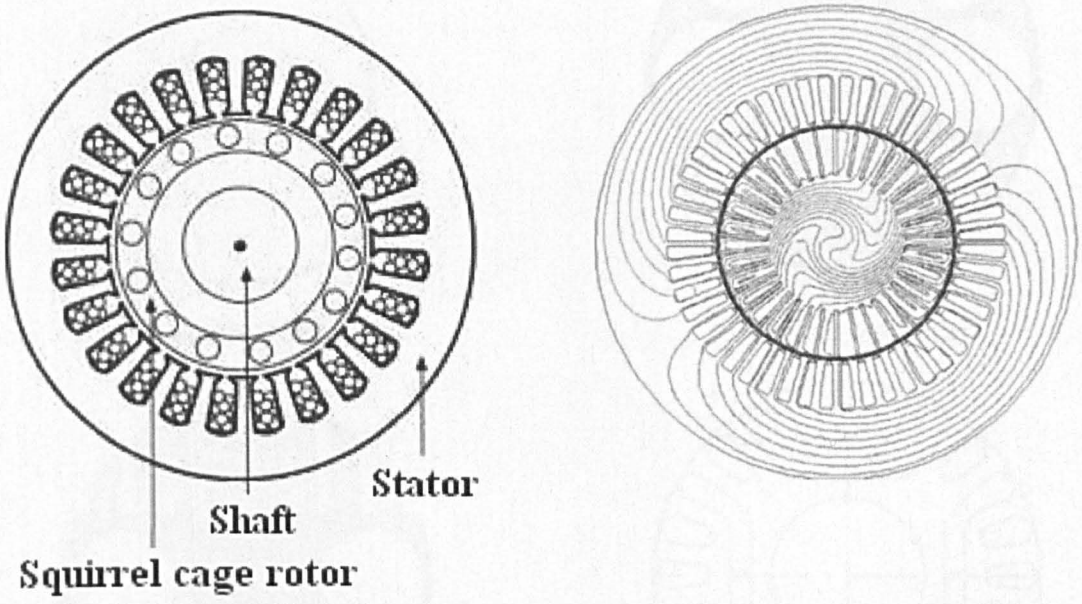

(a) Squirrel cage rotor (b) Slitted solid rotor

Figure 1.1 Induction machine topology with squirrel cage rotor

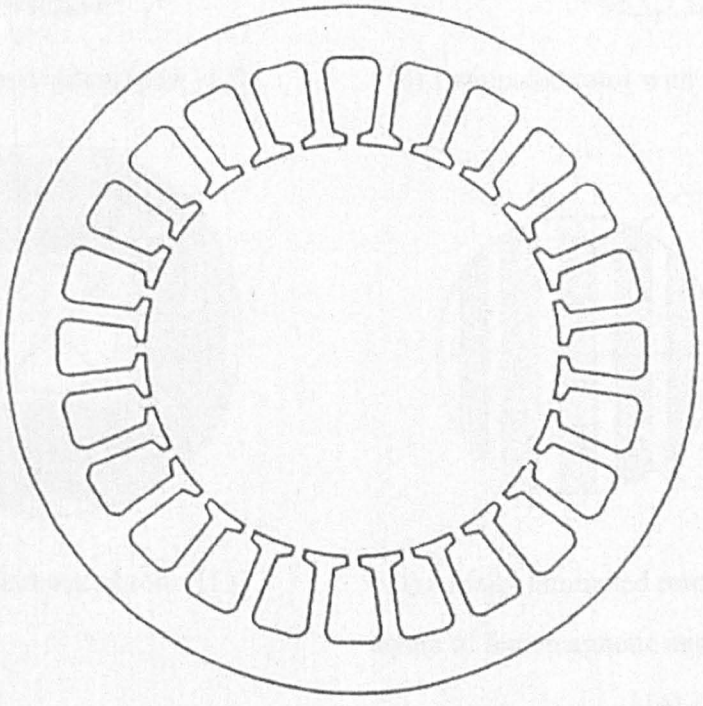

Figure 1.2 Synchronous reluctance machine stator topology.

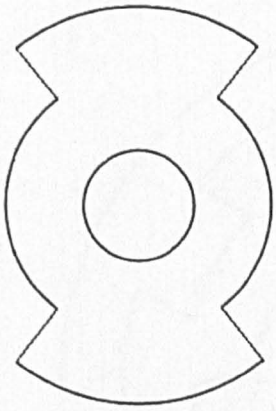

(a) Classical salient rotor

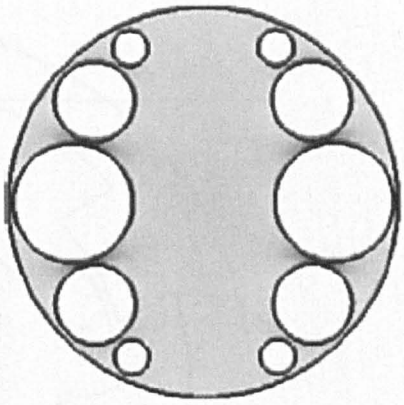

(b) Drilled rotor [12]

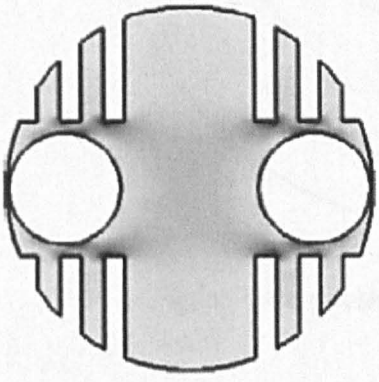

(c) Drilled and slitted rotor [12]

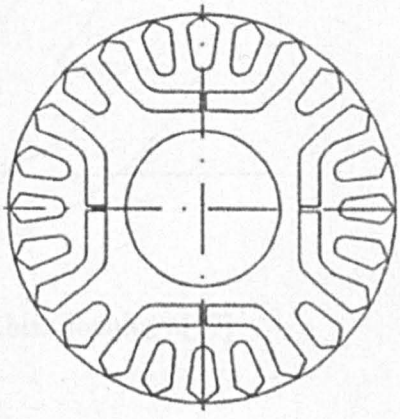

(d) Laminated rotor with flux barriers [14]

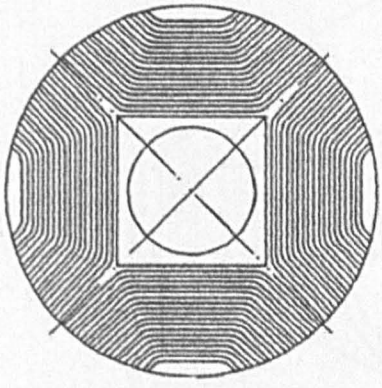

(e) Axially laminated rotor [13]

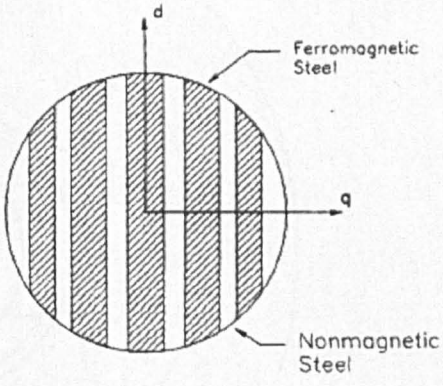

(f) Axially laminated rotor with alternating layers of ferromagnetic and nonmagnetic steel [14]

Figure 1.3 Synchronous reluctance machine rotor topologies.

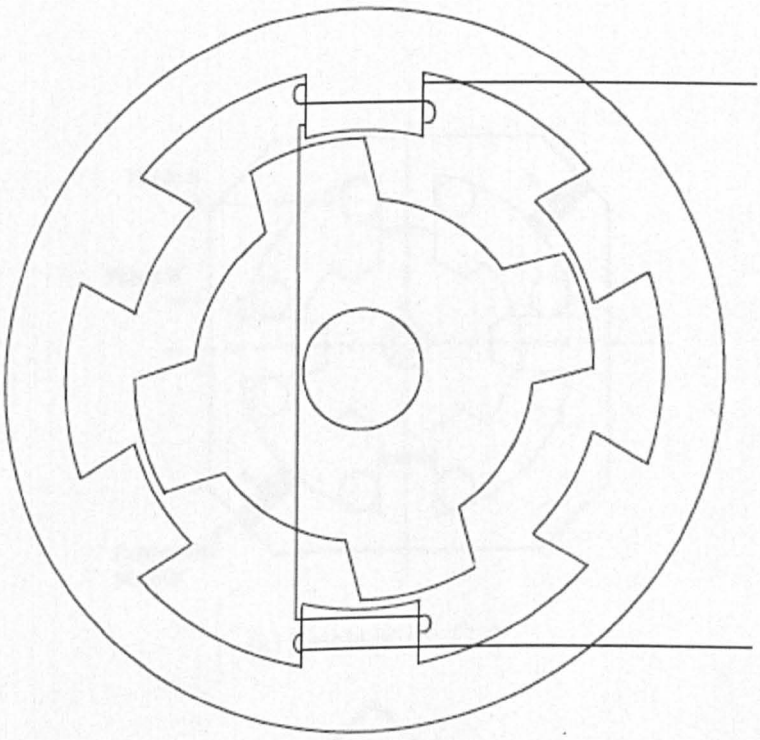

Figure 1.4 Switched reluctance machine topology.[17]

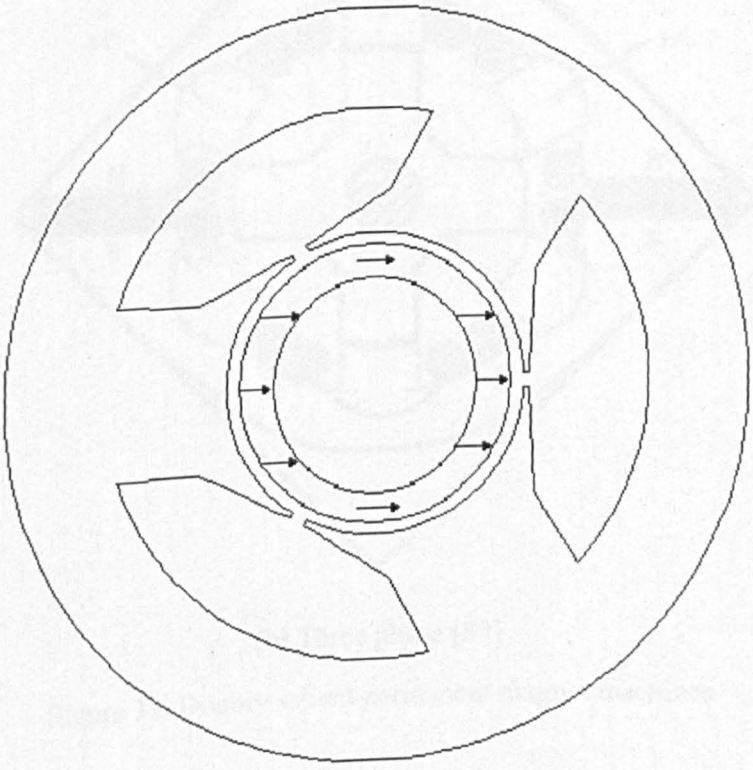

Figure 1.5 Conventional permanent magnet machines

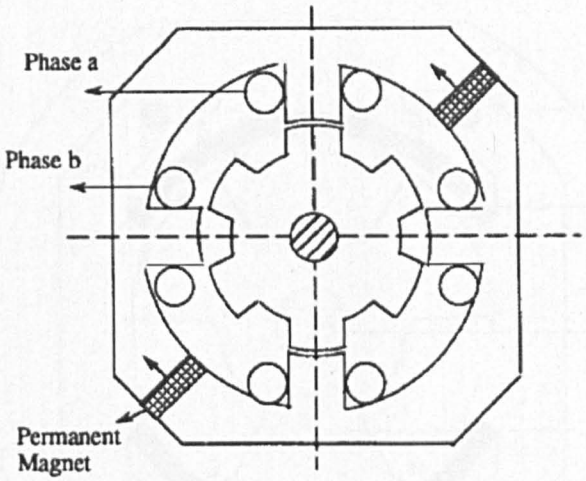

(a) Single phase [33]

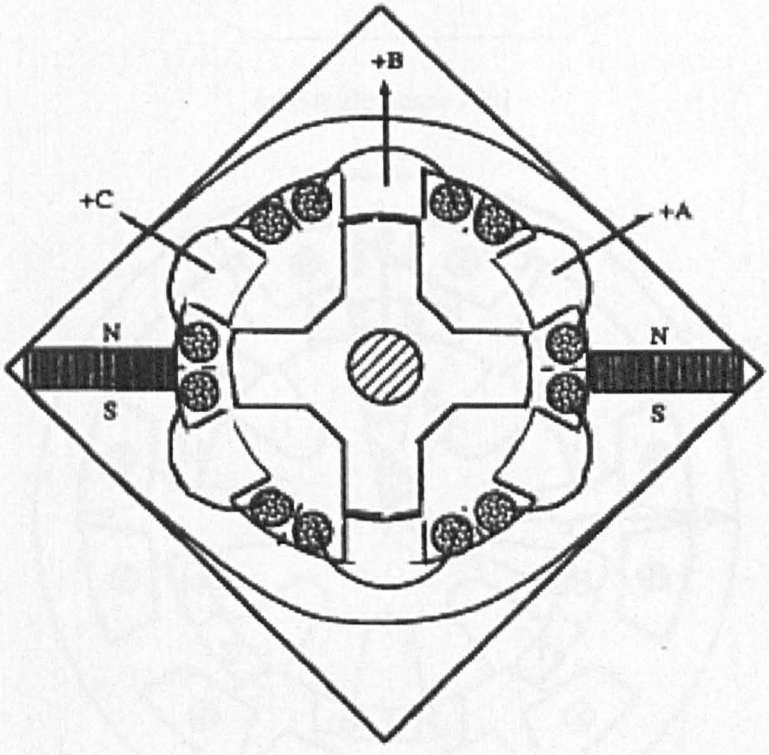

(b) Three phase [89]

Figure 1.6 Doubly salient permanent magnet machines

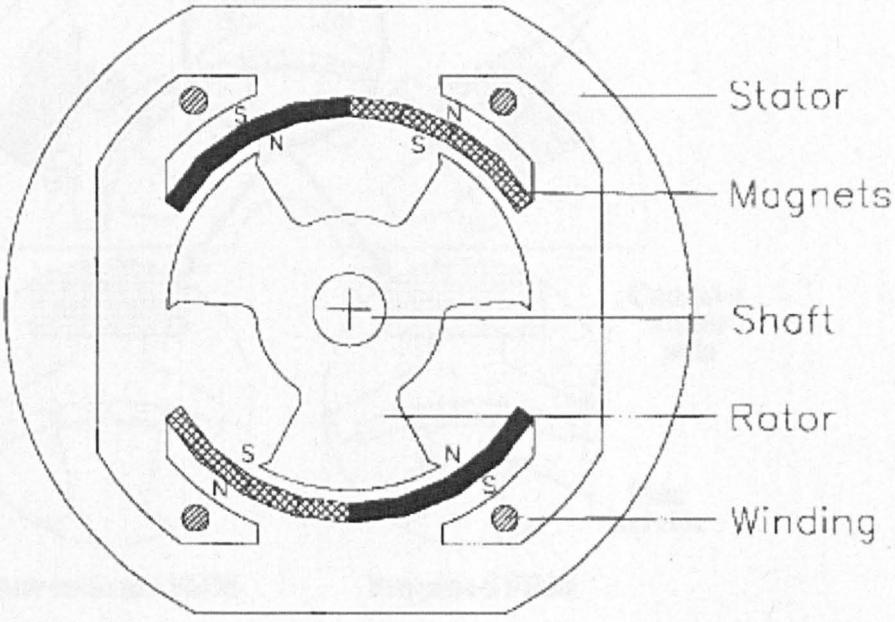

(a) Single phase [90]

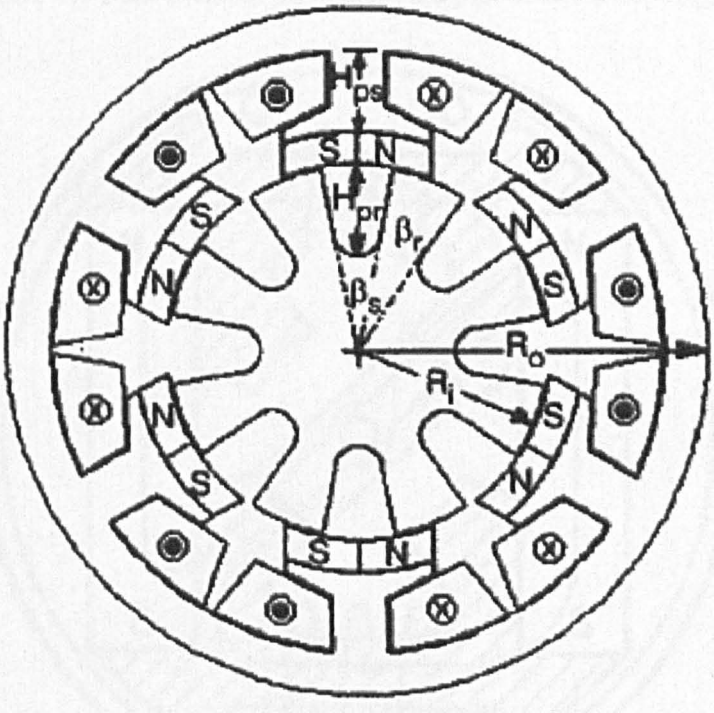

(b) Three phase [91]

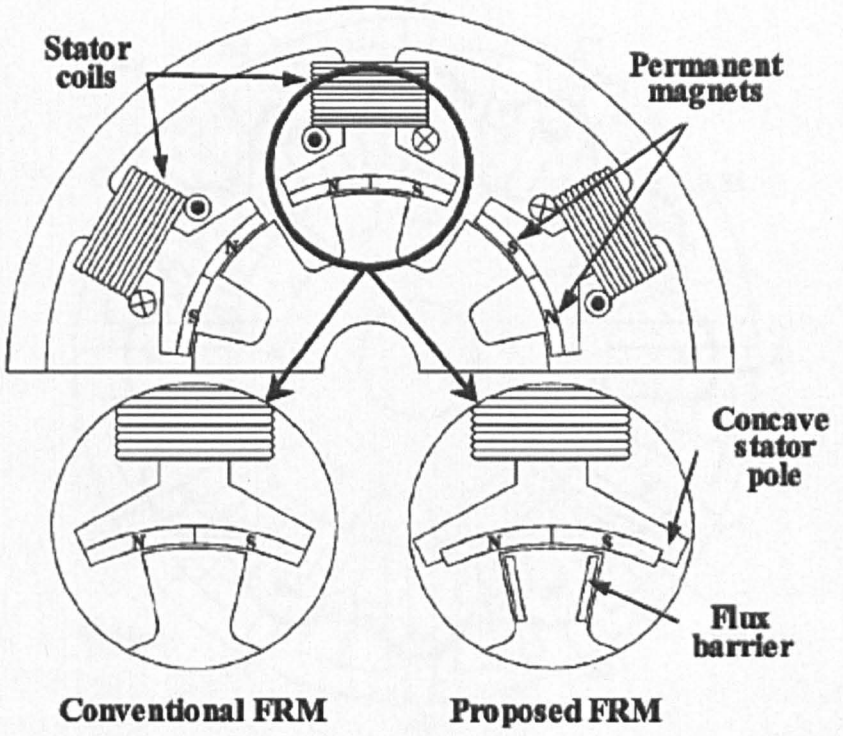

(c) Three phase with concave stator pole and flux barrier [35]

Figure 1.7 Flux reversal permanent magnet machine topologies

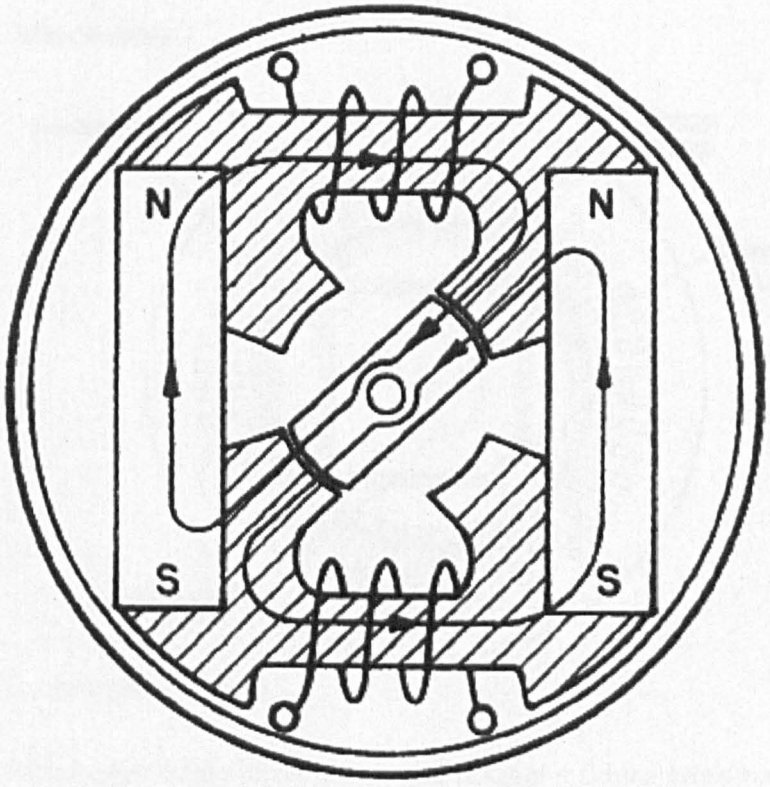

(a) Single phase [92]

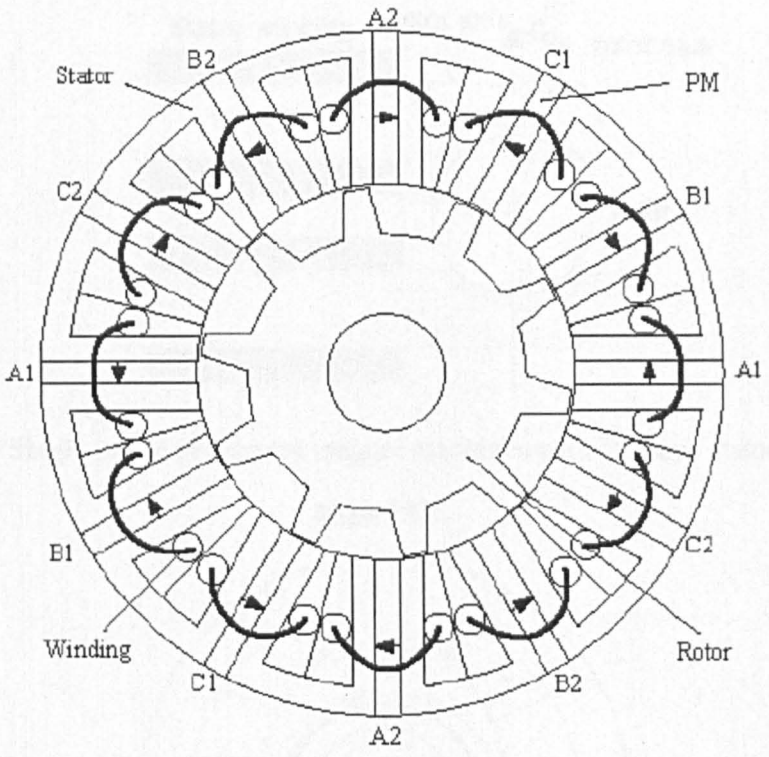

(b) Three phase [36]

Figure 1.8 Flux switching permanent magnet machine topologies

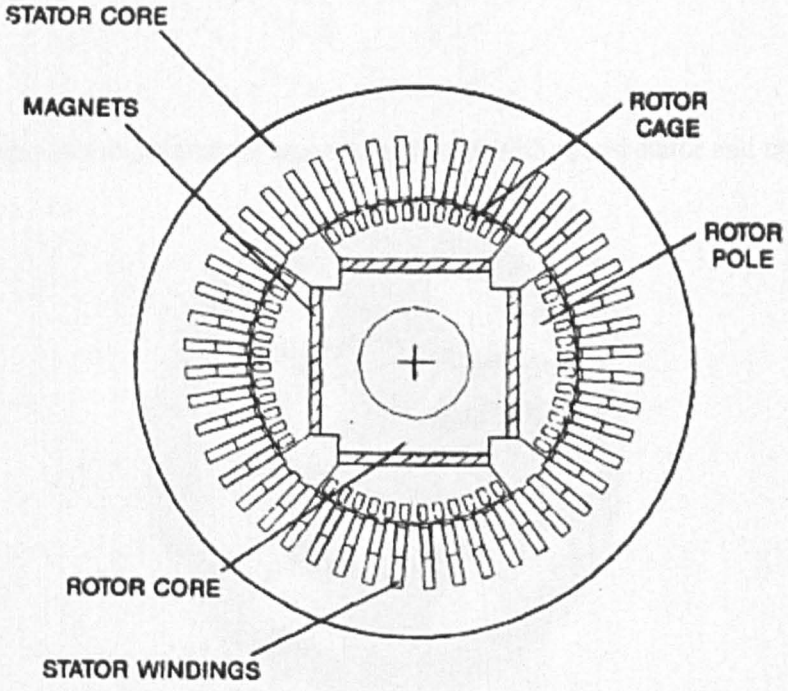

Figure 1.9 Line-start single-phase permanent magnet machine cross-section [54].

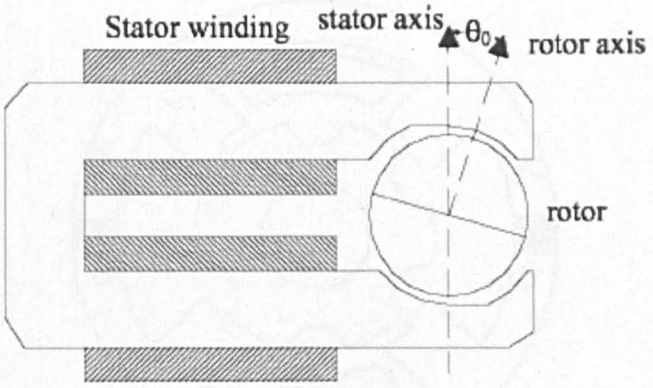

Figure 1.10 Single-phase permanent magnet machines with U-shape stator and taped arigap[93].

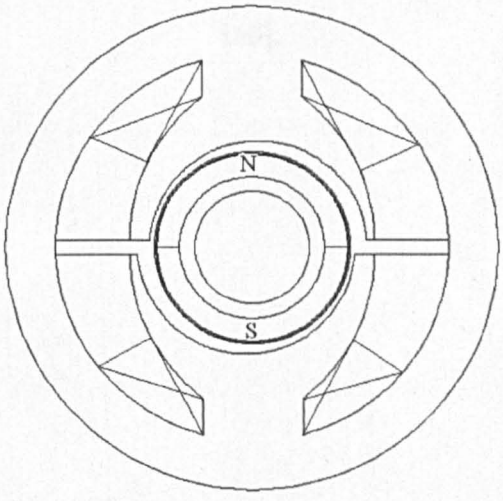

Figure 1.11 Single-phase permanent magnet machines with round stator and tapered airgap.

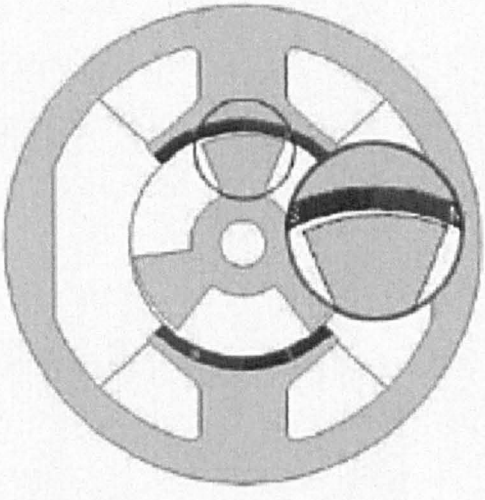

Figure 1.12 Single-phase flux reversal permanent magnet machines with tapered airgap [39].

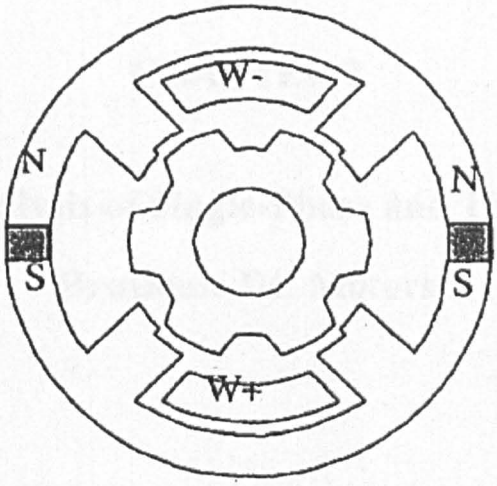

Figure 1.13 Single-phase flux switching permanent magnet machines with stepped airgap [60].

CHAPTER 2

Design and Analysis of Single-Phase and Three-Phase PM Brushless DC Motors

2.1 Introduction

As reviewed in Chapter 1, PM brushless motors have been widely used for the high-speed applications due to their high efficiency, high power density, small size and reliability. The most commonly used PM brushless motors are three-phase motors, which generally represents the best trade-off of the motor iron and copper utilization with the cost of the inverter. Alternatively, single-phase PM brushless motors can offer a relatively low cost, which is always desirable in cost sensitive domestic appliance applications.

In this chapter, a three-phase and a single-phase high-speed PM brushless DC motors, designed for use of the pump application, are analysed. Both motors are designed to operate at speed of 45,000rpm with 1,100W output power. The additional specifications required by the customer are given in Table 2.1.

The three-phase PM brushless DC motor is designed by the CAD package, ERINI, which was developed within the Electrical Machines and Drives Group at the University of Sheffield. The dynamic simulation model is developed to predict its electromagnetic performances. The three-phase motor is driven by a six-pulse full-bridge inverter, with the aid of FEM predicted inductance, back-EMF and cogging torque. Then, the simulated phase current waveform is fed back to FEM to analyse the stator iron loss and the rotor eddy current loss. Finally, the prototype of the three-phase motor is built and tested.

Table 2.1 Specifications of high-speed PM brushless motors.

Output power (W)	1,100
Speed (rpm)	45,000
Rotor outer diameter (mm)	~25
Three-phase stator outer diameter (mm)	70
Single-phase stator outer diameter (mm)	64.5
Stator axial length (mm)	30 ± 10
Power source	230V AC, 50Hz
Rotor containment	Stainless steel sleeve of 0.6mm

An equivalent single-phase PM brushless motor is designed as well. For sake of simplicity, the rotor outer diameter is kept the same as that of three-phase motor. Since the stator outer diameter is specified by the customer, the axial length is adjusted to achieve the required power. In addition, a simplified analytical model is developed to examine the optimal ratio of stator bore to stator outer diameter for the maximum electromagnetic torque at a given copper loss. Dynamic simulation models are developed for the single-phase motors which are driven by either full-bridge inverter or half-bridge inverter employing the bifilar windings, respectively. The simulated phase current waveform is fed back to FEM to analyse the stator iron loss and rotor eddy current loss. Again, the prototype of the single-phase motor is built and tested.

2.2 Rotor design

As high-energy magnets lead to a high power density and low rotor diameter, which is beneficial to reduce the centrifugal force on the magnet and the sleeve thickness, it is desirable to choose the rare earth magnets. Further, because of harsh working environment, SmCo magnets are selected rather than NdFeB, due to its high corrosion resistance and high temperature stability.

The PM motors designed in this Chapter have the magnets on the rotor. The magnets can be either mounted on the surface of the rotor or buried into the rotor. As discussed in Chapter

1.2.3, the surface mounted magnets are commonly used due to its simple rotor structure, easy assembly process and high mechanical integrity if the sleeve is fitted. Hence, the surface mounted magnets are employed to design the high-speed three-phase and single-phase PM motors. Since SmCo magnets have a relatively low mechanical strength, the non-magnetic containment sleeve is necessarily required for the safety of the magnets under the high-speed operation. Considering its low cost, moderate electrical conductivity, strong mechanical strength and good thermal conductivity, the non-magnetic stainless steel is selected for the rotor sleeve.

As the speed increases, the switching frequency of the inverter devices and the variation of the flux in the stator iron and rotor magnet will increase. Consequently, the inverter switching loss, the iron loss and the rotor eddy current loss increase significantly and dominantly affect the motor efficiency. Hence, 2-ploe rotors are preferred for high-speed applications to increase the motor efficiency and will be adopted for the motors designed in this chapter.

The magnets can be magnetized in the parallel direction, the radial direction or the Hallbach array. Parallel magnetisation and Hallbach array can deliver a sinusoidal airgap flux density distribution, while radial magnetisation has a trapezoidal airgap flux density distribution. Since trapezoidal field distribution contains significant high-order field harmonics which will induce more stator iron loss than sinusoidal field distribution. It is also found that trapezoidal field distribution has more torque ripple and on-load rotor eddy current loss than sinusoidal field distribution in the single-phase PM brushless motor, as will be discussed in Chapter 4.7. Further, parallel magnetisation is relatively easier to be processed than radial magnetisation, while a 2-pole diametrically magnetised magnet (parallel magnetisation) is a special case of Hallbach array. Hence, a 2-pole SmCo with the parallel magnetisation is mounted on the surface of the rotor and retained by a non-magnetic stainless steel sleeve to form a rotor as shown in Figure 2.1.

2.3 Three-phase PM motor design

2.3.1 CAD design

Compared to the overlapping distributed windings, the non-overlapping concentrated windings have a simple construction and compact end windings which lead to be cost effective and low copper loss. Further, the axial length of the rotor is reduced. Consequently, the critical speed and stiffness can be increased [1], as they are very important aspects for high-speed motor. Hence, 3-slot stator carrying non-overlapping concentrated windings is selected to be the three-phase stator. The stator core is structured by 0.35mm silicon-iron (Si-Fe) lamination steel, Transil300_16T. The properties of the motor material are summarised in Table 2.2.

Table 2.2 Properties of motor materials

Permanent magnet	Material	Sm_2Co_{17} S3/225
	Magnetisation	Parallel
	Residual induction B_r @20°C (T)	1.04
	Magnetic recoil permeability	1.1
	Temperature coefficient of B_r (%/°C)	-0.035
	Electrical conductivity ($10^{-6}\ \Omega \cdot cm$)	1.43×10^6
Stator and rotor lamination	Material	Transil300_16T
	Lamination thickness	0.35 mm
	Hysteresis loss factor k_h	1.55e-02
	Hysteresis loss factor α_h	2.45
	Eddy current loss factor k_e	1.0e-04
	Electrical conductivity ($\Omega^{-1} \cdot m^{-1}$)	1.33×10^6
Sleeve	Material	Stainless steel
	Electrical conductivity ($\Omega^{-1} \cdot m^{-1}$)	1.39×10^6

The three-phase PM motor was designed by the CAD motor design package ERINI developed within the Electrical Machines and Drives Group at the University of Sheffield. Output torque, speed and dimension constrains were given to ERINI as the input parameters. This software rapidly generated a range of different feasible motor dimensions, which met the requirements.

With the aid of its post-process toolbox, by examining the more detailed motor properties, such as efficiency, peak flux density, and magnet size and so on, the suitable designs could be chosen for further investigation. Initially two motors, **Design A** and **Design B**, as shown in Figure 2.2, are selected for further investigations. Finally **Design A** is prototyped as shown in Figure 2.3. Their leading dimensions and performance are given in Table 2.3.

Table 2.3 Leading dimensions and performance of three-phase PM motors

	Design A	**Design B**
Performance		
DC link voltage (V)	290	290
Rated speed (rpm)	45,000	45,000
Input power (W)	1,310	1,310
Output power (W)	1,120	1,100
Copper loss (W)	14.87	30.06
Iron loss (W)	27.55	17.66
Friction Loss (W)	150	150
Drive ohmic loss (W)	9.98	12.34
Efficiency	84.7%	84.0%
Stator dimensions		
Outer diameter (mm)	70.0	70.0
Inner diameter (mm)	28.0	28.0
Back-iron thickness (mm)	9.4	7.2
Lamination axial length (mm)	32.0	15.1
End winding length (mm)	11.5	14.95
Motor axial length (mm)	55.0	45.0
Motor volume[1] (mm^3)	2.12×10^5	1.73×10^5
Tooth width (mm)	16.3	12.2
Tip edge thickness (mm)	0.4	0.4
Slot opening (mm)	1.5	1.5
Wedge angle (deg.)	151.6	144.8
Rotor dimensions		
Magnet outer diameter (mm)	25.0	25.0
Magnet inner diameter (mm)	19.0	19.0
Rotor axial length (mm)	34.3	18.1
Effective airgap length (mm)	1.5	1.5
Sleeve thickness (mm)	0.6	0.6

Pole-arc/pole-pitch ratio	1.00	1.00
Winding details		
Connection	Star	Star
Number of phase	3	3
Coil per phase	1	1
Turns per coil	61	103
Wire diameter (mm)	1.01	0.96
Packing factor	0.4	0.4
Phase resistance (mΩ)	243.2	378.17
Phase self-inductance[2] (mH)	1.144	1.684
End winding inductance (mH)	0.048	0.179
Phase mutual-inductance (mH)	-0.471	-0.645

[1] Motor volume includes the end winding space.

[2] Phase self-inductance includes the end winding inductance.

It can be seen that both **Design A** and **Design B** can meet the specifications with similar efficiency. However, it is difficult to identify which one is the better solution by only examining the CAD generated results. Further, only open-circuit iron loss can be predicted by the CAD package, which will compromise its accuracy, particularly considering the significant on-load iron loss and rotor eddy current loss for the high-speed motors. Hence, it is desirable to predict these losses accurately. In order to obtain the on-load loss, the dynamic model is developed to simulate the dynamic phase current. Then the simulated phase current is fed into finite element model (FEM). By rotating the rotor over a complete electrical cycle, the rotor eddy current loss can be obtained from FEM directly. Further, the radial and circumferential components of flux density in each element of the mesh model can be synthesized as a function of rotor position. The total iron loss can be calculated as the sum of the loss components associated with the radial and tangential flux density waveforms in each element. Its flowchart is illustrated in Figure 2.4.

2.3.2 FEM validation

Compared to CAD package, FEM can give relatively more accurate results. The reason is that

the local saturation and slot openings can be properly modelled in FEM. In addition, FEM is capable of predicting the on-load stator iron loss and rotor eddy current loss. Therefore, **Design A** and **Design B** are modelled in FEM, using the commercial FE package, i.e. *MEGA*, for further investigation.

2.3.2.1 Back-EMF

2D FEM predicted open-circuit flux distributions are shown in Figure 2.5 and corresponding airgap flux density distributions are shown in Figure 2.6. Due to the diametrically magnetised permanent magnet, the sinusoidal open-circuit airgap flux density is achieved. Hence, the back-EMF waveform is essentially sinusoidal, as shown in Figure 2.7. According to Figure 2.7(a), 2D FEM predicted and measured back-EMFs of **Design A** are in a good agreement.

2.3.2.2 Cogging torque

Cogging torque results from the interaction of the rotor permanent magnets with the stator teeth, and may cause the undesirable torque and speed ripple and induce vibrations and resonances. Hence, cogging torque needs to be examined at the motor design stage. The 2D FEM predicted cogging torque waveforms are shown in Figure 2.8, it can be seen that:

- The periodicity of the cogging torque waveform is determined by the least common multiple, N_{cm}, between the number of slots, N_s, and the number of poles, $2p$, i.e. $360^\circ / N_{cm}$ [94]. For this 3-slot/2-pole three-phase motor, N_{cm} is 6 and the periodicity is 60°.
- Compared to the rated load, i.e. 0.233Nm, the cogging torque of the three-phase motor is very small. Hence, it will be neglected in the dynamic simulation model as described later.

2.3.2.3 Inductances

The winding inductances play an important role in the dynamic performance of high-speed brushless motor [1]. As the speed increases, the inductive reactance of the windings results in a bigger time constant, and consequently it is relatively difficult for the winding current to reach its rated value within the phase-conductive interval. Further, it can cause a significant phase delay in the phase current waveform with respect to the induced back-EMF waveform. Hence, the negative torque is generated which results in a reduction of the overall torque capability and maximum operating speed.

Since the rotor is non-salient, the winding inductances do not vary with the rotor position. To calculate the self- and mutual-inductances in the FEM, the permanent magnet material was set to be fully demagnetised. By exciting only one phase with the rated current I, the self-inductance L can be calculated from:

$$L = \frac{2W_1}{I^2} \quad \text{(H)} \tag{2-1}$$

where W_1 -- Energy stored in the winding which can be obtained from the FEM; Joules

Then two phases are excited with the rated current. The total energy $W2$ stored in the windings can be obtained form the FEM. The mutual-inductance M can be calculated from:

$$M = \frac{W_2 - 2W_1}{I^2} \quad \text{(H)} \tag{2-2}$$

FEM and CAD calculated winding inductances are compared in Table 2.4. Since the end winding was not taken into account in FEM, CAD predicted self-inductance with due account for the end winding is slightly bigger than the FEM predicted value.

Table 2.4 Comparison of FEM and CAD predicted winding inductance.

	Design A			Design B		
	FEM	CAD		FEM	CAD	
		With end winding	Without end winding		With end winding	Without end winding
Self-inductance (mH)	1.101	1.144	1.096	1.557	1.684	1.505
Mutual-inductance (mH)	-0.49	-0.471		-0.696	-0.645	

2.3.2.4 Loss analysis

As is well known, for a given PM brushless motor and its cooling system, there is a thermal limit relating to the winding insulation class and the withstanding capability of the magnet demagnetisation which are influenced by the stator loss and rotor loss, respectively. In addition, less loss is always desired to improve the system efficiency. Hence, at the motor design stage, each loss component needs to be investigated such as winding copper loss, stator iron loss and rotor eddy current loss.

A. Copper loss

The total winding copper loss can be calculated by:

$$P_{cu} = 3I_{rms}{}^2 R \quad \text{(W)} \tag{2-3}$$

where I_{rms} -- Root mean square of the phase current; A

R -- Phase resistance at the operating temperature $T_{\theta_{cu}}$ (°C), and can be given by:

$$R = R_0[1 + (T_{\theta_{cu}} - T_0)\alpha_{cu}] \quad (\Omega) \tag{2-4}$$

where, R_0 -- Phase resistance at the reference temperature T_0 (°C); Ω

α_{cu} -- Copper temperature coefficiency; $^{\circ}C^{-1}$

According to Table 2.3, **Design A** has a less copper loss due to its relatively smaller winding resistance.

B. Stator iron loss

As the speed increases, the stator iron loss increases dramatically. Hence, it is important to predict the stator iron at the design stage for high-speed motors. Under the alternating flux conditions, the total stator iron loss density P_t can be separated into a hysteresis component P_h and an eddy current component P_d [1]:

$$P_t = P_h + P_d \qquad \text{(W/kG)} \tag{2-5}$$

The hysteresis component is attributed to the net energy loss associated with sudden irreversible changes within the domain structure as the magnetization is increased or decreased. Under the alternating flux condition and no minor hysteresis loops, the hysterisis loss density can be expressed as [1]:

$$P_h = k_h f B_m^{\alpha_h} \qquad \text{(W/kG)} \tag{2-6}$$

where f -- Frequency of flux density; Hz

B_m -- Peak flux density; Hz

k_h -- Experimentally determined hysterisis loss constant, as given in Table 2.2.

α_h -- Experimentally determined hysterisis loss constant, as given in Table 2.2.

The eddy current loss is the Joule loss caused by the eddy currents which are induced by the time-varying field. The eddy current loss density can be decomposed into classical eddy current loss P_c and excess eddy current loss P_e as expressed by [1]:

$$P_c = \frac{\sigma d^2}{12\rho T}\int_T \left(\frac{dB}{dt}\right)^2 dt \qquad \text{(W/kG)} \tag{2-7}$$

$$P_e = \frac{k_e}{T}\int_T \left|\frac{dB}{dt}\right|^{1.5} dt \quad \text{(W/kG)} \tag{2-8}$$

where, σ -- Electrical conductivity of lamination; $\Omega^{-1}\cdot m^{-1}$

d -- Lamination thickness; m

ρ -- Mass density of lamination; kG/m^3

k_e -- Eddy current loss constant, which is again determined experimentally and given in Table 2.2.

A self-written post-processing programme in MATLAB environment is used to obtain the variation of the radial and circumferential components of the flux density from the FEM as the rotor is incrementally rotated through a complete electrical cycle, on an element-by-element basis. The iron loss density of each element can be calculated as the sum of the loss density associated with the radial and circumferential flux density waveforms. The total stator iron loss can be computed as the sum of the loss dissipated in each element:

$$P_s = l_a \frac{\rho}{k_{fe}} \sum_{n=1}^{N_e} \left[(P_h + P_c + P_e)A_n\right] \quad \text{(W)} \tag{2-9}$$

where l_a -- Stator lamination axial length; m

k_{fe} -- Stacking factor.

A_n -- Area of the n^{th} finite element; m^2

N_e -- Total number of stator lamination mesh elements.

The phase current waveform, as shown in Figure 2.9(a), required for the calculation of the stator iron loss under load condition is determined from a dynamic simulation model which will be described later. The local flux density waveforms against the rotor rotation position in each element are synthesized and shown in Figure 2.10 and Figure 2.11 for elements in the middle of stator back-iron and tooth body of **Design A** under open-circuit and load condition, respectively. It shows that under both open-circuit and load condition, the flux at back-iron is an alternating type, while the flux through out the teeth is a rotating type in a high-speed

brushless motor in which the stator flux density is usually designed to be lower than that in a conventional motor in order to reduce the stator iron loss and hence the ratio of tooth width to tooth height is relatively small. It also clearly shows that on open-circuit the flux density waveforms are essentially sinusoidal, but on load they are significantly distorted. The stator iron losses of **Design A** and **Design B** are compared in Table 2.5. It could be noted that **Design A** has slightly more stator iron loss than **Design B**.

The finite element technique is also employed to analysis the stator iron loss of **Design A** under different operating conditions:

(a) Sinusoidal current BLAC operation at rated load;

(b) 120° conduction BLDC operation without PWM voltage control at rated load;

(c) 120° conduction BLDC operation with PWM voltage control at rated load;

(d) 120° conduction BLDC operation with PWM current control at rated load.

The corresponding phase current waveforms at 45krpm, deduced from dynamic simulation, are shown in Figure 2.9. It should be noted that the current waveform in Figure 2.9(b) was obtained by controlling the dc-link voltage, i.e. by employing a dc chopper to achieve the required rotational speed, while the current waveform shown in Figure 2.9(c) was obtained with the rated dc-link voltage and a PWM voltage controller (14kHz, duty cycle=84%). The equivalent current waveform which would result from a PWM current controller has been simplified as a 120° rectangular current waveform, as shown in Figure 2.9(d), in which high-order PWM harmonics are neglected. The fundamental component of the various current waveforms is similar to that shown in Figure 2.9(a), which corresponds to BLAC operation. Table 2.6 compares the stator iron loss of Design A with alternative current waveforms. It will be seen that when operated in sinusoidal current BLAC mode the stator iron loss at rated load increases only slightly, compared with that on no-load. However, when operated in BLDC mode the iron loss increases significantly both with and without PWM voltage control, PWM current control resulting in the highest iron loss.

Table 2.5 Comparison of stator iron loss (W) of **Design A** and **Design B** at 45,000rpm under open-circuit and load conditions.

	Design A		**Design B**	
	Open-circuit	**On load**	**Open circuit**	**On load**
Hysteresis loss	5.47	7.11	3.72	7.2
Classical eddy current loss	11.33	17.59	7.8	16.87
Excess eddy current loss	10.48	14.22	6.14	10.89
Total stator iron loss	**27.27**	**38.92**	**17.67**	**34.98**

Table 2.6 Comparison of stator iron loss (W) of **Design A** under different operating conditions.

	BLAC	**BLDC**		
		No PWM	**PWM voltage control**	**PWM current control**
Hysteresis loss	5.77	7.06	7.11	7.72
Classical eddy current loss	12.56	17.28	17.59	30.00
Excess eddy current loss	11.24	14.11	14.22	19.15
Total stator iron loss	**29.57**	**38.46**	**38.92**	**56.87**

C. Rotor eddy current loss

The pulsations of the flux density in the rotor induce the eddy current loss in the solid cylindrical PM and retaining sleeve (if fitted and electrically conductive). As the speed increases, this undesirable rotor eddy current loss increases significantly. Since the heat on the rotor is difficult to be dissipated, the consequent temperature rise can deteriorate the PM performance and cause the irreversible demagnetisation. Hence, it is necessary to predict the rotor eddy current loss at the motor design stage.

The rotor eddy current loss can be predicted by either time-stepped finite element method or

analytical model. The analytical model will be described in Chapter 3.

In *MEGA*, the PM and the retaining sleeve are modelled as a ring shape with the electrical conductivity as given in Table 2.2. A time step of 6°_{mech} has been used for dynamic rotor movement, which is equivalent to a time step of 2.2222e-5 second at 45krpm. The FEM predicted rotor eddy current losses of **Design A** and **Design B** are compared in Table 2.7. It can be seen that the rotor loss is due to high order flux harmonics, which are primarily due to the stator slotting on open-circuit, whereas on load they are produced by both stator slotting and time and spatial mmf harmonics that are not in synchronism with the rotor rotation. For both **Design A** and **Design B** motors, the rotor loss is dominantly produced by mmf harmonics, while those due to stator slotting are negligible due to relatively small slot opening. Hence, rotor loss on open-circuit is much smaller than those on load, being almost negligible. However, it becomes very significant at rated load due to spatial and time mmf harmonics. Further, **Design B** has a much bigger load eddy current loss than **Design A**. It indicates that **Design A** has better performances such as higher efficiency and lower rotor temperature resulting in a higher withstanding capability of the magnet demagnetisation. Further, according to Table 2.3, **Design A** has less copper loss. Hence. **Design A** is selected as the final design for three-phase PM brushless DC motor, even though it has slightly higher stator iron loss.

The rotor eddy current loss of **Design A** under different operating conditions with the simulated phase currents, as shown in Figure 2.9, are investigated by FEM and compared in Table 2.8. It can be seen that even under BLAC operation mode, there is a significant rotor eddy current loss which is dominantly due to the spatial mmf harmonics due to the concentrated and non-overlapping windings. BLDC operation results in a significantly higher rotor eddy current loss as a result of additional time mmf harmonics. PWM current controlled BLDC operation results in higher rotor loss than PWM voltage controlled BLDC operation because of more time mmf harmonics. The rotor loss is essentially the same both with and without PWM voltage control.

Table 2.7 Comparison of rotor eddy current losses of **Design A** and **Design B** at 45,000rpm under open-circuit and load conditions.

	Design A		**Design B**	
	Open-circuit	**On load**	**Open circuit**	**On load**
Magnet	0.41	47.57	0.44	77.35
Sleeve	0.36	18.39	0.27	28.30
Total rotor eddy current loss	0.77	65.96	0.7	105.65

Table 2.8 Comparison of rotor eddy current loss of **Design A** under different operating conditions.

	BLAC	**BLDC**		
		No PWM	**PWM voltage control**	**PWM current control**
Magnet	34.46	46.87	47.57	50.63
Sleeve	13.49	18.14	18.39	20.40
Total rotor eddy current loss	**47.95**	**65.01**	**65.96**	**71.03**

2.3.3 Dynamic simulation model

The dynamic simulation model is highly desirable as it allows to predict the motor performance under many different design variations and control strategies without having to physically construct and test all of them. Hence, a dynamic simulation model has been developed in the MATLAB environment. The following assumption has been made:

- The motor is unsaturated.
- The eddy current and hysteresis effects on the motor's magnetic materials have negligible influence on the phase current.
- The DC link voltage is constant.
- There is no saliency and therefore the self and mutual inductance are constant and independent of the rotor position.
- The switching devices in the inverter are ideal.

Above assumptions are valid for the simulation model of the single-phase PM brushless DC motor as will be described later.

The analysis in this work is based on the circuit diagram shown in Figure 2.12. The three-phase PM brushless DC motor having star-connected windings is controlled by a 120° conduction and fixed six-step commutation mode in accordance with the rotor position that is provided by three Hall sensors mounted on the stator. The voltage controlled PWM (14 kHz) strategy is employed to adjust the DC link voltage to control the motor operating speed. If the PWM is out of its duty cycle, the lower-side IGBT will be switched off which is named as free-wheeling mode. The states of the inverter's IGBTs are summarised in Table 2.9, where the 0°_{mech} of the rotor position corresponds to the position where the back-EMF of phase A is zero.

Table 2.9 Inverter's IGBT states

Rotor Position ($^{\circ}_{mech}$)	PWM Signal[1]	G1[2]	G2	G3	G4	G5	G6
[-30, 30]	0	0	0	1	0	1	0
	1	0	0	1	0	0	0
[30, 90]	0	1	0	0	0	1	0
	1	1	0	0	0	0	0
[90, 150]	0	1	0	0	0	0	1
	1	1	0	0	0	0	0
[150,210]	0	0	1	0	0	0	1
	1	0	1	0	0	0	0
[210,270]	0	0	1	0	1	0	0
	1	0	1	0	0	0	0
[270,330]	0	0	0	1	1	0	0
	1	0	0	1	0	0	0

[1]PWM signal=1, it is out of the duty cycle; Otherwise it is inside the duty cycle.

[2]G1=1, IGBT1 is switched on; Otherwise it is switched off.

The phase voltage equations can be written as:

$$\begin{cases} v_a = e_a + Ri_a + L\dfrac{di_a}{dt} + M\dfrac{di_b}{dt} + M\dfrac{di_c}{dt} \\ v_b = e_b + Ri_b + L\dfrac{di_b}{dt} + M\dfrac{di_a}{dt} + M\dfrac{di_c}{dt} \\ v_c = e_c + Ri_c + L\dfrac{di_c}{dt} + M\dfrac{di_a}{dt} + M\dfrac{di_b}{dt} \end{cases} \tag{2-10}$$

where v_a, v_b and v_c -- Phase terminal voltage; V

e_a, e_b and e_c -- Phase back-EMF which can be obtained from FEM; V

i_a, i_b and i_c -- Phase current; A

The inverter intervals can be classified as three categories:

- Conduction mode where only two phases are conducting via two IGBTs.

For example, by considering the case where the current flows in phase A and phase B during conduction as shown in Figure 2.13, the following equations can be obtained:

$$\begin{cases} \left(e_a + Ri_a + L\dfrac{di_a}{dt} + M\dfrac{di_b}{dt}\right) - \left(e_b + Ri_b + L\dfrac{di_b}{dt} + M\dfrac{di_a}{dt}\right) = V_{DC} \\ i_a = -i_b \end{cases} \tag{2-11}$$

Hence, it can be rewritten by:

$$\begin{cases} \dfrac{di_a}{dt} = -\dfrac{R}{L-M}i_a + \dfrac{V_{DC} - (e_a - e_b)}{2(L-M)} \\ \dfrac{di_b}{dt} = -\dfrac{di_a}{dt} \\ \dfrac{di_c}{dt} = 0 \end{cases} \tag{2-12}$$

- Free-wheeling mode where only two phases are conducting but via one IGBT and one diode.

For example, the current flows in Phase A and Phase B via IGBT 1 and diode 2 as shown in Figure 2.14. The following equations can be obtained:

$$\begin{cases} \left(e_a + Ri_a + L\frac{di_a}{dt} + M\frac{di_b}{dt}\right) - \left(e_b + Ri_b + L\frac{di_b}{dt} + M\frac{di_a}{dt}\right) = 0 \\ i_a = -i_b \end{cases} \tag{2-13}$$

Hence, it can be rewritten by:

$$\begin{cases} \frac{di_a}{dt} = -\frac{R}{L-M}i_a - \frac{(e_a - e_b)}{2(L-M)} \\ \frac{di_b}{dt} = -\frac{di_a}{dt} \\ \frac{di_c}{dt} = 0 \end{cases} \tag{2-14}$$

- Commutation mode where all three phases are conducting.

For example, when the conducting phase is switched from phase B to phase C, i.e. IGBT 5 is switched off and IGBT 6 is switched on, all three phases are conducting as shown in Figure 2.15. The following equations can be obtained:

$$\begin{cases} \left(e_a + Ri_a + L\frac{di_a}{dt} + M\frac{di_b}{dt}\right) - \left(e_b + Ri_b + L\frac{di_b}{dt} + M\frac{di_a}{dt}\right) = 0 \\ \left(e_a + Ri_a + L\frac{di_a}{dt} + M\frac{di_c}{dt}\right) - \left(e_c + Ri_c + L\frac{di_c}{dt} + M\frac{di_a}{dt}\right) = V_{DC} \\ i_a + i_b + i_c = 0 \end{cases} \tag{2-15}$$

Hence, it can be rewritten by:

$$\begin{cases} \frac{di_a}{dt} = -\frac{R}{L-M}i_a + \frac{V_{DC} - 2e_a + e_b + e_c}{3(L-M)} \\ \frac{di_b}{dt} = -\frac{R}{L-M}i_b + \frac{V_{DC} + e_a - 2e_b + e_c}{3(L-M)} \\ \frac{di_c}{dt} = -\frac{R}{L-M}i_c - \frac{2V_{DC} - e_a - e_b + 2e_c}{3(L-M)} \end{cases} \tag{2-16}$$

At each simulation step, the phase current is updated by:

$$\begin{cases} i_{a(n+1)} = i_{a(n)} + di_a \\ i_{b(n+1)} = i_{b(n)} + di_b \\ i_{c(n+1)} = i_{c(n)} + di_c \end{cases} \tag{2-17}$$

Once the phase currents are obtained, the electromagnetic torque can be calculated by:

$$T_{em} = \frac{(e_a i_a + e_b i_b + e_c i_c)}{\omega_r} \quad \text{(Nm)} \tag{2-18}$$

where ω_r -- Rotation speed; rad/s

Hence, the dynamic speed can be obtained by the mechanical equations, as expressed by:

$$T_{em} - T_{load} - T_f = J\frac{d\omega_r}{dt} \quad \text{(Nm)} \tag{2-19}$$

where T_{load} -- Load torque; Nm

T_f -- Friction torque; Nm

J -- Rotor inertia; Kg·m^2

The friction torque is assumed to be:

$$T_f = k_f \omega_r^3 \quad \text{(Nm)} \tag{2-20}$$

Since the customer specifies that the friction loss under the rated speed, 45000rpm, is 150W, the friction coefficient k_f is 3.042×10^{-13}.

2.4 Single-phase PM motor design

Due to simple construction, few power switches, low cost and high reliability, an equivalent single-phase PM brushless dc motor is designed to meet the specifications as given in Table 2.1. It is aimed to have the same rotor dimensions as three-phase PM brushless DC motor designed in previous section. Since the single-phase PM motors have null-points in their

torque waveforms, it may fail to start. Hence, a special design is required to overcome the starting problem. As reviewed in Chapter 1, tapered airgap is the most appropriate solution to solve the starting issue since it results in a high starting torque and a smooth resultant torque waveform without introducing an additional cost [61, 64]. Therefore, a tapered airgap is employed to introduce the starting torque and impart a preferred direction with excited phase current. Further, considering its less leakage flux and consequent better performance, the stator is formed in the cylindrical shape rather than the U-shape. Its cross-section is shown in Figure 2.16, where O is the center of the rotor and O' is the center of the stator bore. Even though the rotor outer diameter and stator outer diameter is constrained by the customer, a simplified analytical model is still developed to examine the optimal ratio of the stator bore to stator outer diameter to obtain the maximum electromagnetic torque at a given copper loss. It can help to optimise the motor design at next stage if it is necessary. Finally, the dynamic simulation models, where the single-phase PM brushless motor is driven by either full-bridge inverter or half-bridge inverter employing bifilar windings, are developed to predict its dynamic performance. The simulated phase current is fed back to the FEM to predict the load stator iron loss and rotor eddy current loss. The prototype of the single-phase PM brushless DC motor is shown in Figure 2.17, and its leading parameters are given in Table 2.10.

Table 2.10 Leading dimensions of single-phase PM brushless DC motor.

Stator dimensions	
Outer diameter (mm)	64.5
Stator bore center O' (mm)	(0.8, 0)
Stator bore diameter (mm)	14.225
Back-iron thickness (mm)	6.5
Lamination axial length (mm)	40.0
End winding length (mm)	22.0
Motor axial length (mm)	84.0
Motor volume (mm^3)	2.74×10^5
Tooth width (mm)	13.0
Tip edge thickness (mm)	2.64/1.0
Slot opening (mm)	1.98
Rotor dimensions	

Magnet outer diameter (mm)	25.0	
Magnet inner diameter (mm)	19.0	
Back-iron thickness (mm)	5.7	
Rotor axial length (mm)	42.3	
Effective airgap length (mm)	0.9 to 2.55	
Sleeve thickness (mm)	0.6	
Pole-arc/pole-pitch ratio	1.00	
Winding details	**Conventional windings**	**Bifilar windings**
Phase resistance (mΩ)	0.56	1.12
Wires per turn	2	1
Turns per coil	50	
Coils per phase	2 coils connected in series	
Packing factor	0.2	
Phase self-inductance (mH)	4.6	

2.4.1 Split ratio

The split ratio is an important design parameter for cylindrical PM brushless motors since it has a significant influence on the torque capability and efficiency and also the cost. However, existing methods for optimal split ratio is mainly focused on multi-phase PM brushless motors [1, 95-96]. In this section, an analytical model is developed to determine the optimal split ratio of the single-phase PM brushless motors, which have the diametrically magnetised rotor, for the maximum torque per volume. This analytical model is restricted to:

- Stator iron loss and rotor eddy current loss are neglected.
- End windings are neglected.
- Sinusoidal back-EMF and phase current are used for the calculation of the torque and copper loss.

For the single-phase PM motor with the concentric airgap, the magnetization of the permanent magnet is in a parallel direction which results in an essential sinusoid back-EMF waveform as shown in Figure 2.18. However, if the tapered airgap is employed to improve the starting

capability, the open-circuit airgap flux density distribution and back-EMF waveform will be distorted relatively as shown in Figure 2.22 and Figure 2.23. In order to simplify the analysis, it is assumed the airgap is concentric and the harmonic components of the back-EMF are neglected. Hence, the amplitude of the sinusoidal phase back-EMF can be given by:

$$e_{ph} = N_{ph} B_g l_a D_s \omega_r \quad \text{(V)} \tag{2-21}$$

where N_{ph} -- Number of turns of phase windings;

B_g -- Amplitude of the open circuit radial airgap flux density; T

D_s -- Stator bore diameter; m

l_a -- Axial length; m

By applying the sinusoidal phase current to the windings, the average electromagnetic torque is:

$$T = \frac{1}{2} N_{ph} B_g l_a D_s I_{ph} \quad \text{(Nm)} \tag{2-22}$$

where I_{ph} -- Amplitude of the sinusoidal phase current; A

The copper loss is given by:

$$P_{cu} = \frac{I_{ph}^2 N_{ph}^2 l_a}{\sigma_{cu} A_s k_p} \quad \text{(W)} \tag{2-23}$$

where σ_{cu} -- Copper electrical conductivity; $\Omega^{-1} \cdot m^{-1}$

A_s -- Winding slot area; m^2

k_p -- is the winding packing factor.

By fixing the copper loss, the temperature rise within a given stator frame diameter is also fixed. (2-23) can be rewritten as $I_{ph} = f(P_{cu})$ and Substituted into (2-22), the electromagnetic torque per motor volume V can be derived as:

$$\frac{T}{V} \propto \frac{D_s}{D_o^2}\sqrt{A_s} \tag{2-24}$$

where D_o -- Stator outer diameter; m

The winding slot area A_s is determined mainly by the required stator tooth-body width, stator tooth tips and stator back-iron thickness that are limited by its maximum flux density B_m.

According to Figure 2.19, the slot area can be expressed as,

$$A_s = 2(A_{s1} + A_{s2}) \quad (\text{m}^2) \tag{2-25}$$

where

$$A_{s1} = \frac{1}{4}\left[\pi\left(\frac{D_o}{2} - h\right)^2 - \pi\left(\frac{D_s}{2} + x_1 + x_2\right)^2 - 2 \times y \times \left(\frac{D_o}{2} - \frac{D_s}{2} - h - x_1 - x_2\right)\right] \tag{2-26}$$

$$A_{s2} \approx \frac{2}{3}(A_{s2} + A_{s3}) = \frac{2}{3} \times \frac{1}{4}\left[\pi\left(\frac{D_s}{2} + x_1 + x_2\right)^2 - \pi\left(\frac{D_s}{2} + x_2\right)^2 - 2 \times y \times x_1\right] \tag{2-27}$$

The tooth tip dimensions are defined by x_1 and x_2 as shown in Figure 2.19 and should be appropriately designed. If x_1 and x_2 are too small, the tooth tips may be subject to the saturation. Consequently, the cogging torque will be increased and back-EMF will be reduced which deteriorates the motor performance undesirably. In this case, they are assumed to be:

$$x_1 = 0.8h \quad (\text{m}) \tag{2-28}$$

$$x_2 = 0.4h \quad \text{(m)} \tag{2-29}$$

As shown in Figure 2.21, the flux in the stator back-iron is approximately half of that in the stator tooth. Hence, in order to keep that same B_m, the stator back-iron thickness is half of the stator tooth width as expressed:

$$y = 2h \quad \text{(m)} \tag{2-30}$$

On the open-circuit with 0°_{mech} of the rotor position, the maximum flux density in the stator tooth or back-iron can be given by:

$$B_m = \frac{\phi_m}{2hl_a} \quad \text{(T)} \tag{2-31}$$

where ϕ_m -- Flux due to the permanent magnet can be given by:

$$\phi_m = l_a \int_0^{\pi} B_g \sin(\alpha) \frac{D_s}{2} d\alpha = B_g l_a D_s \qquad \text{(Wb)} \tag{2-32}$$

Hence, the stator back-iron thickness is:

$$h = \frac{B_g D_s}{2B_m} \qquad \text{(m)} \tag{2-33}$$

By substituting (2-26) to (2-33) into (2-25), the slot area can be obtained as,

$$A_s = \frac{\pi}{8} D_o^2 - \left(\frac{\pi}{4} + \frac{1}{2}\right) \frac{B_g}{B_m} D_o D_s + \left[\left(\frac{41}{50} + \frac{13}{200}\pi\right) \left(\frac{B_g}{B_m}\right)^2 + \left(\frac{1}{2} - \frac{\pi}{6}\right) \frac{B_g}{B_m} - \frac{\pi}{8} \right] D_s^2 \tag{2-34}$$

Substituting (2-34) into (2-24) the relationship between T/V and D_s/D_o can be obtained, and the optimal split ratio for maximum torque per motor volume can be obtained by differentiating T/V with respect to D_s/D_o and equating to zero. The optimal ratio of D_s/D_o is given by

$$\left(\frac{D_s}{D_o}\right)=\frac{-b-\sqrt{b^2-4ac}}{2a} \tag{2-35}$$

where

$$a=4\left[\left(\frac{1}{3}+\frac{31}{600}\pi\right)\left(\frac{B_g}{B_m}\right)^2+\left(\frac{1}{2}-\frac{\pi}{6}\right)\frac{B_g}{B_m}-\frac{\pi}{8}\right] \tag{2-36}$$

$$b=-3\left(\frac{\pi}{4}+\frac{1}{2}\right)\frac{B_g}{B_m} \tag{2-37}$$

$$c=\frac{\pi}{4} \tag{2-38}$$

According to (2-30) and (2-33), with the increase of B_g / B_m, the stator tooth width and back iron thickness will be reduced to maintain the same magnetic saturation level. As a consequence, the winding slot area is reduced. However, for the purpose of the same copper loss or effectively the same winding slot area, the stator bore diameter has to be reduced. Hence, the optimal split ratio is reduced as shown in Figure 2.20.

The peak of the airgap flux density at the stator bore is given by [1]:

$$B_g = B_r\left(\frac{R_m}{R_s}\right)^2 \qquad \text{(T)} \tag{2-39}$$

If it is assumed that the airgap is concentric and airgap length is the same as that of the three-phase PM brushless motor, $B_r = 1.01$ T, $R_m = 12.5$ mm, and $R_s = 14.0$ mm. Thus $B_g = 0.8$ T. The allowable maximum flux density in the stator B_m is assumed to be 1.7T. Hence, $\frac{B_g}{B_m} = 0.47$, the corresponding optimal split ratio $\frac{D_s}{D_o} = 0.35$ and the optimal rotor to stator diameter ratio is 0.31.

However, the rotor to stator diameter ratio of the prototype of the single-phase motor is 0.39 which is higher than the optimal ratio. The eccentric airgap gives a relatively lower peak

open-circuit flux density, $B_g = 0.67$ as shown in Figure 2.22. Hence, $\frac{B_g}{B_m} = 0.39$, the corresponding optimal split ratio $\frac{D_s}{D_o} = 0.39$ and the optimal rotor to stator diameter ratio is 0.35, which is close to the ratio of the prototype.

2.4.2 FEM validation

2.4.2.1 Back-EMF, cogging torque and inductance

2D FEM predicted open-circuit flux distribution of single-phase PM motor is shown in Figure 2.21 and corresponding airgap flux density distribution is shown in Figure 2.22. 2D FEM predicted and tested back-EMF waveforms are compared in Figure 2.23. Because of the tapered airgap, back-EMF is distorted from the essentially sinusoidal waveform as shown in Figure 2.18 where the concentric airgap is employed.

2D FEM and tested cogging torque waveforms are compared in Figure 2.24. It can be seen that they have a good agreement. Its periodicity is 180o. Compared to the three-phase PM brushless DC motor, single-phase PM motor has much bigger cogging torque, which may induce significant torque and speed ripple. Hence, it needs to be modelled in the dynamic simulation properly.

Using the same method as described in section 2.3.2.3, the inductance of the single-phase PM brushless DC motor can be obtained by FEM and is given in Table 2.10.

2.4.2.2 Stator iron loss

By employing the same method as described in 2.3.2.4 for three-phase PM brushless motors, the stator iron loss of single-phase PM brushless motors are predicted by FEM under open-circuit and rated load conditions. The rated phase current, Figure 2.25, is simulated by a

dynamic simulation model where an H-bridge inverter is used to drive the motor as will be described later. The FEM predicted stator iron loss is given in Table 2.11. It can be noted that the stator iron loss under the rated load are slightly higher than that under the open-circuit condition. However, because of the eccentric airgap, both are much bigger than that of the three-phase PM brushless motors.

Table 2.11 Stator iron loss (W) of single-phase PM brushless motor under open-circuit and rated load conditions

	Open-circuit	**On load**
Hysteresis loss	12.41	14.52
Classical eddy current loss	23.04	24.47
Excess eddy current loss	17.39	18.41
Total stator iron loss	52.85	57.4

2.4.2.3 Rotor eddy current loss

The rotor eddy current loss is also investigated with the FEM. Further, unlike the three-phase PM brushless motors, an eccentric airgap is employed in the single-phase PM brushless motors to improve its starting capability. However, it will introduce more airgap permeance harmonics, and thus the rotor eddy current loss will be affected significantly. Hence, the eccentric airgap needs to be designed appropriately with the due account for its effect on the rotor eddy current loss.

Table 2.12 Airgap and slot opening dimensions.

	Design C	**Design D**	**Design E**	**Design F**
Airgap length range (mm)	0.9	0.9 to 1.9	0.9 to 2.55	0.9 to 1.9
Slot opening (mm)	1.98	1.98	1.98	1.5

Table 2.13 Open-circuit rotor eddy current loss @45krpm.

	Design C	**Design D**	**Design E**	**Design F**
Magnet (W)	0.15	23.4	50.3	22.63
Sleeve (W)	0.03	2.13	4.45	2.09
Total rotor eddy current loss (W)	**0.18**	**25.53**	**54.75**	**24.72**

Table 2.14 On load rotor eddy current loss @45krpm.

	Design C	**Design D**	**Design E**	**Design F**
Magnet (W)	104.6	43.71	28.32	40.28
Sleeve (W)	3.51	3.23	2.12	2.91
Total rotor eddy current loss (W)	**108.11**	**46.94**	**30.44**	**43.19**

Four single-phase PM brushless motors, having the same rotor and stator dimensions except the airgap and slot opening as summarised in Table 2.12, are examined in terms of their rotor eddy current loss under open-circuit and rated load conditions. **Design C**, **Design D** and **Design E** have the same slot opening but different airgap. Particularly **Design C** has a concentric airgap. **Design D** and **Design F** have the same eccentric airgap but different slot openings. The corresponding open-circuit and on load rotor eddy current loss are compared in Table 2.13 and Table 2.14, respectively. It can be noted that the open-circuit rotor eddy current loss increases with the eccentric airgap. However, the on load rotor eddy current loss decreases with the eccentric airgap. Further investigation as will be described in Chapter 4 shows that for a given phase current, there is an optimal eccentric airgap to give the minimum on load rotor eddy current loss. In this case, **Design E** is the optimised one. It can also be seen that **Design D** and **Design F** have similar rotor eddy current loss. It indicates that compared to the eccentric airgap, the slot opening has less effect on the rotor eddy current loss.

2.4.3 Dynamic simulation model and test results

A single-phase PM brushless dc motor may be fed from either a full-bridge inverter [82, 97] or, if the motor is equipped with a bifilar winding, from a half-bridge inverter [59], as shown in Figure 2.26. Compared with a full-bridge inverter, a half-bridge inverter has half the

number of power switches, only two switches and two freewheeling diodes are required, both being referred to ground, which simplifies the control strategy and reduces the cost. However, the motor then requires two bifilar-wound coils, so that the copper utilization is reduced since only half the conductors are active in producing torque at any instant. While the stator iron loss, rotor eddy current loss and the friction loss may often be neglected in low speed simulations [59, 82, 97], as will be shown, they can have a significant effect on the dynamic performance of a high-speed motor.

Similar to three-phase PM brushless motors, the voltage controlled PWM (14kHz) strategy is employed to adjust the DC link voltage to control the motor operating speed in accordance with the rotor position that is provided by two Hall sensors mounted on the stator. The Hall signal is illustrated in Figure 2.27.

2.4.3.1 Single-phase PM brushless motor model

The dynamic simulation model of the single-phase PM brushless motor is derived based on its equivalent electrical and mechanical equations as follows:

$$v = Ri + L\frac{di}{dt} + e_{PM} \qquad \text{(V)} \tag{2-40}$$

$$T_{em} - T_{load} - T_f = J\frac{d\omega_r}{dt} \qquad \text{(Nm)} \tag{2-41}$$

where v -- Winding terminal voltage; V

e_{PM} --Back-EMF; V

i -- Phase current; A

R -- Phase resistance; Ω

L -- Phase inductance; H

The electromagnetic torque T_{em} can be expressed by:

$$T_{em} = \frac{ie_{PM}}{\omega_r} + T_c \qquad \text{(Nm)} \tag{2-42}$$

where ω_r -- Rotation speed; rad/s

T_c -- Cogging torque which can be obtained from FEM; Nm

With a high fundamental operating frequency (750Hz for a 2-pole motor running at 45,000rpm), the stator iron loss, P_s, and the rotor eddy current loss, P_r, can have a significant influence on the performance. Thus, various loss components are pre-calculated as a function of both the load and the speed, using FEM as discussed in the previous section. The loss is then represented by an equivalent load torque:

$$T_{loss} = (P_s + P_r)/\omega_r \qquad \text{(Nm)} \tag{2-43}$$

Equation (2-41) can then be rewritten as:

$$T_{em} - T_{load} - T_{loss} - T_f = J\frac{d\omega_r}{dt} \qquad \text{(Nm)} \tag{2-44}$$

2.4.3.2 Full-bridge inverter model

Figure 2.26(a) shows the circuit diagram of the single-phase drive system with the half-bridge inverter. According to (2-40) (2-42) (2-44), in order to predict the phase current, torque and dynamic performance, it is necessary to determine the winding terminal voltage at each simulation time step, which is determined by the inverter intervals based on the Hall signal and PWM signal. During conduction mode, if the PWM is out of its duty cycle, the lower-side IGBT will be switched off which is named as free-wheel mode. During off mode, all of IGBTs are switched off. Hence, five inverter intervals are summarised in Table 2.15. Based on the phase current of the previous time step, the winding terminal voltage is given in Table 2.16.

Table 2.15 Inverter intervals of full-bridge inverter

Inverter interval	Rotor position θ_r ($^o_{mech}$)	Hall Signal 1	Hall Signal 2	PWM signal	G 1	G 2	G 3	G 4
1	$[0, \theta_c]$	1	0	0	1	0	0	1
2	$[0, \theta_c]$	1	0	1	1	0	0	0
3	$[180, 180+\theta_c]$	0	1	0	0	1	1	0
4	$[180, 180+\theta_c]$	0	1	1	0	0	1	0
5	$[\theta_c, 180]$	1	1		0	0	0	0
	$[180+\theta_c, 360]$	0	0					

Table 2.16 Winding terminal voltage at different inverter intervals of full-bridge inverter.

Inverter interval	$i > 0$	$i < 0$	$i = 0$
1	V_{DC}	V_{DC}	
2	0	V_{DC}	
3	$-V_{DC}$	$-V_{DC}$	e_{PM}
4	$-V_{DC}$	0	
5	$-V_{DC}$	V_{DC}	

2.4.3.3 Half-bridge inverter model

Figure 2.26(b) shows the circuit diagram of the single-phase drive system with the half-bridge inverter employing a bifilar winding and the polarities of winding terminal voltage, back-EMF, and current. It is assumed that winding 1 and winding 2 have the same self-inductance, i.e. L, and there is no leakage flux, therefore, the mutual inductance, M, is assumed to be equal to the self-inductance. The electrical equations of the bifilar windings can be expressed as follows:

$$v_1 = Ri_1 + L\frac{di_1}{dt} + M\frac{di_2}{dt} + e_{PM} \quad \text{(V)} \tag{2-45}$$

$$v_2 = Ri_2 + L\frac{di_2}{dt} + M\frac{di_1}{dt} + e_{PM} \quad \text{(V)} \tag{2-46}$$

$$T_{em} = \frac{(i_1 + i_2)e_{PM}}{\omega_r} + T_c \quad \text{(Nm)} \tag{2-47}$$

where v_1, v_2 -- Terminal voltage of two couple windings; V

i_1, i_2 -- Phase current of two coupled windings; A

e_{PM} -- Back-EMF; V

According to the rotor position and PWM controller signal, 4 inverter intervals are considered in the simulation:

- **Interval 1:** $0 \le \theta_r < \theta_c$, T1 is switched on, while T2 is switched off. The current flows from the supply to the winding 1.
- **Interval 2:** $\theta_c \le \theta_r < 180^\circ$, T1 and T2 are both switched off. The current in the winding 1 is reduced to zero and the corresponding stored magnetic energy is transferred to the winding 2 instantaneously. As the winding 2 is wound in the opposite direction to the winding 1, the current in this winding is positive and will decrease as energy is returned to the supply via the freewheel diode.
- **Interval 3:** $180^\circ \le \theta_r < 180^\circ + \theta_c$, T2 is switched on, while T1 is switched off. The current flows from the supply to the winding 2 to provide the reversed MMF so as to produce positive torque.
- **Interval 4:** $180^\circ + \theta_c \le \theta_r < 360^\circ$, T1 and T2 are both switched off. The stored magnetic energy is transferred from the winding 2 to the winding 1, the current in the winding 2 being reduced to zero instantaneously.

Furthermore, in **interval 1**, if the PWM controller sends a signal to switch off T1, it can be regarded as **interval 2**, while in **interval 3**, if the PWM voltage controller sends a signal to switch off T2, it can be regarded as **interval 4**. This commutation process continues cyclically in synchronism with the rotor rotation. The winding terminal voltages and currents at different inverter intervals are given in Table 2.17.

In the simulation, at the start of each time step, the inverter interval is based on the rotor position at the end of the previous time step. The corresponding back-EMF, cogging torque and winding terminal voltage are determined. Then the motor state variables can be simulated by using (2-44) to (2-47). However, it should be noted that, when one of IGBTs is switched off during **interval 2** or **4**, it is assumed in the simulation that the currents between two coupled windings are transferred instantaneously. Therefore, at this instant the winding currents will not be determined by (2-45) and (2-46). In contrast, the current in one winding connected to the IGBT which is being switched off will be set to zero and the current in other winding will be set to the value of the first winding current at last time step.

Table 2.17 Winding terminal voltage at different inverter intervals of half-bridge inverter.

Inverter interval	i_1	i_2	v_1	v_2
1	>0	=0	V_{DC}	$v_1 - i_1 R$
2	=0	>0	$v_2 - i_2 R$	$-V_{DC}$
	=0	=0	e_{PM}	e_{PM}
3	=0	<0	$v_2 - i_2 R$	$-V_{DC}$
	<0	=0	V_{DC}	$v_1 - i_1 R$
4	=0	=0	e_{PM}	e_{PM}

2.4.3.4 Simulation and test results

Based on the above simulation models, the dynamic simulation performance is investigated for the single-phase PM brushless motor drive system. The motor parameters are given in Table 2.10. The prototype of this single-phase PM brushless DC motor is shown in Figure 2.17. In the simulation model, its back-EMF and cogging torque are pre-calculated by FEM. The phase current is taken from measurements and fed into FEM to calculate the stator iron loss and the rotor eddy current loss. Three conditions, as described in Table 2.18, have been carried out in the simulation to compare with the measured results such as motor speed and phase current waveforms. In addition, for each condition, a separate simulation has been

carried out without considering the stator and rotor loss to investigate the influence of the loss on the motor dynamic performance. The simulated and measured speeds are compared in Table 2.19. The simulated and measured phase current waveforms are compared in Figure 2.28, Figure 2.29 and Figure 2.30, respectively. It can be seen that by considering the stator iron loss and rotor eddy current loss, the simulated speed becomes lower and is much closer to the measured speed, while the simulated currents become higher and the waveforms are much closer to the measured current waveforms. Overall, good agreement between simulated and measured speeds and current waveforms has been achieved. However, at high speed (~45,000rpm), the difference increases, which may be due to:

- The actual drive is supplied from the AC mains through a front-end diode bridge rectifier. Hence, DC link voltage ripple exists which is not modelled in the simulation model.
- The tolerance of the Hall sensor location introduces the error in the conduction angle and commutation angle.
- The motor parameters such as phase resistance and inductance used in simulation model may not be accurately predicted.
- The friction loss which is assumed to be 150W at the rated speed may not be accurate.
- For bifilar winding, the leakage flux between two windings is neglected in the simulation model.

Table 2.18 Simulation descriptions

	Condition 1	**Condition 2**	**Condition 3**
Inverter type	Full-bridge	Half-bridge	Half-bridge
V_{DC} (V)		290	
θ_c ($^{o}_{mech}$)		126	
Load (Nm)	0.25	0.24	0.24
PWM duty cycle (%)	18.6	71.1	100

Table 2.19 Comparison of simulated and measured speed.

	Condition 1		Condition 2		Condition 3	
Stator iron loss (W)	0	4.5	0	25.7	0	63
Rotor eddy current loss (W)	0	7.9	0	45.0	0	54
Simulated speed (krpm)	**7.4**	**7.1**	**27.1**	**25.7**	**50.7**	**46.4**
Measured speed (krpm)	**6.4**		**26.0**		**46.0**	

2.5 Comparison of three-phase and single-phase PM brushless DC motors

The performance of the three-phase and single-phase PM brushless DC motors, which are predicted by the dynamic simulation models, are compared in Table 2.20 under the rated load and the rated speed.

- The three-phase PM brushless DC motor has the less copper loss and stator iron loss, but higher rotor eddy current loss. Hence, its efficiency is slightly less than the single-phase PM brushless DC motor driven by the full-bridge inverter.
- The single-phase PM brushless DC motors driven by the full-bridge or the half-bridge inverter have almost the same effective winding current, Figure 2.31. Consequently, they have the same stator iron loss and the rotor eddy current loss.
- If the single-phase PM brushless DC motor having bifilar windings is driven by the half-bridge inverter, only half of the windings are utilized at any instant. Consequently, the copper loss will be doubled which results in 2.5% less efficiency than that driven by the full-bridge inverter.
- Compared to the three-phase PM brushless motor, the single-phase PM brushless motor has longer end winding length. As a result, it has bigger motor volume and less power density.
- According to Figure 2.32, the single-phase PM brushless DC motor has much bigger torque ripple than the three-phase PM brushless DC motor, which may introduce the undesirable vibration and acoustical noise.
- The single-phase PM brushless DC motor with the bifilar windings requires the least number of IGBTs and Hall sensors, and thus potentially the lowest cost.

Table 2.20 Comparison of three-phase and single-phase PM brushless DC motors and their drive system.

	Three-phase	Single-phase	
		Full-bridge	Half-bridge
DC link voltage (V)		290	
Speed (rpm)		45,000	
Output power (W)		1100	
Copper loss (W)	14.2	22.1	45.7
Rotor eddy current loss (W)	66.0	30.4	30.4
Stator iron loss (W)	38.9	57.4	57.4
Friction loss (W)	150.0	150.0	150.0
Input power (W)	1369.1	1359.9	1383.5
Efficiency (%)	80.3	80.9	79.5
Volume (m^3)	2.12×10^{-4}	2.74×10^{-4}	2.74×10^{-4}
Power density (W/m^3)	5.19×10^{6}	4.01×10^{6}	4.01×10^{6}
IGBT devices	6	4	2
Hall sensors	3	2	2

2.6 Summary

In this chapter, a three-phase high-speed PM brushless DC motor has been designed for the pump application. It is driven by six-pulse full-bridge inverter and its dynamic simulation is described and developed to predict its dynamic performance. The FEM is employed to predict the stator iron loss and rotor eddy current loss under open-circuit and load conditions.

An equivalent single-phase high-speed PM brushless DC motor has been designed. A simplified analytical model has been developed to examine its optimal split ratio and found that the split ratio of the prototype, which is constrained by the customer, is higher than its optimum value.

Two inverters, i.e. full-bridge inverter and half-bridge inverter, have been employed to drive the single-phase PM brushless DC motor. The half-bridge inverter requires the bifilar phase winding topologies. Their dynamic simulation models have been described and developed to

investigate its dynamic performance with due account of the stator and rotor losses. Compared to the measured phase current and speed, it is found that by considering the stator and rotor losses in the simulation, the simulated results agree better with the measured results, although at high speed, some difference still exists and needs further investigation.

The stator iron loss and rotor eddy current loss of the single-phase motor are predicted by FEM. It has been found that the eccentric airgap has significant effect on the rotor eddy current loss, and compared to the eccentric airgap the slot opening has the less effect on the rotor eddy current loss. Further, for a given phase current, there is an optimal eccentric airgap which results in a minimum on-load rotor eddy current loss. It will be fully investigated in Chapter 4.

Compared to three-phase PM brushless DC motor, single-phase motor has relatively smaller power density and bigger torque ripple, and thus potentially higher vibration and acoustics noise. If the single-phase motor is driven by the full-bridge inverter, it has a slightly better efficiency due to its relatively lower rotor eddy current loss. If the single-phase motor with bifilar windings is driven by the half-bridge inverter, its efficiency will be worst due to its relatively higher copper loss. However, it has the lowest cost in terms of the drive system.

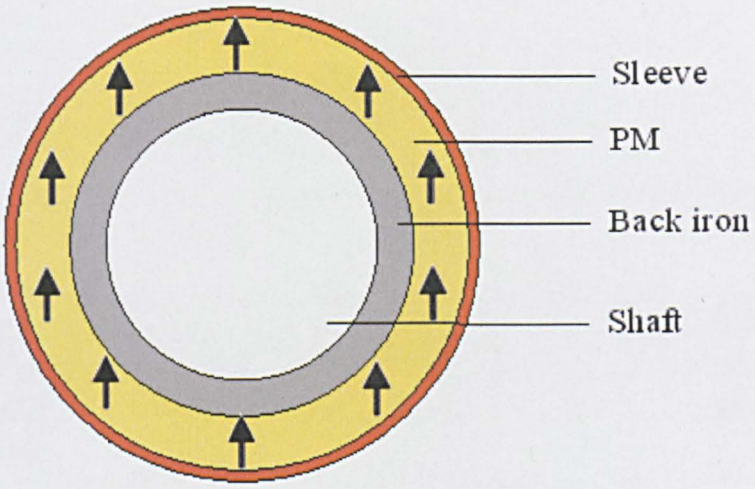

Figure 2.1 Cross-section of rotor.

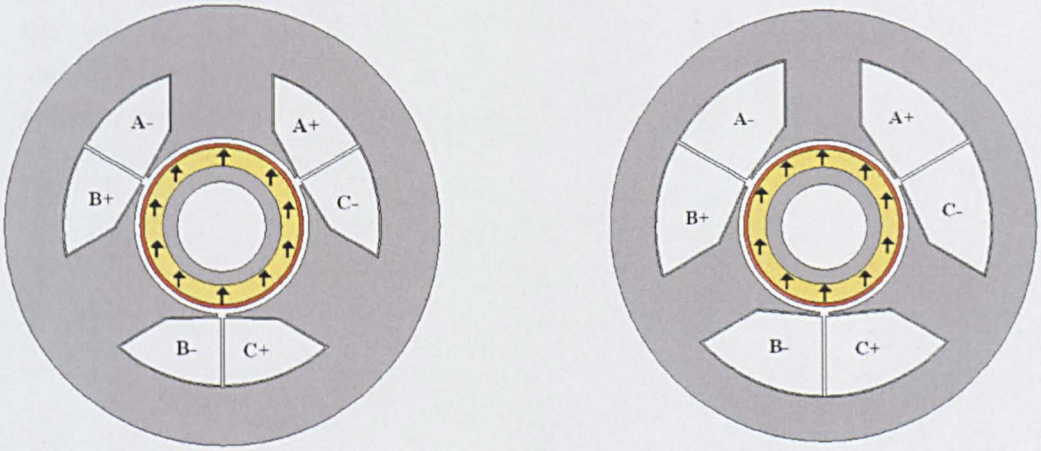

(a) **Design A** (b) **Design B**

Figure 2.2 Cross-section of three-phase PM brushless DC motors.

Figure 2.3 Prototype of three-phase PM brushless DC motor, **Design A**.

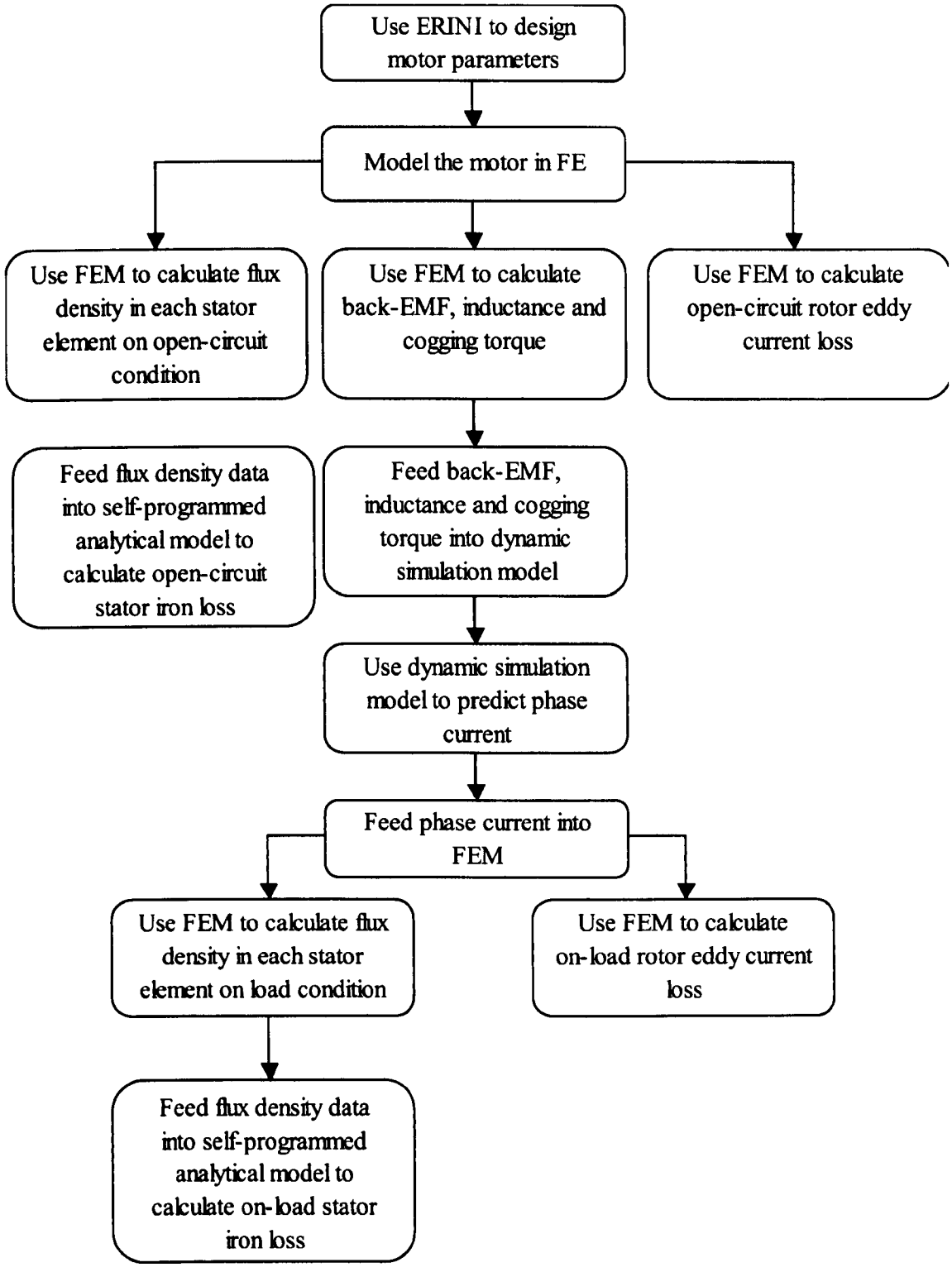

Figure 2.4 Flowchart of motor design and analysis procedure.

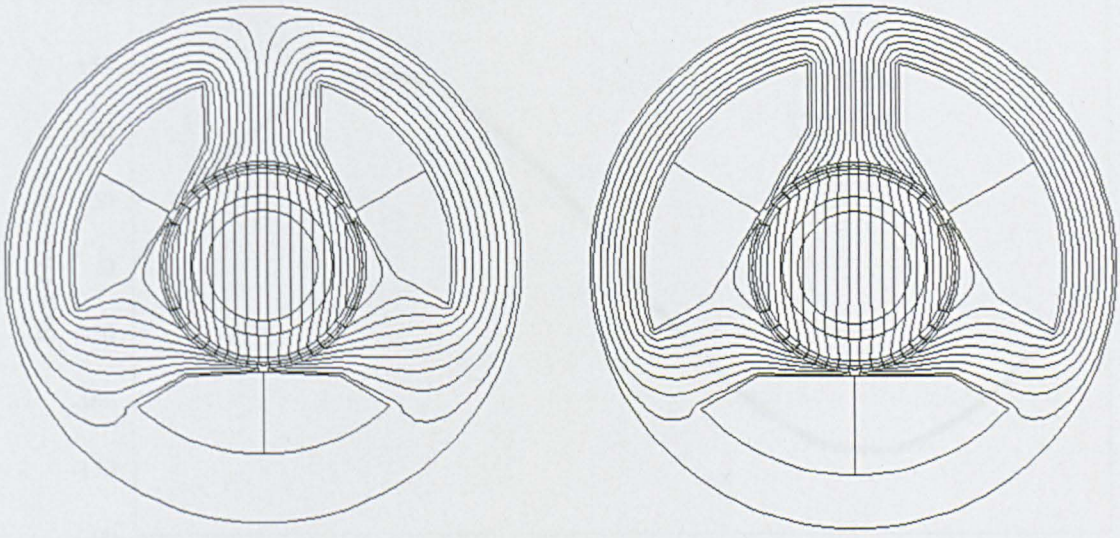

(a) **Design A** (b) **Design B**

Figure 2.5 Open-circuit flux distribution of three-phase PM brushless DC motors. (Rotor position=0°_{mech})

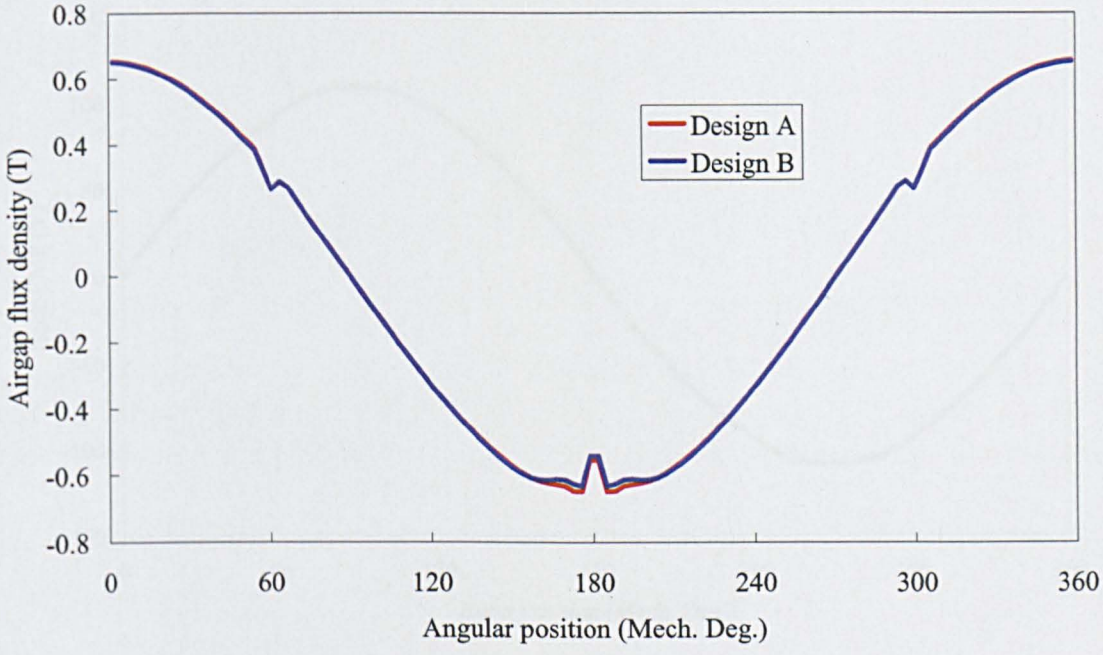

Figure 2.6 Open-circuit airgap flux density distribution of three-phase PM brushless DC motors. (Rotor position=0°_{mech})

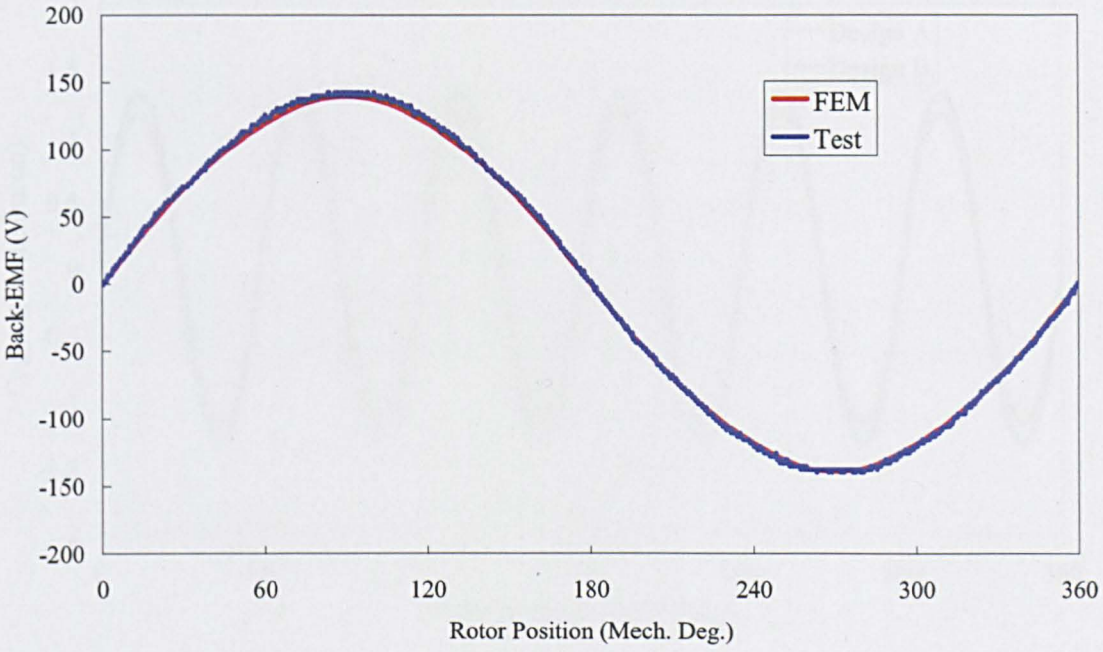

(a) **Design A**

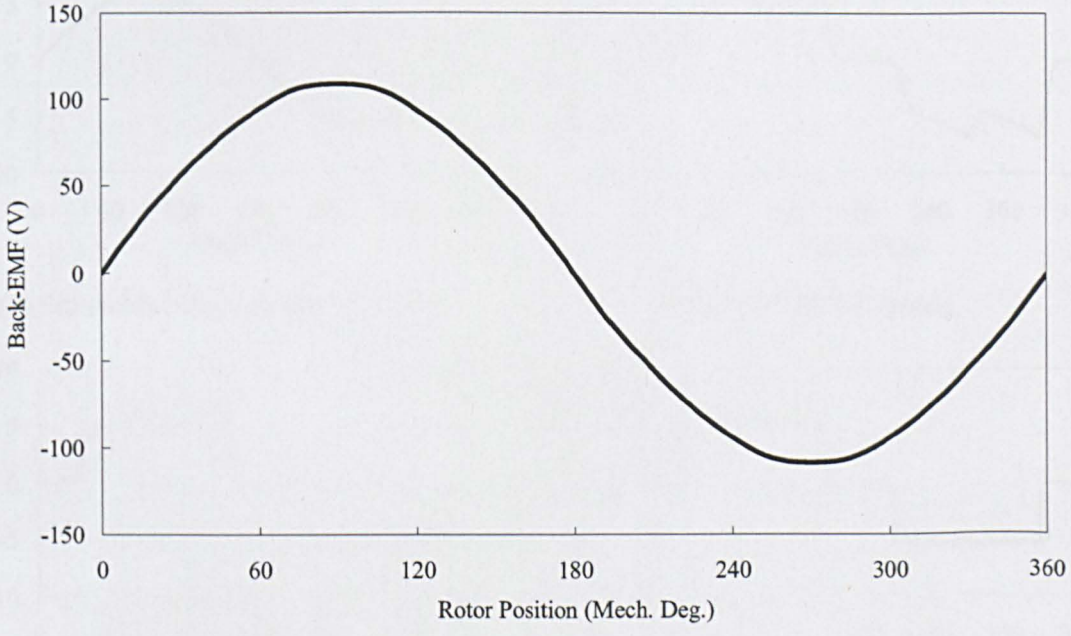

(b) **Design B**

Figure 2.7 Back-EMF waveforms of three-phase PM brushless DC motors. (Speed=45,000rpm)

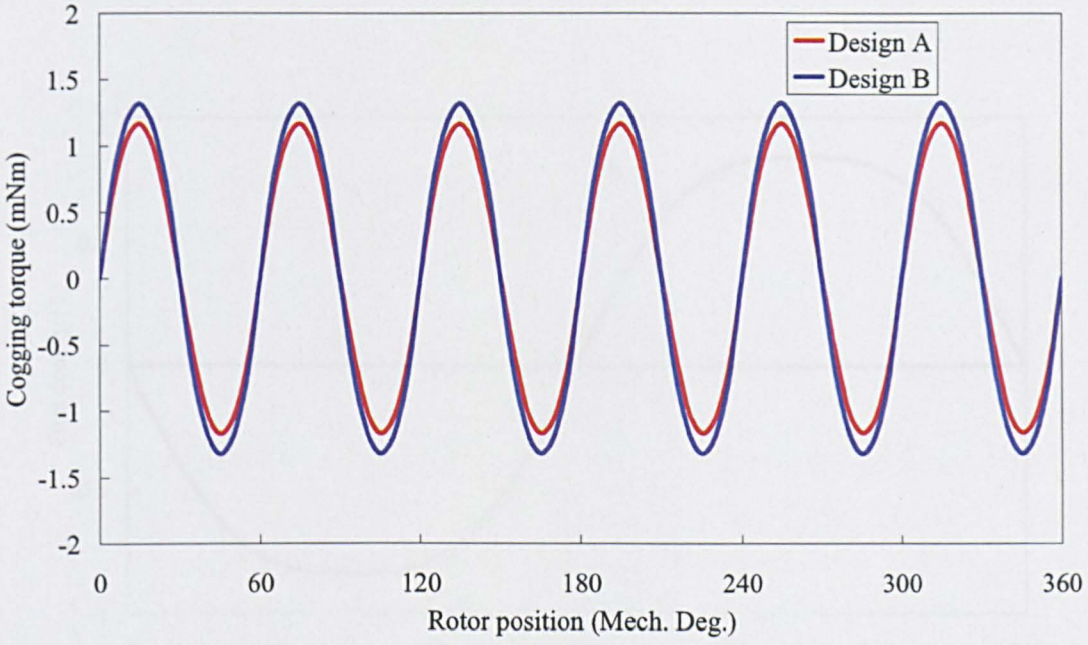

Figure 2.8 Cogging torque waveforms of three-phase PM brushless DC motors.

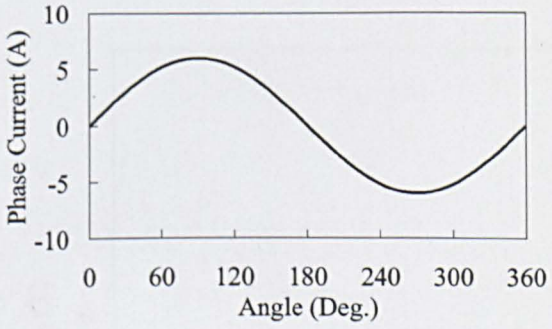

(a) Sinusoidal current, BLAC mode.

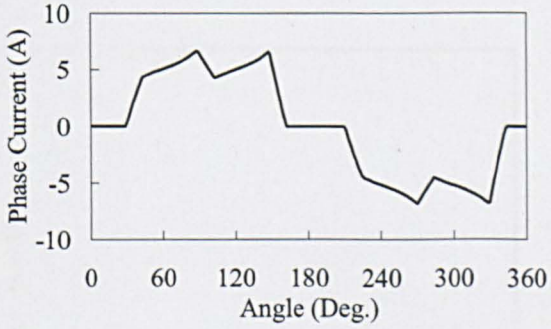

(b) 120° BLDC mode.

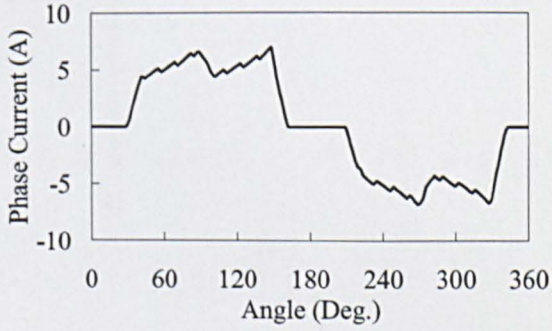

(c) 120° BLDC mode, PWM voltage control.

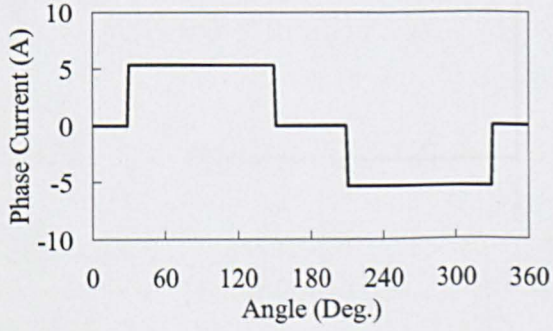

(d) 120° LDC mode, PWM current control.

Figure 2.9 Simulated phase current waveforms of **Design A** at rated load(0.23Nm) and rated speed(45,000rpm).

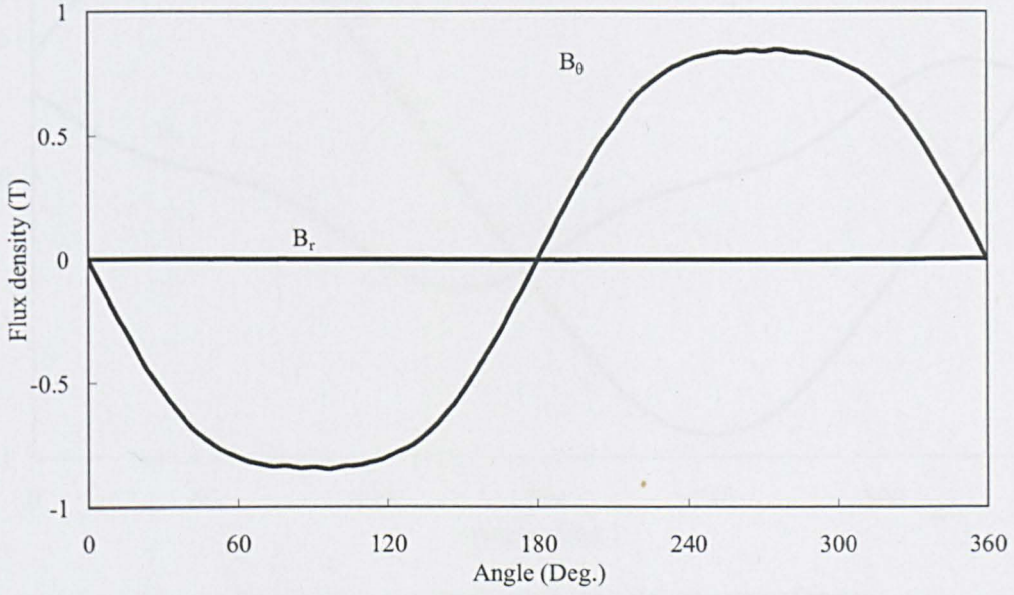

(i) Radial and circumferential flux density waveforms.

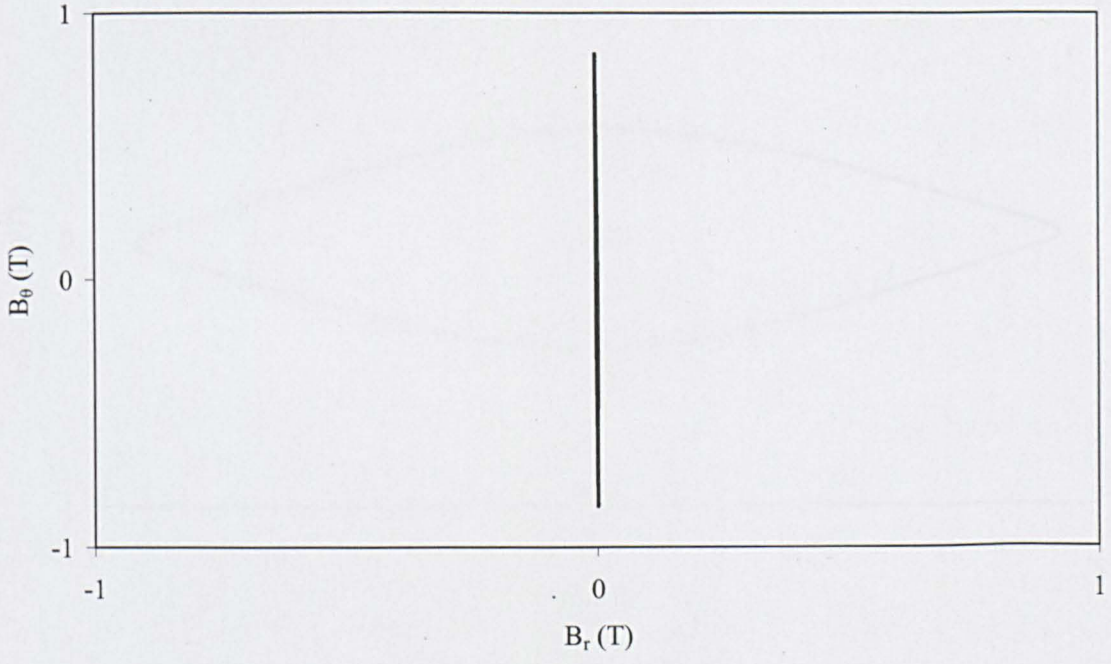

(ii) Flux density loci.

(a) In stator back-iron.

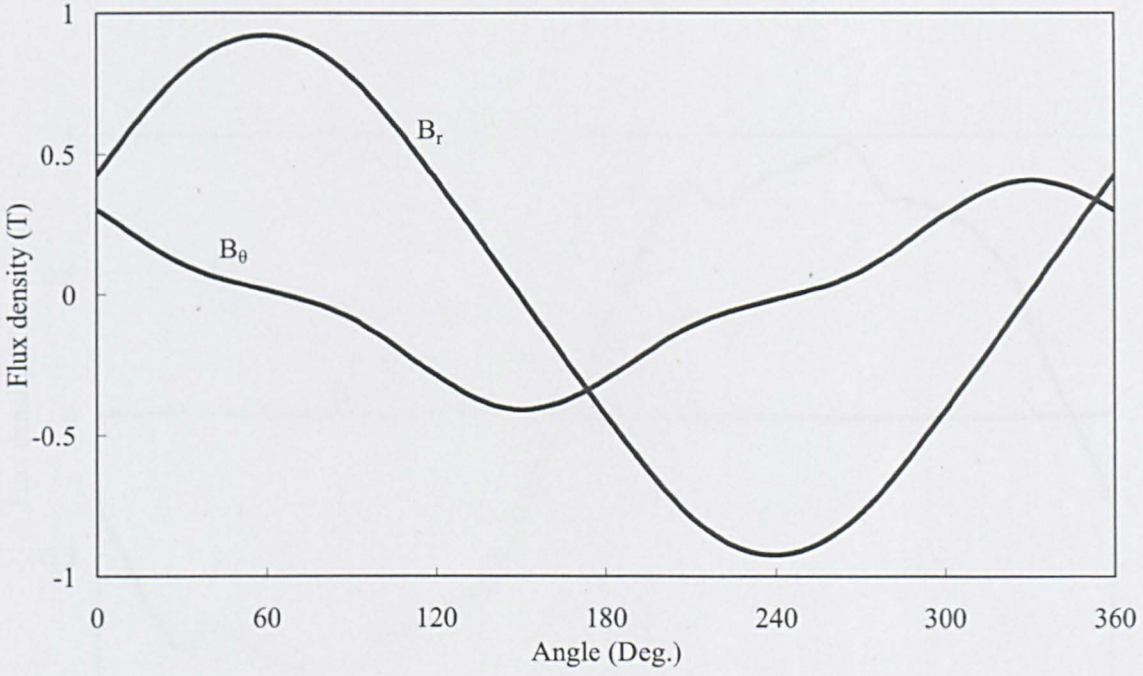

(i) Radial and circumferential flux density waveforms.

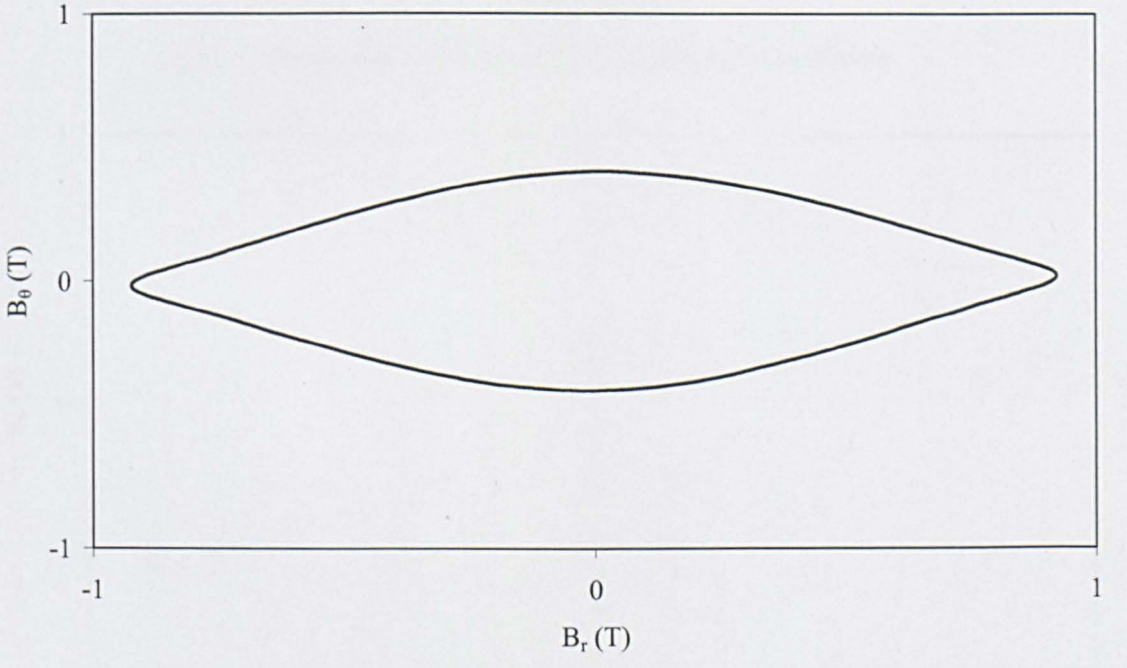

(ii) Flux density loci.

(b) In stator tooth.

Figure 2.10 Radial and circumferential flux density waveforms and resultant flux density loci under open circuit.

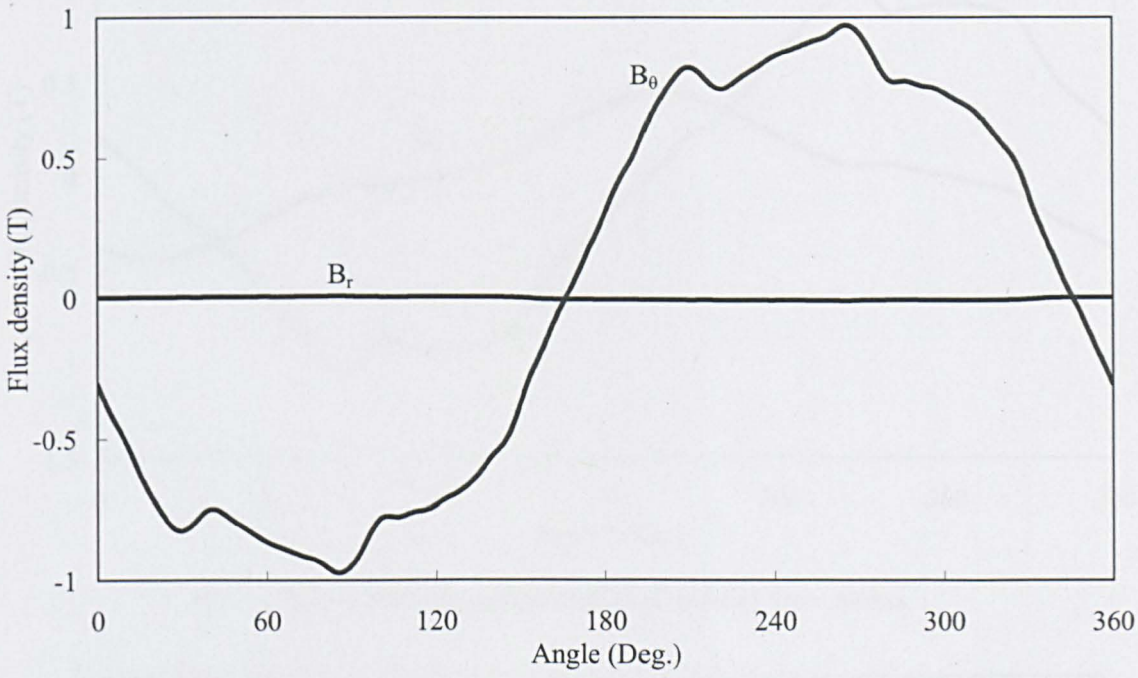

(i) Radial and circumferential flux density waveforms.

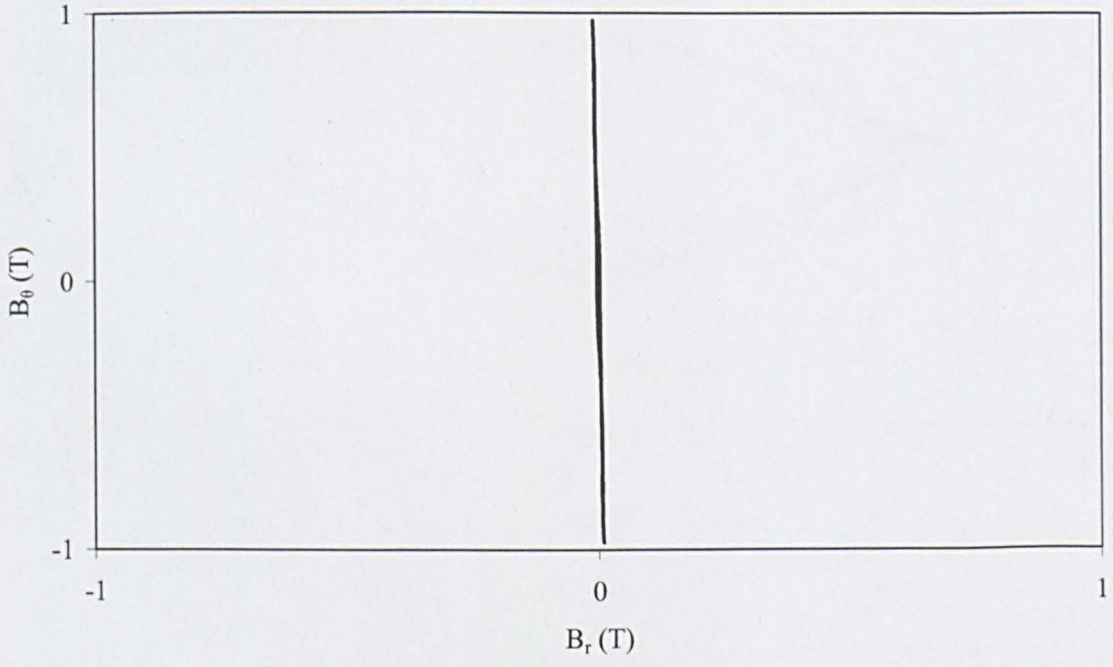

(ii) Flux density loci.

(a) In stator back-iron.

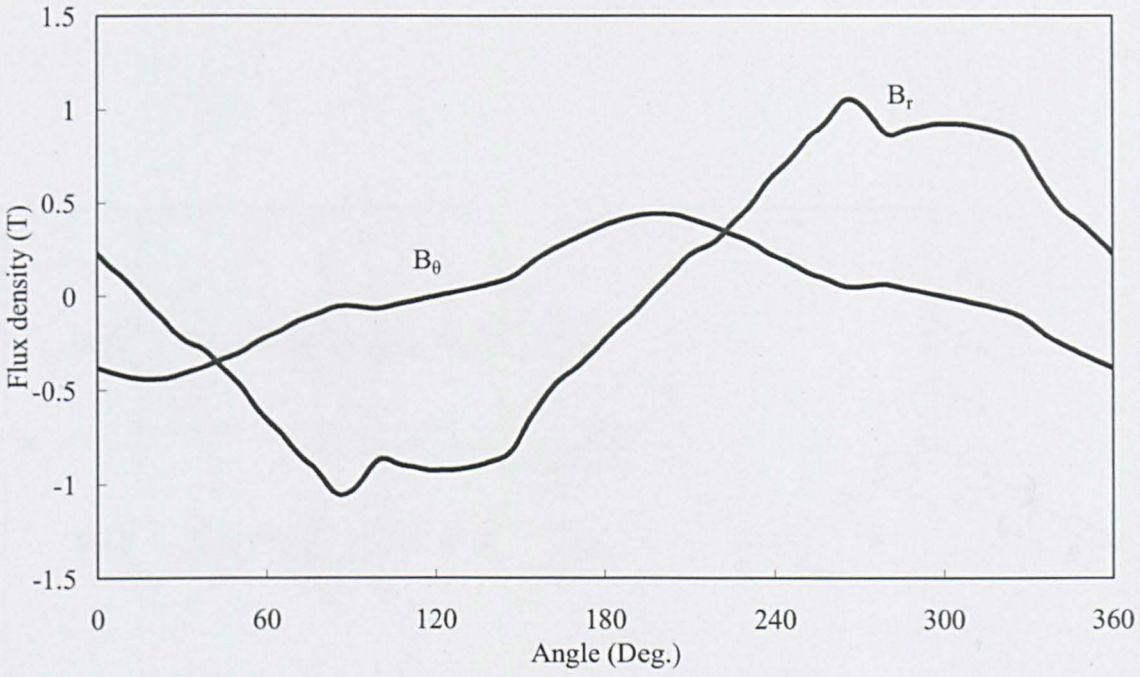

(i) Radial and circumferential flux density waveforms.

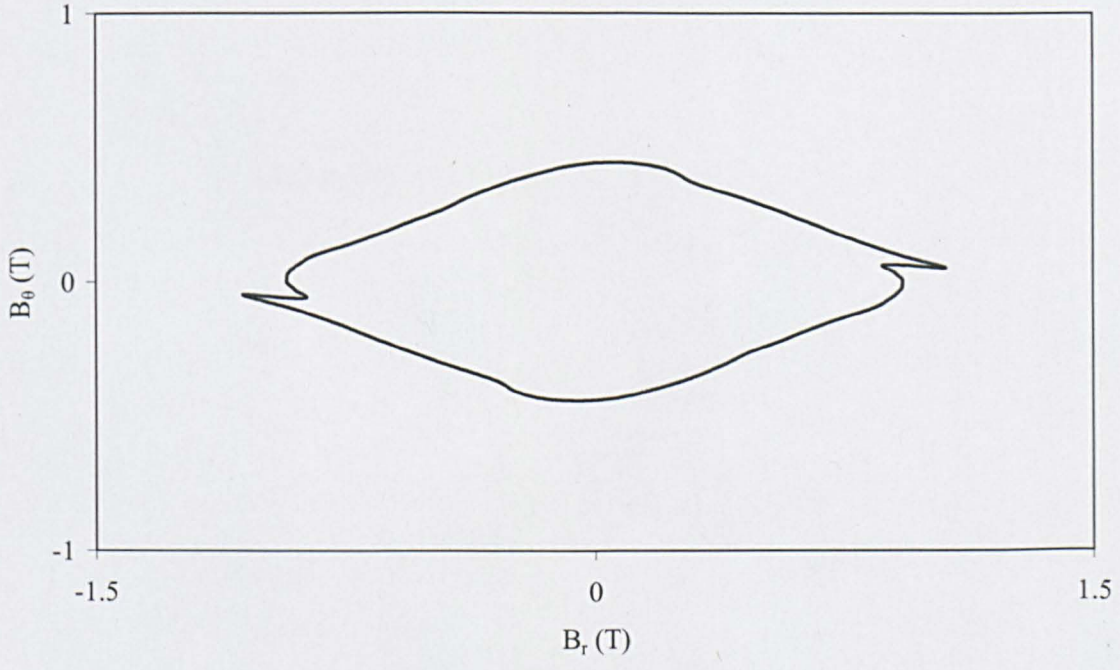

(ii) Flux density loci.

(b) In stator tooth.

Figure 2.11 Radial and circumferential flux density waveforms and resultant flux density loci at rated load.

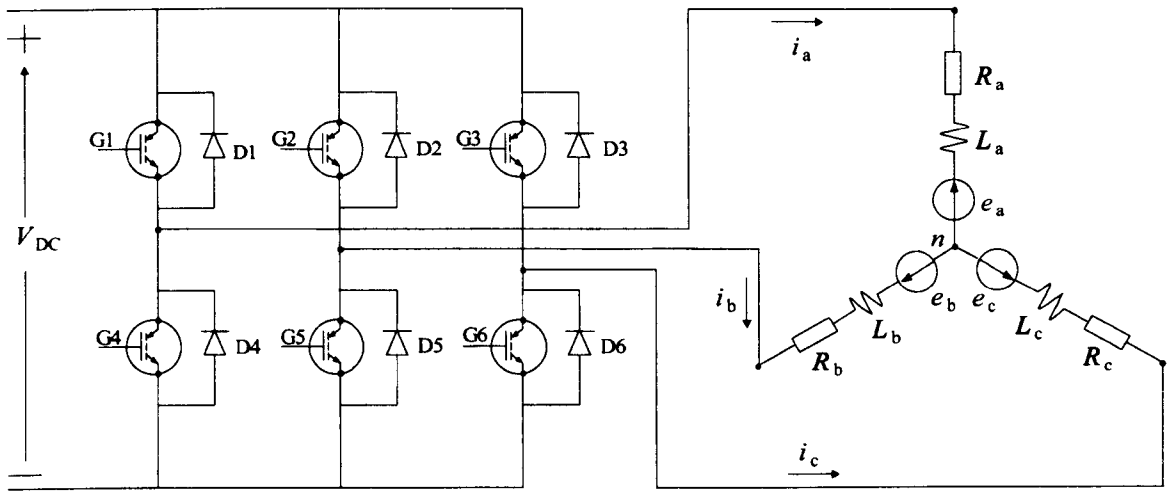

Figure 2.12 Circuit diagram of three-phase brushless PM motor drive system.

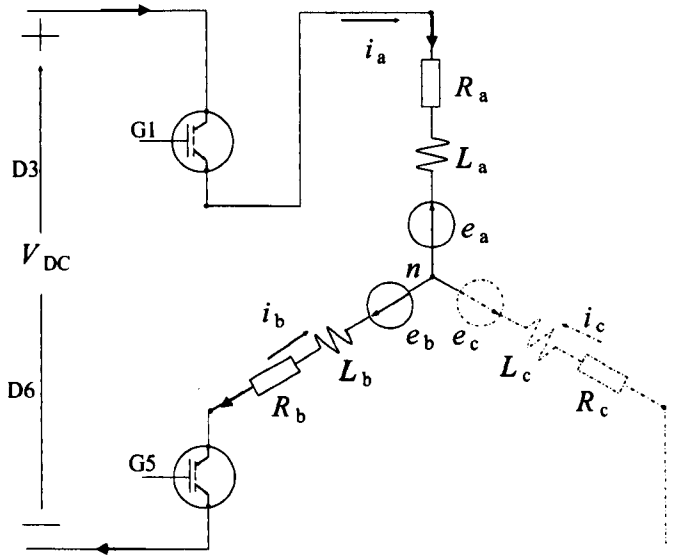

Figure 2.13 Circuit diagram of conduction mode.

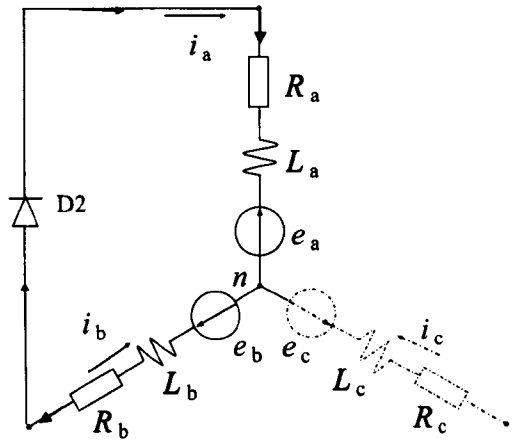

Figure 2.14 Circuit diagram of free-wheeling mode.

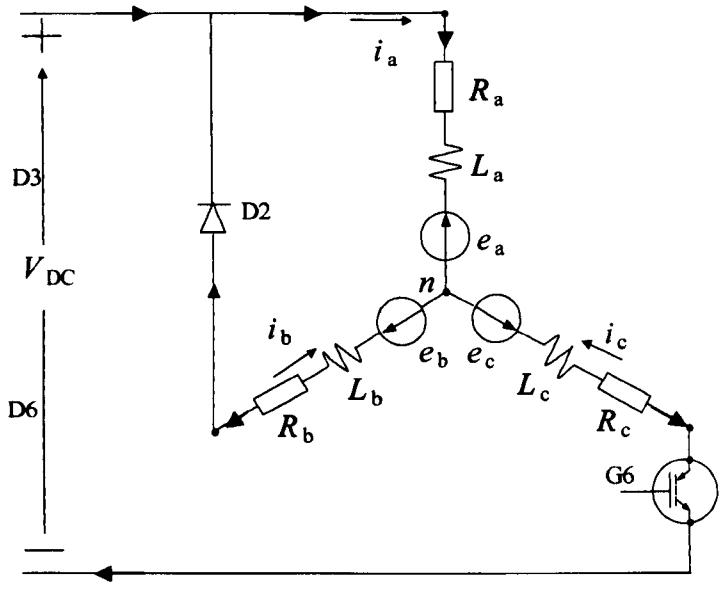

Figure 2.15 Circuit diagram of commutation mode.

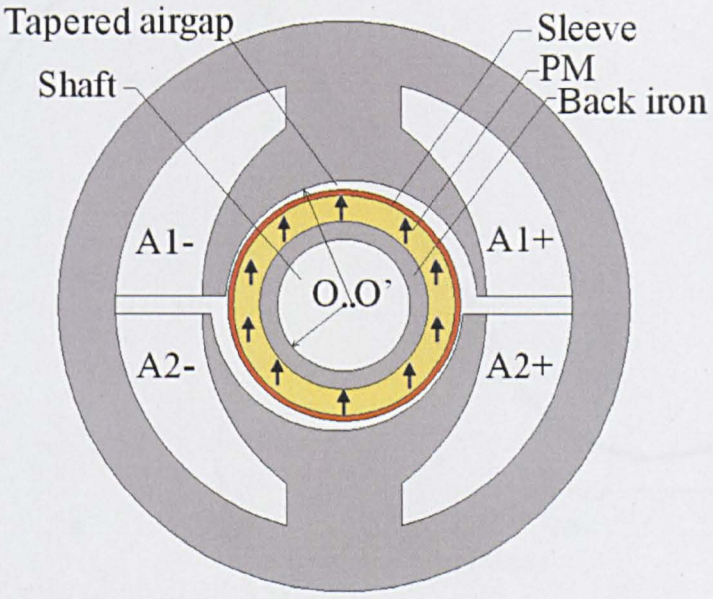

Figure 2.16 Cross-section of single-phase PM brushless DC motor with tapered airgap.

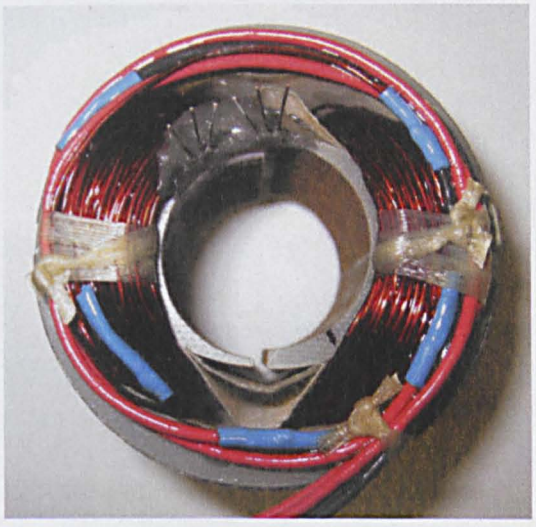

(a) Stator

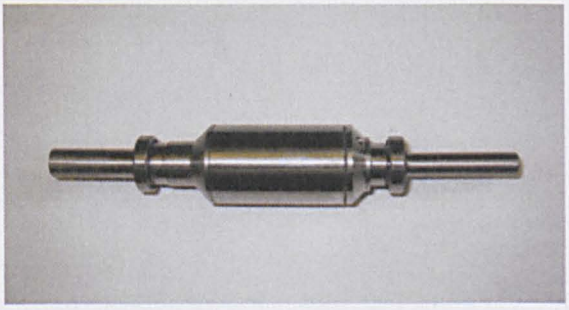

(b) Rotor

Figure 2.17 Prototype of single-phase PM brushless DC motor, **Design E.**

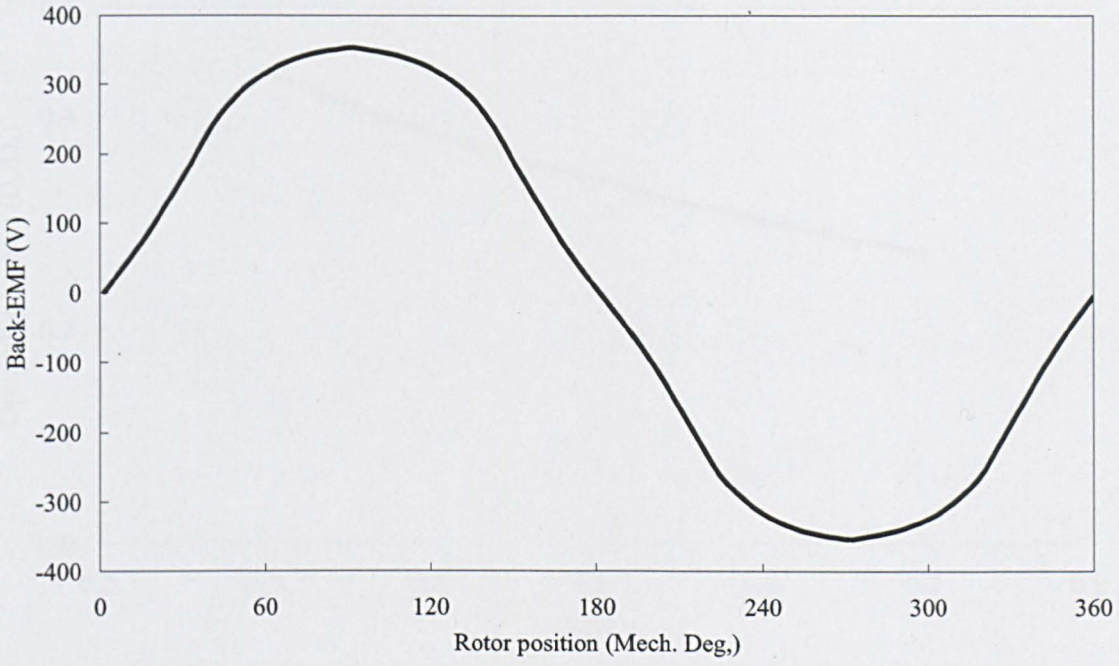

Figure 2.18 2D FEM predicted back-EMF of single-phase PM brushless DC motor having concentric airgap. (Speed=45,000rpm)

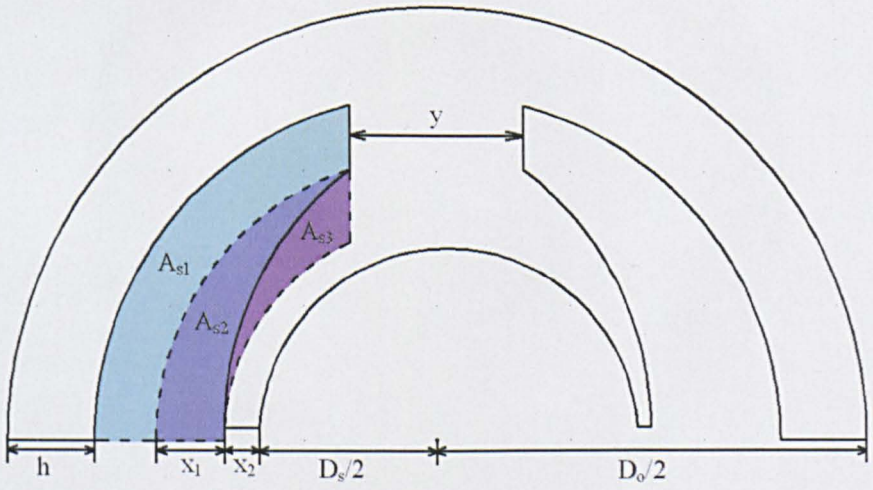

Figure 2.19 Stator illustration.

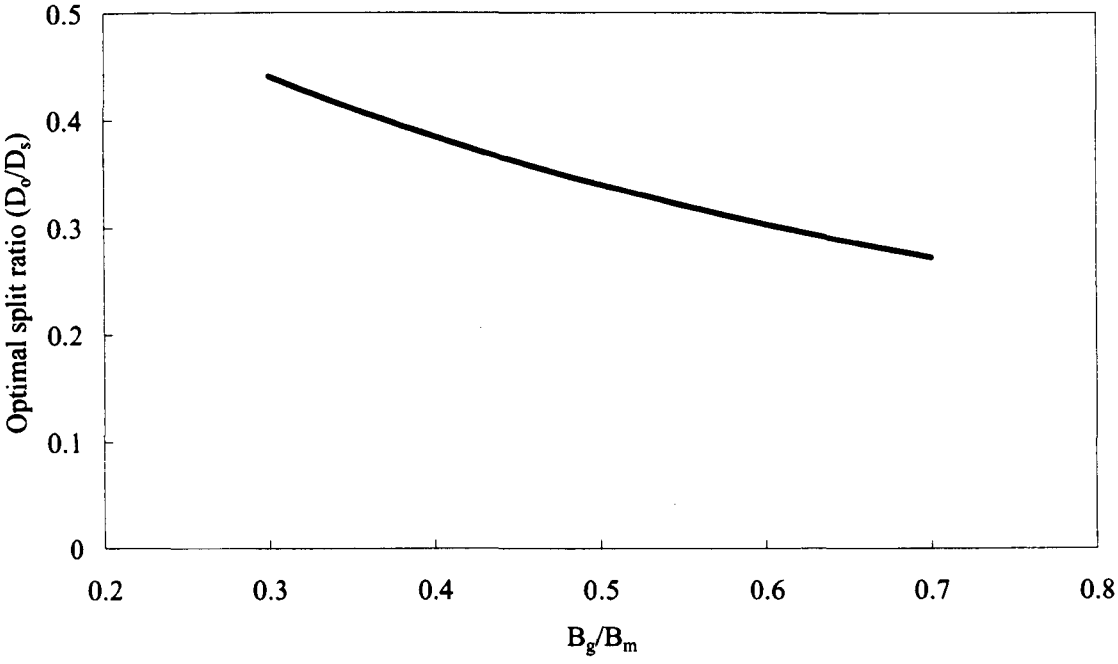

Figure 2.20 Variation of the optimal split ratio D_o / D_s with B_g / B_m.

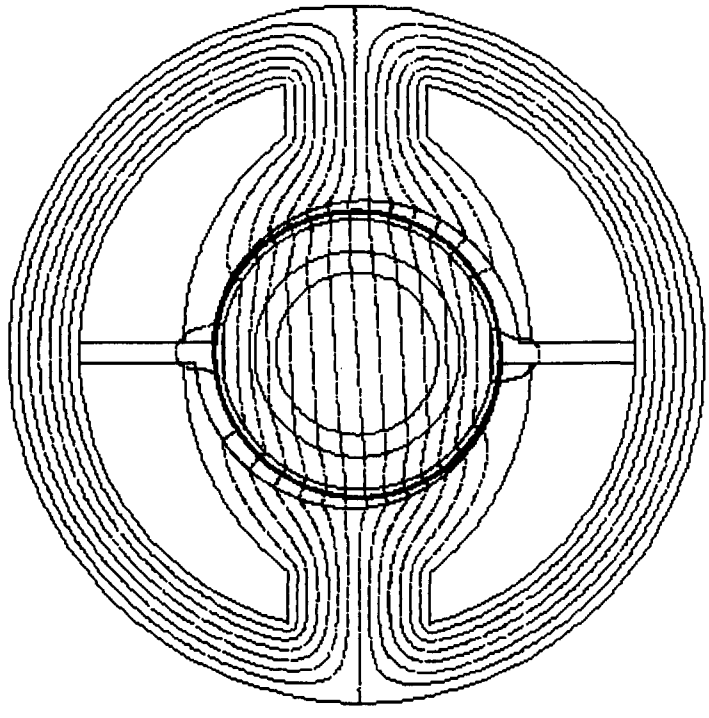

Figure 2.21 Open-circuit flux distribution of single-phase PM brushless DC motor. (Rotor position=0°_{mech})

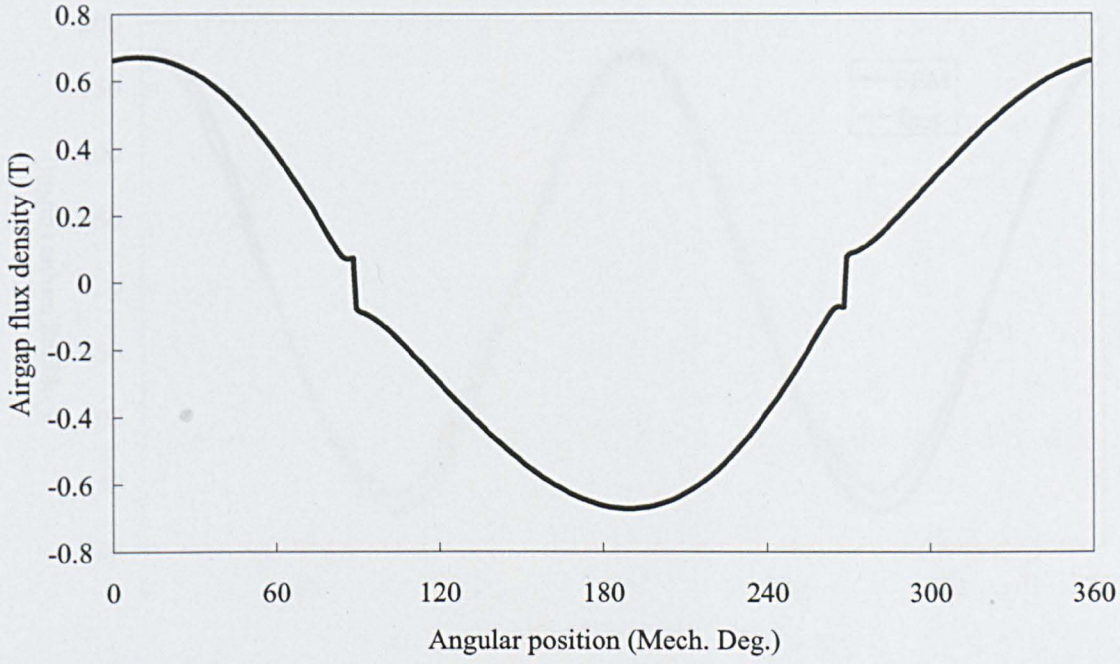

Figure 2.22 Open-circuit airgap flux density of single-phase PM brushless DC motor. (Rotor position=0^{o}_{mech})

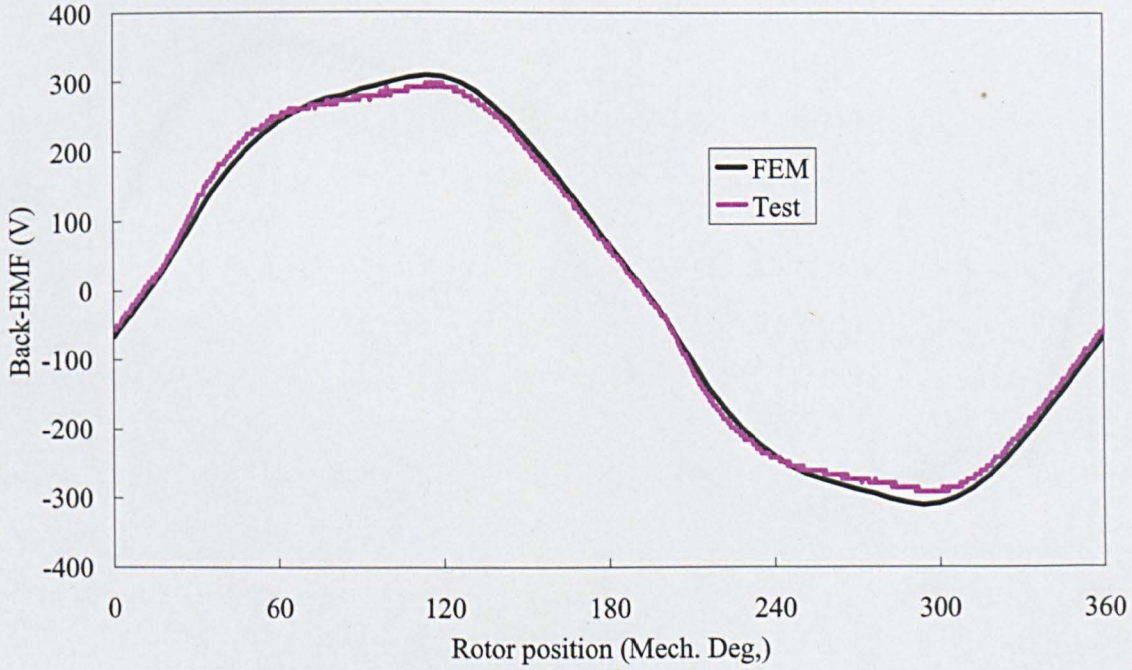

Figure 2.23 Back-EMF of single-phase PM brushless DC motor. (Speed=45,000rpm)

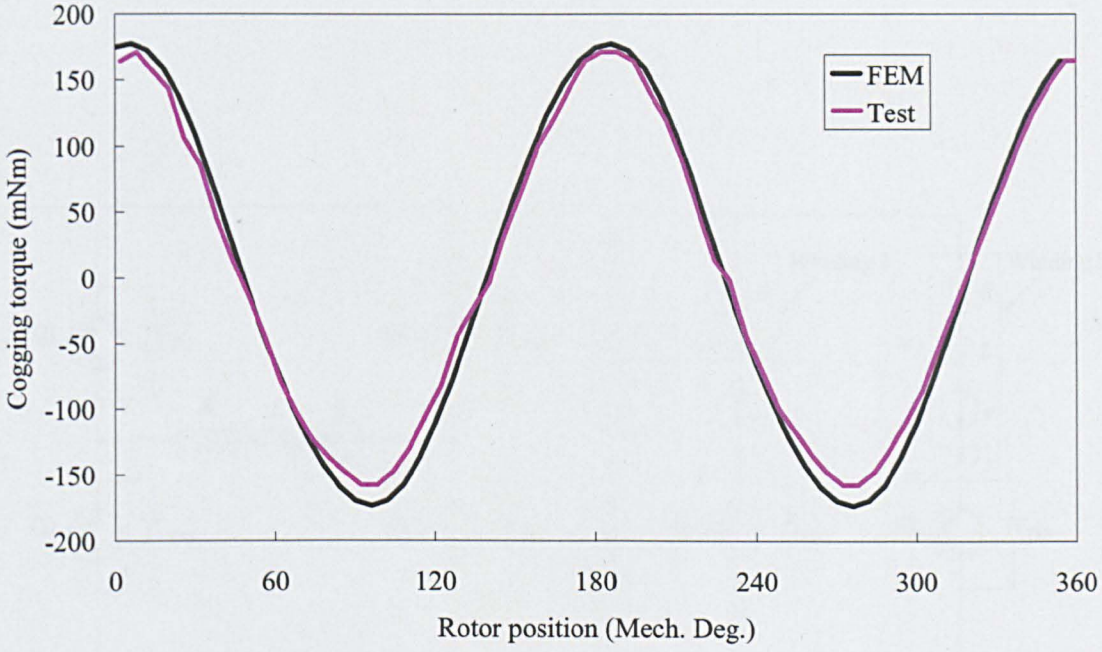

Figure 2.24 Cogging torque of single-phase PM brushless DC motor.

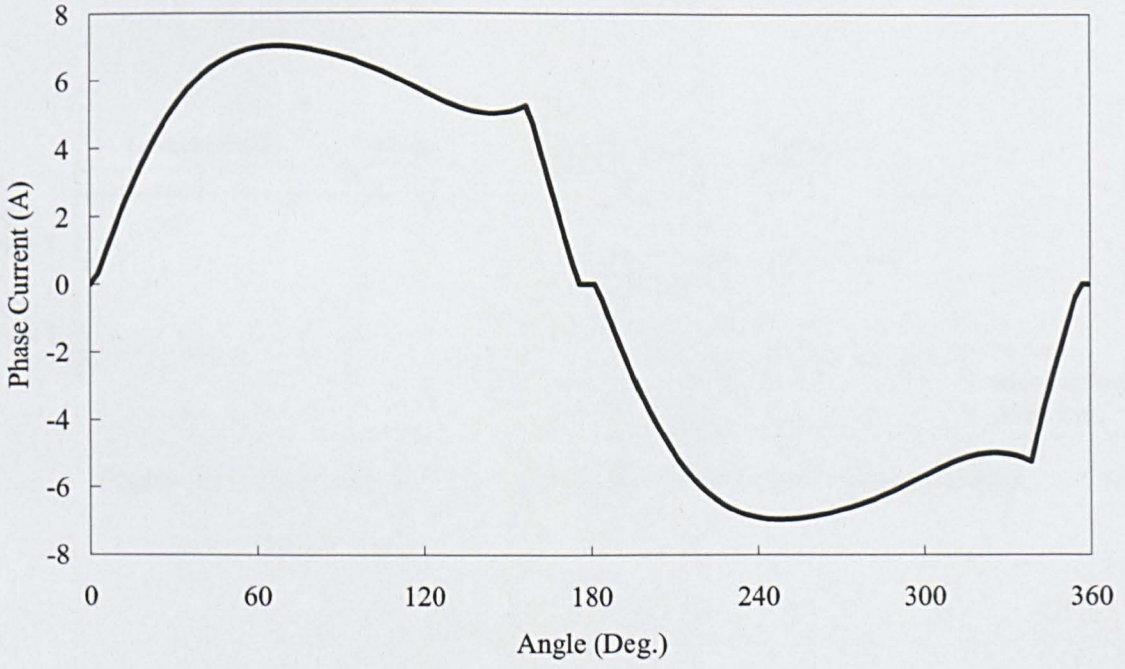

Figure 2.25 Simulated rated phase current. (Speed=45,000rpm)

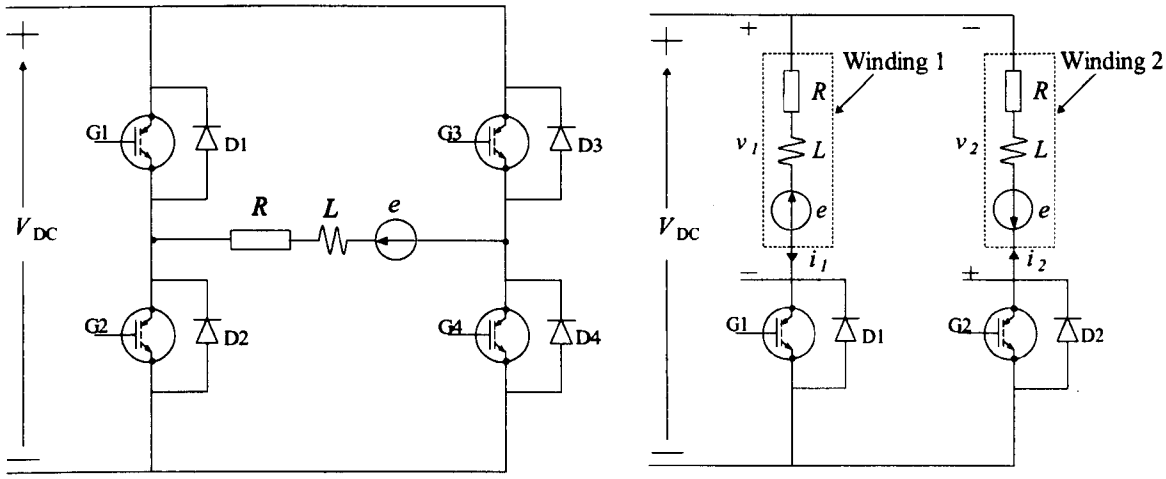

(a) Full-bridge inverter (b) Half-bridge inverter

Figure 2.26 Inverter circuits for single-phase PM brushless motor.

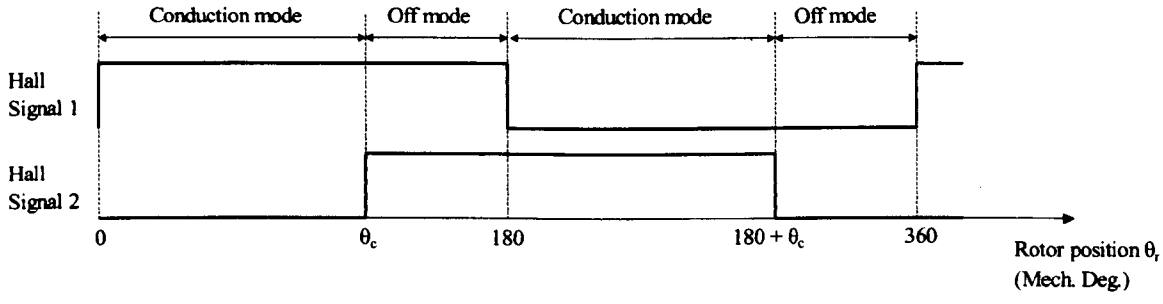

Figure 2.27 Illustration of Hall signal of single-phase PM brushless motors.

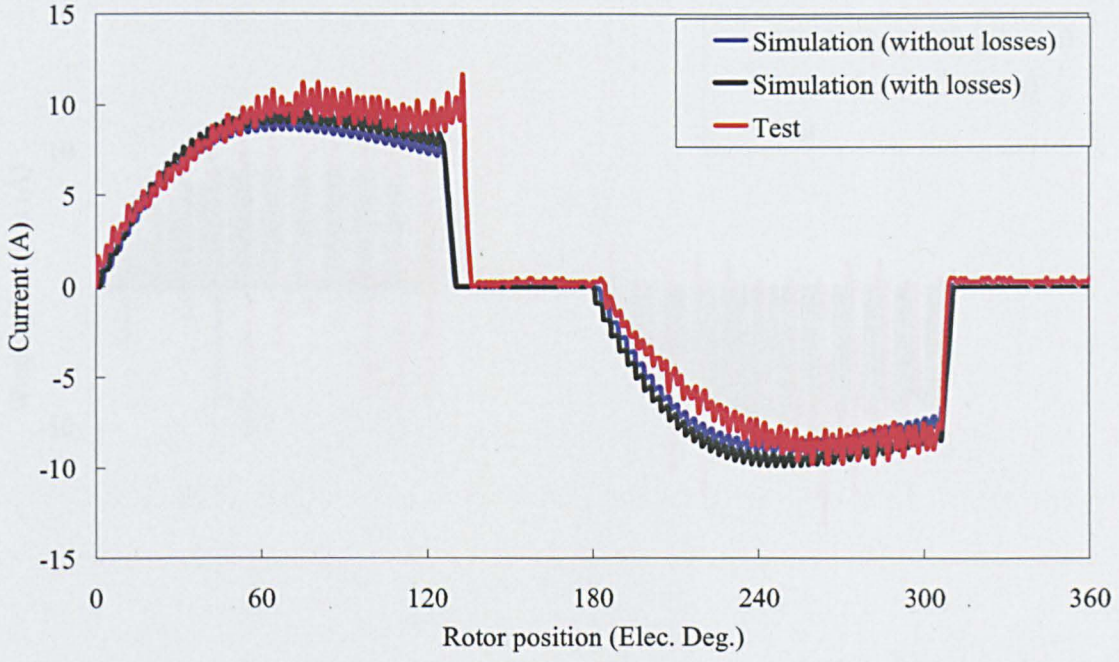

Figure 2.28 Tested and simulated phase current waveforms with full-bridge inverter under condition 1.

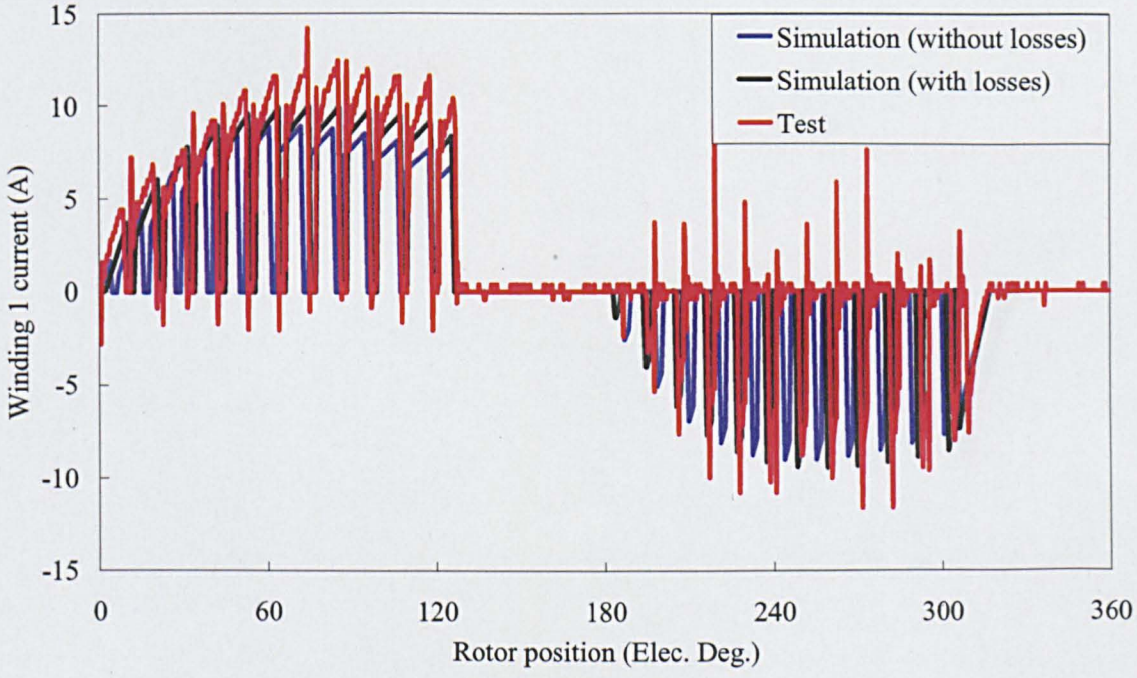

(a) Winding 1 current waveforms.

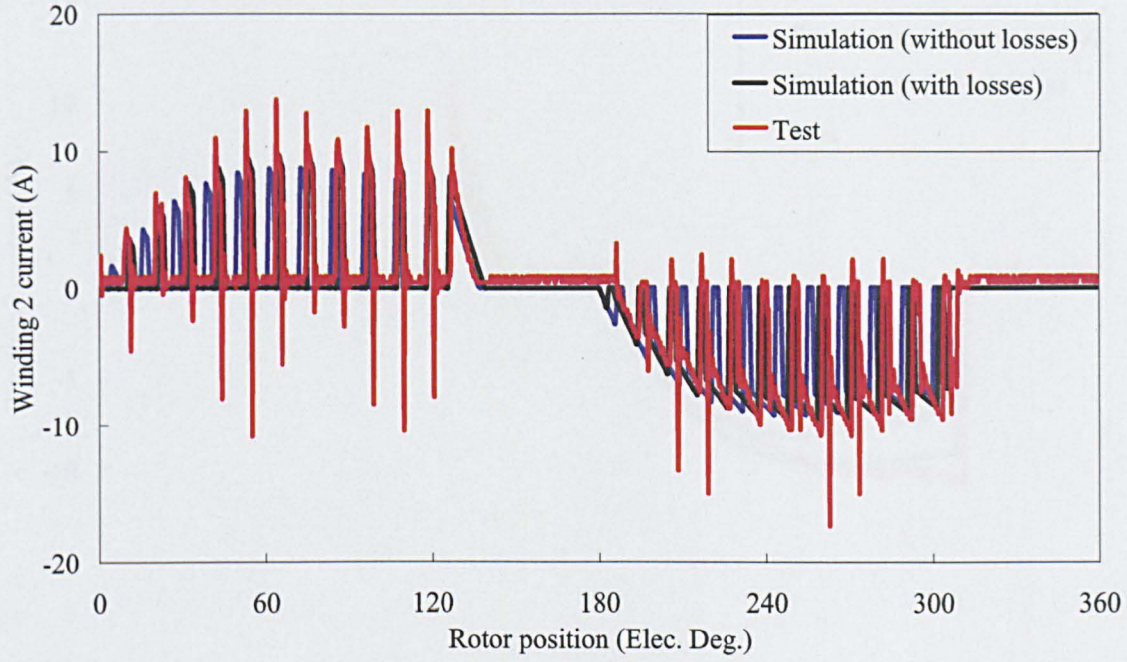

(b) Winding 2 current waveforms.

Figure 2.29 Tested and simulated phase current waveforms with half-bridge inverter under condition 2.

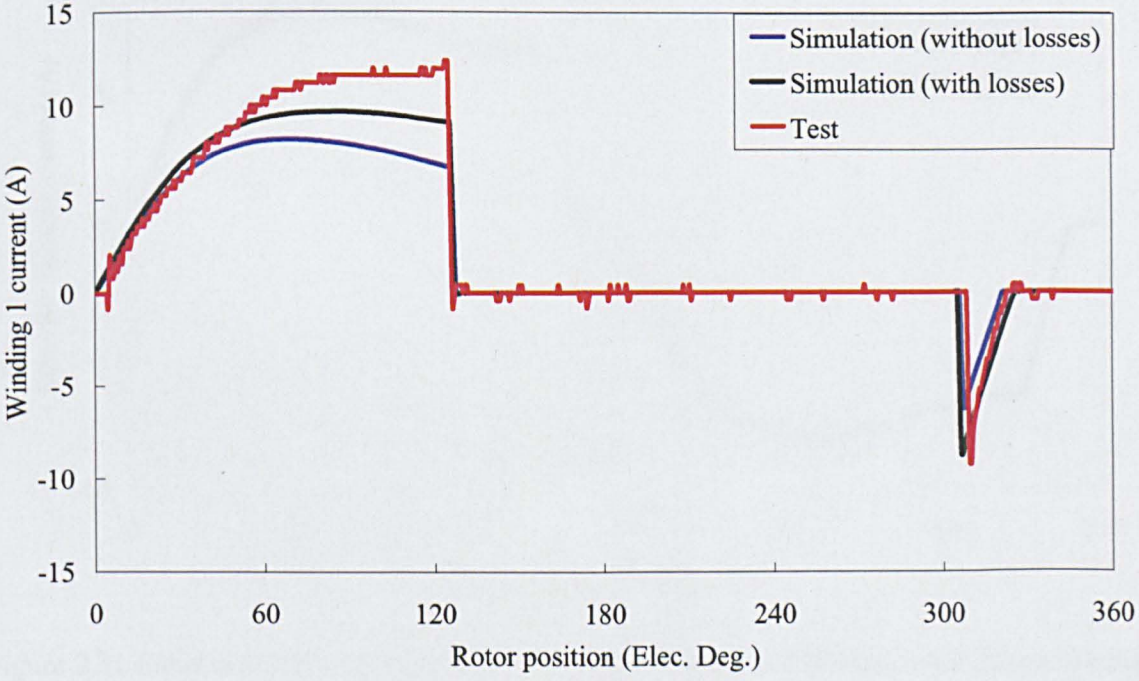

(a) Winding 1 current waveforms.

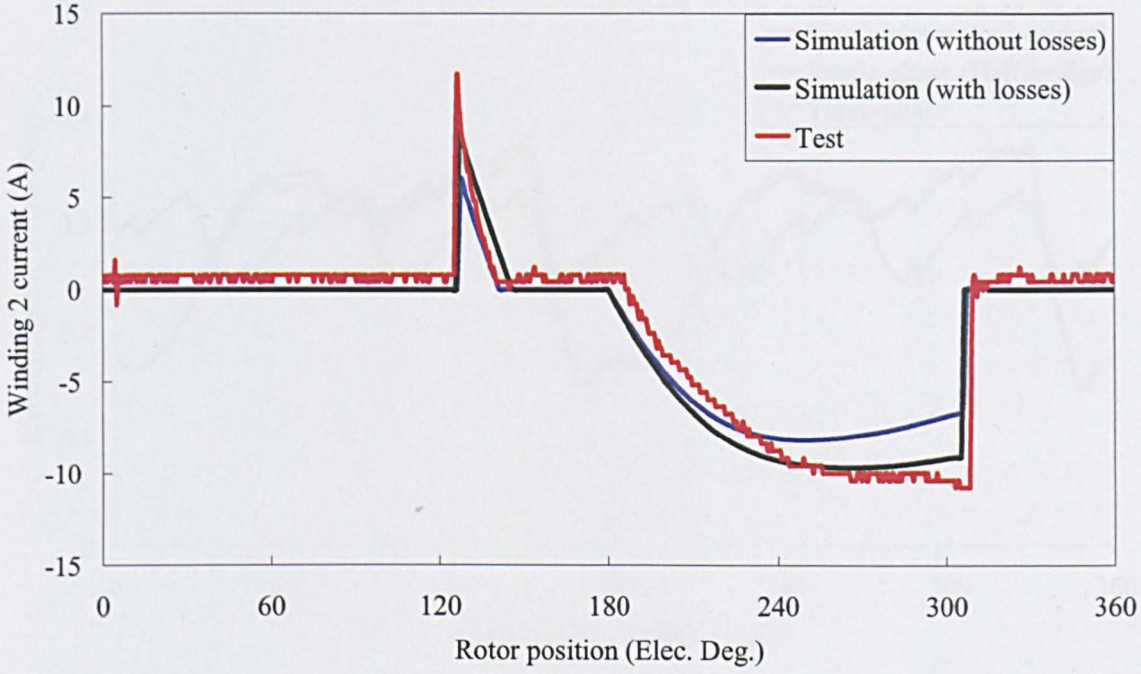

(b) Winding 2 current waveforms.

Figure 2.30 Tested and simulated phase current waveforms with half-bridge inverter under condition 3.

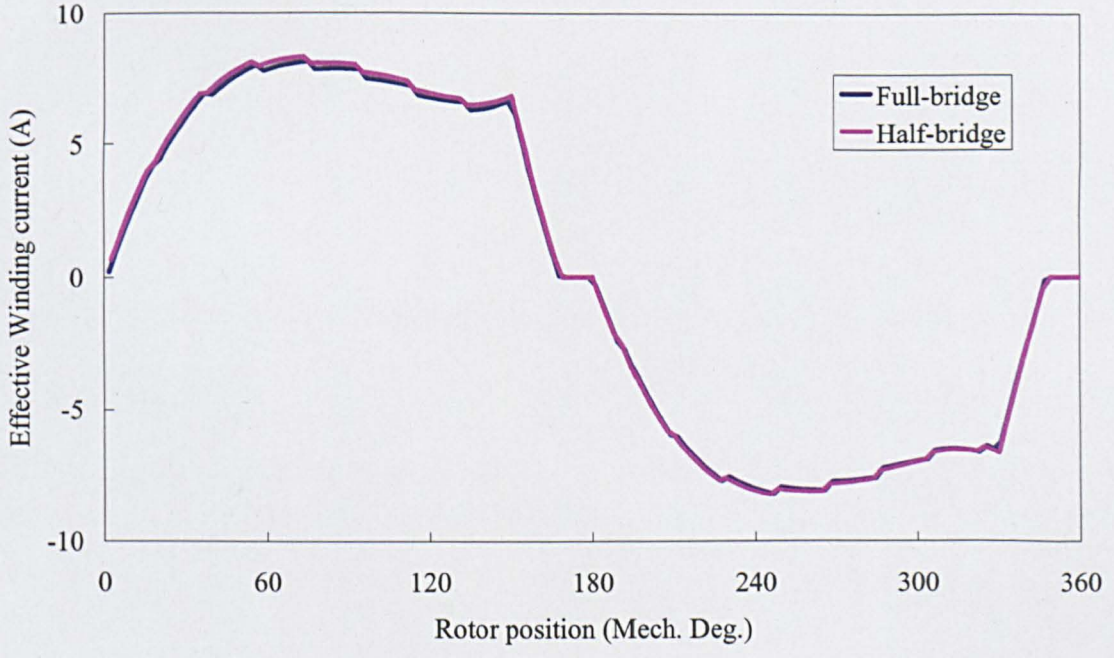

Figure 2.31 Simulated effective phase current of single-phase PM brushless DC motor at rated load(0.23Nm) and rated speed(45,000rpm).

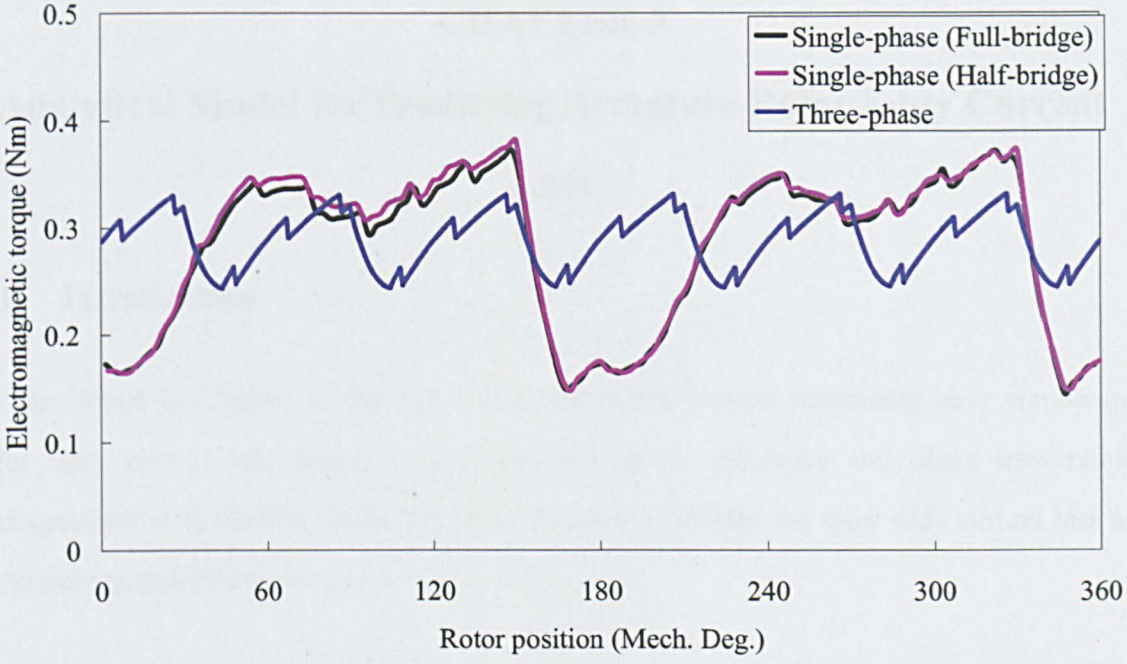

Figure 2.32 Simulated electromagnetic torque at rated load and rated speed.

CHAPTER 3

Analytical Model for Predicting Armature Rotor Eddy Current Loss

3.1 Introduction

As mentioned in Chapter 1, the high-speed PM BLDC motors potentially have significant rotor eddy current loss which may reduce the motor efficiency and cause irreversible demagnetisation of the PM. Therefore, it is necessary to predict the rotor eddy current loss as accurately as possible at the motor design stage.

For three-phase PM BLDC motors, the open-circuit rotor eddy current loss can usually be neglected due to the relatively small stator slotting and concentric airgap. Therefore, only rotor eddy current loss due to armature mmfs is calculated by analytical models and validated by FEM in this chapter.

As reviewed in section 1.4.2, various analytical models have been developed to calculate the armature rotor eddy current loss for three-phase PM BLDC motors. In this chapter, a static analytical model [69] and an improved analytical model [75] will be presented. Both static and improved models are formulated in the 2D polar coordinates which can account for the curvature effect. The winding current is represented by an equivalent current sheet distributed across the stator slot openings to account for the space and time harmonics of the stator mmfs. Further, the eddy current loss occurring in the conducting retained sleeve (if fitted) can be modelled as well. The improved analytical model can account for the influence of the eddy current reaction field on the armature rotor eddy current loss which is neglected in the static analytical model. Both analytical models predicted the armature rotor eddy current loss is compared to the FEM predicted results.

However, up to date, no paper has addressed the analytical model for single-phase PM BLDC.

In this chapter, a static and an improved analytical models are developed and presented for predicting the armature rotor eddy current loss in the single-phase PM BLDC motors having a concentric airgap.

However, in order to improve the starting capability and facilitate the unidirectional rotation in the single-phase PM motors, an eccentric airgap is usually employed, which makes above developed analytical model invalid. Due to its eccentric airgap, it is not convenient for analytical model to express the boundary condition at the interface between the stator inner bore and airgap in the 2D polar coordinates. Therefore, in this chapter FEM is proposed to calculate the boundary condition at the middle of the airgap by applying a unit (1A) current to the windings. Then further static and improved analytical models will be developed for calculating the armature rotor eddy current loss in the PM and the sleeve (if fitted) in the single-phase PM BLDC motors which has an eccentric airgap. Compared to the direct FEM, this method requires less time to calculate the armature rotor eddy current loss with acceptable accuracy.

3.2 Analytical model with equivalent current sheet

The time-varying magnetic field distribution in the rotor is required to predict the load eddy current loss. The 2D time-varying field is formulated in polar coordinates by assuming:

- End-effects are ignored, and the resulting eddy currents in the conductive regions flow in the axially-direction only.
- The winding current is represented by an equivalent current sheet of infinitesimal thickness distributed across the stator slot openings.
- The permeance variation due to stator slotting is neglected.
- The stator iron and rotor core are infinitely permeable and have zero electrical conductivity.
- The PM and the retaining sleeve are homogeneous and isotropic, and characterized by the constant relative recoil magnetic permeabilities, μ_m and μ_{sl}, and the constant

electrical conductivity, σ_m, and σ_{sl}.

3.2.1 Equivalent current sheet for 2-slot/2-pole single-phase motor

A single coil with N_c turns is wound around a single stator tooth, as shown in Figure 3.1, where α is with reference to a stationary reference frame, $\alpha = 0$ corresponds with the axis of the coil, i.e., midway between the two slot openings. The winding current can be represented by an equivalent current sheet of infinitesimal thickness distributed across the stator slot opening, i.e. b_o.

The equivalent current density distribution is given by:

$$J_s(\alpha) = \begin{cases} \dfrac{N_c i}{b_o}, & -\dfrac{\alpha_{cp}}{2} - \dfrac{b_o}{2R_s} \le \alpha \le -\dfrac{\alpha_{cp}}{2} + \dfrac{b_o}{2R_s} \\ 0, & -\dfrac{\alpha_{cp}}{2} + \dfrac{b_o}{2R_s} < \alpha < \dfrac{\alpha_{cp}}{2} - \dfrac{b_o}{2R_s} \\ -\dfrac{N_c i}{b_o}, & \dfrac{\alpha_{cp}}{2} - \dfrac{b_o}{2R_s} \le \alpha \le \dfrac{\alpha_{cp}}{2} + \dfrac{b_o}{2R_s} \end{cases} \quad \text{(A/m)} \qquad (3\text{-}1)$$

where N_c -- Number of turns per coil;

i -- Winding current; A

R_s -- Inner stator radius; m

α_{cp} -- Coil-pitch; $2\pi / N_s$

N_s -- Number of stator slots (in this case N_s=2).

Therefore, the Fourier series expansion is,

$$J_s(a) = \frac{a_0}{2} + \sum_{v}^{\infty} a_v \sin(v\alpha) + \sum_{v}^{\infty} b_v \cos(v\alpha) \qquad \text{(A/m)} \qquad (3\text{-}2)$$

Since the fundamental waveform of the current density sheet is sinusoidal and concentric

about $\alpha = 0^o$, the cosine terms b_v is zero, and the dc component $\frac{a_0}{2}$ is also zero. Thus, only the coefficients a_v of the sine terms of the Fourier series has to be determined,

$$\begin{aligned} a_v &= \frac{1}{\pi}\int_{-\pi}^{\pi} J_s \sin(v\alpha)d\alpha \\ &= \frac{N_c i}{b_0 \pi}\int_{\frac{\alpha_{cp}}{2}-\frac{b_o}{2R_s}}^{\frac{\alpha_{cp}}{2}+\frac{b_o}{2R_s}} \sin(v\alpha)d\alpha \\ &= \frac{4N_c i}{\pi b_o}\frac{1}{v}\sin\left(\frac{va_{cp}}{2}\right)\sin\left(\frac{vb_o}{2R_s}\right) \\ &= \frac{2N_c i}{\pi R_s}\frac{\sin\left(v\frac{b_o}{2R_s}\right)}{v\frac{b_o}{2R_s}}\sin\left(v\frac{a_{cp}}{2}\right) \\ &= \frac{2N_c i}{\pi R_s}K_{sov}K_{pv} \end{aligned} \tag{3-3}$$

Thus, the equivalent current density distribution is given by,

$$J_s(\alpha) = \frac{2N_c i}{\pi R_s}\sum_{v}^{\infty} K_{sov}K_{pv}\sin(v\alpha) \qquad \text{(A/m)} \tag{3-4}$$

where $K_{sov} = \sin\left(v\frac{b_o}{2R_s}\right)/\left(v\frac{b_o}{2R_s}\right)$ is the slot opening factor. $K_{pv} = \sin(va_{cp}/2)$ is the coil-pitch factor.

The phase current can be expressed as a Fourier series,

$$i(t) = \sum_{u}^{\infty} I_u \sin(up\omega_r t + \theta_u) \qquad \text{(A)} \tag{3-5}$$

where p -- Number of pole pairs (in this case $p = 1$);

ω_r -- Rotor angular velocity; rad/s

I_u -- Magnitude of u^{th} harmonic current; A

θ_u -- Angle of u^{th} harmonic current; rad

Substituting equation (3-5) into equation (3-4), the equivalent current sheet of N_c turns wound around a single stator tooth can be given by,

$$J_s(\alpha) = \frac{2N_c}{\pi R_s}\sum_u^{\infty} I_u \sum_v^{\infty} K_{sov}K_{pv}\sin(u\omega_r t + \theta_u)\sin(v\alpha)$$
$$= \sum_u^{\infty}\sum_v^{\infty} J_{uv}[\cos(u\omega_r t + \theta_u - v\alpha) - \cos(u\omega_r t + \theta_u + v\alpha)] \quad \text{(A/m)} \tag{3-6}$$

where $J_{uv} = \frac{2N_c}{\pi R_s} I_u K_{sov} K_{pv}$.

For the single-phase PM BLDC motor, each single stator tooth has N_c turns winding (i.e. the total number of turns per phase is $2N_c$ for a 2-slot/2-pole single-phase motor). Hence,

$$J_{uv} = \frac{2N_c}{\pi R_s} I_u K_{sov} K_{pv} = \frac{N_{ph}}{\pi R_s} I_u K_{sov} K_{pv} \tag{3-7}$$

where the number of turns of per phase $N_{ph} = 2N_c$.

According to equation (3-6), it can be noted that the equivalent current sheet has two components, corresponding to the forward and backward rotating harmonic mmfs, which exist simultaneously for a given time harmonic order, i.e. u, and spatial harmonic order, i.e. v. Among them, the asynchronous harmonic mmfs with the rotor can induce the eddy current loss in the rotor.

3.2.2 Equivalent current sheet for 3-slot/2-pole three-phase motor

Based on the previous section, the equivalent current sheet for 3-slot/2-pole three-phase winding currents, as shown in Figure 3.2, can be expressed by,

$$J_{s\_a}(\alpha) = \frac{2N_c i_a}{\pi R_s}\sum_v^{\infty} K_{sov}K_{pv}\sin(v\alpha) \quad \text{(A/m)} \tag{3-8}$$

$$J_{s\_b}(\alpha)=\frac{2N_c i_b}{\pi R_s}\sum_{v}^{\infty}K_{sov}K_{pv}\sin\left[v\left(\alpha-\frac{2\pi}{3}\right)\right] \quad \text{(A/m)} \tag{3-9}$$

$$J_{s\_c}(\alpha)=\frac{2N_c i_c}{\pi R_s}\sum_{v}^{\infty}K_{sov}K_{pv}\sin\left[v\left(\alpha+\frac{2\pi}{3}\right)\right] \quad \text{(A/m)} \tag{3-10}$$

The phase current can be expressed as a Fourier series:

$$i_a(t)=\sum_{u}^{\infty}I_u\sin(u\omega_r t+\theta_u) \quad \text{(A)} \tag{3-11}$$

$$i_b(t)=\sum_{u}^{\infty}I_u\sin\left[u\left(\omega_r t-\frac{2\pi}{3}\right)+\theta_u\right] \quad \text{(A)} \tag{3-12}$$

$$i_c(t)=\sum_{u}^{\infty}I_u\sin\left[u\left(p_r\omega_r t+\frac{2\pi}{3}\right)+\theta_u\right] \quad \text{(A)} \tag{3-13}$$

Therefore, the equivalent current sheet can be written by,

$$\begin{aligned}J_s(\alpha)&=J_{s\_a}(\alpha)+J_{s\_b}(\alpha)+J_{s\_c}(\alpha)\\&=\begin{cases}\sum_{u}^{\infty}\sum_{v}^{\infty}J_{uv}\cos(u\omega_r t-v\alpha+\theta_u), & v-u=3c,c=0,\pm1,\pm2\cdots\\-\sum_{u}^{\infty}\sum_{v}^{\infty}J_{uv}\cos(u\omega_r t+v\alpha+\theta_u), & v+u=3c,c=0,\pm1,\pm2\cdots\end{cases}\end{aligned} \quad \text{(A/m)} \tag{3-14}$$

where $J_{uv}=\frac{3N_c}{\pi R_s}I_u K_{sov}K_{pv}$.

For 3-slot/2-pole three-phase PM BLDC motors, the number of series turns per phase $N_{ph}=N_c$. Hence,

$$J_{uv}=\frac{3N_{ph}}{\pi R_s}I_u K_{sov}K_{pv} \tag{3-15}$$

Compared to the equivalent current sheet for single-phase PM BLDC motors, the equivalent current sheet for three-phase PM BLDC motors also has two components, corresponding to the forward and backward harmonic mmfs. However, only one of components exists as determined by the time and spatial harmonic order.

3.3 Analytical model for three-phase PM BLDC motors

3.3.1 Static analytical model

In addition to the assumptions made in section 3.2, in order to simplify the analysis, the relative recoil permeability of the PM and the retaining sleeve are $\mu_m = 1$ and $\mu_{sl} = 1$, respectively.

By neglecting the eddy current reaction field in the magnet and the retained sleeve, in terms of the magnetic vector potential A, the Laplace's equation which governs the armature reaction field in the airgap, magnet and sleeve regions, as,

$$\nabla^2 A = 0 \tag{3-16}$$

Its general solution is

$$A = \sum_{\nu}^{\infty} \left(C_\nu r^\nu + D_\nu r^{-\nu} \right) \cos(\nu\alpha) \qquad \text{(A/m)} \tag{3-17}$$

where C_ν and D_ν are constants to be determined for the boundary conditions.

The radial and circumferential components of the armature reaction field can be derived from A as,

$$B_r = \frac{1}{r}\frac{\partial A}{\partial \alpha} \qquad \text{(T)} \tag{3-18}$$

$$B_\alpha = -\frac{\partial A}{\partial r} \qquad \text{(T)} \tag{3-19}$$

By assuming both the stator and rotor irons to be infinitely permeable, the boundary conditions are given by,

$$\text{At } r = R_s \quad H_\alpha\big|_{r=R_s} = J_s(\alpha) \qquad \text{(A/m)} \tag{3-20}$$

$$\text{At } r = R_r \quad B_\alpha\big|_{r=R_r} = 0 \qquad \text{(T)} \tag{3-21}$$

According to equations (3-14) and (3-17) to (3-21), the analytical expressions for the

magnetic vector potential can be derived as:

$$A(r,\alpha,t)=$$

$$\begin{cases} -\mu_0\sum_u^{\infty}\sum_v^{\infty}\dfrac{J_{uv}R_s^{-v+1}}{G_v v}\left(r^v+R_r^{2v}r^{-v}\right)\cos(u\omega_r t+\theta_u-v\alpha), & v-u=3c, c=0,\pm1,\pm2\cdots \\ \mu_0\sum_u^{\infty}\sum_v^{\infty}\dfrac{J_{uv}R_s^{-v+1}}{G_v v}\left(r^v+R_r^{2v}r^{-v}\right)\cos(u\omega_r t+\theta_u+v\alpha), & v+u=3c, c=0,\pm1,\pm2\cdots \end{cases} \quad (3\text{-}22)$$

The radial and circumferential component of flux density is:

$$B_r(r,\alpha,t)=$$

$$\begin{cases} -\mu_0\sum_u^{\infty}\sum_v^{\infty}\dfrac{J_{uv}R_s^{-v+1}}{G_v}\left(r^{v-1}+R_r^{2v}r^{-v-1}\right)\sin(u\omega_r t+\theta_u-v\alpha), & v-u=3c, c=0,\pm1,\pm2\cdots \\ -\mu_0\sum_u^{\infty}\sum_v^{\infty}\dfrac{J_{uv}R_s^{-v+1}}{G_v}\left(r^{v-1}+R_r^{2v}r^{-v-1}\right)\sin(u\omega_r t+\theta_u+v\alpha), & v+u=3c, c=0,\pm1,\pm2\cdots \end{cases} \quad (3\text{-}23)$$

$$B_\alpha(r,\alpha,t)=$$

$$\begin{cases} \mu_0\sum_u^{\infty}\sum_v^{\infty}\dfrac{J_{uv}R_s^{-v+1}}{G_v}\left(r^{v-1}-R_r^{2v}r^{-v-1}\right)\cos(u\omega_r t+\theta_u-v\alpha), & v-u=3c, c=0,\pm1,\pm2\cdots \\ -\mu_0\sum_u^{\infty}\sum_v^{\infty}\dfrac{J_{uv}R_s^{-v+1}}{G_v}\left(r^{v-1}-R_r^{2v}r^{-v-1}\right)\cos(u\omega_r t+\theta_u+v\alpha), & v+u=3c, c=0,\pm1,\pm2\cdots \end{cases} \quad (3\text{-}24)$$

where $G_v=1-\left(\dfrac{R_r}{R_s}\right)^{2v}$.

In order to determine the induced eddy currents and the associated loss in the rotor, the above analytical expressions for the equivalent current sheet and magnetic vector potential have to be transformed from the stationary reference frame α to the rotating reference frame θ with the transformation $\alpha=\theta+\omega_r t$. Hence,

$$J_s(\theta)=\begin{cases} \sum_u^{\infty}\sum_v^{\infty}J_{uv}\cos[(u-v)\omega_r t+\theta_u-v\theta], & v-u=3c, c=0,\pm1,\pm2\cdots \\ -\sum_u^{\infty}\sum_v^{\infty}J_{uv}\cos[(u+v)\omega_r t+\theta_u+v\theta], & v+u=3c, c=0,\pm1,\pm2\cdots \end{cases} \quad \text{(A/m)} \quad (3\text{-}25)$$

$$A(r,\theta,t)=$$

$$\begin{cases} -\mu_0\sum_u^{\infty}\sum_v^{\infty}\dfrac{J_{uv}R_s^{-v+1}}{G_v v}\left(r^v+R_r^{2v}r^{-v}\right)\cos[(u-v)\omega_r t+\theta_u-v\theta], & v-u=3c, c=0,\pm1,\pm2\cdots \\ \mu_0\sum_u^{\infty}\sum_v^{\infty}\dfrac{J_{uv}R_s^{-v+1}}{G_v v}\left(r^v+R_r^{2v}r^{-v}\right)\cos[(u+v)\omega_r t+\theta_u+v\theta], & v+u=3c, c=0,\pm1,\pm2\cdots \end{cases}$$

(3-26)

The induced eddy current density in the PM and the retaining sleeve due to the time-varying armature reaction field can be calculated by

$$J_m(r,\theta,t) = -\sigma_m \frac{\partial A(r,\theta,t)}{\partial t} + C_m(t) \qquad (\mathrm{A/m^2}) \tag{3-27}$$

$$J_{sl}(r,\theta,t) = -\sigma_{sl} \frac{\partial A(r,\theta,t)}{\partial t} + C_{sl}(t) \qquad (\mathrm{A/m^2}) \tag{3-28}$$

where C_m and C_{sl} are the integration constant which ensure that the net total current flowing in each magnet segment and the sleeve to be zero at any instant, respectively, i.e.

$$\int_{R_r}^{R_m} \int_{-\frac{\alpha_p}{2}}^{\frac{\alpha_p}{2}} J_m r dr d\theta = 0 \tag{3-29}$$

$$\int_{R_m}^{R_{sl}} \int_{-\pi}^{\pi} J_{sl} r dr d\theta = 0 \tag{3-30}$$

where R_r, R_m and R_{sl} are the magnet inner radius, the magnet outer radius and the retaining sleeve outer radius, respectively. α_p is the pole-arc of the per magnet segment and is given by,

$$\alpha_p = \frac{2\pi}{N} \tag{3-31}$$

where N is the number of magnet segments.

From equations (3-26) to (3-28):

$$-\sigma_m \frac{\partial A(r,\theta,t)}{\partial t} =$$

$$\begin{cases} -\sigma_m \omega_r \mu_0 \sum_u^{\infty} \sum_v^{\infty} (u-v) \frac{J_{uv} R_s^{-v+1}}{G_v v} \left(r^v + R_r^{2v} r^{-v}\right) & v-u = 3c, c = 0, \pm 1, \pm 2 \cdots \\ \sin\left[(u-v)\omega_r t - v\theta + \theta_u\right], & \\ \sigma_m \omega_r \mu_0 \sum_u^{\infty} \sum_v^{\infty} (u+v) \frac{J_{uv} R_s^{-v+1}}{G_v v} \left(r^v + R_r^{2v} r^{-v}\right) & v+u = 3c, c = 0, \pm 1, \pm 2 \cdots \\ \sin\left[(u+v)\omega_r t + v\theta + \theta_u\right], & \end{cases} \tag{3-32}$$

$$-\sigma_{sl}\frac{\partial A(r,\theta,t)}{\partial t}=$$

$$\begin{cases} -\sigma_{sl}\omega_r\mu_0\sum_u^{\infty}\sum_v^{\infty}(u-v)\dfrac{J_{uv}R_s^{-v+1}}{G_v v}\left(r^v+R_r^{2v}r^{-v}\right) & v-u=3c, c=0,\pm1,\pm2\cdots \\ \sin[(u-v)\omega_r t-v\theta+\theta_u], & \\ \sigma_{sl}\omega_r\mu_0\sum_u^{\infty}\sum_v^{\infty}(u+v)\dfrac{J_{uv}R_s^{-v+1}}{G_v v}\left(r^v+R_r^{2v}r^{-v}\right) & v+u=3c, c=0,\pm1,\pm2\cdots \\ \sin[(u+v)\omega_r t+v\theta+\theta_u], & \end{cases} \tag{3-33}$$

Hence, according to equations (3-27) and (3-30), the integration constant $C_{sl}(t)=0$ and the integration constant C_m can be given by,

- If $N=1, C_m=0$
- If $N>1$,

$$C_m=\begin{cases} \dfrac{2N\sigma_m\omega_r\mu_0}{\pi\left(R_m^2-R_r^2\right)}\sum_u^{\infty}\sum_v^{\infty}\dfrac{J_{uv}R_s^{-v+1}}{G_v v^2}\left[\dfrac{R_m^{v+2}-R_r^{v+2}}{v+2}+R_r^{2v}E_{pmv}\right] & v-u=3c, c=0,\pm,\pm2\cdots \\ (u-v)\sin\left(v\dfrac{\pi}{N}\right)\sin[(u-v)\omega_r t+\theta_u], & \\ \dfrac{-2N\sigma_m\omega_r\mu_0}{\pi\left(R_m^2-R_r^2\right)}\sum_u^{\infty}\sum_v^{\infty}\dfrac{J_{uv}R_s^{-v+1}}{G_v v^2}\left[\dfrac{R_m^{v+2}-R_r^{v+2}}{v+2}+R_r^{2v}E_{pmv}\right] & v+u=3c, c=0,\pm,\pm2\cdots \\ (u+v)\sin\left(v\dfrac{\pi}{N}\right)\sin[(u+v)\omega_r t+\theta_u], & \end{cases}$$

where

$$E_{pmv}=\begin{cases} \ln\left(\dfrac{R_m}{R_r}\right), & v=2 \\ \dfrac{R_m^{-v+2}-R_r^{-v+2}}{-v+2} & v\neq 2 \end{cases}$$

Therefore, the eddy current losses in the total magnets and the sleeve are:

$$P_m=N\frac{L_a\omega_r}{2\pi}\int_{R_r}^{R_m}\int_0^{\frac{2\pi}{\omega_r}}\int_{-\frac{\alpha_p}{2}}^{\frac{\alpha_p}{2}}\frac{1}{\sigma_m}J_m^2 r\,dr\,dt\,d\theta=\sum_u^{\infty}\sum_v^{\infty}\left(P_{cuv}+P_{auv}\right)\quad\text{(W)} \tag{3-34}$$

$$P_{sl} = \frac{L_a \omega_r}{2\pi} \int_{R_m}^{R_{sl}} \int_{0}^{\frac{2\pi}{\omega_r}} \int_{-\pi}^{\pi} \frac{1}{\sigma_{sl}} J_{sl}^2 r dr dt d\theta = \sum_{u}^{\infty} \sum_{v}^{\infty} P_{sluv} \qquad \text{(W)} \tag{3-35}$$

where L_a is the axial length of the PM and the retaining sleeve, which is assumed to be the same as the axial length of the stator lamination.

P_{cuv} is given by,

$$P_{cuv} = \begin{cases} \dfrac{\pi L_a \sigma_m \omega_r^2 \mu_0^2 J_{uv}^2 R_s^{-2v+2} (u-v)^2}{G_v^2 v^2} \\ \left[\dfrac{R_m^{2v+2} - R_r^{2v+2}}{2v+2} + R_r^{2v} \left(R_m^2 - R_r^2 \right) + R_r^{4v} F_{pmv} \right], \end{cases} \quad v - u = 3c, c = 0, \pm 1, \pm 2 \cdots$$

$$\begin{cases} \dfrac{\pi L_a \sigma_m \omega_r^2 \mu_0^2 J_{uv}^2 R_s^{-2v+2} (u+v)^2}{G_v^2 v^2} \\ \left[\dfrac{R_m^{2v+2} - R_r^{2v+2}}{2v+2} + R_r^{2v} \left(R_m^2 - R_r^2 \right) + R_r^{4v} F_{pmv} \right], \end{cases} \quad v + u = 3c, c = 0, \pm 1, \pm 2 \cdots$$

where $F_{pmv} = \begin{cases} \ln\left(\dfrac{R_m}{R_r} \right), & v = 1 \\ \dfrac{R_m^{-2v+2} - R_r^{-2v+2}}{-2v+2}, & v \neq 1 \end{cases}$

P_{auv} is given by,

- If $N = 1$, $P_{auv} = 0$.
- If $N > 1$

$$P_{auv}=\begin{cases}-N^2\dfrac{2L_a\sigma_m\omega_r^2\mu_0^2J_{uv}^2\sin^2\left(v\dfrac{\pi}{N}\right)(u-v)^2}{\pi G_v^2v^4\left(R_m^2-R_r^2\right)} & v-u=3c,c=0,\pm,\pm2\cdots\\ \left(\dfrac{R_m^{v+2}-R_r^{v+2}}{v+2}+R_r^{2v}E_{pmv}\right)^2, & \\ -N^2\dfrac{2L_a\sigma_m\omega_r^2\mu_0^2J_{uv}^2\sin^2\left(v\dfrac{\pi}{N}\right)(u+v)^2}{\pi G_v^2v^4\left(R_m^2-R_r^2\right)} & v+u=3c,c=0,\pm,\pm2\cdots\\ \left(\dfrac{R_m^{v+2}-R_r^{v+2}}{v+2}+R_r^{2v}E_{pmv}\right)^2, & \end{cases}$$

P_{sluv} is given by,

$$P_{sluv}=\begin{cases}\dfrac{\pi L_a\sigma_{sl}\omega_r^2\mu_0^2J_{uv}^2R_s^{-2v+2}(u-v)^2}{G_v^2v^2} & \\ \left[\dfrac{R_{sl}^{2v+2}-R_m^{2v+2}}{2v+2}+R_r^{2v}\left(R_{sl}^2-R_m^2\right)+R_r^{4v}F_{slv}\right], & v-u=3c,c=0,\pm,\pm2\cdots\\ \dfrac{\pi L_a\sigma_{sl}\omega_r^2\mu_0^2J_{uv}^2R_s^{-2v+2}(u+v)^2}{G_v^2v^2} & \\ \left[\dfrac{R_{sl}^{2v+2}-R_m^{2v+2}}{2v+2}+R_r^{2v}\left(R_{sl}^2-R_m^2\right)+R_r^{4v}F_{slv}\right], & v+u=3c,c=0,\pm,\pm2\cdots\end{cases}$$

where $F_{slv}=\begin{cases}\ln\left(\dfrac{R_{sl}}{R_m}\right), & v=1\\ \dfrac{R_{sl}^{-2v+2}-R_m^{-2v+2}}{-2v+2}, & v\neq1\end{cases}$

3.3.2 Improved analytical model

If the motor operation speed is relatively high, the skin effect associated with the field harmonics may be relatively smaller than the pole arc and the radial thickness of the PM and the retaining sleeve. Hence, the static analytical model may significantly overestimate the rotor eddy current loss due to neglecting the influence of the eddy current reaction field. Therefore, an improved analytical model is going to be developed to account for the eddy

current reaction field by employing Bessel functions having complex arguments. Further, the improved analytical model can cater for motors with/without the conducting sleeve.

The expression (3-14) for the equivalent current sheet distribution over the stator slotting can be rewritten by,

$$J_s(\alpha)=\begin{cases}\sum_{u}^{\infty}\sum_{v}^{\infty}\mathrm{Re}\left[J_{uv}e^{j(u\omega_r t+\theta_u-v\alpha)}\right] & v-u=3c, c=0,\pm1,\pm2\cdots\\ \sum_{u}^{\infty}\sum_{v}^{\infty}\mathrm{Re}\left[-J_{uv}e^{j(u\omega_r t+\theta_u+v\alpha)}\right] & v+u=3c, c=0,\pm1,\pm2\cdots\end{cases} \quad \text{(A/m)} \qquad (3\text{-}36)$$

In terms of the magnetic vector potential A_I, Laplace's equation, which governs the armature reaction field in the airgap, i.e. $(R_{sl}\le r\le R_s)$ is,

$$\frac{\partial^2 A_I}{\partial r^2}+\frac{1}{r}\frac{\partial A_I}{\partial r}+\frac{1}{r^2}\frac{\partial^2 A_I}{\partial \alpha^2}=0 \qquad (3\text{-}37)$$

For which, the general solution due to each component of the equivalent current sheet, i.e. equation (3-36), is,

$$A_I=\begin{cases}\sum_{u}^{\infty}\sum_{v}^{\infty}\mathrm{Re}\left[\left(Ar^{v}+Br^{-v}\right)e^{j(u\omega_r t-v\alpha+\theta_u)}\right], v-u=3c, c=0,\pm1,\pm2...\\ \sum_{u}^{\infty}\sum_{v}^{\infty}\mathrm{Re}\left[\left(Ar^{v}+Br^{-v}\right)e^{j(u\omega_r t+v\alpha+\theta_u)}\right], v+u=3c, c=0,\pm1,\pm2...\end{cases} \quad \text{(A/m)} \qquad (3\text{-}38)$$

The radial and circumferential components of the armature reaction field can be derived from A_I as,

$$B_{rI}(\alpha)=\frac{1}{r}\frac{\partial A_I}{\partial \alpha}=$$

$$\begin{cases}\sum_{u}^{\infty}\sum_{v}^{\infty}\mathrm{Re}\left[-j\frac{v}{r}\left(Ar^{v}+Br^{-v}\right)e^{j(u\omega_r t-v\alpha+\theta_u)}\right], v-u=3c, c=0,\pm1,\pm2... & \text{(T)}\\ \sum_{u}^{\infty}\sum_{v}^{\infty}\mathrm{Re}\left[j\frac{v}{r}\left(Ar^{v}+Br^{-v}\right)e^{j(u\omega_r t+v\alpha+\theta_u)}\right], v+u=3c, c=0,\pm1,\pm2...\end{cases} \qquad (3\text{-}39)$$

$$H_{\alpha l}(\alpha) = -\frac{1}{\mu_0}\frac{\partial A_l}{\partial r} =$$

$$\begin{cases} \sum_u^{\infty}\sum_v^{\infty} \mathrm{Re}\left[-\frac{v}{r\mu_0}\left(Ar^v - Br^{-v}\right)e^{j(u\omega_r t - v\alpha + \theta_u)}\right], v-u = 3c, c = 0,\pm1,\pm2\ldots \\ \sum_u^{\infty}\sum_v^{\infty} \mathrm{Re}\left[-\frac{v}{r\mu_0}\left(Ar^v - Br^{-v}\right)e^{j(u\omega_r t + v\alpha + \theta_u)}\right], v+u = 3c, c = 0,\pm1,\pm2\ldots \end{cases} \quad \text{(A/m)} \tag{3-40}$$

In the sleeve (if fitted), i.e. $R_m \le r \le R_{sl}$, the magnetic vector potential A satisfy the following equation:

$$\nabla^2 A = \sigma_{sl}\mu_0\mu_{sl}\frac{\partial A}{\partial t} \tag{3-41}$$

The induced eddy current density in the sleeve can be give by:

$$J_{zll} = -\frac{\partial A}{\partial t} \qquad (\mathrm{A/m^2}) \tag{3-42}$$

According to (3-41) and (3-42), the induced eddy current density due to the equivalent current sheet can be calculated by solving the following diffusion equations,

$$\begin{cases} \frac{\partial^2 J_{zll}}{\partial r^2} + \frac{1}{r}\frac{\partial J_{zll}}{\partial r} + \frac{1}{r^2}\frac{\partial^2 J_{zll}}{\partial \alpha^2} - j(u-v)\omega_r\sigma_{sl}\mu_0\mu_{sl}J_{zll} = 0, v \ne u, v-u = 3c, c = 0,\pm1,\pm2\ldots \\ \frac{\partial^2 J_{zll}}{\partial r^2} + \frac{1}{r}\frac{\partial J_{zll}}{\partial r} + \frac{1}{r^2}\frac{\partial^2 J_{zll}}{\partial \alpha^2} - j(u+v)\omega_r\sigma_{sl}\mu_0\mu_{sl}J_{zll} = 0, v+u = 3c, c = 0,\pm1,\pm2\ldots \end{cases} \tag{3-43}$$

i.e.

$$\frac{\partial^2 J_{zll}}{\partial r^2} + \frac{1}{r}\frac{\partial J_{zll}}{\partial r} + \frac{1}{r^2}\frac{\partial^2 J_{zll}}{\partial \alpha^2} + \tau_{sl}^{\ 2} J_{zll} = 0$$

where $\tau_{sl} = \dfrac{-1+j}{\delta_{sl}}$, and $\delta_{sl} = \begin{cases} \sqrt{\dfrac{2}{(u-v)\omega_r\sigma_{sl}\mu_0\mu_{sl}}}, v \ne u, v-u = 3c, c = 0,\pm1,\pm2\ldots \\ \sqrt{\dfrac{2}{(u+v)\omega_r\sigma_{sl}\mu_0\mu_{sl}}}, v+u = 3c, c = 0,\pm1,\pm2\ldots \end{cases}$ is the skin depth of the retaining sleeve.

It can be noted that if $v = u$, the corresponding stator mmfs is synchronous with the rotor and

will not induce the eddy current in the rotor.

The general solution for the eddy current density in the retaining sleeve, due to asynchronous stator mmfs, is:

$$J_{zII}(\alpha)=\begin{cases}\sum_{u}^{\infty}\sum_{v}^{\infty}\mathrm{Re}\left\{\left[CJ_v(\tau_{sl}r)+DY_v(\tau_{sl}r)\right]e^{j(u\omega_r t-v\alpha+\theta_u)}\right\}, v\neq u, v-u=3c, c=0,\pm1,\pm2\ldots \\ \sum_{u}^{\infty}\sum_{v}^{\infty}\mathrm{Re}\left\{\left[CJ_v(\tau_{sl}r)+DY_v(\tau_{sl}r)\right]e^{j(u\omega_r t+v\alpha+\theta_u)}\right\}, v+u=3c, c=0,\pm1,\pm2\ldots\end{cases} \tag{3-44}$$

The radial and circumferential field components in the sleeve may be found by applying Maxwell's equation,

$$\nabla\times\vec{E}_{II}=-\frac{\partial\vec{B}_{II}}{\partial t} \tag{3-45}$$

which yields,

$$\frac{1}{r\sigma_{sl}}\frac{\partial J_{zII}}{\partial\alpha}=-j(u\pm v)\omega_r B_{rII} \tag{3-46}$$

i.e.

$$B_{rII}(\alpha)=$$
$$\begin{cases}\sum_{u}^{\infty}\sum_{v}^{\infty}\mathrm{Re}\left\{-j\frac{v}{r}\frac{\mu_0\mu_{sl}}{\tau_{sl}^2}\left[CJ_v(\tau_{sl}r)+DY_v(\tau_{sl}r)\right]e^{j(u\omega_r t-v\alpha+\theta_u)}\right\}, v\neq u, v-u=3c, c=0,\pm1,\pm2\ldots \\ \sum_{u}^{\infty}\sum_{v}^{\infty}\mathrm{Re}\left\{j\frac{v}{r}\frac{\mu_0\mu_{sl}}{\tau_{sl}^2}\left[CJ_v(\tau_{sl}r)+DY_v(\tau_{sl}r)\right]e^{j(u\omega_r t+v\alpha+\theta_u)}\right\}, v+u=3c, c=0,\pm1,\pm2\ldots\end{cases} \tag{3-47}$$

$$-\frac{1}{\sigma_{sl}}\frac{\partial J_{zII}}{\partial r}=-j(u\pm v)\omega_r\mu_0\mu_{sl}H_{\alpha II} \tag{3-48}$$

i.e.

$$H_{all}(\alpha)=$$

$$\begin{cases} \sum_{u}^{\infty}\sum_{v}^{\infty}\mathrm{Re}\left\{-\frac{v}{r\tau_{sl}^2}\left\{\begin{matrix} C\left[\frac{\tau_{sl}r}{v}J_{v-1}(\tau_{sl}r)-J_v(\tau_{sl}r)\right] \\ +D\left[\frac{\tau_{sl}r}{v}Y_{v-1}(\tau_{sl}r)-Y_v(\tau_{sl}r)\right]\end{matrix}\right\}e^{j(u\omega_r t-v\alpha+\theta_u)}\right\}, v\neq u, v-u=3c, c=0,\pm1,\pm2... \\ \sum_{u}^{\infty}\sum_{v}^{\infty}\mathrm{Re}\left\{-\frac{v}{r\tau_{sl}^2}\left\{\begin{matrix} C\left[\frac{\tau_{sl}r}{v}J_{v-1}(\tau_{sl}r)-J_v(\tau_{sl}r)\right] \\ +D\left[\frac{\tau_{sl}r}{v}Y_{v-1}(\tau_{sl}r)-Y_v(\tau_{sl}r)\right]\end{matrix}\right\}e^{j(u\omega_r t+v\alpha+\theta_u)}\right\}, v+u=3c, c=0,\pm1,\pm2... \end{cases}$$

(3-49)

where J_v, Y_v and J_{v-1}, Y_{v-1} are Bessel functions of the first and second kind of order v and $v-1$, respectively.

Similarly, the eddy current density in the rotor PM, i.e. $R_r \le r \le R_m$, also satisfy the diffusion equation,

$$\begin{cases} \frac{\partial^2 J_{zIII}}{\partial r^2}+\frac{1}{r}\frac{\partial J_{zIII}}{\partial r}+\frac{1}{r^2}\frac{\partial^2 J_{zIII}}{\partial \alpha^2}-j(u-v)\omega_r\sigma_m\mu_0\mu_m J_{zIII}=0, v\neq u, v-u=3c, c=0,\pm1,\pm2... \\ \frac{\partial^2 J_{zIII}}{\partial r^2}+\frac{1}{r}\frac{\partial J_{zIII}}{\partial r}+\frac{1}{r^2}\frac{\partial^2 J_{zIII}}{\partial \alpha^2}-j(u+v)\omega_r\sigma_m\mu_0\mu_m J_{zIII}=0, v+u=3c, c=0,\pm1,\pm2... \end{cases}$$

(3-50)

i.e.

$$\frac{\partial^2 J_{zIII}}{\partial r^2}+\frac{1}{r}\frac{\partial J_{zIII}}{\partial r}+\frac{1}{r^2}\frac{\partial^2 J_{zIII}}{\partial \alpha^2}+\tau_m{}^2 J_{zIII}=0$$

where $\tau_m=\frac{-1+j}{\delta_m}$, and $\delta_m=\begin{cases}\sqrt{\frac{2}{(u-v)\omega_r\sigma_m\mu_0\mu_m}}, v\neq u, v-u=3c, c=0,\pm1,\pm2... \\ \sqrt{\frac{2}{(u+v)\omega_r\sigma_m\mu_0\mu_m}}, v+u=3c, c=0,\pm1,\pm2...\end{cases}$ is the skin depth of the magnet.

The general solution for the eddy current density in the PM, due to asynchronous stator mmfs, is:

$$J_{zIII}(\alpha)=\begin{cases}\sum_{u}^{\infty}\sum_{v}^{\infty}\mathrm{Re}\left\{\left[EJ_v(\tau_m r)+FY_v(\tau_m r)\right]e^{j(u\omega_r t-v\alpha+\theta_u)}\right\}, v\neq u, v-u=3c, c=0,\pm1,\pm2\ldots\\ \sum_{u}^{\infty}\sum_{v}^{\infty}\mathrm{Re}\left\{\left[EJ_v(\tau_m r)+FY_v(\tau_m r)\right]e^{j(u\omega_r t+v\alpha+\theta_u)}\right\}, v+u=3c, c=0,\pm1,\pm2\ldots\end{cases} \quad (3\text{-}51)$$

Therefore, the radial and circumferential field components in the magnets is

$$B_{rIII}(\alpha)=\begin{cases}\sum_{u}^{\infty}\sum_{v}^{\infty}\mathrm{Re}\left\{-j\frac{v}{r}\frac{\mu_0\mu_m}{\tau_m^2}\left[EJ_v(\tau_m r)+FY_v(\tau_m r)\right]e^{j(u\omega_r t-v\alpha+\theta_u)}\right\}, v\neq u, v-u=3c, c=0,\pm1,\pm2\ldots\\ \sum_{u}^{\infty}\sum_{v}^{\infty}\mathrm{Re}\left\{j\frac{v}{r}\frac{\mu_0\mu_m}{\tau_m^2}\left[EJ_v(\tau_m r)+FY_v(\tau_m r)\right]e^{j(u\omega_r t+v\alpha+\theta_u)}\right\}, v+u=3c, c=0,\pm1,\pm2\ldots\end{cases} \quad (3\text{-}52)$$

$$H_{\alpha III}(\alpha)=\begin{cases}\sum_{u}^{\infty}\sum_{v}^{\infty}\mathrm{Re}\left\{-\frac{v}{r\tau_m^2}\left\{E\left[\frac{\tau_{ml}r}{v}J_{v-1}(\tau_m r)-J_v(\tau_m r)\right]+F\left[\frac{\tau_m r}{v}Y_{v-1}(\tau_m r)-Y_v(\tau_m r)\right]\right\}e^{j(u\omega_r t-v\alpha+\theta_u)}\right\}, v\neq u, v-u=3c, c=0,\pm1,\pm2\ldots\\ \sum_{u}^{\infty}\sum_{v}^{\infty}\mathrm{Re}\left\{-\frac{v}{r\tau_m^2}\left\{E\left[\frac{\tau_{ml}r}{v}J_{v-1}(\tau_m r)-J_v(\tau_m r)\right]+F\left[\frac{\tau_m r}{v}Y_{v-1}(\tau_m r)-Y_v(\tau_m r)\right]\right\}e^{j(u\omega_r t+v\alpha+\theta_u)}\right\}, v+u=3c, c=0,\pm1,\pm2\ldots\end{cases} \quad (3\text{-}53)$$

In order to determine the induced eddy currents and the associated loss in the rotor, above analytical expressions for the equivalent current sheet and the armature reaction field have to be transformed from the stationary reference frame α to the rotating reference frame θ with the transformation $\alpha=\theta+\omega_r t$. Hence, the equivalent current sheet which is able to induce the eddy current in the rotor is,

$$J_s(\theta)=\begin{cases}\sum_{u}^{\infty}\sum_{v}^{\infty}\mathrm{Re}\left[J_{uv}e^{j\phi_1}\right] & v\neq u, v-u=3c, c=0,\pm1,\pm2\cdots\\ \sum_{u}^{\infty}\sum_{v}^{\infty}\mathrm{Re}\left[-J_{uv}e^{j\phi_2}\right] & v+u=3c, c=0,\pm1,\pm2\cdots\end{cases} \quad \text{(A/m)} \quad (3\text{-}54)$$

where $\phi_1=(u-v)\omega_r t-v\theta+\theta_u$ and $\phi_2=(u+v)\omega_r t+v\theta+\theta_u$.

The armature reaction field which can produce the eddy current in the rotor is:

- In the airgap,

$$B_{rl}(\theta)=\begin{cases}\sum_{u}^{\infty}\sum_{v}^{\infty}\mathrm{Re}\left[-j\frac{v}{r}\left(Ar^{v}+Br^{-v}\right)e^{j\phi_1}\right], v\neq u, v-u=3c, c=0,\pm1,\pm2...\\ \sum_{u}^{\infty}\sum_{v}^{\infty}\mathrm{Re}\left[j\frac{v}{r}\left(Ar^{v}+Br^{-v}\right)e^{j\phi_2}\right], v+u=3c, c=0,\pm1,\pm2...\end{cases} \quad (\mathrm{T}) \qquad (3\text{-}55)$$

$$H_{\alpha l}(\theta)=\begin{cases}\sum_{u}^{\infty}\sum_{v}^{\infty}\mathrm{Re}\left[-\frac{v}{r\mu_0}\left(Ar^{v}-Br^{-v}\right)e^{j\phi_1}\right], v\neq u, v-u=3c, c=0,\pm1,\pm2...\\ \sum_{u}^{\infty}\sum_{v}^{\infty}\mathrm{Re}\left[-\frac{v}{r\mu_0}\left(Ar^{v}-Br^{-v}\right)e^{j\phi_2}\right], v+u=3c, c=0,\pm1,\pm2...\end{cases} \quad (\mathrm{A/m}) \qquad (3\text{-}56)$$

- In the sleeve,

$$B_{rll}(\theta)=$$

$$\begin{cases}\sum_{u}^{\infty}\sum_{v}^{\infty}\mathrm{Re}\left\{-j\frac{v}{r}\frac{\mu_0\mu_{sl}}{\tau_{sl}^2}\left[CJ_v(\tau_{sl}r)+DY_v(\tau_{sl}r)\right]e^{j\phi_1}\right\}, v\neq u, v-u=3c, c=0,\pm1,\pm2...\\ \sum_{u}^{\infty}\sum_{v}^{\infty}\mathrm{Re}\left\{j\frac{v}{r}\frac{\mu_0\mu_{sl}}{\tau_{sl}^2}\left[CJ_v(\tau_{sl}r)+DY_v(\tau_{sl}r)\right]e^{j\phi_2}\right\}, v+u=3c, c=0,\pm1,\pm2...\end{cases} \quad (\mathrm{T}) \qquad (3\text{-}57)$$

$$H_{\alpha ll}(\theta)=$$

$$\begin{cases}\sum_{u}^{\infty}\sum_{v}^{\infty}\mathrm{Re}\left\{-\frac{v}{r\tau_{sl}^2}\left\{C\left[\frac{\tau_{sl}r}{v}J_{v-1}(\tau_{sl}r)-J_v(\tau_{sl}r)\right]+D\left[\frac{\tau_{sl}r}{v}Y_{v-1}(\tau_{sl}r)-Y_v(\tau_{sl}r)\right]\right\}e^{j\phi_1}\right\}, v\neq u, v-u=3c, c=0,\pm1,\pm2...\\ \sum_{u}^{\infty}\sum_{v}^{\infty}\mathrm{Re}\left\{-\frac{v}{r\tau_{sl}^2}\left\{C\left[\frac{\tau_{sl}r}{v}J_{v-1}(\tau_{sl}r)-J_v(\tau_{sl}r)\right]+D\left[\frac{\tau_{sl}r}{v}Y_{v-1}(\tau_{sl}r)-Y_v(\tau_{sl}r)\right]\right\}e^{j\phi_2}\right\}, v+u=3c, c=0,\pm1,\pm2...\end{cases} \quad (\mathrm{A/m})$$

(3-58)

- In the magnets,

$$B_{rIII}(\theta)=$$

$$\begin{cases} \sum_{u}^{\infty}\sum_{v}^{\infty}\mathrm{Re}\left\{-j\frac{v}{r}\frac{\mu_0\mu_m}{\tau_m^2}\left[EJ_v(\tau_m r)+FY_v(\tau_m r)\right]e^{j\phi_1}\right\}, v\neq u, v-u=3c, c=0,\pm1,\pm2... \\ \sum_{u}^{\infty}\sum_{v}^{\infty}\mathrm{Re}\left\{j\frac{v}{r}\frac{\mu_0\mu_m}{\tau_m^2}\left[EJ_v(\tau_m r)+FY_v(\tau_m r)\right]e^{j\phi_2}\right\}, v+u=3c, c=0,\pm1,\pm2... \end{cases} \text{(T)} \quad (3\text{-}59)$$

$$H_{\alpha III}(\theta)=$$

$$\begin{cases} \sum_{u}^{\infty}\sum_{v}^{\infty}\mathrm{Re}\left\{-\frac{v}{r\tau_m^2}\left\{E\left[\frac{\tau_{mI}r}{v}J_{v-1}(\tau_m r)-J_v(\tau_m r)\right]+F\left[\frac{\tau_m r}{v}Y_{v-1}(\tau_m r)-Y_v(\tau_m r)\right]\right\}e^{j\phi_1}\right\}, v\neq u, v-u=3c, c=0,\pm1,\pm2... \\ \sum_{u}^{\infty}\sum_{v}^{\infty}\mathrm{Re}\left\{-\frac{v}{r\tau_m^2}\left\{E\left[\frac{\tau_{mI}r}{v}J_{v-1}(\tau_m r)-J_v(\tau_m r)\right]+F\left[\frac{\tau_m r}{v}Y_{v-1}(\tau_m r)-Y_v(\tau_m r)\right]\right\}e^{j\phi_2}\right\}, v+u=3c, c=0,\pm1,\pm2... \end{cases} \text{(A/m)}$$

(3-60)

By assuming both of the stator and rotor iron to be infinitely permeable, the boundary conditions at the interface between the different regions are given by,

$$H_{\alpha I}(\theta)\big|_{r=R_s}=J_s(\theta) \quad \text{(A/m)} \quad (3\text{-}61)$$

$$B_{rI}(\theta)\big|_{r=R_{sI}}=B_{rII}(\theta)\big|_{r=R_{sI}} \quad \text{(T)} \quad (3\text{-}62)$$

$$H_{\alpha I}(\theta)\big|_{r=R_{sI}}=H_{\alpha II}(\theta)\big|_{r=R_{sI}} \quad \text{(A/m)} \quad (3\text{-}63)$$

$$B_{rII}(\theta)\big|_{r=R_m}=B_{rIII}(\theta)\big|_{r=R_m} \quad \text{(T)} \quad (3\text{-}64)$$

$$H_{\alpha II}(\theta)\big|_{r=R_m}=H_{\alpha III}(\theta)\big|_{r=R_m} \quad \text{(A/m)} \quad (3\text{-}65)$$

$$H_{\alpha III}(\theta)\big|_{r=R_r}=0 \quad \text{(A/m)} \quad (3\text{-}66)$$

According to above boundary conditions, the coefficients A, B, C, D, E and F can be resolved by the following equation,

$$[K][X]=[Y]\Rightarrow[X]=[K]^{-1}[Y] \quad (3\text{-}67)$$

where $[K]=\begin{bmatrix} K_{11} & K_{12} & 0 & 0 & 0 & 0 \\ K_{21} & K_{22} & K_{23} & K_{24} & 0 & 0 \\ K_{31} & K_{32} & K_{33} & K_{34} & 0 & 0 \\ 0 & 0 & K_{43} & K_{44} & K_{45} & K_{46} \\ 0 & 0 & K_{53} & K_{54} & K_{55} & K_{56} \\ 0 & 0 & 0 & 0 & K_{65} & K_{66} \end{bmatrix}$, $[X]=\begin{bmatrix} A \\ B \\ C \\ D \\ E \\ F \end{bmatrix}$, $[Y]=\begin{bmatrix} Y_1 \\ 0 \\ 0 \\ 0 \\ 0 \\ 0 \end{bmatrix}$

where $Y_1=\begin{cases} -J_{uv}, v \neq u, v-u=3c, c=0,\pm1,\pm2... \\ J_{uv}, v+u=3c, c=0,\pm1,\pm2... \end{cases}$ and $J_{uv}=\frac{3N_{ph}}{\pi R_s} I_u K_{sov} K_{pv}$

$$K_{11}=\frac{v}{\mu_0} R_s^{v-1},\ K_{12}=-\frac{v}{\mu_0} R_s^{-v-1};$$

$$K_{21}=R_{sl}^{v},\ K_{22}=R_{sl}^{-v},\ K_{23}=-\frac{\mu_0\mu_{sl}}{\tau_{sl}^2} J_v(\tau_{sl}R_{sl}),\ K_{24}=-\frac{\mu_0\mu_{sl}}{\tau_{sl}^2} Y_v(\tau_{sl}R_{sl});$$

$$K_{31}=R_{sl}^{v},\ K_{32}=-R_{sl}^{-v},\ K_{33}=-\frac{\mu_0}{\tau_{sl}^2}\left[\frac{\tau_{sl}R_{sl}}{v} J_{v-1}(\tau_{sl}R_{sl})-J_v(\tau_{sl}R_{sl})\right],$$

$$K_{34}=-\frac{\mu_0}{\tau_{sl}^2}\left[\frac{\tau_{sl}R_{sl}}{v} Y_{v-1}(\tau_{sl}R_{sl})-Y_v(\tau_{sl}R_{sl})\right];$$

$$K_{43}=\frac{\mu_{sl}}{\tau_{sl}^2} J_v(\tau_{sl}R_m),\ K_{44}=\frac{\mu_{sl}}{\tau_{sl}^2} Y_v(\tau_{sl}R_m),$$

$$K_{45}=-\frac{\mu_m}{\tau_m^2} J_v(\tau_m R_m), K_{46}=-\frac{\mu_m}{\tau_m^2} Y_v(\tau_m R_m);$$

$$K_{53}=\frac{1}{\tau_{sl}^2}\left[\frac{\tau_{sl}R_m}{v} J_{v-1}(\tau_{sl\_1}R_m)-J_v(\tau_{sl\_1}R_m)\right],$$

$$K_{54}=\frac{1}{\tau_{sl}^2}\left[\frac{\tau_{sl}R_m}{v} Y_{v-1}(\tau_{sl}R_m)-Y_v(\tau_{sl}R_m)\right],$$

$$K_{55}=-\frac{1}{\tau_m^2}\left[\frac{\tau_m R_m}{v} J_{v-1}(\tau_m R_m)-J_v(\tau_m R_m)\right],$$

$$K_{56}=-\frac{1}{\tau_m^2}\left[\frac{\tau_m R_m}{v} Y_{v-1}(\tau_m R_m)-Y_v(\tau_m R_m)\right];$$

$$K_{65}=\frac{\tau_m R_r}{v} J_{v-1}(\tau_m R_r)-J_v(\tau_m R_r),\ K_{66}=\frac{\tau_m R_r}{v} Y_{v-1}(\tau_m R_r)-Y_v(\tau_m R_r).$$

The eddy current densities induced in the retaining sleeve and the PM in the rotating reference frame θ are as follows, respectively,

$$J_{zII}(\theta)=\begin{cases}\sum_{u}^{\infty}\sum_{v}^{\infty}\mathrm{Re}\left\{\left[CJ_v(\tau_{sl}r)+DY_v(\tau_{sl}r)\right]e^{j\phi_1}\right\}, v\neq u, v-u=3c, c=0,\pm1,\pm2... \\ \sum_{u}^{\infty}\sum_{v}^{\infty}\mathrm{Re}\left\{\left[CJ_v(\tau_{sl}r)+DY_v(\tau_{sl}r)\right]e^{j\phi_2}\right\}, v+u=3c, c=0,\pm1,\pm2...\end{cases} \quad (\mathrm{A/m^2}) \quad (3\text{-}68)$$

$$J_{zIII}(\theta)=\begin{cases}\sum_{u}^{\infty}\sum_{v}^{\infty}\mathrm{Re}\left\{\left[EJ_v(\tau_{m}r)+FY_v(\tau_{m}r)\right]e^{j\phi_1}\right\}, v\neq u, v-u=3c, c=0,\pm1,\pm2... \\ \sum_{u}^{\infty}\sum_{v}^{\infty}\mathrm{Re}\left\{\left[EJ_v(\tau_{m}r)+FY_v(\tau_{m}r)\right]e^{j\phi_2}\right\}, v+u=3c, c=0,\pm1,\pm2...\end{cases} \quad (\mathrm{A/m^2}) \quad (3\text{-}69)$$

According to the Poynting's theorem [98], the average eddy current loss over an electrical cycle $T=2\pi/\omega_r$ can be calculated by

$$P=\frac{L_a}{T}\int_0^T\oint_S \mathrm{Re}(E\times H)\cdot dSdt \qquad (\mathrm{W}) \qquad (3\text{-}70)$$

where the surface S bounds the conducting region.

In polar coordinate, due to $E_z=\frac{J_z}{\sigma}$, the eddy current loss of the annual region with outer and inner radius R_1 and R_2, respectively, can be rewritten by,

$$P=\frac{L_a}{T\sigma}\int_0^T\int_{\theta_1}^{\theta_2}(J_{z1}H_{t1})_{r=R_1}R_1dtd\theta-\frac{L_a}{T\sigma}\int_0^T\int_{\theta_1}^{\theta_2}(J_{z2}H_{t2})_{r=R_2}R_2dtd\theta \qquad (\mathrm{W}) \qquad (3\text{-}71)$$

where J_{z1}, J_{z2} -- Eddy current density induced in the axial direction; $\mathrm{A/m^2}$

$H_{\alpha1}$, $H_{\alpha2}$ -- Circumferential component of the magnetic field at the surface of the conducting region of the radius R_1 and R_2; A/m

θ_1, θ_2 -- Angle which spans the conducting region, e.g. the pole-arc when calculating the loss per magnet segment, and 2π when calculating the loss in the retaining sleeve.

Hence, the eddy current loss in the PM is,

$$P_m = \frac{2\pi}{\alpha_p}\frac{L_a}{T\sigma_m}\int_0^T\int_{-\frac{\alpha_p}{2}}^{\frac{\alpha_p}{2}}(J_{zIII}H_{\alpha III})_{r=R_m}R_m dtd\theta - \frac{2\pi}{\alpha_p}\frac{L_a}{T\sigma_m}\int_0^T\int_{-\frac{\alpha_p}{2}}^{\frac{\alpha_p}{2}}(J_{zIII}H_{\alpha III})_{r=R_r}R_r dtd\theta \quad \text{(W)} \qquad (3\text{-}72)$$

i.e.

$$P_m = \frac{\pi L_a}{\sigma_m}\sum_u^\infty\sum_v^\infty\left[|X1_m||Y1_m|\cos(\phi_{x1m}-\phi_{y1m})R_m - |X2_m||Y2_m|\cos(\phi_{x2m}-\phi_{y2m})R_r\right] \quad \text{(W)} \qquad (3\text{-}73)$$

where $X1_m = EJ_v(\tau_m R_m) + FY_v(\tau_m R_m) = |X1_m|e^{j\phi_{x1m}}$

$$X2_m = EJ_v(\tau_m R_r) + FY_v(\tau_m R_r) = |X2_m|e^{j\phi_{x2m}}$$

$$Y1_m = -\frac{v}{R_m\tau_m^2}\left\{\begin{array}{l} E\left[\frac{\tau_m R_m}{v}J_{v-1}(\tau_m R_m) - J_v(\tau_m R_m)\right] \\ +F\left[\frac{\tau_1 R_m}{v}Y_{v-1}(\tau_m R_m) - Y_v(\tau_m R_m)\right]\end{array}\right\} = |Y1_m|e^{j\phi_{y1m}}$$

$$Y2_m = -\frac{v}{R_r\tau_m^2}\left\{\begin{array}{l} E\left[\frac{\tau_{m\_2} R_r}{v}J_{v-1}(\tau_m R_r) - J_v(\tau_m R_r)\right] \\ +F\left[\frac{\tau_{m\_2} R_r}{v}Y_{v-1}(\tau_m R_r) - Y_v(\tau_m R_r)\right]\end{array}\right\} = |Y2_m|e^{j\phi_{y2m}}$$

The eddy current loss in the retaining sleeve is,

$$P_{sl} = \frac{L_a}{T\sigma_{sl}}\int_0^T\int_{-\pi}^{\pi}(J_{zII}H_{tII})_{r=R_{sl}}R_{sl}dtd\theta - \frac{L_a}{T\sigma_{sl}}\int_0^T\int_{-\pi}^{\pi}(J_{zIII}H_{tIII})_{r=R_m}R_m dtd\theta \qquad \text{(W)} \qquad (3\text{-}74)$$

i.e.

$$P_{sl} = \frac{\pi L_a}{\sigma_{sl}}\sum_u^\infty\sum_v^\infty\left[|X1_{sl}||Y1_{sl}|\cos(\phi_{x1sl}-\phi_{y1sl})R_{sl} - |X2_{sl}||Y2_{sl}|\cos(\phi_{x2sl}-\phi_{y2sl})R_m\right] \quad \text{(W)} \qquad (3\text{-}75)$$

where $X1_{sl} = CJ_v(\tau_{sl}R_{sl}) + DY_v(\tau_{sl}R_{sl}) = |X1_{sl}|e^{j\phi_{x1sl}}$

$$X2_{sl} = CJ_v(\tau_{sl}R_m) + DY_v(\tau_{sl}R_m) = |X2_{sl}|e^{j\phi_{x2sl}}$$

$$Y1_{sl} = -\frac{v}{R_{sl}\tau_{sl}^2}\left\{\begin{array}{l} C\left[\frac{\tau_{sl}R_{sl}}{v}J_{v-1}(\tau_{sl}R_{sl}) - J_v(\tau_{sl}R_{sl})\right] \\ +D\left[\frac{\tau_{sl\_1}R_{sl}}{v}Y_{v-1}(\tau_{sl}R_{sl}) - Y_v(\tau_{sl}R_{sl})\right]\end{array}\right\} = |Y1_{sl}|e^{j\phi_{y1sl}}$$

$$Y2_{sl} = -\frac{\nu}{R_m \tau_{sl}^2}\left\{\begin{array}{l} C\left[\frac{\tau_{sl}R_m}{\nu} J_{\nu-1}(\tau_{sl}R_m) - J_\nu(\tau_{sl}R_m)\right] \\ + D\left[\frac{\tau_{sl}R_m}{\nu} Y_{\nu-1}(\tau_{sl}R_m) - Y_\nu(\tau_{sl}R_m)\right] \end{array}\right\} = |Y2_{sl}|e^{j\phi_{y2sl}}$$

3.4 Analytical model for single-phase PM BLDC motors with concentric airgap

3.4.1 Static analytical model A

Similar to the static analytical model for the three-phase PM BLDC motors, by employing an equivalent current sheet as discussed in section 3.2.1, the time-varying armature reaction field in the PM and the retaining sleeve can be calculated in the rotating reference frame. Hence, the eddy current and associated loss in the rotor can be determined.

The expressions for the armature reaction field, eddy currents and associated loss in the rotor are listed in this section. The detailed derivation of the static analytical model can be found in Appendix A.

The magnetic vector potential, radial and circumferential components of the armature reaction field, which is expressed in the stationary reference frame, are,

$$A(r,\alpha,t) =$$
$$-\mu_0 \sum_u^\infty \sum_\nu^\infty \frac{J_{u\nu} R_s^{-\nu+1}}{G_\nu \nu}\left(r^\nu + R_r^{2\nu} r^{-\nu}\right)\left[\cos(u\omega_r t + \theta_u - \nu\alpha) - \cos(u\omega_r t + \theta_u + \nu\alpha)\right] \text{(A/m)} \quad (3\text{-}76)$$

$$B_r(r,\alpha,t) =$$
$$-\sum_u^\infty \sum_\nu^\infty \frac{\mu_0 J_{u\nu} R_s^{-\nu+1}}{G_\nu}(r^{\nu-1} + R_r^{2\nu} r^{-\nu-1})\left[\sin(u\omega_r t + \theta_u - \nu\alpha) + \sin(u\omega_r t + \theta_u + \nu\alpha)\right] \text{(T)} \quad (3\text{-}77)$$

$$B_\alpha(r,\alpha,t) =$$
$$\sum_u^\infty \sum_\nu^\infty \frac{\mu_0 J_{u\nu} R_s^{-\nu+1}}{G_\nu}(r^{\nu-1} - R_r^{2\nu} r^{-\nu-1})\left[\cos(u\omega_r t + \theta_u - \nu\alpha) - \cos(u\omega_r t + \theta_u + \nu\alpha)\right] \text{(T)} \quad (3\text{-}78)$$

where $G_v = 1 - \left(\frac{R_r}{R_s}\right)^{2v}$ and $J_{uv} = \frac{N_{ph}}{\pi R_s} I_u K_{sov} K_{pv}$.

The eddy current density in the magnet and the retaining sleeve which are expressed in the rotating reference frame, are,

$$J_m = J_{m1} + J_{m2} + C_{m1} + C_{m2} \qquad (\text{A/m}^2) \tag{3-79}$$

$$J_{sl} = J_{sl1} + J_{sl2} \qquad (\text{A/m}^2) \tag{3-80}$$

where

$$J_{m1} = -\sigma_m \omega_r \mu_0 \sum_u^\infty \sum_v^\infty (u - v) \frac{J_{uv} R_s^{-v+1}}{G_v v} \left(r^v + R_r^{2v} r^{-v}\right) \sin[(u - v)\omega_r t - v\theta + \theta_u]$$

$$J_{m2} = \sigma_m \omega_r \mu_0 \sum_u^\infty \sum_v^\infty (u + v) \frac{J_{uv} R_s^{-v+1}}{G_v v} \left(r^v + R_r^{2v} r^{-v}\right) \sin[(u + v)\omega_r t + v\theta + \theta_u]$$

$$J_{sl1} = -\sigma_{sl} \omega_r \mu_0 \sum_u^\infty \sum_v^\infty (u - v) \frac{J_{uv} R_s^{-v+1}}{G_v v} \left(r^v + R_r^{2v} r^{-v}\right) \sin[(u - v)\omega_r t - v\theta + \theta_u]$$

$$J_{sl2} = \sigma_{sl} \omega_r \mu_0 \sum_u^\infty \sum_v^\infty (u + v) \frac{J_{uv} R_s^{-v+1}}{G_v v} \left(r^v + R_r^{2v} r^{-v}\right) \sin[(u + v)\omega_r t + v\theta + \theta_u]$$

and,

- If $N = 1$, $C_{m1} = C_{m2} = 0$
- If $N > 1$,

$$C_{m1} = N \frac{2\sigma_m \omega_r \mu_0}{\pi\left(R_m^2 - R_r^2\right)} \sum_u^\infty \sum_v^\infty (u - v) \frac{J_{uv} R_s^{-v+1}}{G_v v^2} \left[\frac{R_m^{v+2} - R_r^{v+2}}{v + 2} + R_r^{2v} E_{mv}\right] \sin\left(v\frac{\pi}{N}\right) \sin[(u - v)\omega_r t + \theta_u]$$

$$C_{m2} = -N \frac{2\sigma_m \omega_r \mu_0}{\pi\left(R_m^2 - R_r^2\right)} \sum_u^\infty \sum_v^\infty (u + v) \frac{J_{uv} R_s^{-v+1}}{G_v v^2} \left[\frac{R_m^{v+2} - R_r^{v+2}}{v + 2} + R_r^{2v} E_{mv}\right] \sin\left(v\frac{\pi}{N}\right) \sin[(u + v)\omega_r t + \theta_u]$$

where $E_{mv} = \begin{cases} \ln\left(\dfrac{R_m}{R_r}\right), & v = 2 \\ \dfrac{R_m^{-v+2} - R_r^{-v+2}}{-v+2} & v \neq 2 \end{cases}$

The eddy current losses in the permanent and the retaining sleeve are,

$$P_m = N\frac{L_a\omega_r}{2\pi}\int_{R_r}^{R_m}\int_{0}^{\frac{2\pi}{\omega_r}}\int_{-\frac{\alpha_p}{2}}^{\frac{\alpha_p}{2}}\frac{1}{\sigma_m}J_m^2 r dr dt d\theta = \sum_u^{\infty}\sum_v^{\infty}\left(P_{cuv} + P_{auv}\right) \quad \text{(W)} \tag{3-81}$$

$$P_{sl} = \frac{L_a\omega_r}{2\pi}\int_{R_m}^{R_{sl}}\int_{0}^{\frac{2\pi}{\omega_r}}\int_{-\pi}^{\pi}\frac{1}{\sigma_{sl}}J_{sl}^2 r dr dt d\theta = \sum_u^{\infty}\sum_v^{\infty}P_{sluv} \quad \text{(W)} \tag{3-82}$$

where

P_{cuv} is given by,

$$P_{cuv} = \frac{\pi L_a\sigma_m\omega_r^2\mu_0^2 J_{uv}^2 R_s^{-2v+2}\left[(u+v)^2 + (u-v)^2\right]}{G_v^2 v^2}\left[\frac{R_m^{2v+2} - R_r^{2v+2}}{2v+2} + R_r^{2v}\left(R_m^2 - R_r^2\right) + R_r^{4v}F_{mv}\right]$$

where $F_{mv} = \begin{cases} \ln\left(\dfrac{R_m}{R_r}\right), & v = 1 \\ \dfrac{R_m^{-2v+2} - R_r^{-2v+2}}{-2v+2}, & v \neq 1 \end{cases}$

P_{auv} is given by,

- If $N = 1, P_{auv} = 0$.
- If $N > 1$

$$P_{auv} = -N^2\frac{2L_a\sigma_m\omega_r^2\mu_0^2 J_{uv}^2 R_s^{-2v+2}\sin^2\left(v\dfrac{\pi}{N}\right)\left[(u+v)^2 + (u-v)^2\right]}{\pi G_v^2 v^4\left(R_m^2 - R_r^2\right)}\left(\frac{R_m^{v+2} - R_r^{v+2}}{v+2} + R_r^{2v}E_{mv}\right)^2$$

P_{sluv} is given by,

$$P_{sluv} = \frac{\pi L_a \sigma_{sl} \omega_r^2 \mu_0^2 J_{uv}^2 R_s^{-2v+2}\left[(u+v)^2+(u-v)^2\right]}{G_v^2 v^2}\left[\frac{R_{sl}^{2v+2}-R_m^{2v+2}}{2v+2}+R_r^{2v}\left(R_{sl}^2-R_m^2\right)+R_r^{4v}F_{slv}\right]$$

where $F_{slv} = \begin{cases} \ln\left(\dfrac{R_{sl}}{R_m}\right), & v=1 \\ \dfrac{R_{sl}^{-2v+2}-R_m^{-2v+2}}{-2v+2}, & v\neq 1 \end{cases}$

3.4.2 Improved analytical model A

Similar to the improved analytical model for the three-phase PM BLDC motors, the expressions for the armature reaction field, the eddy currents and associated loss in the rotor are listed in this section. The detailed derivation of the improved analytical model can be found in Appendix B.

The radial and circumferential components of the armature reaction field produced by the equivalent current sheet in the stationary frame are,

- In the airgap, i.e. $(R_{sl} \le r \le R_s)$

$$B_{rl}(\alpha) = B_{rl\_1}(\alpha) + B_{rl\_2}(\alpha) \quad \text{(T)} \tag{3-83}$$

$$B_{\alpha l}(\alpha) = B_{\alpha l\_1}(\alpha) + B_{\alpha l\_2}(\alpha) \quad \text{(T)} \tag{3-84}$$

where $B_{rl\_1}(\alpha) = \sum_u^\infty \sum_v^\infty \mathrm{Re}\left[-j\frac{v}{r}\left(A_1 r^v + B_1 r^{-v}\right)e^{j(u\omega_r t - v\alpha + \theta_u)}\right], u \neq v$

$$B_{rl\_2}(\alpha) = \sum_u^\infty \sum_v^\infty \mathrm{Re}\left[j\frac{v}{r}\left(A_2 r^v + B_2 r^{-v}\right)e^{j(u\omega_r t + v\alpha + \theta_u)}\right]$$

$$B_{\alpha l\_1}(\alpha) = \sum_u^\infty \sum_v^\infty \mathrm{Re}\left[-\frac{v}{r}\left(A_1 r^v - B_1 r^{-v}\right)e^{j(u\omega_r t - v\alpha + \theta_u)}\right], u \neq v$$

$$B_{\alpha l\_2}(\alpha) = \sum_u^\infty \sum_v^\infty \mathrm{Re}\left[-\frac{v}{r}\left(A_2 r^v - B_2 r^{-v}\right)e^{j(u\omega_r t + v\alpha + \theta_u)}\right]$$

- In the retaining sleeve, i.e. $R_m \le r \le R_{sl}$

$$B_{rII}(\alpha) = B_{rII\_1}(\alpha) + B_{rII\_2}(\alpha) \qquad \text{(T)} \tag{3-85}$$

$$B_{\alpha II}(\alpha) = B_{\alpha II\_1}(\alpha) + B_{\alpha II\_2}(\alpha) \qquad \text{(T)} \tag{3-86}$$

where

$$B_{rII\_1}(\alpha) = \sum_u^{\infty}\sum_v^{\infty} \mathrm{Re}\left\{ -j\frac{v}{r}\frac{\mu_0\mu_{sl}}{\tau_{sl\_1}^2}\left[C_1 J_v(\tau_{sl\_1} r) + D_1 Y_v(\tau_{sl\_1} r)\right] e^{j(u\omega_r t - v\alpha + \theta_u)} \right\}, u \ne v$$

$$B_{rII\_2}(\alpha) = \sum_u^{\infty}\sum_v^{\infty} \mathrm{Re}\left\{ j\frac{v}{r}\frac{\mu_0\mu_{sl}}{\tau_{sl\_2}^2}\left[C_2 J_v(\tau_{sl\_2} r) + D_2 Y_v(\tau_{sl\_2} r)\right] e^{j(u\omega_r t + v\alpha + \theta_u)} \right\}$$

$$H_{\alpha II\_1}(\alpha) = \sum_u^{\infty}\sum_v^{\infty} \mathrm{Re}\left\{ -\frac{v}{r\tau_{sl\_1}^2}\left\{ \begin{array}{l} C_1\left[\frac{\tau_{sl\_1} r}{v} J_{v-1}(\tau_{sl\_1} r) - J_v(\tau_{sl\_1} r)\right] \\ + D_1\left[\frac{\tau_{sl\_1} r}{v} Y_{v-1}(\tau_{sl\_1} r) - Y_v(\tau_{sl\_1} r)\right] \end{array} \right\} e^{j(u\omega_r t - v\alpha + \theta_u)} \right\}, u \ne v$$

$$H_{\alpha II\_2}(\alpha) = \sum_u^{\infty}\sum_v^{\infty} \mathrm{Re}\left\{ -\frac{v}{r\tau_{sl\_2}^2}\left\{ \begin{array}{l} C_2\left[\frac{\tau_{sl\_2} r}{v} J_{v-1}(\tau_{sl\_2} r) - J_v(\tau_{sl\_2} r)\right] \\ + D_2\left[\frac{\tau_{sl\_2} r}{v} Y_{v-1}(\tau_{sl\_2} r) - Y_v(\tau_{sl\_2} r)\right] \end{array} \right\} e^{j(u\omega_r t + v\alpha + \theta_u)} \right\}$$

where $\tau_{sl\_1} = \dfrac{-1+j}{\delta_{sl\_1}}$, and $\delta_{sl\_1} = \sqrt{\dfrac{2}{(u-v)\omega_r \sigma_{sl}\mu_0\mu_{sl}}}$

$$\tau_{sl\_2} = \frac{-1+j}{\delta_{sl\_2}}, \text{ and } \delta_{sl\_2} = \sqrt{\frac{2}{(u+v)\omega_r \sigma_{sl}\mu_0\mu_{sl}}}$$

- In the PM, i.e. $R_r \le r \le R_m$

$$B_{rIII}(\alpha) = B_{rIII\_1}(\alpha) + B_{rIII\_2}(\alpha) \qquad \text{(T)} \tag{3-87}$$

$$B_{\alpha III}(\alpha) = B_{\alpha III\_1}(\alpha) + B_{\alpha III\_2}(\alpha) \qquad \text{(T)} \tag{3-88}$$

where

$$B_{rIII\_1}(\alpha) = \sum_u^{\infty}\sum_v^{\infty} \mathrm{Re}\left\{ -j\frac{v}{r}\frac{\mu_0\mu_m}{\tau_{m\_1}^2}\left[E_1 J_v(\tau_{m\_1} r) + F_1 Y_v(\tau_{m\_1} r)\right] e^{j(u\omega_r t - v\alpha + \theta_u)} \right\}, u \ne v$$

$$B_{rIII\_2}(\alpha) = \sum_u^{\infty}\sum_v^{\infty} \mathrm{Re}\left\{ j\frac{v}{r}\frac{\mu_0\mu_m}{\tau_{m\_2}^2}\left[E_2 J_v(\tau_{m\_2} r) + F_2 Y_v(\tau_{m\_2} r)\right] e^{j(u\omega_r t + v\alpha + \theta_u)} \right\}$$

$$H_{\alpha III\_1}(\alpha)=\sum_{u}^{\infty}\sum_{v}^{\infty}\mathrm{Re}\left\{-\frac{v}{r\tau_{m\_1}^2}\left\{\begin{array}{l}E_1\left[\frac{\tau_{m\_1}r}{v}J_{v-1}(\tau_{m\_1}r)-J_v(\tau_{m\_1}r)\right]\\+F_1\left[\frac{\tau_{m\_1}r}{v}Y_{v-1}(\tau_{m\_1}r)-Y_v(\tau_{m\_1}r)\right]\end{array}\right\}e^{j(u\omega_r t-v\alpha+\theta_u)}\right\},u\neq v$$

$$H_{\alpha III\_2}(\alpha)=\sum_{u}^{\infty}\sum_{v}^{\infty}\mathrm{Re}\left\{-\frac{v}{r\tau_{m\_2}^2}\left\{\begin{array}{l}E_2\left[\frac{\tau_{m\_2}r}{v}J_{v-1}(\tau_{m\_2}r)-J_v(\tau_{m\_2}r)\right]\\+F_2\left[\frac{\tau_{m\_2}r}{v}Y_{v-1}(\tau_{m\_2}r)-Y_v(\tau_{m\_2}r)\right]\end{array}\right\}e^{j(u\omega_r t+v\alpha+\theta_u)}\right\}$$

where $\tau_{m\_1}=\dfrac{-1+j}{\delta_{m\_1}}$, and $\delta_{m\_1}=\sqrt{\dfrac{2}{(u-v)\omega_r\sigma_m\mu_0\mu_m}}$

$$\tau_{m\_2}=\frac{-1+j}{\delta_{m\_2}},\text{ and }\delta_{m\_2}=\sqrt{\frac{2}{(u+v)\omega_r\sigma_m\mu_0\mu_m}}$$

According to boundary conditions, the coefficients A_1, B_1, C_1, D_1, E_1 F_1 and A_2, B_2, C_2, D_2, E_2 F_2 can be resolved by following equations. Details can be referred to Appendix B.

$$[K1][X1]=[Y1]\Rightarrow[X1]=[K1]^{-1}[Y1] \tag{3-89}$$

$$[K2][X2]=[Y2]\Rightarrow[X2]=[K2]^{-1}[Y2] \tag{3-90}$$

where $[K1]=\begin{bmatrix}K_{11}&K_{12}&0&0&0&0\\K_{21}&K_{22}&K_{23}&K_{24}&0&0\\K_{31}&K_{32}&K_{33}&K_{34}&0&0\\0&0&K_{43}&K_{44}&K_{45}&K_{46}\\0&0&K_{53}&K_{54}&K_{55}&K_{56}\\0&0&0&0&K_{65}&K_{66}\end{bmatrix},[X1]=\begin{bmatrix}A_1\\B_1\\C_1\\D_1\\E_1\\F_1\end{bmatrix},[Y1]=\begin{bmatrix}-J_{uv}\\0\\0\\0\\0\\0\end{bmatrix}$.

$[K2]=\begin{bmatrix}K_{11}^{'}&K_{12}^{'}&0&0&0&0\\K_{21}^{'}&K_{22}^{'}&K_{23}^{'}&K_{24}^{'}&0&0\\K_{31}^{'}&K_{32}^{'}&K_{33}^{'}&K_{34}^{'}&0&0\\0&0&K_{43}^{'}&K_{44}^{'}&K_{45}^{'}&K_{46}^{'}\\0&0&K_{53}^{'}&K_{54}^{'}&K_{55}^{'}&K_{56}^{'}\\0&0&0&0&K_{65}^{'}&K_{66}^{'}\end{bmatrix},[X2]=\begin{bmatrix}A_2\\B_2\\C_2\\D_2\\E_2\\F_2\end{bmatrix},[Y2]=\begin{bmatrix}J_{uv}\\0\\0\\0\\0\\0\end{bmatrix}$.

The eddy current densities induced in the retaining sleeve and the PM in the rotating reference frame θ are as follows, respectively,

$$J_{zII}(\theta) = J_{zII\_1}(\theta) + J_{zII\_2}(\theta) \qquad (\text{A/m}^2) \tag{3-91}$$

$$J_{zIII}(\theta) = J_{zIII\_1}(\theta) + J_{zIII\_2}(\theta) \qquad (\text{A/m}^2) \tag{3-92}$$

where $J_{zII\_1}(\theta) = \sum_{u}^{\infty}\sum_{v}^{\infty} \text{Re}\left\{\left[C_1 J_v(\tau_{sl} r) + D_1 Y_v(\tau_{sl} r)\right] e^{j\phi_1}\right\}, v \neq u$

$$J_{zII\_2}(\theta) = \sum_{u}^{\infty}\sum_{v}^{\infty} \text{Re}\left\{\left[C_2 J_v(\tau_{sl} r) + D_2 Y_v(\tau_{sl} r)\right] e^{j\phi_2}\right\}$$

$$J_{zIII\_1}(\theta) = \sum_{u}^{\infty}\sum_{v}^{\infty} \text{Re}\left\{\left[E_1 J_v(\tau_m r) + F_1 Y_v(\tau_m r)\right] e^{j\phi_1}\right\}, v \neq u$$

$$J_{zIII\_2}(\theta) = \sum_{u}^{\infty}\sum_{v}^{\infty} \text{Re}\left\{\left[E_2 J_v(\tau_m r) + F_2 Y_v(\tau_m r)\right] e^{j\phi_2}\right\}$$

$$\phi_1 = (u - v)\omega_r t - v\theta + \theta_u \quad \text{and} \quad \phi_2 = (u + v)\omega_r t - v\theta + \theta_u$$

According to the Poynting's theorem, the eddy current loss in the PM and the retaining sleeve can be determined by,

$$P_m = P_{m1} + P_{m2} \qquad (\text{W}) \tag{3-93}$$

$$P_{sl} = P_{sl1} + P_{sl2} \qquad (\text{W}) \tag{3-94}$$

where

$$P_{m1} = \frac{\pi L_a}{\sigma_m}\sum_{u}^{\infty}\sum_{v}^{\infty}\left[|X1_m||Y1_m|\cos(\phi_{x1m} - \phi_{y1m})R_m - |X3_m||Y3_m|\cos(\phi_{x3m} - \phi_{y3m})R_r\right], u \neq v$$

$$P_{m2} = \frac{\pi L_a}{\sigma_m}\sum_{u}^{\infty}\sum_{v}^{\infty}\left[|X2_m||Y2_m|\cos(\phi_{x2m} - \phi_{y2m})R_m - |X4_m||Y4_m|\cos(\phi_{x4m} - \phi_{y4m})R_r\right]$$

$$P_{sl1} = \frac{\pi L_a}{\sigma_{sl}}\sum_{u}^{\infty}\sum_{v}^{\infty}\left[|X1_{sl}||Y1_{sl}|\cos(\phi_{x1sl} - \phi_{y1sl})R_{sl} - |X3_{sl}||Y3_{sl}|\cos(\phi_{x3sl} - \phi_{y3sl})R_m\right], u \neq v$$

$$P_{sl2} = \frac{\pi L_a}{\sigma_{sl}}\sum_{u}^{\infty}\sum_{v}^{\infty}\left[|X2_{sl}||Y2_{sl}|\cos(\phi_{x2sl} - \phi_{y2sl})R_{sl} - |X4_{sl}||Y4_{sl}|\cos(\phi_{x4sl} - \phi_{y4sl})R_m\right]$$

where $X1_m = E_1 J_v(\tau_{m\_1} R_m) + F_1 Y_v(\tau_{m\_1} R_m) = |X1_m| e^{j\phi_{x1m}}$

$$X2_m = E_2 J_v(\tau_{m\_2} R_m) + F_2 Y_v(\tau_{m\_2} R_m) = |X2_m| e^{j\phi_{x2m}}$$

$$X3_m = E_1 J_v(\tau_{m\_1} R_r) + F_1 Y_v(\tau_{m\_1} R_r) = |X3_m| e^{j\phi_{x3m}}$$

$$X4_m = E_2 J_v(\tau_{m\_2} R_r) + F_2 Y_v(\tau_{m\_2} R_r) = |X4_m| e^{j\phi_{x4m}}$$

$$Y1_m = -\frac{v}{R_m \tau_{m\_1}^2} \left\{ \begin{array}{l} E_1 \left[\frac{\tau_{m\_1} R_m}{v} J_{v-1}(\tau_{m\_1} R_m) - J_v(\tau_{m\_1} R_m) \right] \\ + F_1 \left[\frac{\tau_{m\_1} R_m}{v} Y_{v-1}(\tau_{m\_1} R_m) - Y_v(\tau_{m\_1} R_m) \right] \end{array} \right\} = |Y1_m| e^{j\phi_{y1m}}$$

$$Y2_m = -\frac{v}{R_m \tau_{m\_2}^2} \left\{ \begin{array}{l} E_2 \left[\frac{\tau_{m\_2} R_m}{v} J_{v-1}(\tau_{m\_2} R_m) - J_v(\tau_{m\_2} R_m) \right] \\ + F_2 \left[\frac{\tau_{m\_2} R_m}{v} Y_{v-1}(\tau_{m\_2} R_m) - Y_v(\tau_{m\_2} R_m) \right] \end{array} \right\} = |Y2_m| e^{j\phi_{y2m}}$$

$$Y3_m = -\frac{v}{R_r \tau_{m\_1}^2} \left\{ \begin{array}{l} E_1 \left[\frac{\tau_{m\_1} R_r}{v} J_{v-1}(\tau_{m\_1} R_r) - J_v(\tau_{m\_1} R_r) \right] \\ + F_1 \left[\frac{\tau_{m\_1} R_r}{v} Y_{v-1}(\tau_{m\_1} R_r) - Y_v(\tau_{m\_1} R_r) \right] \end{array} \right\} = |Y3_m| e^{j\phi_{y3m}}$$

$$Y4_m = -\frac{v}{R_r \tau_{m\_2}^2} \left\{ \begin{array}{l} E_2 \left[\frac{\tau_{m\_2} R_r}{v} J_{v-1}(\tau_{m\_2} R_r) - J_v(\tau_{m\_2} R_r) \right] \\ + F_2 \left[\frac{\tau_{m\_2} R_r}{v} Y_{v-1}(\tau_{m\_2} R_r) - Y_v(\tau_{m\_2} R_r) \right] \end{array} \right\} = |Y4_m| e^{j\phi_{y4m}}$$

and

$$X1_{sl} = E_1 J_v(\tau_{sl\_1} R_{sl}) + F_1 Y_v(\tau_{sl\_1} R_{sl}) = |X1_{sl}| e^{j\phi_{x1sl}}$$

$$X2_{sl} = E_2 J_v(\tau_{sl\_2} R_{sl}) + F_2 Y_v(\tau_{sl\_2} R_{sl}) = |X2_{sl}| e^{j\phi_{x2sl}}$$

$$X3_{sl} = E_1 J_v(\tau_{sl\_1} R_m) + F_1 Y_v(\tau_{sl\_1} R_m) = |X3_{sl}| e^{j\phi_{x3sl}}$$

$$X4_{sl} = E_2 J_v(\tau_{sl\_2} R_m) + F_2 Y_v(\tau_{sl\_2} R_m) = |X4_{sl}| e^{j\phi_{x4sl}}$$

$$Y1_{sl} = -\frac{v}{R_{sl} \tau_{sl\_1}^2} \left\{ \begin{array}{l} E_1 \left[\frac{\tau_{sl\_1} R_{sl}}{v} J_{v-1}(\tau_{sl\_1} R_{sl}) - J_v(\tau_{sl\_1} R_{sl}) \right] \\ + F_1 \left[\frac{\tau_{sl\_1} R_{sl}}{v} Y_{v-1}(\tau_{sl\_1} R_{sl}) - Y_v(\tau_{sl\_1} R_{sl}) \right] \end{array} \right\} = |Y1_{sl}| e^{j\phi_{y1sl}}$$

$$Y2_{sl} = -\frac{v}{R_{sl}\tau_{sl\_2}^2}\left\{\begin{array}{l} E_2\left[\frac{\tau_{sl\_2}R_{sl}}{v}J_{v-1}(\tau_{sl\_2}R_{sl}) - J_v(\tau_{sl\_2}R_{sl})\right] \\ +F_2\left[\frac{\tau_{sl\_2}R_{sl}}{v}Y_{v-1}(\tau_{sl\_2}R_{sl}) - Y_v(\tau_{sl\_2}R_{sl})\right] \end{array}\right\} = |Y2_{sl}|e^{j\phi_{v2sl}}$$

$$Y3_{sl} = -\frac{v}{R_m\tau_{sl\_1}^2}\left\{\begin{array}{l} E_1\left[\frac{\tau_{sl\_1}R_m}{v}J_{v-1}(\tau_{sl\_1}R_m) - J_v(\tau_{sl\_1}R_m)\right] \\ +F_1\left[\frac{\tau_{sl\_1}R_m}{v}Y_{v-1}(\tau_{sl\_1}R_m) - Y_v(\tau_{sl\_1}R_m)\right] \end{array}\right\} = |Y3_{sl}|e^{j\phi_{v3sl}}$$

$$Y4_{sl} = -\frac{v}{R_m\tau_{sl\_2}^2}\left\{\begin{array}{l} E_2\left[\frac{\tau_{sl\_2}R_m}{v}J_{v-1}(\tau_{sl\_2}R_m) - J_v(\tau_{sl\_2}R_m)\right] \\ +F_2\left[\frac{\tau_{sl\_2}R_m}{v}Y_{v-1}(\tau_{sl\_2}R_m) - Y_v(\tau_{sl\_2}R_m)\right] \end{array}\right\} = |Y4_{sl}|e^{j\phi_{v4sl}}$$

3.5 Analytical model for single-phase PM BLDC motors with eccentric airgap

Due to the eccentric airgap which is often employed in the single-phase BLDC PM motor to overcome the starting problem, it is not convenient to express the boundary conditions at the interface between the stator inner bore and the airgap. Thus, the foregoing developed analytical models have to be modified for the motors having eccentric airgap.

As mentioned above, the difficulty for analytical model is to determine the boundary condition. However, for FEM, one of advantages is its capability of easily coping with the complex geometry. Therefore, by setting the magnet as unmagnetised region and applying a unit current (1A) to the windings in the FE model, the corresponding armature reaction field at a specified boundary can be achieved. Further, if the motor saturation is neglected, for single-phase PM BLDC motors, the instantaneous armature reaction field is approximately proportional to the instantaneous phase current. Hence, for a given phase current, the armature reaction field at the specific boundary can be calculated and fed back to the analytical model. Thus, it becomes feasible for analytical model to carry out the calculation for the rotor eddy current loss. The radius of the boundary is the middle of the airgap, i.e. $R_a = 13.25mm$. The

circumferential armature reaction flux density distribution at the boundary is shown in Figure 3.3.

If the rotation speed is relatively low which gives a greater skin depth associated with the inducing eddy current reaction field compared with the radial thickness of the magnets and the retaining sleeve, the armature reaction field at the specified boundary can be achieved by magnetostatic FE analysis. Otherwise, time-stepped moving-boundary FE analysis which is much time-consuming is required to account for the effect of the eddy current reaction field.

Compared to direct FEM, this method requires less time to calculate the armature rotor eddy current loss with acceptable accuracy. In this section, the static and improved analytical models, which are able to account for the eccentric airgap, are presented and validated by FEM.

3.5.1 Static analytical model B

In magnetostatic FEM, the magnet is removed and a unit current, i.e. 1A, is applied to the windings. The circumferential flux density B_α at the specified boundary, i.e. middle of the airgap, is obtained and expressed in the stationary frame α as follows,

$$B_\alpha\Big|_{r=R_a} = B_\alpha^*(\alpha) \qquad \text{(T)} \tag{3-95}$$

where R_a -- Radius of the middle airgap; m

$B_\alpha^*(\alpha)$ -- Circumferential airgap flux density with 1A phase current, which is obtained from FEM. It can be expressed as a Fourier series, viz.,

$$B_\alpha^*(\alpha) = \sum_{\nu}^{\infty} B_{\alpha\nu} \sin(\nu\alpha + \theta_\nu) \qquad \text{(T)} \tag{3-96}$$

where $B_{\alpha\nu}$ -- Magnitude ν^{th} space harmonic produced by the unit phase current.

θ_v -- Angle of the v^{th} space harmonic produced by the unit phase current.

If the motor saturation is neglected, for a given phase current, the circumferential flux density at $r = R_a$ can be given by,

$$B_\alpha(\alpha) = i(t)B_\alpha^*(\alpha) = \sum_v^\infty i(t)B_{\alpha v}\sin(v\alpha + \theta_v) \qquad \text{(A)} \tag{3-97}$$

where the phase current can be expressed as a Fourier series, viz.,

$$i(t) = \sum_u^\infty I_u \sin(u\omega_r t + \theta_u) \qquad \text{(A)} \tag{3-98}$$

Hence,

$$B_\alpha(\alpha) = \sum_u^\infty \sum_v^\infty I_u B_{\alpha v}\sin(v\alpha + \theta_v)\sin(u\omega_r t + \theta_u) \qquad \text{(T)} \tag{3-99}$$

The magnetic vector potential A can be written by,

$$A = \sum_v^\infty (C_v r^v + D_v r^{-v})\cos(v\alpha) \qquad \text{(A/m)} \tag{3-100}$$

The radial and circumferential components of the armature reaction field can be derived from A as,

$$B_r(\alpha) = \frac{1}{r}\frac{\partial A}{\partial \alpha} \qquad \text{(T)} \tag{3-101}$$

$$B_\alpha(\alpha) = -\frac{\partial A}{\partial r} \qquad \text{(T)} \tag{3-102}$$

And the boundary conditions are given by,

$$B_\alpha\big|_{r=R_r} = 0 \qquad \text{(T)} \tag{3-103}$$

$$B_\alpha\big|_{r=R_a} = B_\alpha(\alpha) \qquad \text{(T)} \tag{3-104}$$

According to equations (3-96) to (3-104), the analytical expressions for the magnetic vector potential can be derived as,

$$A(r,\alpha,t) = -\sum_{u}^{\infty}\sum_{v}^{\infty} \frac{I_u B_{\alpha v}}{v} \frac{r^v + R_r^{2v} r^{-v}}{R_a^{v-1} - R_r^{2v} R_a^{-v-1}} \sin(u\omega_r t + \theta_u)\sin(v\alpha + \theta_v) \quad \text{(A/m)} \qquad (3\text{-}105)$$

Therefore, the radial and circumferential components of the armature reaction field are,

$$B_r(r,\alpha,t) = -\sum_{u}^{\infty}\sum_{v}^{\infty} \frac{I_u B \alpha_{tv}}{r} \frac{r^v + R_r^{2v} r^{-v}}{R_a^{v-1} - R_r^{2v} R_a^{-v-1}} \sin(u\omega_r t + \theta_u)\cos(v\alpha + \theta_v) \quad \text{(T)} \qquad (3\text{-}106)$$

$$B_\alpha(r,\alpha,t) = \sum_{u}^{\infty}\sum_{v}^{\infty} I_u B_{\alpha v} \frac{r^{v-1} - R_r^{2v} r^{-v-1}}{R_a^{v-1} - R_r^{2v} R_a^{-v-1}} \sin(u\omega_r t + \theta_u)\sin(v\alpha + \theta_v) \quad \text{(T)} \qquad (3\text{-}107)$$

With the similar procedure for eddy current loss calculations for single-phase PM BLDC motors having concentric airgap, the eddy current density in the magnet and the retaining sleeve which are expressed in the rotating reference frame θ, are,

$$J_m = J_{m1} + J_{m2} + C_{m1} + C_{m2} \qquad \text{(A/m}^2\text{)} \qquad (3\text{-}108)$$

$$J_{sl} = J_{sl1} + J_{sl2} \qquad \text{(A/m}^2\text{)} \qquad (3\text{-}109)$$

where

$$J_{m1} = -\frac{\sigma_m \omega_r}{2} \sum_{u}^{\infty}\sum_{v}^{\infty} (u-v) \frac{I_u B_{\alpha v}\left(r^v + R_r^{2v} r^{-v}\right)}{v\left(R_a^{v-1} - R_r^{2v} R_a^{-v-1}\right)} \sin[(u-v)\omega_r t - v\theta + \theta_u - \theta_v]$$

$$J_{m2} = \frac{\sigma_m \omega_r}{2} \sum_{u}^{\infty}\sum_{v}^{\infty} (u+v) \frac{I_u B_{\alpha v}\left(r^v + R_r^{2v} r^{-v}\right)}{v\left(R_a^{v-1} - R_r^{2v} R_a^{-v-1}\right)} \sin[(u+v)\omega_r t + v\theta + \theta_u + \theta_v]$$

$$J_{sl1} = -\frac{\sigma_{sl} \omega_r}{2} \sum_{u}^{\infty}\sum_{v}^{\infty} (u-v) \frac{I_u B_{\alpha v}\left(r^v + R_r^{2v} r^{-v}\right)}{v\left(R_a^{v-1} - R_r^{2v} R_a^{-v-1}\right)} \sin[(u-v)\omega_r t - v\theta + \theta_u - \theta_v]$$

$$J_{sl2} = \frac{\sigma_{sl} \omega_r}{2} \sum_{u}^{\infty}\sum_{v}^{\infty} (u+v) \frac{I_u B_{\alpha v}\left(r^v + R_r^{2v} r^{-v}\right)}{v\left(R_a^{v-1} - R_r^{2v} R_a^{-v-1}\right)} \sin[(u+v)\omega_r t + v\theta + \theta_u + \theta_v]$$

and,

- If $N = 1$, $C_{m1} = C_{m2} = 0$
- If $N > 1$,

$$C_{m1} = N \frac{\sigma_m \omega_r \mu_0}{\pi\left(R_m^2 - R_r^2\right)} \sum_{u}^{\infty}\sum_{v}^{\infty} \frac{(u-v) I_u B_{\alpha v}}{v^2\left(R_a^{v-1} - R_r^{2v} R_a^{-v-1}\right)} \left[\frac{R_m^{v+2} - R_r^{v+2}}{v+2} + R_r^{2v} E_{mv}\right] \sin\left(\frac{v\pi}{N}\right)\sin[(u-v)\omega_r t + \theta_u - \theta_v]$$

$$C_{m2} = -N\frac{\sigma_m \omega_r \mu_0}{\pi\left(R_m^2 - R_r^2\right)}\sum_u^{\infty}\sum_v^{\infty}\frac{(u+v)I_u B_{\alpha v}}{v^2\left(R_a^{\,v-1} - R_r^{\,2v}R_a^{\,-v-1}\right)}\left[\frac{R_m^{v+2} - R_r^{v+2}}{v+2} + R_r^{2v}E_{mv}\right]$$
$$\sin\left(\frac{v\pi}{N}\right)\sin\left[(u+v)\omega_r t + \theta_u + \theta_v\right]$$

where $E_{mv} = \begin{cases} \ln\left(\dfrac{R_m}{R_r}\right), & v = 2 \\ \dfrac{R_m^{-v+2} - R_r^{-v+2}}{-v+2} & v \neq 2 \end{cases}$

The eddy current losses in the permanent and the retaining sleeve are,

$$P_m = N\frac{L_a\omega_r}{2\pi}\int_{R_r}^{R_m}\int_0^{\frac{2\pi}{\omega_r}}\int_{-\frac{\alpha_p}{2}}^{\frac{\alpha_p}{2}}\frac{1}{\sigma_m}J_m^2 r\,dr\,dt\,d\theta = \sum_u^{\infty}\sum_v^{\infty}\left(P_{cuv} + P_{auv}\right) \quad \text{(W)} \tag{3-110}$$

$$P_{sl} = \frac{L_a\omega_r}{2\pi}\int_{R_m}^{R_{sl}}\int_0^{\frac{2\pi}{\omega_r}}\int_{-\pi}^{\pi}\frac{1}{\sigma_{sl}}J_{sl}^2 r\,dr\,dt\,d\theta = \sum_u^{\infty}\sum_v^{\infty}P_{sluv} \quad \text{(W)} \tag{3-111}$$

where

P_{cuv} is given by,

$$P_{cuv} = \frac{\pi L_a\sigma_m\omega_r^2 I_u^2 B_{\alpha v}^2\left[(u+v)^2 + (u-v)^2\right]}{4v^2\left(R_a^{v-1} - R_r^{2v}R_a^{-v-1}\right)^2}\left[\frac{R_m^{2v+2} - R_r^{2v+2}}{2v+2} + R_r^{2v}\left(R_m^2 - R_r^2\right) + R_r^{4v}F_{mv}\right]$$

where $F_{mv} = \begin{cases} \ln\left(\dfrac{R_m}{R_r}\right), & v = 1 \\ \dfrac{R_m^{-2v+2} - R_r^{-2v+2}}{-2v+2}, & v \neq 1 \end{cases}$

P_{auv} is given by,

- If $N = 1$, $P_{auv} = 0$
- If $N > 1$,

$$P_{auv} = -N^2\frac{L_a\sigma_m\omega_r^2 I_u^2 B_{\alpha v}^2\sin^2\left(v\dfrac{\pi}{N}\right)\left[(u+v)^2 + (u-v)^2\right]}{2\pi v^4\left(R_m^2 - R_r^2\right)\left(R_a^{v-1} - R_r^{2v}R_a^{-v-1}\right)^2}\left(\frac{R_m^{v+2} - R_r^{v+2}}{v+2} + R_r^{2v}E_{mv}\right)^2$$

P_{sluv} is given by,

$$P_{sluv} = \frac{\pi L_a \sigma_{sl} \omega_r^2 I_u^2 B_{\alpha v}^2 \left[(u+v)^2 + (u-v)^2\right]}{4v^2 \left(R_a^{v-1} - R_r^{2v} R_a^{-v-1}\right)^2} \left[\frac{R_{sl}^{2v+2} - R_m^{2v+2}}{2v+2} + R_r^{2v}\left(R_{sl}^2 - R_m^2\right) + R_r^{4v} F_{slv} \right]$$

where $F_{slv} = \begin{cases} \ln\left(\dfrac{R_{sl}}{R_m}\right), & v = 1 \\ \dfrac{R_{sl}^{-2v+2} - R_m^{-2v+2}}{-2v+2}, & v \neq 1 \end{cases}$

3.5.2 Improved analytical model B

The boundary condition (3-97) at the middle of the airgap achieved from FEM can be rewritten in the rotational reference frame, by letting $\alpha = \theta + \omega_r t$,

$$\begin{aligned} & B_\alpha(\theta) \\ &= \sum_u^\infty \sum_v^\infty I_u B_{\alpha v} \sin\left[v(\theta + \omega_r t) + \theta_v\right] \sin\left(u\omega_r t + \theta_u\right) \\ &= \sum_u^\infty \sum_v^\infty \frac{1}{2} I_u B_{\alpha v} \left\{\cos\left[(u-v)\omega_r t - v\theta + \theta_u - \theta_v\right] - \cos\left[(u+v)\omega_r t + v\theta + \theta_u + \theta_v\right]\right\} \\ &= B_{\alpha\_1}(\theta) + B_{\alpha\_2}(\theta) \end{aligned} \quad \text{(T)} \quad (3\text{-}112)$$

where $B_{\alpha\_1}(\theta)$ and $B_{\alpha\_2}(\theta)$ are related to the forward and backward rotating mmfs which are rotating in asynchronous with the rotor, and can be given by,

$$B_{\alpha\_1}(\theta) = \sum_u^\infty \sum_v^\infty \frac{I_u B_{\alpha v}}{2} \cos(\phi_1), u \neq v \quad \text{(T)} \quad (3\text{-}113)$$

$$B_{\alpha\_2}(\theta) = -\sum_u^\infty \sum_v^\infty \frac{I_u B_{\alpha v}}{2} \cos(\phi_2) \quad \text{(T)} \quad (3\text{-}114)$$

where $\phi_1 = (u-v)\omega_r t - v\theta + \theta_u - \theta_v$, $\phi_2 = (u+v)\omega_r t + v\theta + \theta_u + \theta_v$.

If $u = v$, the forward rotating mmfs is in synchronous with the rotor and will not induce the eddy current in the rotor. Thus, the boundary equations at the middle of the airgap can be

written by,

$$H_{\alpha I\_1}\Big|_{r=R_a} = \frac{B_{\alpha\_1}(\theta)}{\mu_0} \quad \text{(A/m)} \tag{3-115}$$

$$H_{\alpha I\_2}\Big|_{r=R_a} = \frac{B_{\alpha\_2}(\theta)}{\mu_0} \quad \text{(A/m)} \tag{3-116}$$

In the equations (3-89) and (3-90), $Y1$ and $Y2$ are rewritten by,

$$[Y1]=\begin{bmatrix} -\frac{I_u B_{av}}{2\mu_0} \\ 0 \\ 0 \\ 0 \\ 0 \\ 0 \end{bmatrix} \text{ and } [Y2]=\begin{bmatrix} \frac{I_u B_{av}}{2\mu_0} \\ 0 \\ 0 \\ 0 \\ 0 \\ 0 \end{bmatrix}$$

Hence, coefficients A_1, B_1, C_1, D_1, E_1, F_1 and A_2, B_2, C_2, D_2, E_2 F_2 can be calculated.

Therefore, the eddy current and associated eddy current loss can be obtained by equations (3-93) and (3-94).

3.6 Comparison of armature rotor eddy current loss predicted by analytical models and FEM

Although the FEM is time consuming, it is useful to validate the analytical models. Thus, in this section, 2D magnetostatic and time-stepping FEM are employed to validate the armature field predicted by static and improved analytical models for a three-phase PM BLDC motor, i.e. **Design A in Chapter 2,** a single-phase PM BLDC motor with concentric arigap, i.e. **Design C** in Chapter 2, and a single-phase PM BLDC motor with eccentric arigap, i.e. **Design E** in Chapter 2. In contrast to the magnetostatic FEM, the effect of the eddy current reaction field on the armature field is taken into account in the time-stepping FEM. Therefore, the time-stepping FEM is taken further to analyse the eddy current and associated loss in the magnet and the sleeve. In order to eliminate the eddy current loss component caused by the

variation of the magnet working point which results from the stator slotting or eccentric airgap, the PMs are assumed to be electrically conductive but to have zero remanence. The detailed FEM investigation will be presented in Chapter 4. The phase current waveforms are predicted by the dynamic simulation models as described in Chapter 2. Figure 3.4 and Figure 3.5 show the simulated phase current waveforms, fundament component and harmonics for a three-phase PM BLDC motor, i.e. **Design A**, and a single-phase PM BLDC motor, i.e. **Design E**, respectively. In this section, fundament component of the phase current is applied to the windings to investigate the armature rotor eddy current loss.

Figure 3.6(a) shows the FEM predicted armature reaction field distribution of three-phase PM BLDC motor which has 0.6mm of sleeve thickness and a ring magnet when $i_a = 0A$, $i_b = -5.2A$ and $i_c = 5.2A$. Figure 3.7 shows its radial and circumferential components of the flux density at the middle of the airgap and middle of the magnet as predicted by static analytical model, magnetostatic and time-stepping FEM. It can be seen that there is good agreement between waveforms predicted by the static analytical model and magnetostatic FEM. However, it is obviously noted that the distribution of the radial component of flux density predicted by the time-stepping FEM at the speed of 45krpm is distorted by the eddy current reaction field. It indicates that the static analytical model is not accurate enough to predict the armature field when the speed is relatively high. By applying the fundament component of phase current, Figure 3.4(a), to the windings, the radial and circumferential components of the flux density at the middle of the airgap and middle of the magnet $@t = 0.001333s$ as predicted by improved analytical model and time-stepping FEM are compared in Figure 3.8. As will be seen, a good agreement is achieved.

Figure 3.6(a) and (b) show the FEM predicted armature reaction field distribution of single-phase PM BLDC motors which have 0.6mm of sleeve thickness and a ring magnet with concentric and eccentric airgap, respectively, when the phase current value is 8A. For single-phase PM BLDC motor having a concentric, two analytical models have been developed to analysis the armature field. One model, i.e. analytical model A, is using

equivalent current sheet over the stator slotting to represent the phase current. Another model, i.e. analytical model B, is using the equivalent boundary condition at the middle of the airgap which is provided by the FEM. By applying the fundamental component of phase current, Figure 3.5(a), to the windings, the armature reaction field distributions predicted by both static and improved analytical models are compared with that predicted by the magnetostatic and time-stepping FEM in Figure 3.9 and Figure 3.10 @ $t = 0.000333s$ when the instantaneous phase current value is 8A. As will be seen, there is a good agreement between static analytical models A, B and magnetostatic FEM. However, when speed is relatively high, as validated by time-stepping FEM, improved analytical models are much more accurate than static analytical models, which is also valid for the single-phase PM brushless DC motors having an eccentric airgap, as shown in Figure 3.11 and Figure 3.12.

As long as the armature field is available, the eddy current and associated loss can be calculated as discussed in above analytical model. The eddy current distribution in the middle of PMs and sleeve of the three phase and single-phase PM BLDC motors predicted by the analytical models and time-stepping FEM are compared in Figures Figure 3.13 and Figure 3.14, respectively. It can be noted that when the speed is relatively lower, for example, in the case of 1krpm, both static and improved analytical models can give a good match with time-stepping FEM. However, the static analytical model will have larger error when the speed is higher, for example, in the case of 45krpm. In contrast, because the improved analytical model has taken the eddy current reaction field into account, it still can give accurate results even the speed is relatively higher. Therefore, as shown in Figure 3.15, Figure 3.16 and Figure 3.17, the static analytical model predicted eddy current loss increases quadratically with the speed and will overestimate the eddy current loss at higher speed. Hence, the improved analytical model is a preferred solution to calculate the eddy current loss accurately, although there is a slight difference between improved analytical model and time-stepping FEM predicted results, which can mainly be attributed to three factors, i.e.:

- In the improved analytical model, Bessel functions of the first and second order, i.e. $J_\nu(\tau \cdot r)$ and $Y_\nu(\tau \cdot r)$, with large order ν and complex arguments $\tau \cdot r$ could lead

to results which are too large to be represented as convenient floating-point values in MATLAB. For the same reason, matrix calculation such as $[X]=[K]^{-1}[Y]$ cannot be executed successfully. Hence, a numerical failure could occur. Neglecting the component of loss whose calculation is failed in analytical model will underestimate the total loss slightly.

- Improved analytical model A neglects the effect of stator slot opening, whereas improved analytical model B accounts for this by employing the equivalent boundary condition at the middle of the airgap which is provided by FEM. Therefore, as shown in Figure 3.16, improved analytical model A predicted loss is slightly higher than that predicted by improved analytical model B and FEM since by considering the influence of slotting the armature reaction field around the slot opening regions is reduced.
- In order to simplify the analytical model B, the equivalent boundary condition at the middle of the airgap is calculated by time-stepping FE model at rated speed, i.e. 45krpm. However, for different speed, because the effect of the eddy current reaction field on the armature reaction field is different, the boundary condition will be affected as well. Hence, applying the equivalent boundary condition, which is specifically ideal for the rated speed, to the full range of speed conditions will introduce some error. However, according to Figure 3.12, the effect of the eddy current reaction field on the circumferential component of armature reaction field at the middle of the airgap is relatively weak. Hence, the calculation error of the loss could be reasonably neglected.
- Generally, the accuracy of FE model is mainly determined by the mesh size. Particularly when the speed is relatively high, in order to accurately model the relatively small skin effect, a sufficient discretization of the interested regions such as magnet and sleeve has to be employed to calculate the eddy current loss. However, smaller mesh size results in more computation time. Therefore, there is a trade-off between the computation time and accuracy.

Overall, by considering the accuracy of the eddy current loss calculation at the rated speed, improved analytical model is a better solution than static analytical model to predict the eddy

current loss. By applying the dynamic simulation model predicted phase current, as shown in Figure 3.4(a) and Figure 3.5(a), to the windings, the eddy current loss of three-phase and single-phase PM BLDC motors are predicted by improved analytical model and time-stepping FEM. As will be evident from Figure 3.18(a), the majority of the loss of the three-phase motor are mainly due to the fundamental current time-harmonic and the second space-harmonic mmfs. Whereas, as shown in Figure 3.18(b), the majority of the loss of the single-phase motor are mainly due to the fundamental current time-harmonic and the fundamental and third space-harmonic mmfs.

3.7 Limitations of analytical model

The developed analytical models in this chapter are adequate to predict the eddy current loss due to the armature reaction field. However, for a realistic motor operating condition, there is another loss component, i.e. open-circuit eddy current loss, which is due to the variation of the magnet working point resulting from the stator slotting or eccentric airgap. Further, the armature eddy current loss and open-circuit eddy current loss cannot simply be added to give the on-load eddy current loss. For three-phase PM BLDC motors, the open-circuit eddy current loss is relatively small. The total on-load eddy current loss is mainly due to the armature reaction field. Therefore, it is acceptable for three-phase PM BLDC motors to predict the on-load current loss by examining the armature eddy current loss only with the developed analytical model. However, for single-phase PM BLDC motors which have an eccentric airgap, there is a significant open-circuit eddy current loss. Hence, analytical model predicted armature eddy current loss may not be accurately enough to represent the on-load eddy current loss. In this case, FEM is required to calculate the on-load eddy current loss directly and accurately, as will be presented in Chapter 4 in detail.

In analytical models, it is assumed that the axial length of the rotor stack is infinite such that the end-effects are ignored and the resulting eddy currents in the conductive regions flow in the axially-direction only. In reality due to the finite axial length, there exists the significant

eddy current flowing in the circumferential direction, which cannot be taken into account in the analytical models. Further, as an effective method to reduce the eddy current loss in the magnet, segmenting the magnet axially or circumferentially may be employed, for which analytical solutions are more difficult. Therefore, FE method is an alternative approach to the solution.

3.8 Summary

The static and improved analytical models for calculating the armature rotor eddy current loss have been developed for three-phase and single-phase PM BLDC motors. By comparing with the FEM predicted results, it was noticed that static analytical model overestimates the loss due to its neglecting the influence of the eddy current on the armature field, particularly at the high speed. Therefore, the improved analytical model is proposed and proved to be able to predict the rotor load eddy current loss more accurately by comparing with the FEM predicted results. For three-phase PM BLDC motor and single-phase PM BLDC having concentric airgap, both static and improved analytical models employ an equivalent current sheet distributed across the stator slot openings to account for the space and time harmonics of the stator mmfs. However, for a single-phase PM BLDC motor having an eccentric airgap, it becomes much more complicated to develop the analytical model based on the equivalent current sheet. Hence, a new method where the boundary condition at the middle of the airgap is provided by FE model is proposed and gives an acceptable result. Due to limitations of the analytical models associated with the on-load rotor eddy current loss for single-phase PM BLDC motor having an eccentric airgap and magnet segment schemes, FE model is an alternative solution which will be investigated in the next chapter.

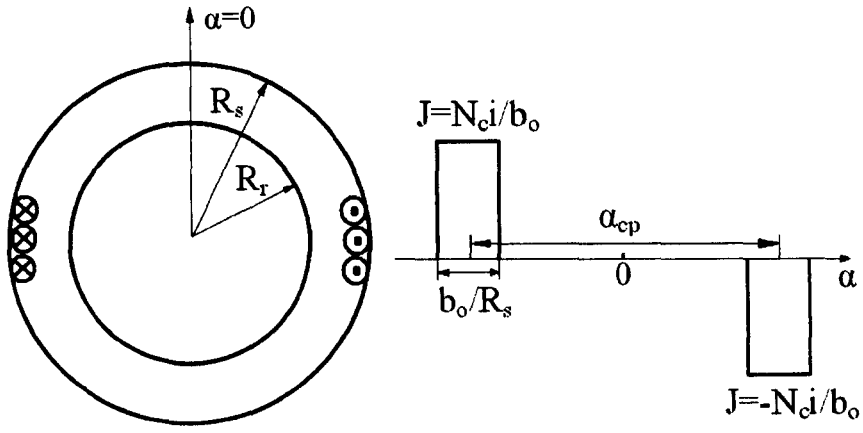

Figure 3.1 Equivalent current sheet of a single coil

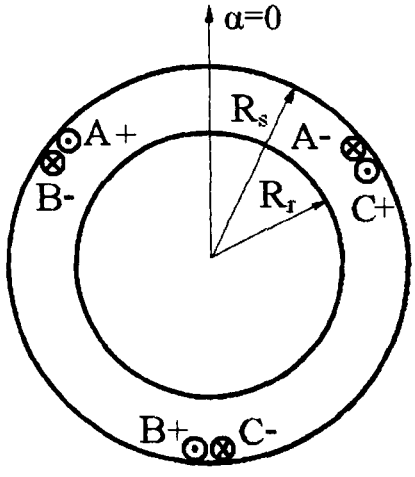

Figure 3.2 Equivalent current sheet of 3-phase coil

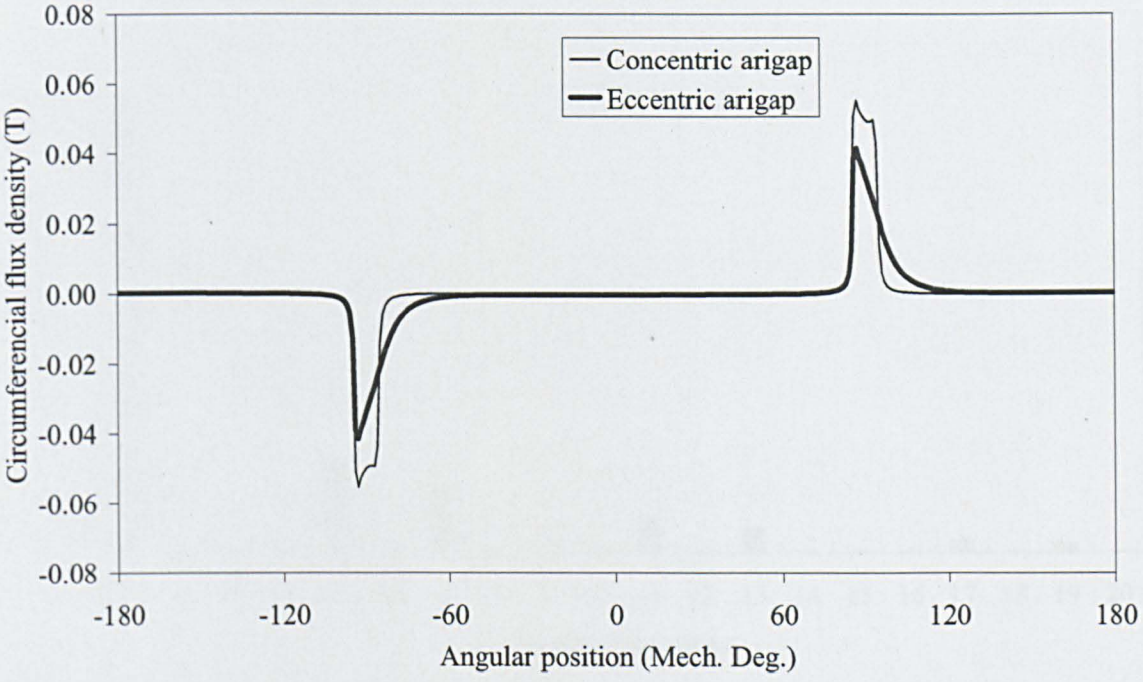

Figure 3.3 FEM predicted circumferential armature reaction flux density at boundary of single-phase PM BLDC motor.

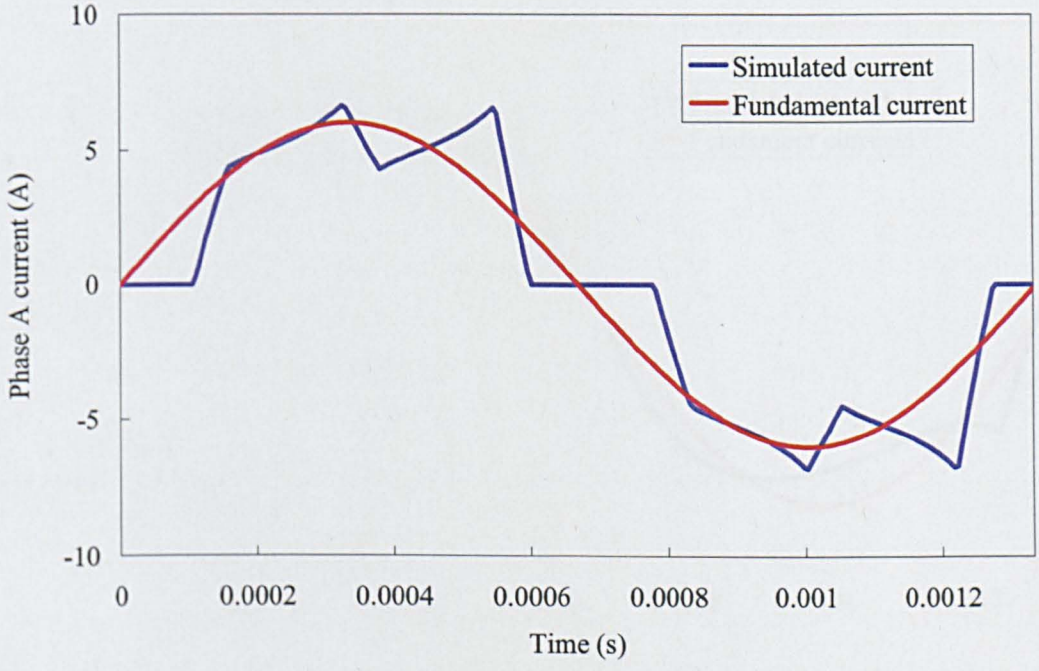

(a) Simulated phase current and its fundamental component.

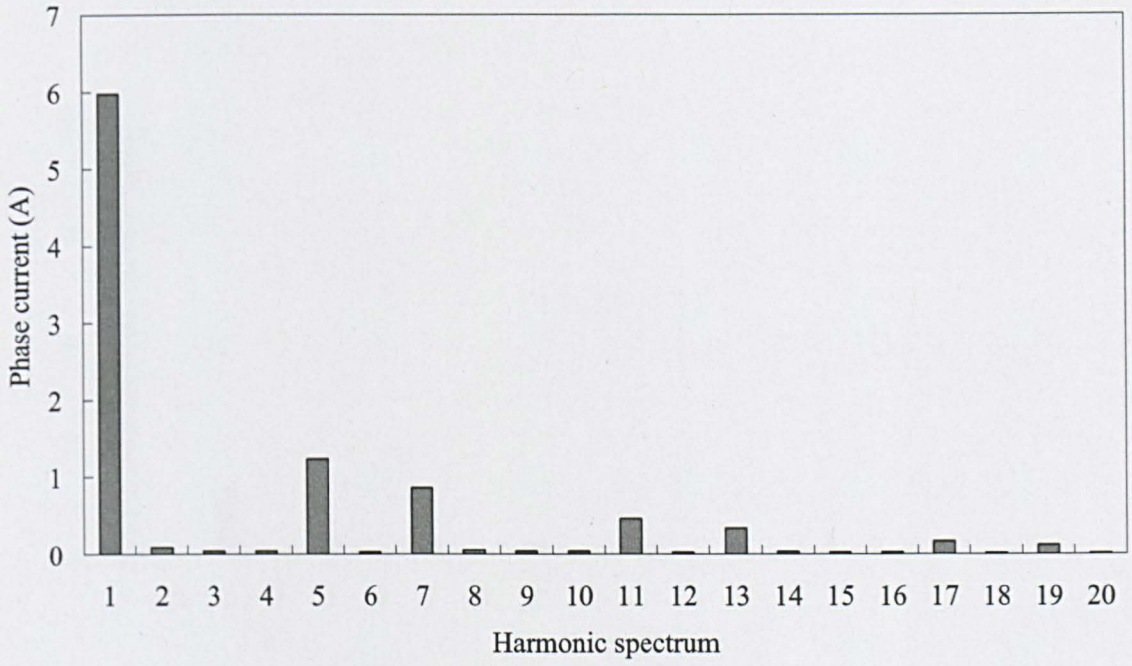

(b) Simulated phase current harmonic spectra.

Figure 3.4 Simulated phase A current of three-phase PM BLDC motor. (Speed=45,000rpm)

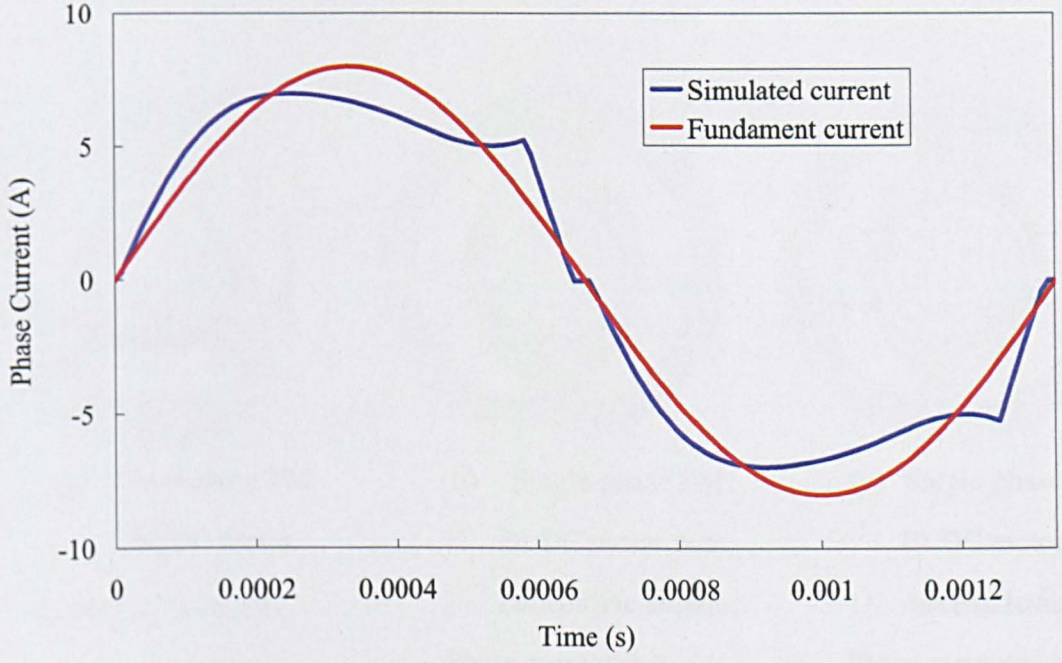

(a) Simulated phase current and its fundamental component.

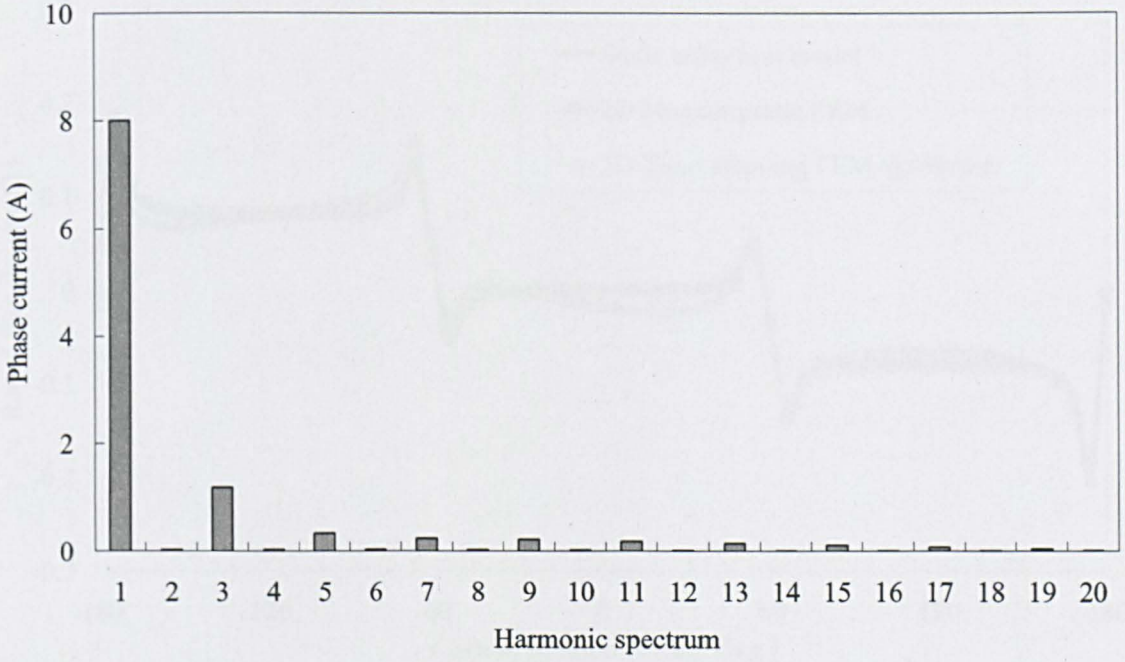

(b) Simulated phase current harmonic spectra.

Figure 3.5 Simulated phase current of single-phase PM BLDC motor. (Speed=45,000rpm)

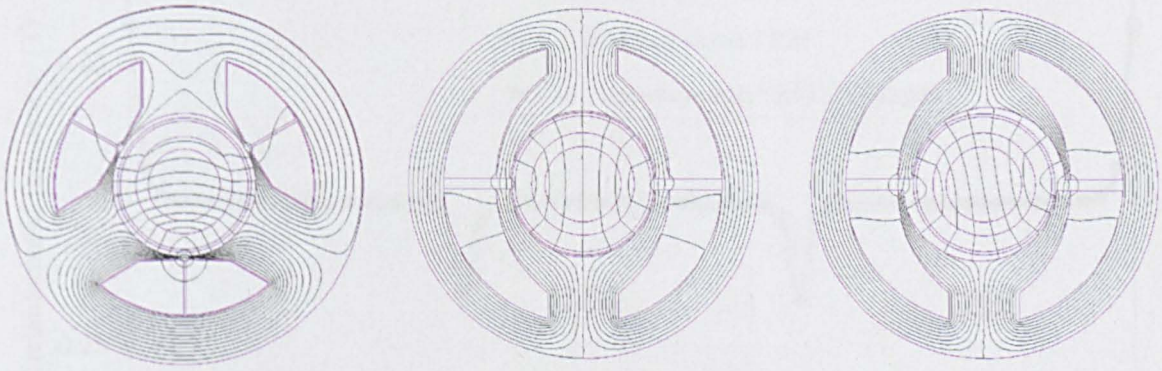

(a) Three-phase PM BLDC motor.

$i_a = 0A, i_b = -5.2A,$

$i_c = 5.2A$

(b) Single-phase PM BLDC motor with **concentric** airgap.

Phase current=8A

(c) Single-phase PM BLDC motor with **eccentric** airgap.

Phase current=8A

Figure 3.6 FEM predicted armature flux distribution.

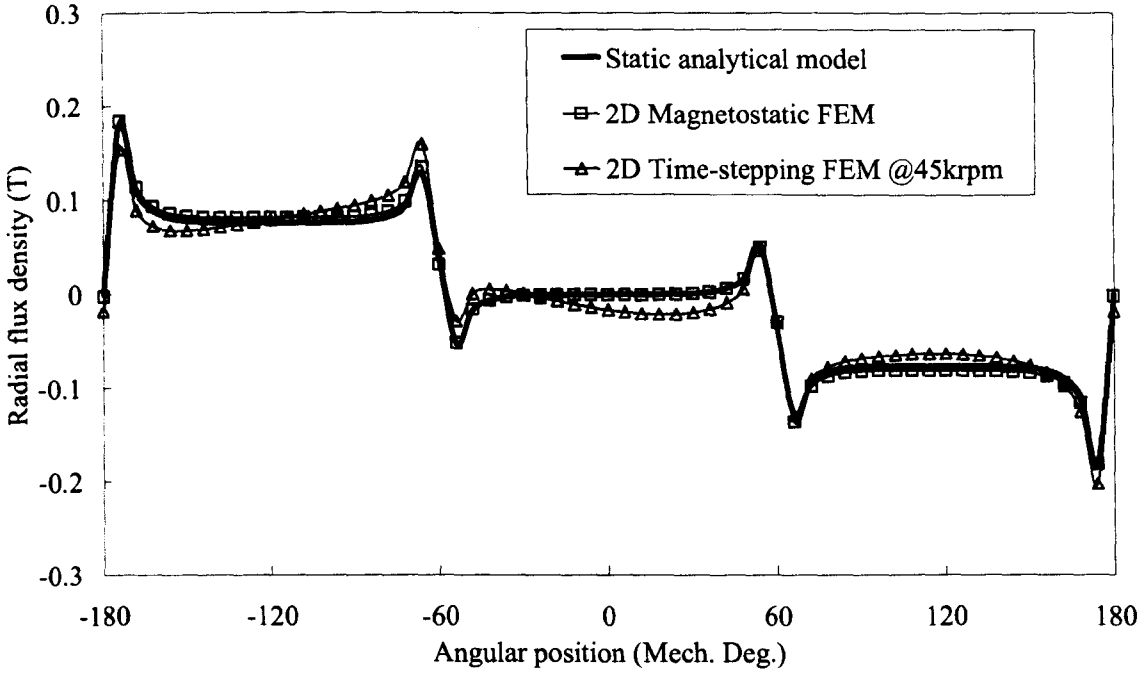

(I) Radial component

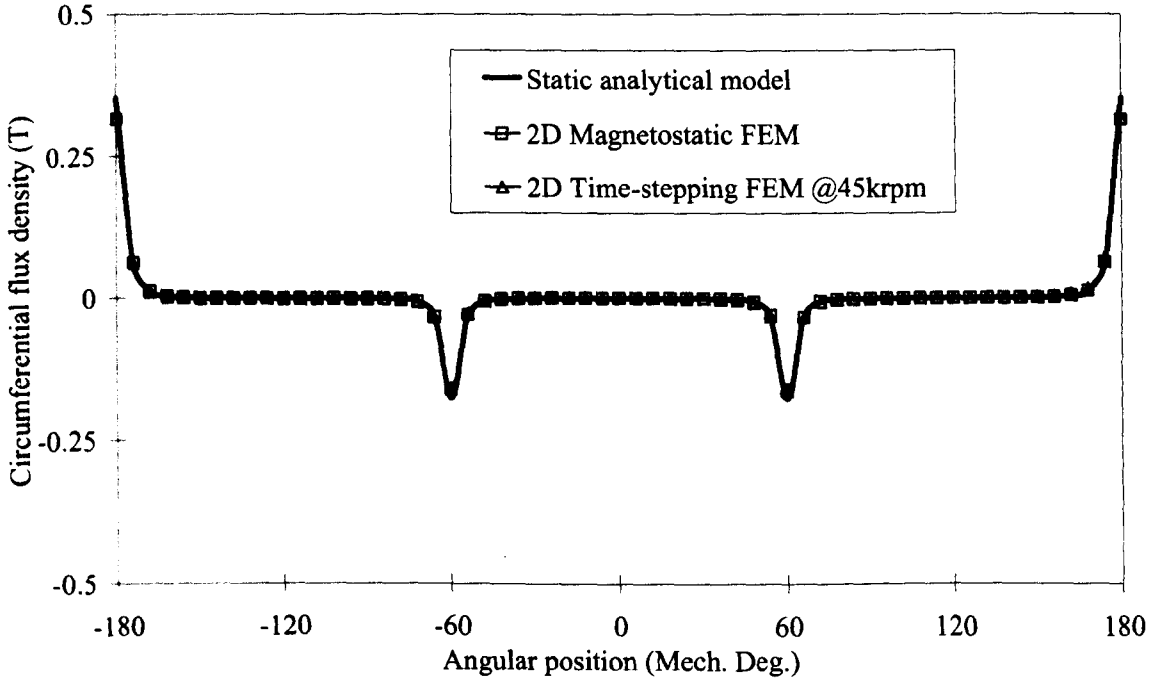

(II) Circumferential component

(a) Middle of airgap

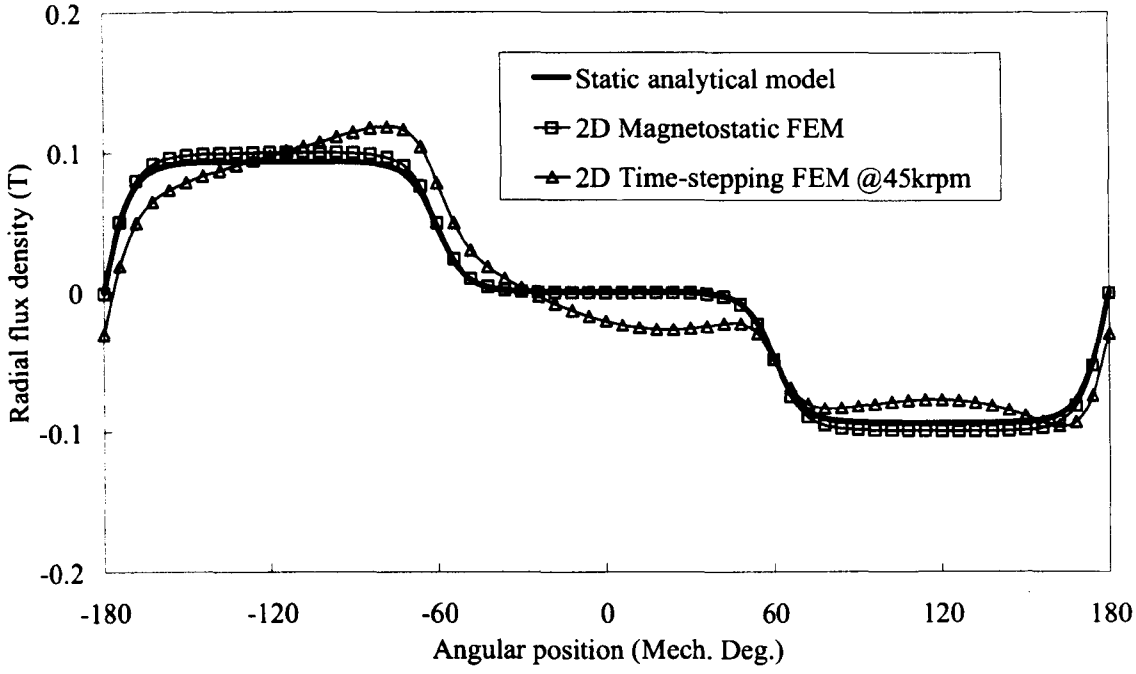

(I) Radial component

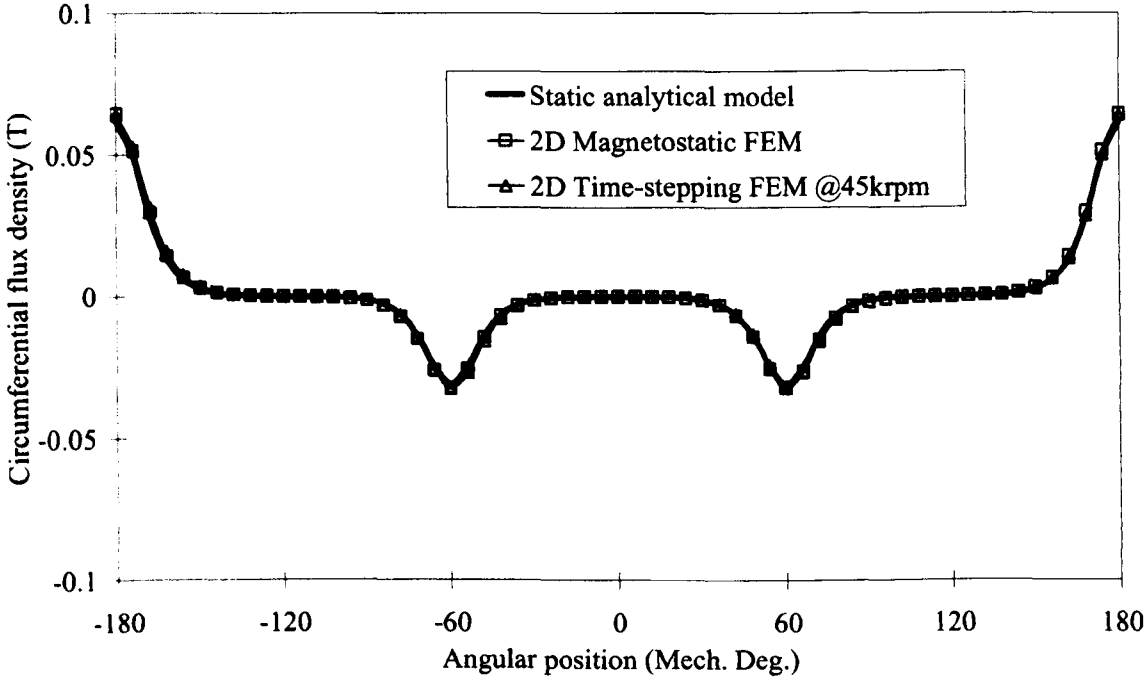

(II) Circumferential component

(b) Middle of PM

Figure 3.7 Comparison of flux distribution predicted by **static** analytical models and FEM for **three-phase** PM brushelss DC motor. ($t = 0.001333s$)

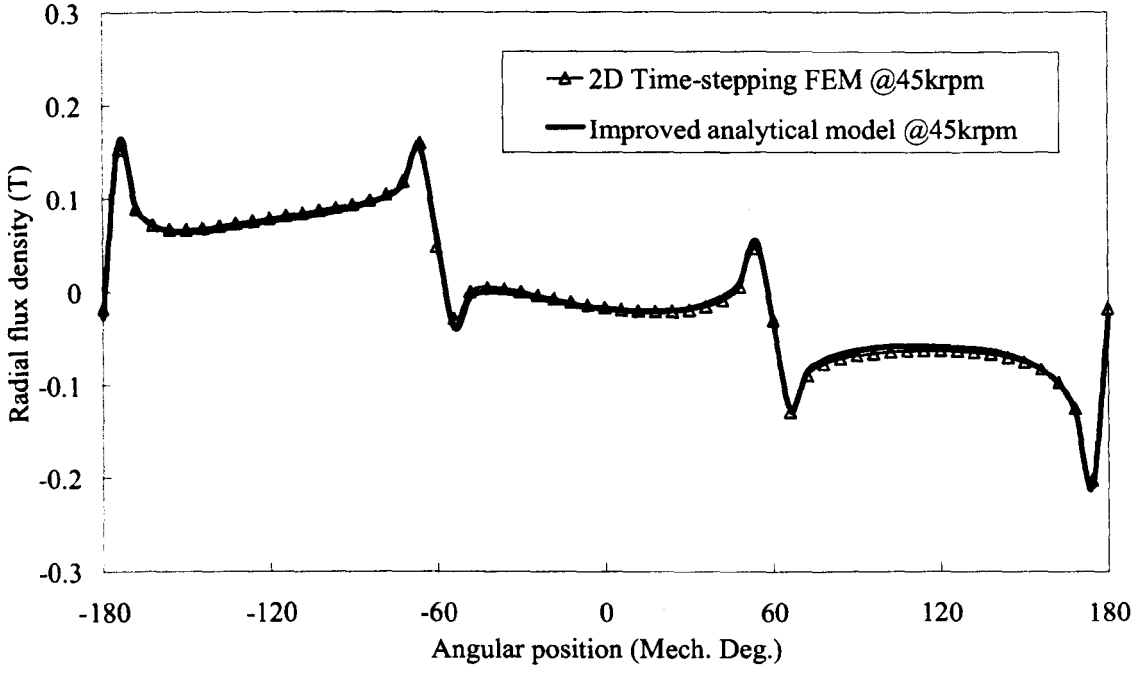

(I) Radial component

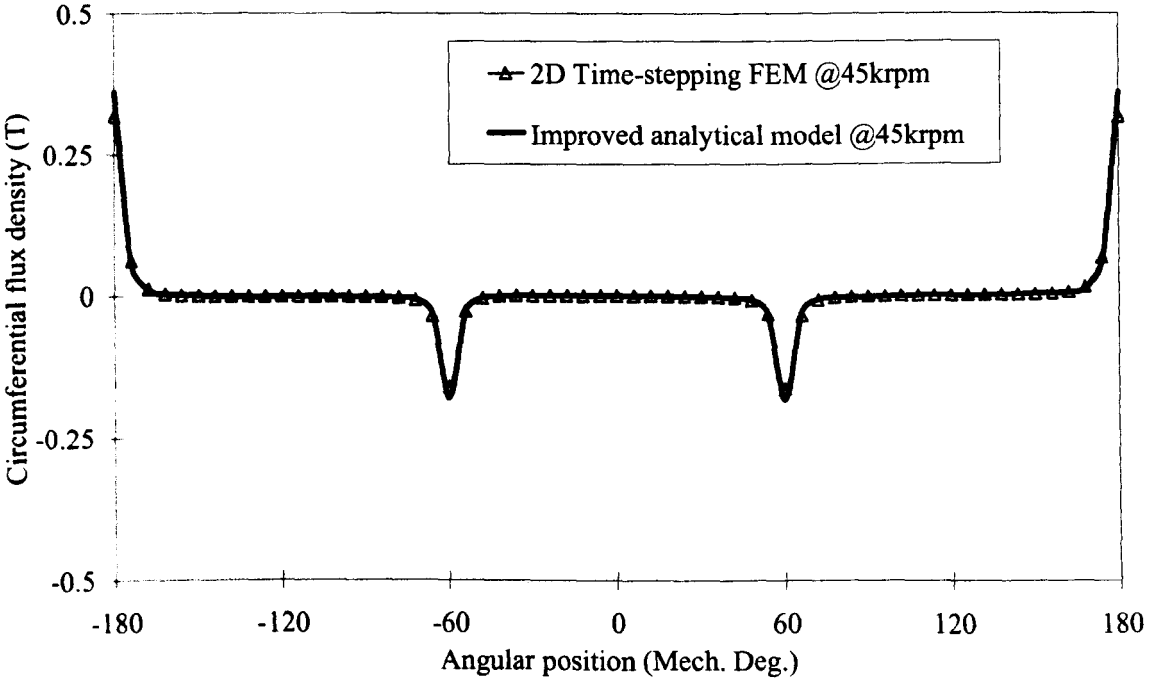

(II) Circumferential component

(a) Middle of airgap

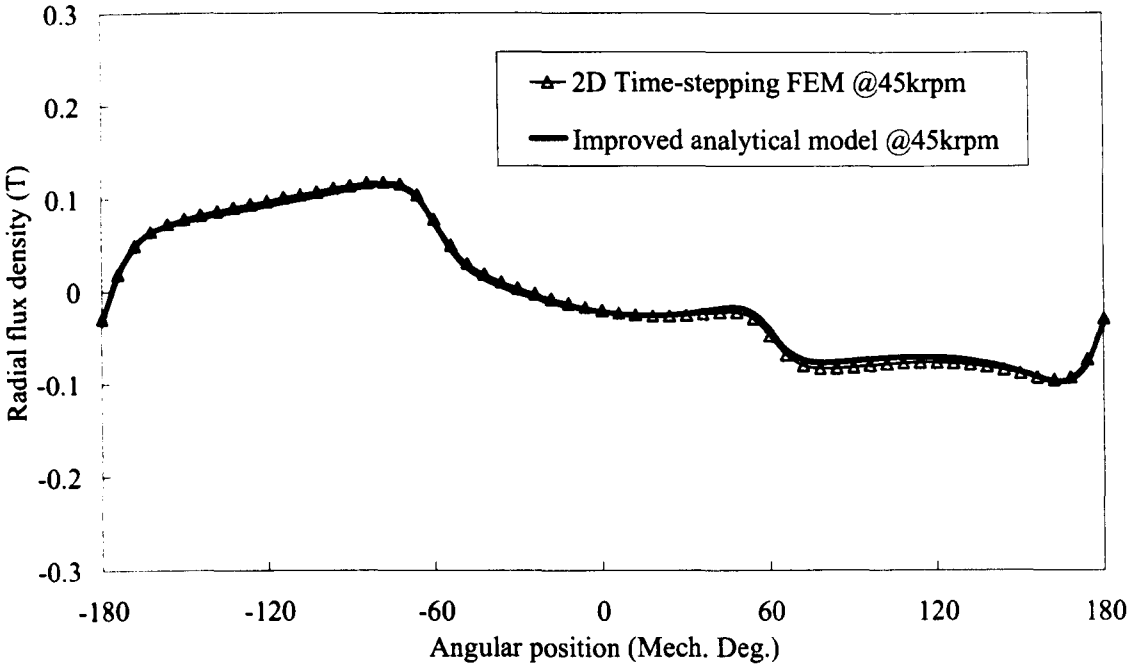

(I) Radial component

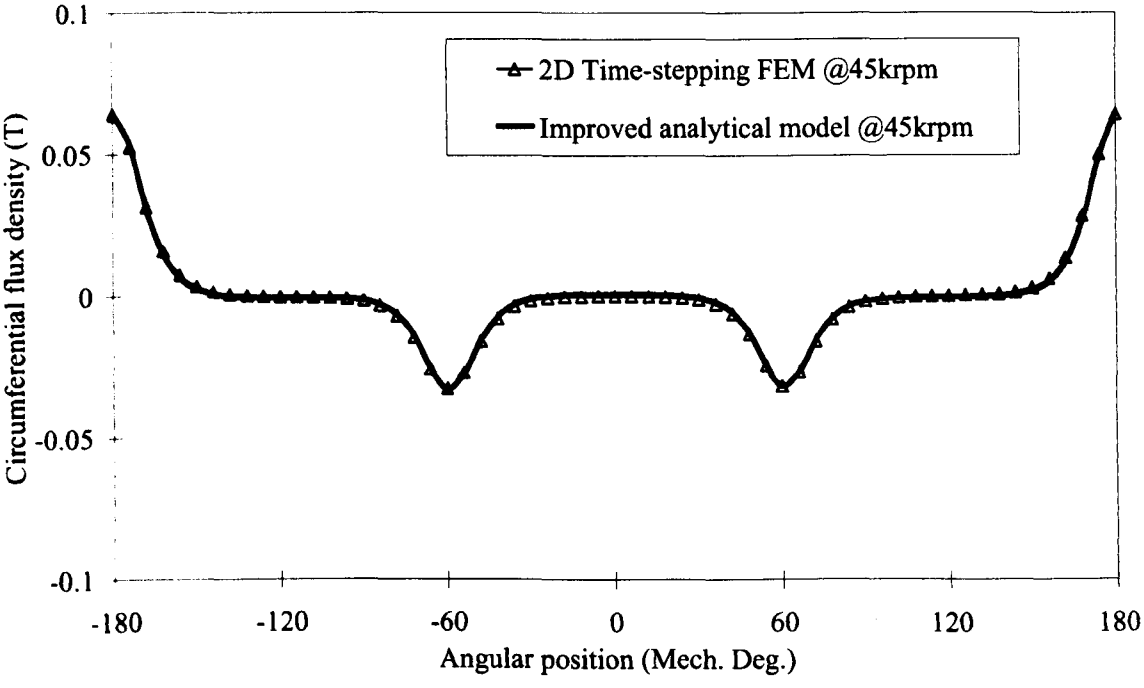

(II) Circumferential component

(b) Middle of PM

Figure 3.8 Comparison of flux distribution predicted by **improved** analytical models and FEM for **three-phase** PM BLDC motor. ($t = 0.001333s$)

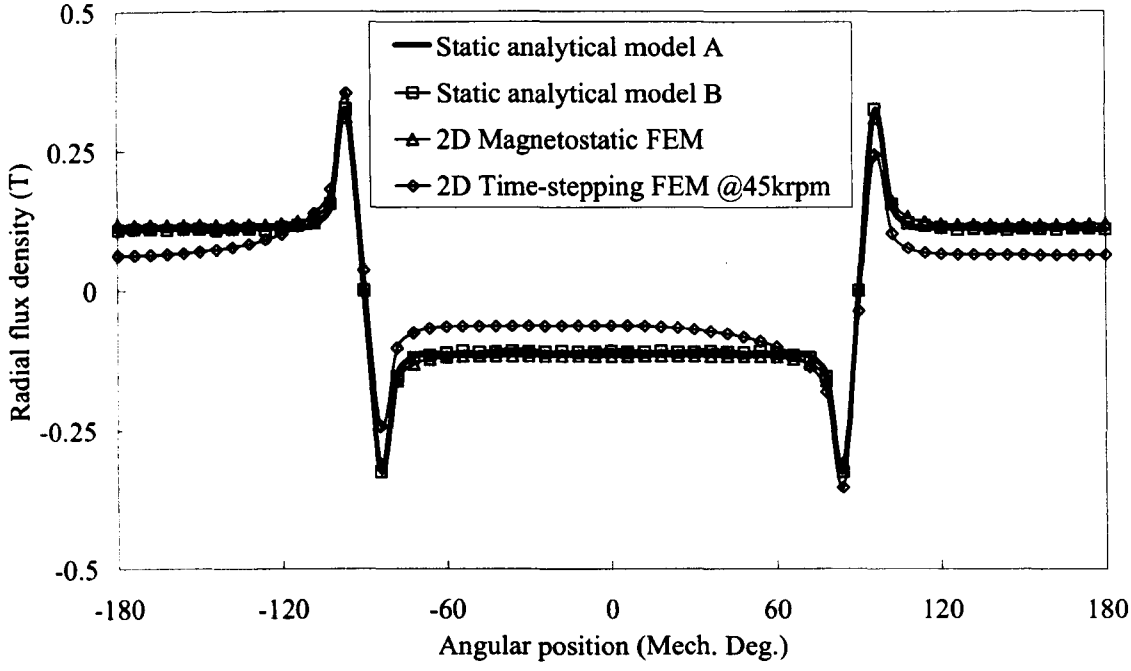

(I) Radial component

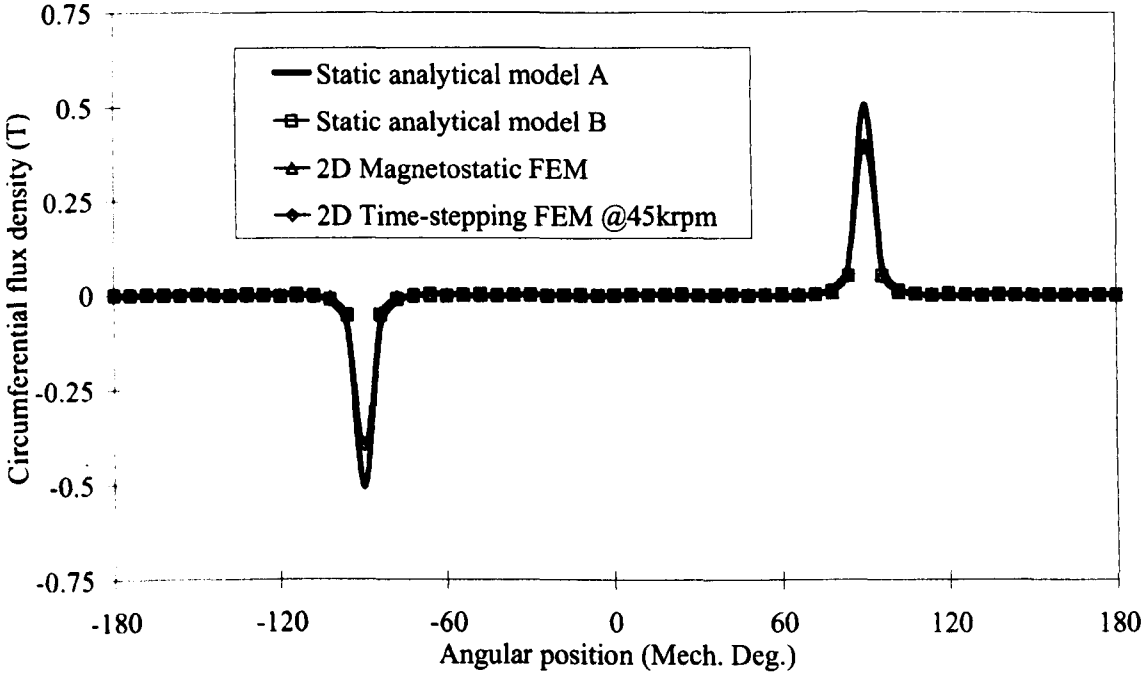

(II) Circumferential component

(a) Middle of airgap

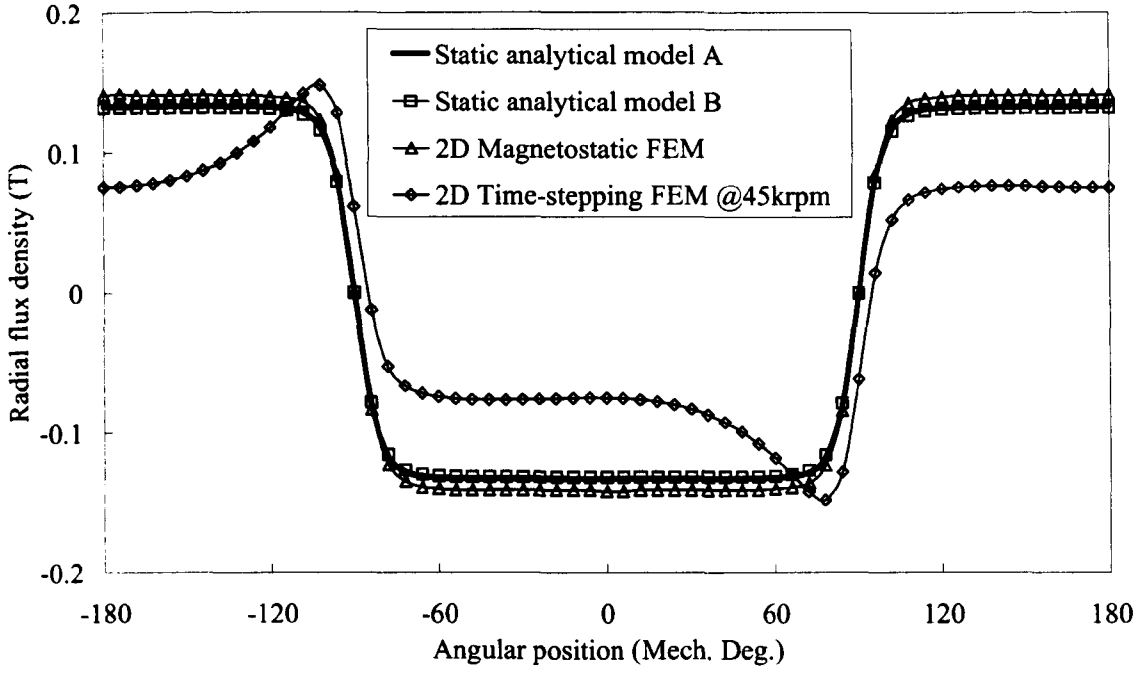

(I) Radial component

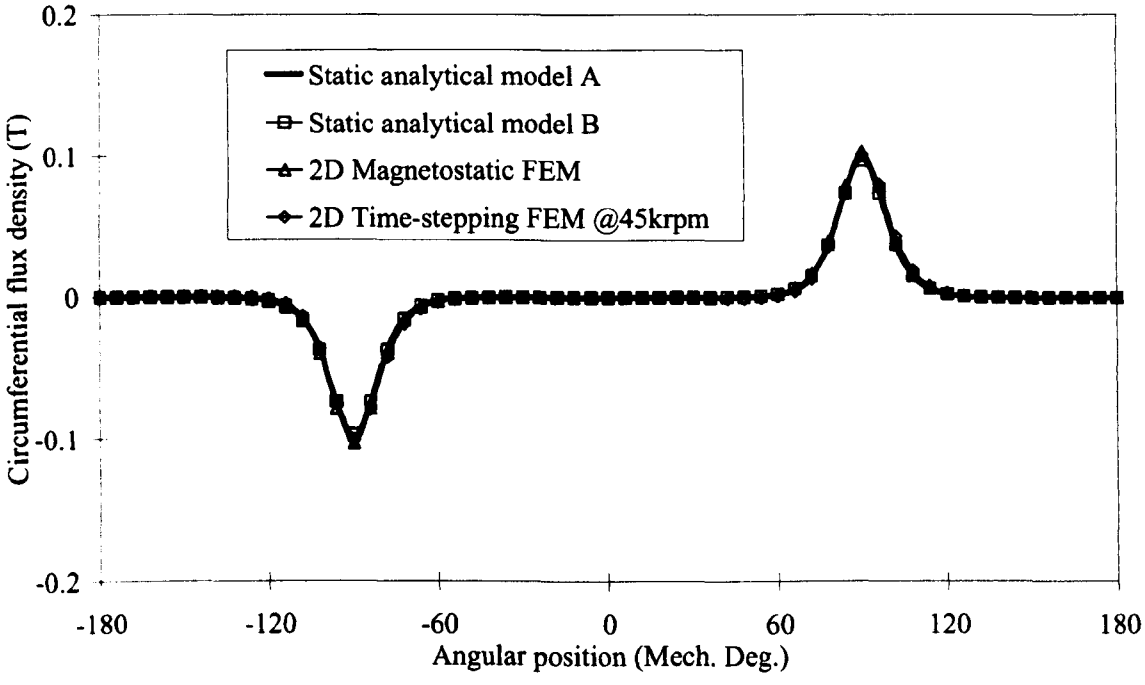

(II) Circumferential component

(b) Middle of PM

Figure 3.9 Comparison of flux distribution predicted by **static** analytical models and FEM for **single-phase** PM BLDC motor having **concentric** airgap. ($t = 0.000333s$)

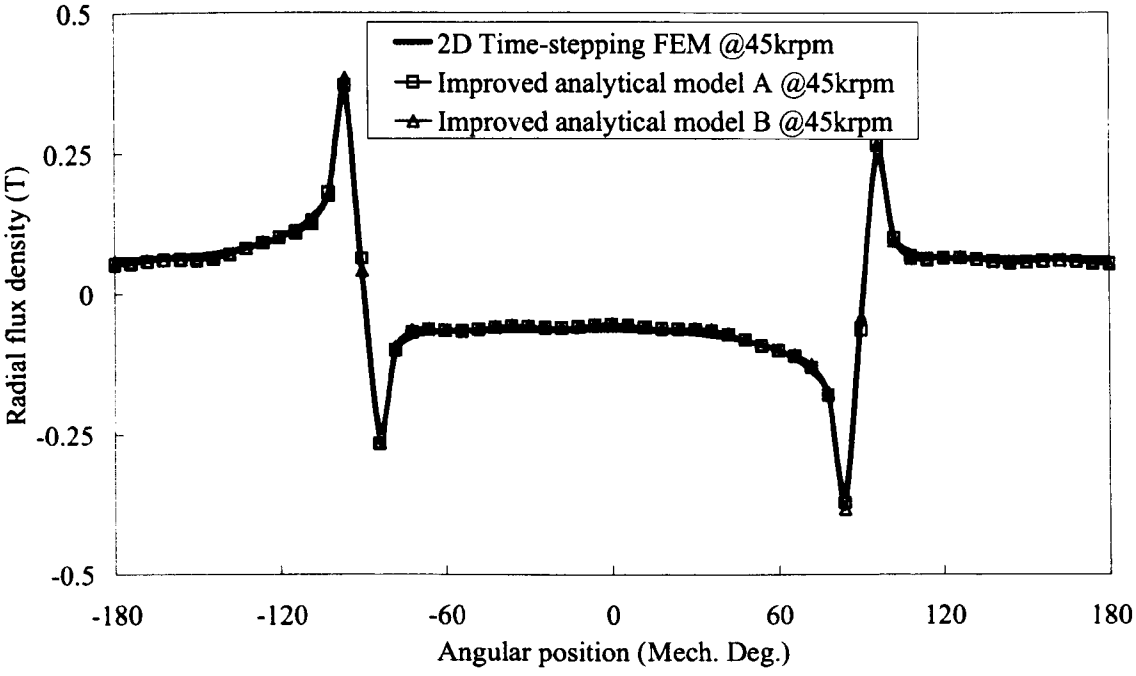

(I) Radial component

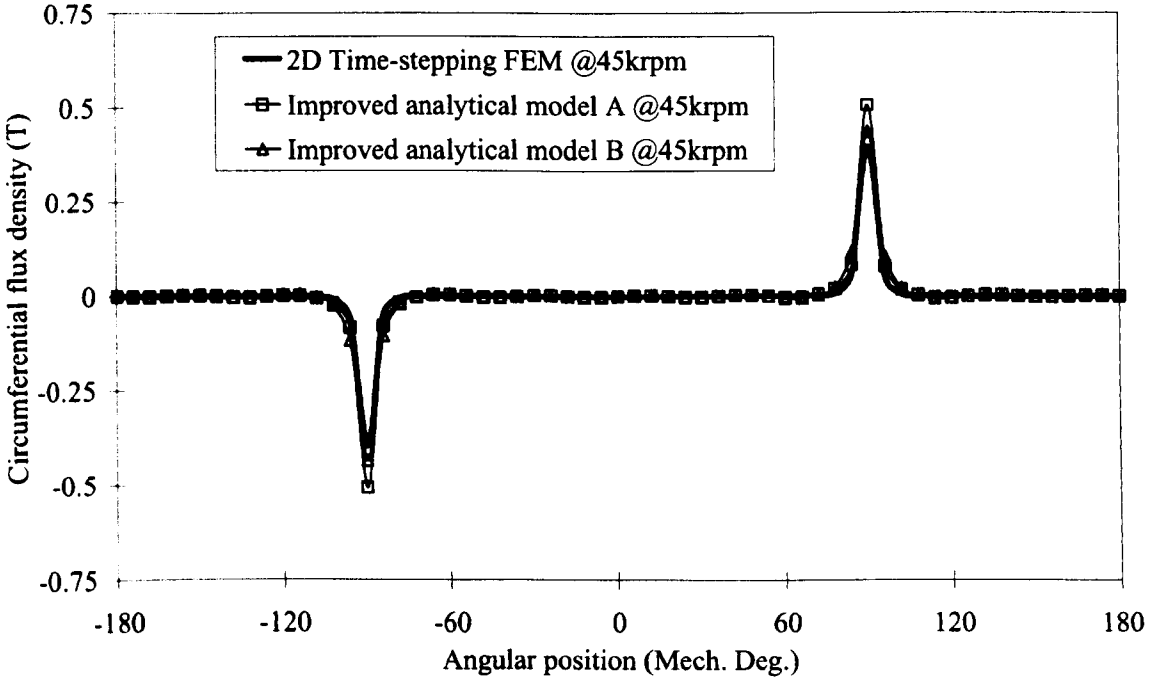

(II) Circumferential component

(a) Middle of airgap

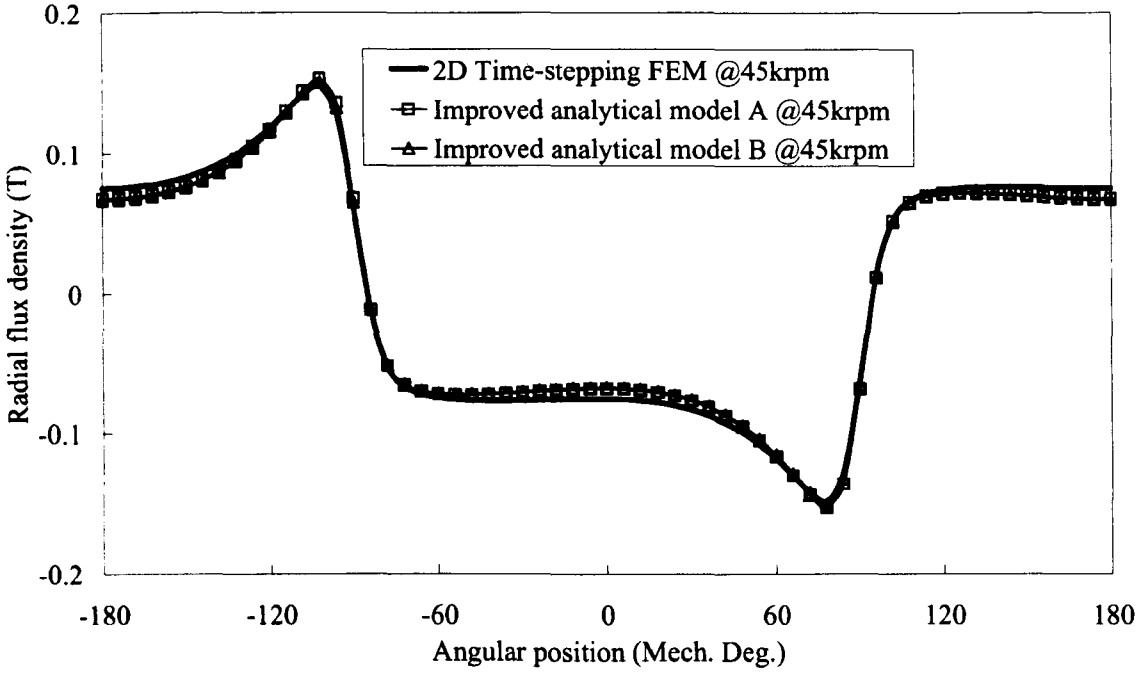

(I) Radial component

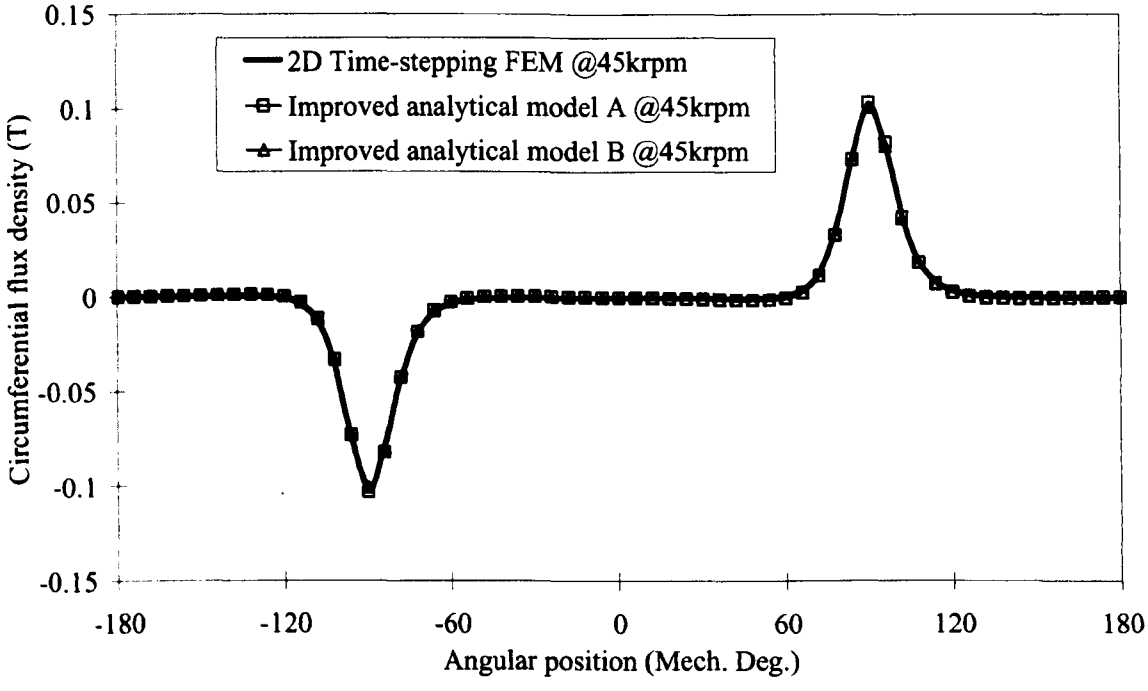

(II) Circumferential component

(b) Middle of PM

Figure 3.10 Comparison of flux distribution predicted by **improved** analytical models and FEM for **single-phase** PM BLDC motor having **concentric** airgap. ($t = 0.000333s$)

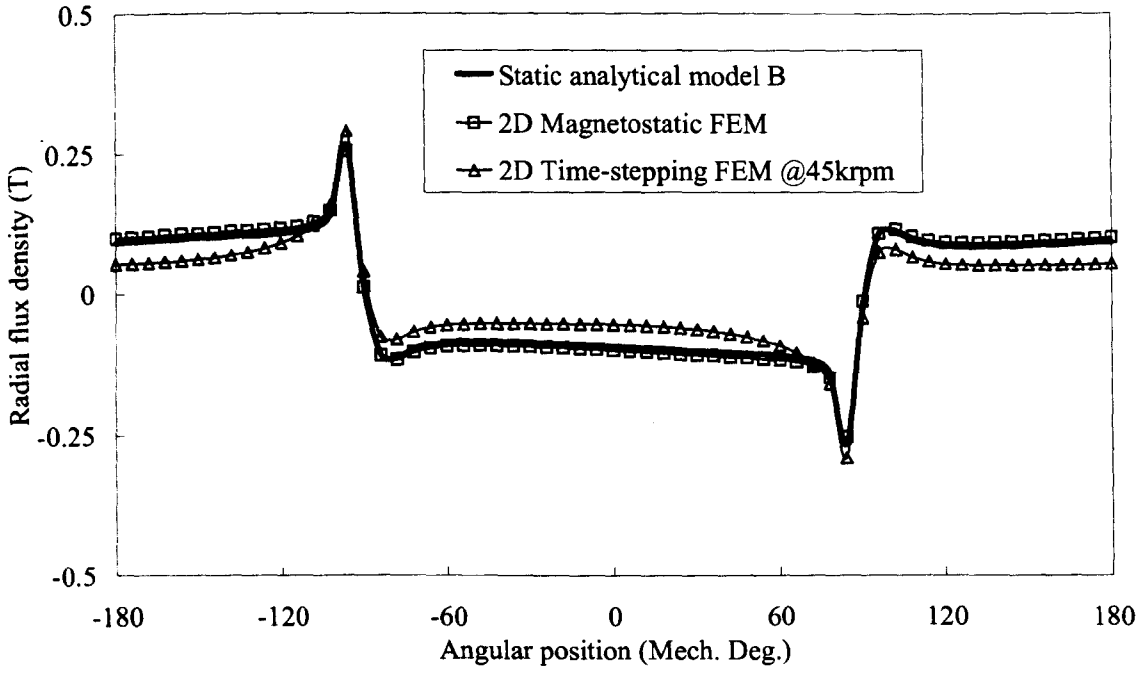

(I) Radial component

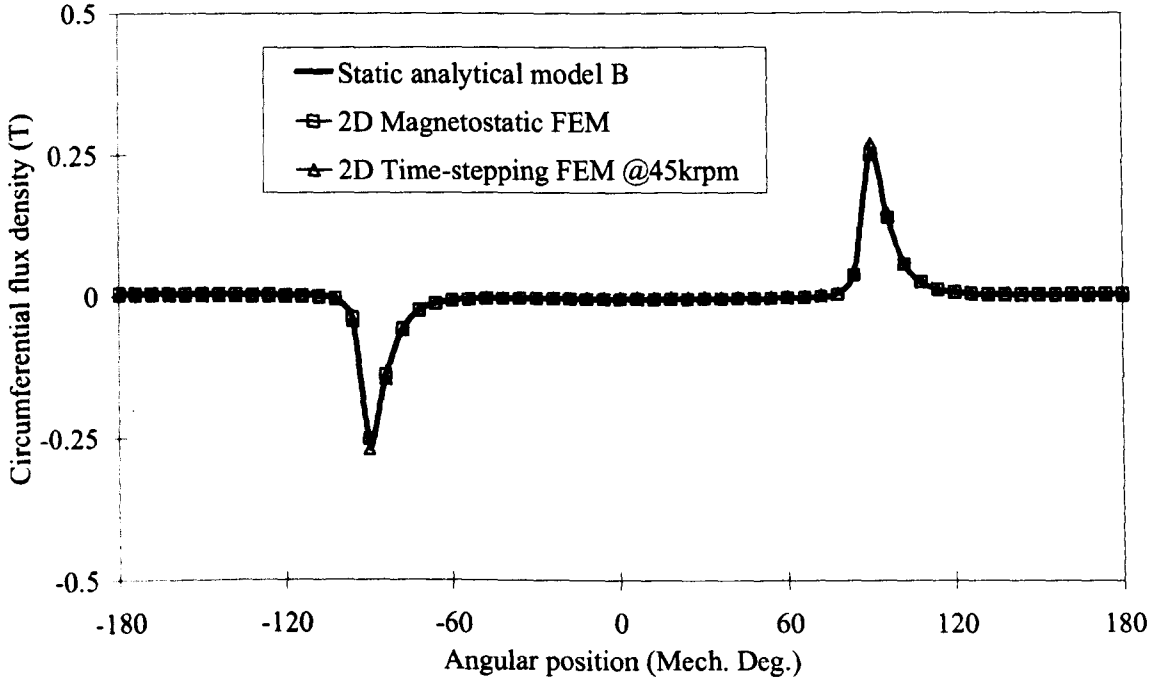

(II) Circumferential component

(a) Middle of airgap

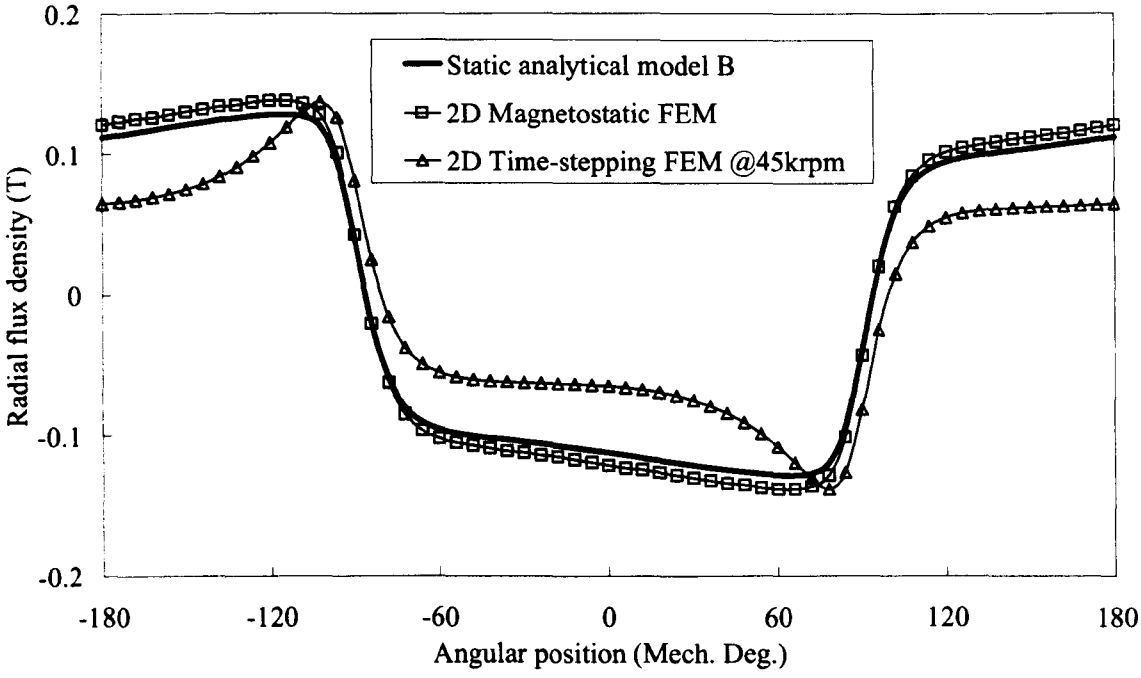

(I) Radial component

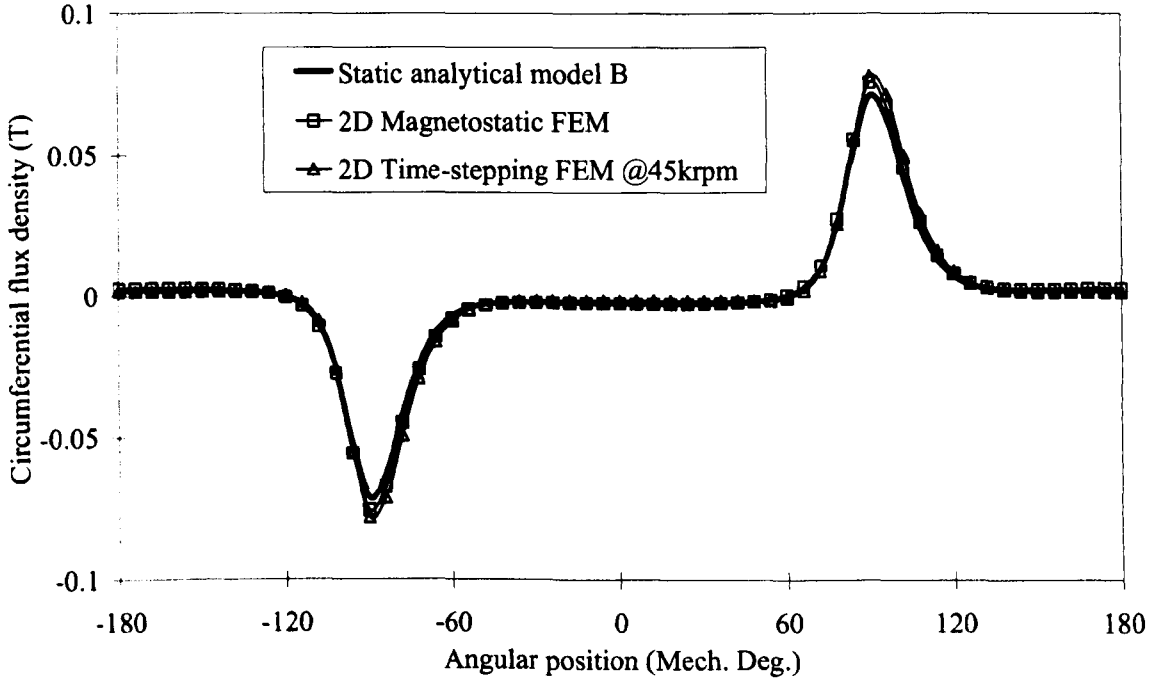

(II) Circumferential component

(b) Middle of PM

Figure 3.11 Comparison of flux distribution predicted by **static** analytical models and FEM for **single-phase** PM BLDC motor having **eccentric** airgap. ($t = 0.000333s$)

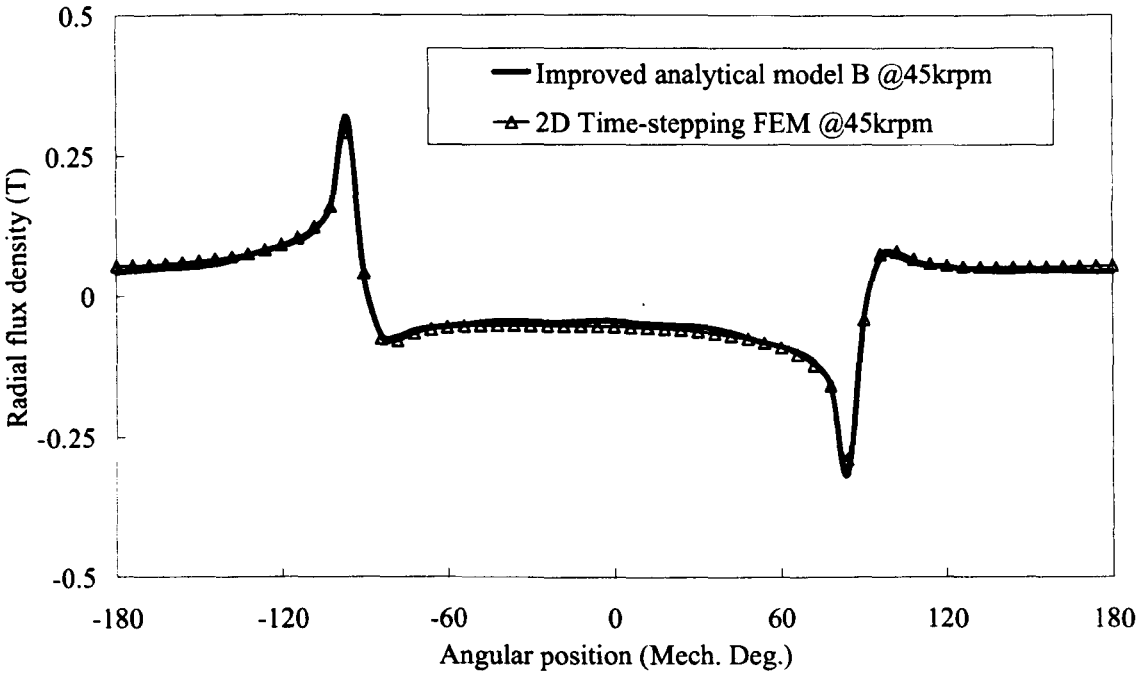

(I) Radial component

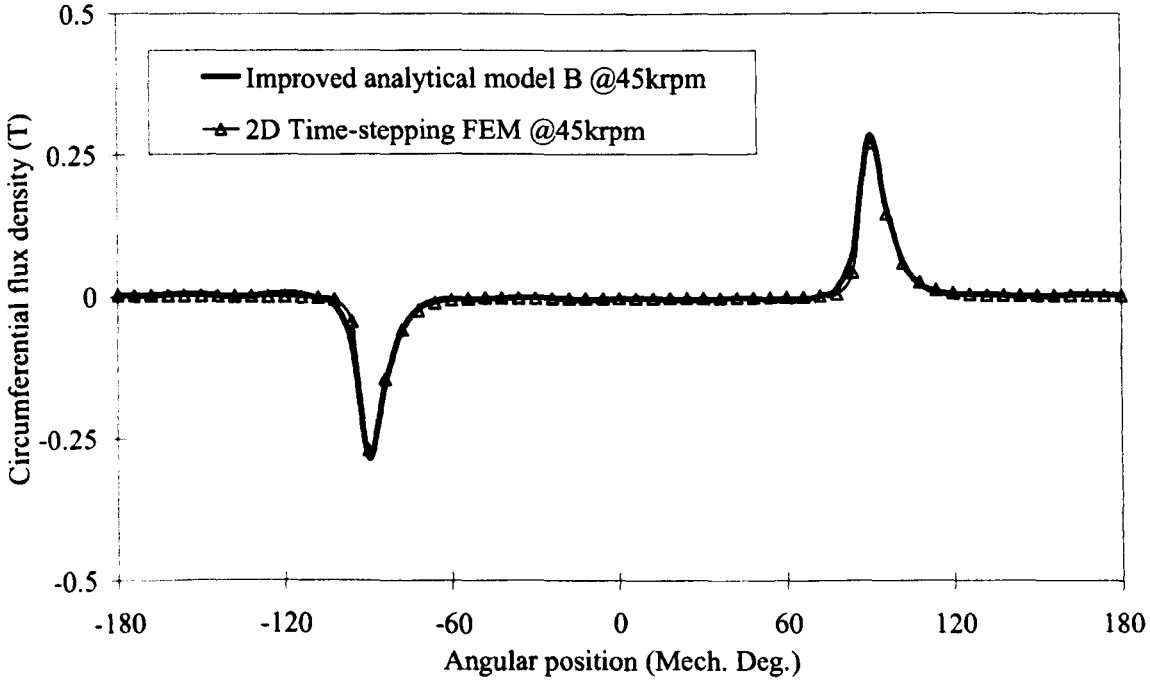

(II) Circumferential component

(a) Middle of airgap

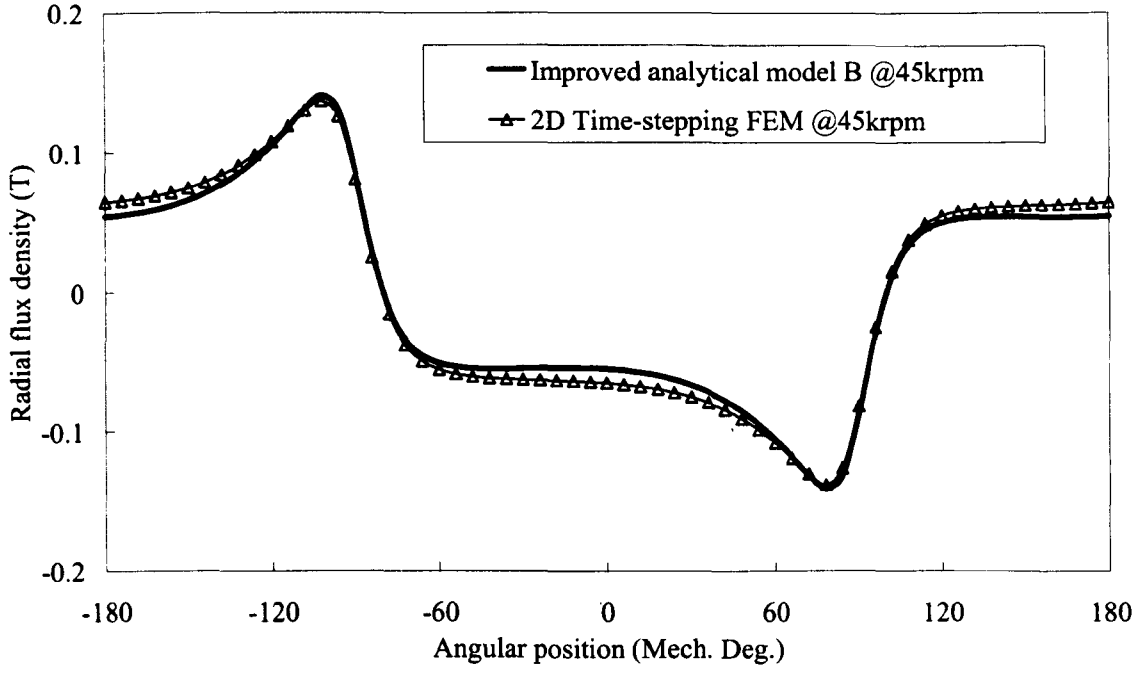

(I) Radial component

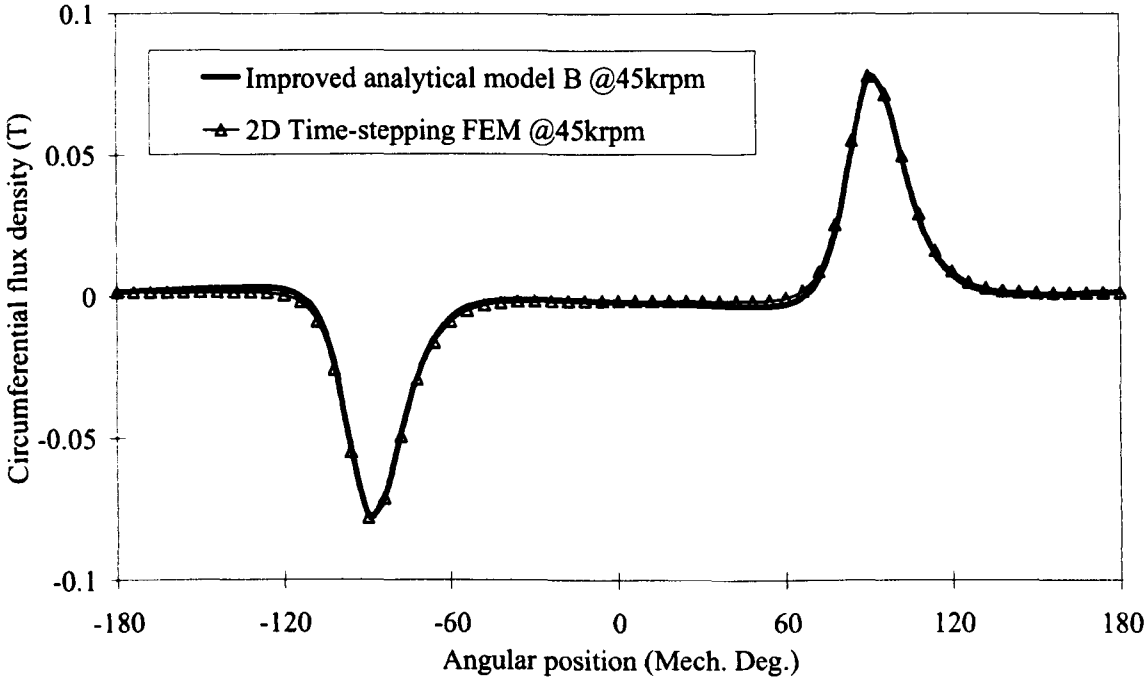

(II) Circumferential component

(b) Middle of PM

Figure 3.12 Comparison of flux distribution predicted by **improved** analytical models and FEM for **single-phase** PM BLDC motor having **eccentric** airgap. ($t = 0.000333s$)

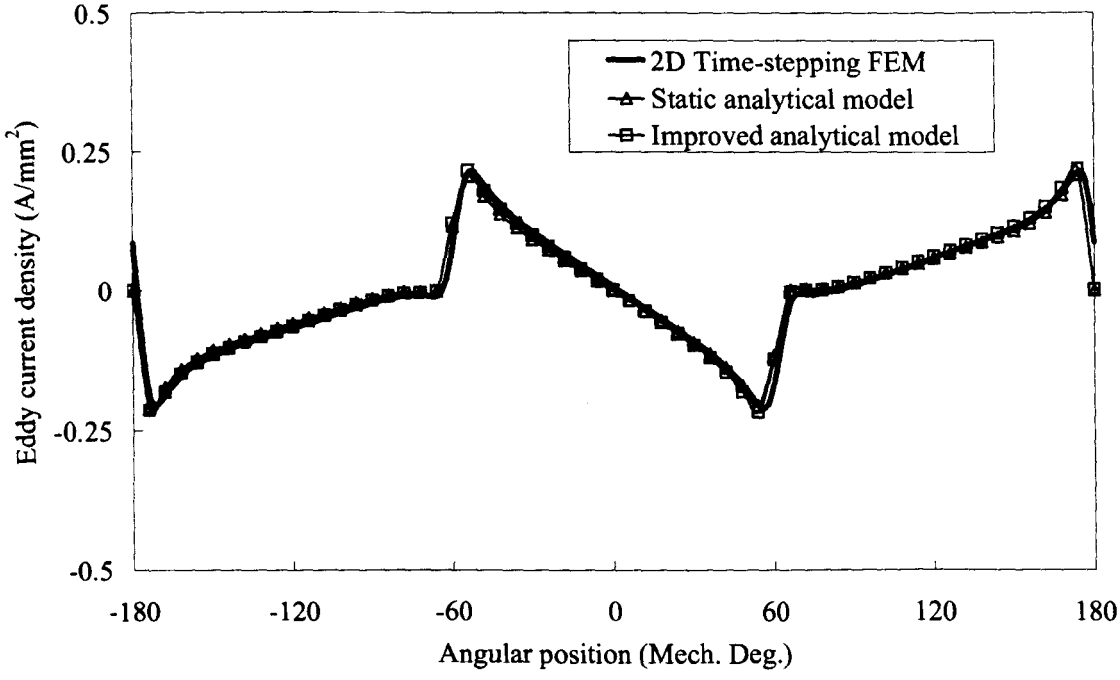

(I) Speed=1krpm, $t = 0.06s$

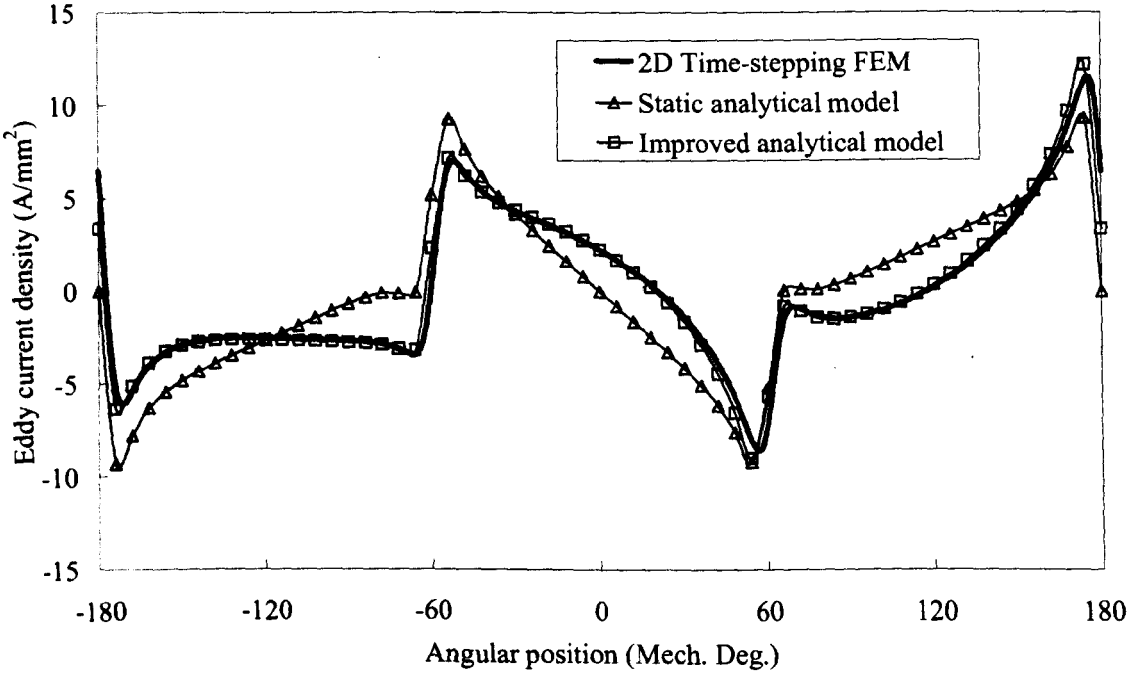

(II) Speed=45krpm, $t = 0.001333s$

(a) Middle of sleeve

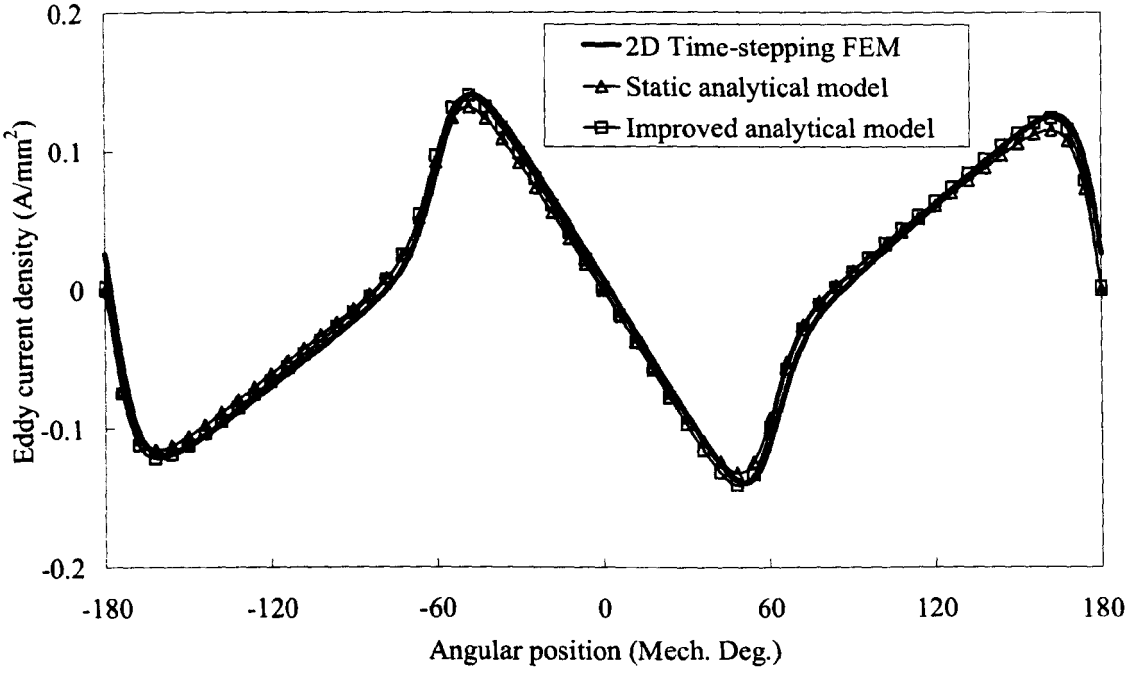

(I) Speed=1krpm, $t = 0.06s$

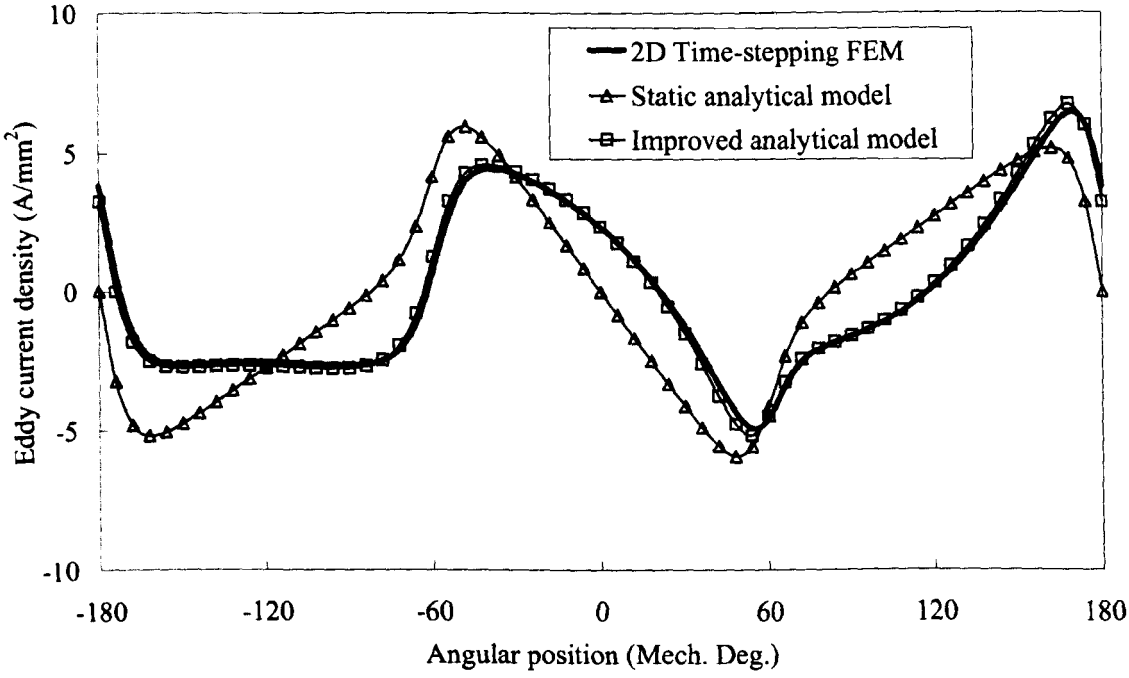

(II) Speed=45krpm, $t = 0.001333s$

(b) Middle of PM

Figure 3.13 Comparison of eddy current distribution predicted by analytical models and FEM for **three-phase** PM BLDC motor. Rotor position=0°.

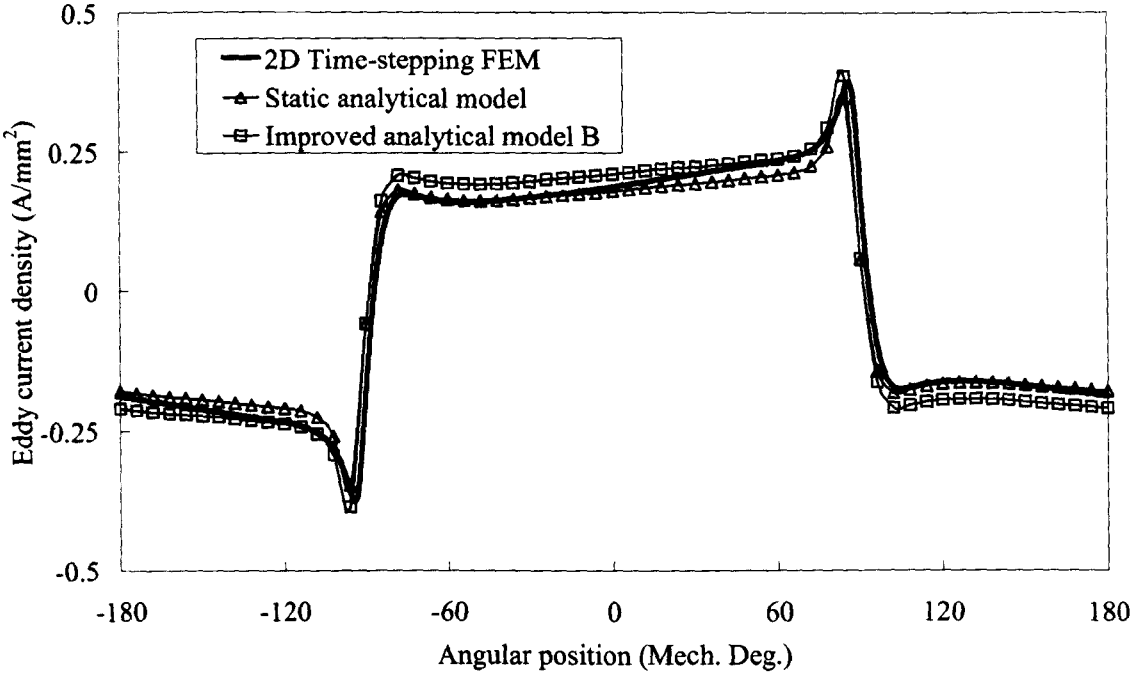

(I) Speed=1krpm, $t = 0.015s$

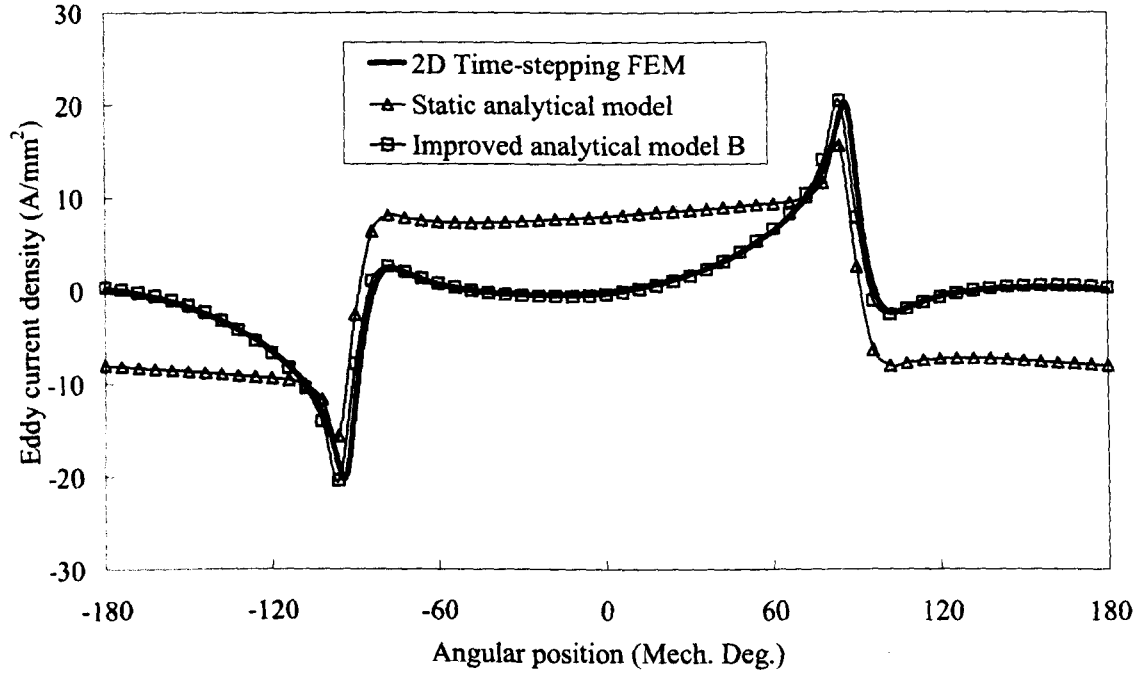

(II) Speed=45krpm, $t = 0.000333s$

(a) Middle of sleeve

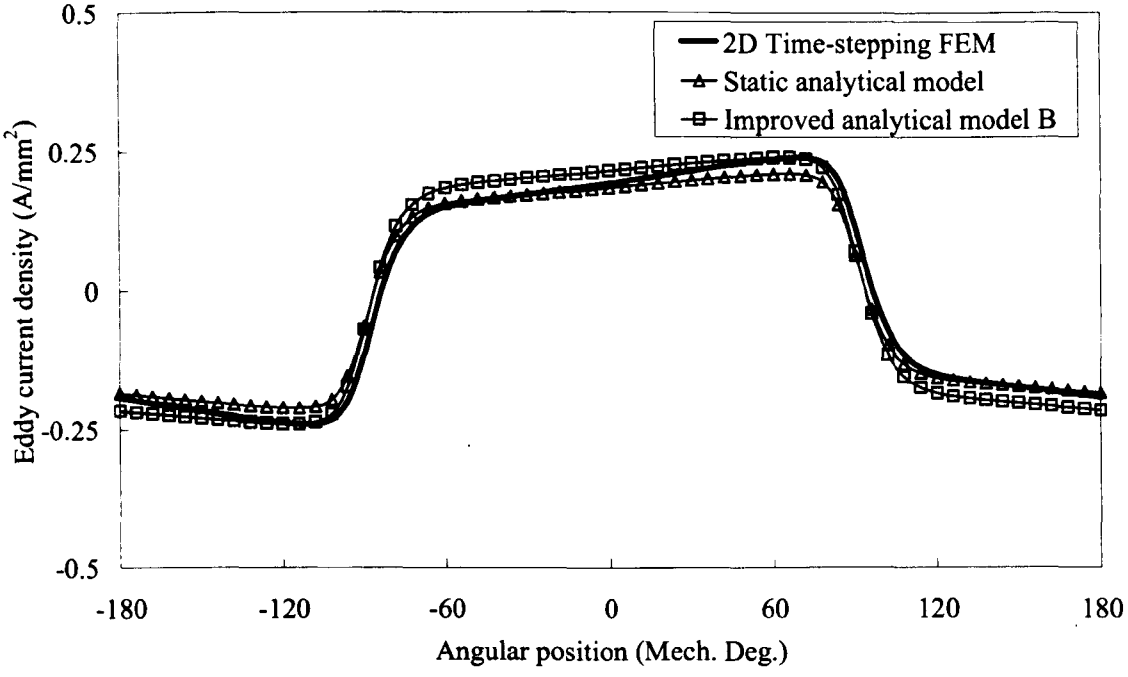

(I) Speed=1krpm, $t = 0.015s$

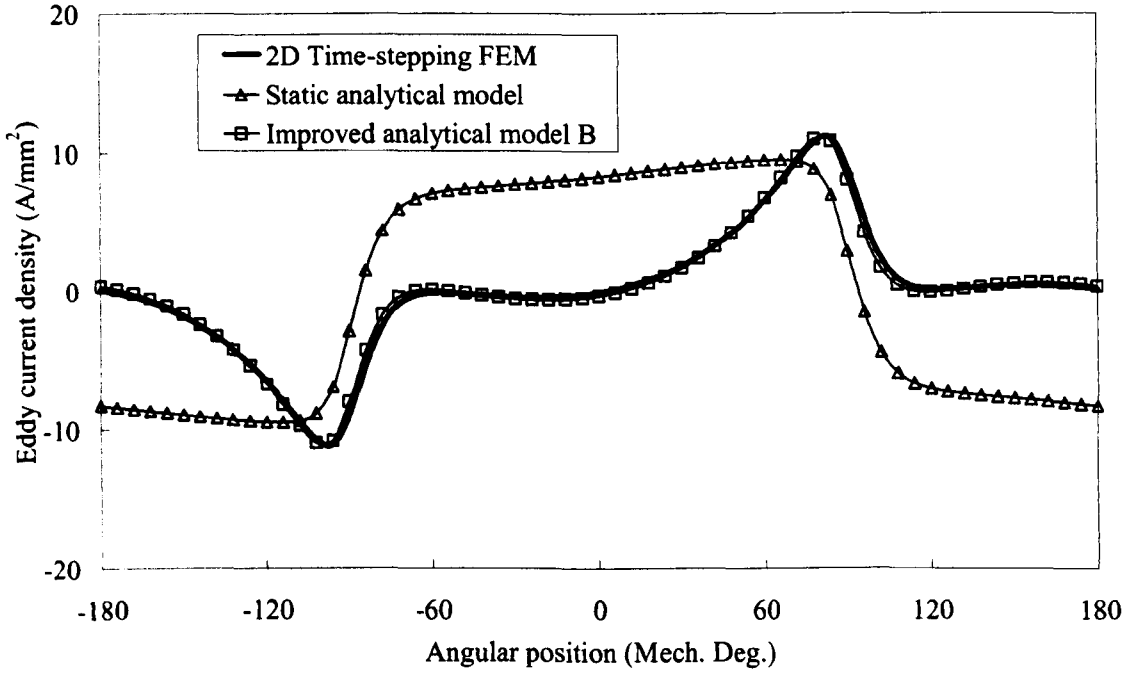

(II) Speed=45krpm, $t = 0.000333s$

(b) Middle of PM

Figure 3.14 Comparison of eddy current distribution predicted by analytical models and FEM for **single-phase** PM BLDC motor having **eccentric** airgap. Rotor position=90°.

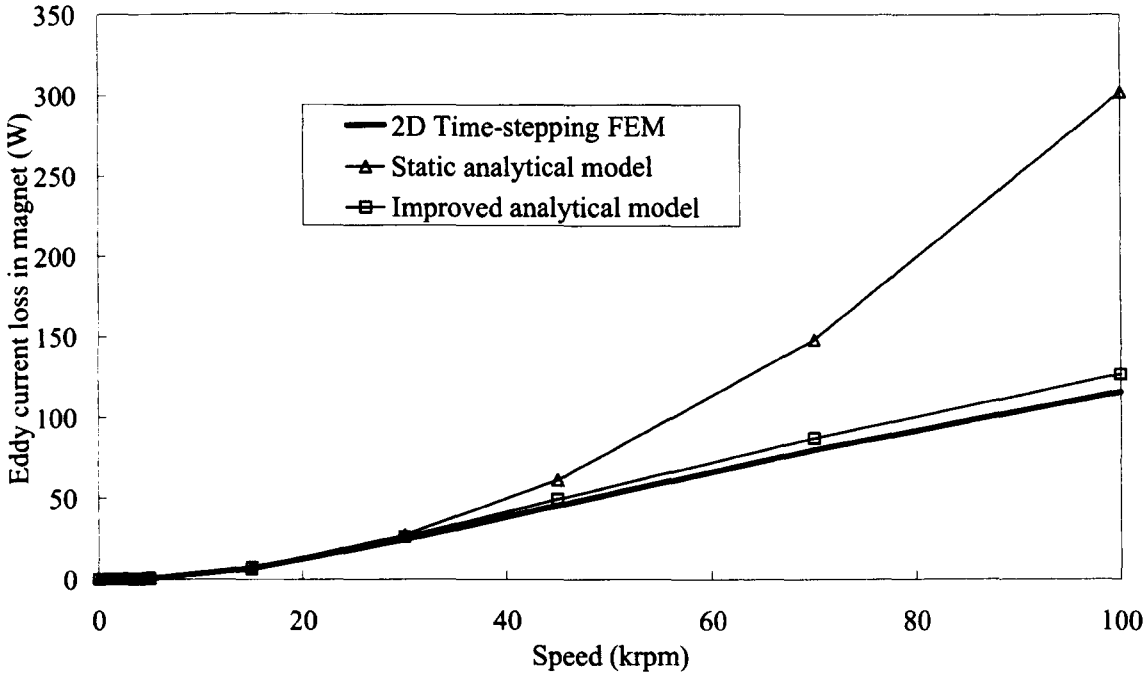

(a) Eddy current loss in PM

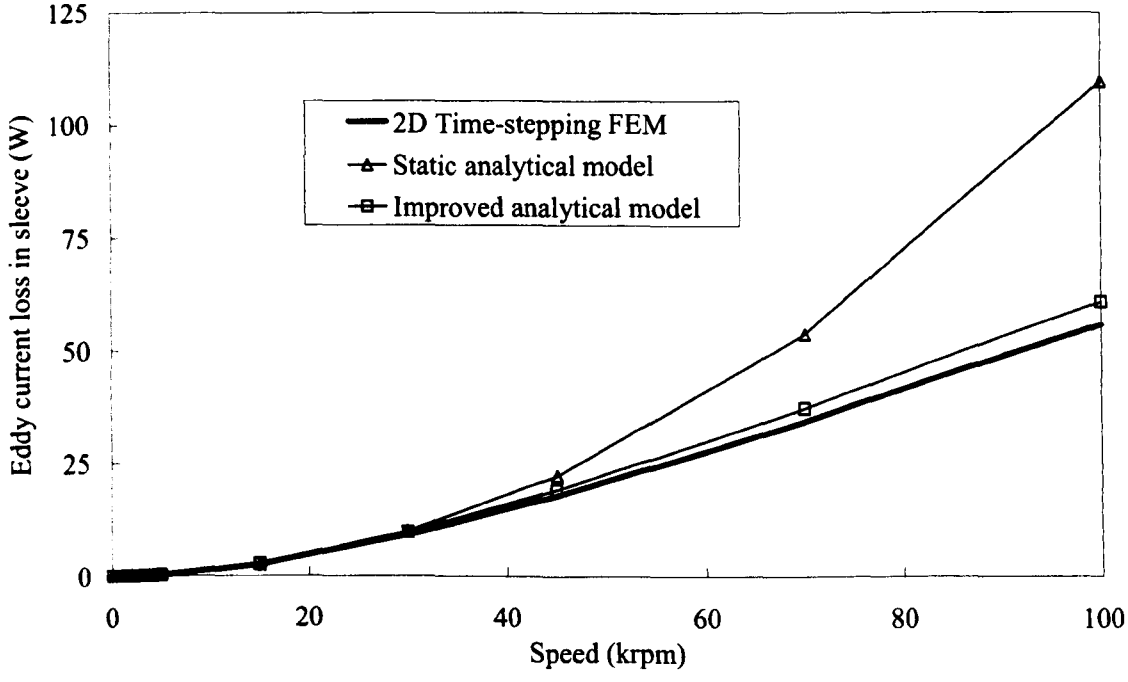

(b) Eddy current loss in sleeve (Sleeve thickness = 0.6mm)

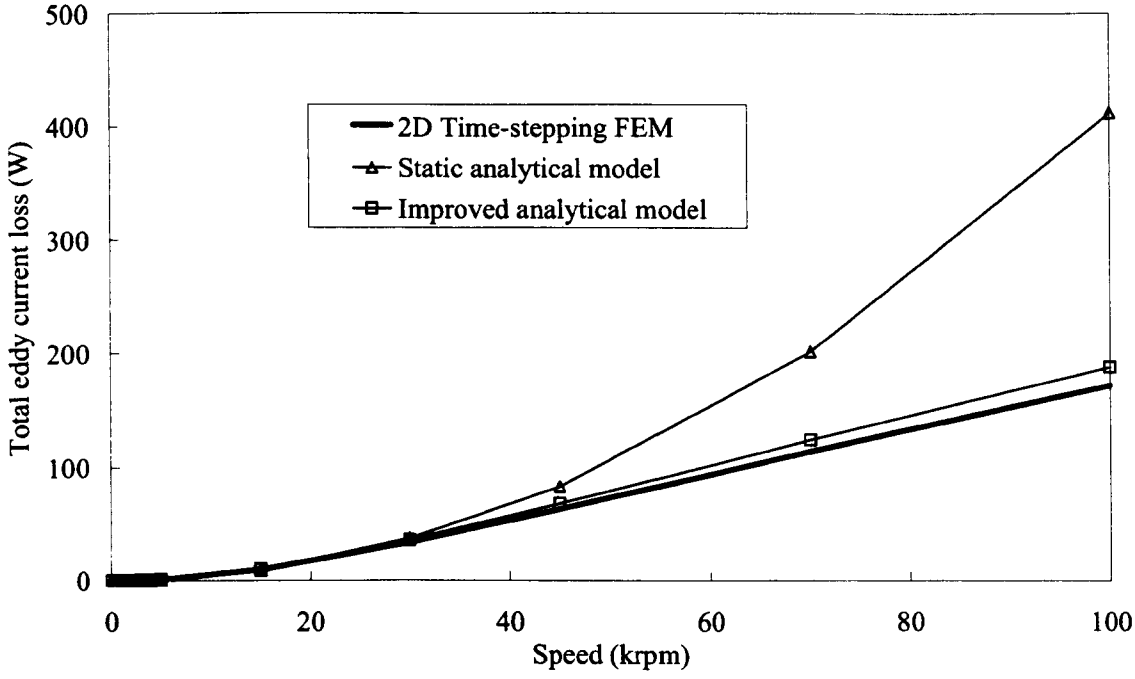

(c) Total eddy current loss

Figure 3.15 Comparison of eddy current loss predicted by analytical models and FEM for **three-phase** PM BLDC motor. $I_{m\_\sin} = 6A$

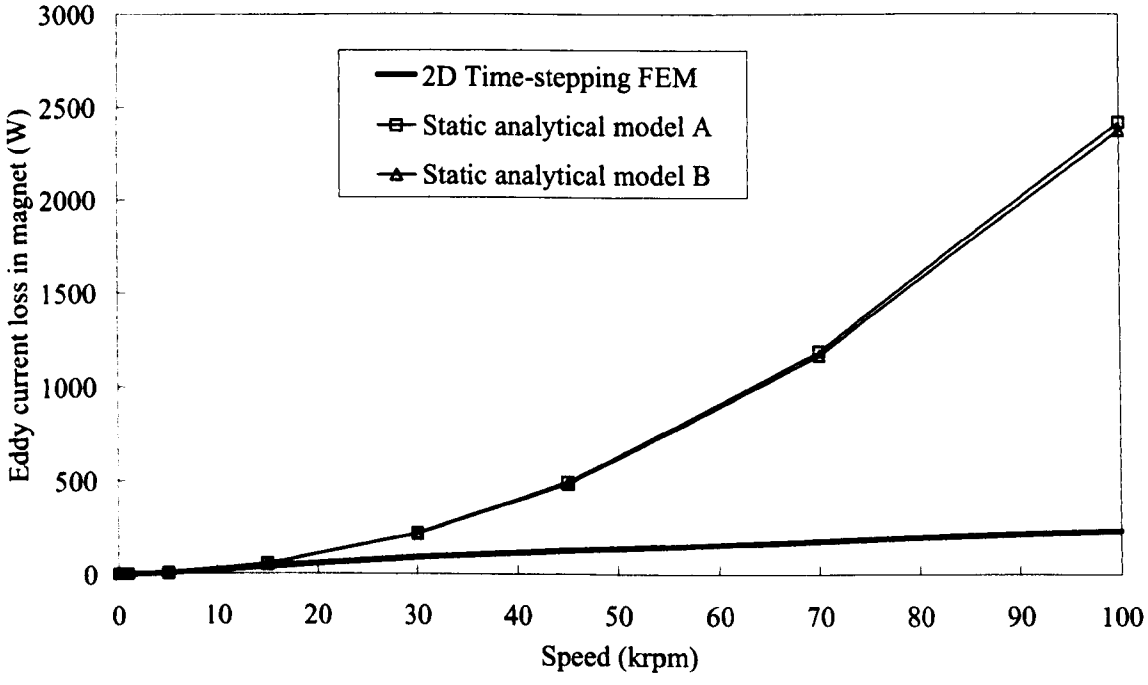

(I) Static analytical model

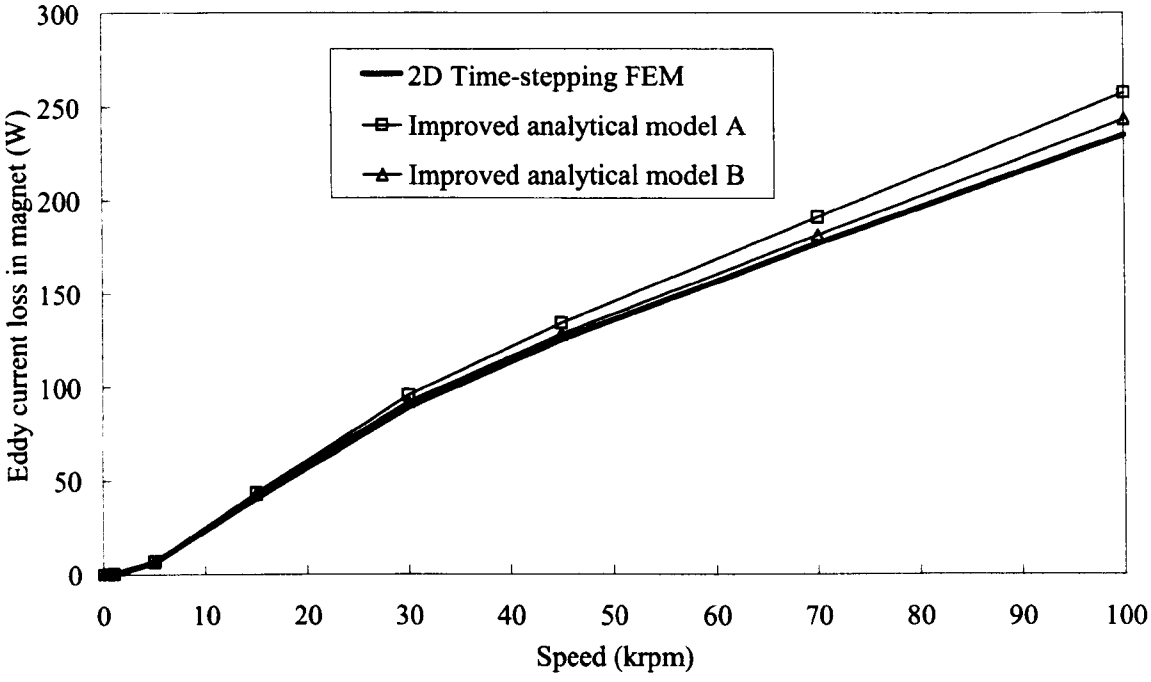

(II) Improved analytical model

(a) Eddy current loss in PM

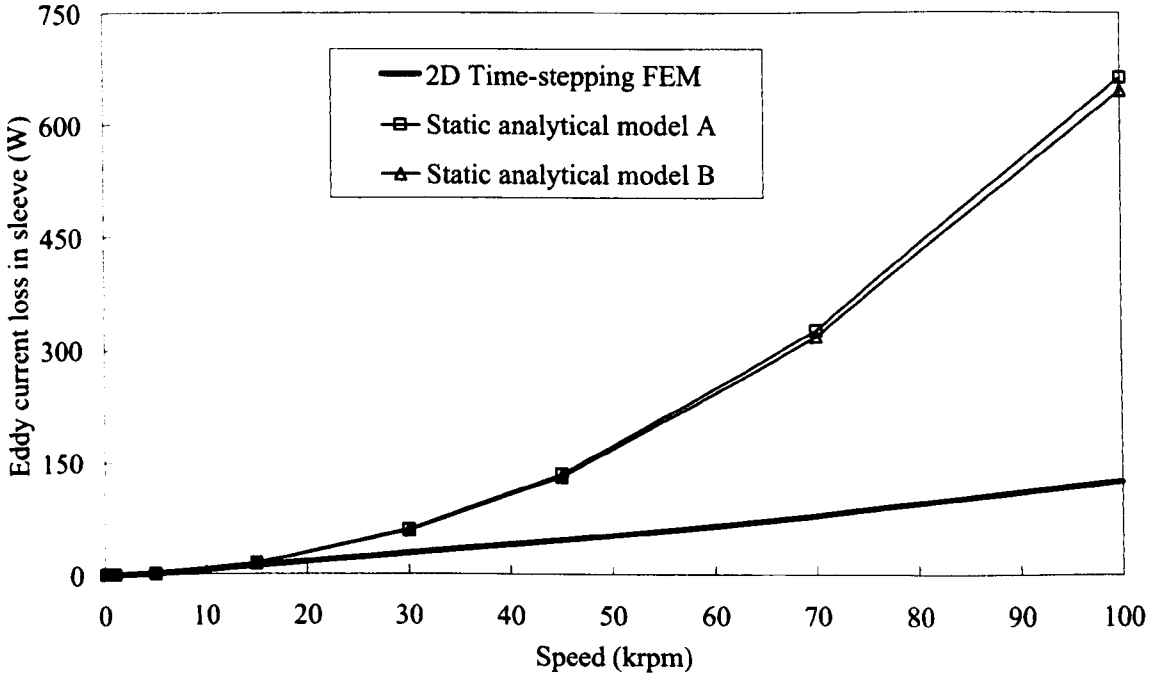

(I) Static analytical model

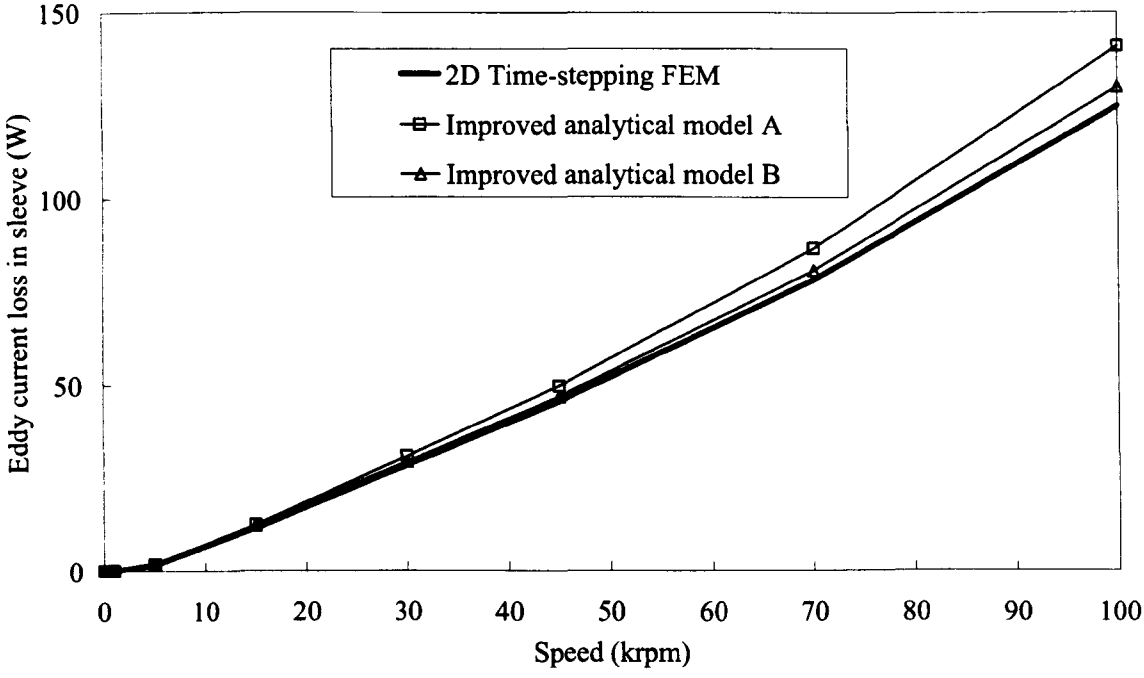

(II) Improved analytical model

(b) Eddy current loss in sleeve (Sleeve thickness = 0.6mm)

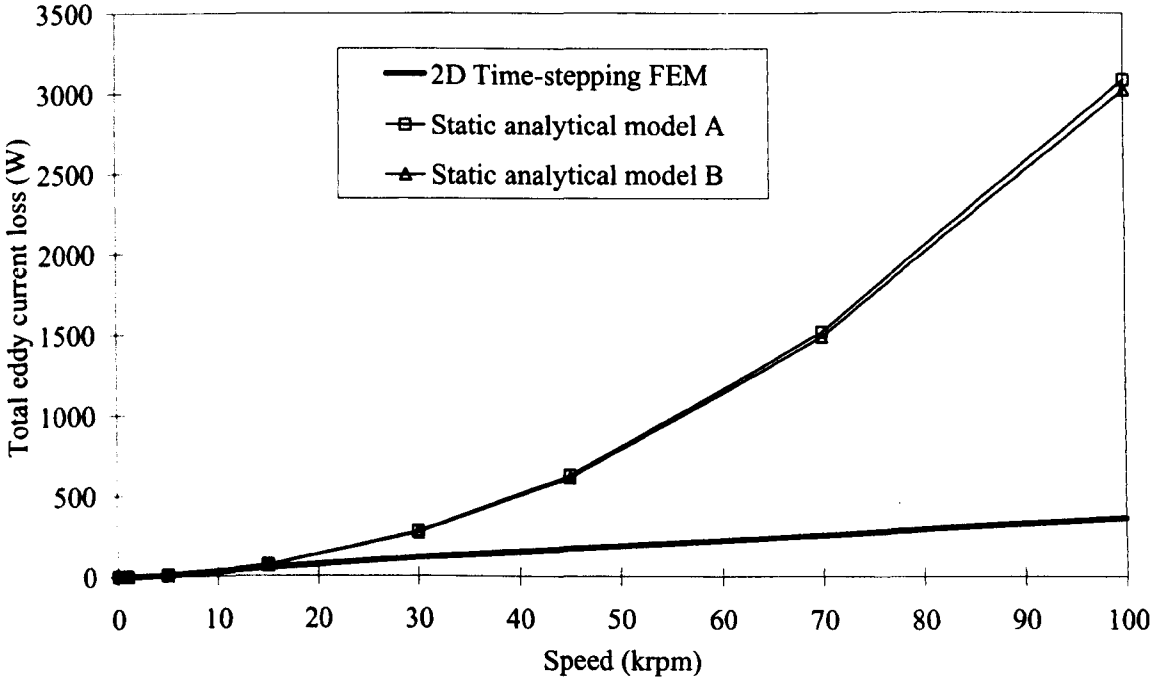

(I) Static analytical model

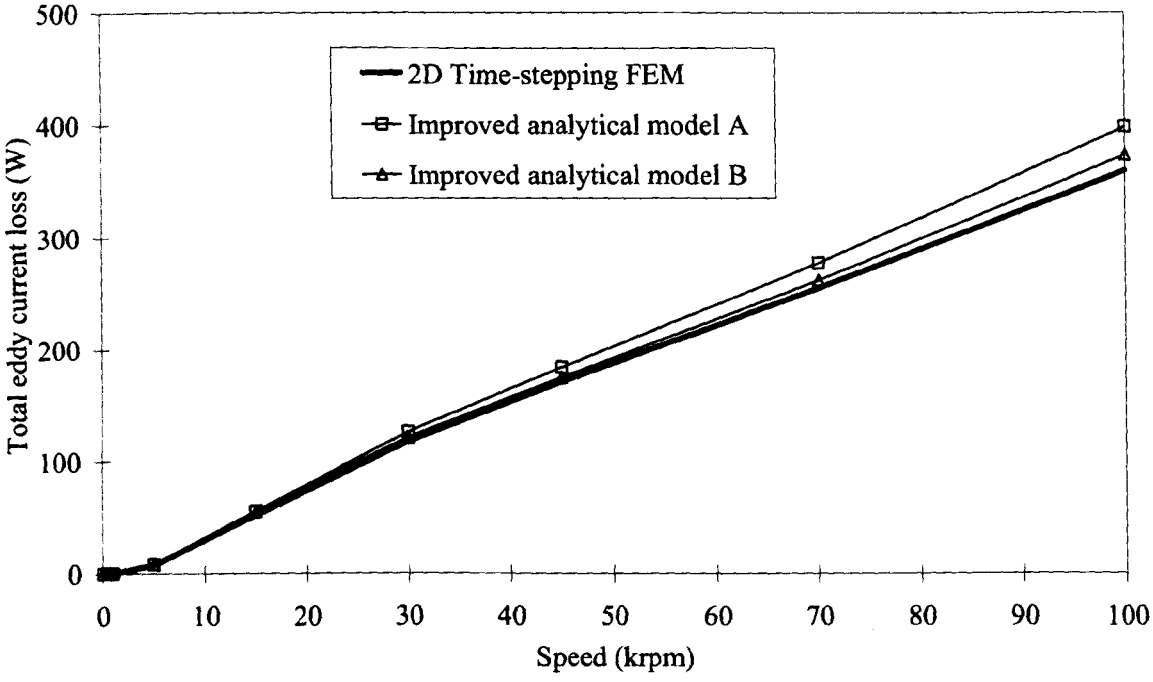

(II) Improved analytical model

(c) Total eddy current loss

Figure 3.16 Comparison of eddy current loss predicted by analytical models and FEM for **single-phase** PM BLDC motor having **concentric** airgap. ($I_{m\_\sin} = 8A$)

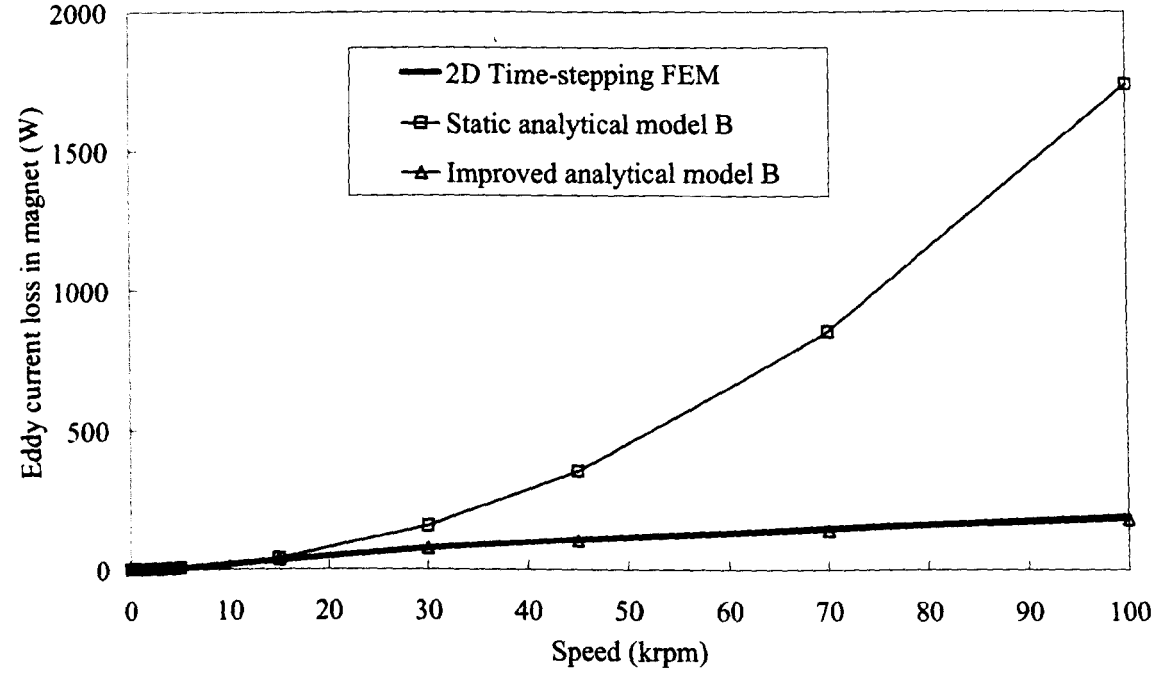

(a) Eddy current loss in PM

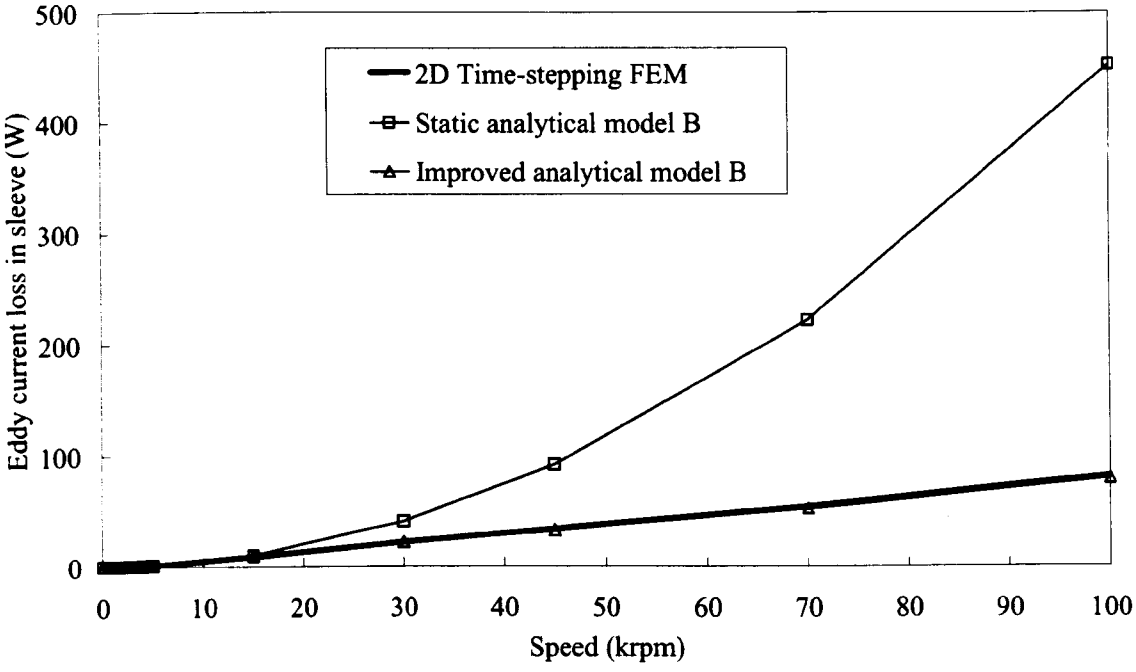

(b) Eddy current loss in sleeve, sleeve thickness = 0.6mm

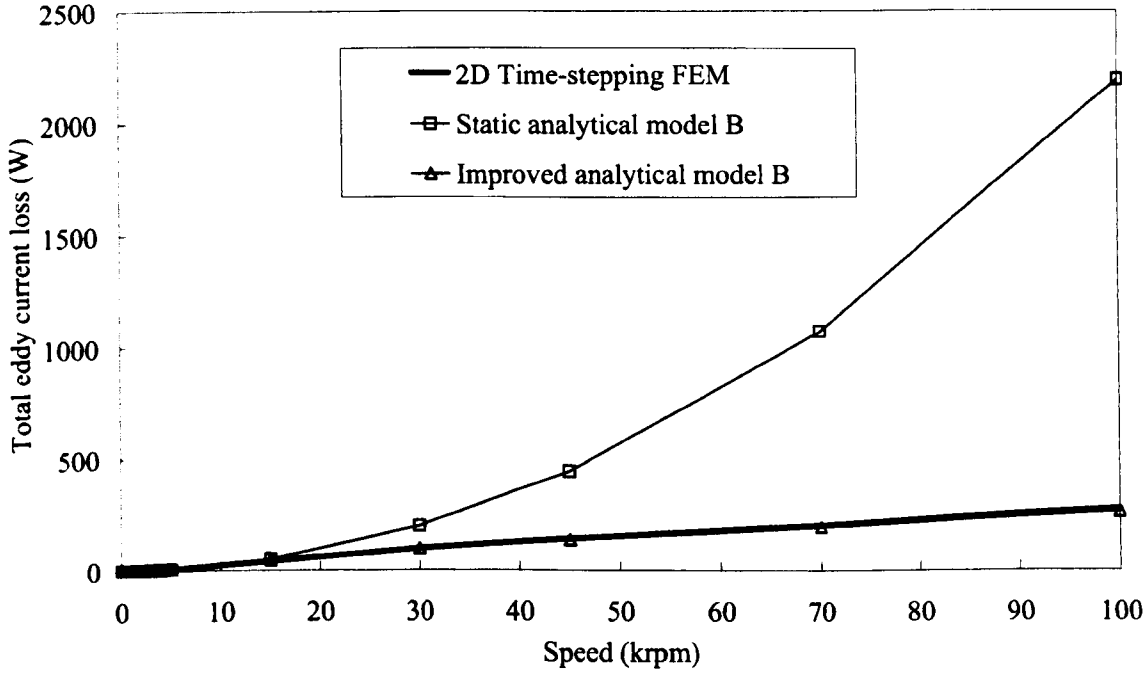

(c) Total eddy current loss

Figure 3.17 Comparison of eddy current loss predicted by analytical models and FEM for **single-phase** PM BLDC motor with **eccentric** airgap. ($I_{m\_\sin} = 8A$)

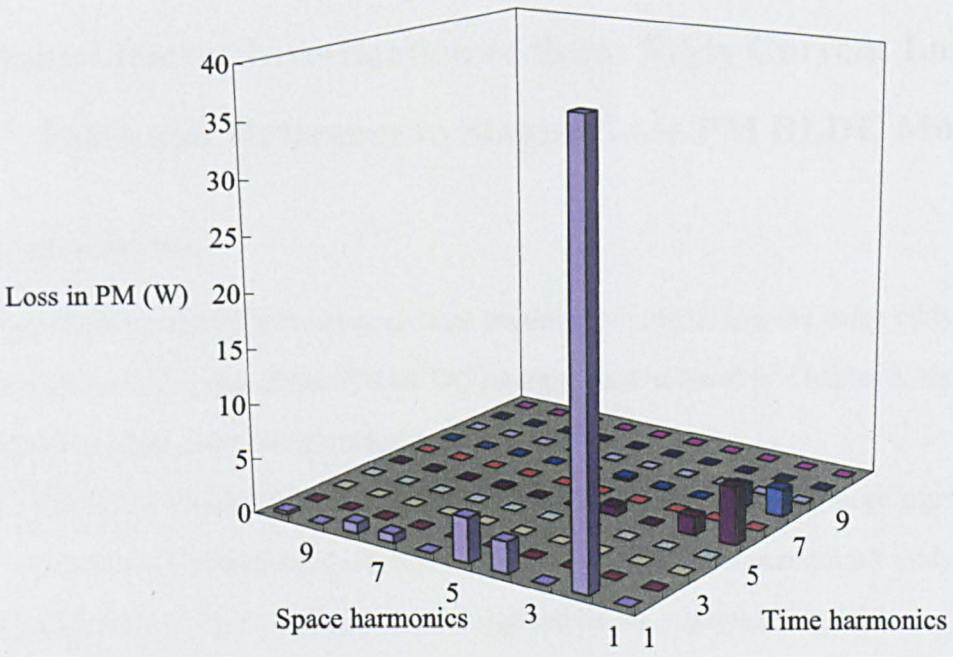

(a) Three-phase PM BLDC motor

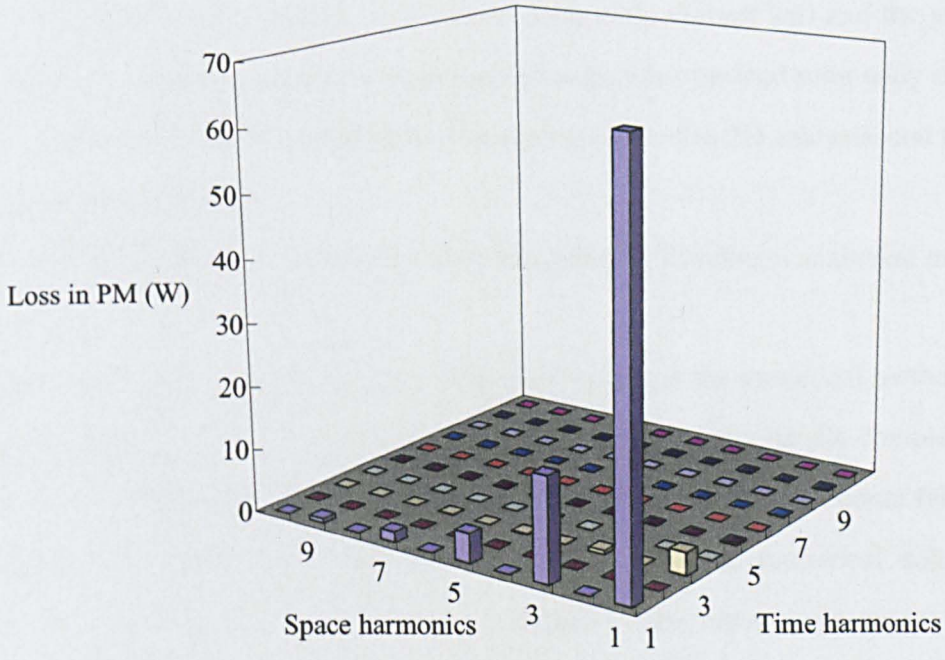

(b) Single-phase PM BLDC motor with **eccentric** airgap

Figure 3.18 Eddy current loss spectra in PM. (Speed = 45krpm; simulated current)

CHAPTER 4

Finite Element Investigation of Rotor Eddy Current Loss with Particular Reference to Single-Phase PM BLDC Motor

4.1 Introduction

Chapter 3 has described various analytical models for calculating the rotor eddy current loss in three-phase and single-phase PM BLDC motors. As discussed in Chapter 3, these analytical models have a few limitations, including

- For single-phase PM BLDC motors having an eccentric airgap, more significant airgap permeance harmonics exist and result in considerable open-circuit eddy current loss which is relatively difficult to be simulated by the analytical model.
- In single-phase PM BLDC motor, the inherent pulsating stator mmf introduces a significant armature rotor eddy current loss. Neither open-circuit rotor eddy current loss nor armature rotor eddy current loss can represent the on-load rotor eddy current loss individually. Further, open-circuit rotor eddy current loss and the armature rotor eddy current loss cannot be simply added to give the on-load rotor eddy current loss.
- Analytical models developed in Chapter 3 is limited to 2D analysis, and hence the end effect is neglected.
- Segmented magnets cannot be easily modelled by developed analytical models.

An alternative way to predict the rotor eddy current loss is the numerical method. One of the attractive features of the numerical method is its ability to easily handle complex geometries. Therefore, eccentric airgap and segmental magnets can be taken into account relatively easily. Generally, due to the large number of iterations required, numerical solutions require relatively long computing times. However, thanks to the rapid development of the digital computer with progressively greater capacity and speed, the numerical model can be solved easily.

The most popular numerical method appears to be the FEM. The commercial FE package, i.e.

FLUX 2D, is employed to build the 2D FE models to analyze the rotor eddy current loss in this chapter. The details of the FEM are well known and will not be described in this thesis. Hence, only the basic background of the FEM will be outlined in this chapter, while some special features of the FLUX 2D will be described briefly.

Firstly, the FEM will be carried out to determine the open-circuit, armature and on-load eddy current losses in the magnets and retaining sleeve for three-phase and single-phase PM BLDC motors, respectively.

Secondly, the FEM is employed to investigate the influence of airgap eccentricity, excitation current waveform, as well as the effectiveness of segmenting the magnet in reducing the induced eddy current in single-phase PM BLDC motors.

Thirdly, the FEM is used to investigate the influence of the thickness and electrical conductivity of the retaining sleeve in single-phase PM BLDC motors.

4.2 FEM predicted rotor eddy current loss

The FLUX-2D has been used to determine the open-circuit, armature and on-load losses in the magnets and retaining sleeve for three-phase and single-phase PM BLDC motors, respectively. In the FE model, an incremental dynamic rotor displacement of 3^{o}_{mech} has been used, which is equivalent to a time step of 1.11e-05 s at 45 krpm. The electrical conductivity of the magnet and retaining sleeve are 1.4286e06 $\Omega^{-1}m^{-1}$ and 1.3889e06 $\Omega^{-1}m^{-1}$, respectively. For the prototype machine, the magnet is composed by two segments which are electrically isolated each other. Figure 4.1, Figure 4.2 and Figure 4.3 show the open-circuit, armature reaction and on-load flux distribution of three-phase PM BLDC motor and single-phase PM BLDC motors having concentric and eccentric airgap, respectively.

4.2.1 FEM predicted open-circuit rotor eddy current loss

The FEM predicted open-circuit rotor eddy current loss for the three-phase and single-phase PM BLDC motors are given in Table 4.1 and their variation is shown in Figure 4.4. On open-circuit, the rotor loss results solely from the stator slot openings. Hence, for the 3-slot, 2-pole three-phase motor, since the smallest common multiple between the number of stator slots and the number of rotor poles is 6, the periodicity of the open-circuit rotor loss variation is $360°/6=60°_{mech}$. However, due to the relatively narrow slot openings the tooth ripple component of eddy current loss is extremely small.

Table 4.1 Open-circuit rotor eddy current loss @45,000rpm with 2 magnet segments.

	Three-phase PM BLDC motor	**Single-phase PM BLDC motor**
Magnet (W)	0.83	60.79
Sleeve (W)	0.54	32.84
Total (W)	1.37	93.63

For the 2-slot, 2-pole single-phase motor, the periodicity of the open-circuit rotor eddy current loss variation is $360°/2=180°_{mech}$. However, due to the eccentric airgap, the open-circuit loss is much higher than that of the three-phase motors. Figure 4.5 shows the variation of open-circuit rotor eddy current loss with airgap eccentricity at the rated speed. It can be clearly seen that the open-circuit rotor eddy current loss increases significantly with the airgap eccentricity. Further, when the single-phase motor has a concentric airgap, i.e; OO'=0mm, the open-circuit rotor eddy current loss is 5.13W which is only due to the stator slot opening. It is much less than that of the single-phase having an eccentric airgap, which indicates that the influence the eccentricity is much greater than that of the stator slot openings.

4.2.2 FEM predicted armature and on-load rotor eddy current loss

By applying the current to the windings, as shown in Figure 4.6, which is obtained by the simulation model as described in Chapter 2, and setting the magnet remanence to zero, the armature rotor eddy current loss solely due to the armature field can be calculated by FEM.

By setting the magnet remanence to 1.04T, together with the current being applied to the windings, the on-load rotor eddy current loss can be determined by FEM, which represents the realistic conditions. The FEM predicted rotor eddy current loss is summarized in Table 4.2 and Table 4.3, and their variations are shown in Figure 4.7 and Figure 4.8. It can be seen that:

- For three-phase motor, the periodicity of the armature and on-load rotor eddy current loss is 60°_{mech}, while for single-phase motor, it is 180°_{mech}.
- For both three-phase and single-phase motors, compared to fundamental component of the winding current, simulated winding current has more time harmonics, which will induce more armature and on-load rotor eddy current loss.
- For three-phase motor, even with sinusoidal winding current, there is considerable armature rotor eddy current loss resulting from the spatial mmfs harmonics. However, the single-phase motor has a significant armature rotor eddy current loss which is more than twice of that of the three-phase motor, even with sinusoidal winding current.
- Further, it can also be noticed that for three-phase motor on-load rotor eddy current loss is 83% of the armature rotor eddy current loss. However, because of the eccentric airgap the on-load rotor eddy current loss is only 16% of the armature rotor eddy current loss, which clearly shows that for single-phase motor the armature rotor eddy current loss cannot represent the on-load rotor eddy current loss accurately.

Table 4.2 Armature rotor eddy current loss @45,000rpm with 2 magnet segments.

	Three-phase PM BLDC motor		**Single-phase PM BLDC motor**	
	Fundamental current	Simulated current	Sinusoidal current	Simulated current
PM (W)	45.53	59.84	84.46	92.89
Sleeve (W)	17.82	23.92	48.07	46.46
Total (W)	63.35	83.76	132.53	139.35

Table 4.3 On-load rotor eddy current loss @45,000rpm with 2 magnet segments.

	Three-phase PM BLDC motor		Single-phase PM BLDC motor	
	Fundamental current	Simulated current	Sinusoidal current	Simulated current
PM (W)	39.01	53.99	12.74	17.51
Sleeve (W)	13.62	19.81	8.41	10.22
Total (W)	52.63	73.80	21.15	27.73

4.3 Pulsating armature reaction field of single-phase PM BLDC motor

As predicted by FEM in the previous section, single-phase motor exhibits significant armature rotor eddy current loss. One of the reasons is that the single-phase motor has an inherent pulsating armature reaction field which will be investigated in this section.

For the armature reaction field and corresponding armature rotor eddy current loss, the magnet remanence is set as zero in the FE model. Meanwhile the fundamental component of the simulated current, i.e. sinusoidal current as shown in Figure 4.6(b), is applied to the windings. Hence, the instantaneous airgap field distribution resulting from the fundamental component of winding current can be obtained by solving the static FE model. Figure 4.9 shows the instantaneous radial airgap flux density distributions due to stator excitation. It is evident that the winding current produces a pulsating field. The space harmonic spectra of the radial airgap flux density distribution corresponding to a stator current of 8A for both concentric and eccentric airgaps are shown in Figure 4.10. As will be seen that the space harmonics are influenced by the eccentricity of the airgap, which, in turn, significantly affects the rotor eddy current loss. Due to its relatively small airgap length, the motor with a concentric airgap (its airgap corresponds to the minimum airgap in the case of eccentric airgap) has greater amplitude of each radial airgap flux density harmonic.

The pulsating instantaneous airgap field distribution also can be expressed by:

$$F(\theta,t) = F_{m1}\sum_{\nu}\frac{1}{\nu}\sin(\omega_r t)\sin(\nu\theta) \qquad \text{(A)} \tag{4-1}$$

where F_{m1} -- Magnitude of fundamental mmfs; A

ν -- Order of space harmonic;

ω_r -- Angular speed; rad/s

θ -- Angular position; rad

Therefore, the ν^{th} mmf harmonic can be resolved into two components:

$$\begin{aligned} F_\nu(\theta,t) &= \frac{F_{m1}}{\nu}\sin(\omega_r t)\sin(\nu\theta) \\ &= \frac{1}{2}\frac{F_{m1}}{\nu}\cos(\omega_r t - \nu\theta) - \frac{1}{2}\frac{F_{m1}}{\nu}\cos(\omega_r t + \nu\theta) \qquad \text{(A)} \\ &= F_\nu^{'}(\theta,t) + F_\nu^{''}(\theta,t) \end{aligned} \tag{4-2}$$

where $F_\nu^{'}(\theta,t)$ and $F_\nu^{''}(\theta,t)$ are the ν^{th} forward and backward rotating harmonic mmfs, each being half the amplitude of the ν^{th} pulsating mmf.

Therefore, in single-phase motor, except the fundamental component of the forward mmfs, both forward and backward rotating harmonic mmfs which do not rotate in synchronism with the rotor can induce a significant rotor eddy current loss. However, three-phase motor has rotating armature reaction field and only $\nu = 6k \pm 1 (k = 1,2,3...)$ harmonic mmfs exits which is much less than single-phase motor.

4.4 On-load rotor eddy current loss of single-phase PM BLDC motor

For the actual machine which is under consideration, the rotor eddy current loss is determined not only by the stator slot openings and the eccentric airgap, but also by the winding current. As mentioned in section 4.2.2, for a single-phase PM BLDC motor, the overall on-load rotor eddy current loss is much less than the open-circuit rotor eddy current loss and the armature rotor eddy current loss. In this section, the magnet working point is examined to investigate

this phenomenon.

As shown in Figure 4.11, two locations in the magnet, i.e. A and B, are being examined in terms of the radial and circumferential flux density variation at three conditions which are:

- Magnetized magnet without winding current, i.e. open-circuit condition;
- Unmagnetized magnet with fundamental component of the winding current, i.e. load condition;
- Magnetized magnet with fundamental component of the winding current i.e. on-load condition.

The variation of the flux density at these two locations in the magnet as it rotates is shown in Figure 4.12. It can be seen that the flux density variation due to stator slot openings and eccentric airgap behaves in opposite way to that due to the winding current. Therefore, the overall flux density variation at the on-load condition is less than at the open-circuit condition and load condition, which results in less rotor eddy current loss. Figure 4.13 shows the field distributions at two rotor positions corresponding to the maximum flux density variation at two locations in the magnet, from which it can be seen that the maximum flux density near the minimum airgap has been significantly reduced. It indicates that there is an optimal combination of the eccentric airgap and winding current resulting in a minimum on-load rotor eddy current loss, which will be investigated in next section.

4.5 Influence of eccentric airgap and winding current on rotor eddy current loss

The eccentric airgap is employed in the single-phase PM BLDC motor to improve the starting capability and facilitate the unidirectional rotation. However, it will have a significant influence not only on the open-circuit rotor eddy current loss as discussed in 4.2.1, but also on the on-load rotor eddy current loss combined with the winding current as mentioned in 4.4. In

this section, FEM is used to investigate the influence of eccentric airgap and winding current on the rotor eddy current loss. Figure 4-10 compares the variation of eddy current losses in the permanent magnet, stainless steel sleeve, and total eddy current loss with eccentric airgap and winding current when the permanent magnet is unmagnetized or magnetized, and the winding current is 180° square waveform and sinusoidal waveform (fundamental), respectively.

It can be seen that,

(1) If the magnet is unmagnetized:

- 180° square current waveform induces much more significant armature rotor eddy current loss than that which results when the motor is supplied with only the fundamental component of the square current waveform. The reason is that 180° square current has considerable odd high time harmonics. Both forward and backward magnetic fields which are associated with these odd high harmonics are all asynchronous with rotor rotation and can induce the eddy current loss.
- The higher winding current introduces a relatively higher flux density in the rotor which results in a relatively higher armature rotor eddy current loss, as shown in Figure 4.14(a) and Figure 4.15.
- For a given winding current, the greater airgap eccentricity has less armature rotor eddy current loss, as shown in Figure 4.14(b) and Figure 4.16. The reason is that, for a given rotor outer diameter, a greater airgap eccentricity means a longer average effective airgap length which will reduce the flux density in the rotor resulting a relative less armature rotor eddy current loss.

(2) If the magnet is magnetized:

- Due to its odd high time harmonics, 180° square current waveform induces much more on-load rotor eddy current loss than its fundamental component, i.e. sinusoidal winding current.
- As shown in Figure 4.14(b) and Figure 4.15(a), for the concentric airgap, i.e. OO'=0mm, the rotor eddy current loss increase with the winding current.

- However, for a given eccentric airgap, there is a particular value of winding current which results in a minimum rotor eddy current loss, since it results in the smallest variation in the magnet working points when the rotor rotates as analyzed in the section 4.4. For example, as shown in Figure 4.15(b), for airgap eccentricity OO'=0.8mm, if the motor is supplied with the sinusoidal winding current, $I_{m\_\sin} = 6A$ gives the minimum rotor eddy current loss. Meanwhile, if the motor is supplied with the 180° square winding current, $(4/\pi)I_{m\_squ} = 4A$ has the minimum rotor eddy current loss. However, it doesn't mean that the motor is working at the best efficiency point which needs more investigation.

Therefore, at the design stage of the single-phase PM BLDC motor, the airgap eccentricity needs to be optimized not only to satisfy the starting requirement, but also to minimize the rotor eddy current loss by considering the winding current, which needs more investigation in the future research, particularly when the overall motor performance is considered.

4.6 Influence of number of PM segments

In order to reduce the risk of the irreversible PM demagnetization, the magnet can be segmented axially or circumferentially. Segmented magnets are insulated electrically, which may result in less PM eddy current loss. Axially segmenting the magnet is not convenient to be modeled in 2D FE model. Therefore, only circumferentially segmenting the magnet is examined by 2D FE model in this section. The influence of the number of circumferential PM segments on the open-circuit and on-load rotor eddy current loss is investigated for both diametrically magnetized PM and radially magnetized PM which are assumed to have the same magnet dimensions, remanence and electrical conductivity.

4.6.1 Diametrically magnetized PM

The lowest number of magnet segment the diametrically magnetized PM can have is one, i.e.

ring magnet. In its simplest form this would consists of only one piece of magnet, which makes it relatively easy to be assembled with the shaft and the sleeve.

Figure 4.17 shows that the eddy current distribution which results on open-circuit when the rotor is equipped with a single ring magnet, both with and without the stainless steel retaining sleeve, at the rotor position of 270°_{mech}h. As will be evident, the diametrically opposite region having the highest eddy current which is adjacent to the slot opening can be seen in the magnet. This indicates that due to 2-pole/2-slot stator, the pole-pitch of the harmonic field which induces the majority of the magnet eddy current loss is 180°. Therefore, the circumferential magnet segmentation is only effective for reducing the magnet eddy current loss when the magnet arc becomes smaller than the pole-pitch of the harmonic field, i.e. 180° in this case.

The illustration of different number of magnet segments is shown in Figure 4.18. It can be noted that whatever the magnet segment number is, the overall direction of the magnetization of the whole magnet is kept as parallel. If the number of the magnet segments is greater than 1, the magnet is divided into several segments evenly. The influence of the number of circumferential magnet segments on the open-circuit and on-load rotor eddy current loss at the speed of 45,000rpm, both with and without the stainless steel sleeve, is shown in Figure 4.19. The fundamental component of the simulated phase current with the amplitude of 8A is applied to the windings on the load condition. It can be seen that:

- If there is no sleeve, for the 2-pole/2-slot stator single ring magnet and 2 pieces of magnet segments produce similar open-circuit eddy current loss in magnet. However, if the stainless steel sleeve is employed, 2 pieces of magnet segments has less open-circuit eddy current loss in magnet than that of single ring magnet. When the number of magnet segments is greater than 2, in these cases the magnet arc becomes smaller than 180°, the open-circuit eddy current loss in magnet reduces significantly regardless of with and without sleeve. Further, open-circuit eddy current loss in sleeve increases gradually with the number of the magnet segments.

- Generally, regardless of with and without sleeve, the on-load eddy current loss in magnet reduces gradually with the increase of the number of magnet segments. However, similar with open-circuit condition, higher number of magnet segments has greater on-load eddy current loss in sleeve.
- Without the stainless steel sleeve, the use of 8 magnet segments reduces the on-load eddy current loss in the permanent magnet by ~70% compared to that which results in a ring magnet (1 segment). With the stainless steel sleeve, the use of 8 magnet segments reduces the on-load eddy current loss in the permanent magnets by ~67% compared to that which results in a ring magnet (1 segment). However, the on-load eddy current loss in the sleeve is increased by ~91%. Consequently, the total on-load rotor eddy current loss is only reduced by ~23%, i.e. increasing the number of magnet segments can reduce the rotor eddy current loss, but becomes less effective when a metallic sleeve is employed to contain the magnets.

Since the overall magnet is magnetized in the parallel direction, for a given number of magnet segments, the magnet can be segmented by different way. By way of example, if the magnet is divided into 2 segments, four possible magnet divisions are shown in Figure 4.20, where the angle α between the magnetized direction and common edge of two magnet segments is 0°, 45°, 90°, and 135°, respectively. In these four cases, the open-circuit and on-load rotor eddy current loss at the speed of 45,000rpm, both with and without the stainless steel sleeve are calculated by 2D FE method and results are shown in Figure 4.21. Again, the fundamental component of the phase current with the amplitude of 8A is being applied to the windings on the load condition. From Figure 4.21, it can be seen that on open-circuit condition, regardless of with or without sleeve, $\alpha = 90^\circ$ has the minimum rotor eddy current loss.

However, on on-load condition, the minimum rotor eddy current loss is achieved at $\alpha = 0^\circ$. When the motor is under normal operating condition, the eddy current loss which should be minimized is the on-load rotor eddy current loss. Therefore, $\alpha = 0^\circ$ is the best choice to

divide the magnet into 2 segments.

4.6.2 Radially magnetized PM

Instead of being magnetized in the diametrical direction, the PM also can be magnetized in the radially direction. In this section, the influence of the number of the magnet segments on the rotor eddy current loss of the single-phase PM BLDC motor which has a radially magnetized PM will be presented and compared to that of diametrically magnetized PM. In order to compare fairly, diametrically magnetized PM and radially magnetized PM have the same dimensions. In the FE model, magnetization direction of each radially magnetized PM segment can only be set as only one direction. In another word, the flux of the PM goes either from inner PM bore to outer PM bore or from outer PM bore to inner PM bore radially. Therefore, unlike 2-pole diametrically magnetized PM, only even number of PM segments exists for 2-pole radially magnetized PM, i.e. 2, 4, 6 and 8, as shown in Figure 4.22. Figure 4.23 and Figure 4.24 compare the open-circuit and on-load eddy current loss in PM, sleeve and rotor between single-phase motor with diametrically magnetized PM and radially magnetized PM at the different number of PM segments.

It can be noticed that:

- With radially magnetized PM, if the number of the magnet segments increases, the open-circuit and on-load eddy current loss in PM decreases gradually, and the open-circuit and on-load eddy current loss in the sleeve increases gradually. Therefore, the overall open-circuit rotor eddy current loss decreases gradually. However, 4 magnet segments gives highest overall rotor eddy current loss.
- Compared to diametrically magnetized PM, radially magnetized PM introduces much more open-circuit and on-load rotor eddy current loss at any number of magnet segments.

In order to further compare these two magnetized PMs, their back-EMF waveforms are compared in Figure 4.25 as well. It can be seen that due to the radial direction of the magnetization, the back-EMF waveform is more likely rectangular rather than

quasi-sinusoidal. By applying the fundamental component of the phase current with the amplitude of 8A to the windings, the static torque waveforms are compared in Figure 4.26 and the average peak-to-peak static torque is summarized in Table 4.4. It can be noticed that the radially magnetized PM produces 9.22% more average static torque than the diametrically magnetized PM. However, the radially magnetized PM has 2.3 times peak-to-peak static torque as the diametrically magnetized PM, which means that the radially magnetized PM introduces much more torque fluctuation.

In summary, radially magnetized PM introduces more open-circuit rotor eddy current loss than the diametrically magnetized PM. For a given sinusoidal phase current, radially magnetized PM can provide higher average static torque, but has higher torque fluctuation and more on-load rotor eddy current loss as well. Further, fabrication of diametrically magnetized PM is much easier than radially magnetized which leads to a lower cost for manufacture. Therefore, overall the diametrically magnetized PM is a more attractive option for domestic applications such as vacuum cleaner, fan, pump, etc., where the cost is very sensitive.

Table 4.4 Comparison of static torque.

	Radially magnetized PM	**Diametrically magnetized PM**
Average static torque (Nm)	0.283	0.259
Peak-to-peak static torque (Nm)	0.406	0.177

4.7 Influence of sleeve thickness and material

For high-speed motors, the centrifugal force on the magnet is relatively high and will be potential danger to the brittle magnet. Therefore, the retaining sleeve is often used to maintain the mechanical integrity of the rotor of the permanent magnet machine. The sleeve is exposed to the fields resulting from the stator slot opening and the mmfs harmonics which are not synchronous with the rotor. Hence, if the sleeve is electrically conductive, the eddy current

loss will be generated in the sleeve. Further, the eddy current in the sleeve acts as a magnetic shield which reduces the amplitude of the varying field to which the magnets are exposed. Consequently, the existing of the retaining sleeve has an influence of the eddy current loss in the magnet. In this section, the influence of the sleeve conductivity and sleeve thickness on the rotor eddy current loss is examined by 2D FEM.

4.7.1 Sleeve material

Due to its high permeability which can reduce the effective airgap length resulting in high magnet working point and open-circuit field, the magnetic sleeve seems an attractive option. However, unfortunately a magnetic sleeve shunts the magnets. Hence, some of the open-circuit flux will go across the sleeve in the interpolar area rather than airgap to the stator, which means that the leakage flux will be increased. Further, the sleeve in the interpolar area will be saturated which can reduce the average magnet working point slightly. Generally, higher ratio between sleeve thickness and pole arc gives a greater saturated flux-shunting zone in the sleeve. The other major disadvantage for the magnetic sleeve is that the electrical conductivity is relatively high. Therefore, the eddy current loss in the sleeve could be significant. As discussed in Chapter 1, for high-speed PM machines, the rotor loss may cause a significant heating of the permanent magnets which may irreversibly demagnetise the partial permanent magnet. Hence, it is desirable to use low conductivity materials to reduce the eddy current loss in the sleeve. The most popular material for the sleeve is non-magnetic stainless steel which combines high strength with low electrical conductivity. There are various other metallic non-steel alternate materials such as titanium, aluminium and copper. Titanium tends to be more expensive. Aluminium and copper have a relative higher electrical conductivity. Non-metallic materials can be adopted as well such as carbon fibre. However, the thermal conductivity is much lower which will make it more difficult to transmit the heat form the magnet and sleeve to the air. Table 4.5 gives the electrical conductivity and relative permeability for some general non-magnetic sleeve materials such as carbon fibre, titanium, stainless steel, aluminium and copper. In order to compare fairly, with the same motor dimensions, magnet properties, sleeve permeability, and motor running speed, the impact of

the sleeve electrical conductivity on the open-circuit rotor eddy current loss is investigated by the 2D FEM, as shown in Figure 4.27(a). Meanwhile, by applying the fundamental component of amplitude of 8A the phase current to the windings, the variation of the on-load rotor eddy current loss with the sleeve electrical conductivity is shown in Figure 4.27(b).

It can be seen that:

- Due to that the magnetic field produced by the eddy current loss in the sleeve can smooth the varying field in the magnet as a magnetic shield, the loss in the magnet is reduced dramatically. Further, the greater the sleeve electrical conductivity is, the stronger the shielding effect. Theoretically, ideal superconductive material for the sleeve results in zero loss in the magnet. Therefore, Figure 4.27 apparently shows that the higher electrical conductivity of the retaining sleeve gives the less eddy current loss in the magnet. By way of example, copper sleeve has the dominant rotor loss and the magnet loss becomes negligible.
- Approximately, aluminium results in maximum sleeve and total rotor eddy current loss. If the sleeve electrical conductivity is greater than aluminium conductivity, the loss in the sleeve decreases slightly with the increase of sleeve conductivity.
- Carbon fibre, titanium and stainless steel have much less rotor eddy current loss than aluminium and copper. By taking into consideration the rotor loss, cost and thermal performance, stainless steel could be a preferred option.

Table 4.5 Sleeve material properties.

	Carbon fibre	**Titanium**	**Stainless steel**	**Aluminium**	**Copper**
Electrical conductivity ($\times 10^6 S \cdot m^{-1}$)	0.033	0.61	1.39	37.7	58.0
Relative permeability			1.0		

4.7.2 Sleeve thickness

In order to investigate the influence of the sleeve thickness on the rotor eddy current loss, Figure 4.28 shows the rotor loss versus the stainless steel sleeve thickness. The same motor dimensions, magnet properties and running conditions as previous section are applied to predict the rotor loss by 2D FEM. Due to the mechanical constrain limit, the sleeve thickness is varying from 0mm to 0.8mm. For this single-phase PM BLDC motor, as shown in Figure 4.10, the major mmfs harmonics which cause a significant rotor eddy current loss are 1st, 3rd and 5th space harmonics. Hence the orders of the harmonics in the rotor are 2nd, 4th and 6th. Table 4.6 summarizes the skin depth in different sleeve materials and magnet related to these harmonics at 45,000rpm of the running speed. It could be noticed that with the stainless steel sleeve, the skin depth is much greater than the maximum possible sleeve thickness, i.e. 0.8mm. Therefore, as will be seen in Figure 4.28 when the sleeve thickness is increased from 0mm to 0.8mm, the eddy current loss in the sleeve always increases due to a drop in overall sleeve resistance. However, for the motor in [78] due to the skin effect, once the sleeve thickness is greater than certain value, there is little further impact upon the loss in the sleeve. It also can be noted that when the sleeve thickness increases the loss in the magnets decreases due to the increasing shielding effect of the sleeve. However, the total rotor eddy current loss is increased.

Skin depth is a term used for the distance over which the amplitude of electromagnetic waves falls to 1/e of its original value. The skin depth can be calculated by following equation which has been used in the improved analytical eddy current loss model as described in Chapter 4:

$$\delta = \sqrt{\frac{2}{nw\sigma\mu_0\mu_r}} \quad \text{(m)} \tag{4-3}$$

where n -- Order of field harmonics;

ω -- Angular frequency of the wave; rad/s

σ -- Electrical conductivity of the material; $\Omega^{-1}\cdot m^{-1}$

μ_0 -- Permeability of free space;$4\pi\times10^{-7}$ N·A^{-2}

μ_r -- Relative permeability of the material.

Table 4.6 Skin depths in different rotor materials, speed=45,000rpm, (mm)

Order of field harmonics	Sm_2Co_{17}	Carbon fibre	Titanium	Stainless steel	Aluminium	Copper
2	10.37	71.53	16.64	11.03	2.12	1.71
4	7.33	50.58	11.77	7.80	1.50	1.21
6	5.98	41.3	9.61	6.37	1.22	0.99

4.8 Summary

The open-circuit, armature and on-load rotor eddy current loss of single-phase and three-phase PM BLDC motors have been predicted by 2D FEM in this chapter, with particular emphasis on the single-phase motor. It is concluded that unlike the three-phase PM BLDC motor, the single-phase PM BLDC has much less on-load rotor eddy current loss than its open-circuit and armature rotor eddy current loss due to its eccentric airgap. By examining the influence of the eccentric airgap combining with the phase current on the on-load rotor eddy current loss, it is found that there is an optimal combination of eccentric airgap and phase current which gives the minimum on-load rotor eddy current loss. By increasing the number of circumferential diametrically magnetized magnet segments, the rotor eddy current loss can be reduced gradually. However, it becomes less effective when a metallic sleeve is employed to contain the magnets. On the same load conditions, the radially magnetized magnets have a higher eddy current loss than the diametrically magnetized magnets. The influence of the sleeve materials and sleeve thickness on the rotor eddy current loss has been investigated as well.

As a summary, for a given phase current, the on-load rotor eddy current loss can be minimized by:

- Optimising the eccentric airgap.
- Diametrically rather than radially magnetizing the magnets.
- Segmenting the magnets circumferentially.

- Selecting the sleeve material with low electrical conductivity.
- Reducing the sleeve thickness.

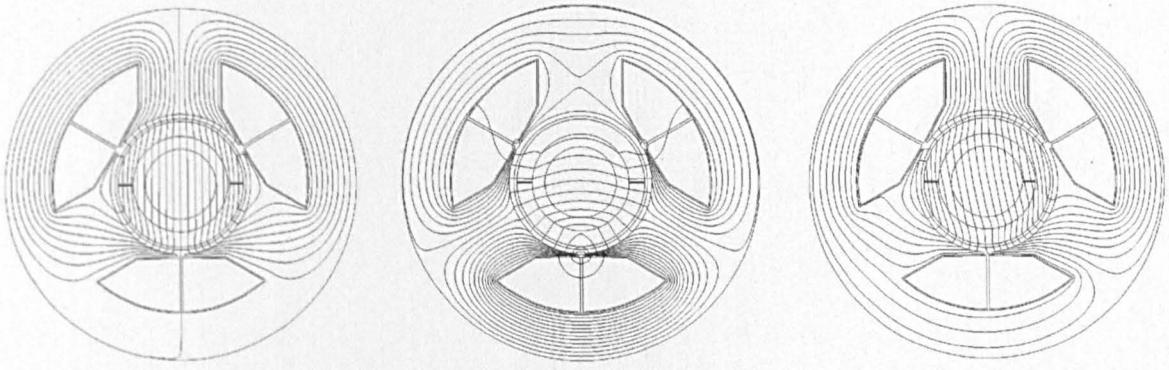

(a) Open-circuit field, Magnetized PM

(b) Armature reaction field, Unmagnetized PM, $i_a = 0A, i_b = -5.2A,$ $i_c = 5.2A$

(c) On-load field, Magnetized PM, $i_a = 0A, i_b = -5.2A,$ $i_c = 5.2A$

Figure 4.1 Flux distribution of three-phase PM BLDC motor.

Rotor position=$0^{o}_{mech.}$

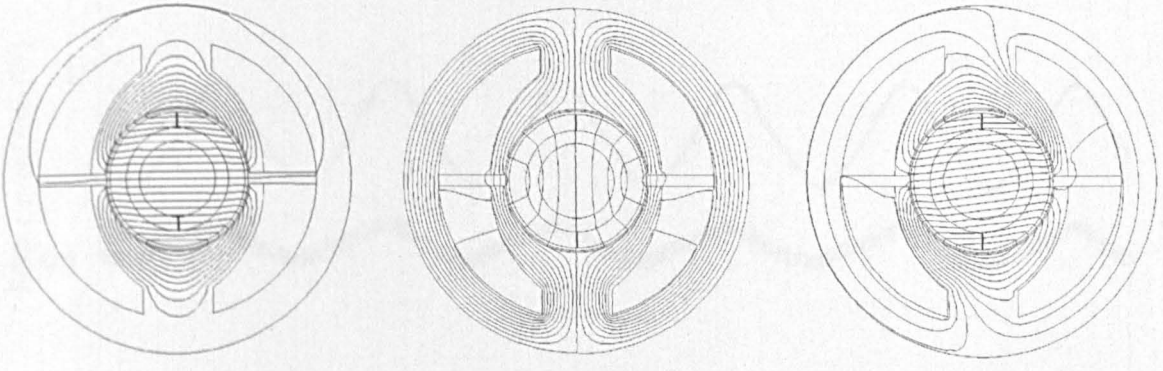

(a) Open-circuit field, Magnetized PM

(b) Armature reaction field, Unmagnetized PM, Phase current=8A

(c) On-load field, Magnetized PM, Phase current=8A

Figure 4.2 Flux distribution of single-phase PM BLDC motor with concentric airgap.

Rotor position=90^{o}_{mech}

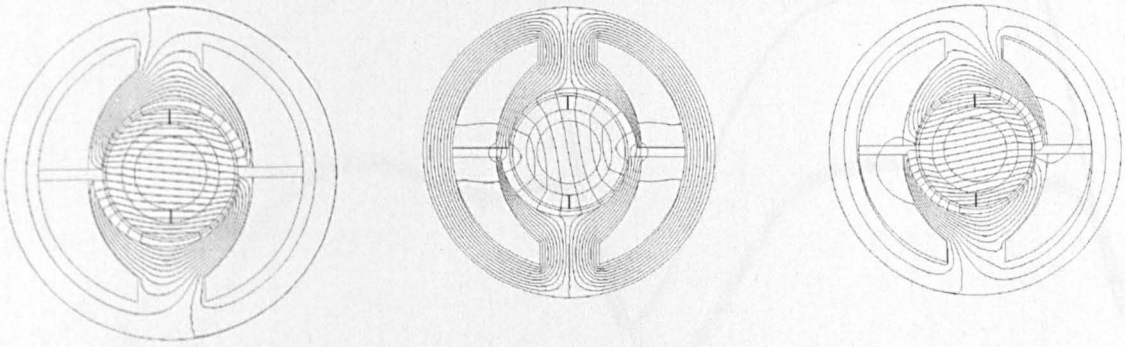

(d) Open-circuit field, Magnetized PM

(e) Armature reaction field, Unmagnetized PM, Phase current=8A

(f) On-load field, Magnetized PM, Phase current=8A

Figure 4.3 Flux distribution of single-phase PM BLDC motor with eccentric airgap. Rotor position=90°_{mech}

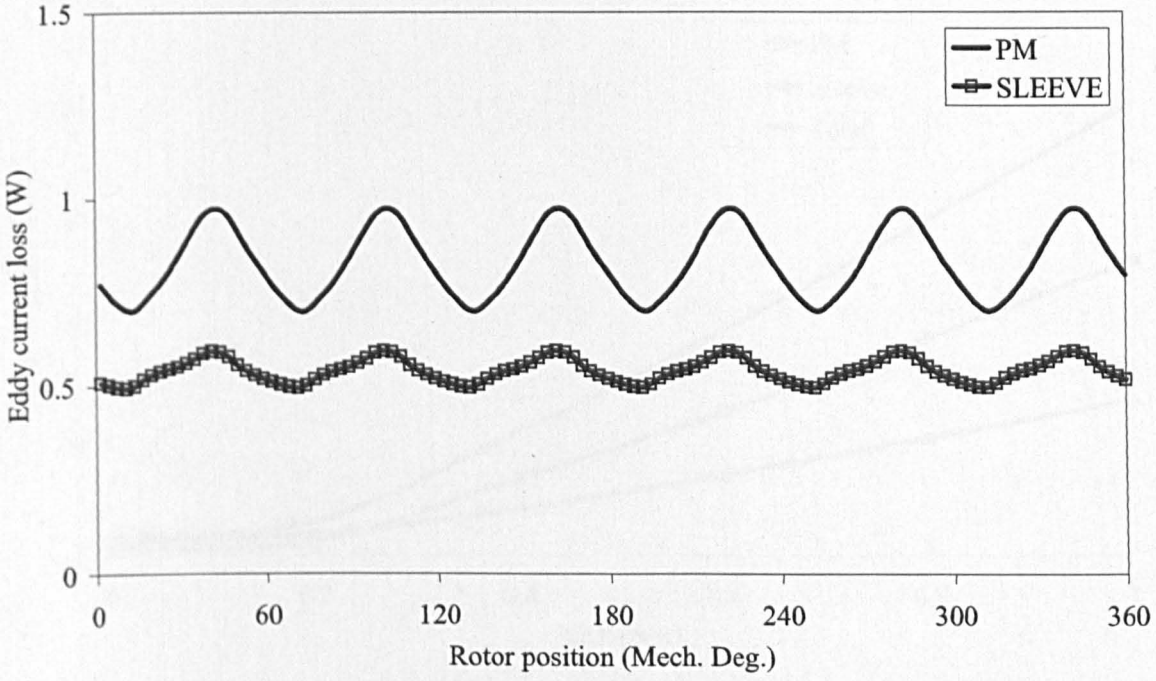

(a) Three-phase

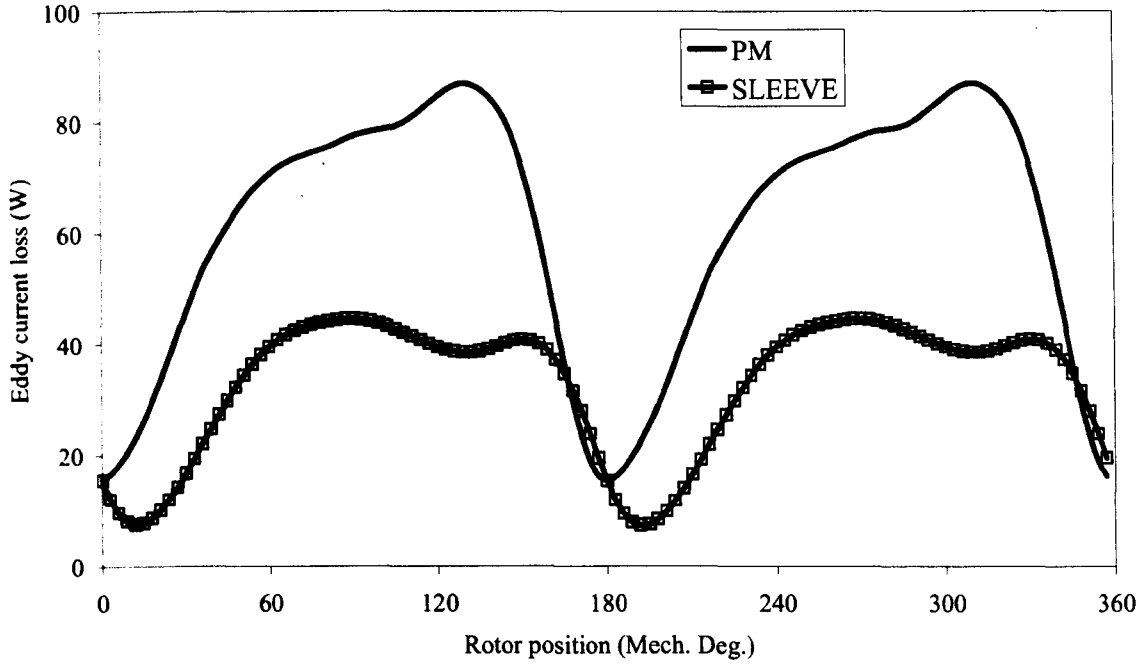

(b) Single-phase with eccentric airgap

Figure 4.4 Open-circuit rotor eddy current loss.

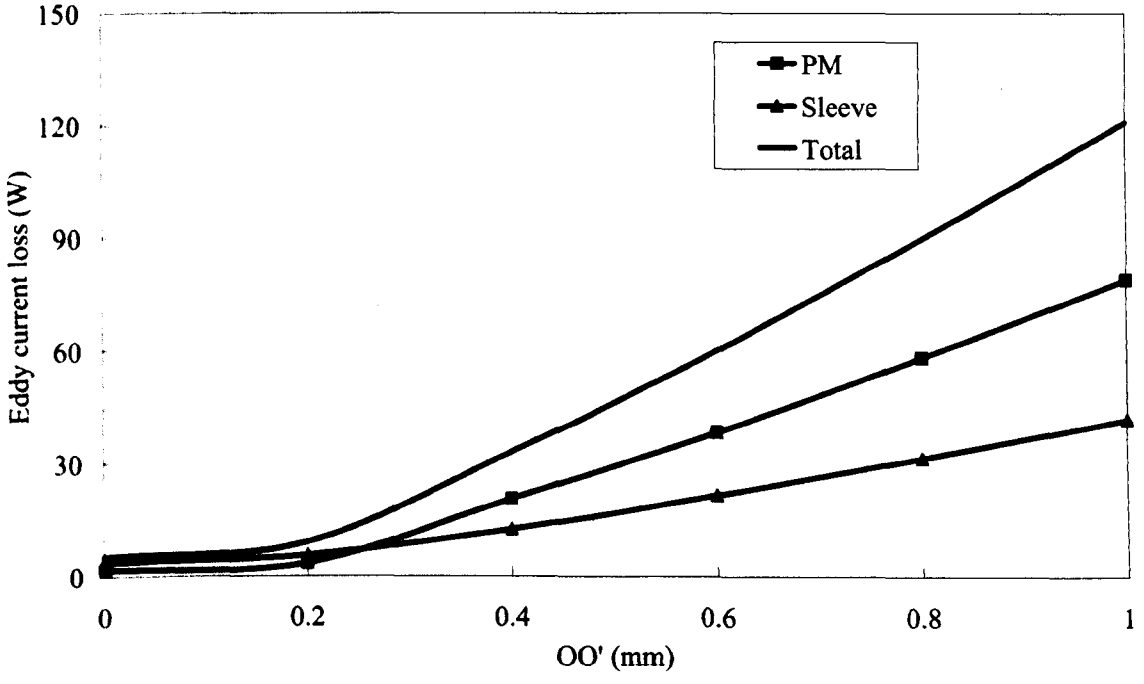

Figure 4.5 Variation of open-circuit rotor eddy current loss with airgap eccentricity.

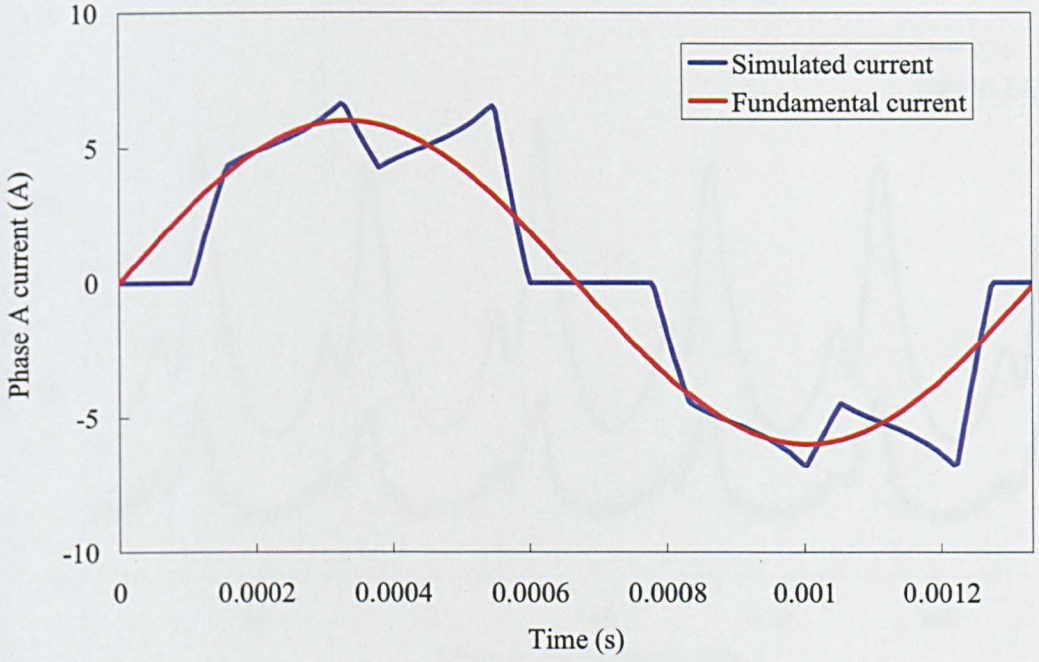

(a) Three-phase PM brushless DC motor

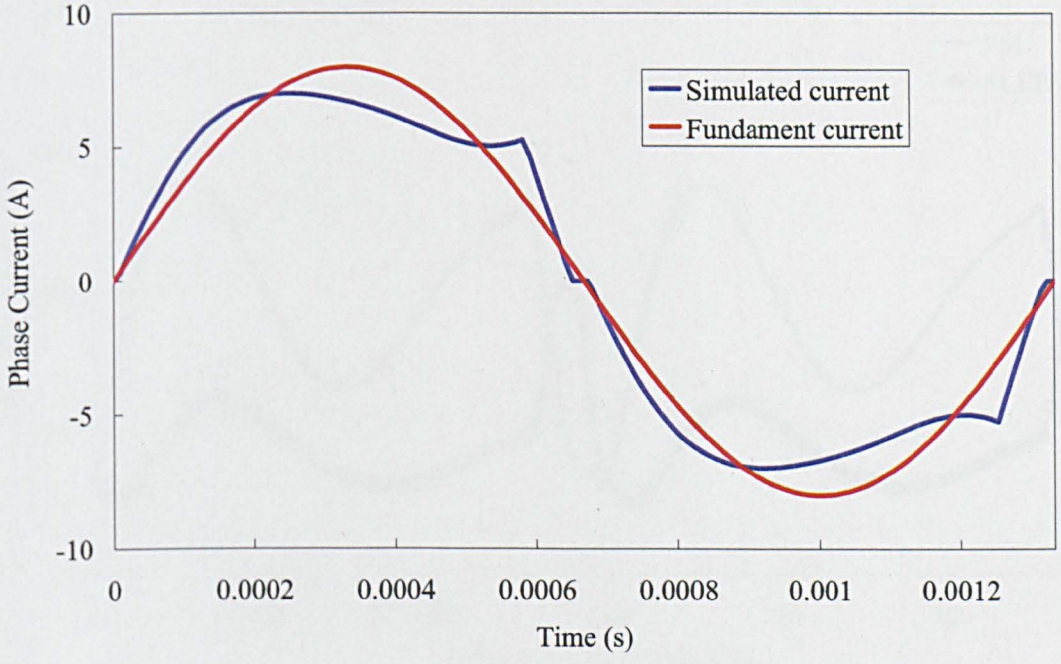

(b) Single-phase PM brushless DC motor

Figure 4.6 Simulated phase current ant its fundamental component.

(Speed=45,000rpm)

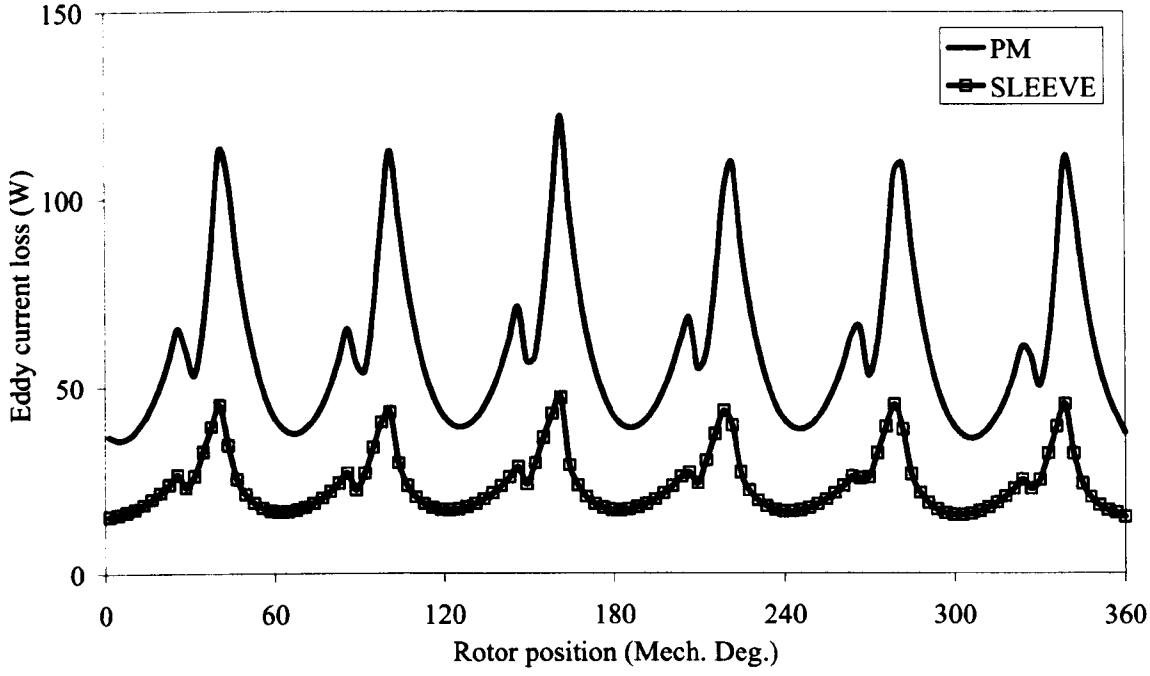

(a) Three-phase PM BLDC motor

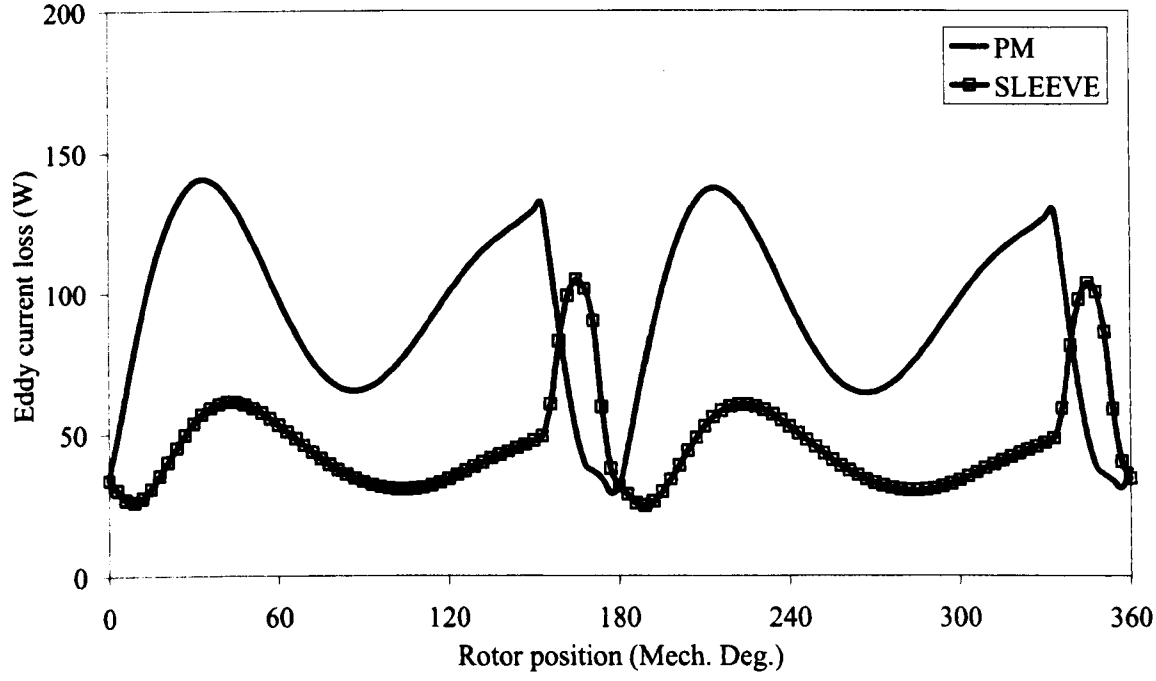

(b) Single-phase PM BLDC motor

Figure 4.7 Armature rotor eddy current loss vs rotor position, simulated current.

(Speed=45,000rpm)

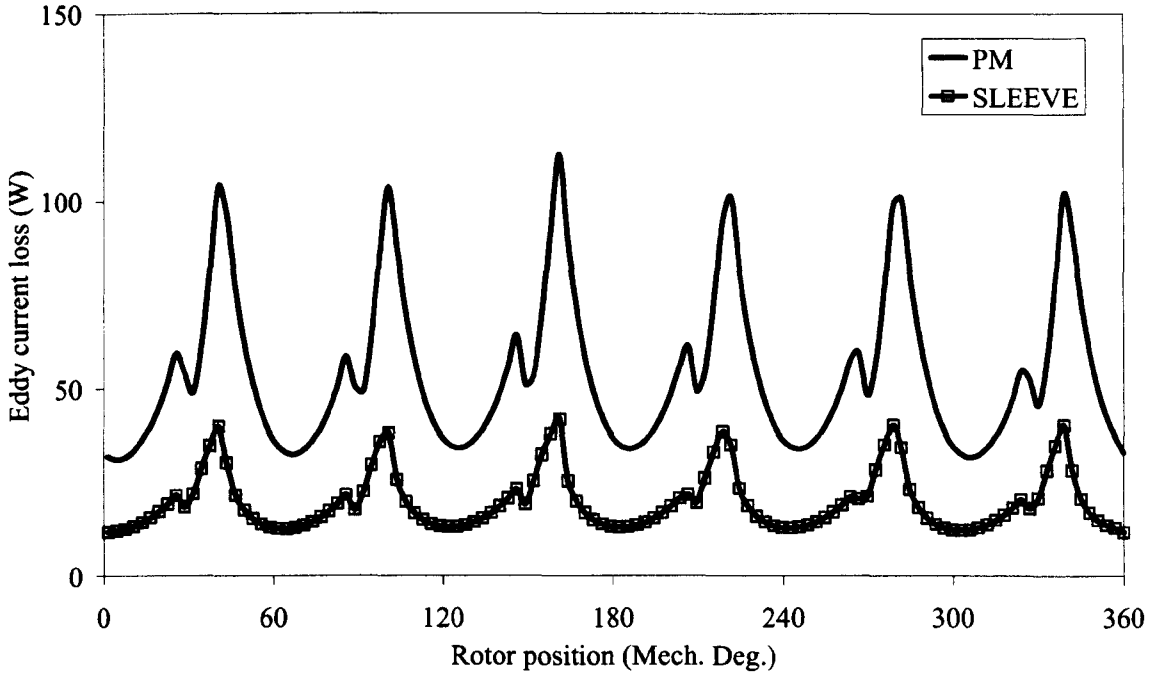

(a) Three-phase PM BLDC motor

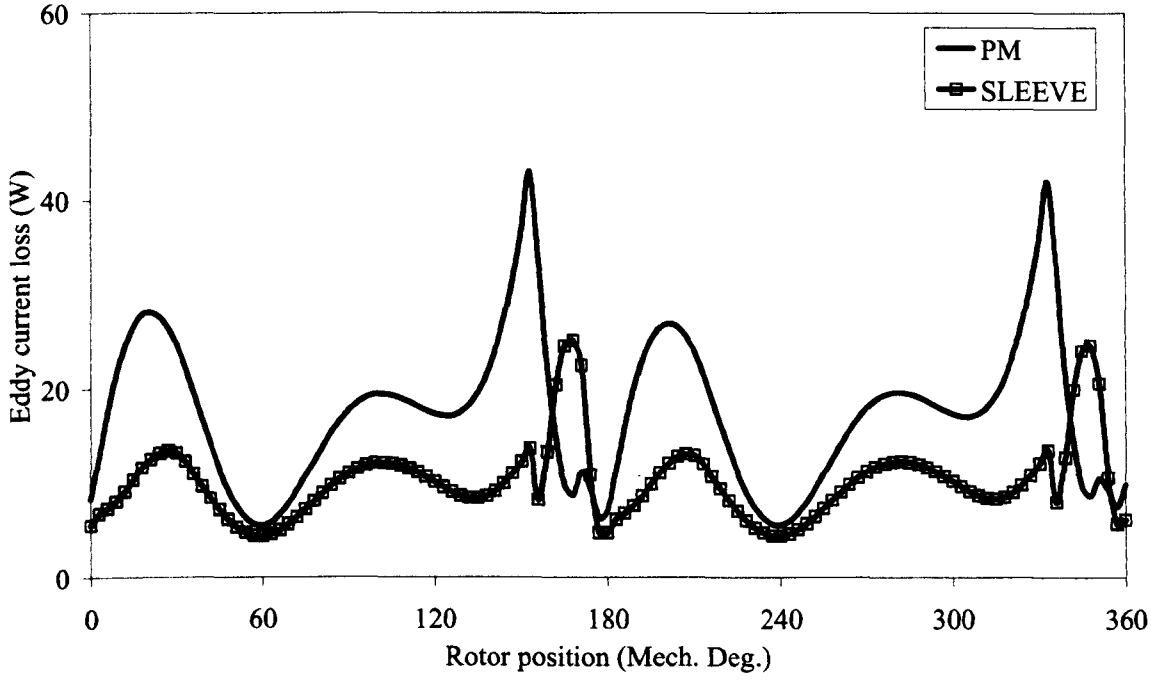

(b) Single-phase PM BLDC motor

Figure 4.8 On-load rotor eddy current loss vs rotor position, simulated current.

(Speed=45,000rpm)

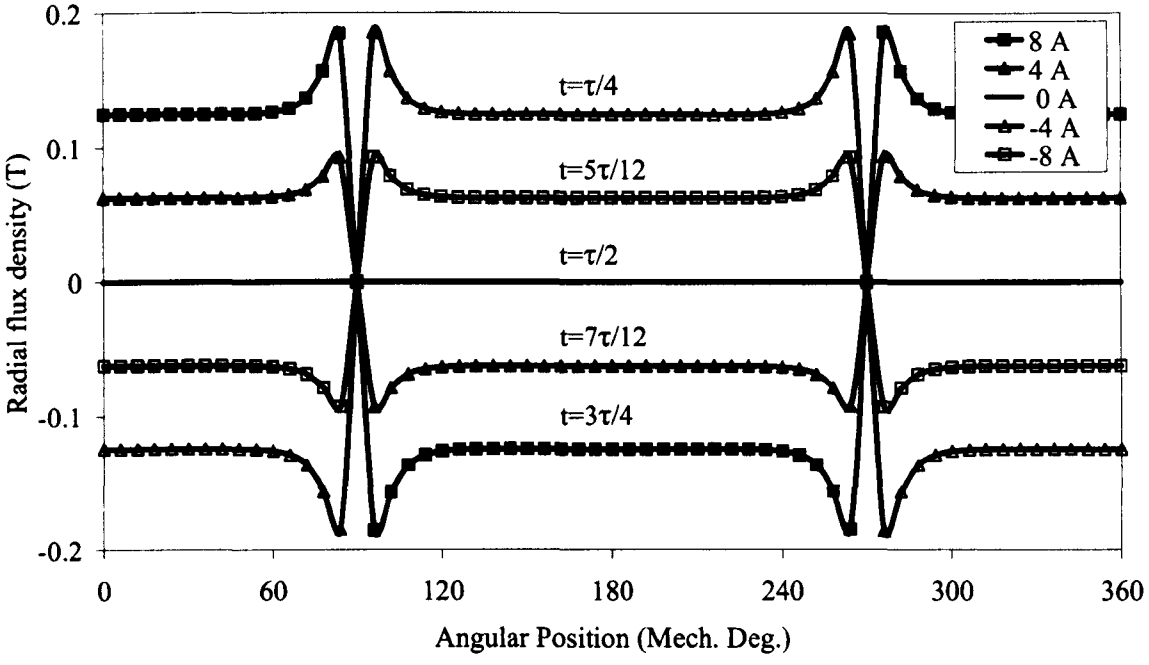

(a) OO'=0.0mm

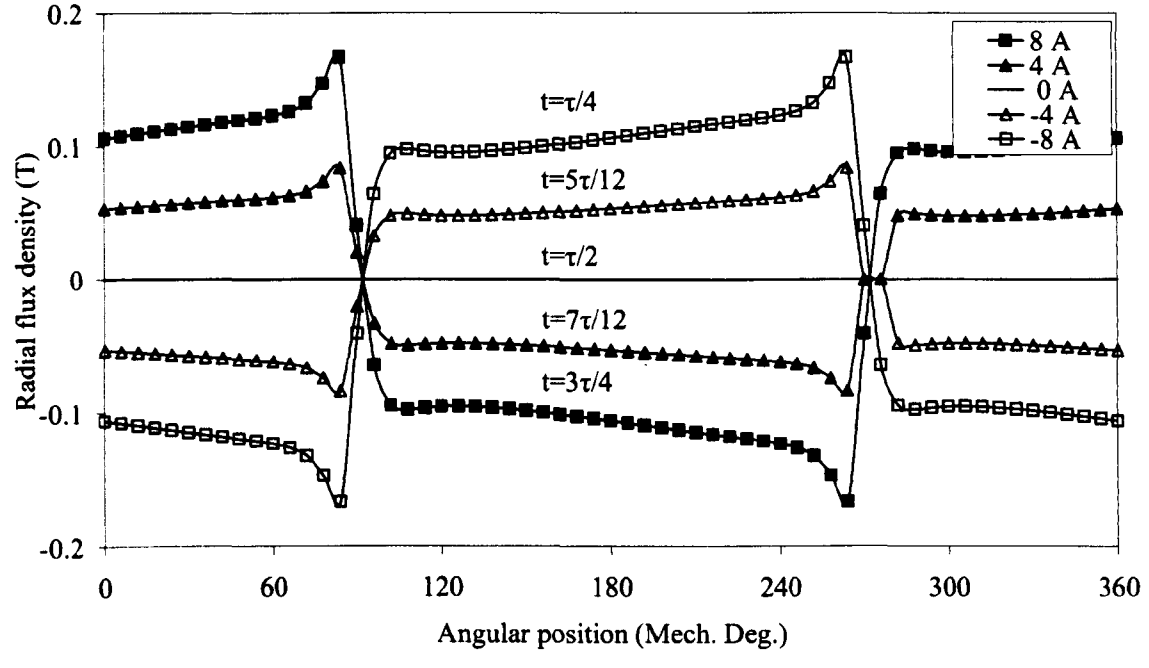

(b) OO'=0.8mm

Figure 4.9 Instantaneous radial airgap flux density distributions due to stator excitation alone.

$$(i = I_{m\_\sin} \sin \omega_r t,\ \ I_{m\_\sin} = 8A,\ \ \tau = 2\pi / \omega_r)$$

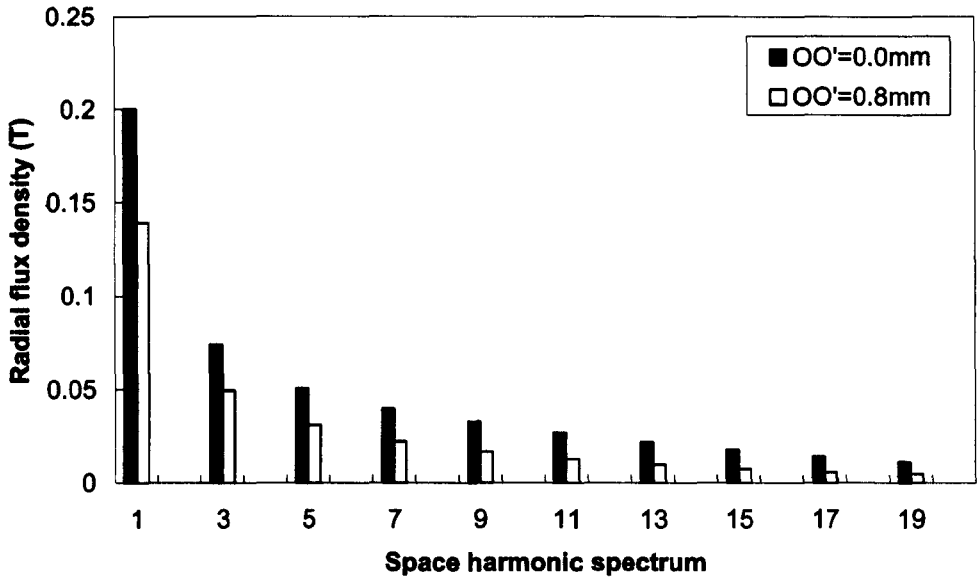

Figure 4.10 Space harmonic spectrum of radial airgap flux density distribution due to stator excitation alone. ($i = 8A$)

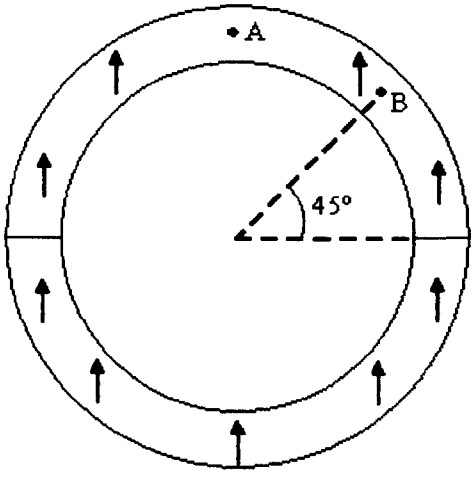

Figure 4.11 Two locations A&B in permanent magnet.

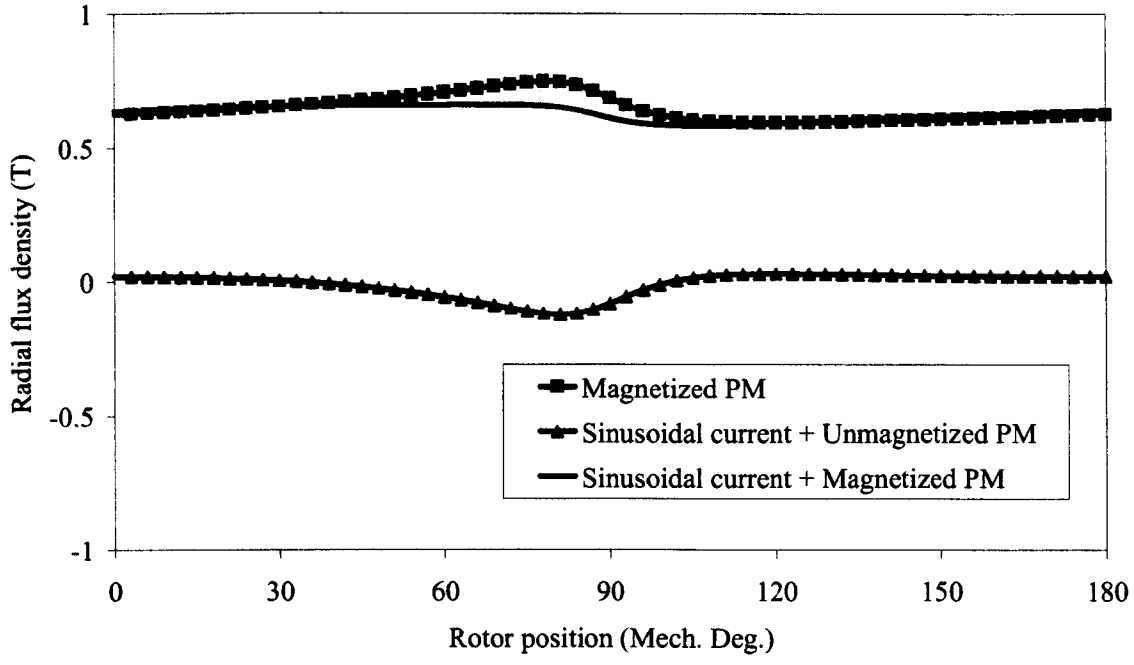

(i) Radial flux density

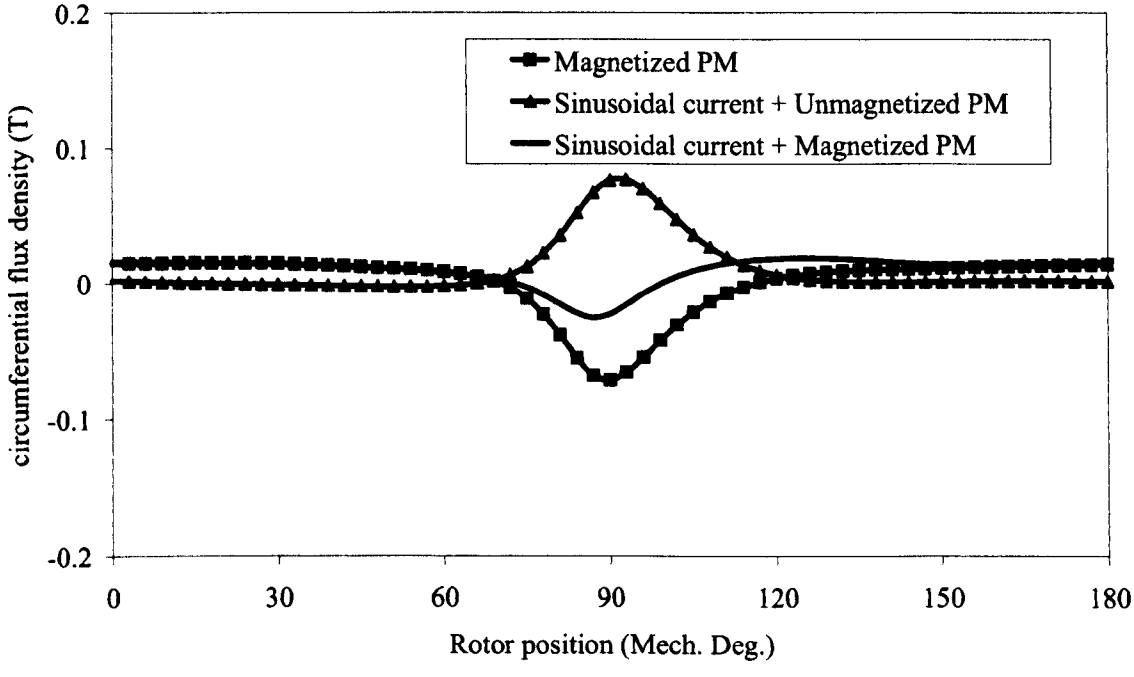

(ii) Circumferential flux density

(a) Location A

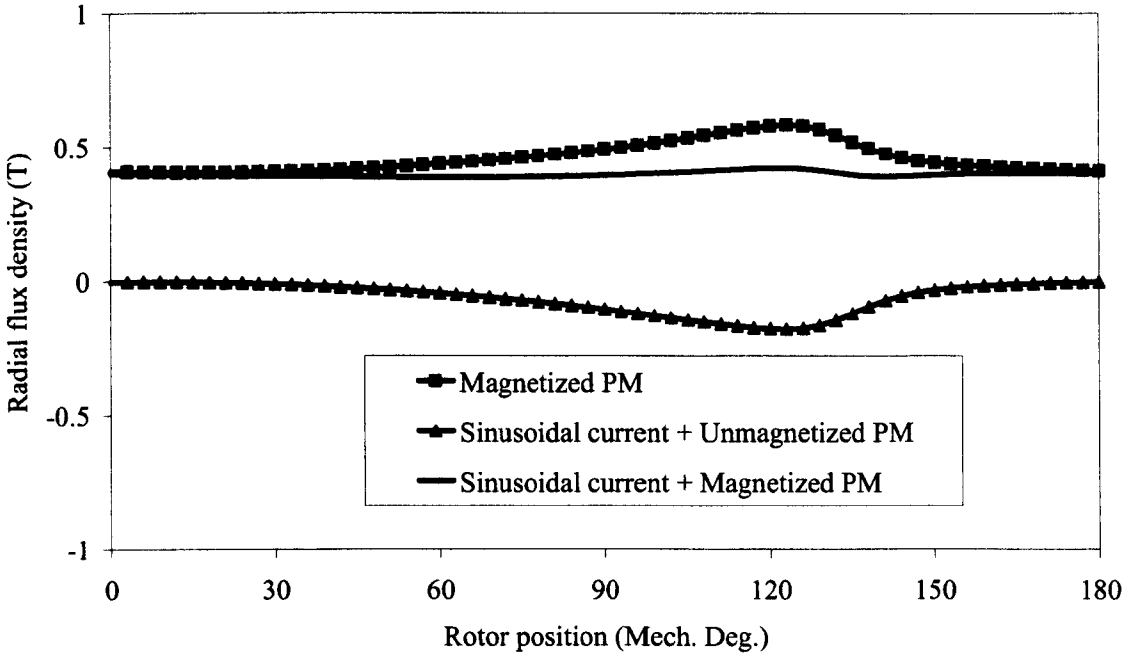

(i) Radial flux density

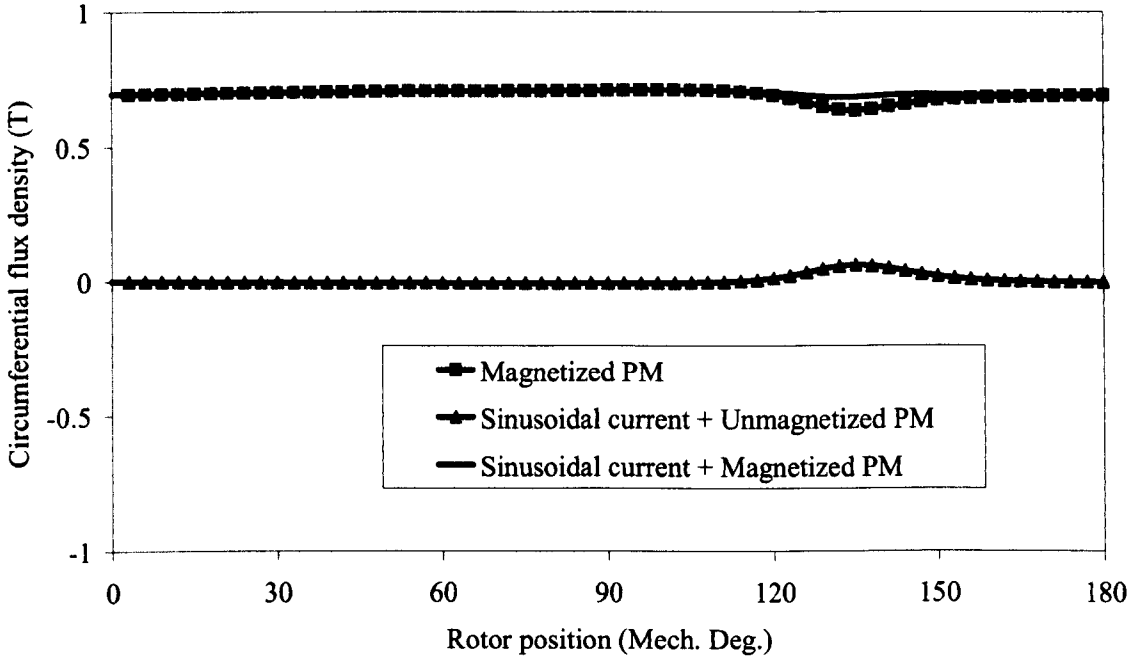

(ii) Circumferential flux density

(b) Location B

Figure 4.12 Variation of flux density in permanent magnet with rotor position.

($I_{m\_\sin} = 8A$, OO'=0.8mm)

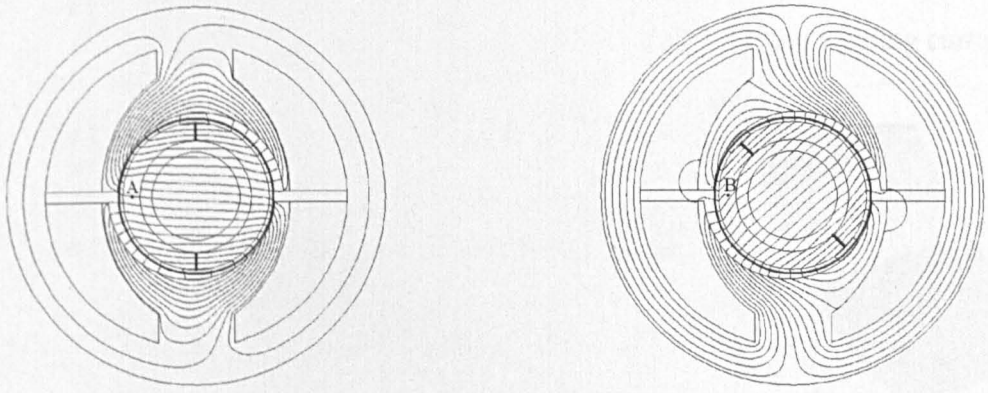

(i) Rotor position=90° (ii) Rotor position=135°

(a) Magnetized PM

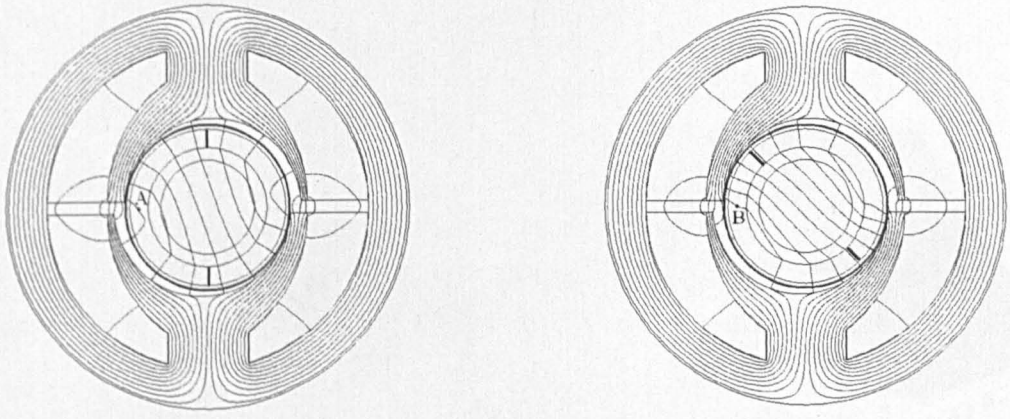

(i) Rotor position=90° (ii) Rotor position=135°

(b) Sinusoidal current + unmagnetized PM

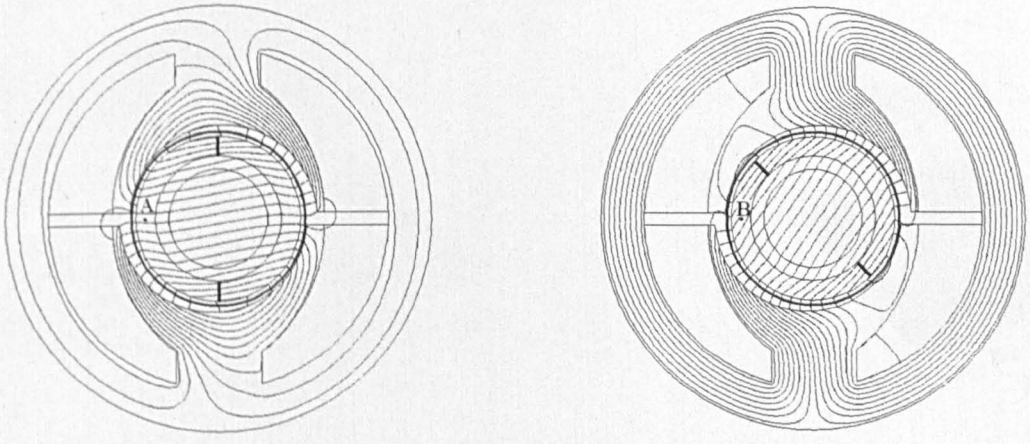

(i) Rotor position=90° (ii) Rotor position=135°

(c) Sinusoidal current + magnetized PM

Figure 4.13 Field distributions due to permanent magnet, stator coil excitation, and resultant load.

Sinusoidal winding current

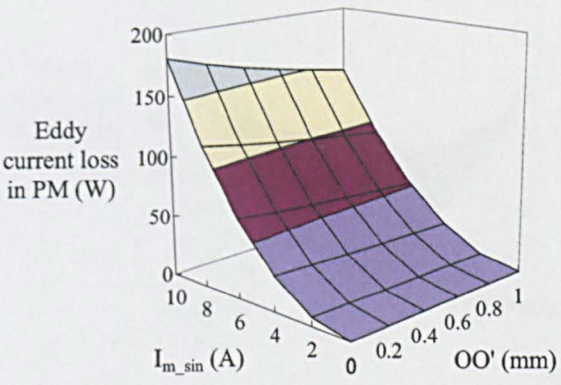

180° square winding current

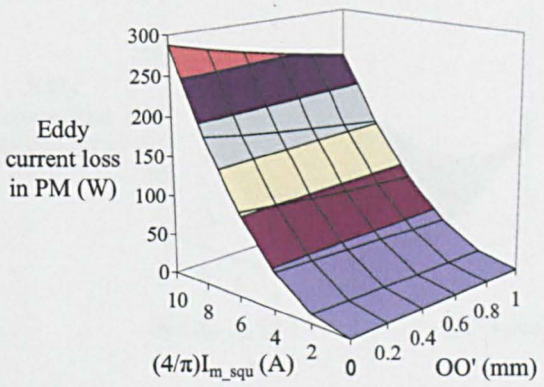

(i) In magnet

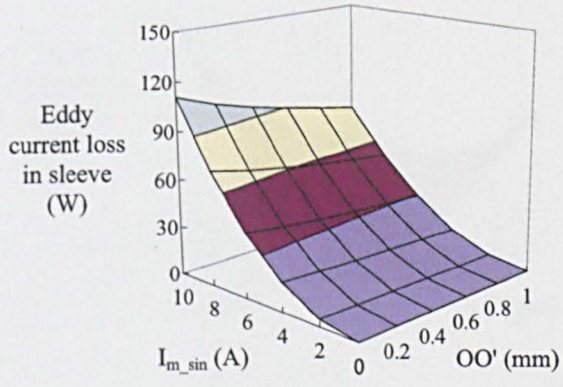

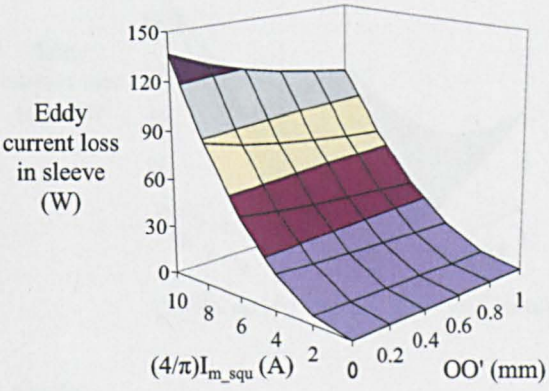

(ii) In sleeve

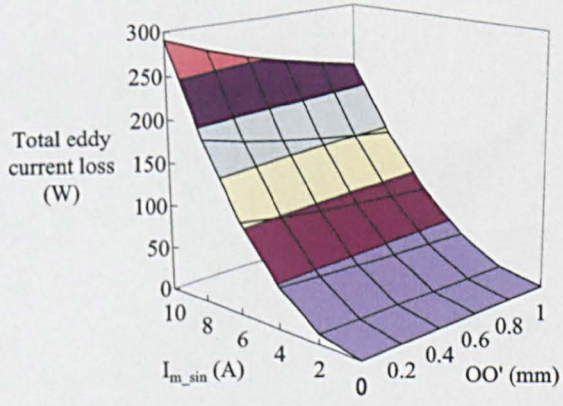

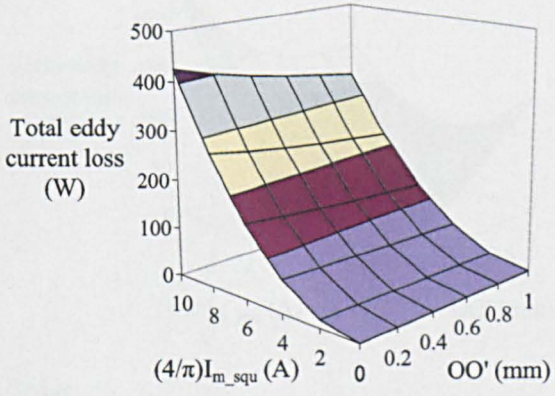

(iii) Total

(a) Armature rotor eddy current loss (Unmagnetized magnet)

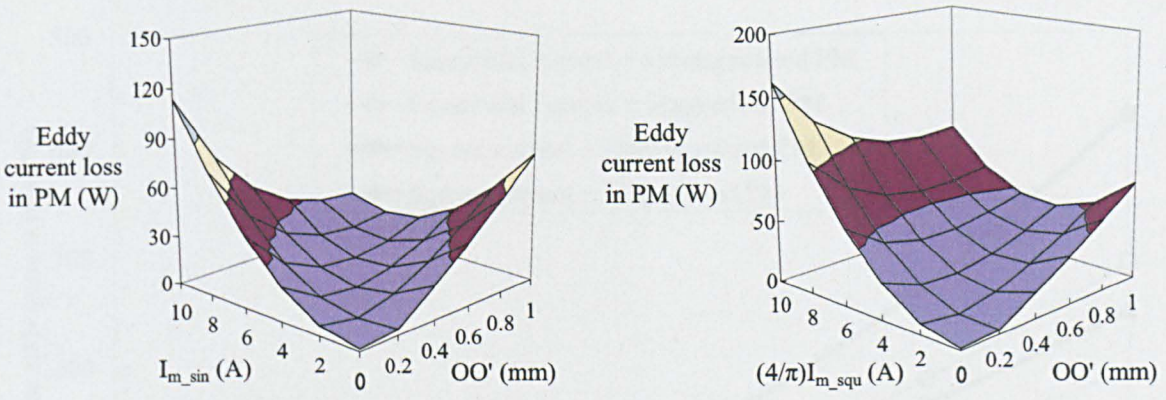

(i) In magnet

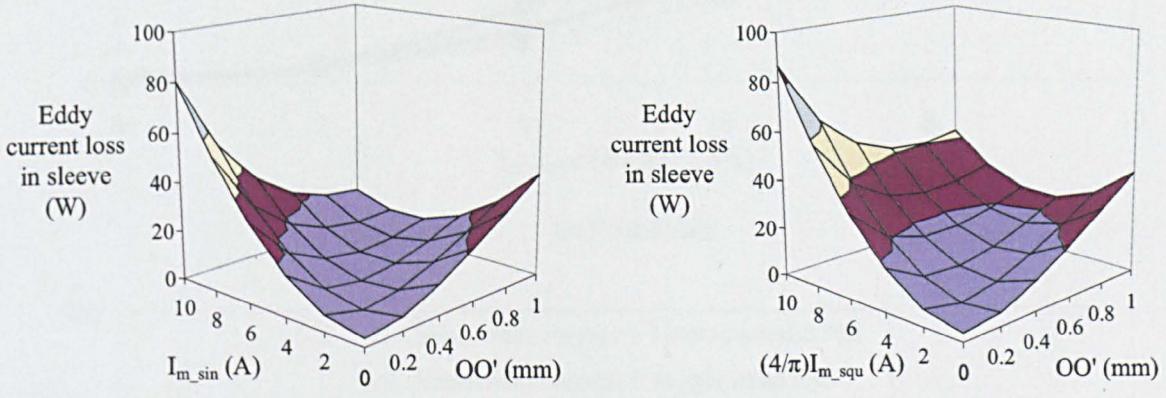

(ii) In sleeve

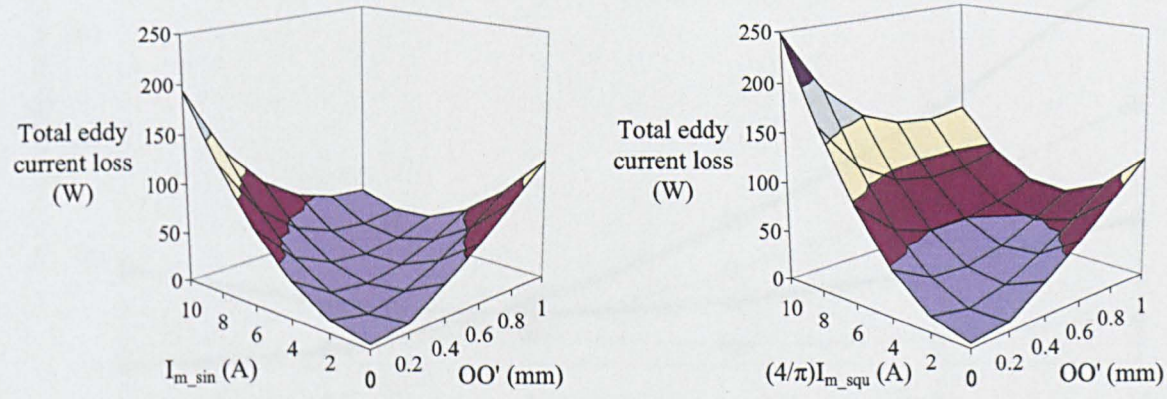

(iii) Total

(b) On-load rotor eddy current loss (Magnetized magnet)

Figure 4.14 Variation of rotor eddy current loss with eccentric airgap and winding current.

(2 pieces of PMs, sleeve thickness=0.6mm, speed=45krpm).

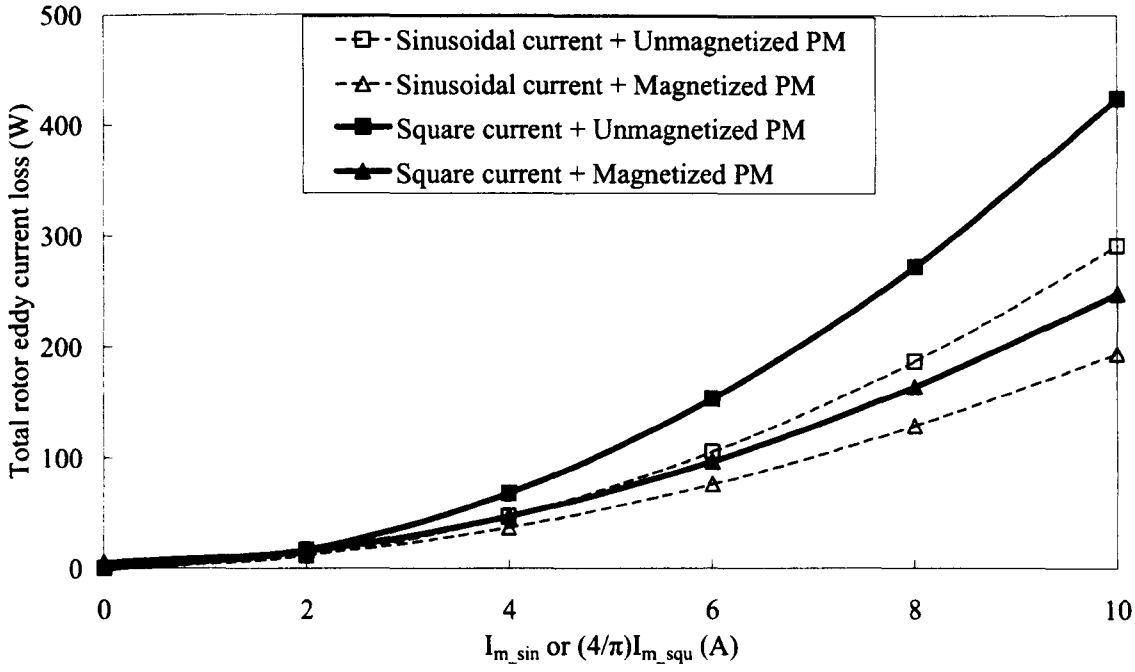

(a) OO'=0.0mm

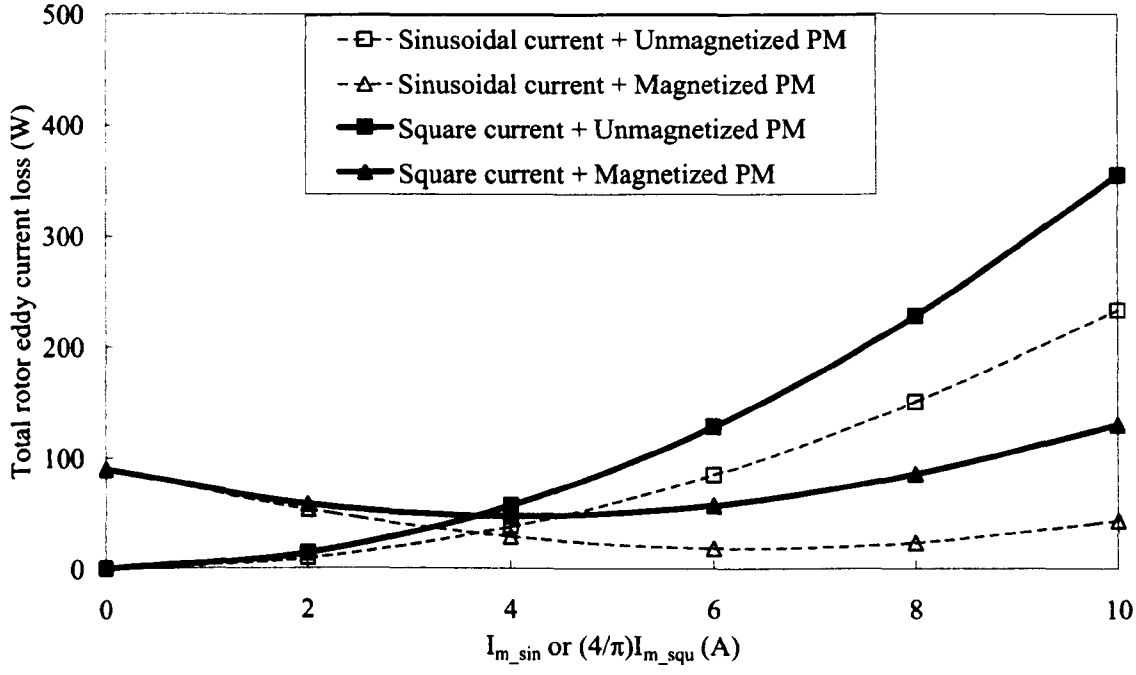

(b) OO'=0.8mm

Figure 4.15 Variation of eddy current loss with winding current.

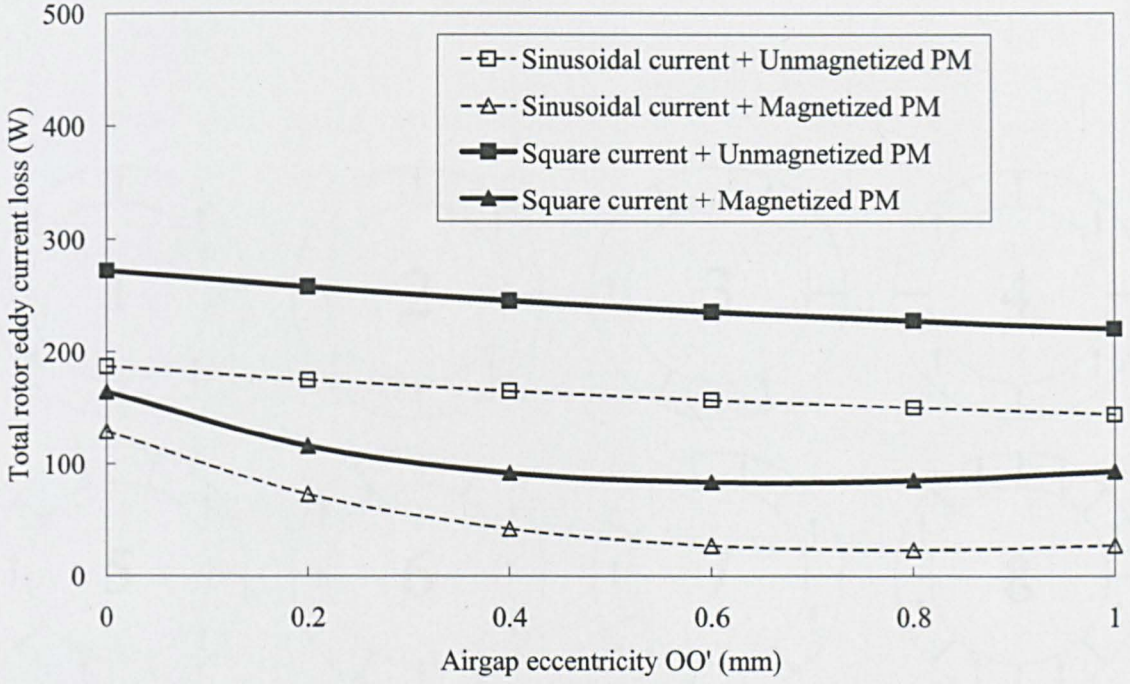

Figure 4.16 Variation of eddy current loss with airgap eccentricity.

$(I_{m\_\sin} = (4/\pi) I_{m\_squ} = 8A)$

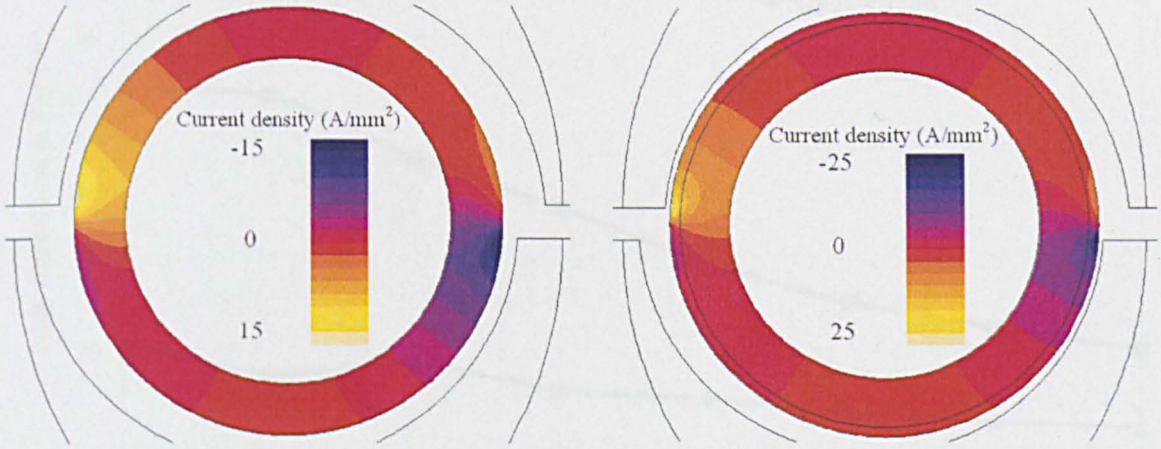

(a) Without sleeve (b) With sleeve (thickness=0.6mm)

Figure 4.17 Eddy current distribution.

(OO'=0.8mm, 1 magnet segment, Speed=45,000rpm, Rotor position=270°)

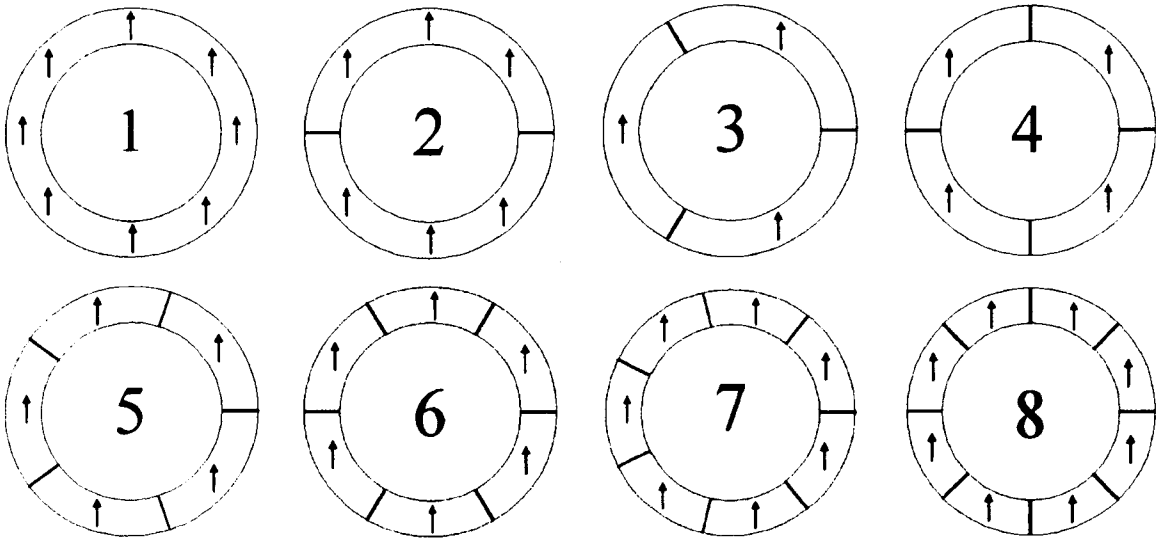

Figure 4.18 Alternative number of diametrically magnetized PM segments.

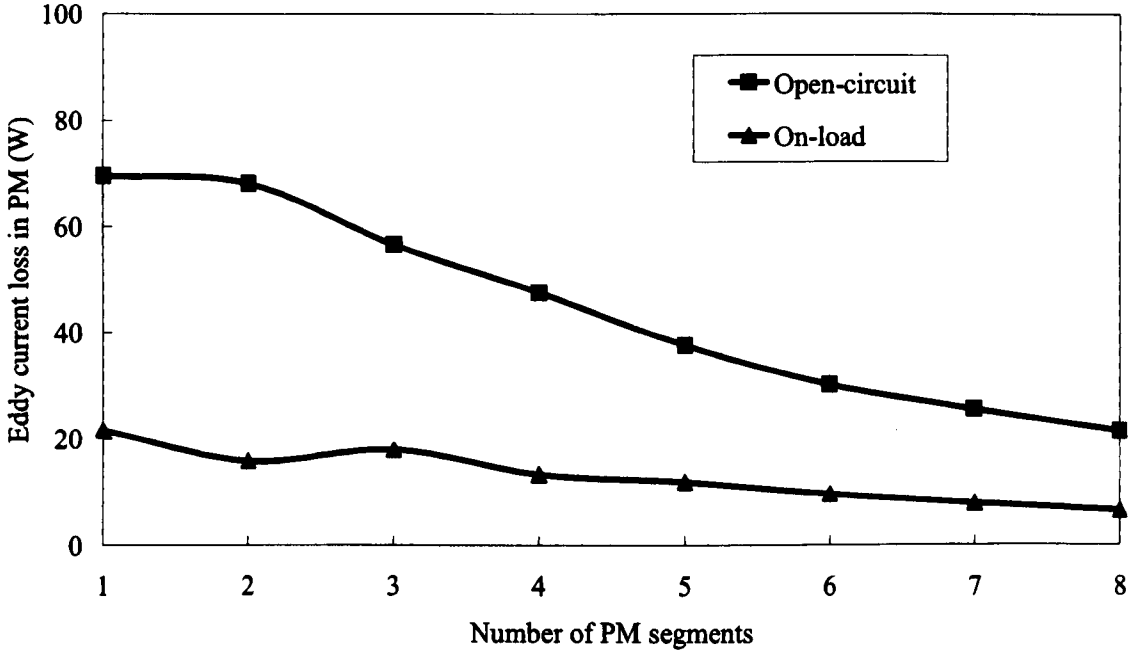

(a) Without sleeve

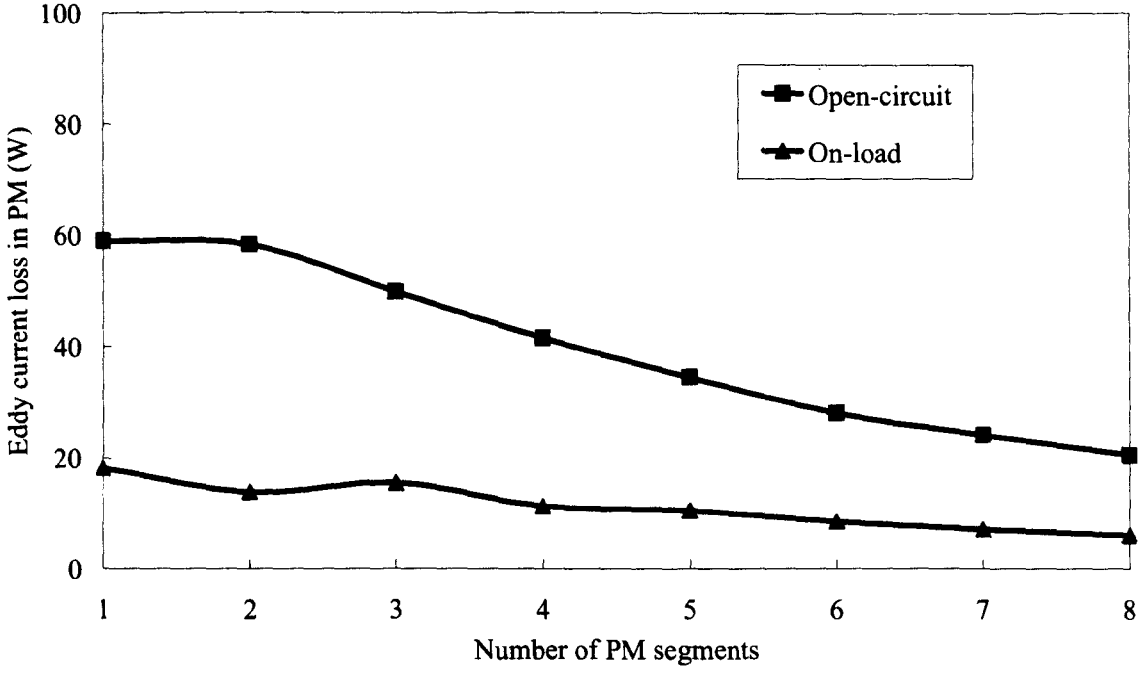

(i) In magnet

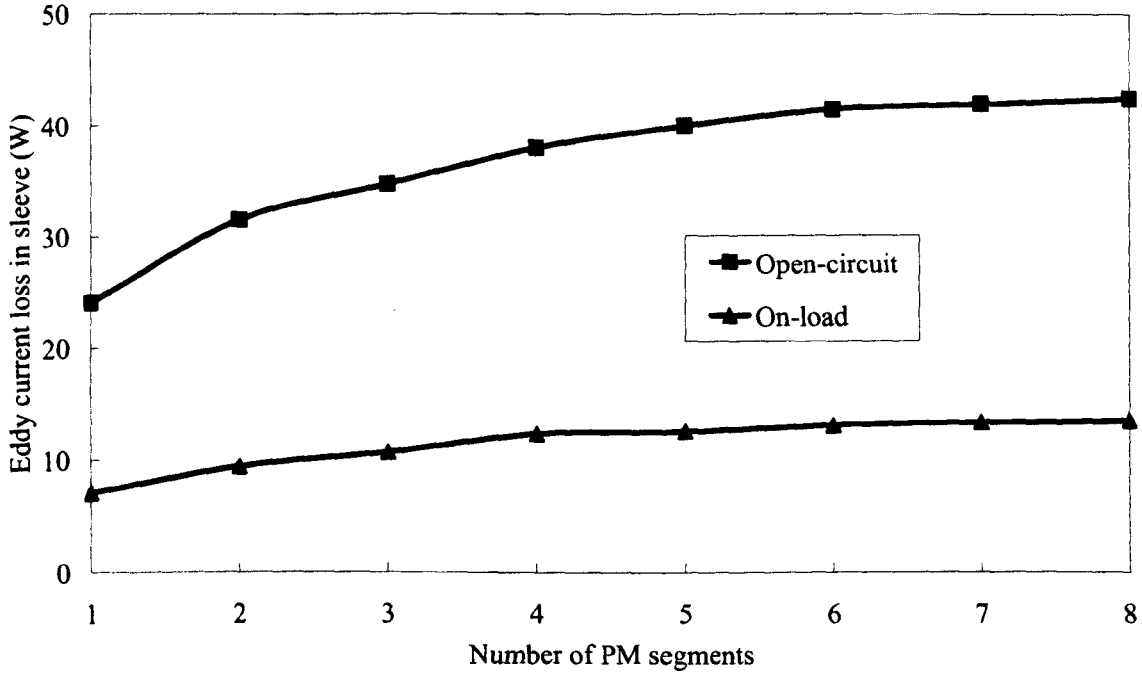

(ii) In sleeve

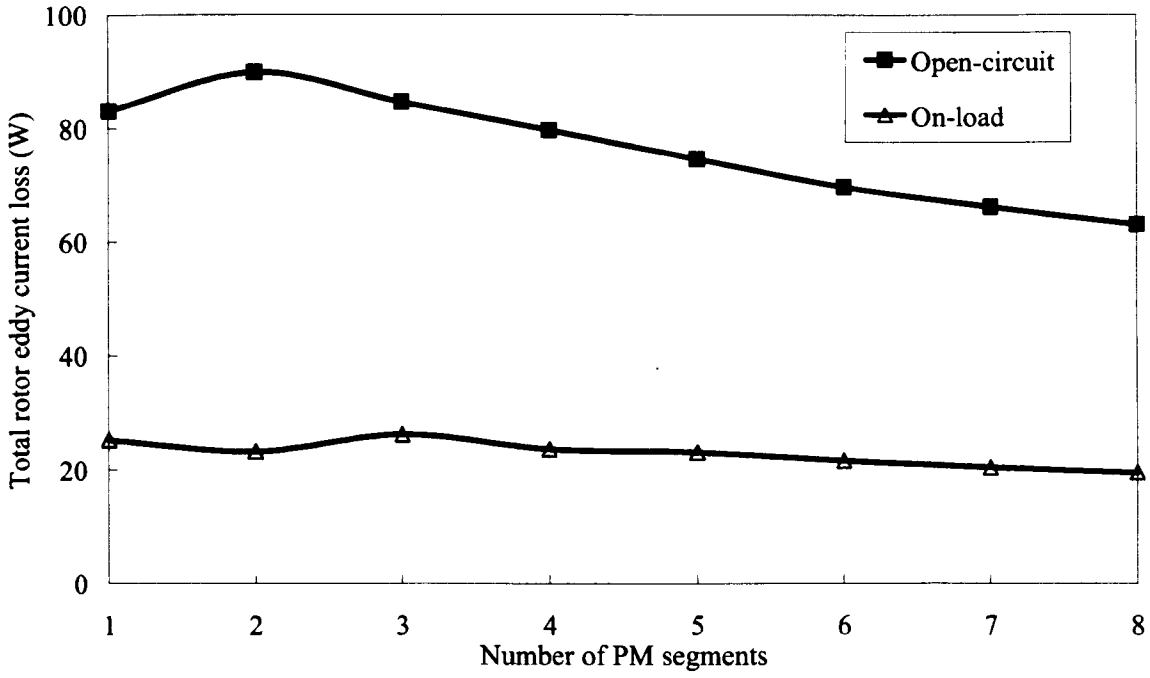

(iii) Total

(b) With sleeve (thickness=0.6mm)

Figure 4.19 Influence of number of magnet segments on rotor eddy current loss.

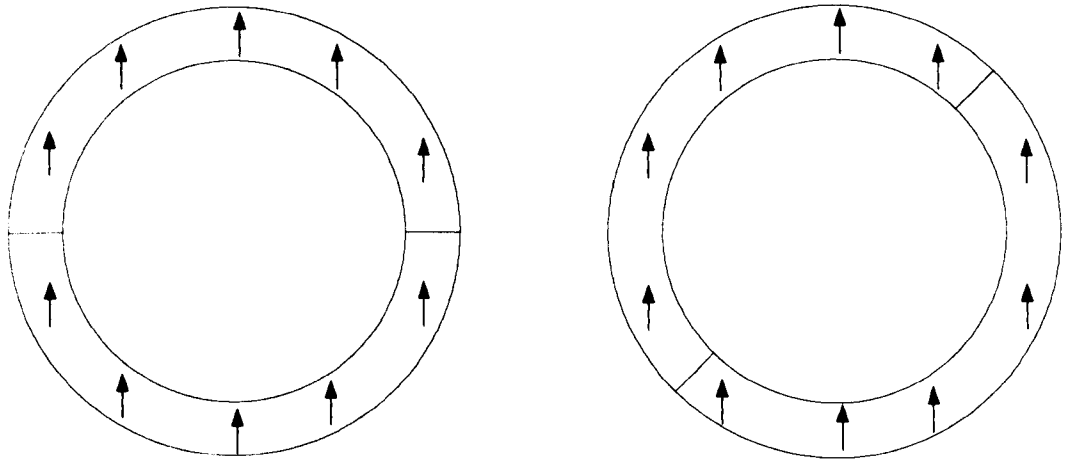

(a) $\alpha = 0°$ (b) $\alpha = 45°$

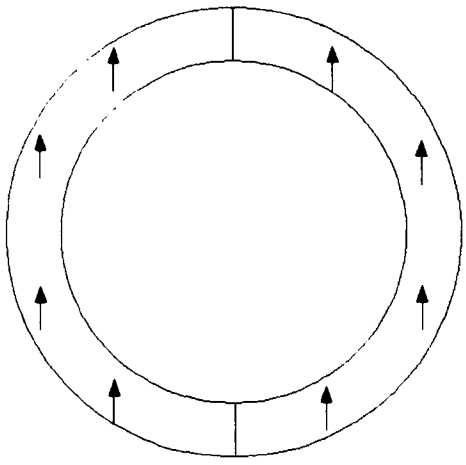

(c) $\alpha = 90°$

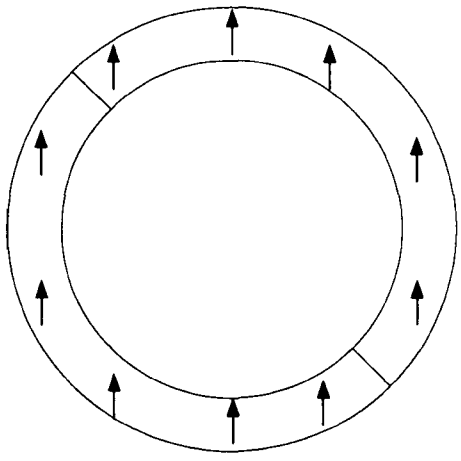

(d) $\alpha = 135°$

Figure 4.20 Alternative divisions of 2 diametrically magnetized PM segments.

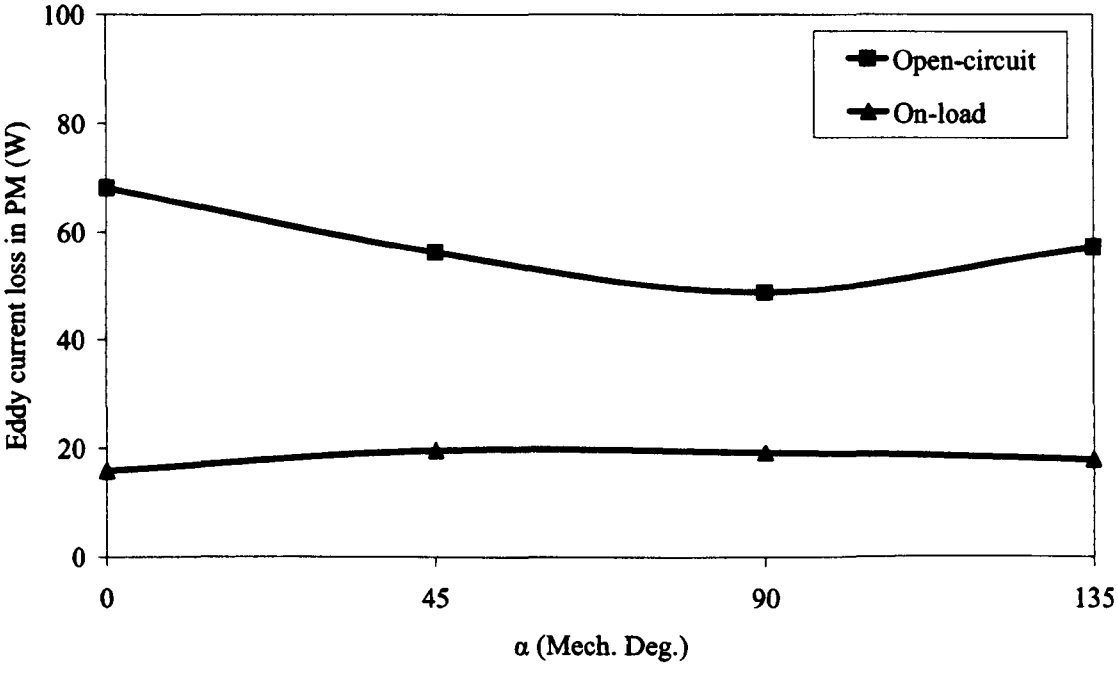

(a) Without sleeve

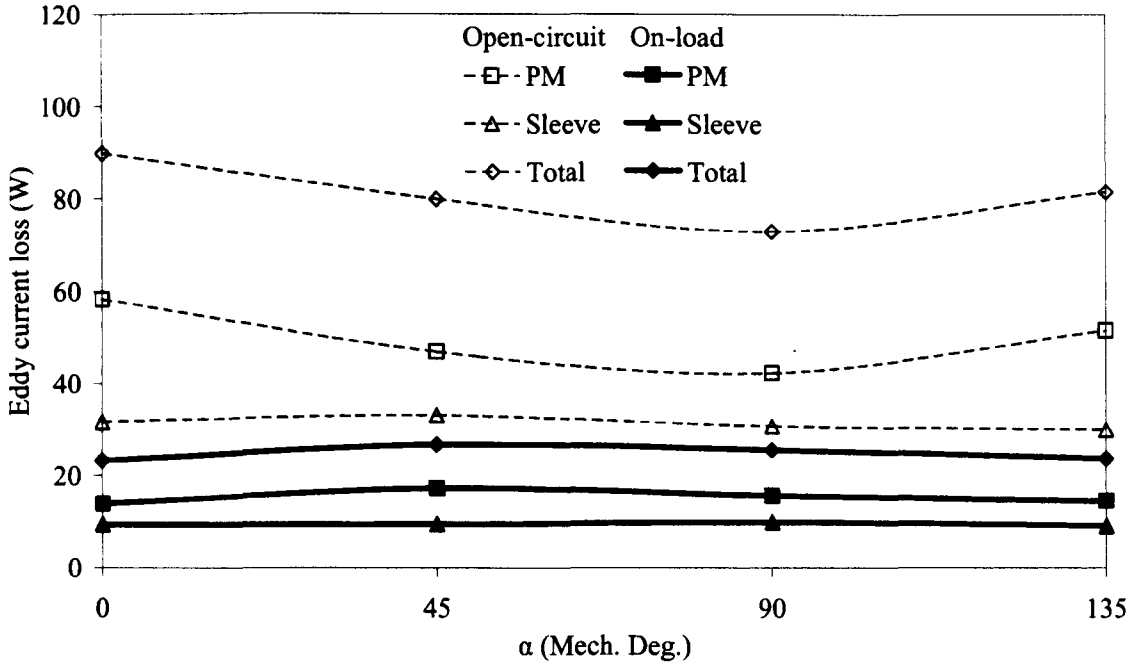

(b) With sleeve (thickness=0.6mm)

Figure 4.21 Influence of alternative divisions of 2 magnet segments on rotor eddy current loss.

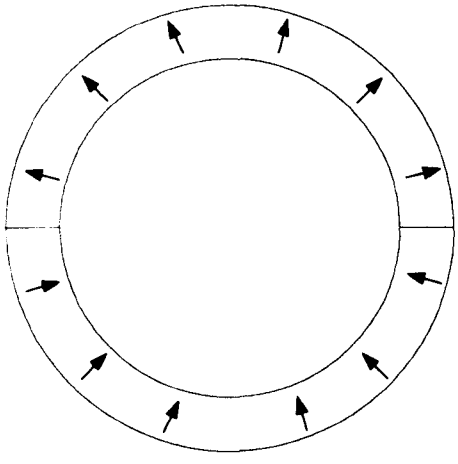

(a) 2 PM segments

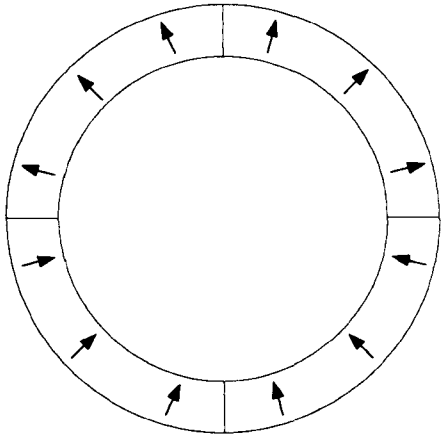

(b) 4 PM segments

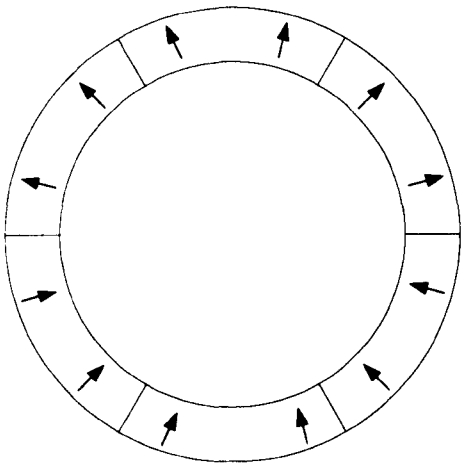

(c) 6 PM segments

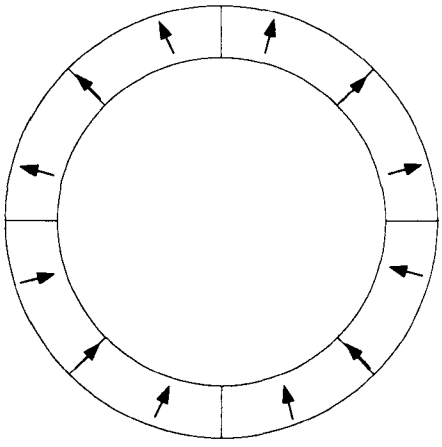

(d) 8 PM segments

Figure 4.22 Alternative number of radially magnetized PM segments.

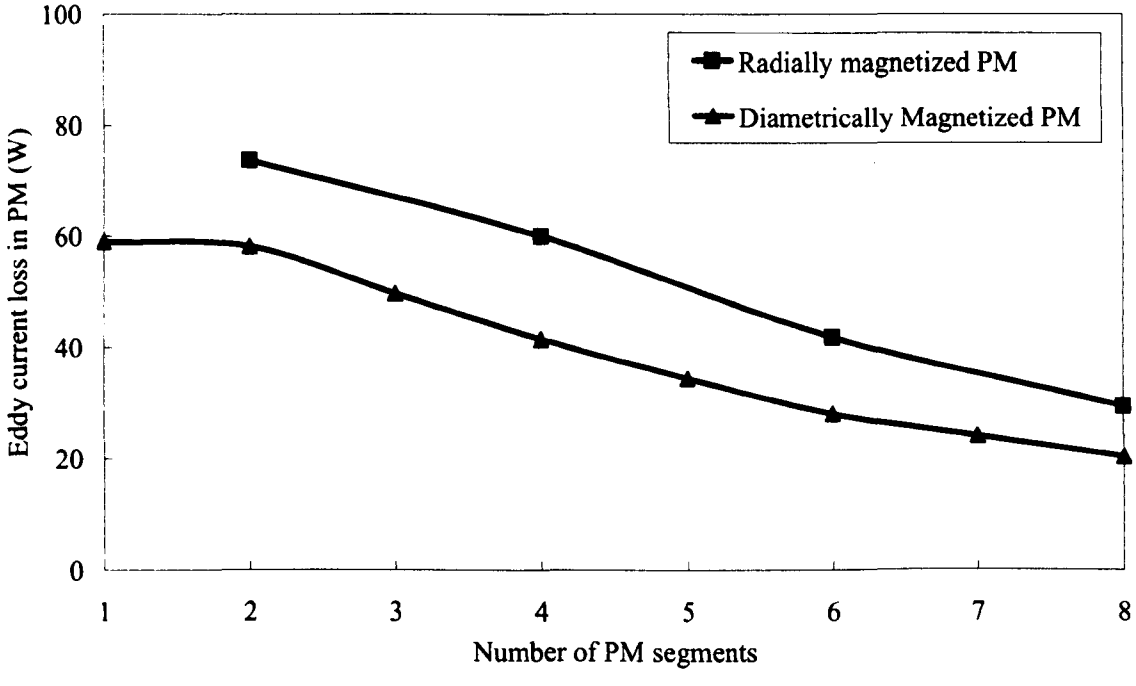

(a) In magnet

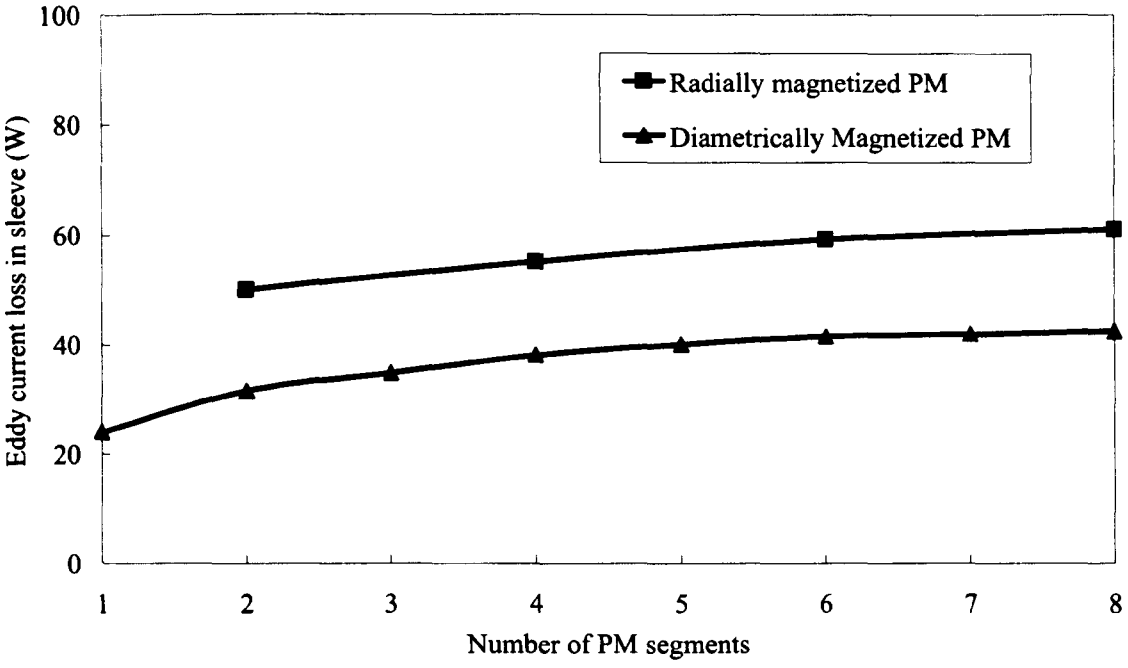

(b) In sleeve

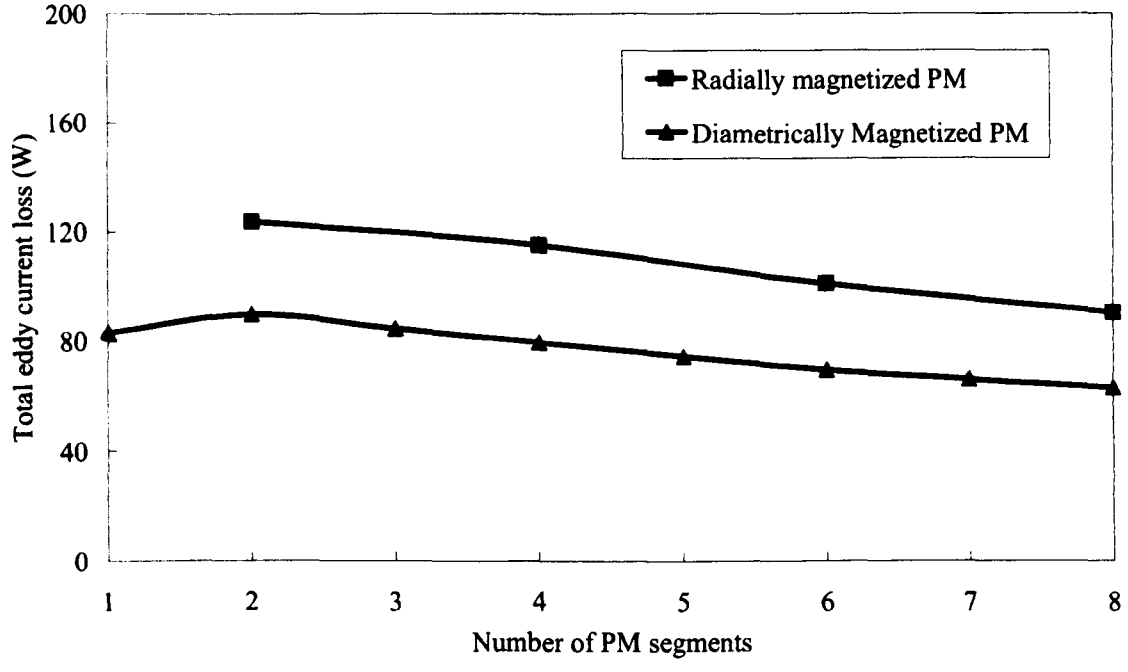

(c) Total

Figure 4.23 Open-circuit rotor eddy current loss of radially and diametrically magnetized PM.

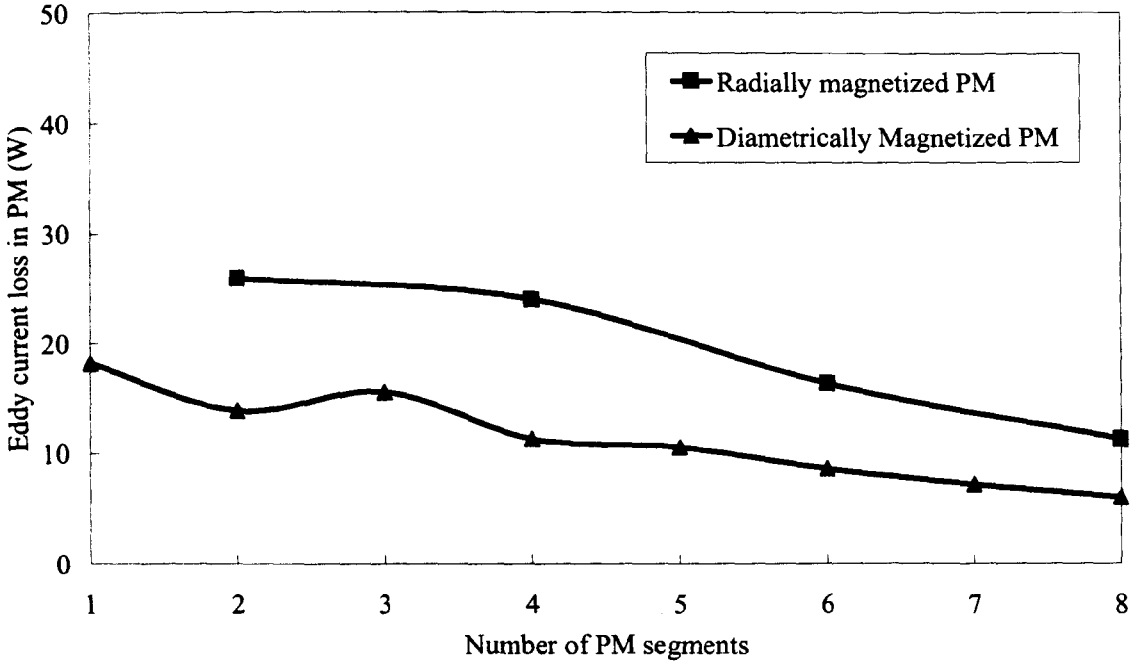

(a) In magnet

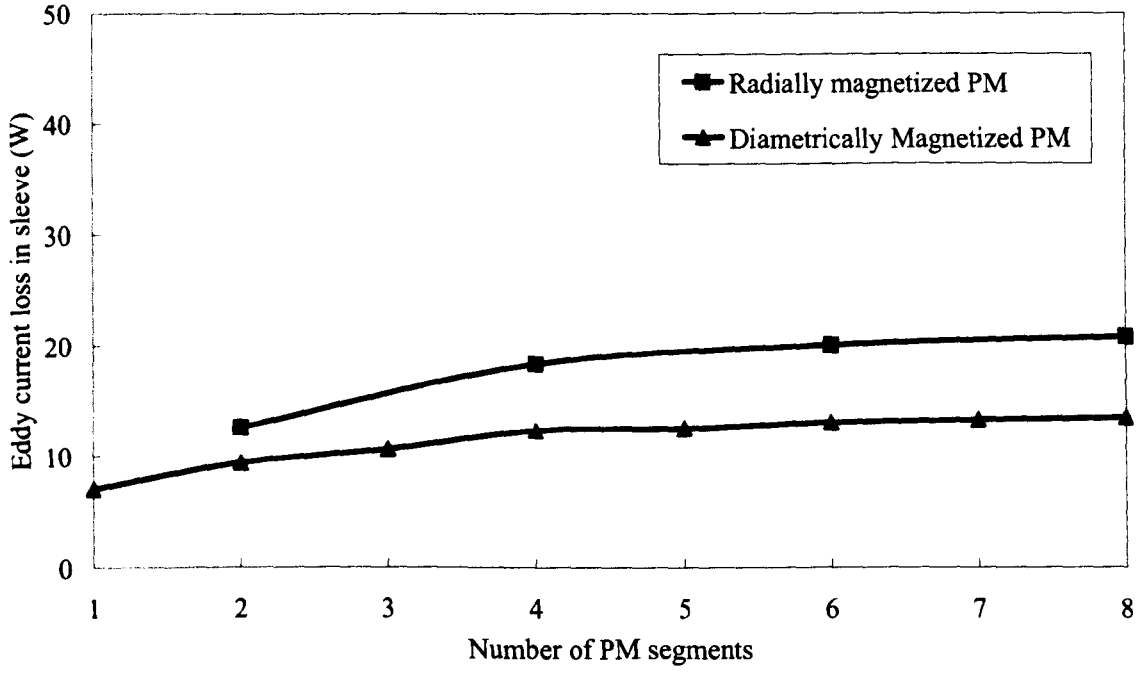

(b) In sleeve

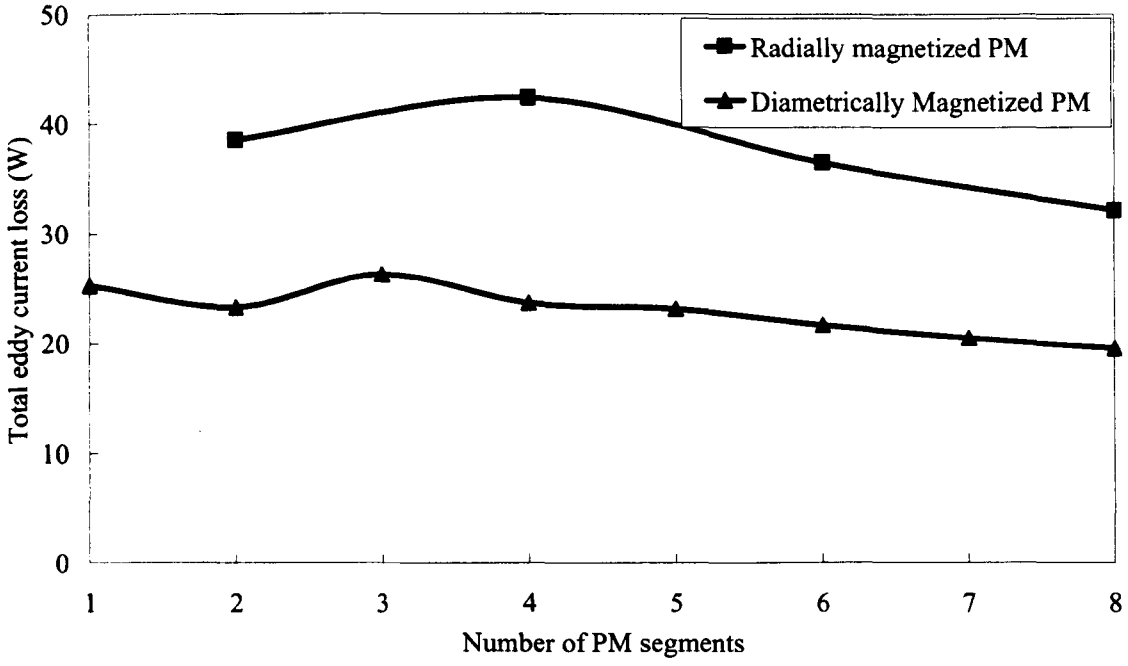

(c) Total

Figure 4.24 On-load rotor eddy current loss of radially and diametrically magnetized PM.

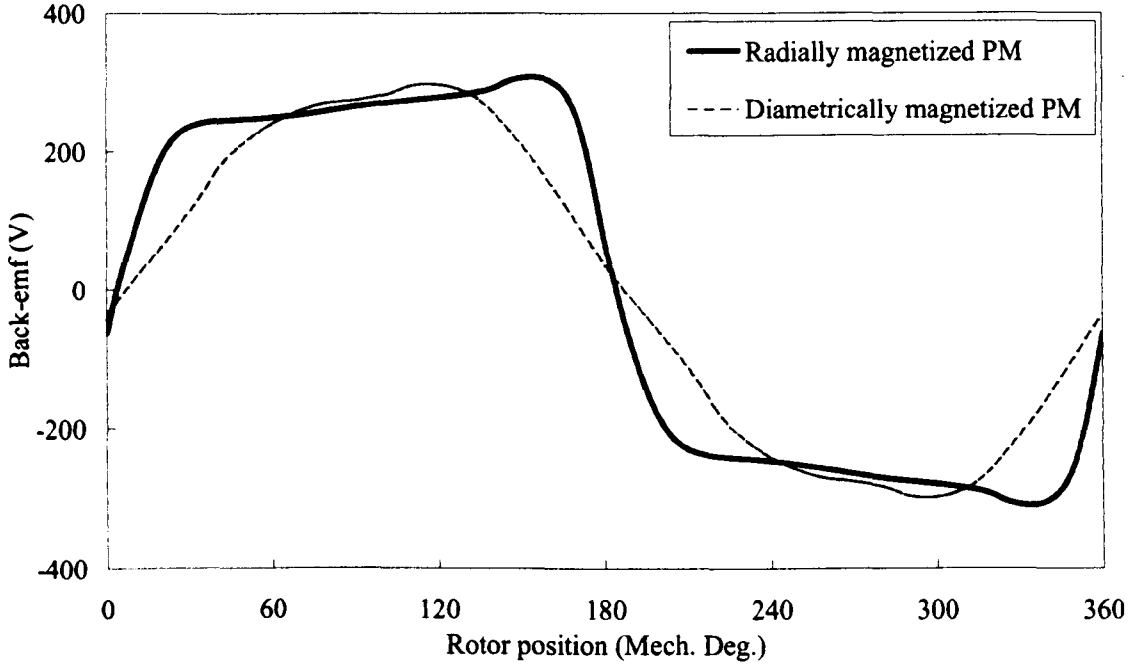

Figure 4.25 Comparison of back-EMF waveforms of radially and diametrically magnetized PM. (Speed=45,000rpm)

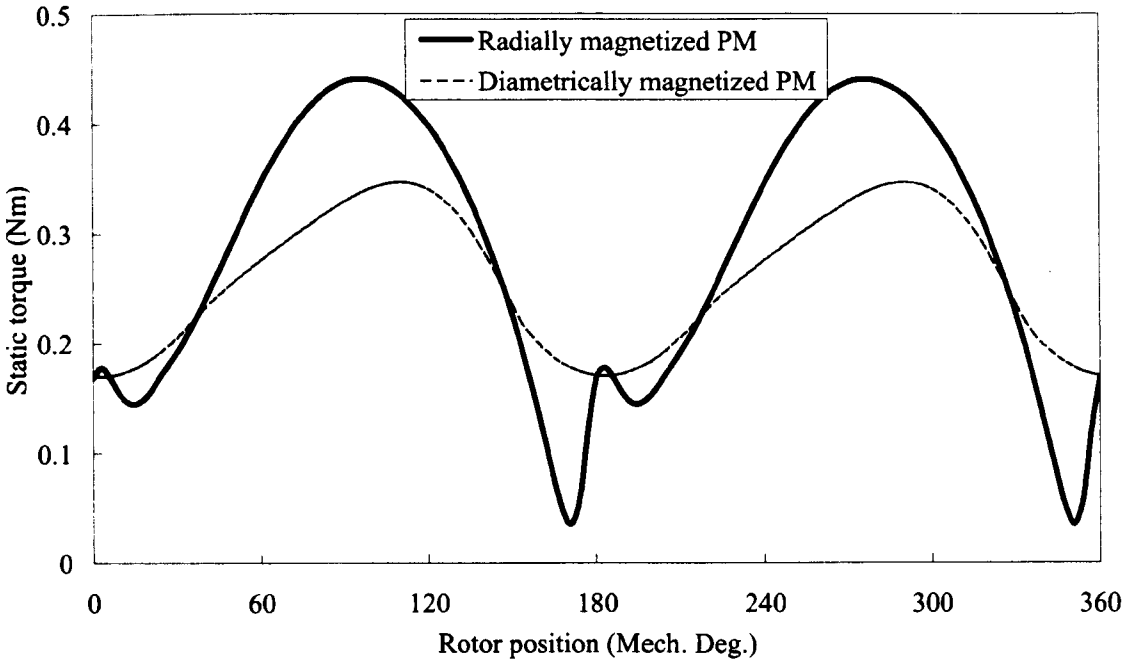

Figure 4.26 Comparison of static torque waveforms.

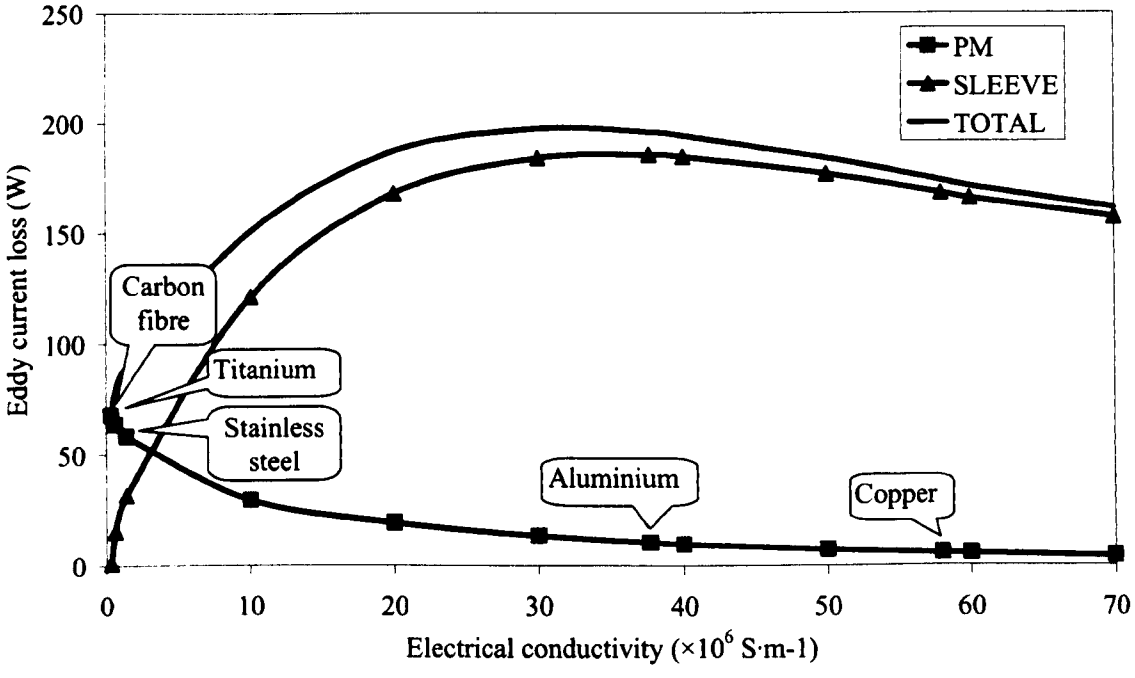

(a) Open-circuit

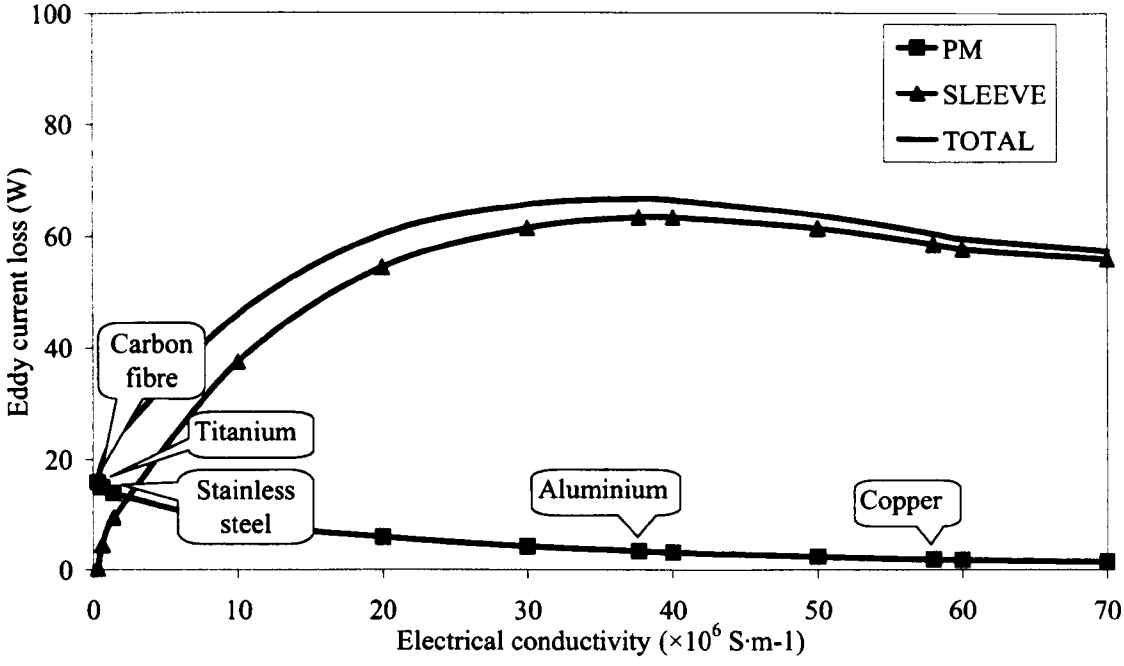

(b) On-load ($I_{m\_\sin} = 8A$)

Figure 4.27 Variation of rotor eddy current loss with sleeve electrical conductivity.

(2 magnet segments, OO'=0.8mm, Sleeve thickness=0.6mm, Speed=45kprm)

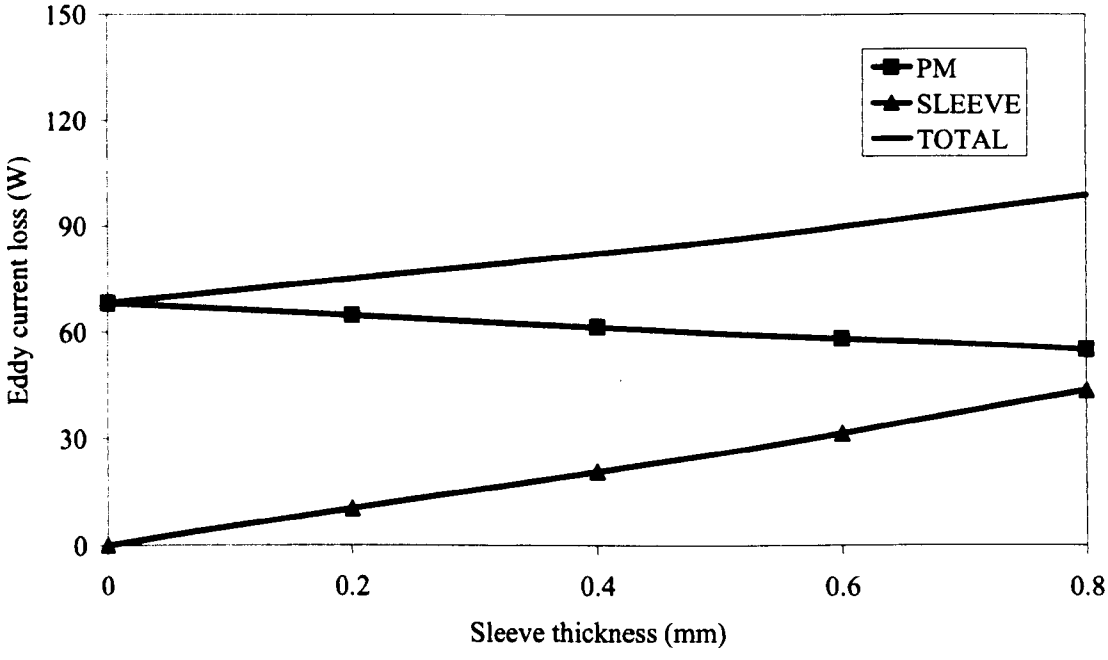

(a) Open-circuit

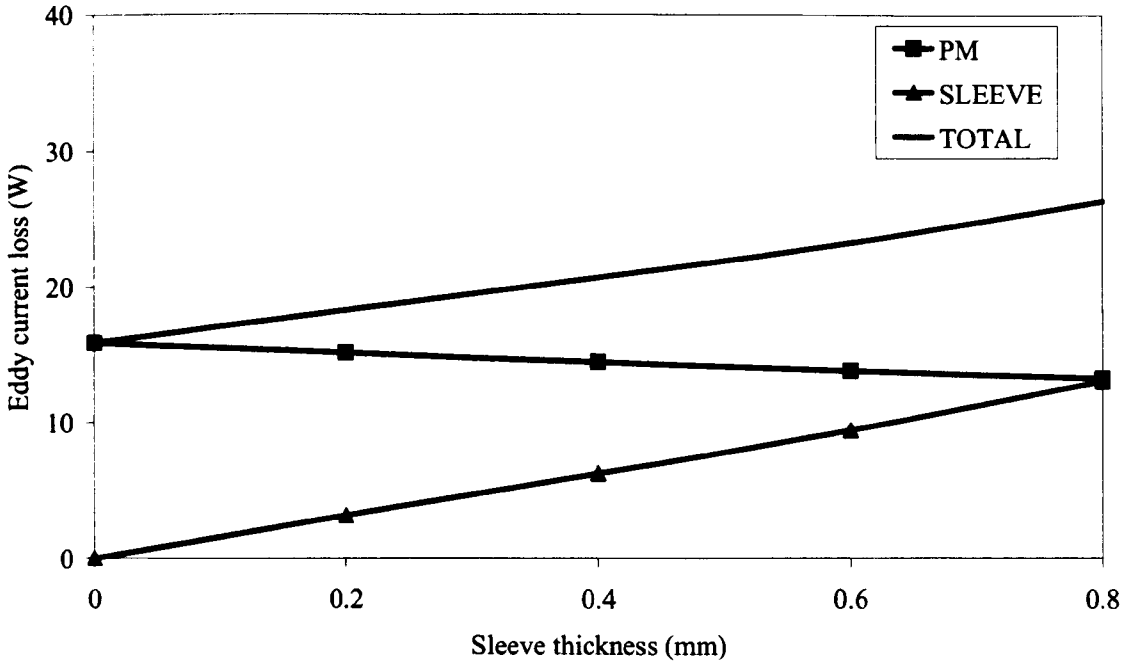

(b) On-load ($I_{m\_\sin} = 8A$)

Figure 4.28 Variation of rotor eddy current loss with sleeve thickness.

(2 magnet segments, OO'=0.8mm, Sleeve thickness=0.6mm, Speed=45kprm)

CHAPTER 5

Investigation of Single-Phase Flux-Switching PM Motor

5.1 Introduction

As presented in previous chapters, single-phase PM BLDC motors offer the advantages of high power density and high efficiency. However, for high-speed applications the containing sleeve is generally required to retain the magnets onto the shaft, since the adhesives between surface mounted PM and shaft is not mechanically strong enough to withstand the centrifugal force against the magnets at the high-speed operation. If the containing sleeve is electrically conductive, such as stainless steel, titanium alloy and copper, etc., a significant eddy current loss will be induced at high-speed in the sleeve and magnet due to pulsating mmfs, time harmonics of phase current and asymmetric airgap. Consequently, not only the motor efficiency could be affected, but also the permanent magnet might suffer from the possibility of the irreversible demagnetization due to high temperature rise. Further, assembling the rotor becomes more complicated and the cost will be higher due to the retaining sleeve.

In order to overcome above drawbacks, another type of PM machine, i.e. FSPM motor, becomes an attractive candidate for high-speed applications. Generally, such machines have salient rotor and stator poles and the permanent magnets are located on the stator. By changing the direction of the current in the armature winding based on the rotor position, the continuous positive torque can be achieved which results in uni-directional rotation. Reversal of the armature winding current causes the stator flux to be switched between two sets of alternate stator teeth. Hence, it is named as flux switching motor.

Compared to PM BLDC motor, the major special feature of a FSPM motor is that the permanent magnets are located on the stator. Hence, it is easier to dissipate heat from the stator, thereby, to limit the temperature rise of the magnet. Further, since the windings and the magnets are effectively magnetically in parallel, rather than in series as in conventional PM

machines, the influence of the armature reaction field on the working point of the magnets is almost eliminated. Consequently, the FSPM machine has high electric loading and torque capability without the risk of irreversible demagnetization of the permanent magnets. In addition, since the flux resulting from the winding current is not going through the magnets, a high per-unit winding inductance can be potentially achieved which gives a high flux-weakening capability. Because of these features, potentially FSPM machine could be a good candidate for high-speed applications.

The first single-phase FSPM motor was proposed by Rauch and Johnson in 1955 [92] and was more recently studied further in [89]. However, zero starting torque at certain rotor positions leads to its suitability primarily for working as a generator. A stepped airgap under the stator poles was employed in [60] to obtain the starting torque of a 4-pole stator and 6-pole rotor (4/6) single-phase FSPM machine which works as a motor. An 8-pole stator and 4-pole rotor (8/4) single-phase FSPM motor was proposed in [99] where the self-starting capability in the desired direction was achieved by modifying the rotor lamination profile to give the required amount of asymmetry. Three-phase FSPM machines based on both the unipolar flux principle [33, 100-101] and the bipolar flux principle [102-103] have recently been described. While the performance of a limited angle form of FS actuator was studied in [104]. Theoretically, the permanent magnets in such FS machines can be replaced by current-carrying coils [105-107].

In order to understand and design the FSPM machine, following issues will be presented for a single-phase FSPM motor:

- The operating principle of a single-phase FSPM motor is introduced in this chapter, together with different motor topologies and winding topologies.
- The influences of key parameters on the motor performance will be investigated by FEM. Particularly, the starting issue is addressed in details.
- 2D and 3D lumped parameter magnetic circuit (LPMC) models are proposed to analyze the motor characteristics by taking the end effect into account.

- After validated by FEM and experiments on the prototyped of the single-phase FSPM motors, LPMC model is used to investigate the influence of motor parameters on the motor characteristics.
- The dynamic simulation model is used to analysis the effect of LPMC predicted back-EMF and inductance on the motor performance.

5.2 Operation principle

For the convenience of discussion, a simple example of single-phase FSPM motor is shown in Figure 5.1. The rotor is 2-salient-pole stack of lamination on the shaft. The stator consists of 4-pole stator and a pair of permanent magnets. Each stator pole carries a concentrated coil. Figure 5.2 shows the open-circuit field distributions at four rotor positions. The flux through the stator tooth is twice of that through the stator back iron. Therefore, the stator tooth width is desired to be twice of the stator yoke width in order to obtain the approximate same flux density. It will be seen that the flux-linkage is zero when the rotor poles align with the stator slot openings, Figure 5.2 (a) and (c), and has a maximum positive value when the rotor poles align with one pair of stator poles, Figure 5.2(b), and a maximum negative value when the rotor poles align with the other pair of stator poles, Figure 5.2(d). Thus, as the rotor rotates, a bipolar flux-linkage through the coils results, as illustrated in Figure 5.3, which also shows idealized back-EMF, winding current and torque waveforms. As can be seen, by applying appropriate priority of current excitation, Figure 5.3, continuous rotation torque can be produced. Because the back-EMF is essentially rectangular, the motor is eminently suitable for single-phase brushless DC drive operation. However, due to influence of flux fringing and winding inductance, the back-EMF and current waveforms will depart from their ideal waveforms, significant torque pulsation and zero torque exist, which may cause starting problem. Hence, as in conventional single-phase brushless DC motor, special design consideration must be taken to ensure the motor can start at any rotor rest position, as will be described later.

In order to provide the magnetic path for switching flux, it is convenient to have the number of stator poles which is twice of the number of permanent magnets. The flux density in the rotor is bipolar and its frequency is proportional to the number of stator poles. For a given speed, higher number of stator poles results in more rotor iron loss, particularly at high-speed applications.

The number of rotor poles determines the frequency of the back-EMF by the following equation:

$$f_{emf} = p\frac{n}{60} \tag{5-1}$$

where n -- Rotating speed; rpm

p -- Number of rotor poles;

f_{emf} -- Frequency of back-EMF, Hz.

It can also be noted that the flux density in the stator back iron is bipolar as well and its frequency is proportional to the number of rotor poles.

By now, the most popular combinations of stator and rotor poles of single-phase FSPM motor are 4/2, 4/6 and 8/4. Since the higher the number of the rotor poles the higher is the frequency of the flux density, which results in the higher iron loss[1]. It is desirable to choose low number of rotor poles to minimize the iron loss. Therefore, this chapter will focus on a 4/2 single-phase FSPM motor which has the lowest number of stator poles and rotor poles. In addition, 4/2-pole motor has a simpler construction than that of 4/6 and 8/4-pole motors. This motor is designed for electrical assisted turbo charge for automotive applications for which the maximum operation speed is 100krpm.

For a single-phase FSPM motor, the winding flux linkage can be divided into two components as follows:

$$\lambda = \lambda_{PM} + \lambda_w \quad \text{(Wb)} \tag{5-2}$$

where λ_{PM} -- Flux linkage produced by permanent magnet; Wb

λ_w -- Armature reaction flux linkage; Wb. It can be given by,

$$\lambda_w = Li \qquad \text{(Wb)} \tag{5-3}$$

where L -- Winding inductance; H

i -- Phase current; A

In order to simplify the model, it is assumed that L varies with the rotor position, but it is current-independent.

The back-EMF induced by the permanent magnet is

$$e_{PM} = \frac{d\lambda_{PM}}{dt} = \frac{d\lambda_{PM}}{d\theta}\omega_r \qquad \text{(V)} \tag{5-4}$$

where θ -- rotor position; rad

ω_r -- rotor angular speed; rad/s

The electromagnetic torque is

$$T_{em} = i\frac{d\lambda_{PM}(\theta)}{d\theta} + \frac{1}{2}i^2\frac{dL(\theta)}{d\theta} + T_c = T_{iPM} + T_r + T_c \qquad \text{(Nm)} \tag{5-5}$$

It can be seen that T_{em} is composed of three components. T_{iPM} is the PM excitation torque which is produced by the interaction between the winding current i and the PM. T_r is the reluctance torque caused by the variation of winding self inductance with rotor position. T_c is the torque that introduced by the cogging torque. T_r and T_c contribute little to the overall output torque but can cause the torque ripples.

Hence, the phase winding terminal voltage equation and mechanical equation are,

$$v = Ri + \frac{d\lambda}{dt} = Ri + \frac{d\lambda_w}{dt} + \frac{d\lambda_{PM}}{dt} = Ri + i\frac{dL_w}{dt} + L\frac{di}{dt} + e_{PM} \qquad \text{(V)} \tag{5-6}$$

$$T_{em} - T_{load} = J\frac{d\omega_r}{dt} \qquad \text{(Nm)} \tag{5-7}$$

where v -- Winding terminal voltage; V

R -- Phase resistance; Ω

J -- Rotor inertia; Kg·m^2

T_{load} -- Load torque; Nm

5.3 Winding topologies

As shown in Figure 5.1, each stator pole carries a concentrated coil. It is named as the short-pitched winding topology. However, the two sets of coils in the slot adjacent to the magnets carry the currents which have the same magnitude but opposite priorities. Hence, the current in these coils does not contribute to the output torque. It indicates that the coils can be wound on the stator spanning two stator poles, rather than on the each stator pole, as shown in Figure 5.5 (a) as known as the full-pitched winding topology. Since the coils are eliminated in the slot adjacent to magnets, more magnets could be placed on the stator to increase the utilization of magnet flux focusing, resulting in a higher power density. In addition, another alternative winding topology, i.e. toroidal winding topology, is illustrated in Figure 5.5 (b), where the coils are wound around the yoke of the stator back iron.

For fair comparison, the single-phase FSPM motors having above three types of winding topologies, as shown in Figure 5.5, have the identical rotor dimensions, airgap length, stator outer diameter, motor axial length and magnet size except the stator slot shape. The leading motor parameters are listed in Table 5.1 and the rotor pole-arc is 80°. In order to keep the same level of the flux density in the stator tooth, these three motors are designed to have approximately the same stator tooth. Therefore, the motors with full-pitched and toroidal windings have the same effective slot area which is about twice of that of the motor with short-pitched windings. Figure 5.6 shows 2D FEM predicted back-EMF, cogging torque and winding inductance waveforms. It can be seen that, with identical rotor and stator magnetic circuits, a toroidally wound machine produces the same back-EMF and cogging torque waveforms, and has a similar winding inductance, as the machine with the full-pitched winding. Due to the asymmetric stator tooth tips, for full-pitched and toroidally wound machines, when the rotor pole is aligned with the coil slot, the overall magnetic circuit is

more heavily saturated compared to the rotor position where the rotor pole is aligned with the PM slot, which results in a relatively lower inductance. However, for the short-pitched wound machine, due to its different asymmetric stator tooth tips, longer tooth tips adjacent to the PM slot means that the overall magnetic circuit is more saturated when the rotor pole is aligned with the PM slot where the lower inductance is achieved, as shown in Figure 5.6 (c).

Generally, in order to achieve a high efficiency, the copper loss should be taken into account during the machine design stage. The copper loss can be calculated by,

$$P_{C_u} = I_{rms}{}^2 R \qquad \text{(W)} \tag{5-8}$$

where I_{rms} -- Root mean square value of phase current; A

R -- Phase resistance at temperature $T_{\theta_{cu}}$ (°C) and can be given by,

$$R = R_0[1 + (T_{\theta_{cu}} - T_0)\alpha_{cu}] \qquad (\Omega) \tag{5-9}$$

where α_{cu} -- Copper temperature coefficiency; $^{\circ}C^{-1}$

R_0 -- Phase resistance at the reference temperature T_0 (°C) and can be given by,

$$R_0 = \frac{1}{\sigma_{C_u}} \frac{l_w}{s_w} \qquad (\Omega) \tag{5-10}$$

where σ_{cu} -- Copper electrical conductivity; $\Omega^{-1}\cdot m^{-1}$

l_w -- Winding length; m

s_w -- Coil area; m^2

Geometrically, the windings are composed by the active windings that are within the motor main body and the end windings located at two ends of the motor as illustrated in Figure 5.7. It is assumed that the end winding has two components: (1) l_e=5mm; (2) A semi-circular component with the average radii being 20mm, 5mm, and 10mm for full-pitched, toroidally and short-pitched wound windings, respectively. Hence, the total winding length is:

$$l_w = \begin{cases} (2l_a + 4l_e + 2\pi R_e)N_{ph} & Full-pitched \\ (4l_a + 8l_e + 4\pi R_e)N_{ph} & Toroidal \\ (4l_a + 8l_e + 4\pi R_e)N_{ph} & Shorted-pitched \end{cases} \quad (m) \qquad (5\text{-}11)$$

where N_{ph} -- Number of turns of phase windings.

The coil area can be calculated by,

$$s_w = k_p A_s / N_{ph} \qquad (m^2) \qquad (5\text{-}12)$$

where k_p -- Wining packing factor and assumed to be 50%.

A_s -- Effective coil slot area, being $0.00022m^2$ for full-pitched and toroidally wound machines and $0.000098m^2$ for short-pitched wound machine. It is evident that for a given number of coil turns and packing factor, short-pitched wound machine has less coil area.

According to the Figure 5.8, regardless of the motor axial length, the short-pitched wound machine has the longest winding length. Combined with its less slot area, a short-pitched wound machine has the highest copper loss, resulting in a smallest average torque/copper loss. It also can be noted that when the motor axial length is less than ~20mm, toroidally wound machine has the shortest winding length due to its relatively short end winding length. However, when the motor axial length is increased, the main winding length becomes a dominant factor rather than the end winding length. Therefore, the full-pitched wound machine which has half main winding length has the shortest winding length, resulting in the less copper loss and higher static torque/(copper loss). In order to accommodate the outer conductors, the overall diameter of the toroidally wound machine is relatively larger. However, it has advantage over the full-pitched wound machine, when the axial length is very short. Since the specification of the axial length required by the customer is 18mm, the focus will be on the analysis of the full-pitched winding machine, since in general it shows advantageous in terms of average torque/(copper loss) and less overall machine volume.

5.4 Cogging torque and starting torque

An 8-pole stator and 4-pole rotor (8/4) single-phase FSPM motor is proposed in [99], where the self-starting capability in the desired direction was achieved by modifying the rotor lamination profile to give the required amount of asymmetry. However, the influence of the rotor pole-arc or the degree of asymmetry of the rotor pole-surface on the starting capability and electromagnetic performance has not been addressed in detail.

In this section, 2D FEM is employed to optimize the asymmetric rotor profile of 4/2 single-phase FSPM motor to increase the starting capability and minimize the cogging toque.

Cogging torque in a FSPM motor results from the interaction of the doubly salient stator and rotor poles under the influence of the permanent magnet excitation. It affects not only the torque ripple but also the rotor rest positions which determine the starting capability. Therefore, cogging torque is an important issue and needs to be fully analyzed considering the inherent starting problem in the single-phase FSPM motor. The rest position is defined as the rotor position where the rotor parks if there is no armature current applied to the windings. In other words, the rotor will rest at the positions where the cogging torque is kept balance with friction torque and load. For applications such as pumps and fans, there is no significant load at the moment of starting. If the friction torque is assumed to be negligible, the rotor will rest at the positions where the cogging torque is zero. However, there are two kinds of rest positions. One is named as stable rest position which corresponds to the rotor angular positions where the slope of cogging torque is negative. Another is named as unstable rest position which corresponds to the rotor angular positions where the slope of cogging torque is positive. Generally, the rotor parks at the stable rest positions. It needs to be investigated that there is enough starting torque to make the rotor rotate in the desired direction at any possible rest positions by applying the proper armature current to the windings.

Three single-phase FSPM motors, i.e. **M1**, **M2** and **M3**, having the same stator and winding topology as shown in Figure 5.5 (a), but different rotor pole-arc, are investigated by 2D FEM.

The corresponding motor leading parameters are listed in Table 5.1. Their cross-sections are shown in Figure 5.9 where the rotor position is zero and the current direction is defined as positive. It is also assumed that the positive electromagnetic torque can make the motor rotate in the counter-clockwise direction.

Table 5.1 Leading parameters of FSPM motors.

	M1	**M2**	**M3**
Rotor pole-arc	60°	80°	100°
Rotor outer diameter, mm		30.0	
Stator outer diameter, mm		64.0	
Airgap length, mm		1.0	
Stator pole-arc		80°	
Stator slot-opening		10°	
Stack axial length, mm		18	
Coils per phase		1	
Turns per coil		4	
Wires per turn		12	
Diameter of wire, mm		1.26	
Magnet size, mm^2		14×5	
PM material		Sintered NdFeB	
PM permeability		1.1	
PM remanence, T		1.2	

2D FEM predicted cogging torque-displacement characteristics of **M1**, **M2** and **M3** are compared in Figure 5.10. It can be seen that the rotor pole-arc can significantly affect the amplitude and waveform of the cogging torque and, therefore, the number and angular location of stable rotor rest positions within one cycle, i.e. 180°_{mech}. Compared to **M1** and **M3**, **M2** has a relatively smaller peak-to-peak cogging torque. It can also be noticed that when the motor is unexcited, the rotor may come to rest at not only the stable rest positions but also a wide range of positions where the cogging torque is very small. By way of example, for **M1** with 60° rotor pole-arc, the rotor can park at the stable rest position, i.e. 48° and 132°, and a large range of positions, i.e. [0°, 20°] and [160°, 180°], due to small cogging torque which is less than 2% of peak cogging torque.

Figure 5.12 shows the 2D FEM predicted static torque-rotor position characteristics by applying an ideal rectangular phase current with 100A amplitude as shown in Figure 5.11. It can be seen that none of the three rotors results in a unidirectional torque being developed over the full angular rotation of the rotor, as the stator coils are excited with bipolar rectangular current waveforms. There are small angular regions over which a torque of opposite polarity is developed, which would clearly compromise the starting capability and may be problematic for achieving smooth operation. Compared with **M2** and **M3**, **M1** has a relatively lower static torque at the stable rest positions of 48° and 132° which may result in the starting problem. However, **M2** with a rotor pole-arc of 80° (i.e. the same as the stator pole-arc) results in a relatively higher starting torque at the rest positions, has the most uniform unidirectional torque and the narrowest region over which the opposite torque is developed. Therefore, from the point of view of starting capability and smooth static torque, **M2** with a rotor pole-arc of 80° is the best option.

In order to eliminate the negative torque, the profile of the rotor pole of **M2** is modified as illustrated in Figure 5.13. This also affects unidirectional rotation. As will be seen from Figure 5.14 and Figure 5.15, the angle over which the pole-faces are chamfered determines the angular position of the negative peak cogging torque and the depth of the chamfer determines the amplitude of the peak cogging torque. The preferred chamfer has a depth of 1mm and extends over an angle of 30°. The torque–displacement characteristics then remains positive over the full angular rotation of the rotor, as shown in Figure 5.16, when the winding is excited by a rectangular current waveform.

Hence, a single-phase FSPM motor having a rotor pole-arc of 80° and a chamfer of 1mm extending over an angle of 30°, and the other design parameters given in Table 5.1, was prototyped for experimental validation of the performance. As shown in Figure 5.17 and Figure 5.18, 2D FEM predicted cogging torque and static torque are much higher than 3D FEM predicted values. Further, it is clearly shows that there is a good match between 3D FEM predict and measured values. It indicates that due to the relatively short motor axial length, i.e. 18mm, and special motor topology, i.e. the magnet is located on the stator; this

single-phase FSPM motor has a significant leakage-flux. Hence, it is very essential to investigate the influence of the leakage-flux on the motor performance.

5.5 End effects in single-phase FSPM motor

As mentioned in above section, FSPM motor has a significant leakage-flux which is also discussed in [105, 108]. This can significantly compromise the motor performance, particularly as the ratio of the axial length to diameter is reduced. Therefore, 3D magnetic field analysis is required to accurately predict the operating characteristics [103, 108-109]. However, 3D FEM analysis is computationally time-consuming. Thus, LPMC analysis is often preferred, since it provides acceptable accuracy for relatively little computational effort [103, 110-112]. In [103] a 3D non-linear LPMC model was developed to predict the electromagnetic performance of a three-phase FSPM motor.

In this section, 2D and 3D LPMC models are developed to investigate the performance of a single-phase FSPM motor. In order to improve the starting capability of a single-phase FSPM motor, the outer surface of the salient rotor poles is usually asymmetric. As discussed in above section, the optimized rotor has 80° pole-arc and the preferred chamfer of rotor pole has a depth of 1mm and extends over an angle of 30°. Hence, an appropriate airgap permeance is required which represents the airgap flux paths and accurately models the asymmetry in the airgap field distribution. The developed 2D and 3D LPMC models are employed to predict the airgap field distribution, back-EMF and inductance characteristics, which are compared with those derived from 2D and 3D FEM and measurements from two prototype motors having symmetric and asymmetric rotors, respectively. The LPMC model is then used to investigate the influence of the motor parameters on the motor performance.

5.5.1 Lumped parameter magnetic circuit (LPMC) model

In order to simplify the analysis, the LPMC is developed on the following assumptions:

- Magnetic materials are isotropic;
- Hysteresis effects are ignored;

- MMF absorbed in the iron is neglected in the linear LPMC model.

Figure 5.19 shows the 3D LPMC model in which the airgap permeances P_1 and P_2 vary with rotor position.

The basic equation which governs each element of the LPMC model is given by [113]:

$$\frac{\Phi}{P} = F \qquad \text{(Wb)} \tag{5-13}$$

where Φ -- Flux; Wb

P -- Permeance; $\text{Wb}\cdot\text{A}^{-1}$

F -- MMF; A

$$P = \mu_r \mu_0 \frac{A_C}{L} \qquad (\text{Wb}\cdot\text{A}^{-1}) \tag{5-14}$$

where A_C -- Cross-sectional area of each element; m^2

L -- Length of each element; m

A. Stator winding

Each coil is modelled as an MMF source, F_W:

$$F_W = IN_c \qquad \text{(A)} \tag{5-15}$$

where I -- Phase current; A

N_c -- Number of turns per coil.

B. Permanent magnets

Each permanent magnet is represented by an MMF source, F_M, in series with an internal permeance, P_M, where,

$$P_M = \frac{\mu_r \mu_0 A_M}{L_M} \qquad (\text{Wb}\cdot\text{A}^{-1}) \tag{5-16}$$

$$F_M = \frac{B_r L_M}{\mu_r \mu_0} \qquad \text{(A)} \tag{5-17}$$

$$A_M = H_M L_a \qquad (m^2) \tag{5-18}$$

where B_r -- Magnet remanence; T

A_M -- Magnet cross-sectional area; m^2

L_M -- Thickness of the magnets in the direction of magnetization; m

H_M -- Length of the magnets in the radial direction; m

L_a -- Axial length of the laminations; m

C. Outer surface leakage-flux

The leakage-flux paths from the outer surface of the stator are assumed to be semi-circular, as shown in Figure 5.20. The permeance, P_o, which is independent of the rotor position, consists of two components, i.e.

$$P_o = P_{o1} + P_{o2} \qquad (Wb \cdot A^{-1}) \tag{5-19}$$

$$P_{o1} = 0.26\mu_0 L_a \qquad (Wb \cdot A^{-1}) \tag{5-20}$$

$$P_{o2} = \frac{\mu_0 \log_e(\frac{\pi R_{so}/2}{L_M/2})}{\pi} L_a \qquad (Wb \cdot A^{-1}) \tag{5-21}$$

where R_{so} -- Stator outer radius; m

D. End leakage-flux

In 2D LPMC model, the end leakage-flux is generally neglected. However, it can be taken into account in 3D LPMC model and its permeance can be deduced from four components, as illustrated in Figure 5.21. P_{e1}, P_{e2}, P_{e3} and P_{e4} are independent of the rotor position and can be expressed as follows,

$$P_{e1} = 0.26\mu_0 H_M \qquad (Wb \cdot A^{-1}) \tag{5-22}$$

$$P_{e2} = \frac{\mu_0 \log_e(1 + (\pi(R_{so} + R_{si})/2 - L_M)/L_M)}{\pi} H_M \qquad (Wb \cdot A^{-1}) \tag{5-23}$$

$$P_{e3} = 0.077\mu_0 L_M \qquad (\text{Wb}\cdot\text{A}^{-1}) \qquad (5\text{-}24)$$

$$P_{e4} = 0.25\mu_0(\pi R_{so} - L_M)/2 \qquad (\text{Wb}\cdot\text{A}^{-1}) \qquad (5\text{-}25)$$

where R_{si} -- Stator inner radius; m .

The total end leakage-flux permeance is, therefore,

$$P_e = 2(P_{e1} + P_{e2} + P_{e3} + P_{e4}) \qquad (\text{Wb}\cdot\text{A}^{-1}) \qquad (5\text{-}26)$$

E. Airgap fluxes

The airgap permeance needs to account for the influence of the pole faces, as well as the fact that the airgap flux distribution varies as the rotor rotates. Hence, LPMC model needs to be adaptively modified in accordance with the rotor position.

In order to determine the airgap permeance and its variation with rotation of the rotor, the airgap is subdivided into angular elements spanning 1°_{mech}, and the rotor is rotated in 6°_{mech}. angular increment. In the angular airgap region the flux is assumed to cross the airgap radially, and the permeance of an angular element is:

$$P_{gi} = \frac{\mu_0 A_i}{g} \qquad (\text{Wb}\cdot\text{A}^{-1}) \qquad (5\text{-}27)$$

$$A_i = \frac{(R_{si} + R_{ro})}{2}\frac{\pi}{180}L_a \qquad (\text{m}^2) \qquad (5\text{-}28)$$

where A_i -- Cross-sectional area of angular element; m^2

g -- Minimum airgap length; m

R_{ro} -- rotor outer radius; m

In the tapered airgap and interpole regions, the flux is assumed to flow radially across the airgap length g and then to take the minimum length path to the rotor. By way of example, a flux line which emanate from point A on the stator core, Figure 5.22, is assumed to pass

through A' to A''. Thus, the effective path length is $(L_m + g)$, and the permeance of the angular element is:

$$P_{gi} = \frac{\mu_0 A_i}{(L_m + g)} \qquad (\mathrm{Wb \cdot A^{-1}}) \qquad (5\text{-}29)$$

However, if the path length $(L_m + g)$ is greater than the length $L_{mm} = \pi r$ of an alternative flux path which passes from the stator core on one side of a magnet to the stator core on the other side, then the contribution of that angular element to the airgap permeance is neglected, since it is then incorporated with the PM slot leakage permeance. The total airgap permeance related to two adjacent stator pole faces, P_1 and P_2 in Figure 5.19, can be deduced by summing up the angular element permeance.

F. PM slot leakage-flux

As show in Figure 5.23, the PM slot leakage-flux permeance, P_{MS}, has four components, viz. P_{MS1}, P_{MS2}, P_{MS3} and P_{MS4}.

P_{MS1}, P_{MS2}, and P_{MS3} are independent of the rotor position and are given by:

$$P_{MS1} = \frac{\mu_0 H_{MS1}}{L_M} L_a \qquad (5\text{-}30)$$

$$P_{MS2} = \frac{\mu_0 H_{MS2}}{L_{MS2}} L_a \qquad (5\text{-}31)$$

$$P_{MS3} = 0.26 \mu_0 L_a \qquad (5\text{-}32)$$

where H_{MS1} -- Radial heights of PM slot; m

H_{MS2} -- Radial heights of PM slot opening; m

L_M -- Circumferential widths of PM slot; m

L_{MS2} -- Circumferential widths of PM slot opening; m

Similar to the procedure for determining the variation of the airgap permeance as the rotor rotates, P_{MS4} is again determined at each rotor position, after which it is compared with the airgap permeance P_{gi} to establish whether it should be contribution to the airgap permeance or PM slot leakage permeance, according to which flux path is shorter. Therefore, the total PM slot leakage-flux permeance is:

$$P_{MS} = P_{MS1} + P_{MS2} + P_{MS3} + P_{MS4} \tag{5-33}$$

The leakage-flux permeance in the slots which accommodate the coils, P_{WS}, Figure 5.19, can be similarly determined. However, on open-circuit, only the PM slot leakage-flux is taken into account, since the MMF dropped in the iron is neglected.

5.5.2 Validation of LPMC model

M2 with symmetric rotor and chamfered rotor, as shown in Figure 5.24, have been prototyped. By using the foregoing developed LPMC model, these two motors' airgap flux density distribution, open circuit phase flux-linkage, back-EMF, winding inductance and average static torque have been calculated and compared with FEM predicted values. Further, it has been validated by the measurements in terms of the back-EMF, inductance and static torque.

Figure 5.25 and Figure 5.26 compare 2D and 3D LPMC and FEM predicted open-circuit airgap flux density distributions, corresponding to a rotor position of 0°_{mech}, and the open circuit phase flux-linkage waveforms, respectively. It shows that there is a good match between the results predicted by LPMC and FEM. It can also be seen that 2D LPMC and FEM predicted results is higher than that predicted by 3D LPMC and FEM.

Compared to FEM, it is relatively convenient for LPMC model to examine each component of the leakage-flux. As discussed in previous section, on the open-circuit condition, 2D LPMC model considers two components of the leakage-flux, i.e. stator out surface leakage-flux and

PM slot leakage-flux. However, there is an extra leakage-flux component, i.e. end leakage-flux, in the 3D LPMC model. Among these leakage-flux components, the stator outer surface leakage-flux permeance and end leakage-flux permeance are both constant at any rotor position. However, the PM slot leakage-flux is dependent of the rotor position. By way of example, each component of the leakage-flux permeance of single-phase FSPM motor with asymmetric rotor on the open-circuit condition at the rotor position of 0°_{mech} is listed in Table 5.2. Among the leakage-flux permeance components, P_{MS}, P_{o2}, $2P_{e2}$ and $2P_{e4}$ are relatively bigger, which indicates that the motor performance will be affected significantly by the associated leakage-flux. Figure 5.27 shows the relative magnitude of the leakage-flux components with reference to the total flux produced by the permanent magnets, with the rotor at 0°_{mech}. It can be seen that the end leakage-flux accounts for ~30% of the total flux produced by the magnets, i.e. it causes ~30% reduction on the phase flux-linkage and the back-EMF compared to values predicted from the 2D analysis, as shown in Figure 5.28. In general, 3D LPMC predicted back-EMF waveform agrees well with the measured waveform.

Table 5.2 3D LPMC model predicted permeance at rotor position of 0°_{mech}. (Asymmetric rotor)

PM slot leakage-flux permeance	P_{MS}	1.87e-08
Stator outer surface leakage-flux permeance	P_{o1}	5.76e-09
	P_{o2}	1.54e-08
End leakage-flux permeance	$2P_{e1}$	9.15e-09
	$2P_{e2}$	3.46e-08
	$2P_{e3}$	9.68e-10
	$2P_{e4}$	2.99e-08

It is obvious that the influence of the end leakage-flux is neglected in the 2D model. From Figure 5.25, Figure 5.26 and Figure 5.28, it can be seen that both the 2D LPMC model and

the 2D FEM analysis over-estimate the airgap field, flux-linkage and back-EMF. When the rotor displacement is between 60° and 135°, the difference between 2D LPMC and 2D FEM predicted phase flux-linkage and back-EMF is larger than that between the 3D LPMC and 3D FEM predicted results, as a consequence of localized magnetic saturation in the stator tooth-tips. As shown in Figure 5.30(b), compared to the rotor position of $0°_{mech}$, the stator tooth tips which are close to the coil slot are heavily saturated at the rotor position of $90°_{mech}$. Therefore, the inductance predicted by 2D LPMC which neglects the iron saturation is higher than that predicted by 2D FEM when rotor position is around $90°_{mech}$, as shown in Figure 5.29. However, when the rotor position is around 0° and $180°_{mech}$, because of the less saturation of the stator, 2D LPMC and 2D FEM predicted inductance has the similar value. The variation of winding inductance with the rotor rotation position is measured by '3522-50 LCR HiTESTER' by setting the frequency of the phase current to 10Hz, and is compared with the inductance predicted by LPMC and FE models in Figure 5.29. Since 3D FEM can take the end effect and magnetic saturation into account accurately, it has the best match with measurements in terms of the inductance.

Although, in general, the magnetic saturation can be catered for in the LPMC model, it is relatively difficult to account for localized magnetic saturation. Particularly, considering that the flux paths passing through the stator tooth and rotor pole vary with the rotor position and complex stator tooth shape, which results in very complex flux paths and is difficult to be represented by equivalent permeances in the LPMC model. However, because of the end leakage-flux, the level of saturation in the 3D model is much lower than that in the 2D model. Therefore, the 3D LPMC predicted results are much closer to the 3D FEM predicted results. Hence, it is reasonable to investigate the open-circuit characteristics by neglecting the iron saturation in 3D LPMC. This can also be seen by comparing back-EMF predicted by 2D linear FEM analysis, in which the stator and rotor iron is assumed to be linear, $\mu_r = 1e+08$, as shown in Figure 5.31. As will be seen, by neglecting the end effect, magnetic saturation is much more prominent in the stator iron than in the rotor iron.

On open-circuit condition, 3D LPMC model can give an acceptable accuracy of the airgap flux density distribution, flux linkage and back-EMF. However, it is more interesting to know whether 3D LPMC can perform properly on load conditions or not. Hence, by applying the ideal rectangular phase current, as shown in Figure 5.11, to the windings, the static electromagnetic toque can be calculated by LPMC model, which is validated by FEM and measurements.

As mentioned in Section 5.2, on load condition, the electromagnetic torque consists of three components, i.e. PM excitation torque, reluctance torque and cogging torque. The overall electromagnetic torque can be measured and predicted by FEM and compared in Figure 5.32. Again, due to neglecting the end leakage-flux, 2D FEM over-estimates the electromagnetic torque. Since it is relatively difficulty for LPMC model to analysis the reluctance torque and the cogging torque. Only PM excitation torque has been predicted by LPMC model. However, over one electrical cycle, the average reluctance torque and cogging torque is zero. Therefore, the average static electromagnetic torque is equal to the average PM excitation torque, which can be expressed by:

$$\overline{T}_{em} = \overline{T}_{iPM} = \frac{1}{T}\int_0^T e_{PM}(t)\cdot i(t)/\omega_r dt \qquad \text{(Nm)} \tag{5-34}$$

where T -- One electrical cycle length, s

To ease comparison, with ideal rectangular phase current, the average static electromagnetic torque predicted by the LPMC model is compared with the measurements and FEM predicted results, as shown in Figure 5.33. It can be seen that, with due account for the stator external leakage-flux and end leakage-flux, the average static torque predicted by 3D FEM and 3D LPMC has a good agreement with the measured result. Further, due to more significant localized magnetic saturation, 2D FEM predicted torque is slightly lower than that predicted by 2D LPMC.

The measured static electromagnetic torque is obtained using an electronic scale to measure the force on an arm which is fixed on the stationary rotor shaft while the stator is hold by the

clamping head of the machine spindle and rotated incrementally by a step of 1°, as shown in Figure 5.34. By rotating the spindle, the rotor position can be changed and recorded. By recording the scale reading, with the specified phase current which is supplied by DC power supply, at a certain rotor position, the static electromagnetic torque can be calculated by:

$$T_s = (M - m)gl \tag{5-35}$$

where, T_s -- Measured static electromagnetic torque; Nm

M -- Scale reading; Kg

m -- Additional weight; Kg

g -- Acceleration of gravity; m/s^2

l -- Half length of the arm; m

5.6 Influence of motor parameters on motor performance

As discussed in the foregoing section, the developed LPMC model can accurately predict the performance of the single-phase FSPM motor, such as open-circuit airgap flux density, open-circuit phase flux-linkage, back-EMF and static torque. Further considering its significantly less computation time, LPMC model is suitable for the initial design and optimization of single-phase FSPM motor, which usually needs to continually vary the motor parameters, but which is often inconvenient to model in FEM.

Hence, in this section, LPMC model is used to examine the influence of the leading design parameters on the single-phase FSPM motor's performance:

- Influence of the rotor pole-arc width on the power density.
- Influence of the motor axial length and magnet dimensions on the end leakage-flux.

5.6.1 Influence of rotor pole-arc width on power density

As validated by 2D FEM in Section 5.4, 80° is the optimal rotor pole-arc width which can achieve the best starting capability. However, can this optimal rotor pole-arc width deliver the

maximum power density? Power density is defined as P_{em}/V, where $P_{em} = T_{em}\omega_r$ is the electromagnetic power, and $V = \pi R_{so}{}^2 l_a$ is the motor volume. It can be seen that, for a given motor volume and motor operating speed, the power density is determined by the electromagnetic torque T_{em}. It has been addressed in the previous section that over one electrical cycle, the average reluctance torque and cogging torque is zero. Therefore, the electromagnetic torque capability can be analyzed by investigating the average PM excitation torque over one electrical cycle only

Equation (5-34) indicates that for a given phase current waveform, the average electromagnetic torque over one electrical cycle is only determined by the back-EMF waveform. Therefore, by examining the influence of the rotor pole-arc width on the back-EMF waveform, the optimal rotor pole-arc width can be achieved to deliver the maximum power density.

Due to the significant end leakage-flux, 2D FEM is not accurate enough to predict the back-EMF waveform, and 3D FEM needs significant computational time. However, by comparing the 3D LPMC model predicted back-EMF with measurements in previous section, it has been proven that the developed 3D LPMC model is accurate enough to simulate the back-EMF. Hence, the 3D LPMC model is adopted to investigate the influence of the rotor pole-arc width on the back-EMF.

To simplify the analysis, the FSPM motor with symmetric rotor topology is investigated which means that the rotor pole is not chamfered for improving the starting capability. Figure 5.35 shows the 3D LPMC predicted back-EMF waveforms of the FSPM motors having different rotor pole-arc width which is varied from 50° to 120°. The peak-to-peak and RMS value of the back-EMF are illustrated in Figure 5.36. It can be seen that:

- Since the iron saturation is neglected in the 3D LPMC model, the rotor pole-arc width does not affect the zero-crossing positions of the back-EMF waveform which are at

the rotor position of 45°_{mech} and 135°_{mech}, where the rotor pole is fully aligned with stator pole.

- Approximately, the peak-to-peak back-EMF is decreased linearly with the increase of the rotor pole-arc width.
- 80° rotor pole-arc width also produces the maximum RMS value of the back-EMF.

If an ideal rectangular phase current with 100A amplitude is applied to the windings, the average electromagnetic torque over one electrical cycle can be calculated by equation (5-34). The influence of the rotor pole-arc width on the average electromagnetic torque is shown in Figure 5.37. It clearly shows that 80° rotor pole-arc width delivers the maximum average torque. Consequently, 80° is the optimal rotor pole-arc width which is able to achieve not only the potential best starting capability by chamfering the rotor pole but also the maximum power density.

5.6.2 Influence of motor axial length and magnet dimensions on end leakage-flux

The 3D LPMC model shows that the single-phase FSPM motor has a significant leakage-flux at not only its stator outer surface but also ends of the stator, since the permanent magnets are located on the stator. This can significantly compromise the performance, particularly as the ratio of the motor axial length to the motor diameter is reduced. By varying the motor lamination axial length, the LPMC model predicted ratio of 3D to 2D peak-to-peak and RMS value of back-EMF of the single-phase FSPM motor is shown in Figure 5.38. Because the end leakage-flux only exists at the ends of the stator as illustrated in Figure 5.21, the end leakage-flux is independent of the motor lamination axial length, and the equations for the end leakage-flux permeance, i.e. equations (5-22) to (5-26), do not contain the motor lamination axial length. Therefore, as the motor lamination axial length is increased, the percentage of the end leakage-flux gradually reduces and the ratio of 3D to 2D back-EMF approaches unity. An ideal rectangular phase current with 100A amplitude, is applied to the windings, the average electromagnetic torque over one electrical cycle can be calculated by equation (5-34) and torque density can be calculated by $\overline{T}_{em} / V$. 3D LPMC predicted torque density is shown

in Figure 5.39, which shows that the torque density is increased by increasing the motor lamination axial length.

According to equations for the end leakage-flux permeance, the end leakage-flux is dependent of the permanent magnet dimensions. As shown in Figure 5.40, by comparing to the influence of the axial length, the magnet dimensions have relatively less influence on the end effect.

5.7 Limitations of LPMC model

The developed LPMC model neglects the MMF dropped in the stator and rotor iron. As a result, the saturation in the iron cannot be taken into account. Particularly without considering the local saturation in the stator tooth tips which is generally relatively severe, the accuracy of the LPMC model predicted motor characteristics could be affected. By examining Figure 5.28, it can be noticed that even though 3D LPMC model predicted back-EMF is very close to the 3D FEM predicted and measured results, the duty cycle is different as summarised in Table 5.3. Further, the difference of the positive peak and negative peak back-EMF is also different as summarised in Table 5.4. It can be seen that compared to 3D FEM predicted and measured back-EMF, 3D LPMC model predicted back-EMF gives a more like symmetric profile.

Table 5.3 Duty cycle of back-EMF. (M2 with asymmetric rotor)

	3D LPMC	**3D FEM**	**Measurement**
Positive length ($^{o}_{mech}$)	90.8	93.1	93.8
Negative length ($^{o}_{mech}$)	89.2	86.9	86.2
Duty cycle[1] (%)	50.44	51.72	52.10

[1]Duty cycle=(positive length / one electrical cycle length) × 100.

Table 5.4 Peak back-EMF. (M2 with asymmetric rotor)

	3D LPMC	3D FEM	Measurement
Positive peak (V)	0.117	0.108	0.108
Negative peak (V)	-0.119	-0.121	-0.120
Error[1] (V)	-0.002	-0.013	-0.012

[1]Error = |Positive peak| - |Negative peak|.

Another limitation of the LPMC model is that the end-winding inductance is not modelled. Therefore, 2D and 3D LPMC model predicted winding inductance is very similar, as shown in Figure 5.29. At the rotor position of 0°_{mech}, the tooth tips is not very saturated, so LPMC model predicted inductance is similar with 2D FEM predicted value, but is lower than 3D LPMC model predicted and measured inductance, as the end-winding inductance is neglected. At the rotor position of 90°_{mech}, since the heavy saturation in the stator tooth tips which are close to the winding slot, LPMC predicted inductance is much higher than 2D FEM predicted value, but it is close to the 3D FEM predicted and measured inductance. The reason is that effect of neglecting both of the saturation and the end-winding inductance in the LPMC model is opposite. Overall, the LPMC model predicted inductance is not good enough to match the measured inductance.

The third limitation of the LPMC model is that the reluctance torque and the cogging torque are relatively difficult to be predicted accurately, particularly when the rotor is chamfered resulting in an asymmetric arigap.

In order to assess the effects of the back-EMF, inductance and cogging torque on the motor dynamic performance, a dynamic simulation model has been developed as described in Appendix C. The simulated phase current waveforms are compared in Figure 5.41, by executing the dynamic simulation model with different combinations of the back-EMF and inductance, as listed in Table 5.5. The simulated results are also compared in Table 5.6. By taking **CASE 1**, where both back-EMF and inductance are predicted by 3D FEM, as the benchmark, it can be found that 3D LPMC model predicted back-EMF has a relatively

smaller effect on the motor dynamic performance. However, 3D LPMC predicted inductance has a significant effect which cannot be ignored. Therefore, it is not acceptable to use LPMC model predicted inductance to investigate the motor dynamic performance.

Table 5.5 Combinations of back-EMF and inductance. (M2 with asymmetric rotor)

	CASE 1	CASE 2	CASE 3	CASE 4
Back-EMF	3D FEM	3D LPMC	3D FEM	3D LPMC
Inductance	3D FEM	3D FEM	3D LPMC	3D LPMC

Table 5.6 Comparisons of simulation results. (M2 with asymmetric rotor)

	CASE 1	CASE 2	CASE 3	CASE 4
DC link voltage (V]		24.0		
Conduction angle (Elec. Deg.)		54.0		
Load (mNm)		114.59		
Speed (Krpm)	99.73	100.45	111.61	111.87
Maximum Phase Current (A)	349.67	313.12	259.26	256.96
Minimum Phase Current (A]	-228.08	-223.94	-248.76	-242.47
Output Power (W]	1196.69	1205.38	1339.30	1342.46

5.8 Summary

The operation principle of the single-phase FSPM motor has been introduced. Three different winding topologies, full-pitched, short-pitched and toroidal have been investigated. By considering the copper loss and overall motor size, it is found that the full-pitched winding topology is the best option for this specific project. The starting issue has been addressed and the starting capability is improved by optimizing the chamfered rotor pole. A LPMC model has been developed to analysis the motor end effect. By comparing with FEM and measurements, it has proven that the developed LPMC can predict the back-EMF waveform very well. Hence, the LPMC model is used to optimise the rotor pole width to increase the motor torque/power density. Further, it has been used to investigate the effect of the magnet dimensions and motor axial length on the motor end effect. However, the inductance cannot be predicted accurately enough because the LPMC model neglects the iron saturation and end

winding inductance. A dynamic simulation model has been developed to assess the effect of the back-EMF and inductance on the motor performance. It has been found that LPMC predicted inductance is not good enough to predict the motor performance accurately. Overall, developed LPMC model in this chapter can provide not only a deeper understanding of the FSPM machine behaviour but also an efficiency way to optimise the motor design.

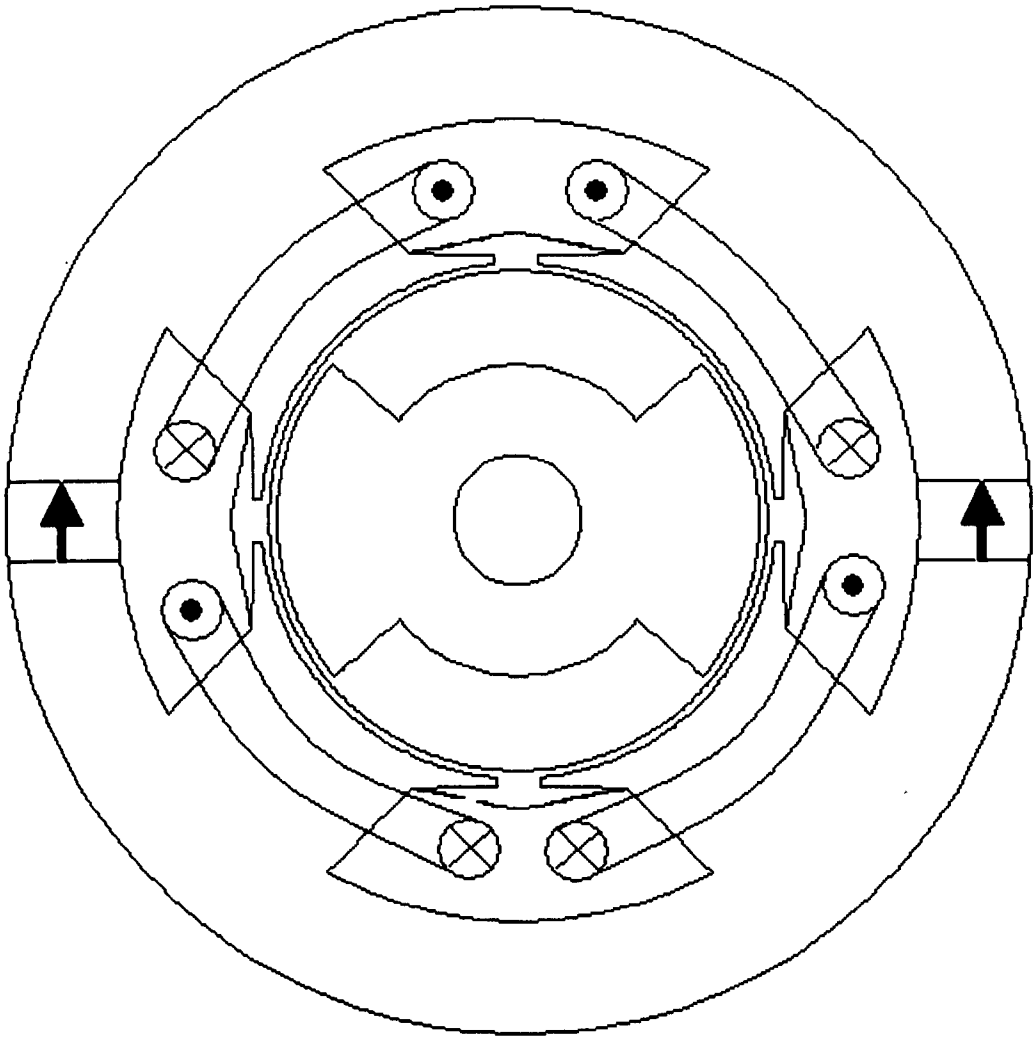

Figure 5.1 Cross-section of single-phase FSPM motor.

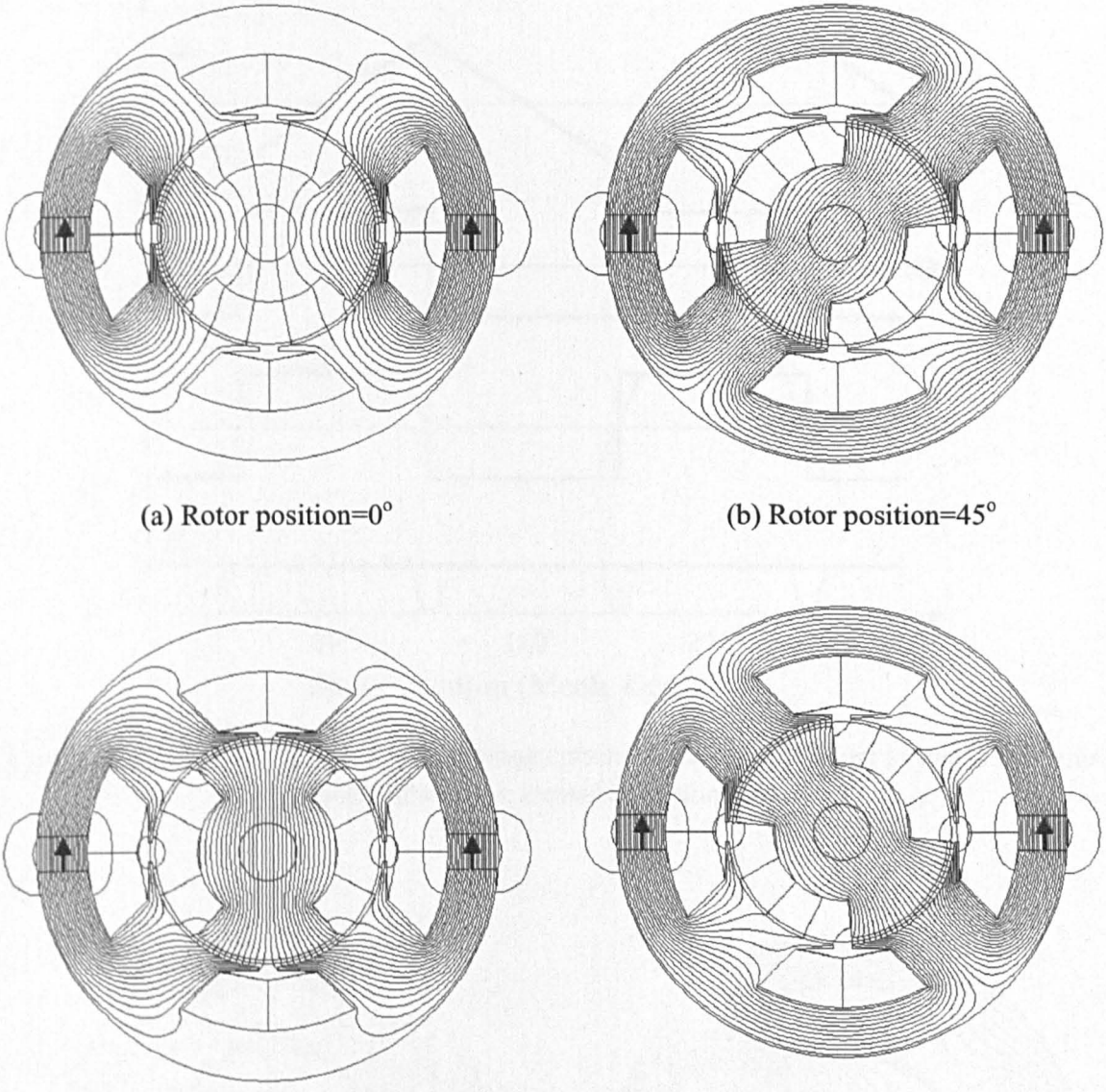

(a) Rotor position=0°

(b) Rotor position=45°

(c) Rotor position = 90°

(d) Rotor position = 135°

Figure 5.2 Flux distribution of single-phase FSPM motor at different rotor position.

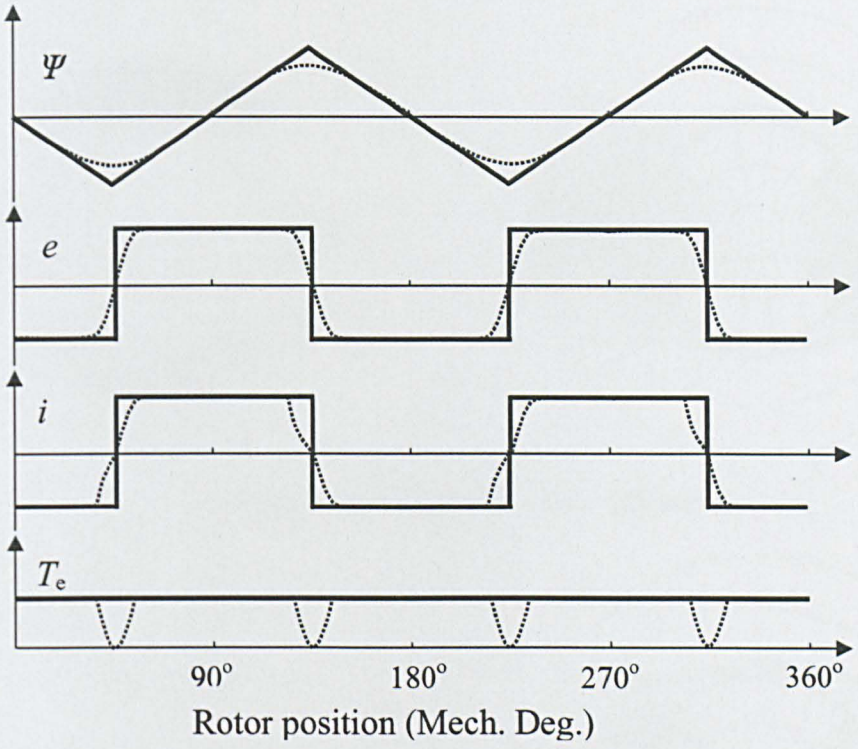

Figure 5.3 Flux-linkage, back-EMF, winding current and electromagnetic torque waveforms. (Solid line: Ideal; Dotted line: None ideal)

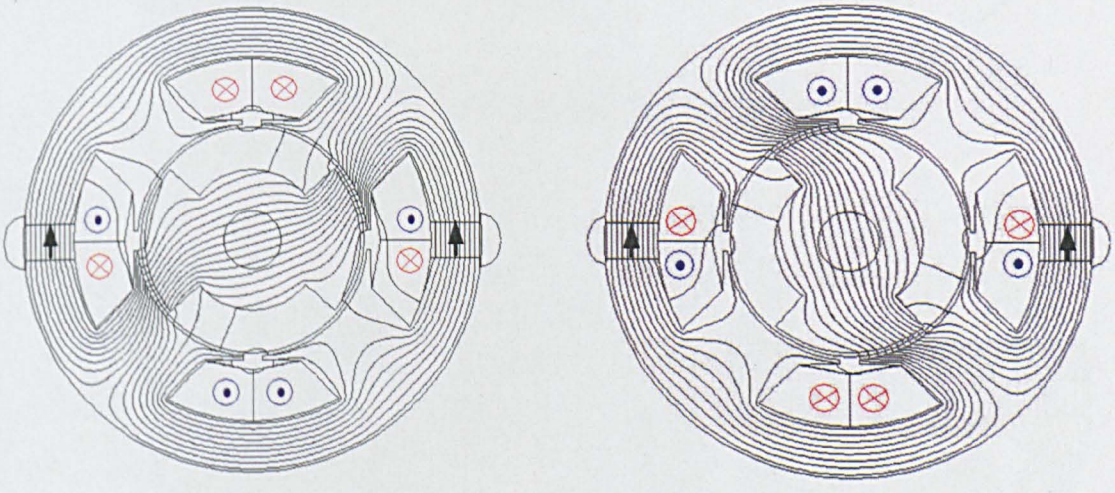

(a) Rotor position=0°

(b) Rotor position=90°

Figure 5.4 Flux-switching and production of rotating torque.

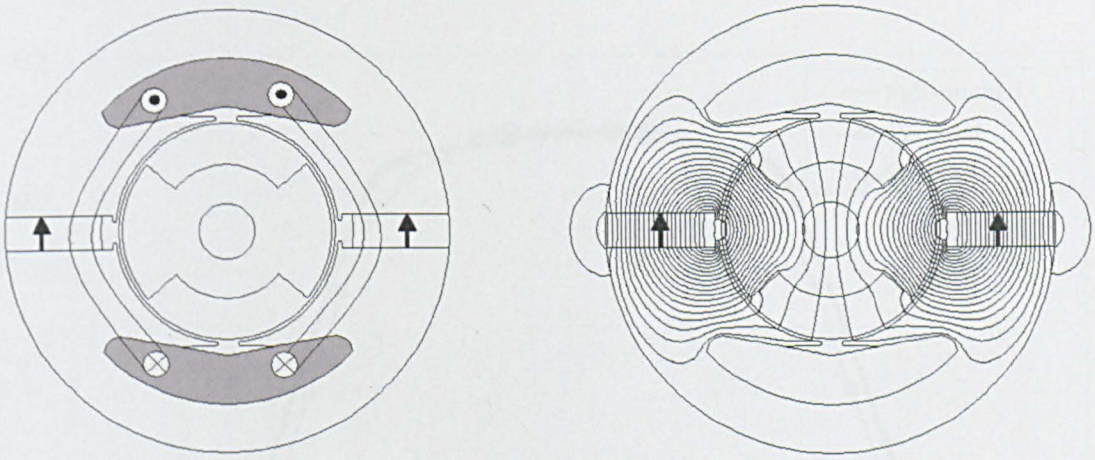

(a) Full-pitched (Stator slot area=220mm^2)

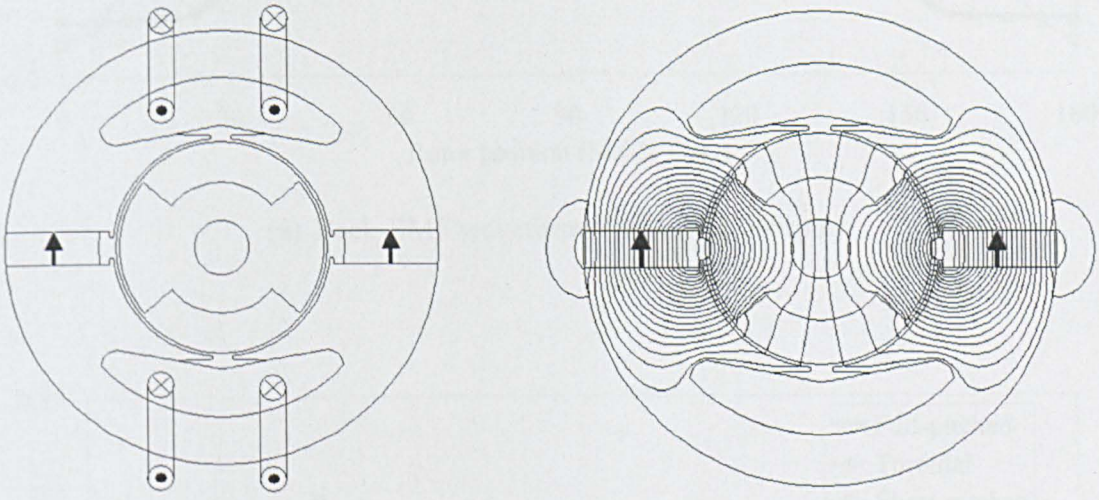

(b) Toroidal (Stator slot area=220mm^2)

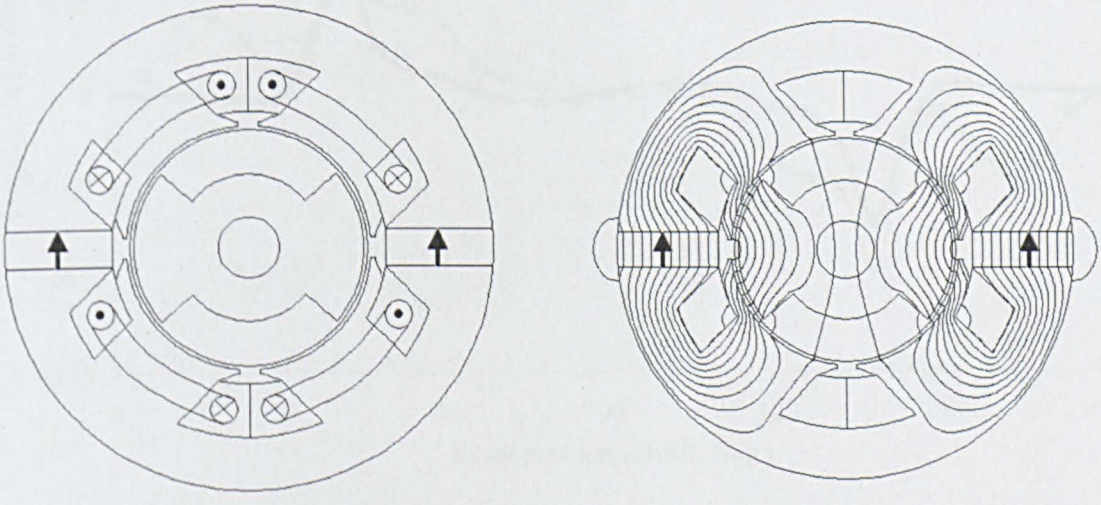

(c) Short-pitched (Stator slot area=98mm^2)

Figure 5.5 Single-phase FSPM machines having different winding topologies.

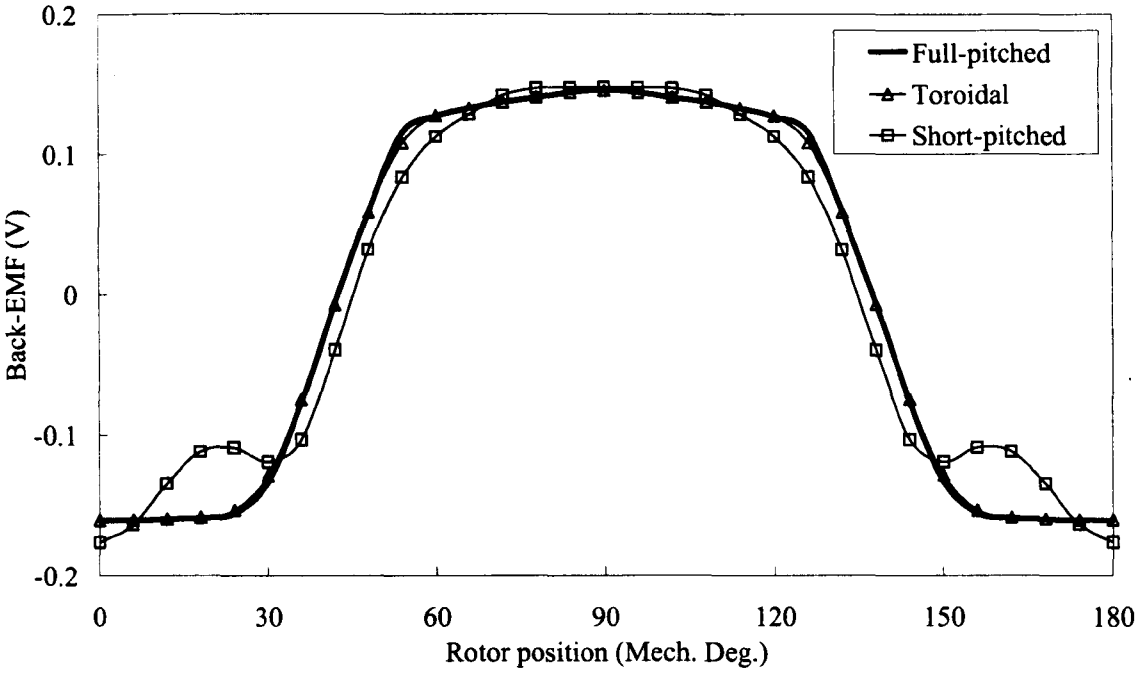

(a) Back-EMF waveforms (Speed= 1,000rpm)

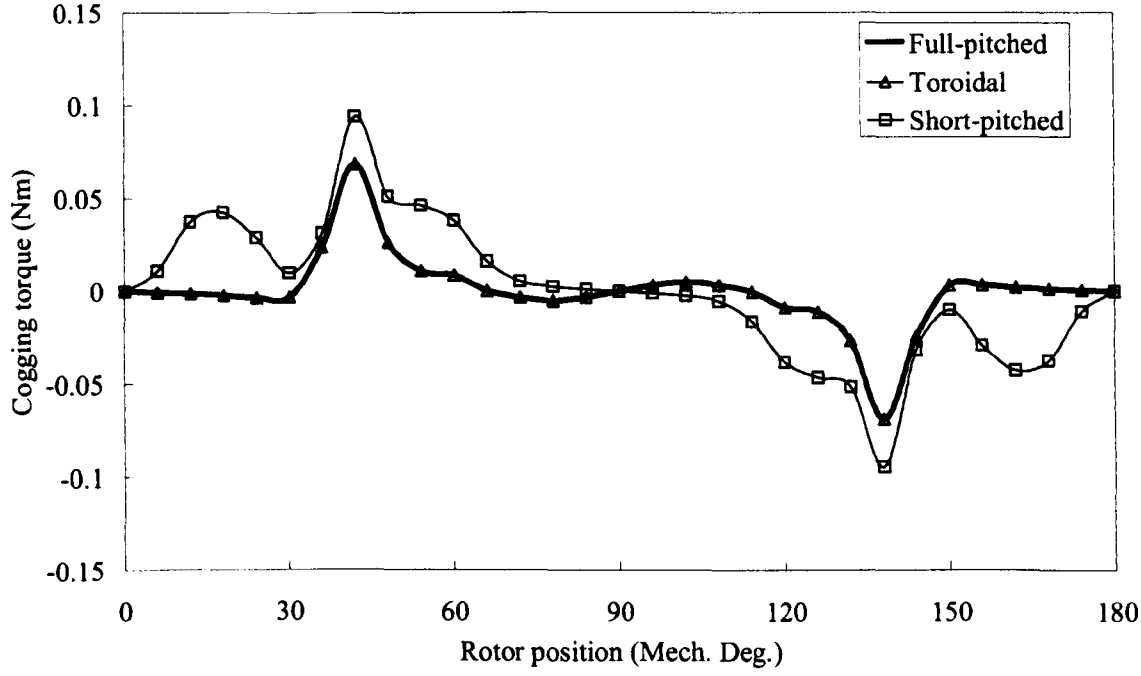

(b) Cogging torque waveforms

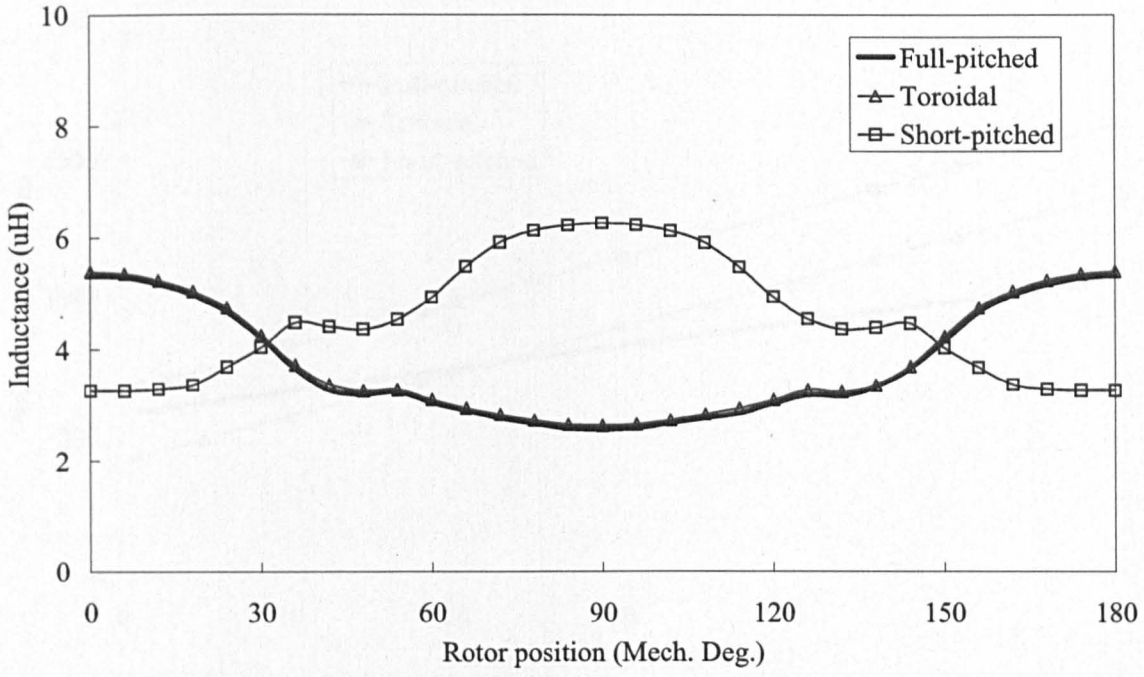

(c) Inductance waveforms

Figure 5.6 2D FEM predicted back-EMF, cogging torque and winding inductance waveforms of single-phase FSPM machines having different winding topologies.

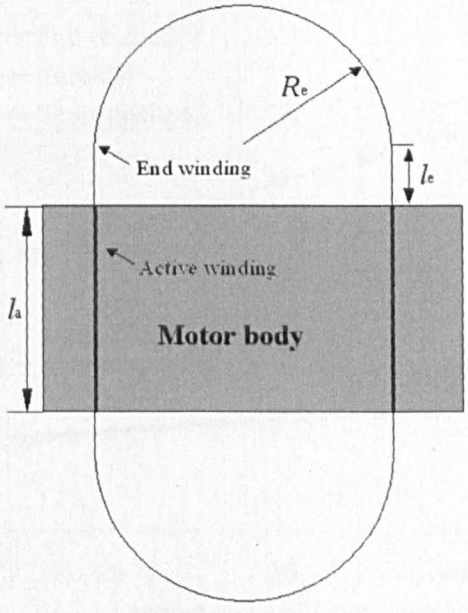

Figure 5.7 Winding illustrations

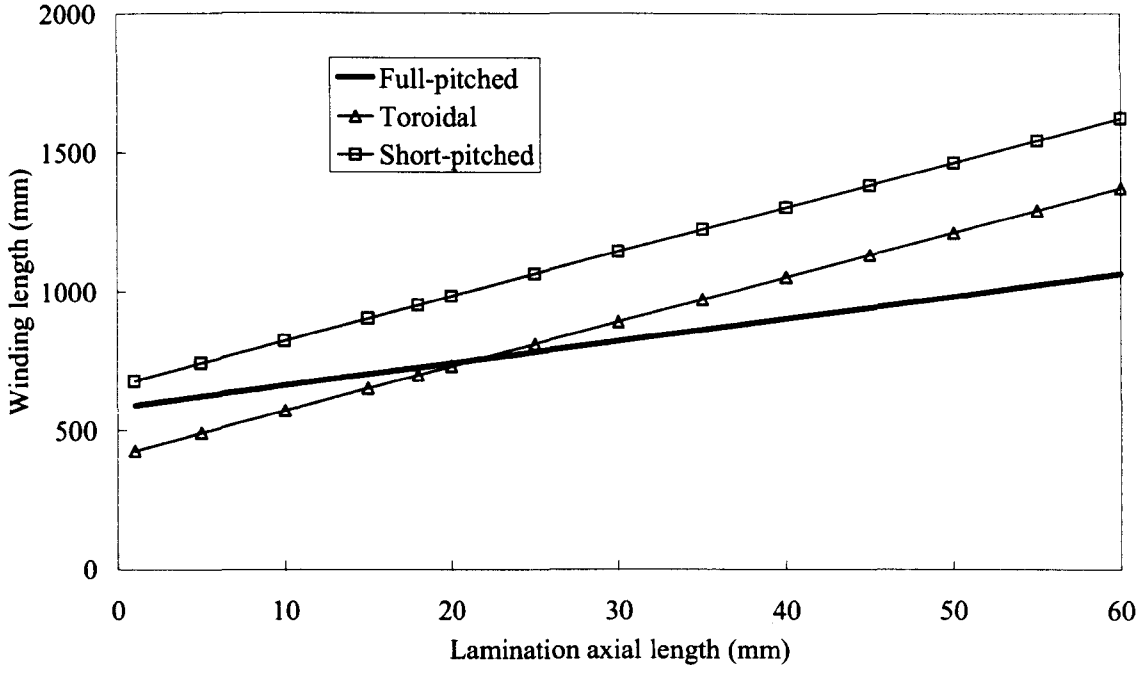

(a) Winding length

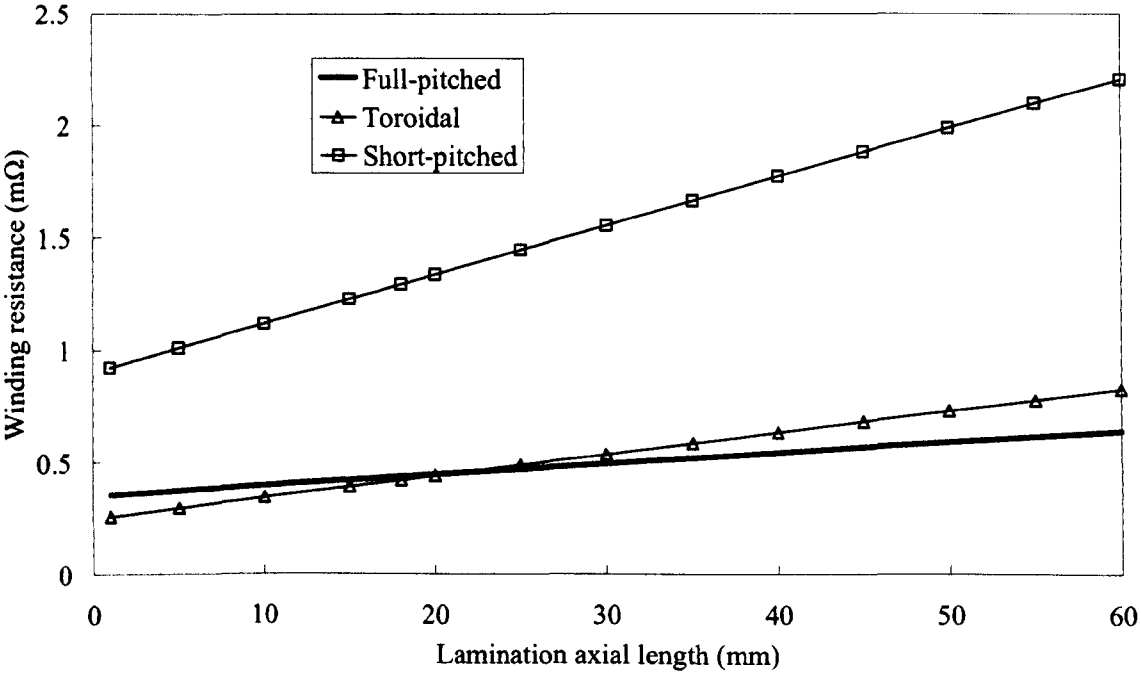

(b) Winding resistance

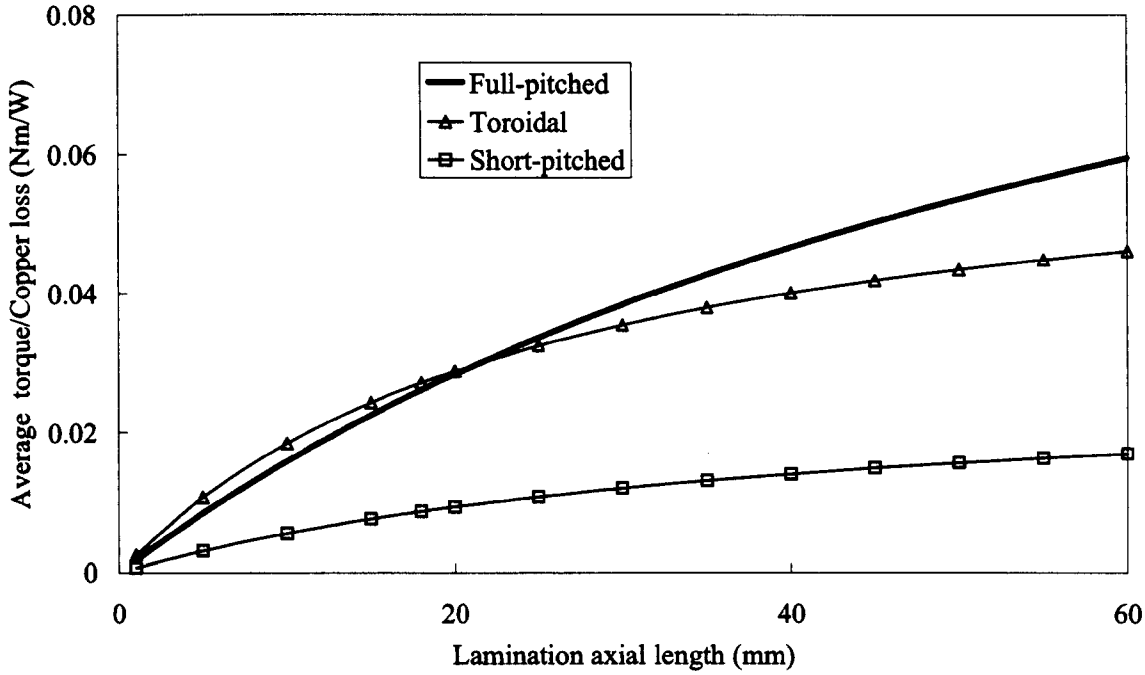

(c) Average static torque/copper loss (Phase current=100A)

Figure 5.8 Variation of winding length, winding resistance and torque/copper loss with motor axial length. (Number of turns per slot=4)

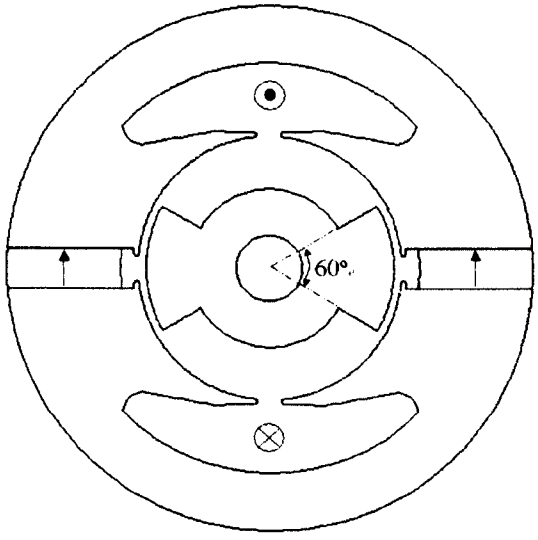

(a) M1; Rotor pole-arc=60°

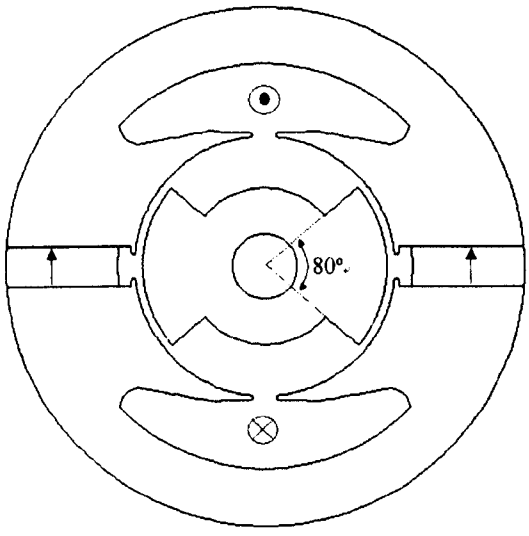

(b) M2; Rotor pole-arc=80°

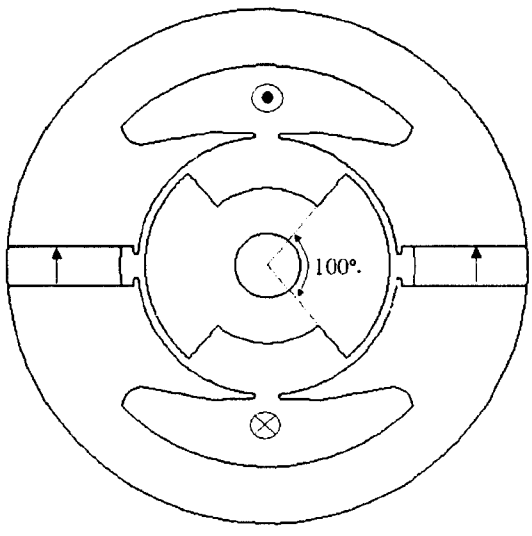

(c) M3; Rotor pole-arc=100°

Figure 5.9 Cross-section of single-phase FSPM motors with different rotor pole-arc.

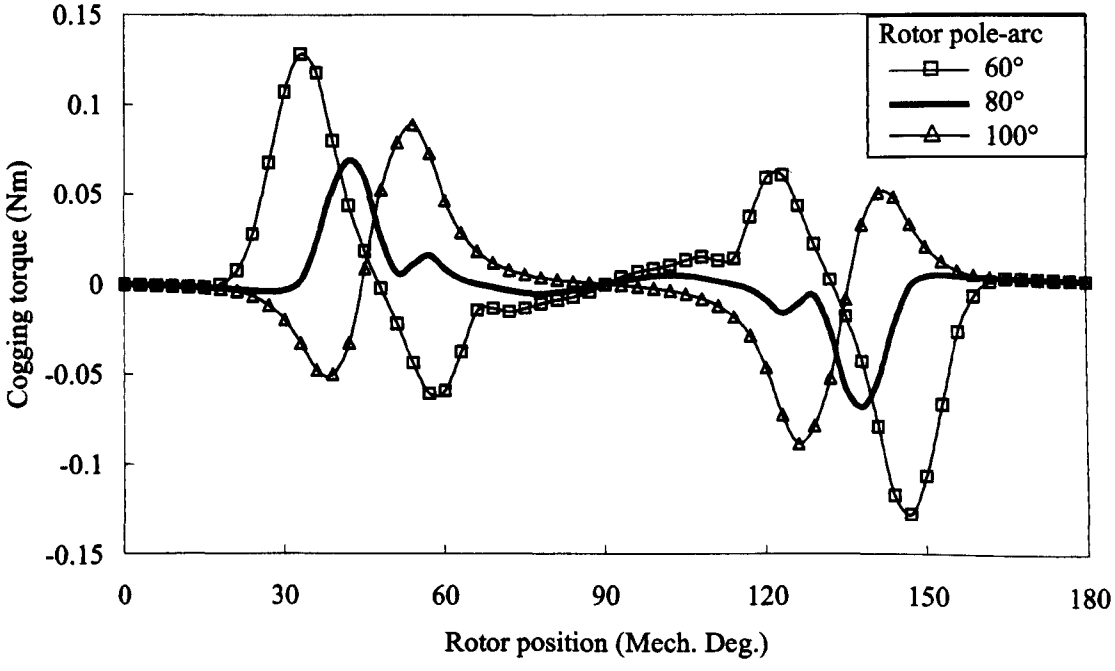

Figure 5.10 2D FEM predicted cogging torque-displacement characteristic of M1, M2 and M3.

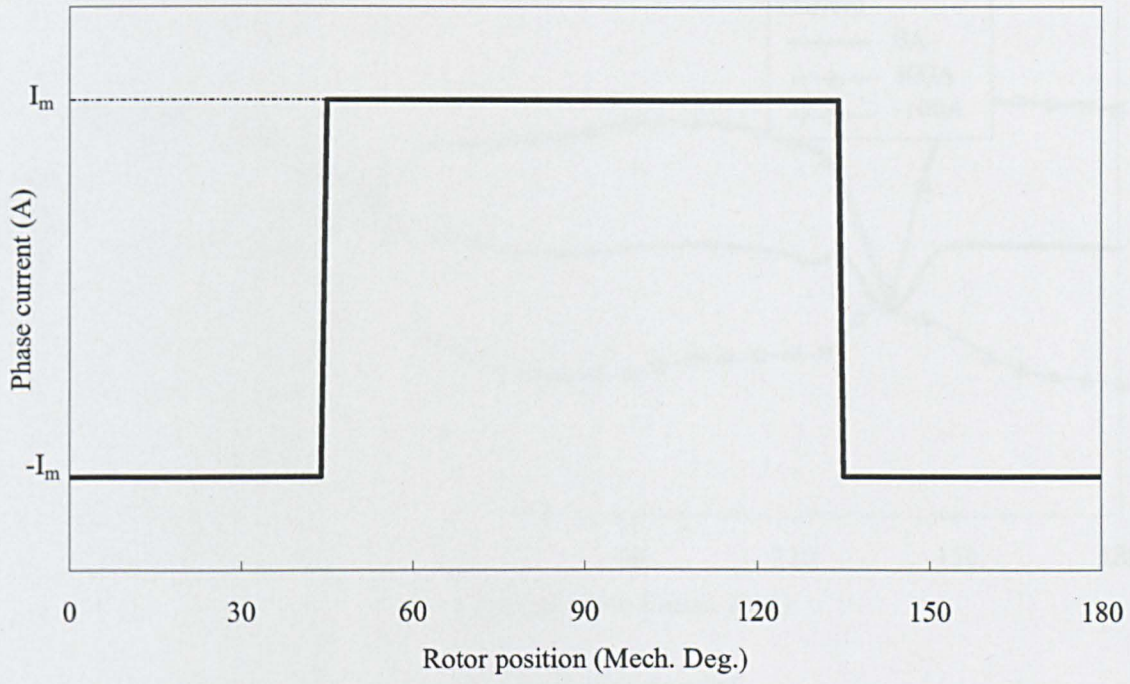

Figure 5.11 Ideal rectangular phase current waveform with amplitude I_m.

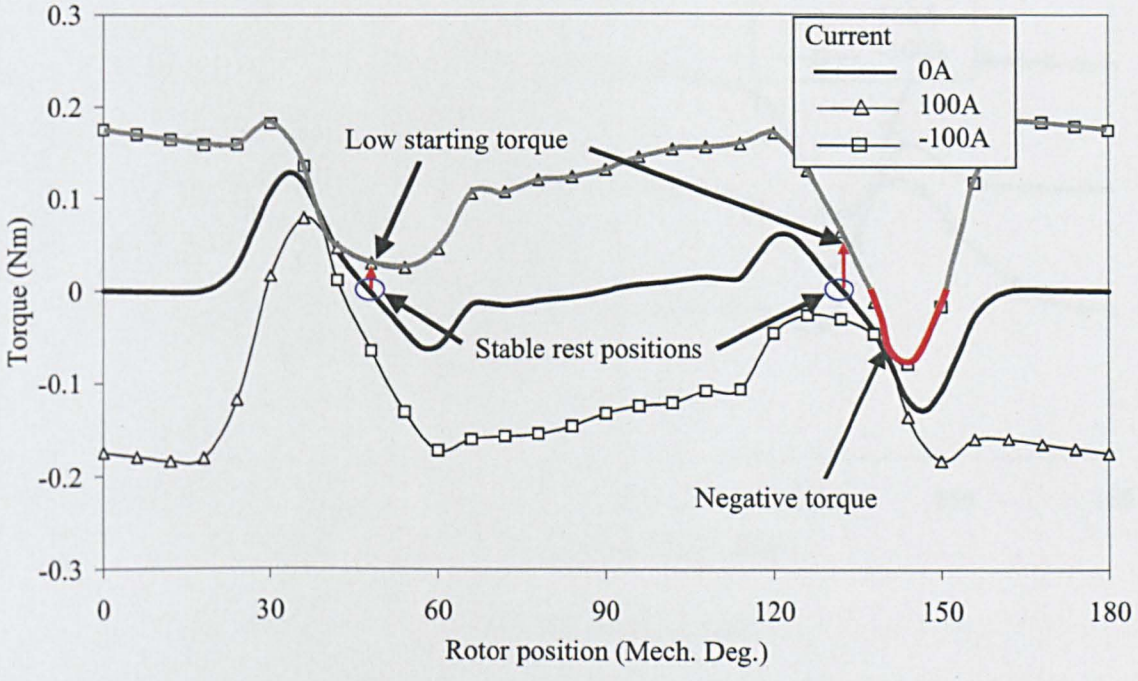

(a) M1, Rotor pole-arc=60°

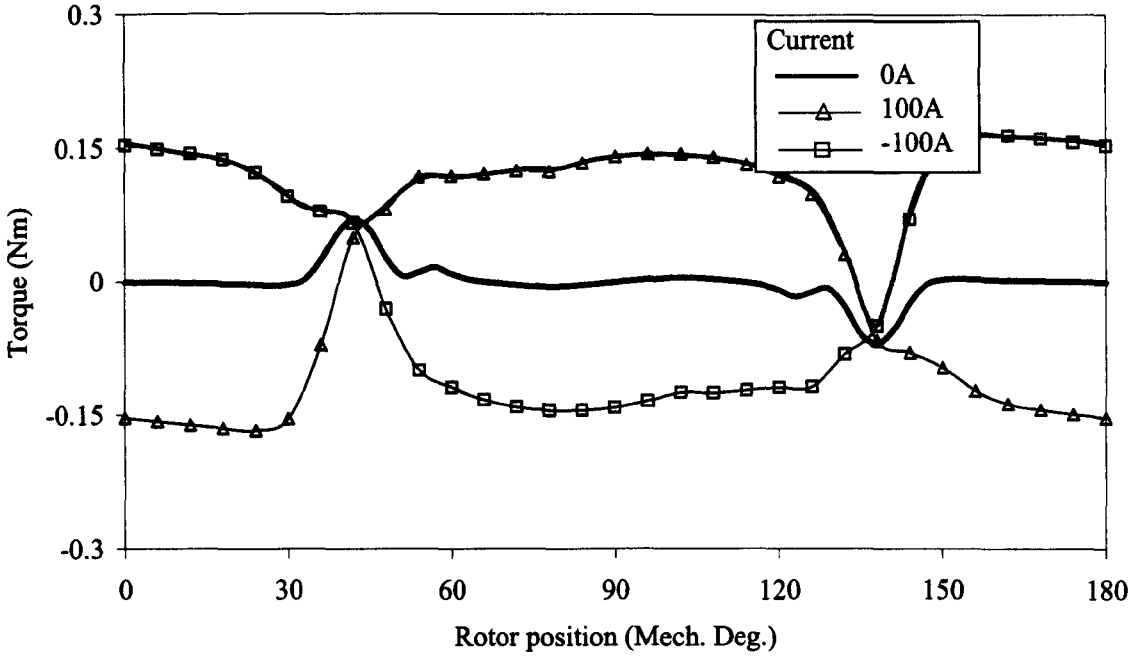

(b) M2, Rotor pole-arc=80°

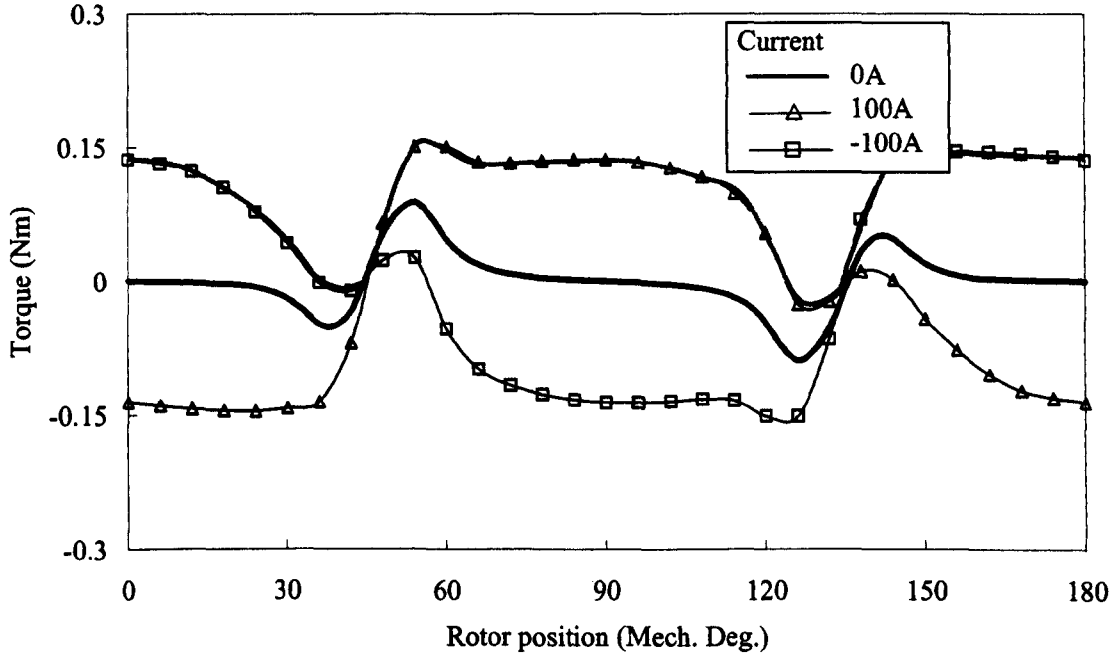

(c) M3, Rotor pole-arc=100°

Figure 5.12 2D FEM predicted static torque-rotor position characteristics of M1, M2 and M3.

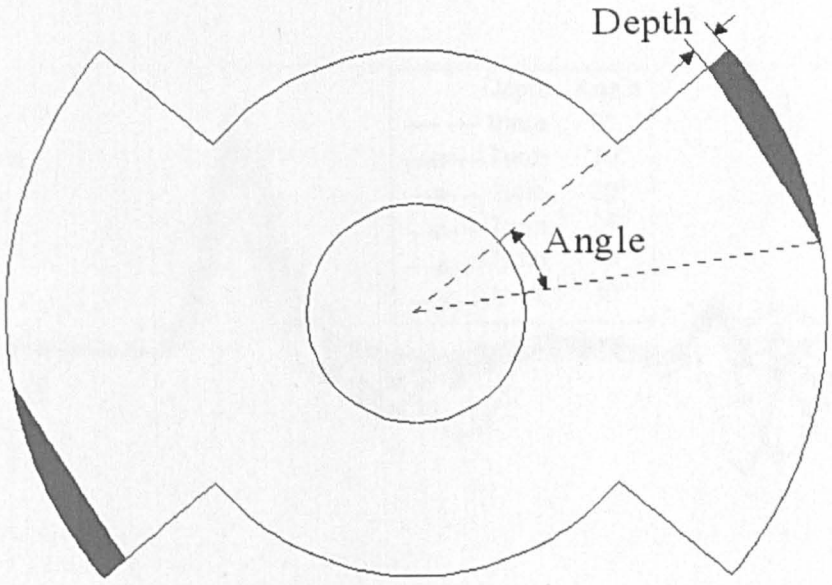

(a) Cross-section of asymmetric rotor

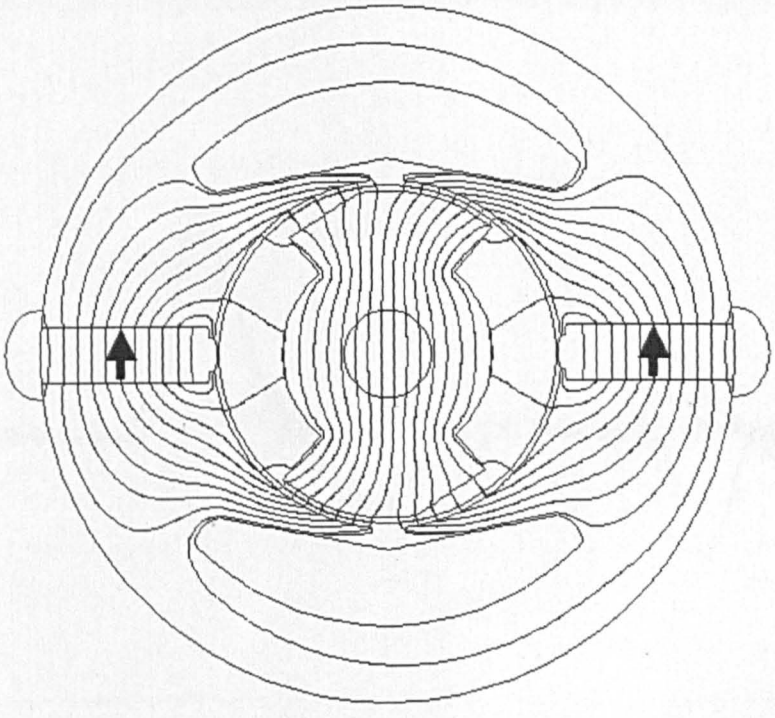

(b) Open-circuit flux distribution of FSPM motor with asymmetric rotor

Figure 5.13 Asymmetric rotor, with pole-arc=80°, and chamfer angle/depth=30°/1mm

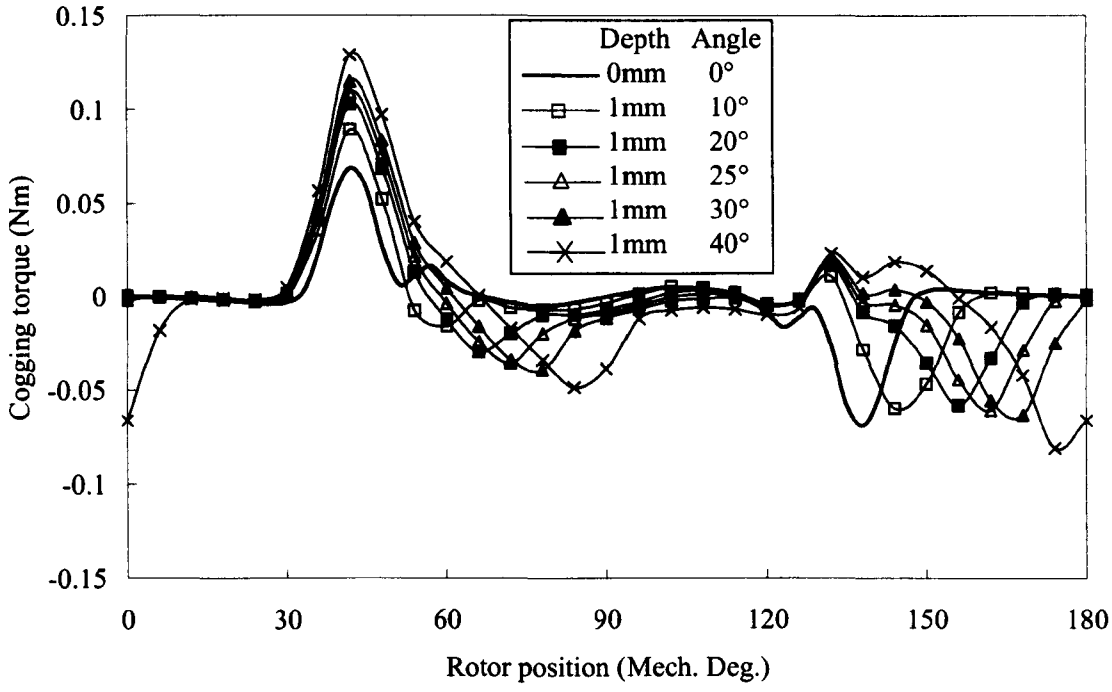

Figure 5.14 2D FEM predicted influence of chamfer angle on cogging torque.

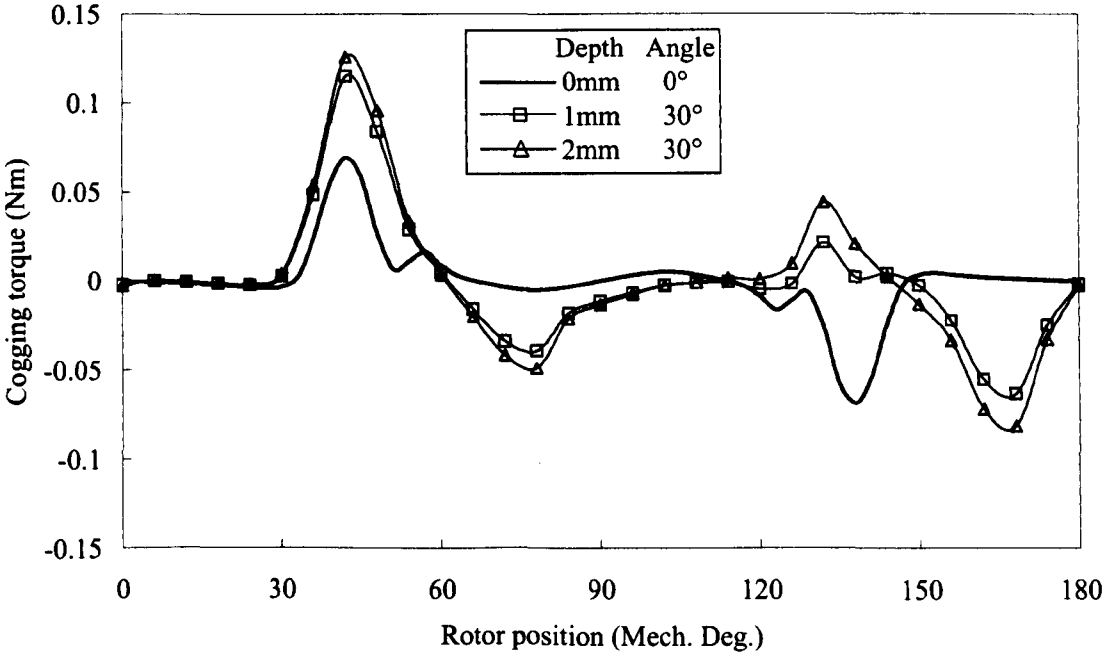

Figure 5.15 2D FEM predicted influence of chamfer depth on cogging torque.

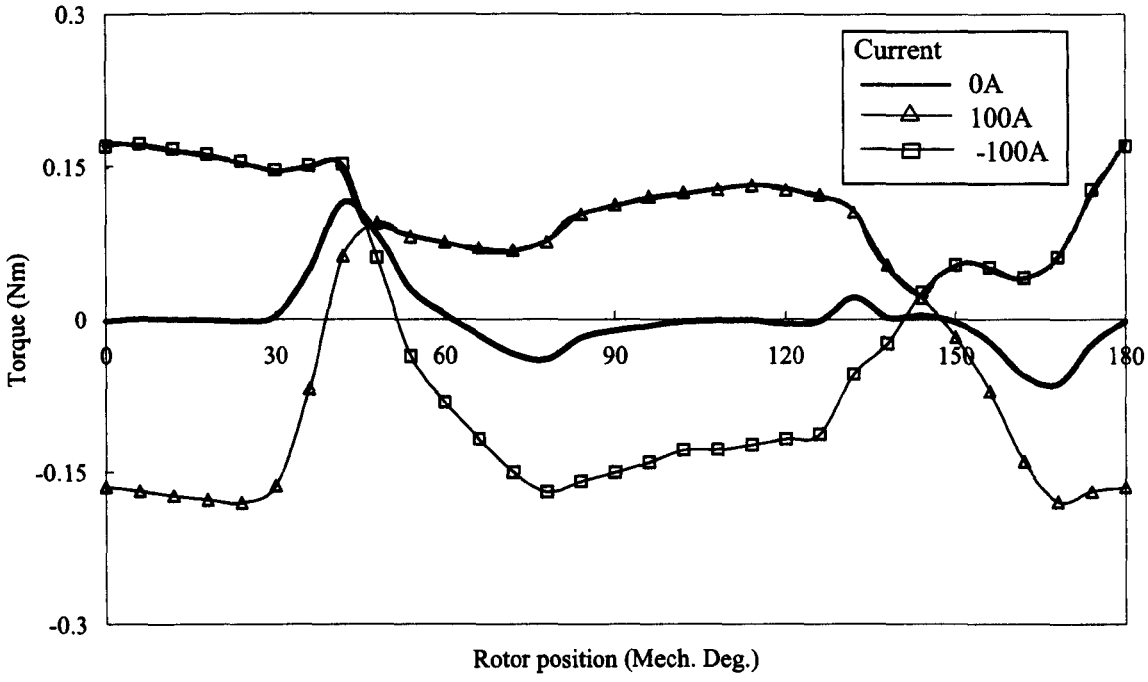

Figure 5.16 2D FEM predicted torque–displacement characteristics with asymmetric rotor (Chamfer depth=1mm, Angle=30°)

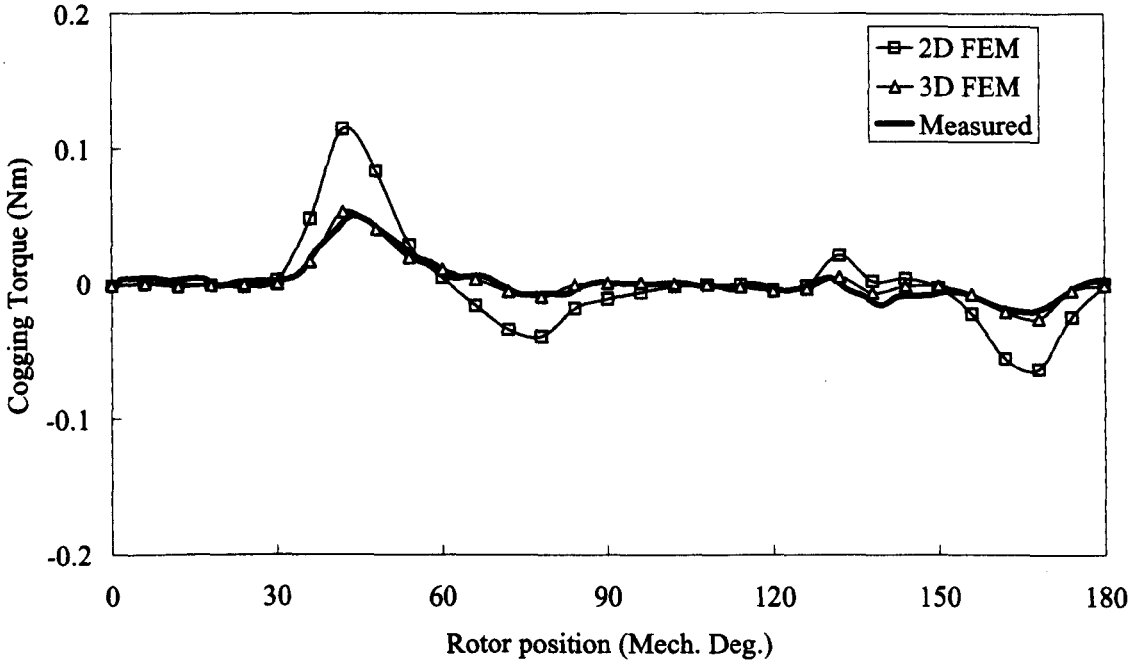

Figure 5.17 2D/3D FEM predicted and measured static torque-rotor position characteristics with asymmetric rotor.

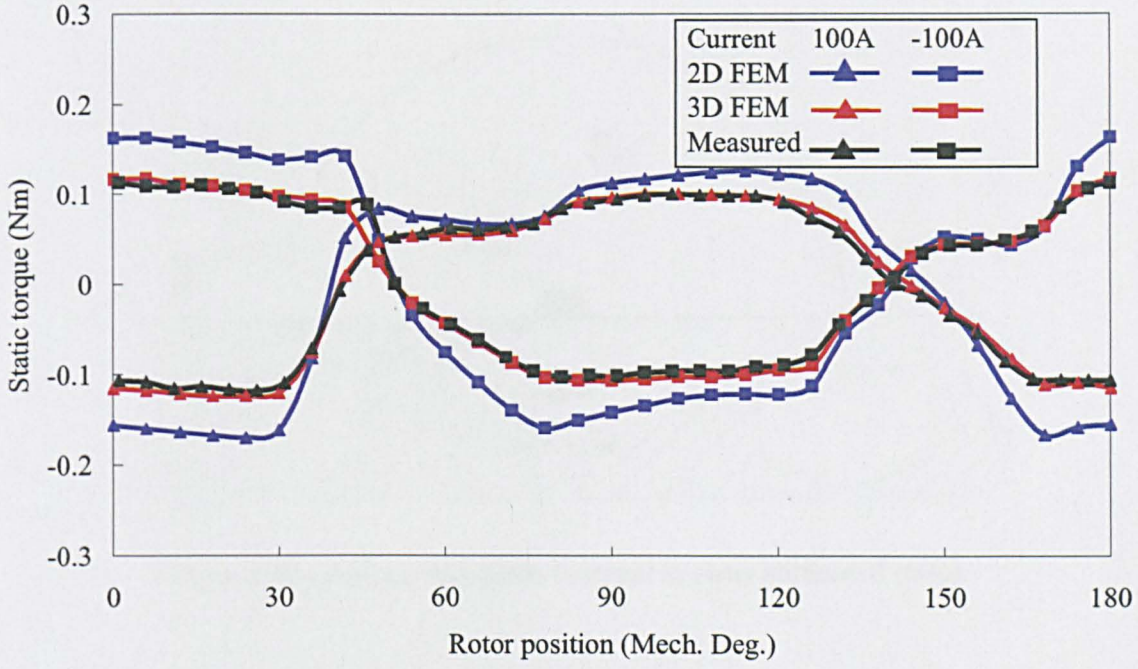

Figure 5.18 2D/3D FEM predicted and measured static torque-rotor position characteristics with asymmetric rotor.

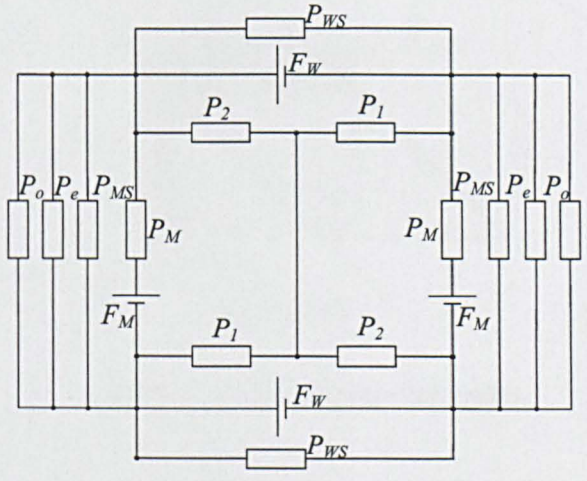

Figure 5.19 3D Lumped parameter magnetic circuit model.

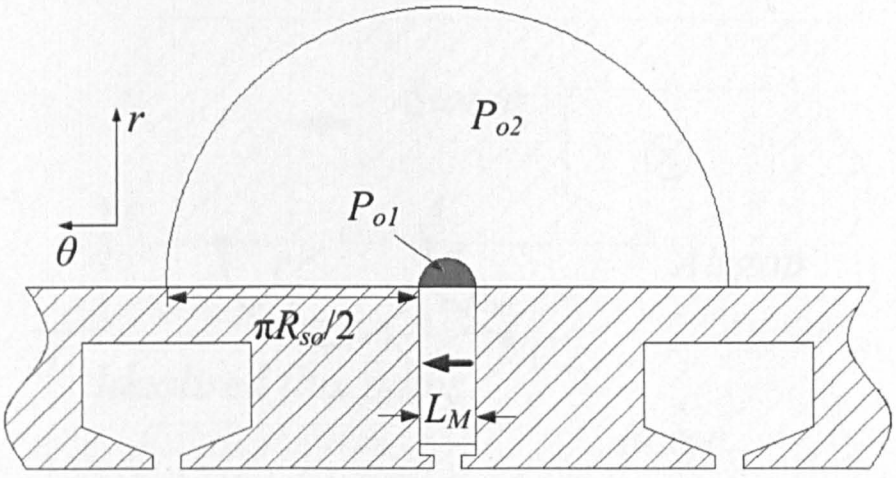

Figure 5.20 Leakage-flux paths external to outer surface of stator.

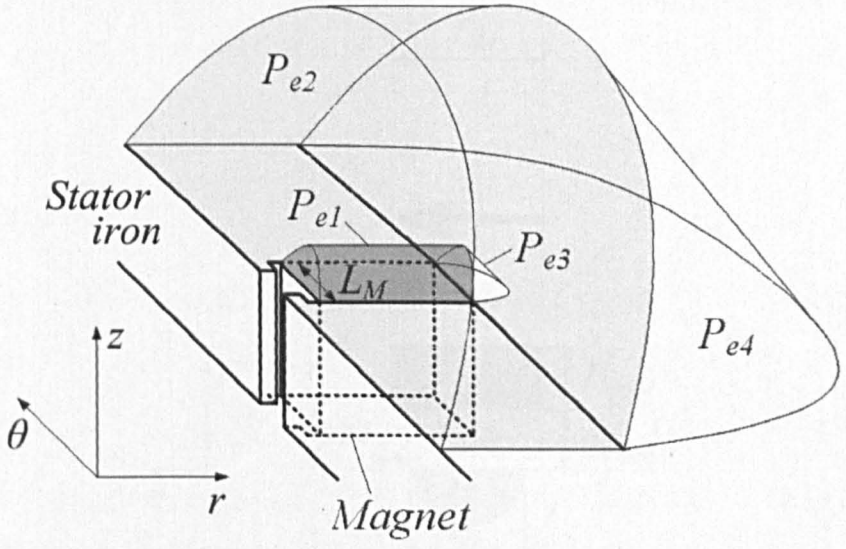

Figure 5.21 End leakage-flux paths.

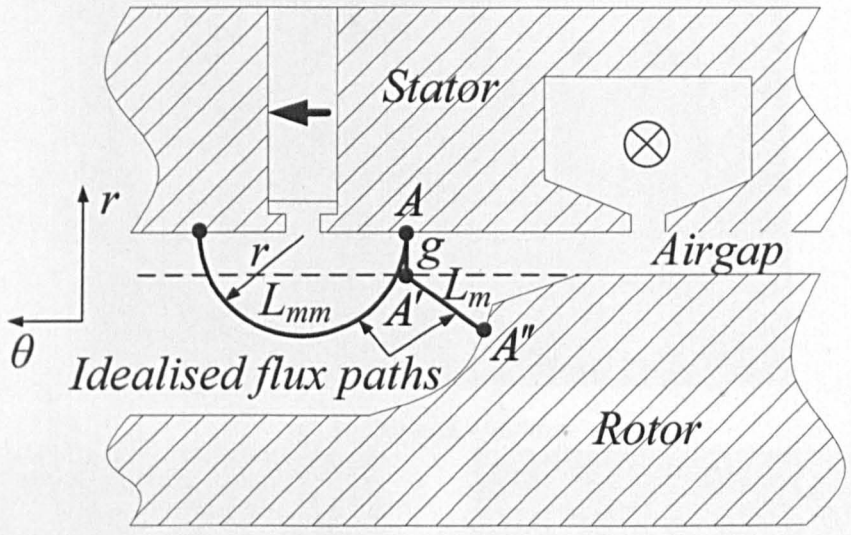

Figure 5.22 Definition of airgap flux path.

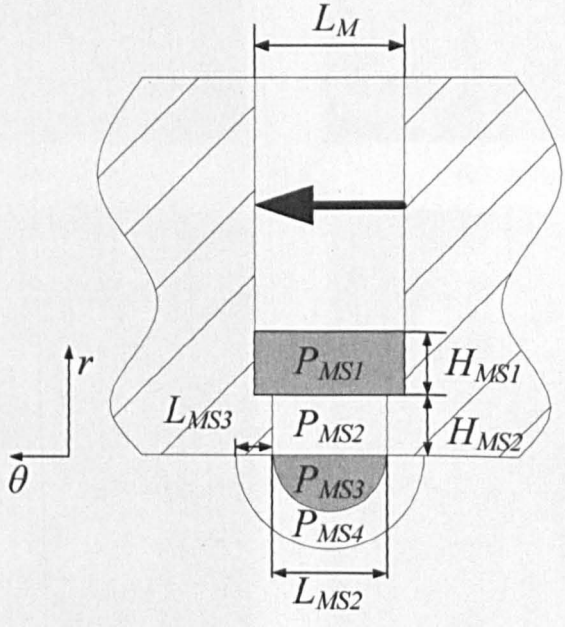

Figure 5.23 PM slot leakage-flux paths.

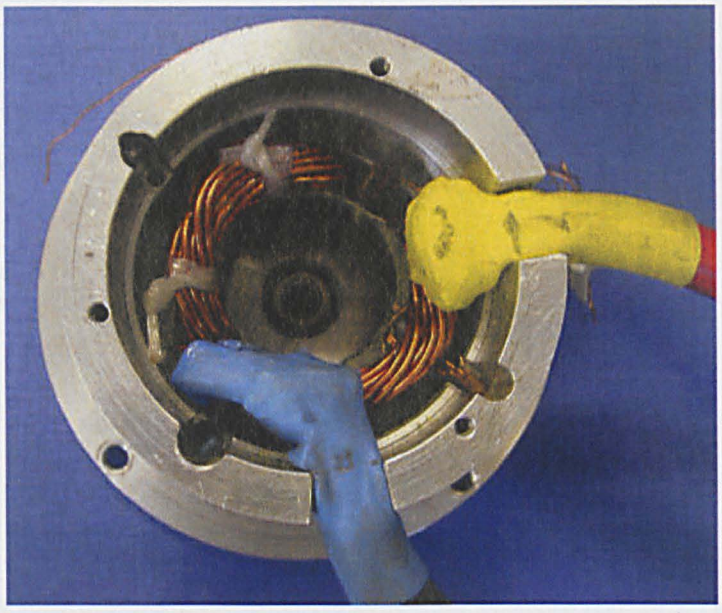

(a) Stator and windings

(b) Symmetric rotor

(c) Asymmetric rotor

(d) Symmetric rotor and stator laminations

(e) Asymmetric rotor and stator laminations

Figure 5.24 Prototypes of single-phase FSPM motors.

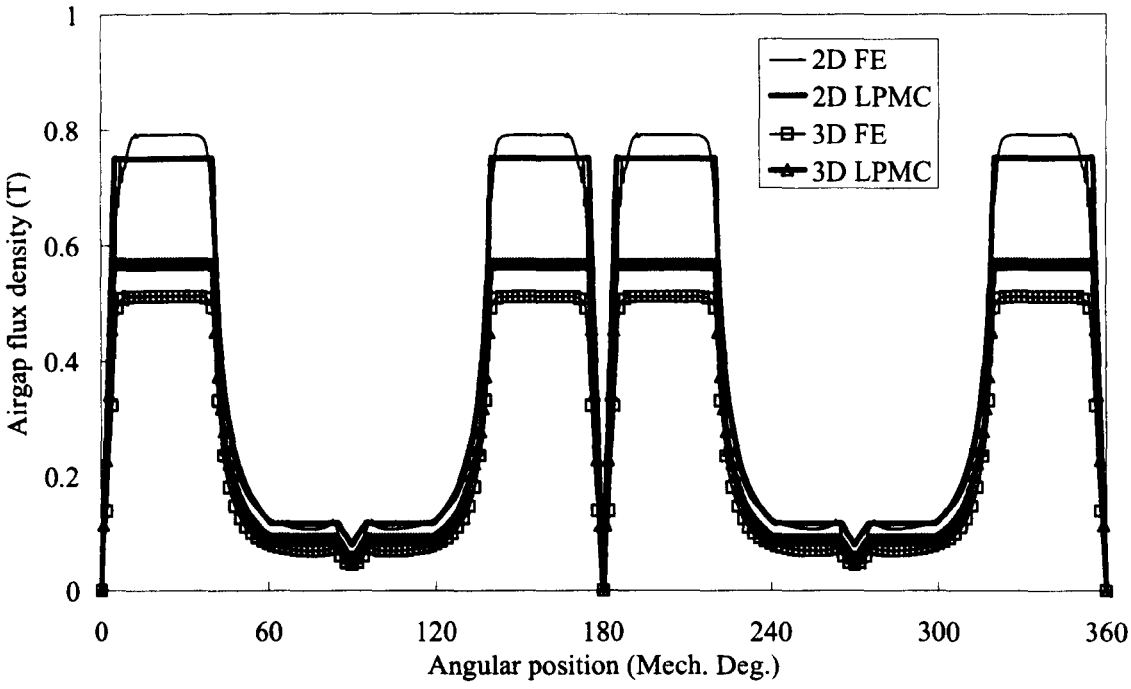

(a) Symmetric rotor

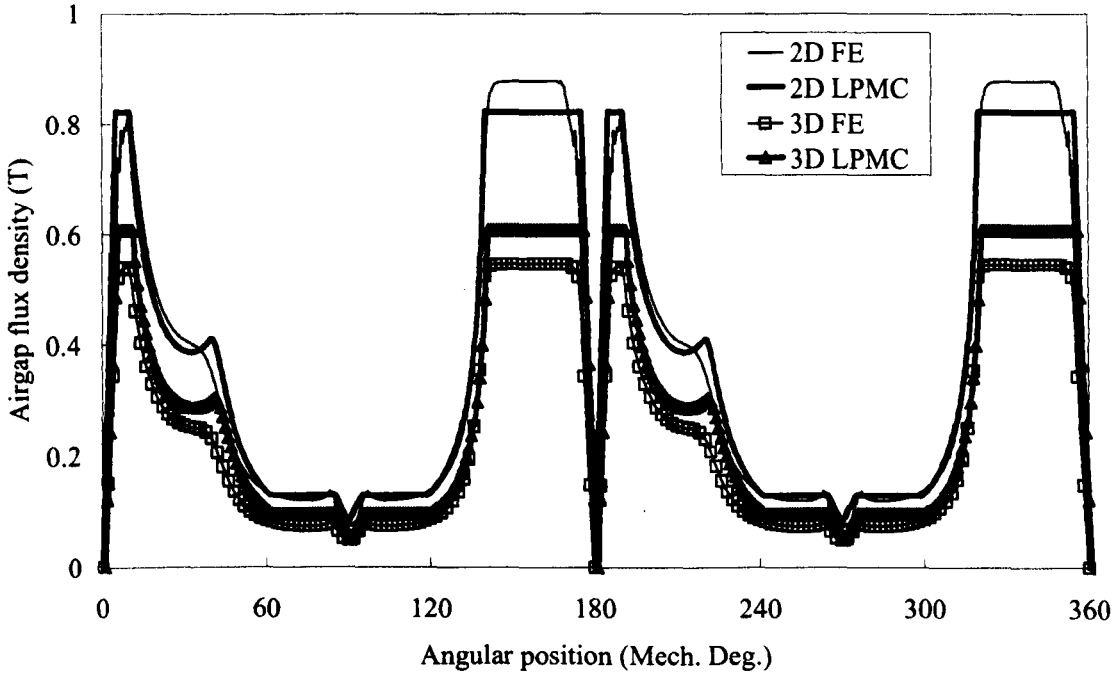

(b) Asymmetric rotor

Figure 5.25 LPMC model and FEM predicted open-circuit airgap flux density distribution (Rotor position=$0°_{mech}$).

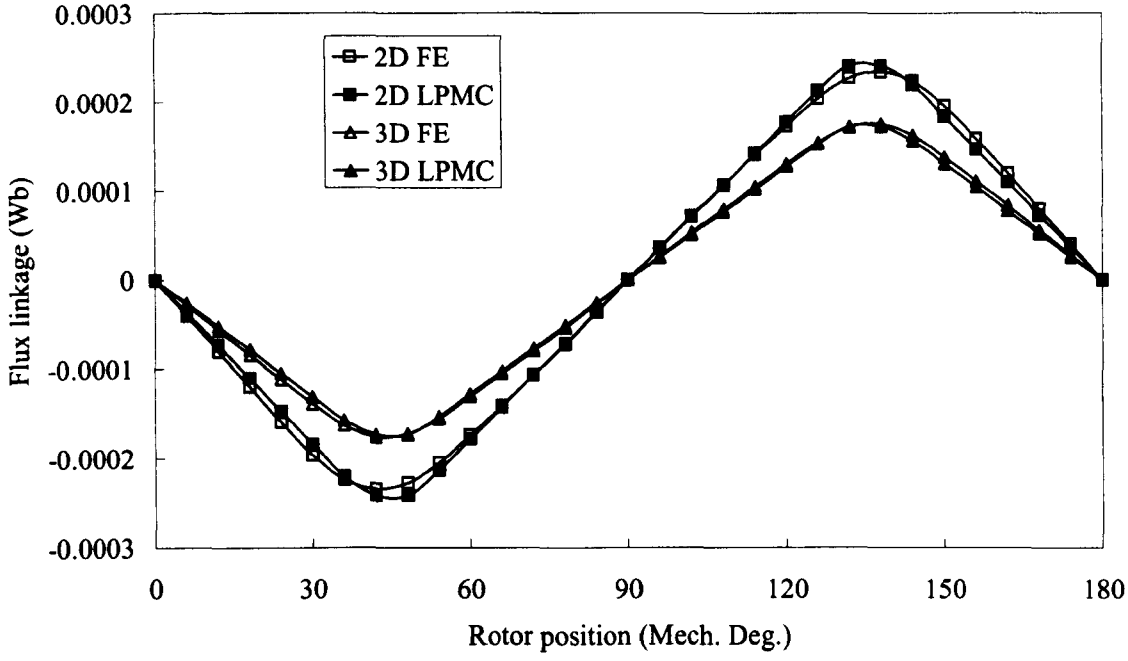

(a) Symmetric rotor

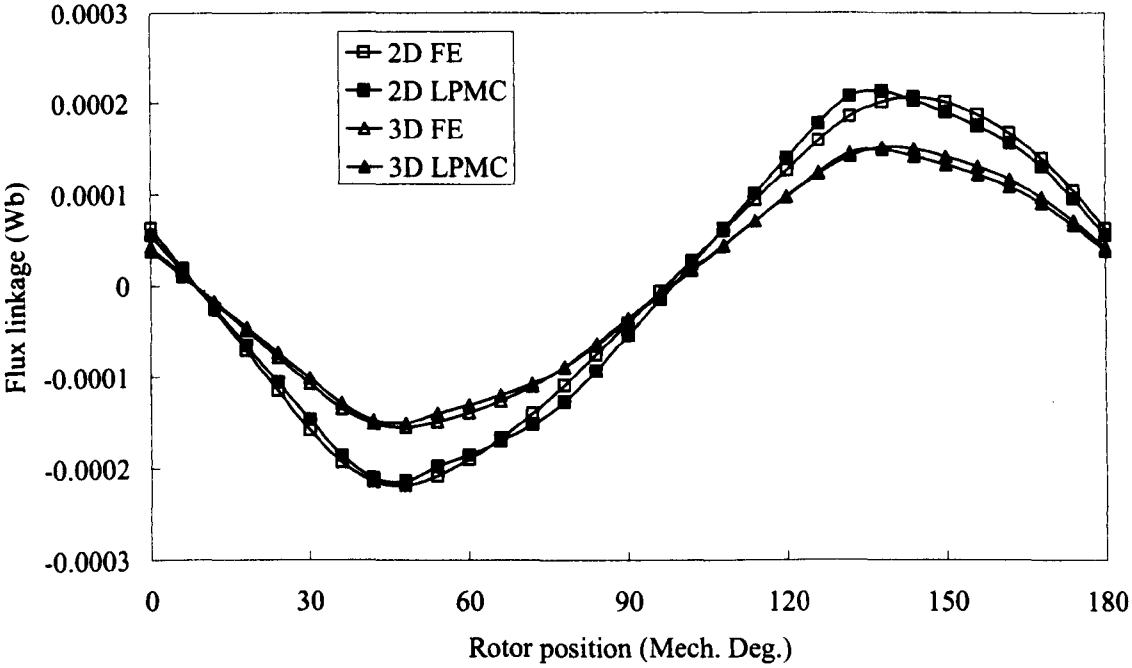

(b) Asymmetric rotor

Figure 5.26 LPMC model and FEM predicted open-circuit phase flux-linkage.

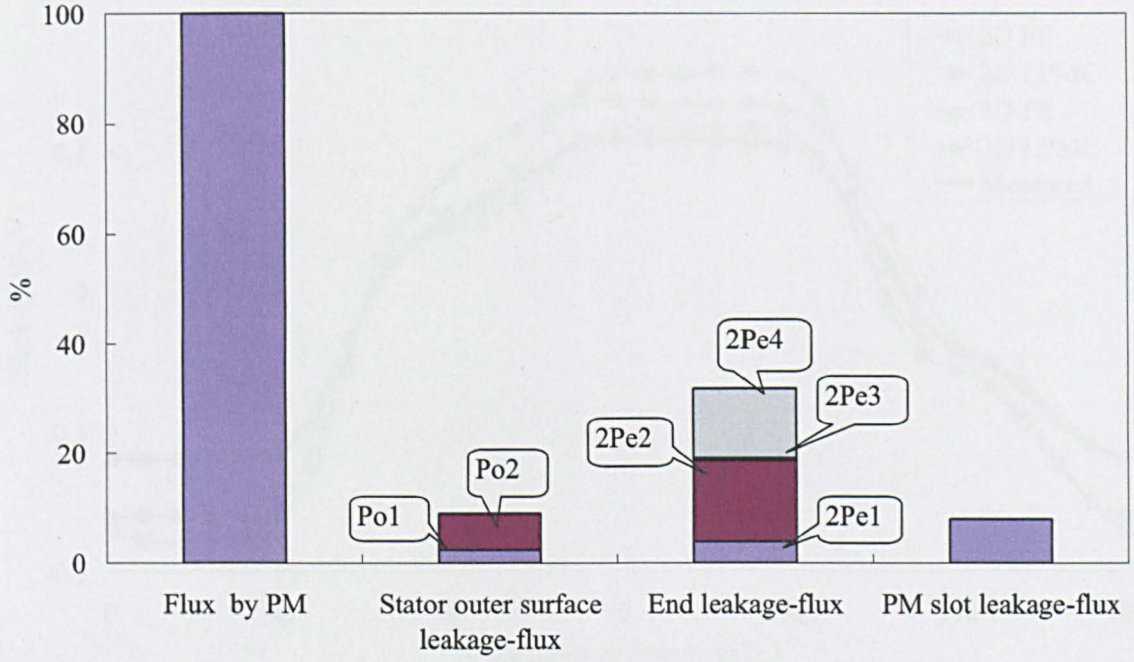

Figure 5.27 3D LPMC model predicted percentage of leakage-flux at rotor position of $0^{\circ}_{mech.}$ (Asymmetric rotor)

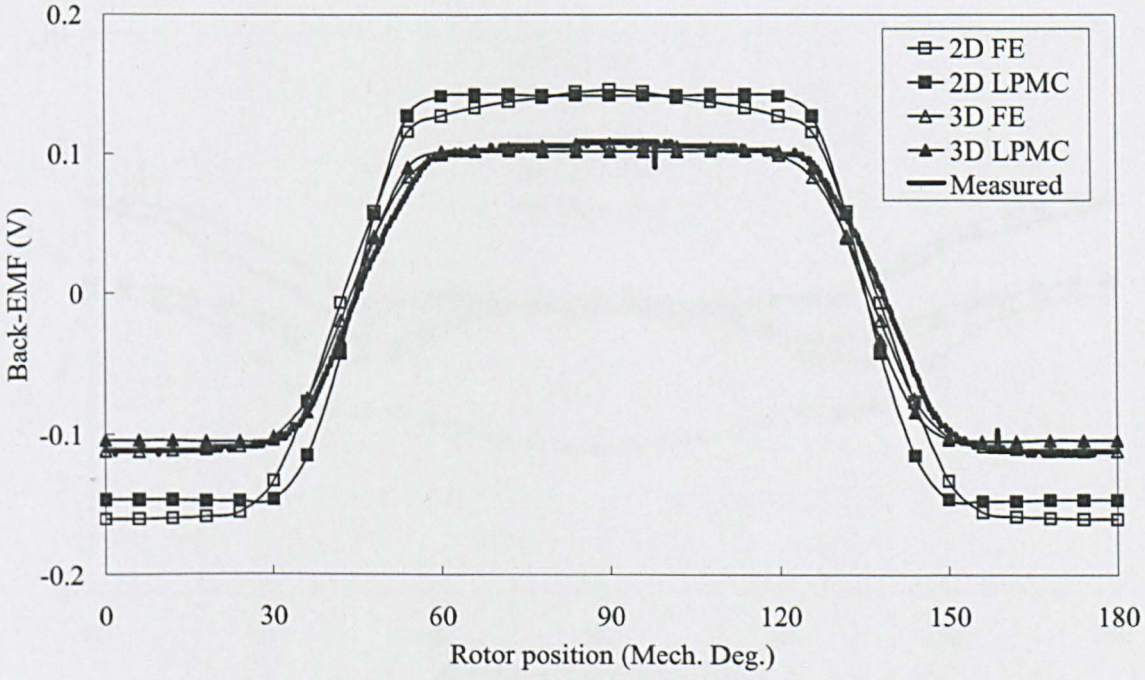

(a) Symmetric rotor

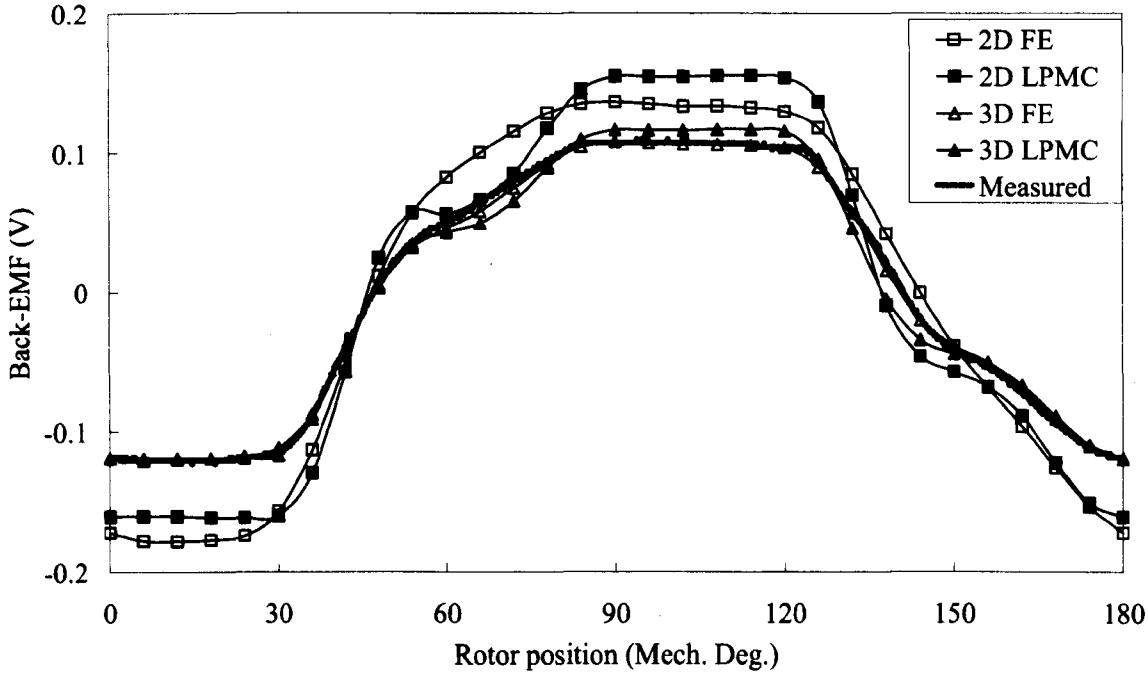

(b) Asymmetric rotor

Figure 5.28 LPMC model and FEM predicted and measured back-EMF waveforms (Speed=1krpm).

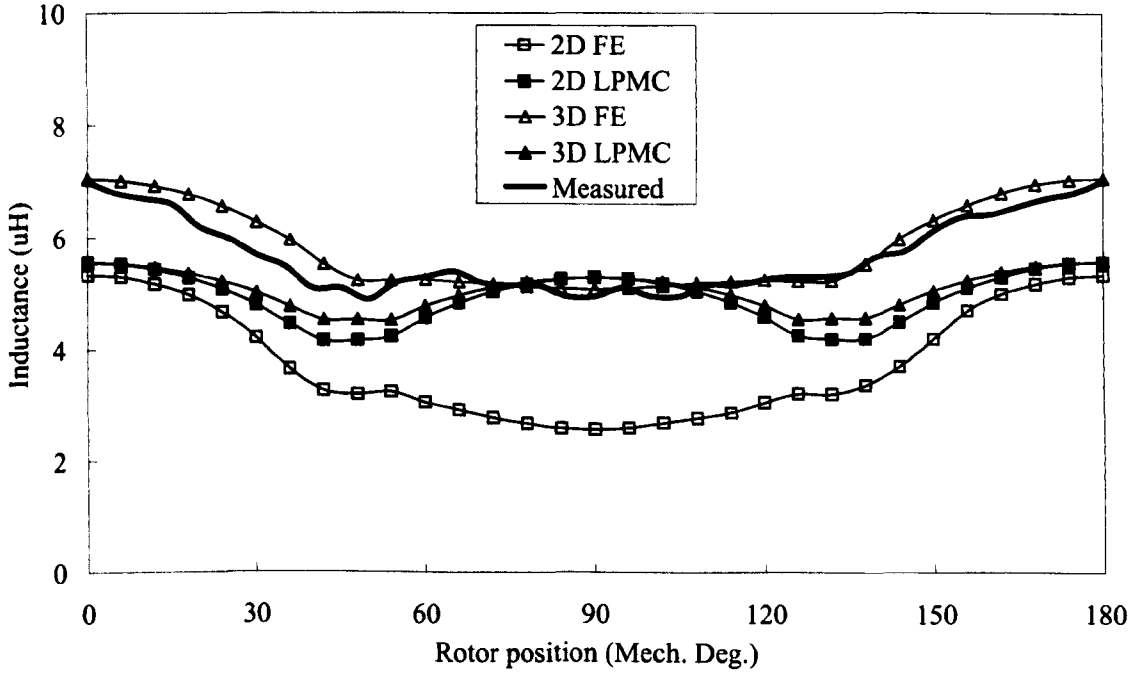

(a) Symmetric rotor

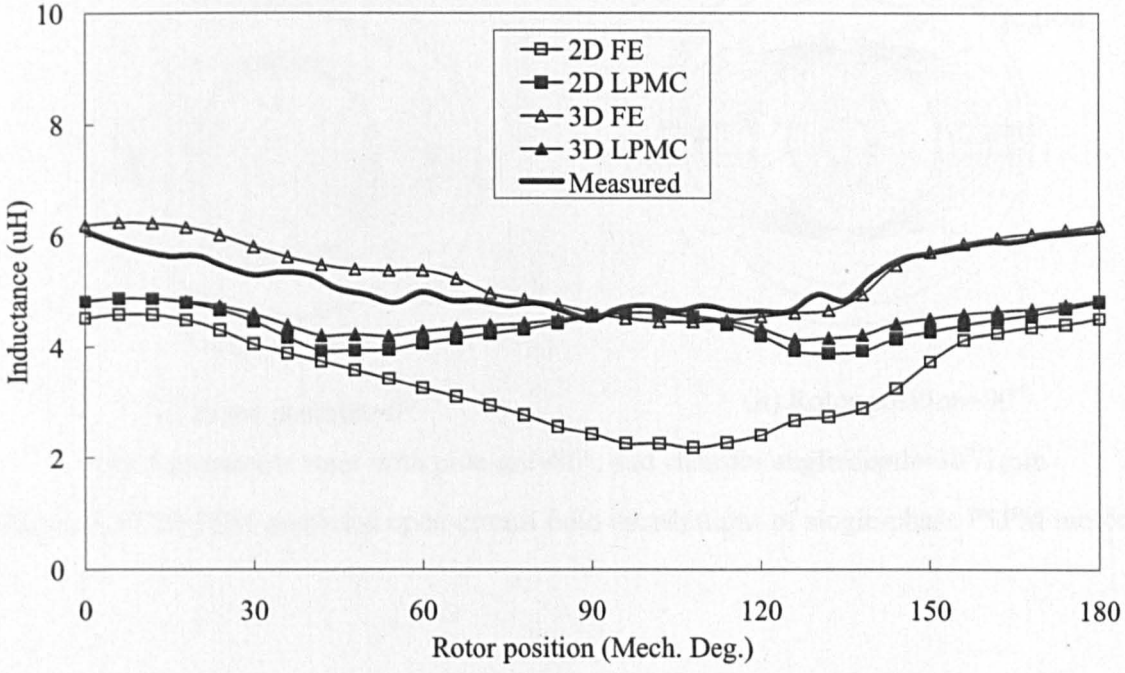

(b) Asymmetric rotor

Figure 5.29 LPMC model, FEM predicted and measured inductance waveforms.

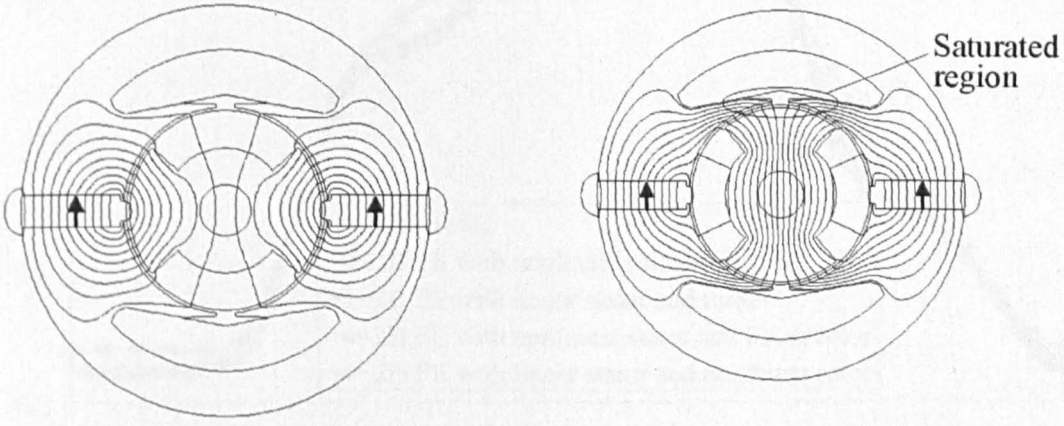

(i) Rotor position=0° (ii) Rotor position=90°

(a) Symmetric rotor with pole-arc=80°

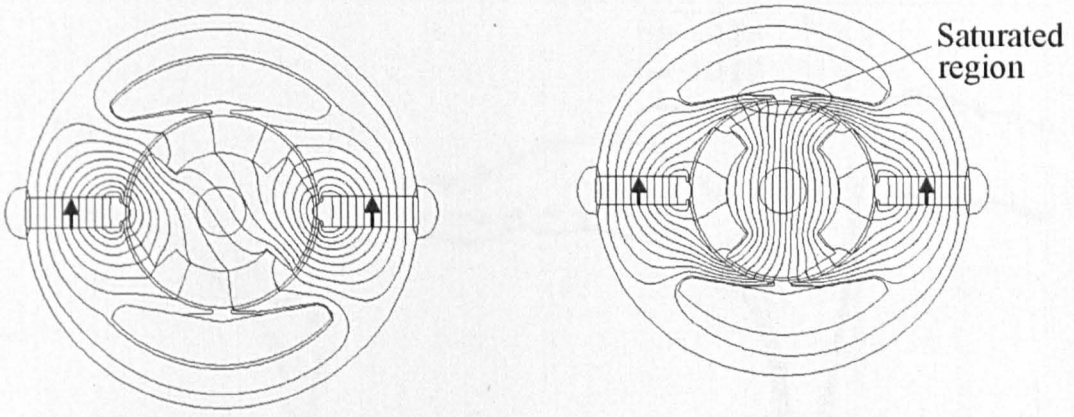

(i) Rotor position=0° (ii) Rotor position=90°

(b) Asymmetric rotor with pole-arc=80°, and chamfer angle/depth=30°/1mm

Figure 5.30 2D FEM predicted open-circuit field distributions of single-phase FSPM motors.

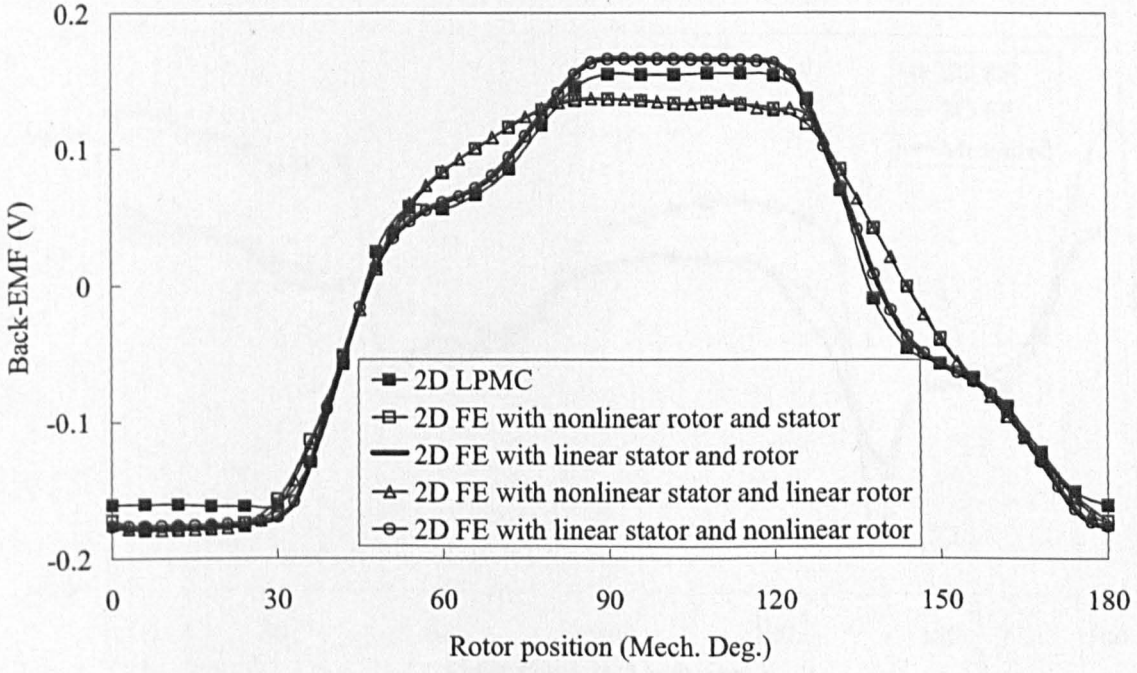

Figure 5.31 Comparison of back-EMF waveforms of single-phase FSPM motor with asymmetric rotor (Speed=1krpm).

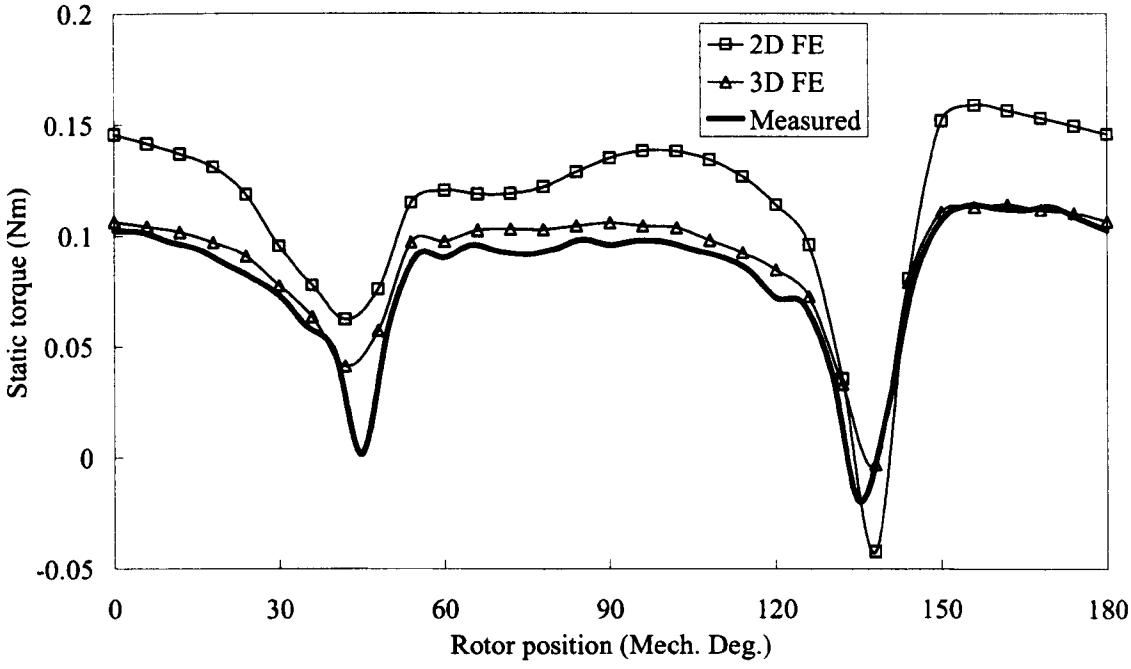

(a) Symmetric rotor

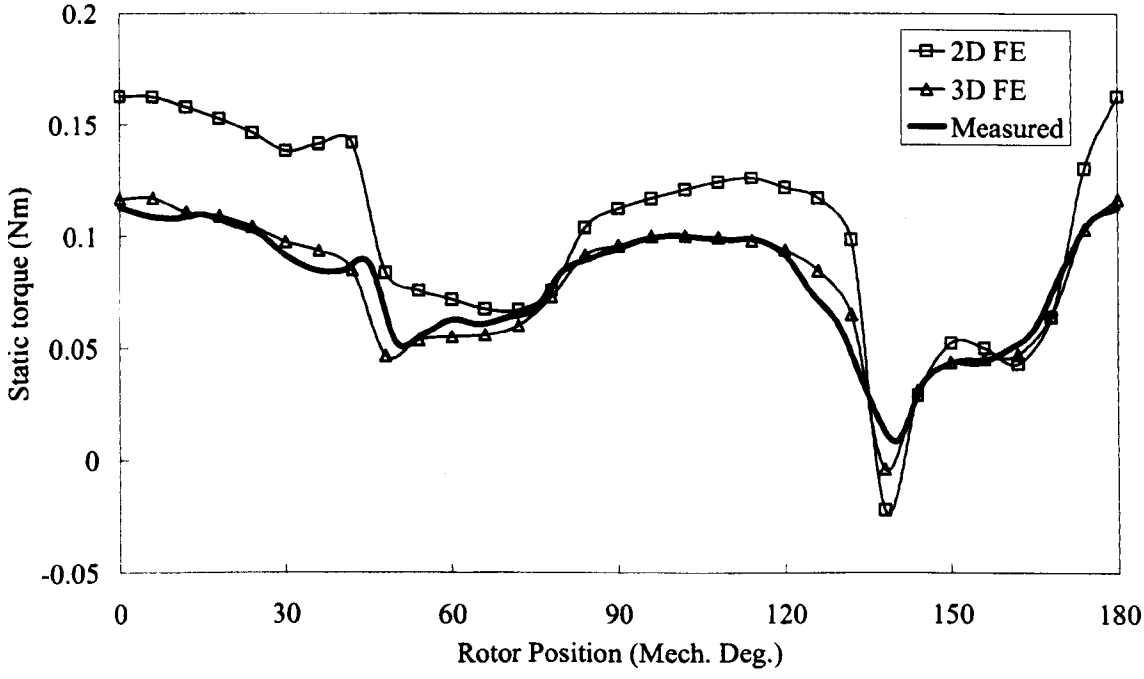

(b) Asymmetric rotor

Figure 5.32 Measured and FEM predicted static electromagnetic torque of single-phase FSPM motor (Current amplitude = 100A).

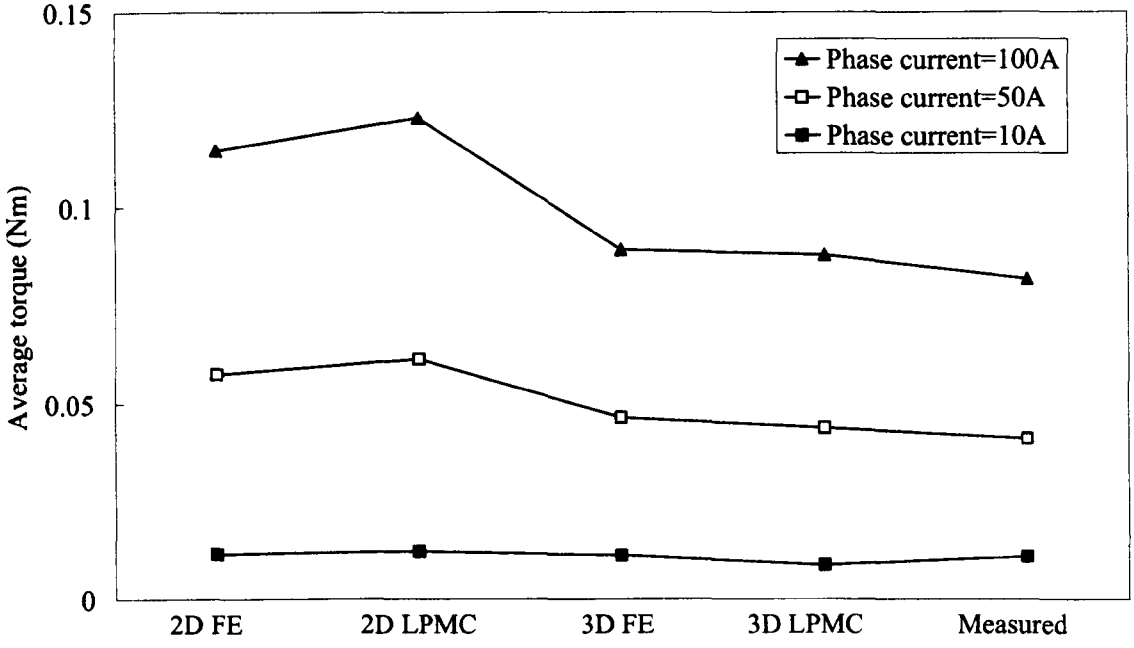

(a) Symmetric rotor

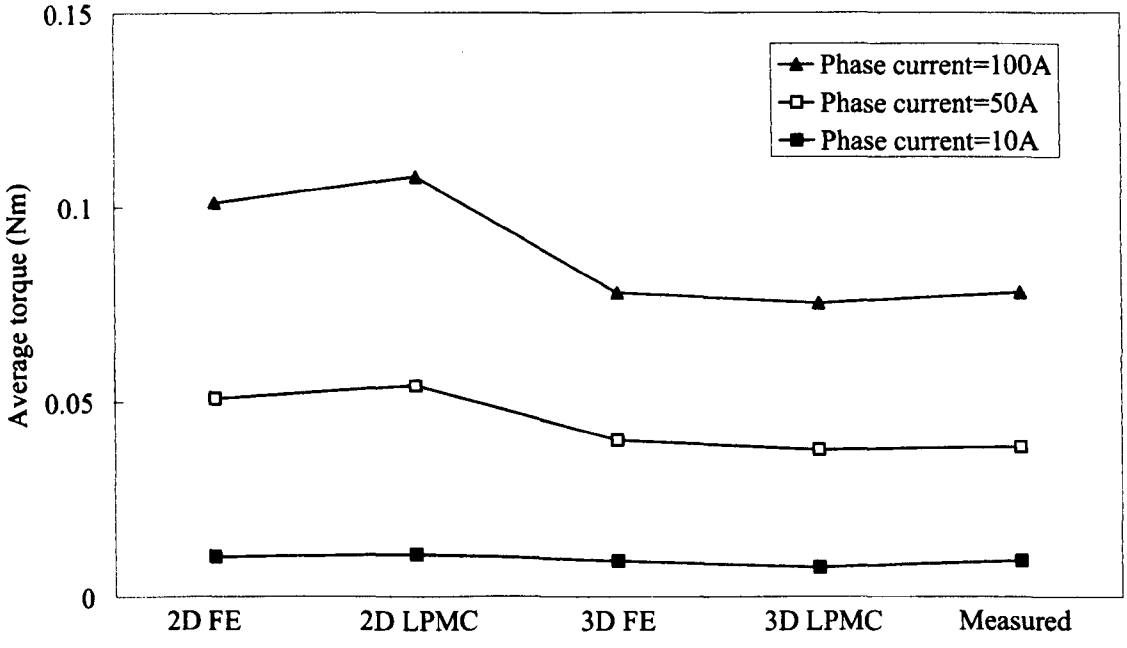

(b) Asymmetric rotor

Figure 5.33 LPMC model, FEM predicted and measured average static torque.

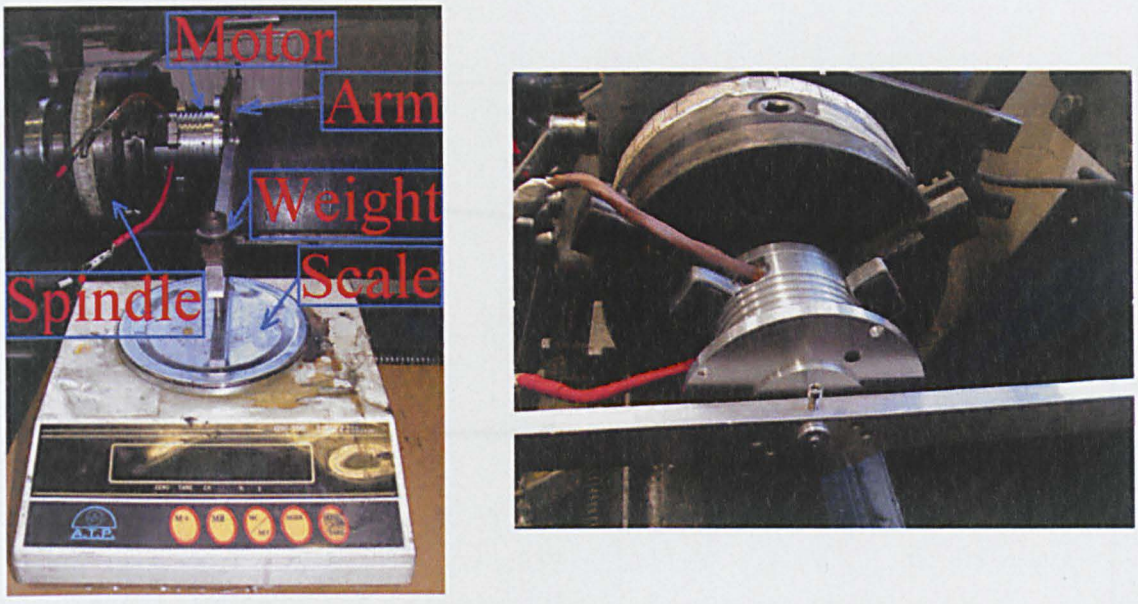

Figure 5.34 Static electromagnetic torque measurement instrumentations

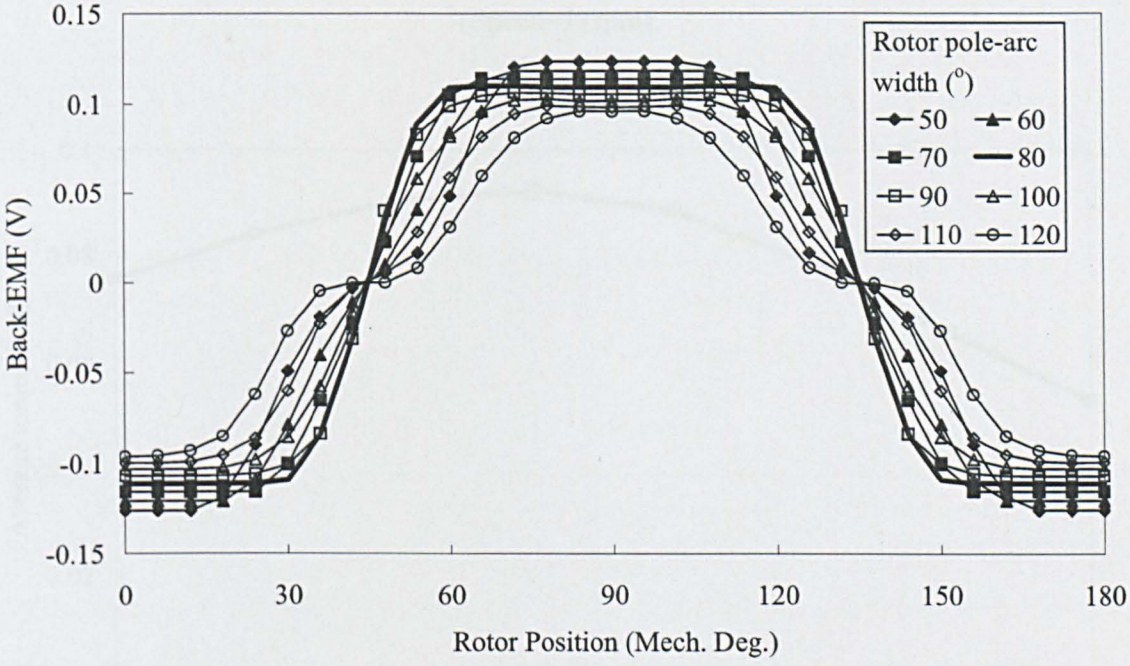

Figure 5.35 Influence of rotor pole-arc width on the back-EMF waveform (Speed=1krpm).

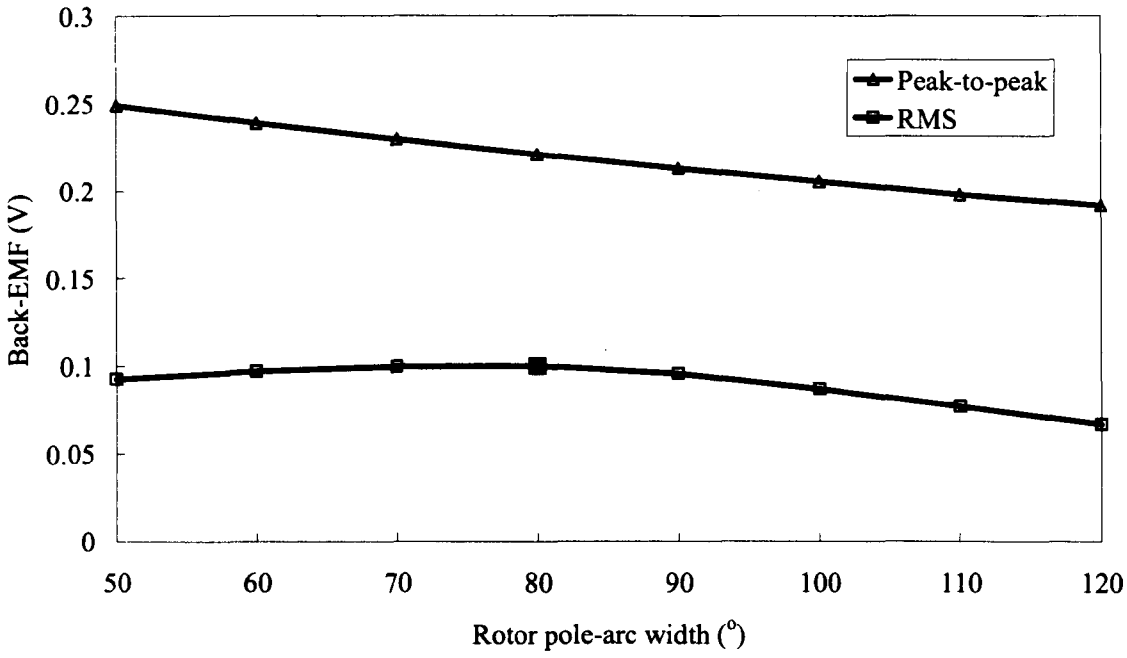

Figure 5.36 Influence of rotor pole-arc width on peak-to-peak and RMS value of back-EMF (Speed=1krpm).

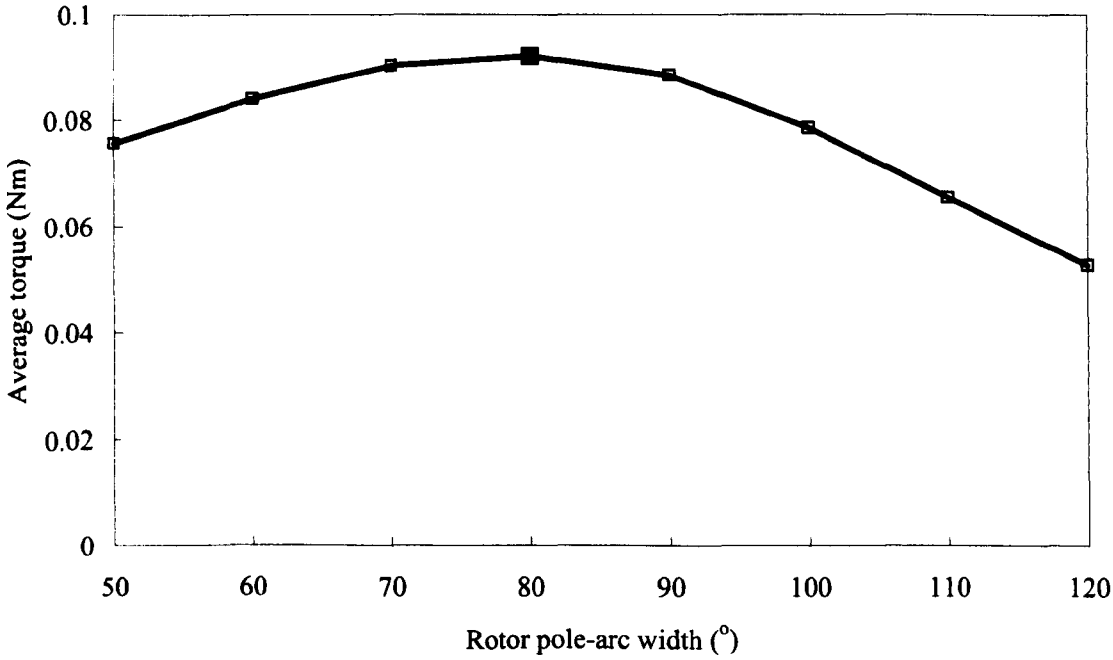

Figure 5.37 Influence of rotor pole-arc width on average torque.

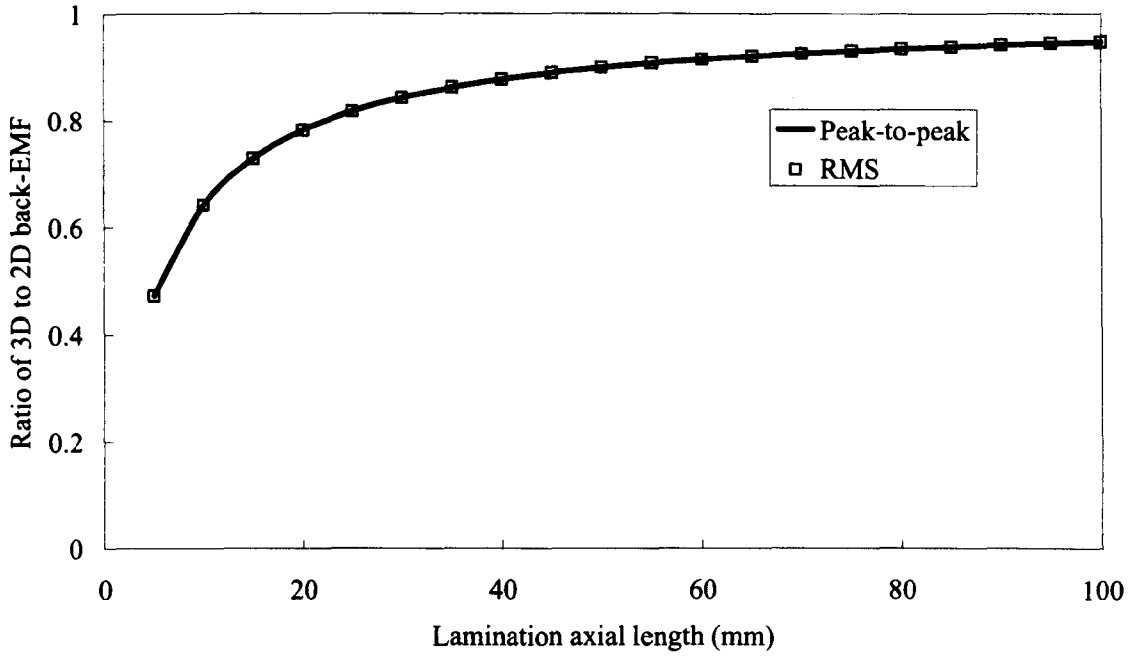

Figure 5.38 Influence of motor lamination axial length on ratio of 3D to 2D back-EMF.

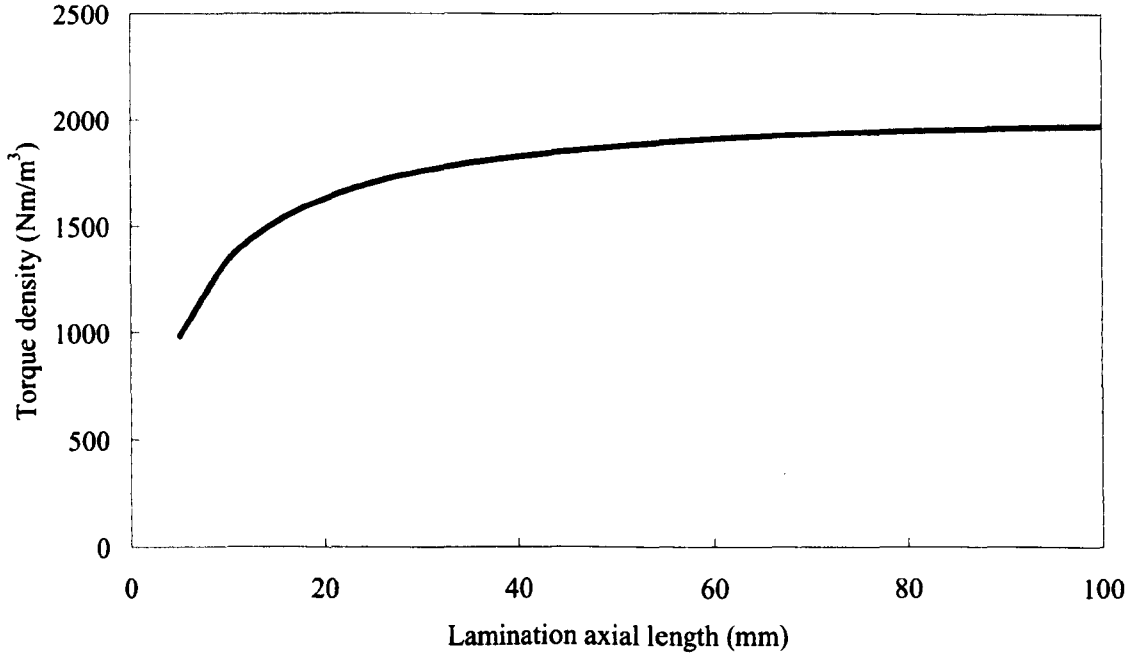

Figure 5.39 3D LPMC model predicted influence of motor lamination axial length on torque density.

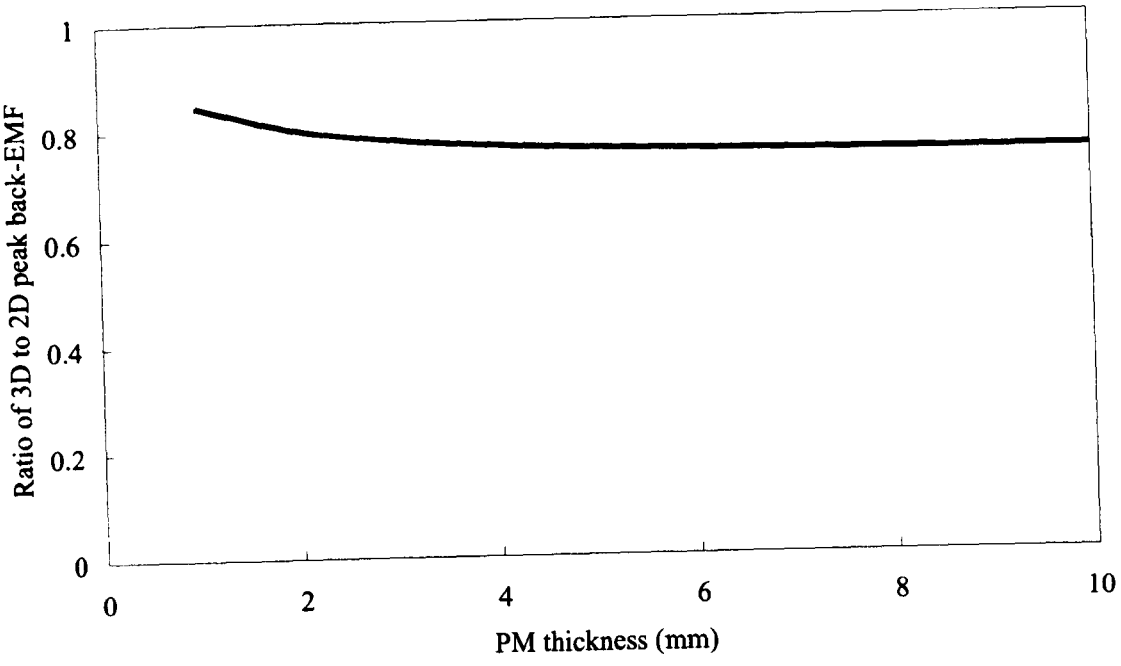

(a) PM thickness (PM radial length=14mm)

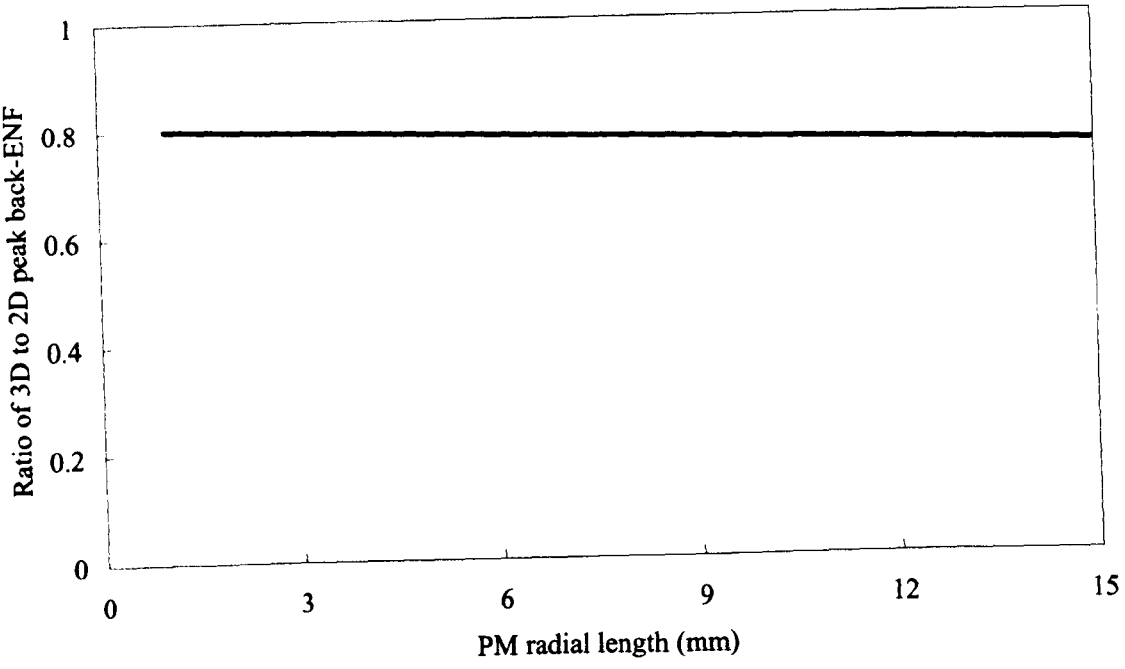

(b) Magnet radial length (PM thickness=5mm)

Figure 5.40 Influence of permanent magnet dimensions on ratio of 3D to 2D back-EMF.

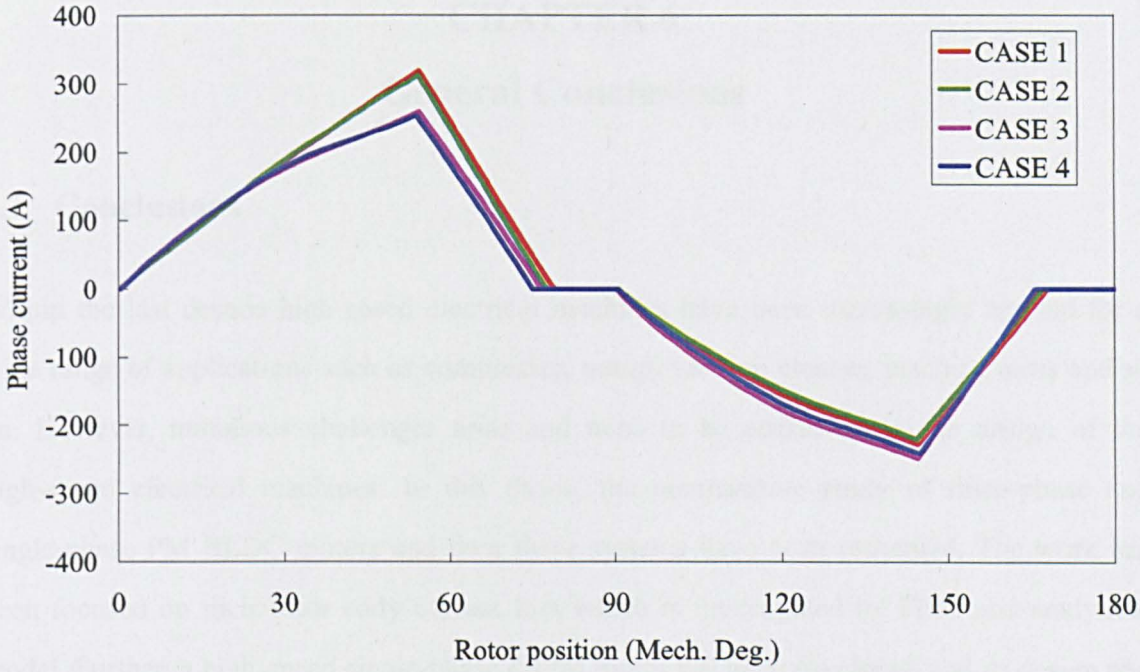

Figure 5.41 Comparison of simulated phase current waveforms.

CHAPTER 6

General Conclusions

6.1 Conclusions

Within the last decade high-speed electrical machines have been increasingly applied for a wide range of applications such as compressor, pump, vacuum cleaner, machine tools and so on. However, numerous challenges arise and need to be addressed in the design of the high-speed electrical machines. In this thesis, the comparative study of three-phase and single-phase PM BLDC motors and their drive systems have been presented. The work has been focused on their rotor eddy current loss which is investigated by FEM and analytical model. Further, a high-speed single-phase FSPM motor has been developed and its design and performance are described.

In Chapter 2, a three-phase 2-pole/3-slot PM BLDC motor and a single-phase 2-pole/2-slot PM BLDC motor having tapered airgap were designed, analysed and constructed. The stator iron loss and rotor eddy current loss have been predicted by the FEM. A simplified analytical model has been derived to find the optimal split ratio of rotor to stator diameter of the single-phase PM BLDC motor. The single-phase PM BLDC motor can be driven by either full-bridge inverter or half-bridge inverter if the bifilar windings are employed. Their dynamic simulation models have been developed to investigate the dynamic performance with due account of the stator and rotor losses. Compared to the measured phase current and speed, it is found that by considering the stator and rotor losses in the simulation, the simulated results agree better with the measured results. It has also been found that together with the phase current the eccentric airgap of single-phase PM BLDC motor plays an important role in the rotor eddy current loss, and consequently the single-phase motor has relatively lower rotor eddy current loss but higher stator iron loss than the three-phase motor on the rated load. Finally, the overall performance comparison of three-phase and single-phase motors has been presented. It shows that three-phase PM BLDC motor has relatively higher power density and less torque ripple but required more electronic devices than single-phase PM BLDC motor.

Since the rotor eddy current loss is increasing significantly as the motor rotating speed increases, the demagnetisation of the PM becomes a concern. Hence, the rotor eddy current loss needs to be investigated at the motor design stage. Due to the relatively small stator slotting and concentric airgap, the open-circuit rotor eddy current loss of the three-phase PM BLDC motor can be negligible. Hence, the rotor eddy current loss due to the armature mmfs becomes dominant. In Chapter 3, by a static analytical model has been developed to predict the armature rotor eddy current loss for three-phase PM BLDC motor and validated by the FEM. Good agreement was obtained at low speed range (<30krpm). However, at high speed range the rotor eddy current loss is significantly overestimated by the static analytical model due to its neglecting the eddy current reaction field. Hence, an improved analytical model has been developed to predict the armature rotor eddy current loss with due account for the eddy current reaction field and validated by the FEM. Good agreement is obtained within full-speed range. In both static and improved analytical models, the winding current is represented by an equivalent current sheet distributed across the stator slot openings to account for the space and time harmonics of the stator mmfs.

Similar technology has been employed to develop the static and improved analytical models to predict the armature rotor eddy current loss of the single-phase PM BLDC motor which has the concentric airgap. Again, the improved analytical model can predict the armature rotor eddy current loss more accurately as validated by the FEM. However, due to the complicated expressions for the boundary condition at the interface between the stator inner bore and airgap in the 2D polar coordinates, this technology is not suitable for the single-phase PM BLDC motor having eccentric airgap. Modified static and improved analytical models, where the boundary conditions at the middle of the airgap were obtained by FEM, have been developed for calculating the armature rotor eddy current loss of the single-phase PM BLDC motor which has either concentric or eccentric airgap. As validated by the FEM, modified improved analytical models can accurately predict the armature rotor eddy current loss over the full speed range.

However, single-phase PM BLDC motor with eccentric airgap has significant airgap permeance harmonics. Consequently considerable open-circuit eddy current loss exists and cannot be predicted by the analytical model. Further, the on-load rotor eddy current loss is affected by the eccentric airgap and phase current and cannot be predicted by the analytical model as well. In addition, the segmented magnets and end effect cannot be modelled in the analytical model. Hence, FEM was employed to investigate the open-circuit, armature and on-load rotor eddy current loss of single-phase and three-phase PM BLDC motors in Chapter 4, with particular emphasis on the single-phase motor. It has been found:

- Unlike the three-phase PM BLDC motor, the single-phase PM BLDC has much less on-load rotor eddy current loss than its open-circuit and armature rotor eddy current loss due to its eccentric airgap.
- An optimal combination of eccentric arigap and phase current exists for a minimum on-load rotor eddy current loss.
- Radially magnetized PM introduces more open-circuit and on-load rotor eddy current loss than the diametrically magnetized PM.
- As the number of circumferential diametrically magnetized magnet segments increases, the rotor eddy current loss can be reduced gradually. However, it becomes less effective when a metallic sleeve is employed to contain the magnets.
- Due to that the magnetic field produced by the eddy current loss in the sleeve can smooth the varying field in the magnet as a magnetic shield, as the sleeve electrical conductivity increases, the eddy current loss in the magnet is reduced dramatically.
- For a given speed, i.e. 45,000rpm and a given sleeve material, i.e. stainless steel, as the sleeve thickness increases, the PM eddy current loss decreases gradually, but the sleeve and overall rotor eddy current loss increases gradually.

For the conventional high-speed PM BLDC motor which has the PM in the rotor, there are two special concerns: Firstly, significant centrifugal force may crack the magnets. Secondly, high temperature resulting from the significant rotor eddy current loss may cause irreversible demagnetisation of the PM. In order to overcome these potential problems, Chapter 5 focused on a single-phase FSPM motor which has the PM in the stator for high-speed applications. Its

operation principle was introduced. Three winding topologies, i.e. full-pitched, short-pitched and toroidal winding, have been investigated with due account for the torque capability at a given winding copper loss and the overall motor size. It has been found that short-pitched winding has the least torque capability and toroidal winding has the biggest motor size. In addition, shorter motor axial length prefers the full-pitched winding. As a single-phase motor, the chamfered rotor pole was employed and optimised to introduce the starting torque. During the investigation, it was also found that a significant end leakage-flux exists. Hence, a 3D LPMC model was developed to predict the motor back-EMF and inductance with due account for the end effect. By comparing with FEM and measurement results, LPMC model can predict the back-EMF very well. However, due to that the simple LPMC model neglects the iron saturation, there was an obvious discrepancy in terms of the inductance prediction. LPMC model was employed to optimise the rotor pole width for increasing the motor power density. It was also used to investigate the influence of the magnet dimensions on the motor end effect. Finally, the dynamic simulation model was developed to investigate its dynamic performance.

6.2 Suggestions for future work

Firstly, the simplified analytical model for the optimum split ratio of the single-phase PM BLDC motor as described in Chapter 2 neglects the stator iron loss and rotor eddy current loss. However at high-speed condition, they may become dominant loss component rather than copper loss. Hence, analytical model needs to be modified to take the stator iron loss and rotor eddy current loss into account for the optimum split ratio when the motor is operating at high speed.

Secondly, the influence of the control strategies such as phase commutation advance and commutation pulse control [97] on the stator iron loss and rotor eddy current loss needs to be investigated for improving the motor efficiency.

Thirdly, the analytically predicted rotor eddy current loss of three-phase and single-phase PM BLDC motors has only been validated by FEM. They need to be further experimentally validated.

Fourthly, the iron loss and PM eddy current loss of the high-speed single-phase FSPM motor need to be investigated.

Fifthly, due to its flux focusing, the FSPM motor is more likely to be saturated. Further, it has doubly salient structure. Hence, its inductance is dependent of not only the phase current but also the rotor position. Hence, a 2D inductance is required for the dynamic simulation to improve the simulation accuracy.

Finally, for the low supply voltage applications, the voltage drop on the MOSFETs/IGBTs cannot be neglected. Hence, the inverter conducting loss and switching loss need to be modelled properly in the dynamics simulation model, particularly at high-speed.

REFERENCES

[1] Z. Q. Zhu, K. Ng and D. Howe, "Design and analysis of high-speed brushless permanent magnet motors," in *Electrical Machines and Drives, 1997 Eighth International Conference on (Conf. Publ. No. 444)*, pp. 381-385, 1997.

[2] J. C. Rama and A. Gieseche, "High-speed electric drives: technology and opportunity," *Industry Applications Magazine, IEEE,* vol. 3, no. 5, pp. 48-55, 1997.

[3] W. L. Soong, G. B. Kliman, R. N. Johnson, R. A. White and J. E. Miller, "Novel high-speed induction motor for a commercial centrifugal compressor," *Industry Applications, IEEE Transactions on,* vol. 36, no. 3, pp. 706-713, 2000.

[4] M. Mekhiche, J. L. Kirtley, M. Tolikas, E. Ognibene, J. Kiley, E. Holmansky and F. Nimblett, "High speed motor drive development for industrial applications," in *Electric Machines and Drives, 1999. International Conference IEMD '99*, pp. 244-248, 1999.

[5] J. Pyrhönen, J. Nerg, A. Mikkola, J. Sopanen and T. Aho, "Electromagnetic and mechanical design aspects of a high-speed solid-rotor induction machine with no separate copper electric circuit in the megawatt range," *Electr Eng,* pp. 35-49, 2009.

[6] J. R. Bumby, E. S. Spooner, J. Carter, H. Tennant, G. G. Mego, G. Dellora, W. Gstrein, H. Sutter and J. Wagner, "Electrical machines for use in electrically assisted turbochargers," in *Power Electronics, Machines and Drives, 2004. (PEMD 2004). Second International Conference on (Conf. Publ. No. 498)*, vol. 1, pp. 344-349, 2004.

[7] M. Ikeda, S. Sakabe and K. Higashi, "Experimental study of high speed induction motor varying rotor core construction," *Energy Conversion, IEEE Transactions on,* vol. 5, no. 1, pp. 98-103, 1990.

[8] N. D. Sharma, R. Anbarasu, J. Nataraj, A. Y. Dangore and B. Bhattacharjee, "Experimental investigations on high speed solid and composite rotor induction motor," in *Power Electronics, Drives and Energy Systems for Industrial Growth, 1996., Proceedings of the 1996 International Conference on*, vol. 2, pp. 913-919, 1996.

[9] H. Walter, A. Moehle and M. Bade, "Asynchronous solid rotors as high-speed drives in the megawatt range," in *Petroleum and Chemical Industry Technical Conference, 2007. PCIC '07. IEEE*, pp. 1-8, 2007.

[10] T. Fukao, A. Chiba and M. Matsui, "Test results on a super-high-speed amorphous-iron reluctance motor," *Industry Applications, IEEE Transactions on,* vol. 25, no. 1, pp. 119-125, 1989.

[11] S. D. Calverley, G. W. Jewell and R. J. Saunders, "Aerodynamic losses in switched reluctance machines," *Electric Power Applications, IEE Proceedings -*, vol. 147, no. 6, pp. 443-448, 2000.

[12] M. El Hadi Zaim, "High-Speed Solid Rotor Synchronous Reluctance Machine Design and Optimization," *Magnetics, IEEE Transactions on,* vol. 45, pp. M. El Hadi Zaim, "High-speed solid rotor synchronous reluctance machine design and optimization," *Magnetics, IEEE Transactions on,* vol. 45, no. 3, pp. 1796-1799, 2009.

[13] I. Boldea, Z. X. Fu and S. A. Nasar, "Performance evaluation of axially-laminated anisotropic (ALA) rotor reluctance synchronous motors," *Industry Applications, IEEE Transactions on,* vol. 30, no. 4, pp. 977-985, 1994.

[14] H. Hofmann and S. R. Sanders, "Synchronous reluctance motor/alternator for flywheel energy storage systems," in *Power Electronics in Transportation, 1996. IEEE*, pp. 199-206, 1996.

[15] H. Hofmann and S. R. Sanders, "High-speed synchronous reluctance machine with minimized rotor losses," *Industry Applications, IEEE Transactions on,* vol. 36, no. 2, pp. 531-539, 2000.

[16] S. R. MacMinn and W. D. Jones, "A very high speed switched-reluctance starter-generator for aircraft engine applications," in *Aerospace and Electronics Conference, 1989. NAECON 1989., Proceedings of the IEEE 1989 National*, vol.4, pp. 1758-1764, 1989.

[17] K. De Brabandere, J. Driesen and R. Belmans, "The control of switched reluctance drives and their use for flywheel energy storage," *Proc. of IEEE Young Researchers Symposium in Electrical Power Engineering,* pp. 1-5, 2002.

[18] I. Takahashi, T. Koganezawa, W. Su and K. Ohyama, "A super high speed PM motor drive system by a quasi-current source inverter," *Industry Applications, IEEE Transactions on,* vol. 30, no. 3, pp. 683-690, 1994.

[19] N. Bianchi, S. Bolognani and F. Luise, "Analysis and design of a brushless motor for high speed operation," in *Electric Machines and Drives Conference, 2003. IEMDC'03. IEEE International*, vol.1, pp. 44-5, 2003.

[20] N. Bianchi, S. Bolognani and F. Luise, "Analysis and design of a PM brushless motor for high-speed operations," *Energy Conversion, IEEE Transactions on,* vol. 20, no. 3, pp. 629-637, 2005.

[21] J. Seok-Myeong, J. Sang-Sub, R. Dong-Wan and C. Sang-Kyu, "Comparison of three types of PM brushless machines for an electro-mechanical battery," *Magnetics, IEEE Transactions on,* vol. 36, no. 5, pp. 3540-3543, 2000.

[22] J. Seok-Myeong, J. Sang-Sub, R. Dong-Wan and C. Sang-Kyu, "Design and analysis of high speed slotless PM machine with Halbach array," *Magnetics, IEEE Transactions on,* vol. 37, no .4, pp.

2827-2830, 2001.

[23] Z. Q. Zhu and D. Howe, "Halbach permanent magnet machines and applications: a review," *Electric Power Applications, IEE Proceedings -*, vol. 148, no. 4, pp. 299-308, 2001.

[24] H. Polinder and M. J. Hoeijmakers, "Eddy-current losses in the segmented surface-mounted magnets of a PM machine," *Electric Power Applications, IEE Proceedings -*, vol. 146, no. 3, pp. 261-266, 1999.

[25] K. Yoshida, Y. Hita and K, kesamaru, "Eddy-current loss analysis in PM of surface-mounted-PM SM for electric vehicles," *Magnetics, IEEE Transactions on,* vol. 36, no. 4, pp. 1941-1944, 2000.

[26] H. Toda, Z. P. Xia, J. B. Wang, K. Atallah and D. Howe, "Rotor eddy-current loss in permanent magnet brushless machines," *Magnetics, IEEE Transactions on,* vol. 40, no. 4, pp. 2104-2106, 2004.

[27] K. Atallah, D. Howe, P. H. Mellor and D. A. Stone, "Rotor loss in permanent-magnet brushless AC machines," *Industry Applications, IEEE Transactions on,* vol. 36, no. 6, pp. 1612-1618, 2000.

[28] B. P. James and B. A. T. Al Zahawi, "A high speed alternator for a small scale gas turbine CHP unit," in *Electrical Machines and Drives, 1995. Seventh International Conference on (Conf. Publ. No. 412)*, pp. 281-285, 1995.

[29] A. A. Pride and P. R. Evison, "100 to 140krpm PM motor / generators for EV applications," in *Electrical Machine Design for All-Electric and Hybrid-Electric Vehicles (Ref. No. 1999/196), IEE Colloquium on*, pp. 6/1-6/5, 1999.

[30] M. E. Leaver, B. C. Mecrow, A. G. Jack, A. Steven and K. E. Austin, "High-speed drives for mass market products," in *Power Electronics, Machines and Drives, 2006. PEMD 2006. The 3rd IET International Conference on*, pp. 586-590, 2006.

[31] M. Hippner and R. G. Harley, "Looking for an optimal rotor for high speed permanent magnet synchronous machine," in *Industry Applications Society Annual Meeting, 1992., Conference Record of the 1992 IEEE*, vol. 1, pp. 265-270, 1992.

[32] A. Binder, T. Schneider and M. Klohr, "Fixation of buried and surface-mounted magnets in high-speed permanent-magnet synchronous machines," *Industry Applications, IEEE Transactions on,* vol. 42, no. 4, pp. 1031-1037, 2006.

[33] L. Yuefeng, L. Feng and T. A. Lipo, "A novel permanent magnet motor with doubly salient structure," *Industry Applications, IEEE Transactions on,* vol. 31, no. 5, pp. 1069-1078, 1995.

[34] I. Boldea, J. C. Zhang and S. A. Nasar, "Theoretical characterization of flux reversal machine in low-speed servo drives-the pole-PM configuration," *Industry Applications, IEEE Transactions on,*

vol. 38, no. 6, pp. 1549-1557, 2002.

[35] K. Tae Heoung and L. Ju, "A study of the design for the flux reversal machine," *Magnetics, IEEE Transactions on,* vol. 40, no. 4, pp. 2053-2055, 2004.

[36] W. Hua, Z. Q. Zhu, M. Cheng, Y. Pang and D. Howe, "Comparison of flux-switching and doubly-salient permanent magnet brushless machines," in *Electrical Machines and Systems, 2005. ICEMS 2005. Proceedings of the Eighth International Conference on*, vol. 1, pp. 165-170, 2005.

[37] A. Thomas, Z. Q. Zhu, G. W. Jewell and D. Howe, "Flux-switching PM brushless machines with alternative stator and rotor pole combinations," in *Electrical Machines and Systems, 2008. ICEMS 2008. International Conference on*, pp. 2986-2991, 2008.

[38] Y. Pang, Z. Q. Zhu, D. Howe, S. Iwasaki, R. Deodhar and A. Pride, "Comparative study of flux-switching and interior permanent magnet machines," in *Electrical Machines and Systems, 2007. ICEMS. International Conference on*, pp. 757-762, 2007.

[39] K. B. Jang, W. Sung Hong, K. Tae Heoung and L. Ju, "Starting and high-speed driving of single-phase flux-reversal motor for vacuum cleaner," *Magnetics, IEEE Transactions on,* vol. 41, no. 10, pp. 3967-3969, 2005.

[40] S. C. LaGrone, M. C. Griggs and M. Bressani, "Application of a 5500 RPM high speed induction motor and drive in a 7000 HP natural gas compressor installation," in *Petroleum and Chemical Industry Conference, 1992, Record of Conference Papers., Industry Applications Society 39th Annual*, pp. 141-146, 1992.

[41] D. C. Gilon, "Design and tests of a 6 MW, 10000 RPM induction motor," in *Electrical Machines and Drives, 1991. Fifth International Conference on (Conf. Publ. No. 341)*, pp. 6-10, 1991.

[42] M. Ahrens, U. Bikle, R. Gotkehaskamp and H. Prenner, "Electrical design of high-speed induction motors of up to 15 MW and 20000 RPM," in *Power Electronics, Machines and Drives, 2002. International Conference on (Conf. Publ. No. 487)*, pp. 381-386, 2002.

[43] M. I. Lamghari-Jamal, J. Fouladgar, E. H. Zaim and D. Trichet, "A magneto-thermal study of a high-speed synchronous reluctance machine," *Magnetics, IEEE Transactions on,* vol. 42, no. 4, pp. 1271-1274, 2006.

[44] http://www.dyson.co.uk/technology/handDryerTech.asp

[45] D. E. Hesmondhalgh, D. Tipping and M. Amrani, "Design and construction of a high-speed high-performance direct-drive handpiece," *Electric Power Applications, IEE Proceedings B,* vol. 134, no. 6, pp. 286-296, 1987.

[46] www.dyson.co.uk/technology/motorTech/default.asp?panel=faster`#ddmSelection

[47] B. A. T. Al Zahawi, B. P. James and F. Starr, "High speed turboalternator for domestic combined heat and power unit," in *Electrical Machines and Drives, 1997 Eighth International Conference on (Conf. Publ. No. 444)*, pp. 215-218, 1997.

[48] K. Miyashita, S. Yamashita, S. Tanabe, T. Shimozu and H. Sento, "Development of a high speed 2-pole permanent magnet synchronous motor," *Power Apparatus and Systems, IEEE Transactions on*, vol. PAS-99, no. 6, pp. 2175-2183, 1980.

[49] J. D. Ede, Z. Q. Zhu and D, Howe, "Design considerations for high-speed sensorless permanent magnet brushless DC motors," in *Power Electronics, Machines and Drives, 2004. (PEMD 2004). Second International Conference on (Conf. Publ. No. 498)*, vol. 2, pp. 686-690, 2004.

[50] J. Oyama, T. Higuchi, T. Abe, K. Shigematsu, X. Yang and E. Matsuo, "A trial production of small size ultra-high speed drive system," in *Electric Machines and Drives Conference, 2003. IEMDC'03. IEEE International*, vol. 1, pp. 31-36, 2003.

[51] Y. Honda, S. Yokote, T. Higaki and Y. Takeda, "Using the Halbach magnet array to develop an ultrahigh-speed spindle motor for machine tools," in *Industry Applications Conference, 1997. Thirty-Second IAS Annual Meeting, IAS '97., Conference Record of the 1997 IEEE*, vol. 1, pp. 56-60, 1997.

[52] M. Mekhiche, S. Nichols, J. L. Kirtley, J. Young, D. Boudreau and R. Jodoin, "High-speed, high-power density PMSM drive for fuel cell powered HEV application," in *Electric Machines and Drives Conference, 2001. IEMDC 2001. IEEE International*, pp. 658-663, 2001.

[53] B. Bon-Ho, S. Seung-Ki, K. Jeong-Hyeck and B. Ji-Seob, "Implementation of sensorless vector control for super-high-speed PMSM of turbo-compressor," *Industry Applications, IEEE Transactions on*, vol. 39, no. 3, pp. 811-818, 2003.

[54] T. J. E. Miller, "Single-phase permanent-magnet motor analysis," *Industry Applications, IEEE Transactions on*, vol. IA-21, no. 3, pp. 651-658, 1985.

[55] K. Kurihara and M. A. Rahman, "High-efficiency line-start interior permanent-magnet synchronous motors," *Industry Applications, IEEE Transactions on*, vol. 40, no. 3, pp. 789-796, 2004.

[56] V. Ostovic, "Performance comparison of U-Core and round-stator single-phase permanent-magnet motors for pump applications," *Industry Applications, IEEE Transactions on*, vol. 38, no. 2, pp. 476-482, 2002.

[57] S. Bentouati, Z. Q. Zhu and D. Howe, "Permanent magnet brushless DC motors for consumer products," in *Electrical Machines and Drives, 1999. Ninth International Conference on (Conf. Publ. No. 468)*, pp. 118-122, 1999.

[58] D. R. Huang, C. Y. Fan, S. J. Wang, H. P. Pan, T. F. Ying, C. M. Chao and E. G. Lean, "A new type single-phase spindle motor for HDD and DVD," *Magnetics, IEEE Transactions on,* vol. 35, no. 2, pp. 839-844, 1999.

[59] J. S. Mayer and O. Wasynczuk, "Analysis and modeling of a single-phase brushless DC motor drive system," *Energy Conversion, IEEE Transactions on,* vol. 4, no. 3, pp. 473-479, 1989.

[60] D. Bian and Q. Zhan, "A novel single phase doubly salient permanent magnet motor," in *Power Electronics and Drive Systems, 1999. PEDS '99. Proceedings of the IEEE 1999 International Conference on*, vol. 2, pp. 725-729, 1999.

[61] L. Iepure, L. Tutelea and I. Boldea, "FEM analysis and control of a tapered airgap single phase PMSM," in *Optimization of Electrical and Electronic Equipment, 2008. OPTIM 2008. 11th International Conference on*, pp. 241-248, 2008.

[62] M. Andriollo, L. Tutelea and I. Boldea, "Performance assessment of a single-phase PM synchronous motor for small fan appliances," in *Electrical Machines, 2008. ICEM 2008. 18th International Conference on*, pp. 1-6, 2008.

[63] H. Ohta, T. Sato, I. Masugane and K. Matsuse, "Rotor pole discrimination and simple starting method of new single-phase PM motor without position sensor," in *Power Electronics and Motion Control Conference, 2000. Proceedings. IPEMC 2000. The Third International*, vol. 2, pp. 616-621, 2000.

[64] S. Bentouati, D. Howe and Z. Q. Zhu, "Influence of design parameters on the starting torque of a single-phase PM brushless DC motor," *Magnetics, IEEE Transactions on,* vol. 36, no. 5, pp. 3533-3536, 2000.

[65] S. H. Won, T. H. Kim, K. B. Jang, S. K. Choi, W. S. Oh and J. Lee, "Effect of design variables on starting torque of single phase flux-reversal machine," *Journal of Applied Physics,* vol. 99, no. 8, pp. 08R312-08R312-3, 2006.

[66] W. Z. Wang, Z. G. Wu, W. B. Jin and J. P. Ying, "Starting methods for hall-less single phase BLDC motor," in *Industrial Electronics Society, 2005. IECON 2005. 31st Annual Conference of IEEE*, pp. 5, 2005.

[67] W. Z. Wang, Z. G. Wu, W. B. Jin and J. P. Ying, "Sensorless control technology for single phase BLDCM based on the winding time-sharing method;" in *Industrial Electronics Society, 2005. IECON 2005. 31st Annual Conference of IEEE*, pp. 5, 2005.

[68] J. R. H. Jr. and T. J. E. Miller, "Design of brushless permanent magnet motor," *Oxford, U.K.: Magna Physics,* 1994.

[69] D. Ishak, Z. Q. Zhu and D. Howe, "Eddy-current loss in the rotor magnets of permanent-magnet brushless machines having a fractional number of slots per pole," *Magnetics, IEEE Transactions on,* vol. 41, no. 9, pp. 2462-2469, 2005.

[70] G. J. Atkinson, B. C. Mecrow, A. G. Jack, D. J. Atkinson, P. Sangha and M. Benarous, "The analysis of losses in high-power fault-tolerant machines for aerospace applications," *Industry Applications, IEEE Transactions on,* vol. 42, no. 5, pp. 1162-1170, 2006.

[71] A. K. Nagarkatti, O. A. Mohammed and N. A. Demerdash, "Special losses in rotors of electronically commutated brushless DC botors induced by non-uniformly rotating amature MMFS," *Power Apparatus and Systems, IEEE Transactions on,* vol. PAS-101, no. 12, pp. 4502-4507, 1982.

[72] D. Fang, "Commutation-caused eddy-current losses in permanent-magnet brushless DC motors," *Magnetics, IEEE Transactions on,* vol. 33, no. 5, pp. 4310-4318, 1997.

[73] D. Fang, "Improved analytical modeling of commutation losses including space harmonic effects in permanent magnet brushless DC motors," in *Industry Applications Conference, 1998. Thirty-Third IAS Annual Meeting. The 1998 IEEE*, vol. 1, pp. 380-386, 1998.

[74] N. Schofield, K. Ng, Z. Q. Zhu and D. Howe, "Parasitic rotor losses in a brushless permanent magnet traction machine," in *Electrical Machines and Drives, 1997 Eighth International Conference on (Conf. Publ. No. 444)*, pp. 200-204, 1997.

[75] Z. Q. Zhu, K. Ng, N. Schofield and D. Howe, "Improved analytical modelling of rotor eddy current loss in brushless machines equipped with surface-mounted permanent magnets," *Electric Power Applications, IEE Proceedings -,* vol. 151, no. 6, pp. 641-650, 2004.

[76] D. Fang and T. W. Nehl, "Analytical modeling of eddy-current losses caused by pulse-width-modulation switching in permanent-magnet brushless direct-current motors," *Magnetics, IEEE Transactions on,* vol. 34, no. 5, pp. 3728-3736, 1998.

[77] N. Boules, "Impact of slot harmonics on losses of high-speed permanent magnet machine with a magnet retaining ring," *Electric Power Components and Systems,* vol. 6, no. 6, pp. 527-539, 1981.

[78] B. C. Mecrow, A. G. Jack and J. M. Masterman, "Determination of rotor eddy current losses in permanent magnet machines," in *Electrical Machines and Drives, 1993. Sixth International Conference on (Conf. Publ. No. 376)*, pp. 299-304, 1993.

[79] M. R. H. S. M. A. Sharkh, and N. T. Irenji, "Computation of no-load electromagnetic rotor loss in high-speed PM machines," *Proc. COMPUMAG,* pp. 715-717, 1977.

[80] Z. Q. Zhu, K. Ng, N. Schofield and D. Howe, "Analytical prediction of rotor eddy current loss in brushless machines equipped with surface-mounted permanent magnets. I. Magnetostatic field

model," in *Electrical Machines and Systems, 2001. ICEMS 2001. Proceedings of the Fifth International Conference on*, vol. 2, pp. 806-809, 2001.

[81] C. B. Rajanathan, H. Acikgoz and R. Egin, "Transient characteristics of the single phase permanent magnet synchronous motor," *Magnetics, IEEE Transactions on*, vol. 35, no. 5, pp. 3589-3591, 1999.

[82] L. A. Pereira, E. R. Locatelli, G. Zolet and V. M. Canalli, "Single phase permanent-magnet motors. I. Parameter determination and mathematical model," in *Electric Machines and Drives Conference, 2001. IEMDC 2001. IEEE International*, pp. 789-793, 2001.

[83] L. A. Pereira, E. R. Locatelli, G. Zolet and V. M. Canalli, "Single phase permanent-magnet motors. II. Performance and test results," in *Electric Machines and Drives Conference, 2001. IEMDC 2001. IEEE International*, pp. 794-797, 2001.

[84] K. J. Binns, P. J. Lisboa and M. S. N. Al-Din, "The use of canned rotors in high speed permanent magnet machines," in *Electrical Machines and Drives, 1991. Fifth International Conference on (Conf. Publ. No. 341)*, pp. 21-25, 1991.

[85] F. Z. Zhu, J. X. Shen, W. Z. Fei and R. G. Lin, "Study of retaining sleeve and conductive shield and their influence on rotor loss in high-speed PM BLDC motors," *Magnetics, IEEE Transactions on*, vol. 42, no. 10, pp. 3398-3400, 2006.

[86] C. Han-Wook, J. Seok-Myeong and C. Sang-Kyu, "A design approach to reduce rotor losses in high-speed permanent magnet machine for turbo-compressor," *Magnetics, IEEE Transactions on*, vol. 42, no. 10, pp. 3521-3523, 2006.

[87] N. Bianchi, S. Bolognani and F. Luise, "Potentials and limits of high-speed PM motors," *Industry Applications, IEEE Transactions on*, vol. 40, no. 6, pp. 1570-1578, 2004.

[88] S. Mabu Sharkh, M. R. Harris and N. T. Irenji, "Calculation of rotor eddy-current loss in high-speed PM alternators," in *Electrical Machines and Drives, 1997 Eighth International Conference on (Conf. Publ. No. 444)*, pp. 170-174, 1997.

[89] B. Sarlioglu, Z. Yifan and T. A. Lipo, "A novel doubly salient single phase permanent magnet generator," in *Industry Applications Society Annual Meeting, 1994., Conference Record of the 1994 IEEE*, vol. 1, pp. 9-15, 1994.

[90] R. P. Deodhar, S. Andersson, I. Boldea and T. J. E. Miller, "The flux-reversal machine: a new brushless doubly-salient permanent-magnet machine," *Industry Applications, IEEE Transactions on*, vol. 33, no. 4, pp. 925-934, 1997.

[91] C. Wang, S. A. Nasar and I. Boldea, "Three-phase flux reversal machine (FRM)," *Electric Power Applications, IEE Proceedings -*, vol. 146, no. 2, pp. 139-146, 1999.

[92] S. E. Rauch and L. J. Johnson, "Design principles of flux-switch alternators," *Power Apparatus and Systems, Part III. Transactions of the American Institute of Electrical Engineers*, vol. 74, no. 3, pp. 1261-1268, 1955.

[93] H. B. Ertan, B. Dag and G. Capolino, "Calculation of parameters of single-phase PM motor for design optimization," *Energy Conversion, IEEE Transactions on*, vol. 20, no. 3, pp. 538-548, 2005.

[94] Z. Q. Zhu and D. Howe, "Influence of design parameters on cogging torque in permanent magnet machines," *Energy Conversion, IEEE Transactions on*, vol. 15, no. 4, pp. 407-412, 2000.

[95] Y. Pang, Z. Q. Zhu and D. Howe, "Analytical determination of optimal split ratio for permanent magnet brushless motors," *Electric Power Applications, IEE Proceedings -*, vol. 153, no. 1, pp. 7-13, 2006.

[96] J. D. Ede, Z. Q. Zhu and D. Howe, "Optimal split ratio for high-speed permanent magnet brushless DC motors," in *Electrical Machines and Systems, 2001. ICEMS 2001. Proceedings of the Fifth International Conference on*, vol. 2, pp. 909-912, 2001.

[97] Z. Q. Zhu, S. Bentouati and D. Howe, "Control of single-phase permanent magnet brushless DC drives for high-speed applications," in *Power Electronics and Variable Speed Drives, 2000. Eighth International Conference on (IEE Conf. Publ. No. 475)*, pp. 327-332, 2000.

[98] Tegopoulos`, J.A.`, and Kriezis`, E.E: "Eddy currents in linear conducting media" (Elsevier`, 1985)

[99] C. Yi, C. Pollock and H. Pollock, "A permanent magnet flux switching motor for low energy axial fans," in *Industry Applications Conference, 2005. Fourtieth IAS Annual Meeting. Conference Record of the 2005*, vol. 3, pp. 2168-2175, 2005.

[100] C. Ming, K. T. Chau and C. C. Chan, "Static characteristics of a new doubly salient permanent magnet motor," *Energy Conversion, IEEE Transactions on*, vol. 16, no. 1, pp. 20-25, 2001.

[101] C. Ming, K. T. Chau, C. C. Chan, E. Zhou and X. Huang, "Nonlinear varying-network magnetic circuit analysis for doubly salient permanent-magnet motors," *Magnetics, IEEE Transactions on*, vol. 36, no. 1, pp. 339-348, 2000.

[102] E. Hoang, A. H. Ben Ahmed and J. Lucidarme, "Switching flux permanent magnet polyphased synchronous machines," *Proc. 7th Conf. on Power Electronics and Applications*, pp. 903-908, 1997.

[103] Z. Q. Zhu, Y. Pang, D. Howe, S. Iwasaki, R. Deodhar and A. Pride, "Analysis of electromagnetic performance of flux-switching permanent-magnet Machines by nonlinear adaptive lumped parameter magnetic circuit model," *Magnetics, IEEE Transactions on*, vol. 41, no. 11, pp. 4277-4287, 2005.

[104] H. R. Bolton and Y. Shakweh, "Performance prediction of Laws's relay actuator," *Electric Power Applications, IEE Proceedings B,* vol. 137, no. 1, pp. 1-13, 1990.

[105] C. Pollock and M. Wallace, "The flux switching motor, a DC motor without magnets or brushes," in *Industry Applications Conference, 1999. Thirty-Fourth IAS Annual Meeting. Conference Record of the 1999 IEEE*, vol. 3, pp. 1980-1987, 1999.

[106] H. Pollock, C. Pollock, R. T. Walter and B. V. Gorti, "Low cost, high power density, flux switching machines and drives for power tools," in *Industry Applications Conference, 2003. 38th IAS Annual Meeting. Conference Record of the*, vol. 3, pp. 1451-1457, 2003.

[107] C. Pollock, H. Pollock, R. Barron, J. R. Coles, D. Moule, A. Court and R. Sutton, "Flux-switching motors for automotive applications," *Industry Applications, IEEE Transactions on,* vol. 42, no. 5, pp. 1177-1184, 2006.

[108] Z. Q. Zhu, Y. Pang, W. Hua, M. Cheng and D. Howe, "Investigation of end effect in permanent magnet brushless machines having magnets on the stator," *Journal of Applied Physics,* vol. 99, no. 8, pp. 08R319-08R319-3, 2006.

[109] Y. Chen, S. Chen, Z. Q. Zhu, D. Howe and Y. Y. Ye, "Starting torque of single-phase flux-switching permanent magnet motors," *Magnetics, IEEE Transactions on,* vol. 42, no. 10, pp. 3416-3418, 2006.

[110] E. C. Lovelace, T. M. Jahns and J. H. Lang, "A saturating lumped-parameter model for an interior PM synchronous machine," *Industry Applications, IEEE Transactions on,* vol. 38, no .3, pp. 645-650, 2002.

[111] J. P. Wang, D. K. Lieu, W. L. Lorimer and A. Hartman, "Comparison of lumped parameter and finite element magnetic modeling in a brushless DC motor," *Magnetics, IEEE Transactions on,* vol. 33, no. 5, pp. 4092-4094, 1997.

[112] M. Moallem and G. E. Dawson, "An improved magnetic equivalent circuit method for predicting the characteristics of highly saturated electromagnetic devices," *Magnetics, IEEE Transactions on,* vol. 34, no. 5, pp. 3632-3635, 1998.

[113] H. C. Rotors, "Electromagnetic devices," New York, London, Wiley, 1941.

APPENDIX A

Static Analytical Model for Single-Phase PM BLDC Motor Having Concentric Airgap

By neglecting the eddy current reaction field in the magnet and the retained sleeve, in terms of the magnetic vector potential A, the Laplace's equation, which governs the armature reaction field in the airgap, magnet and sleeve regions is given by,

$$\nabla^2 A = 0 \tag{A-1}$$

Its general solution is,

$$A = \sum_{\nu}^{\infty} \left(C_\nu r^\nu + D_\nu r^{-\nu} \right) \cos(\nu\alpha) \qquad \text{(A/m)} \tag{A-2}$$

where C_ν and D_ν are constants to be determined from the boundary conditions.

The radial and circumferential components of the armature reaction field can be derived from A as,

$$B_r = \frac{1}{r}\frac{\partial A}{\partial \alpha} \qquad \text{(T)} \tag{A-3}$$

$$B_\alpha = -\frac{\partial A}{\partial r} \qquad \text{(T)} \tag{A-4}$$

By assuming both of the stator and rotor iron to be infinitely permeable, the boundary conditions are given by,

$$\text{At } r = R_s \quad H_\alpha\big|_{r=R_s} = J_s(\alpha) \qquad \text{(A/m)} \tag{A-5}$$

$$\text{At } r = R_r \quad B_\alpha\big|_{r=R_r} = 0 \qquad \text{(T)} \tag{A-6}$$

According to equations (3-6) and (A-2) to (A-6), the analytical expressions for the magnetic vector potential can be derived as:

$$A(r,\alpha,t)=$$
$$-\mu_0\sum_u^\infty\sum_v^\infty\frac{J_{uv}R_s^{-v+1}}{G_v v}\left(r^v+R_r^{2v}r^{-v}\right)\left[\cos(u\omega_r t+\theta_u-v\alpha)-\cos(u\omega_r t+\theta_u+v\alpha)\right] \quad \text{(A-7)}$$

where $G_v=1-\left(\frac{R_r}{R_s}\right)^{2v}$.

Therefore, the radial and circumferential components of the armature reaction field are,

$$B_r(r,\alpha,t)=$$
$$-\sum_u^\infty\sum_v^\infty\frac{\mu_0 J_{uv}R_s^{-v+1}}{G_v}(r^{v-1}+R_r^{2v}r^{-v-1})\left[\sin(u\omega_r t+\theta_u-v\alpha)+\sin(u\omega_r t+\theta_u+v\alpha)\right] \text{(T)} \quad \text{(A-8)}$$

$$B_\alpha(r,\alpha,t)=$$
$$\sum_u^\infty\sum_v^\infty\frac{\mu_0 J_{uv}R_s^{-v+1}}{G_v}(r^{v-1}-R_r^{2v}r^{-v-1})\left[\cos(u\omega_r t+\theta_u-v\alpha)-\cos(u\omega_r t+\theta_u+v\alpha)\right] \text{(T)} \quad \text{(A-9)}$$

In order to determine the induced eddy currents and the associated loss in the rotor, above analytical expressions for the equivalent current sheet and magnetic vector potential have to be transformed from the stationary reference frame α to the rotating reference frame θ with the transformation $\alpha=\theta+\omega_r t$.

Hence,

$$J_s(\theta)=\sum_u^\infty\sum_v^\infty J_{uv}\left\{\cos\left[(u-v)\omega_r t-v\theta+\theta_u\right]-\cos\left[(u+v)\omega_r t+v\theta+\theta_u\right]\right\} \quad \text{(A/m)} \quad \text{(A-10)}$$

$$A(r,\theta,t)=$$
$$-\mu_0\sum_u^\infty\sum_v^\infty\frac{J_{uv}R_s^{-v+1}}{G_v v}\left(r^v+R_r^{2v}r^{-v}\right)\left\{\cos\left[(u-v)\omega_r t-v\theta+\theta_u\right]-\cos\left[(u+v)\omega_r t+v\theta+\theta_u\right]\right\} \text{(A/m)} \quad \text{(A-11)}$$

The induced eddy current density in the permanent magnet and the retaining sleeve due to the time-varying armature reaction field can be calculated by,

$$J_m(r,\theta,t)=-\sigma_m\frac{\partial A(r,\theta,t)}{\partial t}+C_m(t) \quad \text{(A/m}^2\text{)} \quad \text{(A-12)}$$

$$J_{sl}(r,\theta,t)=-\sigma_{sl}\frac{\partial A(r,\theta,t)}{\partial t}+C_{sl}(t) \quad \text{(A/m}^2\text{)} \quad \text{(A-13)}$$

where C_m and C_{sl} are the integration constant which ensure that the net total current flowing in each magnet segment and the sleeve to be zero at any instant, respectively. i.e.

$$\int_{R_r}^{R_m}\int_{-\frac{\alpha_p}{2}}^{\frac{\alpha_p}{2}} J_m r dr d\theta = 0 \tag{A-14}$$

$$\int_{R_m}^{R_{sl}}\int_{-\pi}^{\pi} J_{sl} r dr d\theta = 0 \tag{A-15}$$

where R_r, R_m and R_{sl} are the magnet inner radius, the magnet outer radius and the retaining sleeve outer radius, respectively. α_p is the pole-arc of the per magnet segment and is given by,

$$\alpha_p = \frac{2\pi}{N} \tag{A-16}$$

where N is the number of magnet segments.

Equations (A-11) to (A-13) yields,

$$-\sigma_m \frac{\partial A(r,\theta,t)}{\partial t} = J_{m1} + J_{m2} \tag{A-17}$$

$$-\sigma_m \frac{\partial A(r,\theta,t)}{\partial t} = J_{sl1} + J_{sl2} \tag{A-18}$$

where

$$J_{m1} = -\sigma_m \omega_r \mu_0 \sum_u^{\infty}\sum_v^{\infty} (u-v)\frac{J_{uv} R_s^{-v+1}}{G_v v}\left(r^v + R_r^{2v} r^{-v}\right)\sin\left[(u-v)\omega_r t + v\theta + \theta_u\right]$$

$$J_{m2} = \sigma_m \omega_r \mu_0 \sum_u^{\infty}\sum_v^{\infty} (u+v)\frac{J_{uv} R_s^{-v+1}}{G_v v}\left(r^v + R_r^{2v} r^{-v}\right)\sin\left[(u+v)\omega_r t + v\theta + \theta_u\right]$$

$$J_{sl1} = -\sigma_{sl} \omega_r \mu_0 \sum_u^{\infty}\sum_v^{\infty} (u-v)\frac{J_{uv} R_s^{-v+1}}{G_v v}\left(r^v + R_r^{2v} r^{-v}\right)\sin\left[(u-v)\omega_r t + v\theta + \theta_u\right]$$

$$J_{sl2} = \sigma_{sl} \omega_r \mu_0 \sum_u^{\infty}\sum_v^{\infty} (u+v)\frac{J_{uv} R_s^{-v+1}}{G_v v}\left(r^v + R_r^{2v} r^{-v}\right)\sin\left[(u+v)\omega_r t + v\theta + \theta_u\right]$$

Hence, according to equations (A-12) to (A-15), the integration constant $C_{sl}(t) = 0$ and the

integration constant C_m can be given by,

$$C_m = C_{m1} + C_{m2} \tag{A-19}$$

where

- If $N=1$, $C_{m1} = C_{m2} = 0$
- If $N>1$,

$$C_{m1} = N\frac{2\sigma_m \omega_r \mu_0}{\pi\left(R_m^2 - R_r^2\right)}\sum_u^\infty\sum_v^\infty (u-v)\frac{R_s^{-v+1}}{G_v v^2}\left[\frac{R_m^{v+2} - R_r^{v+2}}{v+2} + R_r^{2v}E_{mv}\right]\sin\left(v\frac{\pi}{N}\right)\sin\left[(u-v)\omega_r t + \theta_u\right]$$

$$C_{m2} = -N\frac{2\sigma_m \omega_r \mu_0}{\pi\left(R_m^2 - R_r^2\right)}\sum_u^\infty\sum_v^\infty (u+v)\frac{R_s^{-v+1}}{G_v v^2}\left[\frac{R_m^{v+2} - R_r^{v+2}}{v+2} + R_r^{2v}E_{mv}\right]\sin\left(v\frac{\pi}{N}\right)\sin\left[(u+v)\omega_r t + \theta_u\right]$$

where

$$E_{mv} = \begin{cases} \ln\left(\dfrac{R_m}{R_r}\right), & v = 2 \\ \dfrac{R_m^{-v+2} - R_r^{-v+2}}{-v+2} & v \neq 2 \end{cases}$$

Therefore, eddy currents in the magnet and the sleeve are,

$$J_m = J_{m1} + J_{m2} + C_{m1} + C_{m2} \tag{A-20}$$

$$J_{sl} = J_{sl1} + J_{sl2} \tag{A-21}$$

The eddy current loss in the total magnets and the sleeve are,

$$P_m = N\frac{L_a \omega_r}{2\pi}\int_{R_r}^{R_m}\int_0^{\frac{2\pi}{\omega_r}}\int_{-\frac{\alpha_p}{2}}^{\frac{\alpha_p}{2}}\frac{1}{\sigma_m}J_m^2 r\,dr\,dt\,d\theta = \sum_u^\infty\sum_v^\infty\left(P_{cuv} + P_{auv}\right) \quad \text{(W)} \tag{A-22}$$

$$P_{sl} = \frac{L_a \omega_r}{2\pi}\int_{R_m}^{R_{sl}}\int_0^{\frac{2\pi}{\omega_r}}\int_{-\pi}^{\pi}\frac{1}{\sigma_{sl}}J_{sl}^2 r\,dr\,dt\,d\theta = \sum_u^\infty\sum_v^\infty P_{sluv} \quad \text{(W)} \tag{A-23}$$

where L_a is the axial length of the PM and the retaining sleeve, which is assumed to be the same as the axial length of the stator lamination.

P_{cuv} is given by,

$$P_{cuv} = \frac{\pi L_a \sigma_m \omega_r^2 \mu_0^2 J_{uv}^2 R_s^{-2v+2}\left[(u+v)^2+(u-v)^2\right]}{G_v^2 v^2}\left[\frac{R_m^{2v+2}-R_r^{2v+2}}{2v+2}+R_r^{2v}\left(R_m^2-R_r^2\right)+R_r^{4v}F_{mv}\right]$$

where $F_{mv} = \begin{cases} \ln\left(\frac{R_m}{R_r}\right), & v=1 \\ \frac{R_m^{-2v+2}-R_r^{-2v+2}}{-2v+2}, & v\neq 1 \end{cases}$

P_{auv} is given by,

- If $N=1$, $P_{auv}=0$
- If $N>1$

$$P_{auv} = -N^2 \frac{2L_a \sigma_m \omega_r^2 \mu_0^2 J_{uv}^2 R_s^{-2v+2} \sin^2\left(v\frac{\pi}{N}\right)\left[(u+v)^2+(u-v)^2\right]}{\pi G_v^2 v^4\left(R_m^2-R_r^2\right)}\left(\frac{R_m^{v+2}-R_r^{v+2}}{v+2}+R_r^{2v}E_{mv}\right)^2$$

P_{sluv} is given by,

$$P_{sluv} = \frac{\pi L_a \sigma_{sl} \omega_r^2 \mu_0^2 J_{uv}^2 R_s^{-2v+2}\left[(u+v)^2+(u-v)^2\right]}{G_v^2 v^2}\left[\frac{R_{sl}^{2v+2}-R_m^{2v+2}}{2v+2}+R_r^{2v}\left(R_{sl}^2-R_m^2\right)+R_r^{4v}F_{slv}\right]$$

where $F_{slv} = \begin{cases} \ln\left(\frac{R_{sl}}{R_m}\right), & v=1 \\ \frac{R_{sl}^{-2v+2}-R_m^{-2v+2}}{-2v+2}, & v\neq 1 \end{cases}$

APPENDIX B

Improved Analytical Model for Single-Phase PM BLDC Motor Having Concentric Airgap

Account for the eddy current redistribution effect, improved analytical model for predicting the eddy current loss in the rotor magnet of single-phase PM BLDC motor having a concentric airgap can be developed.

The equation (3-6) for the equivalent current sheet over the stator slot openings of the single-phase BLDC PM motors which can induce the eddy current in the rotor can be rewritten as,

$$J_s(\alpha)=\sum_u^{\infty}\sum_v^{\infty}J_{uv}[\cos(u\omega_r t+\theta_u-v\alpha)-\cos(u\omega_r t+\theta_u+v\alpha)]=J_{s\_1}(a)+J_{s\_2}(\alpha)\quad \text{(A/m)} \tag{B-1}$$

where $J_{s\_1}(\alpha)$ and $J_{s\_2}(\alpha)$ are related to the forward and backward rotating mmfs which are rotating in asynchronous with the rotor, and can be given by,

$$J_{s\_1}(\alpha)=\sum_u^{\infty}\sum_v^{\infty}J_{uv}\cos(u\omega_r t+\theta_u-v\alpha)=\sum_u^{\infty}\sum_v^{\infty}\mathrm{Re}\left[J_{uv}e^{j(u\omega_r t+\theta_u-v\alpha)}\right]u\neq v\quad \text{(A/m)} \tag{B-2}$$

$$J_{s\_2}(\alpha)=-\sum_u^{\infty}\sum_v^{\infty}J_{uv}\cos(u\omega_r t+\theta_u+v\alpha)=\sum_u^{\infty}\sum_v^{\infty}\mathrm{Re}\left[-J_{uv}e^{j(u\omega_r t+\theta_u+v\alpha)}\right]\quad \text{(A/m)} \tag{B-3}$$

If $u=v$, the forward rotating mmfs is in synchronous with the rotor and will not induce the eddy current in the rotor.

In terms of the magnetic vector potential A_{1_1} and A_{1_2}, rotating in asynchronous with the rotor, Laplace's equation, which governs the armature reaction field in the airgap, i.e. $(R_{sl}\le r\le R_s)$ are,

$$\frac{\partial^2 A_{l\_1}}{\partial r^2}+\frac{1}{r}\frac{\partial A_{l\_1}}{\partial r}+\frac{1}{r^2}\frac{\partial^2 A_{l\_1}}{\partial \alpha^2}=0 \tag{B-4}$$

$$\frac{\partial^2 A_{l\_2}}{\partial r^2}+\frac{1}{r}\frac{\partial A_{l\_2}}{\partial r}+\frac{1}{r^2}\frac{\partial^2 A_{l\_2}}{\partial \alpha^2}=0 \tag{B-5}$$

For which, the general solutions due to each component of the equivalent current sheet, i.e. equations (B-2) and (B-3), are,

$$A_{l\_1}=\sum_{u}^{\infty}\sum_{v}^{\infty}\mathrm{Re}\left[\left(A_1 r^{v}+B_1 r^{-v}\right)e^{j(u\omega_r t-v\alpha+\theta_u)}\right], u\neq v \qquad \text{(A/m)} \tag{B-6}$$

$$A_{l\_2}=\sum_{u}^{\infty}\sum_{v}^{\infty}\mathrm{Re}\left[\left(A_2 r^{v}+B_2 r^{-v}\right)e^{j(u\omega_r t+v\alpha+\theta_u)}\right] \qquad \text{(A/m)} \tag{B-7}$$

The radial and circumferential components of the armature reaction field can be derived from A_{l_1} and A_{l_2} as,

$$B_{rl}(\alpha)=\frac{1}{r}\frac{\partial A_l}{\partial \alpha}=B_{rl\_1}(\alpha)+B_{rl\_2}(\alpha) \qquad \text{(T)} \tag{B-8}$$

$$B_{al}(\alpha)=-\frac{\partial A_l}{\partial r}=B_{al\_1}(\alpha)+B_{al\_2}(\alpha) \qquad \text{(T)} \tag{B-9}$$

which can be written as,

$$B_{rl\_1}(\alpha)=\sum_{u}^{\infty}\sum_{v}^{\infty}\mathrm{Re}\left[-j\frac{v}{r}\left(A_1 r^{v}+B_1 r^{-v}\right)e^{j(u\omega_r t-v\alpha+\theta_u)}\right], u\neq v \qquad \text{(T)} \tag{B-10}$$

$$B_{rl\_2}(\alpha)=\sum_{u}^{\infty}\sum_{v}^{\infty}\mathrm{Re}\left[j\frac{v}{r}\left(A_2 r^{v}+B_2 r^{-v}\right)e^{j(u\omega_r t+v\alpha+\theta_u)}\right] \qquad \text{(T)} \tag{B-11}$$

$$B_{al\_1}(\alpha)=\sum_{u}^{\infty}\sum_{v}^{\infty}\mathrm{Re}\left[-\frac{v}{r}\left(A_1 r^{v}-B_1 r^{-v}\right)e^{j(u\omega_r t-v\alpha+\theta_u)}\right], u\neq v \qquad \text{(T)} \tag{B-12}$$

$$B_{al\_2}(\alpha)=\sum_{u}^{\infty}\sum_{v}^{\infty}\mathrm{Re}\left[-\frac{v}{r}\left(A_2 r^{v}-B_2 r^{-v}\right)e^{j(u\omega_r t+v\alpha+\theta_u)}\right] \qquad \text{(T)} \tag{B-13}$$

In the sleeve, i.e. $R_m \le r \le R_{sl}$, the induced eddy current density due to the equivalent current sheet can be found by solving the diffusion equations,

$$\frac{\partial^2 J_{zll\_1}}{\partial r^2}+\frac{1}{r}\frac{\partial J_{zll\_1}}{\partial r}+\frac{1}{r^2}\frac{\partial^2 J_{zll\_1}}{\partial \alpha^2}-j(u-v)\omega_r\sigma_{sl}\mu_0\mu_{sl}J_{zll\_1}=0, u\neq v \tag{B-14}$$

$$\frac{\partial^2 J_{zll\_2}}{\partial r^2}+\frac{1}{r}\frac{\partial J_{zll\_2}}{\partial r}+\frac{1}{r^2}\frac{\partial^2 J_{zll\_2}}{\partial \alpha^2}-j(u+v)\omega_r\sigma_{sl}\mu_0\mu_{sl}J_{zll\_2}=0 \tag{B-15}$$

i.e.

$$\frac{\partial^2 J_{zll\_1}}{\partial r^2}+\frac{1}{r}\frac{\partial J_{zll\_1}}{\partial r}+\frac{1}{r^2}\frac{\partial^2 J_{zll\_1}}{\partial \alpha^2}+\tau_{sl\_1}{}^2 J_{zll\_1}=0, u\neq v \tag{B-16}$$

$$\frac{\partial^2 J_{zll\_2}}{\partial r^2}+\frac{1}{r}\frac{\partial J_{zll\_2}}{\partial r}+\frac{1}{r^2}\frac{\partial^2 J_{zll\_2}}{\partial \alpha^2}+\tau_{sl\_2}{}^2 J_{zll\_2}=0 \tag{B-17}$$

where $\tau_{sl\_1}=\dfrac{-1+j}{\delta_{sl\_1}}$, and $\delta_{sl\_1}=\sqrt{\dfrac{2}{(u-v)\omega_r\sigma_{sl}\mu_0\mu_{sl}}}, u\neq v$;

$\tau_{sl\_2}=\dfrac{-1+j}{\delta_{sl\_2}}$, and $\delta_{sl\_2}=\sqrt{\dfrac{2}{(u+v)\omega_r\sigma_{sl}\mu_0\mu_{sl}}}$.

The general solution, due to the stator current sheet, is,

$$J_{zll\_1}(\alpha)=\sum_u^{\infty}\sum_v^{\infty}\mathrm{Re}\left\{\left[C_1J_v(\tau_{sl\_1}r)+D_1Y_v(\tau_{sl\_1}r)\right]e^{j(u\omega_r t-v\alpha+\theta_u)}\right\}, u\neq v \quad (\mathrm{A/m^2}) \tag{B-18}$$

$$J_{zll\_2}(\alpha)=\sum_u^{\infty}\sum_v^{\infty}\mathrm{Re}\left\{\left[C_2J_v(\tau_{sl\_1}r)+D_2Y_v(\tau_{sl\_1}r)\right]e^{j(u\omega_r t+v\alpha+\theta_u)}\right\} \quad (\mathrm{A/m^2}) \tag{B-19}$$

The radial and circumferential field components in the sleeve can be found by applying Maxwell's equation,

$$\nabla\times\vec{E}_{ll}=-\frac{\partial\vec{B}_{ll}}{\partial t} \tag{B-20}$$

which yields,

$$\frac{1}{r\sigma_{sl}}\frac{\partial J_{zll}}{\partial\alpha}=-j(u\pm v)\omega_r B_{rll} \tag{B-21}$$

i.e.

$$B_{rll\_1}(\alpha)=\sum_u^{\infty}\sum_v^{\infty}\mathrm{Re}\left\{-j\frac{v}{r}\frac{\mu_0\mu_{sl}}{\tau_{sl\_1}^2}\left[C_1J_v(\tau_{sl\_1}r)+D_1Y_v(\tau_{sl\_1}r)\right]e^{j(u\omega_r t-v\alpha+\theta_u)}\right\}, u\neq v \tag{B-22}$$

$$B_{rll\_2}(\alpha)=\sum_{u}^{\infty}\sum_{v}^{\infty}\mathrm{Re}\left\{ j\frac{v}{r}\frac{\mu_0\mu_{sl}}{\tau_{sl\_2}^2}\left[C_2J_v(\tau_{sl\_2}r)+D_2Y_v(\tau_{sl\_2}r)\right]e^{j(u\omega_r t+v\alpha+\theta_u)}\right\} \tag{B-23}$$

and,

$$-\frac{1}{\sigma_{sl}}\frac{\partial J_{zll}}{\partial r}=-j(u\pm v)\omega_r\mu_0\mu_{sl}H_{all} \tag{B-24}$$

i.e.

$$H_{all\_1}(\alpha)=\sum_{u}^{\infty}\sum_{v}^{\infty}\mathrm{Re}\left\{-\frac{v}{r\tau_{sl\_1}^2}\left\{\begin{array}{l}C_1\left[\frac{\tau_{sl\_1}r}{v}J_{v\_1}(\tau_{sl\_1}r)-J_v(\tau_{sl\_1}r)\right]\\+D_1\left[\frac{\tau_{sl\_1}r}{v}Y_{v\_1}(\tau_{sl\_1}r)-Y_v(\tau_{sl\_1}r)\right]\end{array}\right\}e^{j(u\omega_r t-v\alpha+\theta_u)}\right\},u\neq v \tag{B-25}$$

$$H_{all\_2}(\alpha)=\sum_{u}^{\infty}\sum_{v}^{\infty}\mathrm{Re}\left\{-\frac{v}{r\tau_{sl\_2}^2}\left\{\begin{array}{l}C_2\left[\frac{\tau_{sl\_2}r}{v}J_{v\_1}(\tau_{sl\_2}r)-J_v(\tau_{sl\_2}r)\right]\\+D_2\left[\frac{\tau_{sl\_2}r}{v}Y_{v\_1}(\tau_{sl\_2}r)-Y_v(\tau_{sl\_2}r)\right]\end{array}\right\}e^{j(u\omega_r t+v\alpha+\theta_u)}\right\} \tag{B-26}$$

Similarly, the eddy current density in the PM, i.e. $R_r\le r\le R_m$, also satisfies the diffusion equation,

$$\frac{\partial^2 J_{zlll\_1}}{\partial r^2}+\frac{1}{r}\frac{\partial J_{zlll\_1}}{\partial r}+\frac{1}{r^2}\frac{\partial^2 J_{zlll\_1}}{\partial\alpha^2}-j(u-v)\omega_r\sigma_m\mu_0\mu_m J_{zlll\_1}=0,u\neq v \tag{B-27}$$

$$\frac{\partial^2 J_{zlll\_2}}{\partial r^2}+\frac{1}{r}\frac{\partial J_{zlll\_2}}{\partial r}+\frac{1}{r^2}\frac{\partial^2 J_{zlll\_2}}{\partial\alpha^2}-j(u+v)\omega_r\sigma_m\mu_0\mu_m J_{zlll\_2}=0 \tag{B-28}$$

i.e.

$$\frac{\partial^2 J_{zlll\_1}}{\partial r^2}+\frac{1}{r}\frac{\partial J_{zlll\_1}}{\partial r}+\frac{1}{r^2}\frac{\partial^2 J_{zlll\_1}}{\partial\alpha^2}+\tau_{m\_1}{}^2J_{zlll\_1}=0,u\neq v \tag{B-29}$$

$$\frac{\partial^2 J_{zlll\_2}}{\partial r^2}+\frac{1}{r}\frac{\partial J_{zlll\_2}}{\partial r}+\frac{1}{r^2}\frac{\partial^2 J_{zlll\_2}}{\partial\alpha^2}+\tau_{m\_2}{}^2J_{zlll\_2}=0 \tag{B-30}$$

where $\tau_{m\_1}=\dfrac{-1+j}{\delta_{m\_1}}$, and $\delta_{m\_1}=\sqrt{\dfrac{2}{(u-v)\omega_r\sigma_m\mu_0\mu_m}},u\neq v$;

$\tau_{m\_2}=\dfrac{-1+j}{\delta_{m\_2}}$, and $\delta_{m\_2}=\sqrt{\dfrac{2}{(u+v)\omega_r\sigma_m\mu_0\mu_m}}$.

The general solution, due to the stator current sheet is,

$$J_{zIII\_1}(\alpha)=\sum_{u}^{\infty}\sum_{v}^{\infty}\mathrm{Re}\left\{\left[E_1 J_v(\tau_{m\_1}r)+F_1 Y_v(\tau_{m\_1}r)\right]e^{j(u\omega_r t-v\alpha+\theta_u)}\right\}, u\neq v \quad (\mathrm{A/m^2}) \quad \text{(B-31)}$$

$$J_{zIII\_2}(\alpha)=\sum_{u}^{\infty}\sum_{v}^{\infty}\mathrm{Re}\left\{\left[E_2 J_v(\tau_{m\_2}r)+F_2 Y_v(\tau_{m\_2}r)\right]e^{j(u\omega_r t+v\alpha+\theta_u)}\right\} \quad (\mathrm{A/m^2}) \quad \text{(B-32)}$$

Therefore, the radial and circumferential field components in the magnets are,

$$B_{rIII\_1}(\alpha)=\sum_{u}^{\infty}\sum_{v}^{\infty}\mathrm{Re}\left\{-j\frac{v}{r}\frac{\mu_0\mu_m}{\tau_{m\_1}^2}\left[E_1 J_v(\tau_{m\_1}r)+F_1 Y_v(\tau_{m\_1}r)\right]e^{j(u\omega_r t-v\alpha+\theta_u)}\right\}, u\neq v \quad \text{(B-33)}$$

$$B_{rIII\_2}(\alpha)=\sum_{u}^{\infty}\sum_{v}^{\infty}\mathrm{Re}\left\{j\frac{v}{r}\frac{\mu_0\mu_m}{\tau_{m\_2}^2}\left[E_2 J_v(\tau_{m\_2}r)+F_2 Y_v(\tau_{m\_2}r)\right]e^{j(u\omega_r t+v\alpha+\theta_u)}\right\} \quad \text{(B-34)}$$

$$H_{\alpha III\_1}(\alpha)=\sum_{u}^{\infty}\sum_{v}^{\infty}\mathrm{Re}\left\{-\frac{v}{r\tau_{m\_1}^2}\left\{\begin{aligned}&E_1\left[\frac{\tau_{m\_1}r}{v}J_{v-1}(\tau_{m\_1}r)-J_v(\tau_{m\_1}r)\right]\\&+F_1\left[\frac{\tau_{m\_1}r}{v}Y_{v-1}(\tau_{m\_1}r)-Y_v(\tau_{m\_1}r)\right]\end{aligned}\right\}e^{j(u\omega_r t-v\alpha+\theta_u)}\right\}, u\neq v \quad \text{(B-35)}$$

$$H_{\alpha III\_2}(\alpha)=\sum_{u}^{\infty}\sum_{v}^{\infty}\mathrm{Re}\left\{-\frac{v}{r\tau_{m\_2}^2}\left\{\begin{aligned}&E_2\left[\frac{\tau_{m\_2}r}{v}J_{v-1}(\tau_{m\_2}r)-J_v(\tau_{m\_2}r)\right]\\&+F_2\left[\frac{\tau_{m\_2}r}{v}Y_{v-1}(\tau_{m\_2}r)-Y_v(\tau_{m\_2}r)\right]\end{aligned}\right\}e^{j(u\omega_r t+v\alpha+\theta_u)}\right\} \quad \text{(B-36)}$$

In order to determine the induced currents, the expressions for the equivalent current sheets and the magnetic vector potential have to be transformed from the stationary reference frame α to the rotational reference frame such that $\alpha=\theta+\omega_r t$. Hence,

The equivalent current sheet is,

$$J_s(\theta)=J_{s\_1}(\theta)+J_{s\_2}(\theta) \quad (\mathrm{A/m}) \quad \text{(B-37)}$$

where $J_{s\_1}(\theta)=\sum_{u}^{\infty}\sum_{v}^{\infty}\mathrm{Re}\left[J_{uv}e^{j\phi_1}\right], u\neq v$, $J_{s\_2}(\theta)=\sum_{u}^{\infty}\sum_{v}^{\infty}\mathrm{Re}\left[-J_{uv}e^{j\phi_2}\right]$,

$\phi_1=(u-v)\omega_r t-v\theta+\theta_u$ and $\phi_2=(u+v)\omega_r t-v\theta+\theta_u$.

The armature reaction field is

- In the airgap, i.e. $(R_{sl}\le r\le R_s)$

$$B_{rI\_1}(\theta)=\sum_{u}^{\infty}\sum_{v}^{\infty}\mathrm{Re}\left[-j\frac{v}{r}\left(A_1 r^{v}+B_1 r^{-v}\right)e^{j\phi_1}\right],u\neq v \qquad \text{(T)} \qquad \text{(B-38)}$$

$$B_{rI\_2}(\theta)=\sum_{u}^{\infty}\sum_{v}^{\infty}\mathrm{Re}\left[j\frac{v}{r}\left(A_2 r^{v}+B_2 r^{-v}\right)e^{j\phi_2}\right] \qquad \text{(T)} \qquad \text{(B-39)}$$

$$B_{\alpha I\_1}(\theta)=\sum_{u}^{\infty}\sum_{v}^{\infty}\mathrm{Re}\left[-\frac{v}{r}\left(A_1 r^{v}-B_1 r^{-v}\right)e^{j\phi_1}\right],u\neq v \text{ (B-40)} \qquad \text{(T)} \qquad \text{(B-41)}$$

$$B_{\alpha I\_2}(\theta)=\sum_{u}^{\infty}\sum_{v}^{\infty}\mathrm{Re}\left[-\frac{v}{r}\left(A_2 r^{v}-B_2 r^{-v}\right)e^{j\phi_2}\right] \qquad \text{(T)} \qquad \text{(B-42)}$$

- In the retaining sleeve, i.e. $R_m \le r \le R_{sl}$

$$B_{rII\_1}(\theta)=\sum_{u}^{\infty}\sum_{v}^{\infty}\mathrm{Re}\left\{-j\frac{v}{r}\frac{\mu_0\mu_{sl}}{\tau_{sl\_1}^2}\left[C_1 J_v(\tau_{sl\_1}r)+D_1 Y_v(\tau_{sl\_1}r)\right]e^{j\phi_1}\right\},u\neq v \qquad \text{(T)} \qquad \text{(B-43)}$$

$$B_{rII\_2}(\theta)=\sum_{u}^{\infty}\sum_{v}^{\infty}\mathrm{Re}\left\{j\frac{v}{r}\frac{\mu_0\mu_{sl}}{\tau_{sl\_2}^2}\left[C_2 J_v(\tau_{sl\_2}r)+D_2 Y_v(\tau_{sl\_2}r)\right]e^{j\phi_2}\right\} \qquad \text{(T)} \qquad \text{(B-44)}$$

$$H_{\alpha II\_1}(\theta)=\sum_{u}^{\infty}\sum_{v}^{\infty}\mathrm{Re}\left\{-\frac{v}{r\tau_{sl\_1}^2}\left\{\begin{array}{l}C_1\left[\frac{\tau_{sl\_1}r}{v}J_{v-1}(\tau_{sl\_1}r)-J_v(\tau_{sl\_1}r)\right]\\+D_1\left[\frac{\tau_{sl\_1}r}{v}Y_{v-1}(\tau_{sl\_1}r)-Y_v(\tau_{sl\_1}r)\right]\end{array}\right\}e^{j\phi_1}\right\},u\neq v \qquad \text{(A/m)} \qquad \text{(B-45)}$$

$$H_{\alpha II\_2}(\theta)=\sum_{u}^{\infty}\sum_{v}^{\infty}\mathrm{Re}\left\{-\frac{v}{r\tau_{sl\_2}^2}\left\{\begin{array}{l}C_2\left[\frac{\tau_{sl\_2}r}{v}J_{v-1}(\tau_{sl\_2}r)-J_v(\tau_{sl\_2}r)\right]\\+D_2\left[\frac{\tau_{sl\_2}r}{v}Y_{v-1}(\tau_{sl\_2}r)-Y_v(\tau_{sl\_2}r)\right]\end{array}\right\}e^{j\phi_2}\right\} \qquad \text{(A/m)} \qquad \text{(B-46)}$$

- In the PM, i.e. $R_r \le r \le R_m$

$$B_{rIII\_1}(\alpha)=\sum_{u}^{\infty}\sum_{v}^{\infty}\mathrm{Re}\left\{-j\frac{v}{r}\frac{\mu_0\mu_m}{\tau_{m\_1}^2}\left[E_1 J_v(\tau_{m\_1}r)+F_1 Y_v(\tau_{m\_1}r)\right]e^{j\phi_1}\right\},u\neq v \qquad \text{(T)} \qquad \text{(B-47)}$$

$$B_{rIII\_2}(\theta)=\sum_{u}^{\infty}\sum_{v}^{\infty}\mathrm{Re}\left\{j\frac{v}{r}\frac{\mu_0\mu_m}{\tau_{m\_2}^2}\left[E_2 J_v(\tau_{m\_2}r)+F_2 Y_v(\tau_{m\_2}r)\right]e^{j\phi_2}\right\} \qquad \text{(T)} \qquad \text{(B-48)}$$

$$H_{\alpha III\_1}(\theta)=\sum_{u}^{\infty}\sum_{v}^{\infty}\mathrm{Re}\left\{-\frac{v}{r\tau_{m\_1}^2}\left\{\begin{array}{l}E_1\left[\frac{\tau_{m\_1}r}{v}J_{v-1}(\tau_{m\_1}r)-J_v(\tau_{m\_1}r)\right]\\+F_1\left[\frac{\tau_{m\_1}r}{v}Y_{v-1}(\tau_{m\_1}r)-Y_v(\tau_{m\_1}r)\right]\end{array}\right\}e^{j\phi_1}\right\},u\neq v \qquad \text{(A/m)} \qquad \text{(B-49)}$$

$$H_{\alpha II\_2}(\theta)=\sum_{u}^{\infty}\sum_{v}^{\infty}\mathrm{Re}\left\{-\frac{v}{r\tau_{m\_2}^{2}}\left\{\begin{aligned}&E_2\left[\frac{\tau_{m\_2}r}{v}J_{v-1}(\tau_{m\_2}r)-J_v(\tau_{m\_2}r)\right]\\&+F_2\left[\frac{\tau_{m\_2}r}{v}Y_{v-1}(\tau_{m\_2}r)-Y_v(\tau_{m\_2}r)\right]\end{aligned}\right\}e^{j\phi_2}\right\} \quad \text{(A/m)} \quad \text{(B-50)}$$

The eddy current densities induced in the retaining sleeve and the permanent magnet in the rotating reference frame θ are as follows, respectively,

$$J_{zII}(\theta)=J_{zII\_1}(\theta)+J_{zII\_2}(\theta) \qquad (\mathrm{A/m^2}) \qquad \text{(B-51)}$$

$$J_{zIII}(\theta)=J_{zIII\_1}(\theta)+J_{zIII\_2}(\theta) \qquad (\mathrm{A/m^2}) \qquad \text{(B-52)}$$

where

$$J_{zII\_1}(\theta)=\sum_{u}^{\infty}\sum_{v}^{\infty}\mathrm{Re}\left\{\left[C_1J_v(\tau_{sl}r)+D_1Y_v(\tau_{sl}r)\right]e^{j\phi_1}\right\}, v\neq u \qquad \text{(B-53)}$$

$$J_{zII\_2}(\theta)=\sum_{u}^{\infty}\sum_{v}^{\infty}\mathrm{Re}\left\{\left[C_2J_v(\tau_{sl}r)+D_2Y_v(\tau_{sl}r)\right]e^{j\phi_2}\right\} \qquad \text{(B-54)}$$

$$J_{zIII\_1}(\theta)=\sum_{u}^{\infty}\sum_{v}^{\infty}\mathrm{Re}\left\{\left[E_1J_v(\tau_mr)+F_1Y_v(\tau_mr)\right]e^{j\phi_1}\right\}, v\neq u \qquad \text{(B-55)}$$

$$J_{zIII\_2}(\theta)=\sum_{u}^{\infty}\sum_{v}^{\infty}\mathrm{Re}\left\{\left[E_2J_v(\tau_mr)+F_2Y_v(\tau_mr)\right]e^{j\phi_2}\right\} \qquad \text{(B-56)}$$

By assuming both of the stator and rotor iron to be infinitely permeable, the boundary conditions at the interface between the different regions are given by,

$$H_{\alpha I\_1}(\theta)\big|_{r=R_s}=J_{s\_1}(\theta),\quad H_{\alpha I\_2}(\theta)\big|_{r=R_s}=J_{s\_2}(\theta) \qquad \text{(B-57)}$$

$$B_{rI\_1}(\theta)\big|_{r=R_{sl}}=B_{rII\_1}(\theta)\big|_{r=R_{sl}},\quad B_{rI\_2}(\theta)\big|_{r=R_{sl}}=B_{rII\_2}(\theta)\big|_{r=R_{sl}} \qquad \text{(B-58)}$$

$$H_{\alpha I\_1}(\theta)\big|_{r=R_{sl}}=H_{\alpha II\_1}(\theta)\big|_{r=R_{sl}},\quad H_{\alpha I\_2}(\theta)\big|_{r=R_{sl}}=H_{\alpha II\_2}(\theta)\big|_{r=R_{sl}} \qquad \text{(B-59)}$$

$$B_{rII\_1}(\theta)\big|_{r=R_m}=B_{rIII\_1}(\theta)\big|_{r=R_m},\quad B_{rII\_2}(\theta)\big|_{r=R_m}=B_{rIII\_2}(\theta)\big|_{r=R_m} \qquad \text{(B-60)}$$

$$H_{\alpha II\_1}(\theta)\big|_{r=R_m}=H_{\alpha III\_1}(\theta)\big|_{r=R_m},\quad H_{\alpha II\_2}(\theta)\big|_{r=R_m}=H_{\alpha III\_2}(\theta)\big|_{r=R_m} \qquad \text{(B-61)}$$

$$H_{\alpha III\_1}(\theta)\big|_{r=R_r}=0,\quad H_{\alpha III\_2}(\theta)\big|_{r=R_r}=0 \qquad \text{(B-62)}$$

According to above boundary conditions, the coefficients A_1, B_1, C_1, D_1, E_1 F_1 and A_2, B_2, C_2, D_2, E_2 F_2 can be resolved by the following equations,

$$[K1][X1]=[Y1]\Rightarrow[X1]=[K1]^{-1}[Y1] \tag{B-63}$$

$$[K2][X2]=[Y2]\Rightarrow[X2]=[K2]^{-1}[Y2] \tag{B-64}$$

where $[K1]=\begin{bmatrix} K_{11} & K_{12} & 0 & 0 & 0 & 0 \\ K_{21} & K_{22} & K_{23} & K_{24} & 0 & 0 \\ K_{31} & K_{32} & K_{33} & K_{34} & 0 & 0 \\ 0 & 0 & K_{43} & K_{44} & K_{45} & K_{46} \\ 0 & 0 & K_{53} & K_{54} & K_{55} & K_{56} \\ 0 & 0 & 0 & 0 & K_{65} & K_{66} \end{bmatrix}$, $[X1]=\begin{bmatrix} A_1 \\ B_1 \\ C_1 \\ D_1 \\ E_1 \\ F_1 \end{bmatrix}$, $[Y1]=\begin{bmatrix} -J_{uv} \\ 0 \\ 0 \\ 0 \\ 0 \\ 0 \end{bmatrix}$

$[K2]=\begin{bmatrix} K_{11}' & K_{12}' & 0 & 0 & 0 & 0 \\ K_{21}' & K_{22}' & K_{23}' & K_{24}' & 0 & 0 \\ K_{31}' & K_{32}' & K_{33}' & K_{34}' & 0 & 0 \\ 0 & 0 & K_{43}' & K_{44}' & K_{45}' & K_{46}' \\ 0 & 0 & K_{53}' & K_{54}' & K_{55}' & K_{56}' \\ 0 & 0 & 0 & 0 & K_{65}' & K_{66}' \end{bmatrix}$, $[X2]=\begin{bmatrix} A_2 \\ B_2 \\ C_2 \\ D_2 \\ E_2 \\ F_2 \end{bmatrix}$, $[Y2]=\begin{bmatrix} J_{uv} \\ 0 \\ 0 \\ 0 \\ 0 \\ 0 \end{bmatrix}$

where

$$K_{11}=\frac{\nu}{\mu_0}R_s^{\nu-1},\quad K_{12}=-\frac{\nu}{\mu_0}R_s^{-\nu-1}$$

$$K_{21}=R_{sl}^{\nu},\quad K_{22}=R_{sl}^{-\nu},\quad K_{23}=-\frac{\mu_0\mu_{sl}}{\tau_{sl\_1}^2}J_\nu\left(\tau_{sl\_1}R_{sl}\right),\quad K_{24}=-\frac{\mu_0\mu_{sl}}{\tau_{sl\_1}^2}Y_\nu\left(\tau_{sl\_1}R_{sl}\right)$$

$$K_{31}=R_{sl}^{\nu},\quad K_{32}=-R_{sl}^{-\nu},\quad K_{33}=-\frac{\mu_0}{\tau_{sl\_1}^2}\left[\frac{\tau_{sl\_1}R_{sl}}{\nu}J_{\nu-1}\left(\tau_{sl\_1}R_{sl}\right)-J_\nu\left(\tau_{sl\_1}R_{sl}\right)\right],$$

$$K_{34}=-\frac{\mu_0}{\tau_{sl\_1}^2}\left[\frac{\tau_{sl\_1}R_{sl}}{\nu}Y_{\nu-1}\left(\tau_{sl\_1}R_{sl}\right)-Y_\nu\left(\tau_{sl\_1}R_{sl}\right)\right]$$

$$K_{43}=\frac{\mu_{sl}}{\tau_{sl\_1}^2}J_\nu\left(\tau_{sl\_1}R_m\right),\quad K_{44}=\frac{\mu_{sl}}{\tau_{sl\_1}^2}Y_\nu\left(\tau_{sl\_1}R_m\right),\quad K_{45}=-\frac{\mu_m}{\tau_{m\_1}^2}J_\nu\left(\tau_{m\_1}R_m\right),$$

$$K_{46}=-\frac{\mu_m}{\tau_{m\_1}^2}Y_\nu\left(\tau_{m\_1}R_m\right)$$

$$K_{53}=\frac{1}{\tau_{sl\_1}^2}\left[\frac{\tau_{sl\_1}R_m}{\nu}J_{\nu-1}\left(\tau_{sl\_1}R_m\right)-J_\nu\left(\tau_{sl\_1}R_m\right)\right],$$

$$K_{54}=\frac{1}{\tau_{sl\_1}^2}\left[\frac{\tau_{sl\_1}R_m}{\nu}Y_{\nu-1}\left(\tau_{sl\_1}R_m\right)-Y_\nu\left(\tau_{sl\_1}R_m\right)\right],$$

$$K_{55}=-\frac{1}{\tau_{m\_1}^2}\left[\frac{\tau_{m\_1}R_m}{\nu}J_{\nu-1}\left(\tau_{m\_1}R_m\right)-J_\nu\left(\tau_{m\_1}R_m\right)\right],$$

$$K_{56}=-\frac{1}{\tau_{m\_1}^2}\left[\frac{\tau_{m\_1}R_m}{\nu}Y_{\nu-1}\left(\tau_{m\_1}R_m\right)-Y_\nu\left(\tau_{m\_1}R_m\right)\right]$$

$$K_{65}=\frac{\tau_{m\_1}R_r}{\nu}J_{\nu-1}\left(\tau_{m\_1}R_r\right)-J_\nu\left(\tau_{m\_1}R_r\right),\quad K_{66}=\frac{\tau_{m\_1}R_r}{\nu}Y_{\nu-1}\left(\tau_{m\_1}R_r\right)-Y_\nu\left(\tau_{m\_1}R_r\right)$$

and

$$K_{11}^{'}=\frac{\nu}{\mu_0}R_s^{\nu-1},\quad K_{12}^{'}=-\frac{\nu}{\mu_0}R_s^{-\nu-1}$$

$$K_{21}^{'}=R_{sl}^{\nu},\quad K_{22}^{'}=R_{sl}^{-\nu},\quad K_{23}^{'}=-\frac{\mu_0\mu_{sl}}{\tau_{sl\_2}^2}J_\nu\left(\tau_{sl\_2}R_{sl}\right),\quad K_{24}^{'}=-\frac{\mu_0\mu_{sl}}{\tau_{sl\_2}^2}Y_\nu\left(\tau_{sl\_2}R_{sl}\right)$$

$$K_{31}^{'}=R_{sl}^{\nu},\quad K_{32}^{'}=-R_{sl}^{-\nu},\quad K_{33}^{'}=-\frac{\mu_0}{\tau_{sl\_2}^2}\left[\frac{\tau_{sl\_2}R_{sl}}{\nu}J_{\nu-1}\left(\tau_{sl\_2}R_{sl}\right)-J_\nu\left(\tau_{sl\_2}R_{sl}\right)\right],$$

$$K_{34}^{'}=-\frac{\mu_0}{\tau_{sl\_2}^2}\left[\frac{\tau_{sl\_2}R_{sl}}{\nu}Y_{\nu-1}\left(\tau_{sl\_2}R_{sl}\right)-Y_\nu\left(\tau_{sl\_2}R_{sl}\right)\right]$$

$$K_{44}^{'}=\frac{\mu_{sl}}{\tau_{sl\_2}^2}Y_\nu\left(\tau_{sl\_2}R_m\right),\quad K_{45}^{'}=-\frac{\mu_m}{\tau_{m\_2}^2}J_\nu\left(\tau_{m\_2}R_m\right),\quad K_{46}^{'}=-\frac{\mu_m}{\tau_{m\_2}^2}Y_\nu\left(\tau_{m\_2}R_m\right)$$

$$K_{53}^{'}=\frac{1}{\tau_{sl\_2}^2}\left[\frac{\tau_{sl\_2}R_m}{\nu}J_{\nu-1}\left(\tau_{sl\_2}R_m\right)-J_\nu\left(\tau_{sl\_2}R_m\right)\right],$$

$$K_{54}^{'}=\frac{1}{\tau_{sl\_2}^2}\left[\frac{\tau_{sl\_2}R_m}{\nu}Y_{\nu-1}\left(\tau_{sl\_2}R_m\right)-Y_\nu\left(\tau_{sl\_2}R_m\right)\right],$$

$$K_{55}^{'}=-\frac{1}{\tau_{m\_2}^2}\left[\frac{\tau_{m\_2}R_m}{\nu}J_{\nu-1}\left(\tau_{m\_2}R_m\right)-J_\nu\left(\tau_{m\_2}R_m\right)\right],$$

$$K_{56}^{'}=-\frac{1}{\tau_{m\_1}^2}\left[\frac{\tau_{m\_1}R_m}{\nu}Y_{\nu-1}\left(\tau_{m\_1}R_m\right)-Y_\nu\left(\tau_{m\_1}R_m\right)\right]$$

$$K'_{65} = \frac{\tau_{m\_2} R_r}{\nu} J_{\nu-1}(\tau_{m\_2} R_r) - J_\nu(\tau_{m\_2} R_r), \quad K'_{66} = \frac{\tau_{m\_2} R_r}{\nu} Y_{\nu-1}(\tau_{m\_2} R_r) - Y_\nu(\tau_{m\_2} R_r)$$

According to the Poynting's theorem, the average eddy current loss over an electrical cycle $T = 2\pi / \omega_r$ can be calculated by,

$$P = \frac{L_a}{T} \int_0^T \oint_S \mathrm{Re}(E \times H) \cdot dS dt \qquad \text{(W)} \tag{B-65}$$

where the surface S bounds the conducting region.

In polar coordinate, due to $E_z = \frac{J_z}{\sigma}$, the eddy current loss of the annual region with outer and inner radius R_1 and R_2, respectively, can be rewritten by,

$$P = \frac{L_a}{T\sigma} \int_0^T \int_{\theta_1}^{\theta_2} (J_{z1} H_{\alpha 1})_{r=R_1} R_1 dt d\theta - \frac{L_a}{T\sigma} \int_0^T \int_{\theta_1}^{\theta_2} (J_{z2} H_{\alpha 2})_{r=R_2} R_2 dt d\theta \qquad \text{(W)} \tag{B-66}$$

where J_{z1} and J_{z2} is the eddy current density induced in the axial direction, H_{t1} and H_{t2} is the circumferential component of the magnetic field at the surface of the conducting region of the radii R_1 and R_2. θ_1 and θ_2 define the angle which spans the conducting region, e.g. the pole-arc when calculating the loss per magnet segment, and 2π when calculating the loss in the retaining sleeve.

Hence, the eddy current loss in the PM is,

$$\begin{aligned} P_m = {} & \frac{2\pi}{\alpha_p} \frac{L_a}{T\sigma_m} \int_0^T \int_{-\frac{\alpha_p}{2}}^{\frac{\alpha_p}{2}} \left[(J_{zIII\_1} + J_{zIII\_2})(H_{\alpha III\_1} + H_{\alpha III\_2}) \right]_{r=R_m} R_m dt d\theta - \\ & \frac{2\pi}{\alpha_p} \frac{L_a}{T\sigma_m} \int_0^T \int_{-\frac{\alpha_p}{2}}^{\frac{\alpha_p}{2}} \left[(J_{zIII\_1} + J_{zIII\_2})(H_{\alpha III\_1} + H_{\alpha III\_2}) \right]_{r=R_r} R_r dt d\theta \end{aligned} \qquad \text{(W)} \tag{B-67}$$

where

$$\left[\left(J_{zIII\_1}+J_{zIII\_2}\right)\left(H_{\alpha III\_1}+H_{\alpha III\_2}\right)\right]_{r=R_m}$$

$$=\sum_u^\infty\sum_v^\infty\left[\mathrm{Re}\left(X1_m e^{j\phi_1}+X2_m e^{j\phi_2}\right)\mathrm{Re}\left(Y1_m e^{j\phi_1}+Y2_m e^{j\phi_2}\right)\right] \tag{B-68}$$

$$=\sum_u^\infty\sum_v^\infty\left\{\begin{array}{l}\left|X1_m\right|\cos\left(\phi_1+\phi_{x1m}\right)\left[\left|Y1_m\right|\cos\left(\phi_1+\phi_{y1m}\right)+\left|Y2_m\right|\cos\left(\phi_2+\phi_{y1m}\right)\right]\\+\left|X2_m\right|\cos\left(\phi_2+\phi_{x2m}\right)\left[\left|Y1_m\right|\cos\left(\phi_1+\phi_{y1m}\right)+\left|Y2_m\right|\cos\left(\phi_2+\phi_{y1m}\right)\right]\end{array}\right\}$$

$$\left[\left(J_{zIII\_1}+J_{zIII\_2}\right)\left(H_{\alpha III\_1}+H_{\alpha III\_2}\right)\right]_{r=R_r}$$

$$=\sum_u^\infty\sum_v^\infty\left[\mathrm{Re}\left(X3_m e^{j\phi_1}+X4_m e^{j\phi_2}\right)\mathrm{Re}\left(Y3_m e^{j\phi_1}+Y4_m e^{j\phi_2}\right)\right] \tag{B-69}$$

$$=\sum_u^\infty\sum_v^\infty\left\{\begin{array}{l}\left|X3_m\right|\cos\left(\phi_1+\phi_{x3m}\right)\left[\left|Y3_m\right|\cos\left(\phi_1+\phi_{y3m}\right)+\left|Y4_m\right|\cos\left(\phi_2+\phi_{y4m}\right)\right]\\+\left|X4_m\right|\cos\left(\phi_2+\phi_{x4m}\right)\left[\left|Y3_m\right|\cos\left(\phi_1+\phi_{y3m}\right)+\left|Y4_m\right|\cos\left(\phi_2+\phi_{y4m}\right)\right]\end{array}\right\}$$

where

$$X1_m=E_1J_v\left(\tau_{m\_1}R_m\right)+F_1Y_v\left(\tau_{m\_1}R_m\right)=\left|X1_m\right|e^{j\phi_{x1m}}$$

$$X2_m=E_2J_v\left(\tau_{m\_2}R_m\right)+F_2Y_v\left(\tau_{m\_2}R_m\right)=\left|X2_m\right|e^{j\phi_{x2m}}$$

$$X3_m=E_1J_v\left(\tau_{m\_1}R_r\right)+F_1Y_v\left(\tau_{m\_1}R_r\right)=\left|X3_m\right|e^{j\phi_{x3m}}$$

$$X4_m=E_2J_v\left(\tau_{m\_2}R_r\right)+F_2Y_v\left(\tau_{m\_2}R_r\right)=\left|X4_m\right|e^{j\phi_{x4m}}$$

$$Y1_m=-\frac{v}{R_m\tau_{m\_1}^2}\left\{\begin{array}{l}E_1\left[\frac{\tau_{m\_1}R_m}{v}J_{v-1}\left(\tau_{m\_1}R_m\right)-J_v\left(\tau_{m\_1}R_m\right)\right]\\+F_1\left[\frac{\tau_{m\_1}R_m}{v}Y_{v-1}\left(\tau_{m\_1}R_m\right)-Y_v\left(\tau_{m\_1}R_m\right)\right]\end{array}\right\}=\left|Y1_m\right|e^{j\phi_{y1m}}$$

$$Y2_m=-\frac{v}{R_m\tau_{m\_2}^2}\left\{\begin{array}{l}E_2\left[\frac{\tau_{m\_2}R_m}{v}J_{v-1}\left(\tau_{m\_2}R_m\right)-J_v\left(\tau_{m\_2}R_m\right)\right]\\+F_2\left[\frac{\tau_{m\_2}R_m}{v}Y_{v-1}\left(\tau_{m\_2}R_m\right)-Y_v\left(\tau_{m\_2}R_m\right)\right]\end{array}\right\}=\left|Y2_m\right|e^{j\phi_{y2m}}$$

$$Y3_m=-\frac{v}{R_r\tau_{m\_1}^2}\left\{\begin{array}{l}E_1\left[\frac{\tau_{m\_1}R_r}{v}J_{v-1}\left(\tau_{m\_1}R_r\right)-J_v\left(\tau_{m\_1}R_r\right)\right]\\+F_1\left[\frac{\tau_{m\_1}R_r}{v}Y_{v-1}\left(\tau_{m\_1}R_r\right)-Y_v\left(\tau_{m\_1}R_r\right)\right]\end{array}\right\}=\left|Y3_m\right|e^{j\phi_{y3m}}$$

$$Y4_m = -\frac{v}{R_r \tau_{m\_2}^2}\left\{\begin{array}{l} E_2\left[\frac{\tau_{m\_2}R_r}{v}J_{v-1}(\tau_{m\_2}R_r) - J_v(\tau_{m\_2}R_r)\right] \\ + F_2\left[\frac{\tau_{m\_2}R_r}{v}Y_{v-1}(\tau_{m\_2}R_r) - Y_v(\tau_{m\_2}R_r)\right] \end{array}\right\} = |Y4_m|e^{j\phi_{y4m}}$$

Therefore, the eddy current loss in the total magnets is given by,

$$P_m = P_{m1} + P_{m2} \qquad \text{(W)} \tag{B-70}$$

where P_{m1} and P_{m2} are the eddy current loss due to the forward asynchronous mmfs and backward asynchronous mmfs, respectively, and can be written by,

$$P_{m1} = \frac{\pi L_a}{\sigma_m}\sum_u^\infty\sum_v^\infty\left[|X1_m||Y1_m|\cos(\phi_{x1m} - \phi_{y1m})R_m - |X3_m||Y3_m|\cos(\phi_{x3m} - \phi_{y3m})R_r\right], u \neq v \tag{B-71}$$

$$P_{m2} = \frac{\pi L_a}{\sigma_m}\sum_u^\infty\sum_v^\infty\left[|X2_m||Y2_m|\cos(\phi_{x2m} - \phi_{y2m})R_m - |X4_m||Y4_m|\cos(\phi_{x4m} - \phi_{y4m})R_r\right] \tag{B-72}$$

Similarly, eddy current loss in the sleeve is given by,

$$\begin{aligned} P_{sl} = {} & \frac{L_a}{T\sigma_{sl}}\int_0^T\int_0^{2\pi}\left[(J_{zII\_1} + J_{zII\_2})(H_{\alpha II\_1} + H_{\alpha II\_2})\right]_{r=R_{sl}} R_{sl}\,dt\,d\theta - \\ & \frac{L_a}{T\sigma_{sl}}\int_0^T\int_0^{2\pi}\left[(J_{zII\_1} + J_{zII\_2})(H_{\alpha II\_1} + H_{\alpha II\_2})\right]_{r=R_m} R_m\,dt\,d\theta \end{aligned} \qquad \text{(W)} \tag{B-73}$$

where

$$\begin{aligned} & \left[(J_{zII\_1} + J_{zII\_2})(H_{\alpha II\_1} + H_{\alpha II\_2})\right]_{r=R_{sl}} \\ & = \sum_u^\infty\sum_v^\infty\left[\mathrm{Re}\left(X1_{sl}e^{j\phi_1} + X2_{sl}e^{j\phi_2}\right)\mathrm{Re}\left(Y1_{sl}e^{j\phi_1} + Y2_{sl}e^{j\phi_2}\right)\right] \\ & = \sum_u^\infty\sum_v^\infty\left\{\begin{array}{l} |X1_{sl}|\cos(\phi_1 + \phi_{x1sl})\left[|Y1_{sl}|\cos(\phi_1 + \phi_{y1sl}) + |Y2_{sl}|\cos(\phi_2 + \phi_{y1sl})\right] \\ + |X2_{sl}|\cos(\phi_2 + \phi_{x2sl})\left[|Y1_{sl}|\cos(\phi_1 + \phi_{y1sl}) + |Y2_{sl}|\cos(\phi_2 + \phi_{y1sl})\right] \end{array}\right\} \end{aligned} \tag{B-74}$$

$$
\begin{aligned}
&\left[\left(J_{zII\_1}+J_{zII\_2}\right)\left(H_{\alpha II\_1}+H_{\alpha II\_2}\right)\right]_{r=R_m} \\
&=\sum_u^\infty\sum_v^\infty\left[\mathrm{Re}\left(X3_{sl}e^{j\phi_1}+X4_{sl}e^{j\phi_2}\right)\mathrm{Re}\left(Y3_{sl}e^{j\phi_1}+Y4_{sl}e^{j\phi_2}\right)\right] \\
&=\sum_u^\infty\sum_v^\infty\left\{\begin{array}{l}\left|X3_{sl}\right|\cos\left(\phi_1+\phi_{x3sl}\right)\left[\left|Y3_{sl}\right|\cos\left(\phi_1+\phi_{y3sl}\right)+\left|Y4_{sl}\right|\cos\left(\phi_2+\phi_{y4sl}\right)\right] \\ +\left|X4_{sl}\right|\cos\left(\phi_2+\phi_{x4sl}\right)\left[\left|Y3_{sl}\right|\cos\left(\phi_1+\phi_{y3sl}\right)+\left|Y4_{sl}\right|\cos\left(\phi_2+\phi_{y4sl}\right)\right]\end{array}\right\}
\end{aligned}
\tag{B-75}
$$

where

$$X1_{sl}=E_1J_v\left(\tau_{sl\_1}R_{sl}\right)+F_1Y_v\left(\tau_{sl\_1}R_{sl}\right)=\left|X1_{sl}\right|e^{j\phi_{x1sl}}$$

$$X2_{sl}=E_2J_v\left(\tau_{sl\_2}R_{sl}\right)+F_2Y_v\left(\tau_{sl\_2}R_{sl}\right)=\left|X2_{sl}\right|e^{j\phi_{x2sl}}$$

$$X3_{sl}=E_1J_v\left(\tau_{sl\_1}R_m\right)+F_1Y_v\left(\tau_{sl\_1}R_m\right)=\left|X3_{sl}\right|e^{j\phi_{x3sl}}$$

$$X4_{sl}=E_2J_v\left(\tau_{sl\_2}R_m\right)+F_2Y_v\left(\tau_{sl\_2}R_m\right)=\left|X4_{sl}\right|e^{j\phi_{x4sl}}$$

$$Y1_{sl}=-\frac{v}{R_{sl}\tau_{sl\_1}^2}\left\{\begin{array}{l}E_1\left[\frac{\tau_{sl\_1}R_{sl}}{v}J_{v-1}\left(\tau_{sl\_1}R_{sl}\right)-J_v\left(\tau_{sl\_1}R_{sl}\right)\right] \\ +F_1\left[\frac{\tau_{sl\_1}R_{sl}}{v}Y_{v-1}\left(\tau_{sl\_1}R_{sl}\right)-Y_v\left(\tau_{sl\_1}R_{sl}\right)\right]\end{array}\right\}=\left|Y1_{sl}\right|e^{j\phi_{y1sl}}$$

$$Y2_{sl}=-\frac{v}{R_{sl}\tau_{sl\_2}^2}\left\{\begin{array}{l}E_2\left[\frac{\tau_{sl\_2}R_{sl}}{v}J_{v-1}\left(\tau_{sl\_2}R_{sl}\right)-J_v\left(\tau_{sl\_2}R_{sl}\right)\right] \\ +F_2\left[\frac{\tau_{sl\_2}R_{sl}}{v}Y_{v-1}\left(\tau_{sl\_2}R_{sl}\right)-Y_v\left(\tau_{sl\_2}R_{sl}\right)\right]\end{array}\right\}=\left|Y2_{sl}\right|e^{j\phi_{y2sl}}$$

$$Y3_{sl}=-\frac{v}{R_m\tau_{sl\_1}^2}\left\{\begin{array}{l}E_1\left[\frac{\tau_{sl\_1}R_m}{v}J_{v-1}\left(\tau_{sl\_1}R_m\right)-J_v\left(\tau_{sl\_1}R_m\right)\right] \\ +F_1\left[\frac{\tau_{sl\_1}R_m}{v}Y_{v-1}\left(\tau_{sl\_1}R_m\right)-Y_v\left(\tau_{sl\_1}R_m\right)\right]\end{array}\right\}=\left|Y3_{sl}\right|e^{j\phi_{y3sl}}$$

$$Y4_{sl}=-\frac{v}{R_m\tau_{sl\_2}^2}\left\{\begin{array}{l}E_2\left[\frac{\tau_{sl\_2}R_m}{v}J_{v-1}\left(\tau_{sl\_2}R_m\right)-J_v\left(\tau_{sl\_2}R_m\right)\right] \\ +F_2\left[\frac{\tau_{sl\_2}R_m}{v}Y_{v-1}\left(\tau_{sl\_2}R_m\right)-Y_v\left(\tau_{sl\_2}R_m\right)\right]\end{array}\right\}=\left|Y4_{sl}\right|e^{j\phi_{y4sl}}$$

Therefore, the eddy current loss in the sleeve is given by,

$$P_{sl}=P_{sl1}+P_{sl2}\qquad\text{(W)}\tag{B-76}$$

where P_{sl1} and P_{sl2} are the eddy current loss due to the forward asynchronous mmfs and backward asynchronous mmfs, respectively, and can be written by,

$$P_{sl1} = \frac{\pi L_a}{\sigma_{sl}} \sum_{u}^{\infty} \sum_{v}^{\infty} \left[\left| X1_{sl} \right| \left| Y1_{sl} \right| \cos\left(\phi_{x1sl} - \phi_{y1sl}\right) R_{sl} - \left| X3_{sl} \right| \left| Y3_{sl} \right| \cos\left(\phi_{x3sl} - \phi_{y3sl}\right) R_m \right], u \neq v$$

(B-77)

$$P_{sl2} = \frac{\pi L_a}{\sigma_{sl}} \sum_{u}^{\infty} \sum_{v}^{\infty} \left[\left| X2_{sl} \right| \left| Y2_{sl} \right| \cos\left(\phi_{x2sl} - \phi_{y2sl}\right) R_{sl} - \left| X4_{sl} \right| \left| Y4_{sl} \right| \cos\left(\phi_{x4sl} - \phi_{y4sl}\right) R_m \right]$$

(B-78)

APPENDIX C

Dynamic Simulation Model for Single-Phase FSPM Motor

The single-phase FSPM motor is driven by a full-bridge inverter consisting of four MOSFETs and diodes, Figure C. 1, in accordance with the rotor position that is provided by two Hall sensors mounted on the stator. The Hall signals are illustrated in Figure C. 2. A numerical time-step simulation model for the single-phase FSPM motor is developed on the MATLAB platform to investigate the motor dynamic performance.

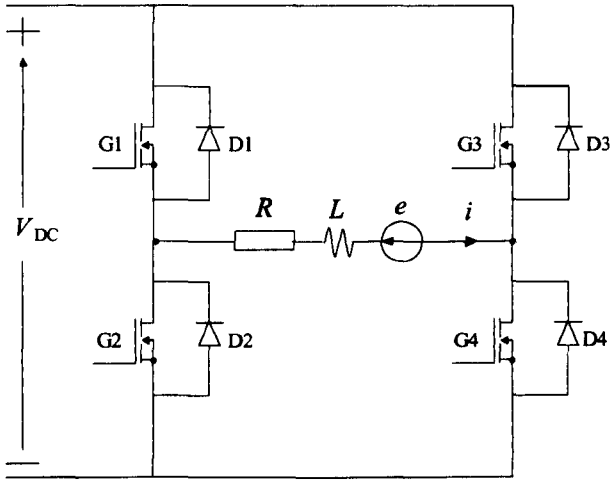

Figure C. 1 Inverter circuits for single-phase FSPM motor.

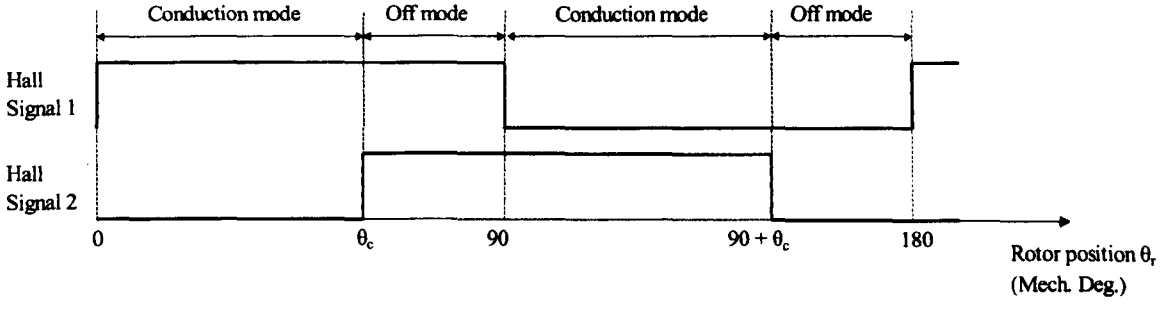

Figure C. 2 Illustration of Hall signals of single-phase FSPM motors.

In order to simplify the dynamic simulation model, the following assumptions have been made:

- Phase inductance is independent of the phase current.
- The eddy current and hysteresis effects on the motor's magnetic materials have negligible influence on the phase current.
- The DC link voltage is constant.
- The voltage drop on the MOSFETs and diodes is 0.35V.

In this numerical time-step simulation model, at each time step, the winding terminal voltage can be updated which is dependent of the inverter states as given in Table C.1 and Table C.2.

Table C.1 Inverter intervals of full-bridge inverter for single-phase FSPM motor.

Inverter interval	Rotor position θ_r ($^{o}_{mech}$)	Hall Signal 1	Hall Signal 2	G 1	G 2	G 3	G 4
1	$[0, \theta_c]$	1	0	1	0	0	1
2	$[90, 90+\theta_c]$	0	1	0	1	1	0
3	$[\theta_c, 90]$	1	1	0	0	0	0
	$[90+\theta_c, 180]$	0	0				

Table C.2 Winding terminal voltage at different inverter intervals of full-bridge inverter for single-phase FSPM motor.

Inverter interval	$i > 0$	$i < 0$	$i = 0$
1	$v_{DC} - 0.7$	$v_{DC} + 0.7$	
2	$-v_{DC} - 0.7$	$-v_{DC} + 0.7$	e_{PM}
3	$-v_{DC} - 0.7$	$v_{DC} + 0.7$	

Therefore, the phase current can be updated by the following equation:

$$i_{(n)} = i_{(n-1)} + \frac{v_{(n)} - Ri_{(n-1)} - i_{n-1}\dfrac{dL_{(n)}}{dt} - e_{PM(n)}}{L_{(n)}} dt \qquad \text{(A)} \qquad \text{(C-1)}$$

Hence, the electromagnetic torque can be updated by:

$$T_{em(n)} = \frac{i_{(n)} e_{PM(n)}}{\omega_{r(n-1)}} + \frac{1}{2} i_{(n)}{}^2 \frac{dL_{(n)}}{\omega_{r(n)} dt} + T_{c(n)} \qquad \text{(Nm)} \qquad \text{(C-2)}$$

And the motor rotation speed and rotor position can be updated by:

$$\omega_{r(n)} = \omega_{r(n-1)} + \frac{T_{em(n)} - T_{load}}{J} dt \qquad \text{(rad/s)} \qquad \text{(C-3)}$$

$$\theta_{r(n)} = \theta_{r(n-1)} + \omega_{r(n)} dt \qquad \text{(rad)} \qquad \text{(C-4)}$$

The back-EMF and inductance can be obtained by the FEM or LPMC model. The cogging torque can be obtained from FEM. Hence, according to equations (C-1) to (C-4), at each simulation time step, the phase voltage, the phase current, the electromagnetic torque, the speed the rotor position can be obtained.

APPENDIX D

Publications Resulted from PhD Study

Journal papers

[1] Y. Chen, Z. Q. Zhu and D. Howe, "Three-dimensional lumped-parameter magnetic circuit analysis of single-phase flux-switching permanent-magnet motor," *IEEE Transactions on Industry Applications,* vol. 44, no. 6, pp. 1701-1710, 2008.

[2] Y. Chen, Z. Q. Zhu, D. Howe and Y. Y. Ye, "Starting torque of single-phase flux-switching permanent magnet motors," *IEEE Transactions on Magnetics,* , vol. 42, no. 10, pp. 3416-3418, 2006.

[3] Z. Q. Zhu, Y. Chen and D. Howe, "Influence of control strategy on stator and rotor losses in high-speed permanent magnet brushless motors," in *Journal of Applied Physics,* vol. 97, no. 10, pp. 10N505-10N505-3, 2005.

[4] Z. Q. Zhu, S. Ruangsinchaiwanich, Y. Chen and D. Howe, "Evaluation of superposition technique for calculating cogging torque in permanent-magnet brushless machines," *IEEE Transactions on Magnetics,* , vol. 42, no. 5, pp. 1597-1603, 2006.

Conference papers

[1] Y. Chen, Z. Q. Zhu, D. Howe and Y. Y. Ye, "Starting torque of single-phase flux-switching permanent magnet motors," in *IEEE International Magnetics Conference, 2006. INTERMAG 2006.*, pp. 189-189, 2006.

[2] Y. Chen, Z. Q. Zhu, D. Howe, "3-D lumped parameter magnetic circuit model for analysing single-phase flux-switching permanent magnet motor," in *Proc. 2006 International Conference on Electrical Machines and Systems(ICEMS2006)*, 20-23 November, 2006, 6 pages.

[3] Y. Chen, Z. Q. Zhu, D. Howe and J. H. Gliemann, "Rotor eddy current loss in single-phase permanent magnet brushless DC motor," in *42nd IAS Annual Meeting. Conference Record of the 2007 IEEE Industry Applications Conference, 2007.*, pp. 537-543, 2007.

[4] Z. Q. Zhu, Y. Chen, J. H. Gliemann, Y. Li, an D. Howe, "Investigation of stator an rotor losses in high-speed PM brushless motors," in *Proc. Int. Conf. on Electrical Machines and Systems*, 2-5 November, 2004, 6 pages.

[5] Z. Q. Zhu, Y. Chen, D. Howe, "Influence of control strategies on stator and rotor losses in high-speed PM brushless motors," in *Proc. MMM2004, 49th Conf. on Magnetism and Magnetic Materials*, 7-11 November, 2004.

[6] Z. Q. Zhu, Y. Chen, Y. Li, D. Howe and J. H. Gliemann, "Dynamic modelling of a high-speed single-phase PM brushless DC drive," in *The 3rd IET International Conference on,Power Electronics, Machines and Drives, 2006.* pp. 484-488, 2006.